Azimuthal asymmetries in semi-inclusive deep-inelastic hadron muoproduction on longitudinally polarized protons

Stefan Sirtl

Fakultät für Mathematik und Physik
Albert-Ludwigs-Universität Freiburg

Azimuthal asymmetries in semi-inclusive deep-inelastic hadron muoproduction on longitudinally polarized protons

Dissertation

zur Erlangung des Doktorgrades
der
Fakultät für Mathematik und Physik
der
Albert-Ludwigs-Universität
Freiburg im Breisgau

vorgelegt von
Stefan Sirtl

Freiburg, April 2016

Dekan:	Prof. Dr. Dietmar Kröner
Leiter der Arbeit	Prof. Dr. Horst Fischer
Referent:	Prof. Dr. Horst Fischer
Koreferent:	Prof. Dr. Karl Jakobs
Tag der Verkündigung des Prüfungsergebnisses:	27.06.2016

Contents

ἐτεῇ δὲ οὐδὲ ἴδμε· ἐ βυθῷ γὰρ ἠ ἀλήθεια.

In truth we know nothing, for truth lies in the depth.

Democritus (460 - 400 BC)

1. Introduction

The exploration of the elementary building blocks of matter and its fundamental properties emerged as a field of particular interest in modern physics. Promoted by the significant technical progress during the last decades, it was possible to advance to smaller and smaller scales and to resolve unexpected phenomena of inspiring challenge for both theoretical and experimental physics. Although tremendous progress has been made from both sides, some questions still remain unanswered.

To the present knowledge, all visible matter is made up by atoms, which in turn are composed by electrons and a compound of nucleons, namely protons and neutrons, forming the atomic core. While the properties of the electron are quite precisely known, nucleons are still subject of ongoing intensive investigations. Ever since the pioneering confirmation of nucleons having a substructure in the late 1960s, a major effort was put into the exploration of their inner structure and the development of adequate theoretical models. The initial interpretation of the nucleon as a static composition of three quasi-free partons, later identified as quarks, soon reached its limits. Today, the most successful interpretation is known as the quantum chromodynamic (QCD) parton model, describing the nucleon as a dynamic compound of three confined valence quarks, surrounded by a cloud of gluons and quark-antiquark fluctuations. This interpretation inevitably raises the question of how the intrinsic properties of nucleons can be explained by their constituents. Concerning mass, charge and longitudinal momentum, satisfying pictures could be composed. However, it remains unclear how the spin of the nucleon is composed by its components.

The spin is a relativistic, quantum mechanical, intrinsic property of particles, which can be related to its magnetic moment. In the present understanding, manifested in the Standard Model of particle physics, all kinds of particles can be divided into two groups according to their spin quantum numbers. These are fermions, characterized by half-integer spin quantum numbers, and bosons, having integer values. Fermions are today associated with elementary matter, while bosons are understood as transmitters of fundamental physical forces. Dennison had already discovered in 1927, that protons must be spin-$\frac{1}{2}$ fermions [1]. During the early days of the constituent parton model interpretation it seemed reasonable to assume, that the three quark spins would simply sum up to the full proton spin. This presumption was ruled out by astonishing results, presented by the EMC[1] at CERN[2] in 1988 [2], indicating that only a marginal fraction of the proton spin is carried by quarks and antiquarks. This observation triggered considerable theoretical activities and new experiments at facilities like CERN, SLAC[3], DESY[4], JLab[5] and BNL[6] in order to verify the EMC result and to understand where the spin of the nucleon comes from.

One of the key tools to experimentally investigate the spin structure of nucleons is by scattering longitudinally polarized high-energetic leptons off optionally longitudinally or transversely polarized nucleons, commonly referred to as polarized deep inelastic scattering (DIS). The lepton acts thereby as an electromagnetic probe, which resolves the nucleon structure through the exchange of a virtual photon. Classical inclusive measurements, where only the scattered lepton is detected in the final state, provide one-dimensional information on how the longitudinal momentum and the helicity of the nucleon is shared between quarks and gluons. Complemented by later semi-inclusive DIS (SIDIS) measurements, where at least one final state hadron is tagged in coincidence with the scattered lepton, comprehensive knowledge on the flavor structure of the nucleon could be obtained. Today, the helicity fraction carried by quarks and antiquarks is quite accurately determined to about 30%. Recent measurements, even if affected by large uncertainties, indicate a rather small gluon polarization [3–5]. These observations inspired to consider also transverse degrees of freedom. Indeed, SIDIS reactions were found to be sensitive to spin-orbit correlations, providing fascinating possibilities to study the three-dimensional nucleon structure in a transverse momentum dependent (TMD) QCD framework.

In the TMD QCD parton model interpretation of SIDIS processes, spin-orbit correlations, as well as scale-suppressed quark-gluon interactions, are expected to affect both the decoupling and the fragmentation mechanism of the struck quark, causing characteristic asymmetric distributions of the detected hadrons with respect to the virtual photon axis. These azimuthal asymmetries are key observables in TMD SIDIS measurements. Thanks to QCD factorization and evolution theorems, they can be used to disentangle conceptual information about transverse momentum dependent parton densities inside nucleons as well as about fragmentation probabilities, encoded in so called parton distribution functions (PDFs) and fragmentation functions (FFs). Huge experimental and theoretical effort was put on the determination of these fundamental quantities during the last decades, combining comprehensive data from fixed target and collider experiments. Although there has been tremendous progress in the understanding of TMD phenomena, the knowledge is still far from being complete.

---

[1] **E**uropean **M**uon **C**ollaboration

[2] **C**onseil **E**uropéen pour la **R**echerche **N**ucléaire (eng.: European Organization for Nuclear Research) in Geneva, Switzerland)

[3] **S**tanford **L**inear **A**ccelerator **C**enter at Stanford University, California, USA

[4] **D**eutsches **E**lektronen-**SY**nchrotron (eng.: German Electron Synchrotron) in Hamburg, Germany)

[5] **J**efferson **Lab**oratory in Virginia, USA

[6] **B**rookhaven **N**ational **L**aboratory in New York, USA

The COMPASS[1] experiment, located at the M2 beam line at CERN, is a fixed target experiment, particularly dedicated to the investigation of the spin structure of the nucleon. Initially proposed to focus on the determination of the gluon polarization, it allows for precise asymmetry measurements through polarized DIS. During the years 2007 and 2011, the COMPASS collaboration collected data by scattering longitudinally polarized muons of 160 GeV/c, respectively 200 GeV/c, off longitudinally polarized protons. This thesis is dedicated to the comprehensive study of this data in view of longitudinal target spin asymmetries in SIDIS, including the extraction of corresponding azimuthal asymmetries in both single hadron and hadron pair muoproduction. The aim of research is to provide new and precise contributions towards a complete understanding of the nucleon spin phenomena inside nucleons and fragmentation mechanisms.

This thesis is organized as follows: in Chapter 2 the theoretical framework for the field of study is outlined. Chapter 3 comprises a brief description of the experimental setup, including the functionality of the relevant components of the COMPASS spectrometer and of the data acquisition system. The first steps of data analysis, namely data stability studies and the selection of events with considered characteristics are presented in Chapter 4. The used methods for the principle extraction of asymmetries are explained in Chapter 5. The main part of the thesis is dedicated to the study of the measured azimuthal asymmetries and the evaluation of their corresponding systematic uncertainties. Following the chronological order of study, the general procedure is in detail explained by the example of leading twist azimuthal hadron pair asymmetries in Chapter 6 and essentially adapted to the study of one hadron azimuthal asymmetries in Chapter 7. A verification of both studies is carried out on the basis of corresponding cross section asymmetries, outlined in Chapter 8. An additional investigation of azimuthal asymmetries of hadron pairs is presented in Chapter 9, considering twist-3 amplitudes in a collinear approach. Each analysis concludes with a discussion of the results and, if available, with a comparison of the results with former measurements and model predictions. An overall summary of the present work is given in Chapter 10.

---

[1] **CO**mmon **M**uon and **P**roton **A**pparatus for **S**tructure and **S**pectroscopy

2. Theoretical Framework

This chapter summarizes the theoretical essentials, the present study is based on. Beginning with an introduction to the general theory of deep inelastic scattering (DIS), the more specific topic of semi-inclusive processes (SIDIS) with at least one single hadron or one hadron pair in the final state, is reviewed. They are discussed in the framework of the quantum chromodynamic (QCD) parton model interpretation, involving the concept of factorization of cross section amplitudes, characterized by so called parton distribution functions (PDFs) and fragmentation functions (FFs). As SIDIS processes turned out to reveal an encouraging experimental approach to investigate the spin structure of the nucleon via the analysis of so called spin asymmetries, they became subject of many recent measurements at various experiments. Their main results are briefly discussed and serve as motivation for the present analysis.

2.1 Deep Inelastic Scattering

The present knowledge about the inner structure of nucleons is mainly due to DIS experiments. By focussing high energy lepton beams on atomic nuclei, their partonic substructure can be resolved via the exchange of a hard virtual boson with sufficiently short wavelength. Already in 1968, this experimental tool led to the confirmation of the existence of point-like constituents inside nucleons at SLAC [6], gradually linked to quarks [7, 8]. During the last decades, polarized DIS evolved as a powerful tool to access information about spin phenomena inside nucleons. This topic is described in Sec. 2.1.2 in more detail.

The following summary on the theoretical principles of deep inelastic scattering is mainly orientated by the reviews in Refs. [9–11]. The common convention $\hbar = c = 1$ is used throughout this chapter. All relevant kinematic variables and their calculation formulae are summarized in Tab. 2.1.

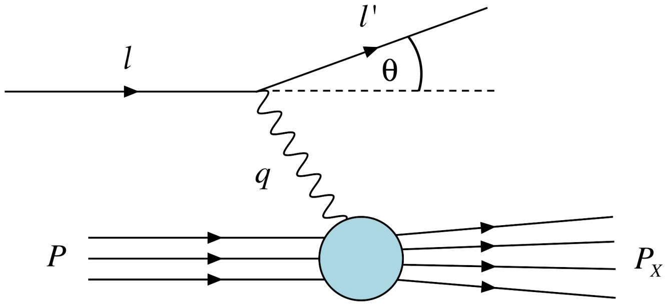

Figure 2.1: Diagram of the considered deep inelastic scattering process in one-photon exchange approximation.

The underlying inelastic process is sketched in Fig. 2.1. An incident lepton ℓ scatters off a target nucleon N at rest and emerges at a scattering angle θ. If the kinematic energy transfer is high enough, meaning the process is inelastic, the partonic compound is shattered and a hadronic system X occurs in the final state. Giving the particle's four-momenta in brackets, this process can be expressed as

$$\ell(l) + N(P) \rightarrow \ell(l') + X(P_X). \tag{2.1}$$

The electromagnetic interaction between the incident lepton and the nucleon is assumed to result of the exchange of a single virtual photon γ^*, carrying the four-momentum $q = l - l'$. This assumption is reasonable, as electromagnetic effects beyond one-photon exchange are suppressed by the electromagnetic constant α_{em}. Weak interactions can be also neglected, because the center-of-mass energy in COMPASS kinematics $\sqrt{s} \approx 17.4\,\mathrm{GeV}$ is much lower than the Z_0 mass.

Unlike elastic processes, where the kinematics is usually well described by the outgoing lepton energy E' and the scattering angle θ, the description of inelastic reactions require two additional variables. It is common to choose them among the invariants

$$Q^2 = -q^2 \qquad \nu = \frac{P \cdot q}{M} \qquad x = \frac{Q^2}{2P \cdot q} \qquad y = \frac{P \cdot q}{P \cdot l}, \tag{2.2}$$

where M denotes the mass of the target nucleon. While Q^2 and ν are the virtuality and the energy of the virtual photon, the Bjorken scaling variable x and y are dimensionless and range in between of 0 and 1. The variable y can be interpreted as the fractional energy of the photon and can be used as a measure of the inelasticity of the reaction.

From theoretical point of view, the DIS regime corresponds to $Q^2, \nu \rightarrow \infty$ at a fixed value of x, called Bjorken limit. In practice, $Q^2 > 1\,(\mathrm{GeV/c})^2$ is required for fixed target experiments.

Table 2.1: Important Variables in DIS and SIDIS. The shortcut TRF indicates the target rest frame.

Variable	**Formula**
Mass of target nucleon	M
Mass of incident lepton	m
Four-momentum of target nucleon	$P \overset{\text{TRF}}{=} (M, 0)$
Four-momentum of incident lepton	$l \overset{\text{TRF}}{=} (E, \boldsymbol{l})$
Four-momentum of scattered lepton	$l' \overset{\text{TRF}}{=} (E', \boldsymbol{l}')$
Four-momentum of virtual photon	$q = l - l'$
Negative squared four-momentum transfer	$Q^2 = -q^2$
Energy of virtual photon	$\nu = \frac{P \cdot q}{M} \overset{\text{TRF}}{=} E - E'$
Fractional energy of the virtual photon	$y = \frac{P \cdot q}{P \cdot l} \overset{\text{TRF}}{=} \frac{\nu}{E}$
Bjorken scaling variable	$x = \frac{Q^2}{2P \cdot q} = \frac{Q^2}{2M\nu}$
Squared invariant center of mass energy	$s = (P + l)^2$
Squared invariant mass of photon-nucleon system	$W^2 = (P + q)^2 =$ $M^2 + 2M\nu - Q^2$

2.1.1 DIS Cross Section and Structure Functions

The total DIS cross section can be written as a contraction of a leptonic tensor $L_{\mu\nu}$ and a hadronic tensor $W^{\mu\nu}$. In terms of the above introduced invariants it reads

$$\frac{d^3\sigma}{dx dy d\phi} = \frac{\alpha_{\text{em}}^2 y}{2Q^4} L_{\mu\nu} W^{\mu\nu}, \tag{2.3}$$

where ϕ describes the angle between the scattering plane and the spin plane, as illustrated in Fig. 2.4. The leptonic tensor contains the information about the emission of the virtual photon by the initial lepton. As leptons are point-like particles it can be calculated in quantum electrodynamics (QED). This is not the case for the hadronic tensor, describing the absorption of the virtual photon, due to non-perturbative effects in strong interactions. Nevertheless, symmetry and conservation laws allow its parametrization with the use of four dimensionless structure functions F_1, F_2, g_1 and g_2.

Both the leptonic and the hadronic tensor can be further decomposed in a symmetric spin-independent (S) and an antisymmetric spin-dependent part (A):

$$L_{\mu\nu} = L^{(S)}_{\mu\nu}(l, l') + iL^{(A)}_{\mu\nu}(l, s_l, l') \tag{2.4}$$

$$W_{\mu\nu} = W^{(S)}_{\mu\nu}(q, P) + iW^{(A)}_{\mu\nu}(q, P, S). \tag{2.5}$$

Here, s_l and S stand for the spin of the incident lepton and the target spin, respectively. Note, that in the calculation of the leptonic tensor it is summed over all spin states of the scattered lepton, as it is usually not measured in practice. Inserting (2.4) and (2.5) in (2.3) the cross section becomes

$$\frac{d^3\sigma}{dxdyd\phi} = \frac{\alpha^2 y}{2Q^4}\Big[L^{(S)}_{\mu\nu}(l, l')W^{\mu\nu(S)}(q, P) - L^{(A)}_{\mu\nu}(l, s_l, l')W^{\mu\nu(A)}(q, P, S)\Big]. \tag{2.6}$$

This implies, that in DIS spin related properties can only be measured using a polarized beam as well as a polarized target. For this purpose, a longitudinally polarized lepton beam with helicity $\lambda_\ell = -1$ and a polarizable target is used at COMPASS.

With α describing the angle between the initial lepton and the target spin as shown in Fig. 2.4, the polarized cross section can be further split into partial cross sections. This leads to

$$\frac{d^3\sigma}{dxdyd\phi} = \frac{d^3\overline{\sigma}}{dxdyd\phi} - \lambda_\ell \cos\alpha \frac{d^3\sigma_\parallel}{dxdyd\phi} - \lambda_\ell \sin\alpha\cos\phi \frac{d^3\sigma_\perp}{dxdyd\phi}. \tag{2.7}$$

with the $\overline{\sigma}$, $\sigma_\parallel$ and $\sigma_\perp$ indicating the unpolarized, the longitudinal and the transverse partial cross section with respect to the direction of the incoming lepton. Defining $\gamma = 2Mx/Q$, the partial cross sections are

$$\frac{d^3\overline{\sigma}}{dxdyd\phi} = \frac{4\alpha^2}{Q^2}\left[\frac{y}{2}F_1(x, Q^2) + \frac{1}{2xy}\left(1 - y - \frac{y^2\gamma^2}{4}\right)F_2(x, Q^2)\right] \tag{2.8}$$

$$\frac{d^3\sigma_\parallel}{dxdyd\phi} = \frac{4\alpha^2}{Q^2}\left[\left(1 - \frac{y}{2} - \frac{y^2\gamma^2}{4}\right)g_1(x, Q^2) - \frac{y}{2}\gamma^2 g_2(x, Q^2)\right] \tag{2.9}$$

$$\frac{d^3\sigma_\perp}{dxdyd\phi} = \frac{4\alpha^2}{Q^2}\left[\gamma\sqrt{1 - y - \frac{y^2\gamma^2}{4}}\left(\frac{y}{2}g_1(x, Q^2) + g_2(x, Q^2)\right)\right]. \tag{2.10}$$

The unpolarized structure functions F_1 and F_2 are measured by several experiments with high accuracy, together covering a wide range of x and Q^2 [12]. As already predicted by J. Bjorken in 1968, both structure functions were found to be almost independent of Q^2 in the valence region [13]. This phenomenon, called Bjorken scaling, is a hint to the point-like nature of partons. Exemplarily, the results for F_2^p, measured in unpolarized DIS off unpolarized proton targets, are shown in Fig. 2.2.

The structure function F_1 results of the magnetic interaction, hence it depends on the spin of the target particle. Considering $S = 1/2$ theoretically leads to the Callan-Gross-Relation [14]

$$2xF_1(x) = F_2(x). \tag{2.11}$$

This, and with that the fermionic nature of the quarks, could be experimentally confirmed in 1969 at SLAC [15].

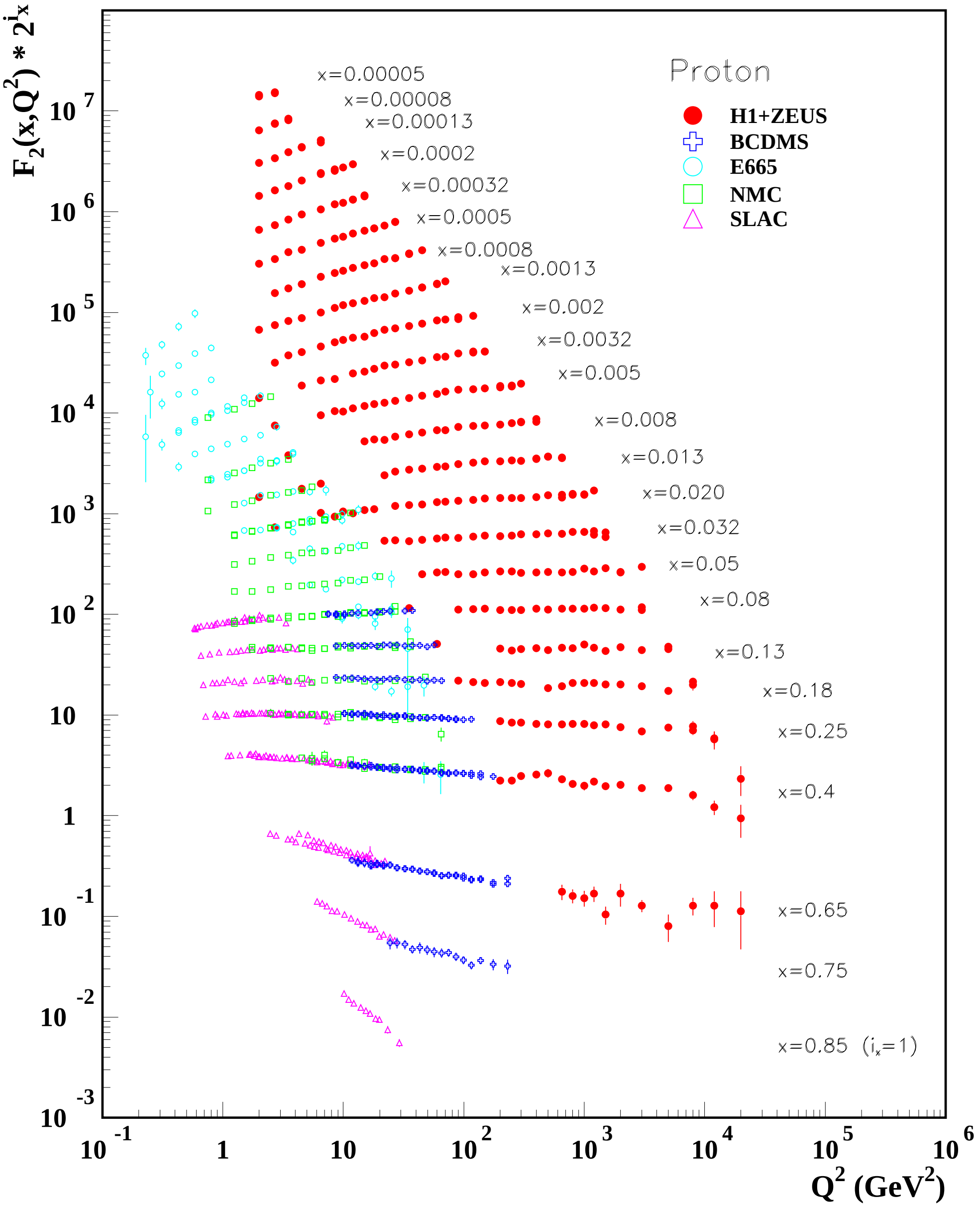

Figure 2.2: The structure function $F_2^p(x, Q^2)$ as a function of Q^2 for several values of x, measured in electromagnetic scattering of protons and positrons (ZEUS [16], H1 [17, 18]), for electrons (SLAC [19]) and muons (BCDMS [20], E665 [21], NMC [22]). For the reason of presentability, the values of each x-bin are multiplied by a factor of 2^{i_x}, where i_x denotes the number of the x-bin and ranges from $i_{0.85} = 1$ to $i_{0.00005} = 24$. Plot from Ref. [12].

2.1.2 Polarized DIS

The spin-dependent structure functions g_1 and g_2 can be probed in polarized DIS, using both a polarized beam and a polarized target. Considering the incoming leptons to have negative helicity ($\leftarrow$), two experimental setups are distinguished: the longitudinal mode, where the target spin is either set parallel ($\Rightarrow$) or antiparallel ($\Leftarrow$) to the incoming lepton direction, and the transverse mode, thus setting the target spin perpendicular to the direction of the lepton ($\Uparrow$ or $\Downarrow$).

The following double spin asymmetries can be measured to access g_1 and g_2:

$$A_{\parallel} = \frac{d^3\sigma^{\leftarrow\Rightarrow} - d^3\sigma^{\leftarrow\Leftarrow}}{d^3\sigma^{\leftarrow\Rightarrow} + d^3\sigma^{\leftarrow\Leftarrow}} = \frac{xy\left(2 - y - \frac{y^2\gamma^2}{2}\right)g_1 - xy^2\gamma^2 g_2}{xy^2F_1 + \left(1 - y - \frac{y^2\gamma^2}{4}\right)F_2}, \tag{2.12}$$

$$A_{\perp} = \frac{d^3\sigma^{\leftarrow\Uparrow} - d^3\sigma^{\leftarrow\Downarrow}}{d^3\sigma^{\leftarrow\Uparrow} + d^3\sigma^{\leftarrow\Downarrow}} = \frac{xy\gamma\sqrt{1 - y - \frac{y^2\gamma^2}{4}}\left(yg_1 + 2g_2\right)}{xy^2F_1 + \left(1 - y - \frac{y^2\gamma^2}{4}\right)F_2}\cos\phi. \tag{2.13}$$

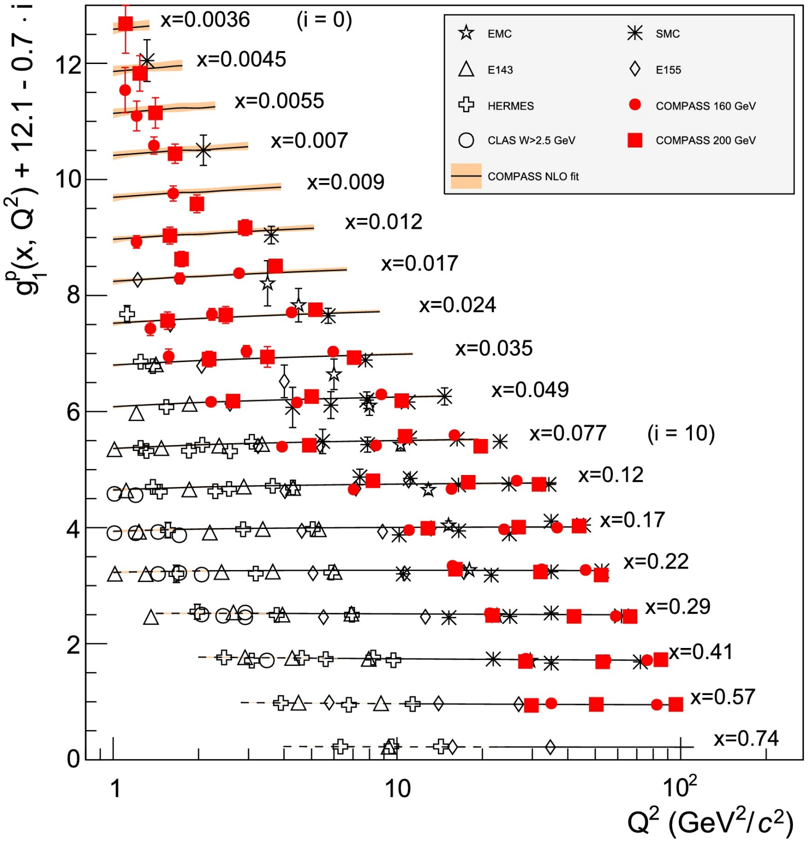

Figure 2.3: World data on the spin-dependent structure function $g_1^p(x, Q^2)$ as a function of Q^2 for several values of x [23]. The red marks indicate COMPASS data from 2007 (circles) and 2011 (squares), also used in the present analysis. For the reason of presentability, the values of each x-bin are vertically shifted by $c_{i_x} = 12.1 - 0.7i_x$, where i_x denotes the number of the x-bin and ranges from $i_{0.0036} = 0$ to $i_{0.74} = 17$.

Obviously, measuring the longitudinal asymmetry $A_{\parallel}$ is the method of choice to extract g_1. In contrast to $A_{\perp}$, where both structure functions contribute with $\mathcal{O}(\gamma)$, only g_2 is strongly suppressed by the factor γ^2 here. The asymmetry $A_{\parallel}$ is hence directly proportional to g_1. However, $A_{\perp}$ serves to extract g_2, once g_1 is known. Fig. 2.3 shows present results for g_1^p as a function of Q^2, including COMPASS data from 2007 and 2011.

2.1.3 Target Polarization Orientation

In the previous chapters, the target polarization was given with respect to the beam axis. This reference system serves well from experimental point of view, although it is theoretically more convenient to choose the direction of the virtual photon as a reference. The process in the two reference systems with the related angles is shown in Fig. 2.4. Note, that three-vectors are indicated by bold letters throughout this work.

Considering the target spin vector $\boldsymbol{S}$ being set transverse to the beam axis ($\alpha = \pi/2$) and neglecting $1/Q^2$ kinematic effects, one finds

$$\cos\beta \simeq \; -\gamma\sqrt{1-y}\cos\phi \tag{2.14}$$

$$\sin\beta \simeq 1, \tag{2.15}$$

and therefore

$$|\boldsymbol{S}_{\perp}| \simeq |\boldsymbol{S}|\,.$$

In longitudinal mode ($\alpha = 0$) it is

$$\cos\beta \simeq 1 \tag{2.16}$$

$$\sin\beta \simeq \gamma\sqrt{1-y}. \tag{2.17}$$

Consequently, with changing the reference system, there enters a small transverse contribution

$$|\boldsymbol{S}_{\perp}| = \sin\beta\,|\boldsymbol{S}| = \gamma\sqrt{1-y}\,|\boldsymbol{S}|\,, \tag{2.18}$$

suppressed by the factor $\gamma \propto M/Q$.

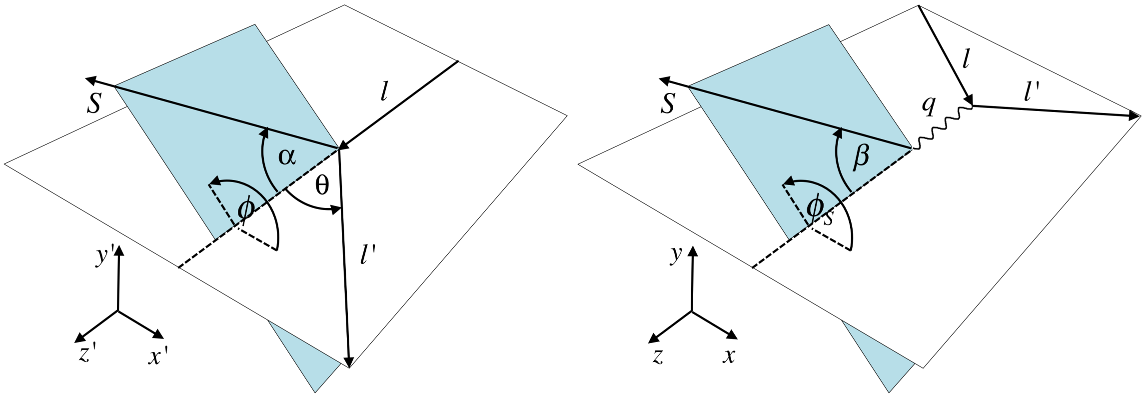

Figure 2.4: Definition of angles with respect to the incoming muon direction (left) and with respect to the virtual photon direction (right). The vector $\boldsymbol{S}$ indicates the target spin.

2.1.4 Parton Distribution Functions

In the late 1960s, the observed Bjorken scaling prompted the interpretation of DIS as an incoherent scattering off charged, point-like, spin 1/2 constituents inside the nucleon, later linked to quarks. This first interpretation is today known as the naive parton model, since later measurements gave evidence of contributions coming from gluons and hence forced an extension of the model on basis of QCD. The theoretical formalism of this development is briefly outlined in the following, including the concept of parton distribution functions (PDFs).

2.1.4.1 Naive Parton Model

In its most simple interpretation, any interaction between the struck quark and the remaining partons, hence the existence of gluons, is ignored. The corresponding Feynman diagram is shown in Fig. 2.5, showing the virtual photon interacting with one quark only. A common reference frame to describe DIS is the so called infinite momentum frame, assuming the proton to move with very large momentum, so that the masses and transverse momenta of the partons can be neglected. In this reference frame, the Bjorken scaling variable x can be interpreted as the momentum fraction carried by the struck quark. The corresponding momentum distributions, denoted by $q(x)$ and referring to a parton with flavor q, are simply called parton distribution functions. By integration over dx they give the probability for finding a quark with flavor q in the nucleon, carrying a fractional momentum in the range $[x; x + dx]$.

In this framework, the total DIS cross section can be formulated as a sum over all contributing partonic cross sections $d\hat{\sigma}$, each weighted with the corresponding PDF $q(x)$ and the squared parton charge e_q:

$$d\sigma(\gamma + N \to X) = \sum_q e_q^2 \int_0^1 dx\, q(x)\, d\hat{\sigma}(\gamma + q \to X). \tag{2.19}$$

This simplified approach allows the calculation of the contributing partonic cross sections in QED and yields the following relations of structure functions and PDFs:

$$\begin{aligned} F_1(x, Q^2) &= \frac{1}{2} \sum_q e_f^2 q(x) && (2.20)\\ F_2(x, Q^2) &= x \sum_q e_q^2 q(x) && (2.21)\\ g_1(x, Q^2) &= \frac{1}{2} \sum_q e_q^2 \Delta q(x) && (2.22)\\ g_2(x, Q^2) &= 0 && (2.23) \end{aligned}$$

with the following compositions of PDFs

$$\begin{aligned} q(x) &= q^+(x) + q^-(x) \qquad \text{Parton Distribution,} && (2.24)\\ \Delta q(x) &= q^+(x) - q^-(x) \qquad \text{Helicity Distribution.} && (2.25) \end{aligned}$$

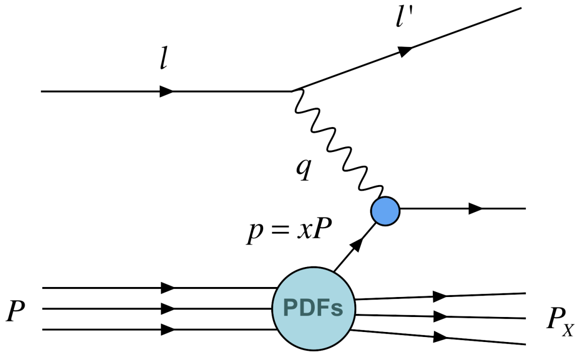

Figure 2.5: Feynman diagram of a DIS process in the naive Parton Model.

Here, the superscripted signs indicate the orientation of the quark spins in the helicity base.

The above Eqs. (2.20)-(2.23) mirror the advantages and disadvantages of the simple parton model. Although it doesn't allow an interpretation of g_2, it predicts the scaling behavior of structure functions as well as the Callan-Gross Relation, both confirmed in early experiments. However, later measurements at higher beam energies revealed non-negligible deviations. So was the longitudinal momentum fraction carried by the valence quarks ($q = u, d$), practically accessible via integrating over F_2 and expected to be 1, found to be less than 0.5. Moreover a weak logarithmic Q^2-dependence of the structure functions was observed, also visible in Fig. 2.2, called scaling violation. Both effects could be ascribed to gluon interactions and necessitate the reformulation of the quark parton model in the framework of QCD.

2.1.4.2 QCD improved Parton Model

QCD is a quantum field theory, developed in the late 1970s in order to describe strong interactions in between of quarks and gluons. In contrast to the electromagnetic counterpart QED, where the photon doesn't carry electrical charge, the field quanta of the strong force, called gluons, do carry a so called color charge and can therefore not only couple to quarks, but also to each other. As a consequence, the theory bases on the non-abelian group SU(3), involving two main characteristic features of QCD: confinement and asymptotic freedom. The former describes the phenomenon, that color charged particles never appear isolated at long distances, while the latter implies their appearance as free particles for short distances. Hence, the coupling constant of the strong force α_S scales with the probing energy. Considering DIS, the assumption of a scattering off free particles is therefore only valid in the theoretical Bjorken Limit $Q^2 \to \infty$, while in case of finite values of Q^2 gluon interactions have to be taken into account.

At sufficiently large Q^2, the DIS process can be expressed by the so called handbag diagram, shown in Fig. 2.6. It considers the process being divided into two parts: a soft part, describing the decoupling of the struck quark from the nucleon, and a hard part, describing the interaction of the virtual photon with the struck quark, carrying a momentum p. The momentum of the quark after the photon absorption thus is $k = p + q$. While the hard part can be calculated order by order in perturbative

QCD, the calculation of the soft part requires non-perturbative QCD methods. It is common to introduce the quark-quark correlator matrix

$$\Phi_{ij}(p,P,S) = \sum_X \int \frac{d^3\boldsymbol{P}_X}{(2\pi)^3 2E_X}(2\pi)^4\delta\left(P-p-P_X\right) \times \left\langle P,S\right| \bar{\psi}_j(0)\left|X\right\rangle \left\langle X\right| \psi_i(0)\left|P,S\right\rangle, \tag{2.26}$$

which encodes the full non-perturbative information of the quark states inside the proton. Here, the sum runs over all possible undetected hadronic final states X with four momenta $P_X = (E_X, \boldsymbol{P}_X)$, while the $\psi_{i,j}$ denotes the quark field operator with spinor index i and j, respectively. Accordingly, the antiquark-antiquark correlator $\bar{\Phi}$ is defined by interchanging ψ and $\bar{\psi}$ in the above formula. For simplicity, its contribution will be omitted in the following.

The completeness of final states $|X\rangle$ and translation invariance allows to fourier-transformate the quark-quark-correlator:

$$\Phi_{ij}(p,P,S) = \int d^4\xi\; e^{ip\cdot\xi}\left\langle P,S\right| \bar{\psi}_j(0)\psi_i(\xi)\left|P,S\right\rangle. \tag{2.27}$$

The hadronic tensor can then be reformulated as a sum over integrated traces:

$$W^{\mu\nu} = \sum_q e_q^2 \int \frac{d^4p}{(2\pi)^4}\delta\left((p+q)^2\right)\mathrm{Tr}\left[\Phi(p,P,S)\gamma^\mu(\not{p}+\not{q})\gamma^\nu\right]. \tag{2.28}$$

As already briefly introduced in 2.1.4.1, PDFs encode the partonic distributions inside the nucleon. In the QCD improved parton model three leading-twist[1] (twist-2) distributions can be identified, derived from projecting the so called integrated correlation function. The determination is usually carried out using light-cone coordinates (see A.1.1) in a collinear infinite momentum frame, allowing the Bjorken

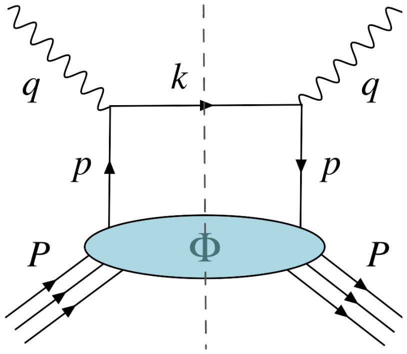

Figure 2.6: The handbag diagram.

---

[1] An observable is twist-t, if its contribution is suppressed by $(M/Q)^{t-2}$.

scaling variable to be interpreted as the longitudinal momentum fraction of the parton $x = p^+/P^+$, hence $p^+ = xP^+$. In this frame, the relevant four-vectors can be approximated in light-cone coordinates as:

$$P^\mu = \left[P^+, \frac{M^2}{2P^+}, \mathbf{0}_T\right] \approx \left[P^+, 0, \mathbf{0}_T\right] \tag{2.29}$$

$$p^\mu = \left[xP^+, \frac{p^2 + |\boldsymbol{p}_T|^2}{2xP^+}, \boldsymbol{p}_T\right] \approx \left[xP^+, 0, \mathbf{0}_T\right] \tag{2.30}$$

$$q^\mu = \left[-xP^+, \frac{Q^2}{2xP^+}, \mathbf{0}_T\right] \approx \left[0, \frac{M\nu}{2xP^+}, \mathbf{0}_T\right], \tag{2.31}$$

and it is $\delta\left[(p+q)^2\right] = \frac{1}{2P\cdot q}\delta(p^+ - xP^+)$. Following the constraint $x = p^+/P^+$ and integrating the correlation function $\Phi_{ij}(x,S)$ over transverse parton momentum components, making up $\boldsymbol{p}_T$, yields

$$\Phi_{ij}(x,S) = \int dp^- d^2\boldsymbol{p}_T \Phi_{ij}(p,P,S)\Big|_{p^+=xP^+} \tag{2.32}$$

$$= \int \frac{d\xi^-}{2\pi}\, e^{-ip\cdot\xi} \left\langle P,S\right| \bar{\psi}_i(\xi)\psi_j(0) \left|P,S\right\rangle\Big|_{\xi^+=0,\xi_T=\mathbf{0}_T}. \tag{2.33}$$

The projected correlation functions $\Phi^{[\Gamma]}$ then read

$$\Phi^{[\Gamma]} = \frac{1}{2}\int dp^- d^2\boldsymbol{p}_T \mathrm{Tr}\left[\Phi(p,P,S)\Gamma\right], \tag{2.34}$$

where Γ are compositions of Dirac matrices (see A.1.2). Three leading-twist PDFs survive the integration[1]:

$$f_1(x) = \Phi^{[\gamma^+]} \quad \text{Parton Distribution,} \tag{2.35}$$

$$g_1(x) = \Phi^{[\gamma^+\gamma_5]} \quad \text{Helicity Distribution,} \tag{2.36}$$

$$h_1(x) = \Phi^{[\gamma^+\gamma^1\gamma_5]} \quad \text{Transversity Distribution.} \tag{2.37}$$

The integrated quark-quark correlation function can then be decomposed in a basis of Dirac matrices. In leading-twist, it reads

$$\Phi(x)\Big|_{\text{twist-2}} = \frac{1}{2}\left\{f_1(x)\not{n}_+ + \lambda_N g_1(x)\gamma_5\not{n}_+ + h_1(x)\frac{\left[\not{S}_T, \not{n}_+\right]\gamma_5}{2}\right\}, \tag{2.38}$$

where the approximation $S \approx \lambda_N \frac{P}{M} + S_T$ was used, with λ_N denoting the helicity of the nucleon and S_T the transverse component of its spin with respect to the nucleon momentum.

---

[1] Here and in the following, the Amsterdam notation (f_1, g_1, h_1) for the set of leading-twist PDFs is used, whereas the indication of the flavor is omitted for clarity.

A probabilistic interpretation of $f_1(x)$ and $g_1(x)$ was already given in the naive parton model, there denoted as $q(x)$ and $\Delta q(x)$. The leading-twist decomposition of the quark-quark-correlator reveals a third distribution, called transversity distribution h_1. It can in analogy be interpreted as the probability-difference of finding a parton being polarized parallel or antiparallel with respect to the spin of a transversely polarized nucleon. Since it is chiral-odd, involving a helicity flip of the struck quark, it can not be connected to any structure function in DIS and can only be measured in connection with an other chiral-odd function. The most promising channels for this purpose are SIDIS, outlined in the next chapter, and Drell-Yan[1] (DY) processes.

Sets of PDFs are obtained by simultaneously fitting global data from various experiments. In the standard fitting procedures, the x-dependence of a certain PDF is evaluated at a sufficiently large initial scale $Q_0^2 > 1\,\mathrm{GeV}^2$ and evolved to other scales using the Dokshitzer-Gribov-Lipatov-Altarelli-Parisi (DGLAP) equations at a certain order N^{m}LO, which refers to the considered order of the running coupling constant $\mathcal{O}(\alpha_S^m)$ in perturbative QCD. Typical parametrizations of the leading twist PDFs are shown in Fig. 2.7, Fig. 2.8 and Fig. 2.9. Detailed information on the certain methods can be found in the corresponding Refs. [24–26].

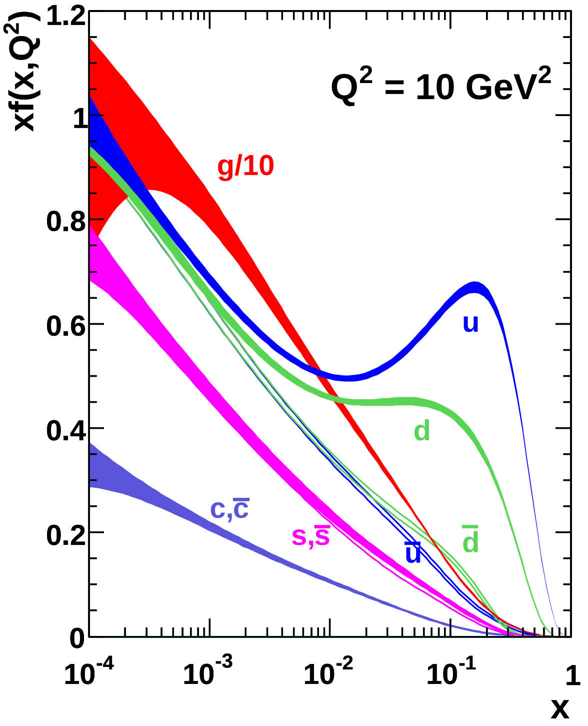

Figure 2.7: Uncertainty bands of x times the unpolarized PDF $f(x)$ for the quark types u_v, d_v, $\bar{u}$, $\bar{d}$, s, c, and gluons g from the NNLO MSTW08 parametrization at $Q^2 = 10$ GeV^2 [24]. Note the scaling of the gluon distribution with a factor 1/10.

---

[1] Drell-Yan processes involve the production of a lepton pair with opposite charge out of a quark-antiquark annihilation $q + \bar{q} \rightarrow l^+ + l^-$. The process can be induced by hadron-hadron collisions.

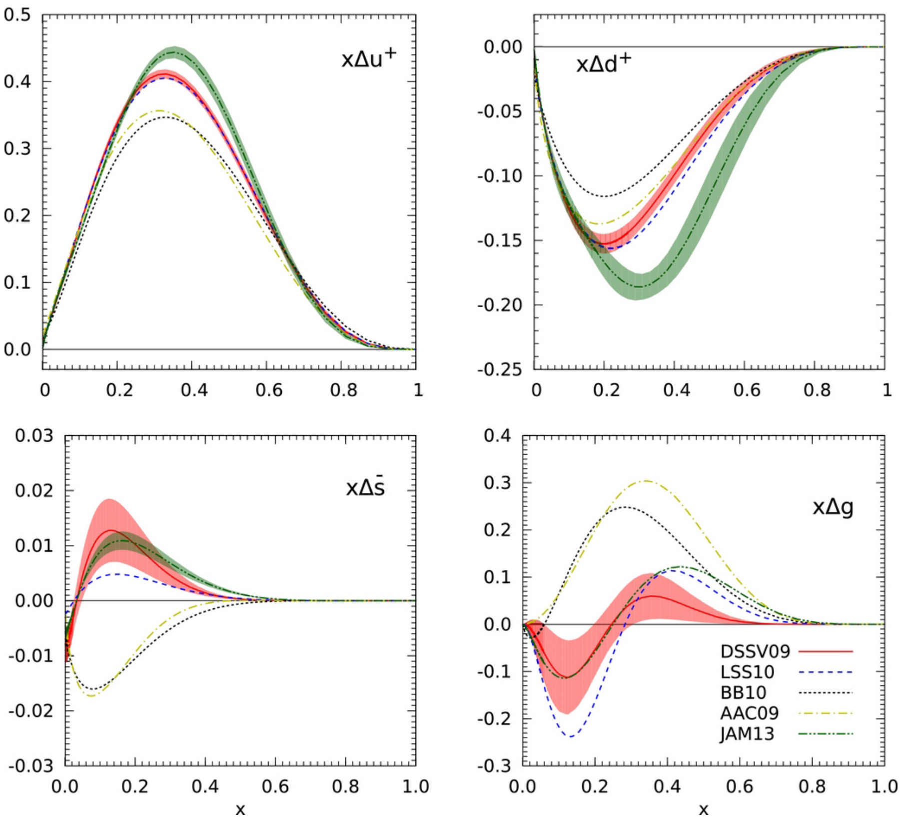

Figure 2.8: The helicity distribution, here named Δq, times x. Displayed are the distributions for the sums $x\Delta u^+ = x(\Delta u + \Delta\bar{u})$ and $x\Delta d^+ = x(\Delta d + \Delta\bar{d})$, for strange sea quarks $x\Delta\bar{s}$ and polarized gluons $x\Delta g$ [25] (modified). The colored lines indicate the different parametrizations from DSSV09 [27], LSS10 [28], BB10 [29], AAC09 [30], and JAM13 [31].

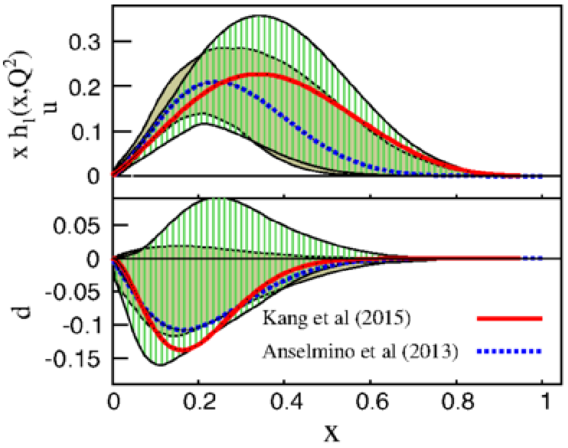

Figure 2.9: The transversity distributions h_1^u and h_1^d times x from different parametrizations, involving data from SIDIS and e^+e^--annihilations [26]. The red lines and vertical-line hashed bands indicates parametrizations from Kang. et. al. [26] at $Q^2 = 2.4\,\mathrm{GeV}^2$, while the dashed blue lines and shaded regions show parametrizations from Anselmino et. al. [32].

2.1.4.3 Transverse Momentum Dependent Distributions

So far intrinsic transverse momenta of the partons were neglected, as it is appropriate in case of inclusive measurements. In early days of the parton model it was indeed naively assumed, that transverse effects arising from the intrinsic motion of partons with respect to the center of mass of the bound state would average out, also when detecting hadronic fragments. However, later measurements enforced their theoretical consideration in order to explain observations, which could not be understood in the collinear approach. Related effects are today known as the Cahn [33], the Sivers [34], the Pretzelosity [35] and the Boer-Mulders [36] effect, just to name a few.

When omitting the integration over $\boldsymbol{p}_T$ in Eq. (2.32), the leading-twist Dirac projections [37] become

$$\Phi^{[\gamma^+]}(x,\boldsymbol{p}_T) = f_1\left(x,p_T^2\right) - \frac{\epsilon_T^{ij} p_{Ti} S_{Tj}}{M} f_{1T}^{\perp}\left(x,p_T^2\right) \tag{2.39}$$

$$\Phi^{[\gamma^+\gamma_5]}(x,\boldsymbol{p}_T) = \lambda_N g_{1L}\left(x,p_T^2\right) - \frac{\boldsymbol{p}_T \cdot \boldsymbol{S}_T}{M} g_{1T}^{\perp}\left(x,p_T^2\right) \tag{2.40}$$

$$\begin{aligned}\Phi^{[\mathrm{i}\gamma^{i+}\gamma_5]}(x,\boldsymbol{p}_T) &= S_T^i h_1\left(x,p_T^2\right) + \lambda_N \frac{p_T^i}{M} h_{1L}^{\perp}\left(x,p_T^2\right) \\ &\quad - \frac{p_T^i p_T^j + \frac{1}{2} p_T^2 g_T^{ij}}{M^2} S_{Tj} h_{1T}^{\perp}\left(x,p_T^2\right) - \frac{\epsilon_T^{ij} p_{Tj}}{M} h_1^{\perp}\left(x,p_T^2\right),\end{aligned} \tag{2.41}$$

where the symbol ϵ_T^{ij} denotes the two-dimensional antisymmetric Levi-Civita tensor. The p_T-dependent projections involve a set of eight transverse momentum dependent (TMD) PDFs. Their probabilistic illustrations are given in Tab. 2.2, ordered with regard to the polarizations of the parton and the parent nucleon. They depend on x and $p_T^2 = |\boldsymbol{p}_T|^2$. The subscripts L or T indicate the polarization orientation of the parent nucleon, either longitudinal or transverse.

Only the three distribution functions $f_1(x,p_T^2)$, $g_{1L}(x,p_T^2)$ and $h_1(x,p_T^2)$ survive the integration over transverse momenta due to their p_T-even structure. They can be connected to ordinary PDFs via

$$f_1(x) = \int d^2\boldsymbol{p}_T\, f_1\left(x,p_T^2\right) \tag{2.42}$$

$$g_1(x) = \int d^2\boldsymbol{p}_T\, g_{1L}\left(x,p_T^2\right) \tag{2.43}$$

$$h_1(x) = \int d^2\boldsymbol{p}_T \Big(\underbrace{h_{1T}\left(x,p_T^2\right) - \frac{p_T^2}{2M^2} h_{1T}^{\perp}\left(x,p_T^2\right)}_{=:\, h_1\left(x,p_T^2\right)} \Big). \tag{2.44}$$

All other TMD PDFs have no counterpart as integrated PDF. The Sivers and the Boer-Mulders function, $f_{1T}^{\perp}(x,p_T^2)$ and $h_1^{\perp}(x,p_T^2)$, are naive T-odd, which means they change sign under usual time reversal without the interchange of initial and final states. As will be outlined in the next subsection, they require additional interaction between the initial and the final state to be non-zero.

TMD PDFs can be studied in deeply inelastic semi-inclusive reactions, such as lepto-production of hadrons and Drell-Yan, using complimentary information from e^+e^--annihilation. The determination of TMD PDFs from data is quite challenging, as both factorization and QCD evolution become more involved when taking into account transverse momenta of quarks. Significant developments have been made during recent years, yielding several phenomenological concepts of TMD factorization and evolution. Summaries of the present status can be found i. e. in the Refs. [38, 39]. First parametrizations have been already extracted, however still suffering from low accuracy due to a lack of data [40]. Up-to-date sets of TMD PDFs are collected in the lately set-up library TMDlib [41].

Table 2.2: Illustration of the probabilistic interpretation of the eight leading-twist TMD PDFs, ordered in regard of the polarization of the nucleon (rows) and the quarks (columns). Black arrows indicate the spin orientation of the nucleon (light blue bulb) and the parton (dark blue bulb). The red arrows symbolize the transverse momentum of the parton with respect to the nucleon momentum direction, which is meant to point to the right here. All TMD PDFs depend on x and p_T^2.

		Quark		
		U	L	T
Nucleon	U	Unpolarized $f_1 =$ 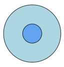		Boer-Mulders $h_1^\perp =$ 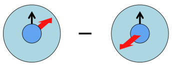
	L		Helicity $g_{1L} =$ 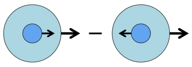	Worm-gear 1 $h_{1L}^\perp =$ 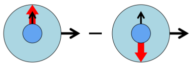
	T	Sivers $f_{1T}^\perp =$ 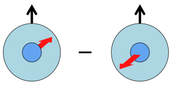	Worm-gear 2 $g_{1T}^\perp =$ 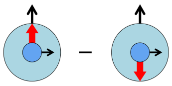	Transversity $h_1 =$ 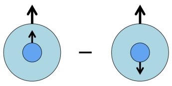 Pretzelosity $h_{1T}^\perp =$ 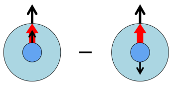

2.1.4.4 Gauge-Link and T-odd Distribution Functions

As already mentioned, the constraint of time-reversal-invariance would naively forbid T-odd TMD PDFs, in particular the Sivers $f_{1T}^{\perp}$ and the Boer-Mulders $h_1^{\perp}$ function. Indeed, this was common belief for more than a decade. However, contrary observations in form of large transverse single spin asymmetries enforced their reconsideration in relation with so far omitted mechanisms. So was the existence of the related Sivers function $f_T^{\perp}$ found to be legitimized by considering initial (DY) or final (SIDIS) state interactions [42, 43]. An example for the latter is given in Fig. 2.10, showing the exchange of a gluon between the nucleon remnant and the current quark.

Such processes theoretically require the insertion of a non-trivial path-dependent link operator $\mathcal{L}$ into the quark-quark correlator to preserve color gauge invariance:

$$\Phi^{\mu}_{A,ij}(p,P,S) = \int d^4\xi \; e^{ip\cdot\xi} \left\langle P,S \right| \bar{\psi}_j(0)\mathcal{L}(0,\xi)\psi_i(\xi) \left| P,S \right\rangle. \tag{2.45}$$

The gauge link $\mathcal{L}(0,\xi)$, also called Wilson line, connects the quark fields at two different points in space and time, 0 and ξ, and can be expressed as a path-ordered exponential of the form

$$\mathcal{L}(0,\xi) = \mathcal{P} \exp\left(-\mathrm{i}\, g \int_0^{\xi} ds_{\mu} A^{\mu}(s) \right), \tag{2.46}$$

where $\mathcal{P}$ indicates the path-ordering of the integral over the gauge field A^{μ} with coupling constant g. The gauge link was so far omitted, as it reduces to unity when considering axial gauge $A^+ = 0$.

Since the gauge link is process-dependent, T-odd distribution functions can not be presumed to be universal. As an example, both the Sivers function $f_{1T}^{\perp}$ and the Boer-Mulders function $h_1^{\perp}$ are predicted to have opposite sign for DY and SIDIS, because the direction of the path is opposite [44].

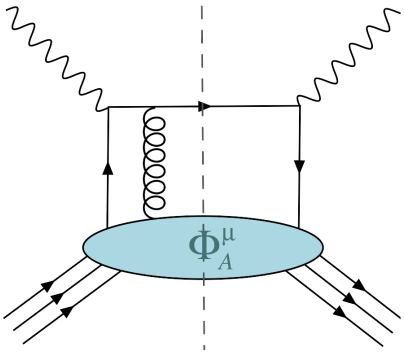

Figure 2.10: The handbag diagram with one-gluon exchange between the nucleon remnant and the quark line.

2.1.4.5 Higher-Twist Distributions

When considering the p_T-dependent quark-quark correlator at subleading twist, 16 additional TMD PDFs appear, characterized through a suppression by one power of P^+ [45]. They have to be understood as effective quantities, incorporating various kinematic and dynamic effects, which arise from the consideration of quark masses, intrinsic transverse motion of quarks and gluon interactions. Unlike leading twist distributions, they consequently don't allow for a simple probabilistic interpretation. The full set of twist-3 TMD PDFs is listed in Tab. 2.3 with regard to the polarization properties of the parent nucleon and the struck quark.

The subleading part of the p_T-integrated quark-quark correlator function can be parametrized by a set of six independent collinear PDFs. Among them, the functions $e(x)$, $g_T(x)$ and $h_L(x)$ are T-even, whereas $f_T(x)$, $e_L(x)$ and $h(x)$ are T-odd and should vanish if the gauge link is the only source of T-odd behavior. The integrated correlator up to twist-3 can be written in their terms as [37]

$$\begin{aligned}\Phi(x)\Big|_{\text{twist 3}} = \Phi(x)\Big|_{\text{twist 2}} \\ + \frac{M}{2P^+}\bigg\{ e(x) - \mathrm{i}\lambda_N e_L(x)\gamma_5 + f_T(x)\epsilon_T^{\rho\sigma} S_{T\rho}\gamma_\sigma + g_T(x)\gamma_5 \not{S}_T \\ + \lambda_N h_L(x)\frac{[\not{n}_+,\not{n}_-]\,\gamma_5}{2} + \mathrm{i}h(x)\frac{[\not{n}_+,\not{n}_-]}{2}\bigg\}. \end{aligned} \tag{2.47}$$

Each twist-3 PDF can be decomposed into three terms, one including a weighted p_T-integrated leading-twist TMD PDF, one depending on the current quark mass, and an interaction dependent term marked with a tilde [46]. For the T-even collinear functions one finds

$$xe(x) = \frac{m}{M} f_1(x) + x\tilde{e}(x) \tag{2.48}$$

$$xg_T(x) = \frac{m}{M} h_1(x) - g_{1T}^{(1)}(x) + x\tilde{g}_T(x) \tag{2.49}$$

$$xh_L(x) = \frac{m}{M} g_1(x) + 2h_{1L}^{\perp(1)}(x) + x\tilde{h}_L(x), \tag{2.50}$$

where the common shorthand notation

$$d^{(n)}(x) = \int d^2\boldsymbol{p}_T \left(\frac{p_T^2}{2M^2}\right)^n d(x, p_T^2) \tag{2.51}$$

for the n-th moment of the TMD PDFs is used to indicate the weighted distributions $g_{1T}^{(1)}(x)$ and $h_{1L}^{\perp(1)}(x)$.

Table 2.3: Twist-3 TMD PDFs, ordered in regard of the polarization of the nucleon (rows) and the quarks (columns). All functions depend on x and p_T^2.

		Quark		
		U	L	T
Nucleon	U	$f^{\perp}$	$g^{\perp}$	h, e
	L	$f_L^{\perp}$	$g_L^{\perp}$	h_L, e_L
	T	f_T, $f_T^{\perp}$	g_T, $g_T^{\perp}$	h_T, e_T, $h_T^{\perp}$, $e_T^{\perp}$

2.2 Semi-Inclusive DIS

A deep inelastic scattering process is called semi-inclusive, if in addition to the scattered muon at least one hadron, produced in the current fragmentation region, is detected. In this section, the theory of one and two hadron SIDIS processes, with at least one, respectively two hadrons in the final state, will be described separately. The involved cross section amplitudes can be interpreted within the QCD parton model in terms PDFs and fragmentation functions (FFs). They can be partly accessed by spin dependent asymmetry measurements. This makes the investigation of SIDIS processes a promising tool to get a further insight in spin dependent phenomena inside the nucleon as well as in fragmentation processes.

With λ_ℓ, $S_\parallel$ and $S_\perp$ being the lepton helicity, respectively the longitudinal and transverse target spin components, the total differential cross section for both considered SIDIS processes can be expressed in terms of partial cross sections as

$$d\sigma = d\sigma_{UU} + \lambda_\ell d\sigma_{LU} + S_\parallel \left(d\sigma_{UL} + \lambda_\ell d\sigma_{LL}\right) + |S_\perp| \left(d\sigma_{UT} + \lambda_\ell d\sigma_{LT}\right). \tag{2.52}$$

The partial cross sections $d\sigma_{XY}$ base on the polarization of the beam (X=U,L) and the target (Y=U,L,T), taking values U (unpolarized), L (longitudinally polarized) and T (transversely polarized). Note, that spin orientations are indicated here with respect to the virtual photon direction. The fact, that the target is practically polarized along the beam direction causes a transverse spin contribution with respect to the virtual photon. As already outlined in Sec. 2.1.3, this transverse spin contribution in case of longitudinally polarized targets are suppressed in COMPASS kinematics. Contributions, coming from transverse polarizations will consequently be omitted in this analysis.

The ratio of longitudinal to transverse photon flux is given by

$$\varepsilon = \frac{1 - y - \frac{1}{4}\gamma^2 y^2}{1 - y + \frac{1}{2}y^2 + \frac{1}{4}\gamma^2 y^2}. \tag{2.53}$$

2.2.1 One Hadron SIDIS

One hadron SIDIS considers the case of at least one detected unpolarized final state hadron with momentum P_h and any, not necessarily detected, rest X in the final state:

$$\ell(l) + N(P) \rightarrow \ell(l') + h(P_h) + X(P_X). \tag{2.54}$$

The corresponding Feynman graph is shown in Fig. 2.11. In addition to the simple DIS process, it involves the fragmentation of the struck quark, also called hadronization, in the QCD parton model theoretically described by fragmentation functions (FFs). The calculation of the respective cross section at lowest order is usually carried out on basis of the extended handbag diagram, shown on the right side of Fig. 2.11, where the fragmentation process is encoded in the fragmentation correlation function Δ, illustrated by the upper bulb. Here, it is convenient to choose a reference frame, where the nucleon and the detected hadron move collinearly, implicating a non-zero transverse component of the virtual photon momentum. In this frame, the relevant light-cone vectors can be parametrized as

$$\begin{aligned} P^\mu &= \left[P^+, \frac{M^2}{2P^+}, \mathbf{0}_T\right] \qquad p^\mu = \left[xP^+, \frac{p^2 + \boldsymbol{p}_T^2}{2xP^+}, \boldsymbol{p}_T\right] \qquad P_h^\mu = \left[\frac{M_h^2}{2P_h^-}, P_h^-, \mathbf{0}_T\right] \\ q^\mu &= \left[-xP^+, \frac{Q^2}{2xP^+}, \boldsymbol{q}_T\right] \quad k^\mu = \left[\frac{z\,(k^2 + \boldsymbol{k}_T^2)}{2P_h^-}, \frac{P_h^-}{z}, \boldsymbol{k}_T\right] \end{aligned} \tag{2.55}$$

where z denotes the fractional energy of the produced hadron, calculable via

$$z = \frac{P \cdot P_h}{P \cdot q} \overset{\text{TRF}}{=} \frac{E_h}{\nu}. \tag{2.56}$$

The transverse component of the virtual photon in this frame can be related up to $1/Q^2$-corrections to the transverse component of the observed hadron momentum

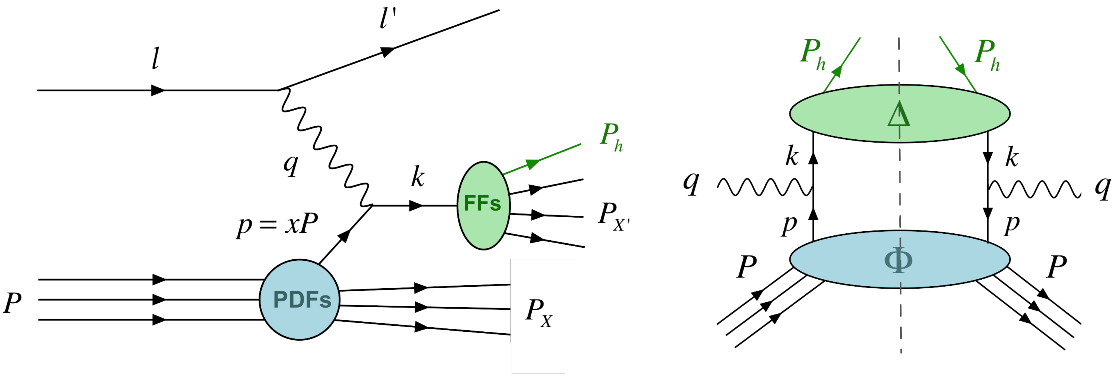

Figure 2.11: The one hadron SIDIS process in leading order. Left: Feynman graph. Right: Handbag diagram.

in respect to the gamma-nucleon system, where the target and the virtual photon momenta are collinear:

$$\boldsymbol{q}_T = -\frac{\boldsymbol{P}_{h\perp}}{z}. \tag{2.57}$$

2.2.1.1 One Hadron Fragmentation Functions

The hadronic tensor, extended by the fragmentation correlation function Δ reads

$$W^{\mu\nu} = \sum_q e_q^2 \int \frac{d^4p}{(2\pi)^4} \int \frac{d^4k}{(2\pi)^4} \delta\left((p+q-k)^2\right) \operatorname{Tr}\left[\Phi(p,P,S)\gamma^\mu \Delta(k,P_h,S_h)\gamma^\nu\right], \tag{2.58}$$

whereas Φ is the quark-quark correlation matrix already encountered in inclusive DIS. The new decay correlator Δ is defined as

$$\Delta_{ij}(k,P_h,S_h) = \sum_X \int \frac{d^3\boldsymbol{P}_X}{(2\pi)^3 2E_X} \int d^4\xi \mathrm{e}^{ik\xi} \left\langle 0\right| \psi_i(\xi) \left|P_h S_h, X\right\rangle \left\langle P_h S_h, X\right| \bar{\psi}_j(0) \left|0\right\rangle. \tag{2.59}$$

The decay matrix can be decomposed in a similar way as it was done for the quark-quark correlation function in Section 2.1.4.2, yielding eight transverse momentum dependent FFs at leading twist. When considering the production of spinless and unpolarized hadrons, it can be parametrized as a combination of the unpolarized FF $D_1(z,k_T^2)$ and the Collins FF $H_1^\perp(z,k_T^2)$ as

$$\Delta(z,k_T)\Big|_{\text{twist 2}} = \frac{1}{2}\left\{D_1(z,k_T^2)\not{n}_- + iH_1^\perp(z,k_T^2)\frac{[\not{k}_T,\not{n}_-]}{2M_h}\right\}. \tag{2.60}$$

The unpolarized FF $D_1(z,k_T^2)$ is chiral- and T-even, i.e. it doesn't change sign under helicity or time reversal operations, while the Collins FF $H_1^\perp(z,k_T^2)$ is chiral-odd and T-odd. In contrast to the case of PDFs, there is no time-reversal constraint for FFs and hence no additional interaction is required between the final or the initial state for T-odd functions to be non-zero, as the hadronic rest in the final state is not known.

The probabilistic interpretation of TMD FFs is analogous to that of the corresponding TMD PDFs at leading twist. In the nucleon-hadron frame, where z can be interpreted as the longitudinal energy fraction of the hadron, the FFs describe the probability differences of finding the struck quark, characterized by a transverse momentum $k_T^2 = |\boldsymbol{k}_T|^2$ and a certain spin state, to fragment into an unpolarized hadron with energy fraction z. The indication of the hadron type in the notation of FFs is neglected here for brevity.

In further analogy to the case of PDFs, four additional TMD FFs appear when considering the fragmentation into unpolarized hadrons at twist-3. The whole set of k_T-dependent FFs is listed in Tab. 2.4 according to the polarization of the fragmenting quark.

Table 2.4: One hadron TMD FFs, describing the fragmentation of a quark (blue bulb) with a certain polarization (rows, black arrows) into an unpolarized hadron (green bulb). All functions depend on z and k_T^2.

		Twist-2	Twist-3
Quark P.	U	Unpolarized $D_1 =$ 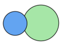	$D^{\perp}$
	L		$G^{\perp}$
	T	Collins $H_1^{\perp} =$ 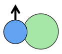 – 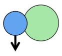	H, E

2.2.1.2 One Hadron SIDIS Cross Section

The cross section of one hadron SIDIS, given in the laboratory frame, can be derived in a model-independent way and is commonly chosen to be differential in the variables x, y, ϕ, z, ϕ_h and $P_{h\perp}^2$, where $d\phi \approx d\phi_S$ in DIS. The azimuthal angle ϕ_h is enclosed by the scattering plane, spread by $\boldsymbol{l}$ and $\boldsymbol{l}'$, and the hadron production plane, spread by $\boldsymbol{P}_h$ and $\boldsymbol{q}$, as shown in Fig. 2.12. Given the momenta in the laboratory frame, it can be explicitly calculated according to

$$\phi_h = \frac{(\boldsymbol{q} \times \boldsymbol{l}) \cdot \boldsymbol{P}_h}{|(\boldsymbol{q} \times \boldsymbol{l}) \cdot \boldsymbol{P}_h|} \arccos\left(\frac{(\boldsymbol{q} \times \boldsymbol{l}) \cdot (\boldsymbol{q} \times \boldsymbol{P}_h)}{|\boldsymbol{q} \times \boldsymbol{l}| \cdot |\boldsymbol{q} \times \boldsymbol{P}_h|}\right). \qquad (2.61)$$

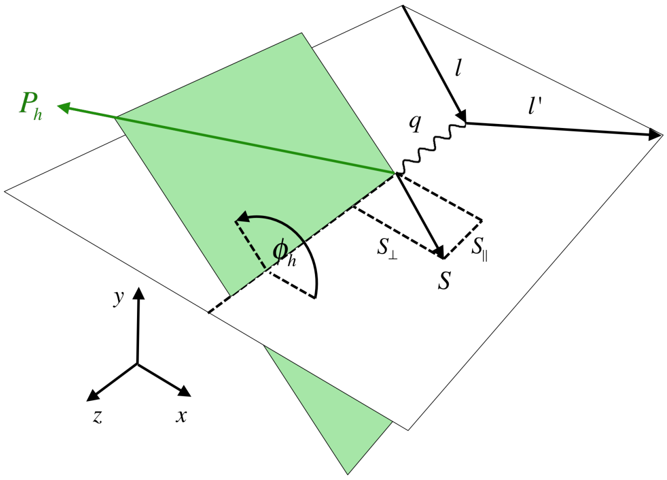

Figure 2.12: Sketch of the considered SIDIS process, including the relevant variables. The nucleon is assumed to be longitudinally polarized either in or against the direction of the incoming lepton.

The partial cross sections at twist-3 level, referring to an either unpolarized or longitudinally polarized target, read

$$d\sigma_{UU} \propto F_{UU,T} + \varepsilon F_{UU,L} + \sqrt{2\varepsilon(1+\varepsilon)}\cos(\phi_h) F_{UU}^{\cos(\phi_h)} + \varepsilon\cos(2\phi_h) F_{UU}^{\cos(2\phi_h)} \quad (2.62)$$

$$d\sigma_{LU} \propto \sqrt{2\varepsilon(1-\varepsilon)}\sin(\phi_h) F_{LU}^{\sin(\phi_h)} \quad (2.63)$$

$$d\sigma_{UL} \propto \sqrt{2\varepsilon(1+\varepsilon)}\sin(\phi_h) F_{UL}^{\sin(\phi_h)} + \varepsilon\sin(2\phi_h) F_{UL}^{\sin(2\phi_h)} \quad (2.64)$$

$$d\sigma_{LL} \propto \sqrt{1-\varepsilon^2} F_{LL} + \sqrt{2\varepsilon(1-\varepsilon)}\cos(\phi_h) F_{LL}^{\cos(\phi_h)}. \quad (2.65)$$

The terms $F_{XY,Z}$, respectively $F_{XY}^{m(\phi_h)}$, denote structure functions, corresponding to a certain azimuthal modulation $m(\phi_h)$, a beam and target polarization X and Y, and a photon polarization Z. In the QCD parton model interpretation, they involve sums of p_T- and k_T-weighted convolutions of TMD PDFs and FFs. Their detailed expressions are summarized in the appendix A.2.1.

An overview about the structure of the particular cross section terms involved in Eq. (2.62) - (2.65), including the contributing particular products of PDFs and FFs, is given in Tab. 2.5. Concerning the target spin dependent azimuthal terms, only the amplitude of the $\sin(2\phi_h)$ modulation is of leading twist, while others are suppressed with M/Q. The twist-3 terms involve contributions of several combinations of either a leading-twist PDF and a twist-3 FF or vice versa. The capital letters marked with tilde are, in analogy to the case of PDFs, twist-3 interaction-dependent FFs.

Table 2.5: Dominating terms of the considered one hadron SIDIS cross section up to twist-3 level. The involved convolutions of PDFs and FFs are also listed. For the detailed expressions of structure functions see Appendix A.2.1.

XY	Twist	$m(\phi_h)$	TMD PDFs and FFs, involved in $F_{XY}^{m(\phi_h)}$
UU	2	1	$f_1 D_1$
	3	$\cos(\phi_h)$	$h H_1^{\perp} + f_1 \tilde{D}^{\perp} + f^{\perp} D_1 + h_1^{\perp} \tilde{H}$
	2	$\cos(2\phi_h)$	$h_1^{\perp} H_1^{\perp}$
LU	3	$\sin(\phi_h)$	$e H_1^{\perp} + f_1 \tilde{G}^{\perp} + g^{\perp} D_1 + h_1^{\perp} \tilde{E}$
UL	3	$\sin(\phi_h)$	$h_L H_1^{\perp} + g_{1L} \tilde{G}^{\perp} + f_L^{\perp} D_1 + h_{1L}^{\perp} \tilde{H}$
	2	$\sin(2\phi_h)$	$h_{1L}^{\perp} H_1^{\perp}$
LL	2	1	$g_{1L} D_1$
	3	$\cos(\phi_h)$	$e_L H_1^{\perp} + g_{1L} \tilde{D}^{\perp} + g_L^{\perp} D_1 + h_{1L}^{\perp} \tilde{E}$

2.2.2 Two Hadron SIDIS

In two hadron SIDIS at least one unpolarized hadron pair, produced in the target fragmentation region, is detected in the final state:

$$\ell(l) + N(P) \to \ell(l') + h_1(P_1) + h_2(P_2) + X(P_X). \tag{2.66}$$

In this thesis pairs of oppositely charged hadrons are studied. For reasons of discriminability, h_1 is defined to be the positively, h_2 the negatively charged hadron. The corresponding Feynman diagram is depicted in Fig. 2.13. Here, the struck quark fragments into two unpolarized hadrons with masses M_1 and M_2 and a common invariant mass M_h.

The theoretical approach to describe the two hadron SIDIS process in leading twist is based on the handbag diagram in Fig. 2.13 and entails basic analogies to the one hadron case. The fragmentation into two hadrons is here encoded in the fragmentation correlation function Ξ, symbolized by the upper bulb, and parametrized by dihadron fragmentation functions (DiFFs).

By choosing a frame, where the hadron-pair has no transverse momentum, the expressions of the light-cone-vectors are identical to the one hadron case, just replacing the one hadron variables with the following corresponding two hadron ones:

$$P_h = P_1 + P_2 \tag{2.67}$$

$$z = z_1 + z_2. \tag{2.68}$$

Additionally, it is common to introduce the relative four-momentum $R = \frac{1}{2}(P_1 - P_2)$, parametrized in light-cone coordinates as

$$R^\mu = \left[\frac{(M_1^2 - M_2^2) - \frac{\xi}{2} M_h^2}{2P_h^-}, \frac{\xi}{2} P_h^-, \boldsymbol{R}_T \right], \tag{2.69}$$

where $\xi = 2R^-/P_h^-$.

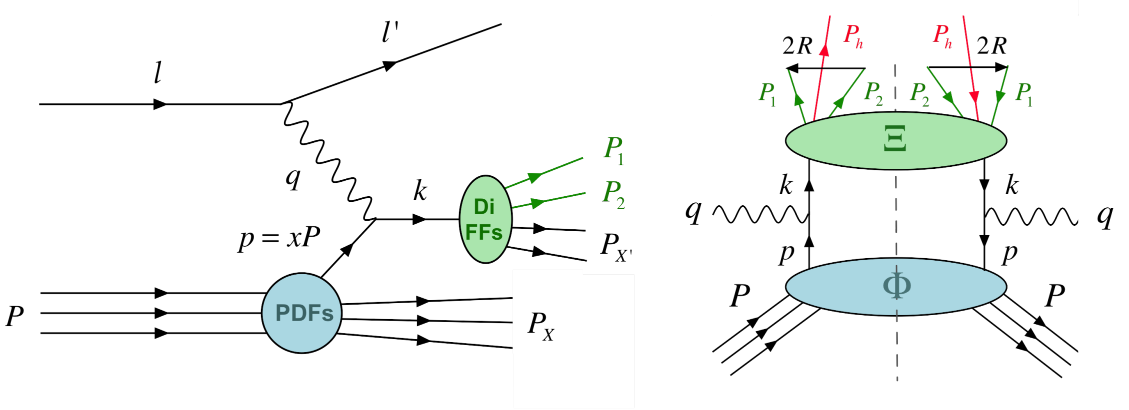

Figure 2.13: The two hadron SIDIS process at leading order. Left: Feynman graph. Right: Handbag diagram.

2.2.2.1 Two Hadron Fragmentation Functions

The hadronic tensor from Eq. (2.58) can be easily adapted to the two hadron case by replacing the fragmentation correlator by the new dihadron fragmentation function

$$\Xi_{ij}(k,P_1,P_2)=\sum_X\int\frac{d^3\boldsymbol{P}_X}{(2\pi)^3 2E_X}\int d^4\zeta \mathrm{e}^{ik\zeta}\left\langle 0\right|\psi_i(\zeta)\left|P_1P_2,X\right\rangle\left\langle P_1P_2,X\right|\bar{\psi}_j(0)\left|0\right\rangle. \tag{2.70}$$

The following k_T-dependent projections emerge at leading twist:

$$\Xi^{[\gamma^-]}(z,\xi,k_T^2,R_T^2,\boldsymbol{k}_T\cdot\boldsymbol{R}_T)=D_1(z,\xi,k_T^2,R_T^2,\boldsymbol{k}_T\cdot\boldsymbol{R}_T) \tag{2.71}$$

$$\Xi^{[\gamma^-\gamma_5]}(z,\xi,k_T^2,R_T^2,\boldsymbol{k}_T\cdot\boldsymbol{R}_T)=\frac{\epsilon_T^{ij}R_{Ti}k_{Tj}}{M_1M_2}G_1^{\perp}(z,\xi,k_T^2,R_T^2,\boldsymbol{k}_T\cdot\boldsymbol{R}_T) \tag{2.72}$$

$$\begin{aligned}\Xi^{[\mathrm{i}\gamma^i\gamma^-\gamma_5]}(z,\xi,k_T^2,R_T^2,\boldsymbol{k}_T\cdot\boldsymbol{R}_T)&=\frac{\epsilon_T^{ij}R_{Tj}}{M_1+M_2}\overline{H}_1^{\sphericalangle}(z,\xi,k_T^2,R_T^2,\boldsymbol{k}_T\cdot\boldsymbol{R}_T)\\&\quad+\frac{\epsilon_T^{ij}k_{Tj}}{M_1+M_2}H_1^{\perp}(z,\xi,k_T^2,R_T^2,\boldsymbol{k}_T\cdot\boldsymbol{R}_T).\end{aligned} \tag{2.73}$$

Four k_T-dependent DiFFs D_1, $G_1^{\perp}$, $\overline{H}_1^{\perp}$ and $H_1^{\sphericalangle}$ are involved, whereas a notational distinction between FFs and DiFFs is omitted. Nevertheless, each DiFF type can be interpreted as the direct counterpart of a corresponding FF with the specification of a hadron pair in the final state. Following the way of illustration in case of FFs, the leading twist DiFFs can be interpreted as probability differences of a quark (blue bulb) with a certain polarization to fragment into unpolarized hadrons (green bulbs):

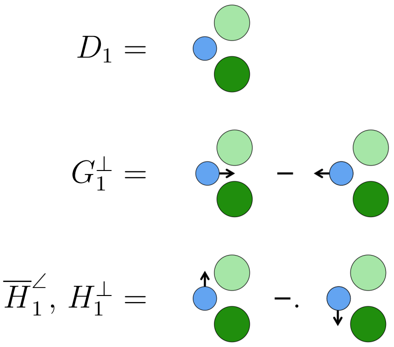

Only the function $G_1^{\perp}$ is k_T-even. The unpolarized DiFF, as well as the functions $\overline{H}_1^{\sphericalangle}$ and $H_1^{\perp}$, both associated to the fragmentation of a transversely polarized quark, survive the integration over k_T. The latter ones merge into one function, H_1, which can be understood as the dihadronic counterpart to the k_T-integrated Collins function. The DiFFs $G_1^{\perp}$, $\overline{H}_1^{\sphericalangle}$ and $H_1^{\perp}$ are naive T-odd. They originate from the interference of two production amplitudes with two different phases and are therefore commonly referred to as interference fragmentation functions (IFFs). A first k_T-dependent analysis of two hadron SIDIS at subleading twist was recently presented in Ref. [47].

2.2.2.2 Partial Wave Expansion

To obtain a detailed structure of the two hadron SIDIS cross section, it is useful to expand the decay correlator into partial waves, considering the center of mass frame of the hadron pair. In this frame, the emission occurs back to back and the key variable can be chosen as the angle θ, which describes the emission angle between the positively charged hadron in the center of mass frame and the momentum of the hadron pair in the target rest frame, as illustrated in Fig. 2.14. So can ξ be expressed as a linear function of $\cos\theta$ as

$$\xi = \frac{1}{M_h}\left(\sqrt{M_1^2 + |\boldsymbol{R}|^2} - \sqrt{M_2^2 + |\boldsymbol{R}|^2} - 2|\boldsymbol{R}|\cos\theta\right), \tag{2.74}$$

where

$$|\boldsymbol{R}| = \frac{1}{2M_h}\sqrt{M_h^2 - 2\left(M_1^2 + M_2^2\right) + \left(M_1^2 - M_2^2\right)^2}. \tag{2.75}$$

If the invariant mass of the hadron pair is small, it can be assumed to be produced mainly in the first two harmonics, namely in s- and the p-wave resonances. By transforming the dependence on $\cos\theta$ in the basis of Legendre polynomials, the extended leading twist k_T-integrated DiFFs read

$$\begin{aligned} D_1(z, \xi(\cos\theta), M_h^2) \approx{} & D_{1,UU}^{ss+pp}(z, M_h^2) + \cos\theta\, D_{1,UL}^{sp}(z, M_h^2) \\ & + \frac{1}{4}(3\cos^2\theta - 1)\, D_{1,LL}^{pp}(z, M_h^2) \end{aligned} \tag{2.76}$$

$$H_1^{\angle}(z, \xi(\cos\theta), M_h^2) \approx H_{1,UT}^{\angle sp}(z, M_h^2) + \cos\theta\, H_{1,LT}^{\angle pp}(z, M_h^2). \tag{2.77}$$

Here, the two additional subscripts indicate the polarization states of the outgoing and the incoming hadron pair, respectively. When applying the concept of partial wave expansion to k_T-dependent DiFFs the situation gets more involved. As they depend on $\boldsymbol{k}_T \cdot \boldsymbol{R}_T$, additional azimuthal modulations emerge. This is studied in detail in Ref. [48], including a thorough derivation of the corresponding leading-twist cross section, summarized in the following section.

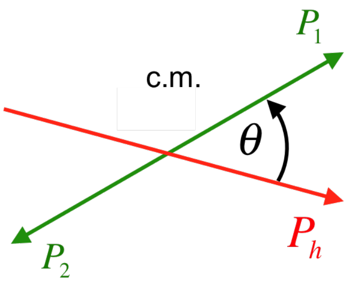

Figure 2.14: Illustration of the emission angle θ in the center of mass frame of the hadron pair.

2.2.2.3 Two Hadron SIDIS Cross Section

The two hadron SIDIS cross section is usually modulated on basis of the azimuthal angles ϕ_h and ϕ_R, illustrated in Fig. 2.15. In the target rest frame, ϕ_h can be calculated according to Eq. 2.61, whereas ϕ_R is defined as the angle between the $\boldsymbol{q}$-$\boldsymbol{R}_\perp$-plane and the scattering plane, hence

$$\phi_R = \frac{(\boldsymbol{q} \times \boldsymbol{l}) \cdot \boldsymbol{R}_\perp}{|(\boldsymbol{q} \times \boldsymbol{l}) \cdot \boldsymbol{R}_\perp|} \arccos \left(\frac{(\boldsymbol{q} \times \boldsymbol{l}) \cdot (\boldsymbol{q} \times \boldsymbol{R}_\perp)}{|\boldsymbol{q} \times \boldsymbol{l}| \cdot |\boldsymbol{q} \times \boldsymbol{R}_\perp|} \right) . \tag{2.78}$$

The vector $\boldsymbol{R}_\perp$ describes the transverse component of $\boldsymbol{R}$ with respect to the virtual photon. For calculations, $\boldsymbol{R}_\perp$ is taken as the transverse vector $\boldsymbol{R}_T$, defined as

$$\boldsymbol{R}_T = \frac{z_2 \boldsymbol{P}_{1T} - z_1 \boldsymbol{P}_{2T}}{z} =: \xi_2 \boldsymbol{P}_{1T} - \xi_1 \boldsymbol{P}_{2T} \tag{2.79}$$

where transverse components are with respect to the lepton axis in the TRF, and $\xi_i = z_i/z$ is the energy fraction of a certain hadron with respect to the total pair energy. This definition of $\boldsymbol{R}_T$ ensures the invariance of ϕ_R against boosts in the direction of the virtual photon and coincides with the general one up to corrections of order $1/Q^2$ [47].

The expanded leading-twist two hadron SIDIS cross section is commonly chosen to be differential in x, y, ϕ_S, z, ϕ_h, $P_{h\perp}^2$, as is the one hadron cross section, and additionally in the dihadronic variables ϕ_R, M_h and $\cos\theta$. The partial cross sections, corresponding to an either unpolarized or longitudinally polarized target, fulfill the proportionalities Eq. (2.80) - Eq. (2.83) [47, 48].

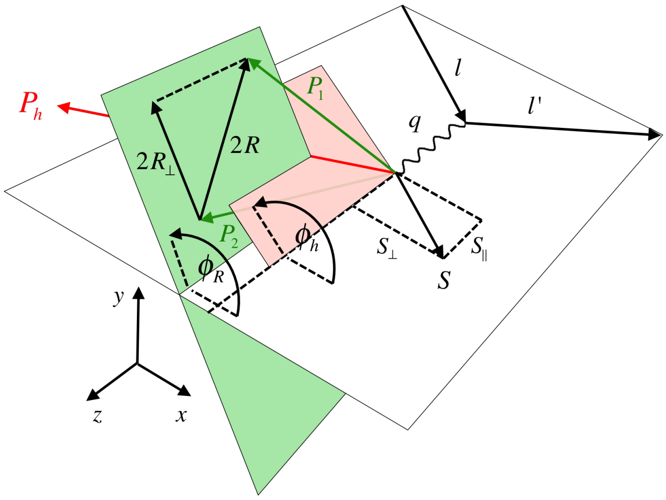

Figure 2.15: Sketch of the considered two hadron SIDIS process, including the relevant variables. The nucleon is assumed to be longitudinally polarized either in or against the direction of the incoming lepton.

$$\begin{aligned}
d^9\sigma_{UU} \propto\ & F_{UU,L} + \cos\theta F_{UU}^{\cos\theta} + \frac{1}{3}\left(3\cos^2\theta - 1\right) F_{UU}^{\frac{1}{3}\left(3\cos^2\theta-1\right)} \\
& + \cos\left(\phi_h - \phi_R\right)\left(\sin\theta F_{UU}^{\cos\left(\phi_h-\phi_R\right)\sin\theta} \sin 2\theta F_{UU}^{\cos\left(\phi_h-\phi_R\right)\sin 2\theta}\right) \\
& + \cos\left(2\phi_h - 2\phi_R\right)\sin^2\theta F_{UU}^{\cos\left(2\phi_h-2\phi_R\right)\sin^2\theta} \\
& + \varepsilon\Bigg\{ F_{UU,T} + \cos\left(2\phi_h\right)\left(F_{UU}^{\cos\left(2\phi_h\right)} + \cos\theta F_{UU}^{\cos\left(2\phi_h\right)\cos\theta} \right.\\
& \left. + \frac{1}{3}\left(3\cos^2\theta - 1\right) F_{UU}^{\cos\left(2\phi_h\right)\frac{1}{3}\left(3\cos^2\theta-1\right)}\right) \\
& + \cos\left(\phi_h + \phi_R\right)\left(\sin\theta F_{UU}^{\cos\left(\phi_h+\phi_R\right)\sin\theta} + \sin 2\theta F_{UU}^{\cos\left(\phi_h+\phi_R\right)\sin 2\theta}\right) \\
& + \cos\left(2\phi_R\right)\sin^2\theta F_{UU}^{\cos\left(2\phi_R\right)\sin^2\theta} \\
& + \cos\left(3\phi_h - \phi_R\right)\left(\sin\theta F_{UU}^{\cos\left(3\phi_h-\phi_R\right)\sin\theta} + \sin 2\theta F_{UU}^{\cos\left(3\phi_h-\phi_R\right)\sin 2\theta}\right) \\
& + \cos\left(4\phi_h - 2\phi_R\right)\sin^2\theta F_{UU}^{\cos\left(4\phi_h-2\phi_R\right)\sin^2\theta}\Bigg\}
\end{aligned} \tag{2.80}$$

$$\begin{aligned}
d^9\sigma_{LU} \propto \sqrt{1-\varepsilon^2}\Bigg\{ & \sin\left(\phi_h - \phi_R\right)\left(\sin\theta F_{LU}^{\sin\left(\phi_h-\phi_R\right)\sin\theta} + \sin 2\theta F_{LU}^{\sin\left(\phi_h-\phi_R\right)\sin 2\theta}\right) \\
& + \sin\left(2\phi_h - 2\phi_R\right)\sin^2\theta F_{LU}^{\sin\left(2\phi_h-2\phi_R\right)\sin^2\theta}\Bigg\}
\end{aligned} \tag{2.81}$$

$$\begin{aligned}
d^9\sigma_{UL} \propto\ & \sin\left(\phi_h - \phi_R\right)\left(\sin\theta F_{UL}^{\sin\left(\phi_h-\phi_R\right)\sin\theta} + \sin 2\theta F_{UL}^{\sin\left(\phi_h-\phi_R\right)\sin 2\theta}\right) \\
& + \sin\left(2\phi_h - 2\phi_R\right)\sin^2\theta F_{UL}^{\sin\left(2\phi_h-2\phi_R\right)\sin^2\theta} \\
& + \varepsilon\Bigg\{ \sin\left(2\phi_h\right)\left(F_{UL}^{\sin\left(2\phi_h\right)} + \cos\theta F_{UL}^{\sin\left(2\phi_h\right)\cos\theta} \right.\\
& \left. + \frac{1}{3}\left(3\cos^2\theta - 1\right) F_{UL}^{\sin\left(2\phi_h\right)\frac{1}{3}\left(3\cos^2\theta-1\right)}\right) \\
& + \sin\left(\phi_h + \phi_R\right)\left(\sin\theta F_{UL}^{\sin\left(\phi_h+\phi_R\right)\sin\theta} + \sin 2\theta F_{UL}^{\sin\left(\phi_h+\phi_R\right)\sin 2\theta}\right) \\
& + \sin\left(2\phi_R\right)\sin^2\theta F_{UL}^{\sin\left(2\phi_R\right)\sin^2\theta} \\
& + \sin\left(3\phi_h - \phi_R\right)\left(\sin\theta F_{UL}^{\sin\left(3\phi_h-\phi_R\right)\sin\theta} + \sin 2\theta F_{UL}^{\sin\left(3\phi_h-\phi_R\right)\sin 2\theta}\right) \\
& + \sin\left(4\phi_h - 2\phi_R\right)\sin^2\theta F_{UL}^{\sin\left(4\phi_h-2\phi_R\right)\sin^2\theta}\Bigg\}
\end{aligned} \tag{2.82}$$

$$\begin{aligned}
d^9\sigma_{LL} \propto \sqrt{1-\varepsilon^2}\Bigg\{ & F_{LL} + \cos\theta F_{LL}^{\cos\theta} + \frac{1}{3}\left(3\cos^2\theta - 1\right) F_{LL}^{\frac{1}{3}\left(3\cos^2\theta-1\right)} \\
& + \cos\left(\phi_h - \phi_R\right)\left(\sin\theta F_{LL}^{\cos\left(\phi_h-\phi_R\right)\sin\theta} + \sin 2\theta F_{LL}^{\cos\left(\phi_h-\phi_R\right)\sin 2\theta}\right) \\
& + \cos\left(2\phi_h - 2\phi_R\right)\sin^2\theta F_{LL}^{\cos\left(2\phi_h-2\phi_R\right)\sin^2\theta}\Bigg\}
\end{aligned} \tag{2.83}$$

Within the Parton Model interpretation, the structure functions $F_{XY,Z}^{m(\phi_h,\phi_R)w(\theta)}$ can be expressed as convolutions of weighted products of TMD PDFs and DiFFs. Please note that, in contrast to Ref. [48], minus signs are absorbed into the definitions of structure functions. Their detailed expressions are given in the appendix A.2.2, using the common abbreviation

$$H_{1,XY}^{\angle} = \overline{H}_{1,XY}^{\angle} + \frac{|\boldsymbol{k}_T|}{|\boldsymbol{R}_T|}\, H_{1,XY}^{\perp}, \tag{2.84}$$

whereas all TMD DiFFs depend on z, k_T^2 and M_h.

The presented cross section formulas involve contributions from several azimuthal modulations in ϕ_h and ϕ_R, whereas their amplitudes are made up by sums of θ-weighted structure functions. As will be shown in Sec. 4.4.1.1, the presented analysis is in first order only sensitive to $\sin\theta$- and the $\sin^2\theta$-weighted terms, due to the symmetric acceptance in θ of the COMPASS detector. The structures of the dominating terms, including the involved TMD PDFs and DiFFs, are summarized in Tab. 2.6. Each structure function $F_{XL}^{m(\phi_h,\phi_R)w(\theta)}$, corresponding to a longitudinally polarized nucleon, involve either the helicity distribution g_{1L} or the Worm-Gear distribution $h_{1L}^{\perp}$, convoluted with a TMD DiFF of a certain partial-wave characteristic.

A detailed study of the two hadron SIDIS cross section at subleading twist, including transverse momenta of involved particles, was recently presented by Gliske et. al. [47]. By introducing a modified definition of DiFFs compared to Ref. [48], a comprehensive framework was proposed, which allows for the derivation of SIDIS cross sections for any final state of any polarization, and links also the one and the two hadron SIDIS cross sections. As already found in Ref. [49], the $P_{h\perp}$-integrated two hadron cross section at twist-3 has a similar structure as the one hadron cross section from Eq. (2.62) - Eq. (2.65), with ϕ_h replaced by ϕ_R.

The presented two hadron analysis concentrates on the study of modulation amplitudes in leading twist from Eq. (2.82) and Eq. (2.83), corresponding to a longitudinally polarized target. Nevertheless, collinear twist-3 amplitudes are considered in an additional extended study, separately outlined in Sec. 9.

Table 2.6: Dominating terms of the considered two hadron SIDIS cross section at leading twist. The involved convolutions of TMD PDFs and DiFFs are also listed. For the detailed expressions of structure functions see A.2.1.

XY	$m(\phi_h, \phi_R)$	$w(\theta)$	TMD PDFs and DiFFs, involved in $F_{XY}^{m(\phi_h,\phi_R)w(\theta)}$
UU	1	1	$f_1 D_{1,UU}$
	$\cos(\phi_h - \phi_R)$	$\sin\theta$	$f_1 D_{1,UT}$
	$\cos(2\phi_h - 2\phi_R)$	$\sin^2\theta$	$f_1 D_{1,TT}$
	$\cos(2\phi_h)$	1	$h_1^\perp H_{1,UU}^\perp$
	$\cos(\phi_h + \phi_R)$	$\sin\theta$	$h_1^\perp H_{1,UT}^\angle$
	$\cos(2\phi_R)$	$\sin^2\theta$	$h_1^\perp H_{1,TT}^\angle$
	$\cos(3\phi_h - \phi_R)$	$\sin\theta$	$h_1^\perp H_{1,UT}^\perp$
	$\cos(4\phi_h - 2\phi_R)$	$\sin^2\theta$	$h_1^\perp H_{1,TT}^\perp$
LU	$\sin(\phi_h - \phi_R)$	$\sin\theta$	$f_1 G_{1,UT}^\perp$
	$\sin(2\phi_h - 2\phi_R)$	$\sin^2\theta$	$f_1 G_{1,TT}^\perp$
UL	$\sin(\phi_h - \phi_R)$	$\sin\theta$	$g_{1L} G_{1,UT}^\perp$
	$\sin(2\phi_h - 2\phi_R)$	$\sin^2\theta$	$g_{1L} G_{1,TT}^\perp$
	$\sin(2\phi_h)$	1	$h_{1L}^\perp H_{1,UU}^\perp$
	$\sin(\phi_h + \phi_R)$	$\sin\theta$	$h_{1L}^\perp H_{1,UT}^\angle$
	$\sin(2\phi_R)$	$\sin^2\theta$	$h_{1L}^\perp H_{1,TT}^\angle$
	$\sin(3\phi_h - \phi_R)$	$\sin\theta$	$h_{1L}^\perp H_{1,UT}^\perp$
	$\sin(4\phi_h - 2\phi_R)$	$\sin^2\theta$	$h_{1L}^\perp H_{1,TT}^\perp$
LL	1	1	$g_{1L} D_{1,UU}$
	$\cos(\phi_h - \phi_R)$	$\sin\theta$	$g_{1L} D_{1,UT}$
	$\cos(2\phi_h - 2\phi_R)$	$\sin^2\theta$	$g_{1L} D_{1,TT}$

2.3 Defininition of Azimuthal Asymmetries

Azimuthal asymmetries are commonly defined in terms of structure functions as

$$A_{XY}^{m(\phi_h,\phi_R)} = \frac{F_{XY}^{m(\phi_h,\phi_R)}}{F_{UU,T} + \varepsilon F_{UU,L}}, \tag{2.85}$$

where $m(\phi_h, \phi_R)$ is a certain azimuthal modulation, contained in the underlying cross section. As the structure functions are composed of convolutions of PDFs and FFs within factorized QCD model interpretation, measuring asymmetries can provide an insight into related spin dependent effects.

The purpose of this work is to measure azimuthal asymmetries in both one and two hadron SIDIS when scattering muons off longitudinally polarized protons. The specific framework is given in the following, separately for the one and the two hadron case.

2.3.1 One Hadron Asymmetries

Using Eq. (2.85) and considering a longitudinally polarized target, one can reformulate the one hadron cross section in terms of asymmetries as

$$\begin{aligned} d\sigma \propto\ & 1 + D_{UU}^{\cos(\phi_h)} A_{UU}^{\cos(\phi_h)} \cos(\phi_h) + D_{UU}^{\cos(2\phi_h)} A_{UU}^{\cos(2\phi_h)} \cos(2\phi_h) \\ & + \lambda_\ell D_{LU}^{\sin(\phi_h)} A_{LU}^{\sin(\phi_h)} \sin(\phi_h) \\ & + S_L \Big(D_{UL}^{\sin(\phi_h)} A_{UL}^{\sin(\phi_h)} \sin(\phi_h) + D_{UL}^{\sin(2\phi_h)} A_{UL}^{\sin(2\phi_h)} \sin(2\phi_h) \Big) \\ & + \lambda_\ell S_L \Big(D_{LL}^{1} A_{LL}^{1} + D_{LL}^{\cos(\phi_h)} A_{LL}^{\cos(\phi_h)} \cos(\phi_h) \Big) \end{aligned} \tag{2.86}$$

with the depolarization factors

$$D_{UU}^{\cos(2\phi_h)} = D_{UL}^{\sin(2\phi_h)} = \varepsilon \tag{2.87}$$

$$D_{UU}^{\cos(\phi_h)} = D_{UL}^{\sin(\phi_h)} = \sqrt{2\varepsilon(1+\varepsilon)} \tag{2.88}$$

$$D_{LU}^{\sin(\phi_h)} = D_{LL}^{\cos(\phi_h)} = \sqrt{2\varepsilon(1-\varepsilon)} \tag{2.89}$$

$$D_{LL}^{1} = \sqrt{1-\varepsilon^2}. \tag{2.90}$$

In total, a set of three longitudinal target-spin azimuthal asymmetries $A_{XL}^{m(\phi)}$ are involved, corresponding to the modulations

$$\begin{aligned} m_1(\phi_h) &= \sin(\phi_h) \\ m_2(\phi_h) &= \sin(2\phi_h) \\ m_3(\phi_h) &= \cos(\phi_h). \end{aligned} \tag{2.91}$$

Here, only $A_{UL}^{\sin(2\phi_h)}$ is of leading twist, while $A_{UL}^{\sin(\phi_h)}$ and $A_{LL}^{\cos(\phi_h)}$ are of twist-3.

2.3.2 Two Hadron Asymmetries

The leading twist partial cross sections for two hadron SIDIS with longitudinally polarized target $d\sigma_{UL}$ (2.82) and $d\sigma_{LL}$ (2.83) contain the nine azimuthal modulations

$$\begin{aligned}
m_1(\phi_h, \phi_R) &= \sin(\phi_h - \phi_R) \\
m_2(\phi_h, \phi_R) &= \sin(2\phi_h - 2\phi_R) \\
m_3(\phi_h, \phi_R) &= \sin(2\phi_h) \\
m_4(\phi_h, \phi_R) &= \sin(\phi_h + \phi_R) \\
m_5(\phi_h, \phi_R) &= \sin(2\phi_R) \\
m_6(\phi_h, \phi_R) &= \sin(3\phi_h - \phi_R) \\
m_7(\phi_h, \phi_R) &= \sin(4\phi_h - 2\phi_R) \\
m_8(\phi_h, \phi_R) &= \cos(\phi_h - \phi_R) \\
m_9(\phi_h, \phi_R) &= \cos(2\phi_h - 2\phi_R).
\end{aligned} \tag{2.92}$$

The cross section at leading twist can be reformulated in terms of asymmetries as

$$\begin{aligned}
d\sigma \propto\ & 1 + D_{UU}^{\cos(\phi_h-\phi_R)} A_{UU}^{\cos(\phi_h-\phi_R)} \cos(\phi_h - \phi_R) + ... \\
& + S_L \left(\sum_{i=1}^{7} D_{UL}^{m_i(\phi_h,\phi_R)} A_{UL}^{m_i(\phi_h,\phi_R)} m_i(\phi_h, \phi_R) \right) \\
& + \lambda_\ell S_L \left(D_{LL}^1 A_{LL}^1 + \sum_{i=8}^{9} D_{LL}^{m_i(\phi_h,\phi_R)} A_{LL}^{m_i(\phi_h,\phi_R)} m_i(\phi_h, \phi_R) \right),
\end{aligned} \tag{2.93}$$

whereas the relevant depolarization factors read

$$D_{UL}^{\sin(\phi_h-\phi_R)} = D_{UL}^{\sin(2\phi_h-2\phi_R)} = 1 \tag{2.94}$$

$$D_{UL}^{\sin(2\phi_h)} = D_{UL}^{\sin(\phi_h+\phi_R)} = D_{UL}^{\sin(2\phi_R)} = D_{UL}^{\sin(3\phi_h-\phi_R)} = D_{UL}^{\sin(4\phi_h-2\phi_R)} = \varepsilon \tag{2.95}$$

$$D_{LL}^1 = D_{LL}^{\cos(\phi_h-\phi_R)} = D_{LL}^{\cos(2\phi_h-2\phi_R)} = \sqrt{1-\varepsilon^2}. \tag{2.96}$$

In total there are seven azimuthal single-spin asymmetries $A_{UL}^{m(\phi_h,\phi_R)}$ and two azimuthal double-spin asymmetries $A_{LL}^{m(\phi_h,\phi_R)}$ involved.

When considering the p_T-integrated two hadron SIDIS cross section at subleading twist, two additional azimuthal target spin asymmetries are involved. These are the single-spin asymmetry $A_{UL}^{\sin(\phi_h)}$ and the double-spin asymmetry $A_{LL}^{\cos(\phi_h)}$. They are studied in a separated analysis in Chapter 9.

2.4 Principles of Measuring Asymmetries

The common approach to experimentally disentangle longitudinal target spin asymmetries in lepton-nucleon scattering is to measure counting rate ratios of type

$$A_{\parallel} = \frac{N^+ - rN^-}{N^+ + rN^-}, \tag{2.97}$$

where $N^{\pm}$ stands for the number of hadrons, respectively hadron pairs, being detected with the target polarization set either in (+) or against (−) the beam direction. The lepton spin, however, is kept being polarized in one orientation along the beam direction. The renormalization factor r accounts for unbalanced statistics of the two data sets with opposite polarizations. Considering an ideal measurement of $A_{\parallel}$, the spin-independent part of the cross section cancels out in the nominator, leaving a pure sensitivity on target spin dependent terms. By fitting $A_{\parallel}$ with an appropriate function, containing the angular modulations of the cross section, asymmetries can be identified as corresponding amplitudes.

However, acceptance and efficiency instabilities during the data taking as well as lepton flux changes, makes this method liable for systematic effects. To reduce these biasing effects, the COMPASS target is built up of three individually polarizable cells, allowing for a simultaneous measurement of both polarization states at the same time. To further cancel acceptance affects, more suitable methods are used in this work. The product ratio method, easy to implement but still prone to biased results due to acceptance variations, and a more sophisticated method, using the likelihood minimization technique, are explained in Sec. 5. In view of this, the theoretical framework is already set up in the following.

As already mentioned, the COMPASS target is made up by three cells, whereas the central cell has double length compared to the outer cells. For analytical purposes, it is convenient to regard the central cell as two cells with same size and polarization state. In longitudinal data taking mode, the polarization configuration is at least once per day changed from $+--+$ to $-++-$, where the signs stand for the polarization direction per cell.

The number of hadron pairs, respectively single hadrons, originating from a cell $i \in \{1, 2, 3, 4\}$ can be written as

$$N_i^{\pm}(\phi_h, \phi_R) = c_i^{\pm}(\phi_h, \phi_R)\left(1 + A_{XU}(\phi_h, \phi_R) \pm A_{XL}(\phi_h, \phi_R)\right), \tag{2.98}$$

with the factor

$$c_i^{\pm}(\phi_h, \phi_R) = \Phi_i^{\pm} a_i^{\pm}(\phi_h, \phi_R) n_i \sigma_{UU}, \tag{2.99}$$

containing the beam flux $\Phi_i^{\pm}$, the angular acceptance $a_i^{\pm}(\phi_h, \phi_R)$ and the number of protons n_i for specific cell i, and the (ϕ_h, ϕ_R)-independent part of the unpolarized cross section σ_{UU}. The terms $A_{XU}(\phi_h, \phi_R)$ and $A_{XL}(\phi_h, \phi_R)$ contain the azimuthal modulations, involved in the certain cross section, with corresponding amplitudes $A_{XY,\mathrm{Raw}}^{m(\phi_h,\phi_R)}$, called raw asymmetries. They read

$$A_{XU}(\phi_h) = A^{\cos(\phi_h)}_{UU,\text{Raw}} \cos(\phi_h) + A^{\cos(2\phi_h)}_{UU,\text{Raw}} \cos(2\phi_h) + A^{\sin(\phi_h)}_{LU,\text{Raw}} \cos(\phi_h) \tag{2.100}$$

$$A_{XL}(\phi_h) = A^{\sin(\phi_h)}_{UL,\text{Raw}} \sin(\phi_h) + A^{\sin(2\phi_h)}_{UL,\text{Raw}} \sin(2\phi_h) + A^{1}_{LL,\text{Raw}} + A^{\cos(\phi_h)}_{LL,\text{Raw}} \cos(\phi_h) \tag{2.101}$$

for the single hadron case, whereas for hadron pairs it is

$$A_{XU}(\phi_h, \phi_R) = A^{\cos(\phi_h-\phi_R)}_{UU,\text{Raw}} \cos(\phi_h - \phi_R) + ... + A^{\sin(2\phi_h-2\phi_R)}_{LU,\text{Raw}} \sin(2\phi_h - 2\phi_R) \tag{2.102}$$

$$\begin{aligned} A_{XL}(\phi_h, \phi_R) = &\sum_{i=1}^{7} A^{m_i(\phi_h,\phi_R)}_{UL,\text{Raw}} m_i(\phi_h, \phi_R) \\ &+ A^{1}_{LL,\text{Raw}} + \sum_{i=8}^{9} A^{m_i(\phi_h,\phi_R)}_{LL,\text{Raw}} m_i(\phi_h, \phi_R). \end{aligned} \tag{2.103}$$

Note, that the cross section in case of single hadrons depends only on the azimuthal angle ϕ_h. Nevertheless, the dependence on both ϕ_h and ϕ_R is kept in the following to allow for a common notation for both types of analyses.

Having extracted the longitudinal raw asymmetries with an appropriate fit, they have to be corrected concerning several factors, in order to obtain the final physical asymmetries:

$$A^{m(\phi_h,\phi_R)}_{UL} = \frac{A^{m(\phi_h,\phi_R)}_{UL,\text{Raw}}}{\langle f|P_T|D^{m(\phi_h,\phi_R)}_{UL}\rangle} \qquad A^{m(\phi_h,\phi_R)}_{LL} = \frac{A^{m(\phi_h,\phi_R)}_{LL,\text{Raw}}}{\langle fP_B|P_T|D^{m(\phi_h,\phi_R)}_{LL}\rangle} \tag{2.104}$$

Here, P_B and P_T are the polarization values of the beam and the target, respectively. $D^{m(\phi_h,\phi_R)}_{XL}$ are the depolarization factors, already defined in Sec. 2.3. The dilution factor f accounts for the fraction of polarizable target material. The asymmetry correction procedure is explained in detail in Sec. 5.3.

2.5 Results from Former Measurements

Measuring spin dependent asymmetries emerged as a powerful tool to investigate spin related phenomena inside nucleons and of hadronic fragmentation processes during recent decades. Since then, various experiments put effort on exploring this field of spin physics. The following summary gives an overview about the present status of analysis of longitudinal target spin asymmetries in SIDIS and serves as classification and motivation of the present work.

2.5.1 One Hadron Azimuthal Asymmetries

The first results on longitudinal target spin azimuthal asymmetries were obtained by the HERMES collaboration in semi-inclusive pion production, scattering positrons off longitudinally polarized protons at 27.6 GeV [50]. While the leading twist asymmetry $A_{UL}^{\sin(2\phi_h)}$ was found to be consistent with zero for both positively and negatively charged pions, the twist-3 asymmetry $A_{UL}^{\sin(\phi_h)}$ turned out to be clearly positive for π^+, characterized by a significant increase with rising x. Results of comparable size were later also reported by HERMES for neutral pions and in the electropdroduction of π^+ and K^+ on a deuterium target [51, 52]. The HERMES results for proton targets are collected in Fig. 2.16.

Measurements at CLAS, using a longitudinally polarized electron beam of 5.7 GeV and a longitudinally polarized proton target, could confirm a sizable $A_{UL}^{\sin(\phi_h)}$ asymmetry in an extended kinematic range and gave first evidence of a non-zero $A_{UL}^{\sin(2\phi_h)}$ asymmetry for both positively and negatively charged pions [55, 56]. As can be seen in the upper plot of Fig. 2.17, the results for π^+ were found to be in agreement with theoretical predictions, based on the PDF $h_{1L}^{\perp}$ from the chiral quark soliton model and the Collins FF $H_1^{\perp}$ extracted from HERMES [57] and Belle [58] data. However,

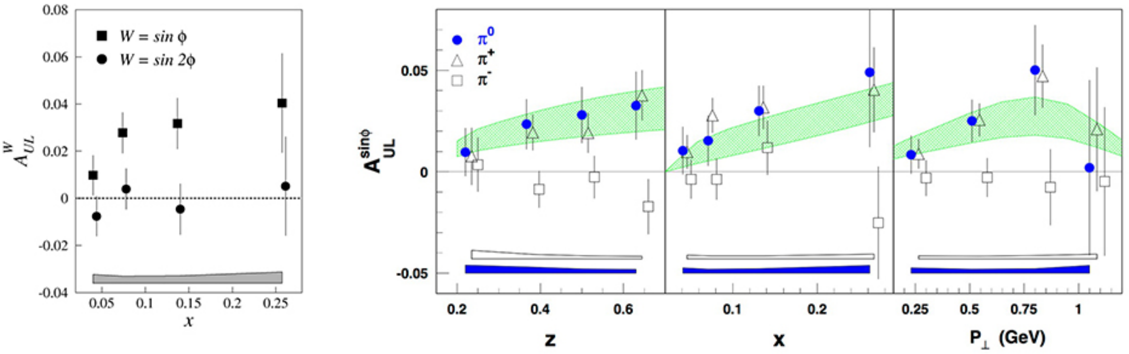

Figure 2.16: Results on longitudinal azimuthal one hadron target asymmetries from HERMES. Left: $A_{UL}^{\sin(\phi)}$ and $A_{UL}^{\sin(2\phi)}$ for π^+ as a function of x [50]. The error band indicates the systematic uncertainties for $A_{UL}^{\sin(\phi)}$. Right: $A_{UL}^{\sin(\phi)}$ for pions as a function of z, x, and of the pion transverse momentum $P_{\perp}$ [51]. The error bands represent the systematic uncertainties for neutral (blue) and charged (white) pions, respectively, whereas the green shaded areas indicate predictions from model calculations for π^0 [53, 54]. Note, that in both plots the asymmetries are not corrected for the depolarization factors.

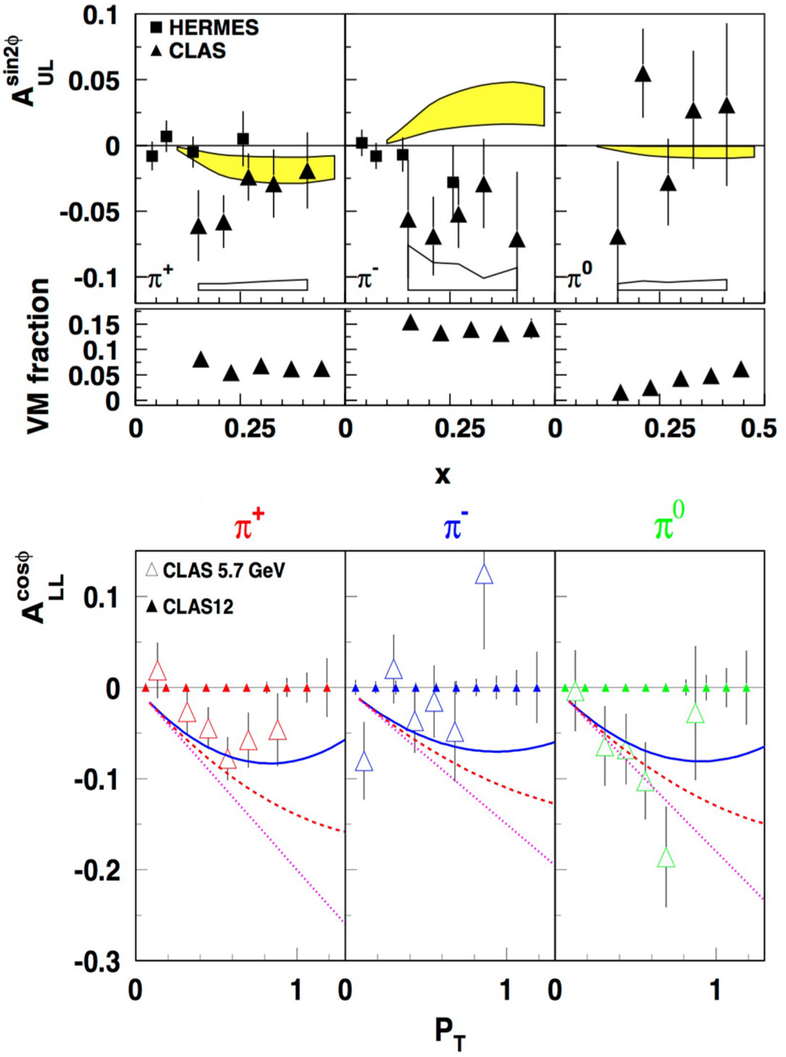

Figure 2.17: Results on longitudinal azimuthal one hadron target asymmetries from CLAS. Top: $A_{UL}^{\sin(2\phi_h)}$ as a function of x [56], compared to the measurement from HERMES. The yellow error bands indicate predictions from model calculations from Ref. [61]. The lower panels show the relative contributions from simulated exclusive ρ-production. Bottom: $A_{LL}^{\cos(\phi_h)}$ as a function of the hadron transverse momentum [60]. Open triangles show preliminary results for 5.7 GeV data, while filled triangles indicate projections of expected results for the proposed data taking for 12 GeV. The lines correspond to model calculations from Ref. [59]. The asymmetries of both plots are not corrected to account for the depolarization factor.

results of opposite sign were expected for π^-. Preliminary CLAS measurements on the double spin asymmetry $A_{LL}^{\cos(\phi_h)}$ as a function of the transverse momentum of the pions are shown on the bottom plot of Fig. 2.17, indicating a sizable negative asymmetry for all pion charges. The results are found to be in agreement with model predictions from Ref. [59], although limited statistics do not allow for further conclusions. However, new data from the CLAS12 program promise a higher precision in a wider kinematic range [60].

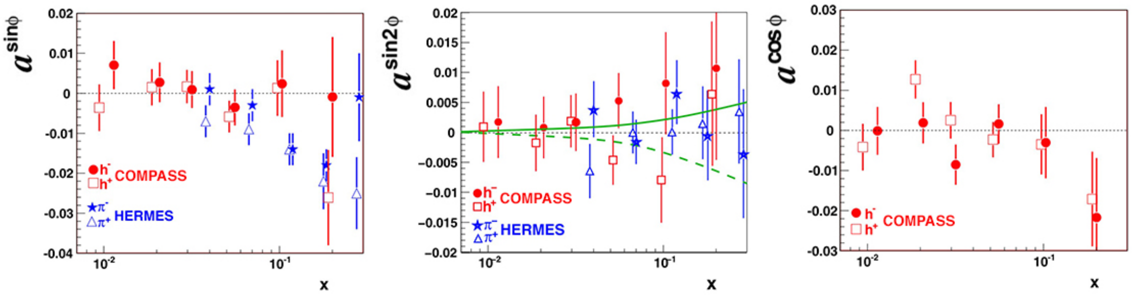

Figure 2.18: Results on azimuthal asymmetries from one hadron SIDIS off longitudinally polarized deuterons as a function of x from COMPASS and HERMES [52, 62] (modified). The green lines indicate model calculations for $A_{UL}^{\sin 2\phi}$ from Ref. [61] for negative (solid) and positive (dashed) hadrons. The asymmetries are not corrected to account for the depolarization factor.

At COMPASS, longitudinal azimuthal target spin asymmetries were so far measured using a polarized LiD target [62]. The results on $A_{UL}^{\sin(\phi_h)}$, $A_{UL}^{\sin(2\phi_h)}$ and $A_{LL}^{\cos(\phi_h)}$ for non-identified hadrons are displayed in Fig. 2.18, exemplarily as a function of x, and compared to HERMES data for charged pions from Ref. [52]. All three asymmetries were found to be in rough agreement with zero, revealing no evident dependence on a wider kinematic range, compared to HERMES results. Sizable negative values for the twist-3 asymmetry $A_{UL}^{\sin(\phi_h)}$, suggested by HERMES measurements in the high-x region for both charges, could not be confirmed. Concerning the leading twist asymmetry $A_{UL}^{\sin(2\phi_h)}$, one is tempted to conclude hints of a mirror asymmetry, as predicted by model calculations from Ref. [61]. The determination of these asymmetries for COMPASS proton data is one of the aims of this work.

2.5.2 Two Hadron Azimuthal Asymmetries

Azimuthal asymmetries in two hadron SIDIS were so far mainly studied on transversely polarized targets. Especially the investigation of the transverse leading-twist asymmetry $A_{UT}^{\sin(\phi_R-\phi_S)}$ became of high interest, as it allows to probe the transversity distribution h_1, being coupled to the collinear dihadron interference FF $H_1^{\angle}$. Unlike to single hadron SIDIS, where transversity can alternatively be accessed via the so called Collins effect, the dihadron amplitude doesn't involve transverse momenta of quarks and, hence, makes it easier to extract transversity. A summary on this topic, including a discussion of up-to-date results from the analysis of both one and two hadron SIDIS processes from COMPASS and HERMES, can be found in Ref. [63].

The main purpose of this work is to provide a first and comprehensive analysis of longitudinal target spin asymmetries in dihadron SIDIS using COMPASS proton data. This includes the determination of all nine dominating modulation amplitudes, involved in the partial-wave expanded two hadron SIDIS TMD cross section at leading twist. Further, collinear twist-3 asymmetries are studied, including the extraction of $A_{UL}^{\sin(\phi_R)}$ and $A_{LL}^{\cos(\phi_R)}$. A similar study is planned at CLAS, aiming to determine collinear beam and target spin asymmetries [64]. Fig. 2.19 shows preliminary results from CLAS, indicating a sizable subleading twist asymmetry $A_{UL}^{\sin(\phi_R)}$ [65].

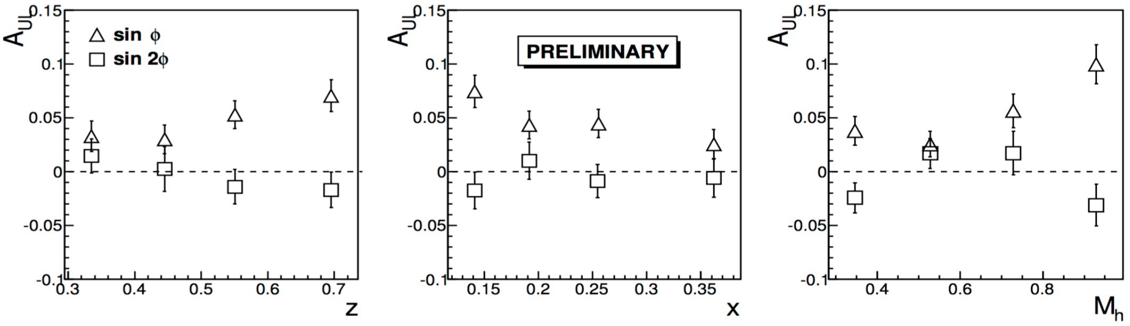

Figure 2.19: Preliminary results on the collinear target spin asymmetries $A_{UL}^{\sin(\phi_R)}$ and $A_{UL}^{\sin(2\phi_R)}$ from CLAS, obtained from semi-inclusive electroproduction of $\pi^+\pi^-$-pairs on a longitudinally polarized NH_3 target [65].

2.5.3 A_1^p Asymmetries

Both, the one and the two hadron analysis performed in this work, give also access to the double spin cross section asymmetries, commonly denoted as A_{1,h^+}^p and A_{1,h^-}^p, respectively $A_{1,h^+h^-}^p$, where the superscripted p indicates the proton. They can be identified as the A_{LL}^1-terms in the previous notation. They can be connected to the non-azimuthal part of the particular partial cross section σ_{LL}, involving the helicity TMD PDF g_1^p and the unpolarized FF D_1, for single hadrons or hadron pairs. This double spin asymmetry has already been extensively studied in one hadron SIDIS at EMC [66], SMC [67], HERMES [68] and COMPASS [69], and could be, in combination with inclusive measurements, used for a flavor decomposition of the helicity distribution.

The COMPASS results [69], obtained from the 2007 proton data, are depicted in Fig. 2.20 as a function of x and compared to HERMES measurements [68], including the inclusive asymmetry (upper left) and semi-inclusive asymmetries for pions (middle) and kaons (right) of positive (top) and negative (bottom) charge. Predictions from the DSSV fit are also shown [27, 70]. A general agreement between the experimental results and with the DSSV parametrization could be concluded. In all cases the asymmetries are found to be clearly positive, indicating a characteristic rise with x.

A comparison of the results from the present work with the results from other measurements will serve as a general consistency check of the performed azimuthal studies. As this work includes also the analysis of 2011 data, a comparison with COMPASS results from 2007 will be of special interest.

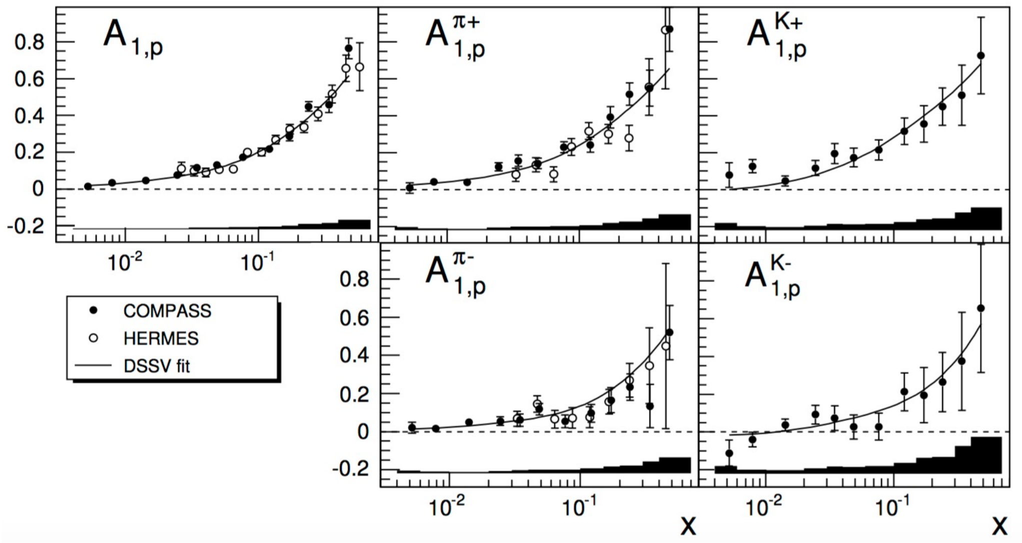

Figure 2.20: Results on A_1^p from inclusive DIS (upper left) and identified charged pions (middle column) and kaons (right column) from SIDIS as a function of x from COMPASS [69], compared to measurements from HERMES [68, 71]. The curves show the predictions of the DSSV fit [27, 70].

3. Experimental Setup of the COMPASS Experiment

The COMPASS experiment is located in the North Area of CERN and operates since 2002. As illustrated in Fig. 3.1, it is connected to the SPS[2] accelerator by the M2 beam line, which was already used for the former experiments EMC, NMC[3] and SMC[4]. It offers the possibility of optionally providing muon or hadron beams of high energy and intensity.

The main focus of research of COMPASS is the inner structure of hadrons, especially their helicity and spin compositions, as well as hadron spectroscopy. To suit the various experimental requirements, the beam, the target, as well as the whole spectrometer allow for a most flexible setup. As this thesis bases on data from the muon programs of 2007 and 2011, the main components and their functionality during these years are briefly described. For more detailed reviews, including also the hadron program setup, see Refs. [72, 73].

Apart from different beam momenta, 160 GeV/c in 2007 and 200 GeV/c in 2011, the experimental setup for both years muon programs is basically identical. The muon beam is first collimated and momentum selected in the M2 beam line before being directed on the polarized fixed target. The reaction particles are then detected in a two-stage spectrometer with a total angular acceptance up to 180 mrad, illustrated in Fig. 3.2. The large angle spectrometer (LAS) serves for the detection of particles with small momenta and hence wide scattering angle, while the particles with higher momenta are detected in the following small angle spectrometer (SAS). Both stages are equipped with the same main components, including a deflecting dipole magnet (SM), an electromagnetic and a hadron calorimeter (ECAL and HCAL), and a muon filter system (MW). Additionally, a Ring Imaging Cherenkov detector (RICH) in the LAS allows for a precise identification of pions, kaons, protons and electrons. The

---

[2] **S**uper **P**roton **S**ynchrotron

[3] **N**ew **M**uon **C**ollaboration

[4] **S**pin **M**uon **C**ollaboration

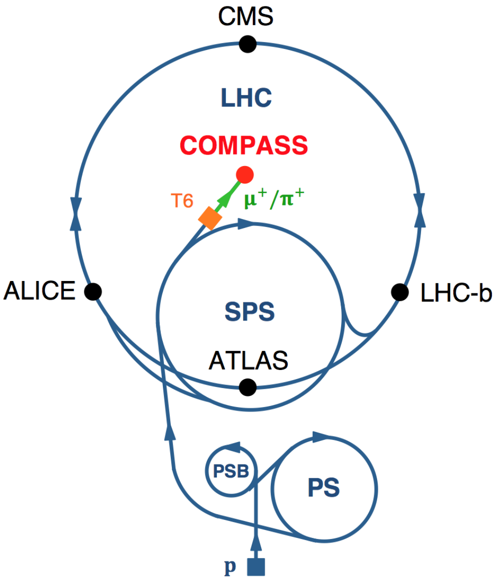

Figure 3.1: Artistic overview of the CERN accelerating complex, including the accelerators PSB (Proton Synchrotron Booster), PS (Proton Synchrotron), SPS (Super Proton Synchrotron) and LHC (Large Hadron Collider). The experiments, located at the LHC, and COMPASS are also indicated.

particles trajectories are tracked by various tracking detectors, placed over the whole spectrometer.

The following chapters summarize the functionality of the main experimental components, including also the trigger, the data acquisition system and the event reconstruction software. Further a description of the offline analysis is given.

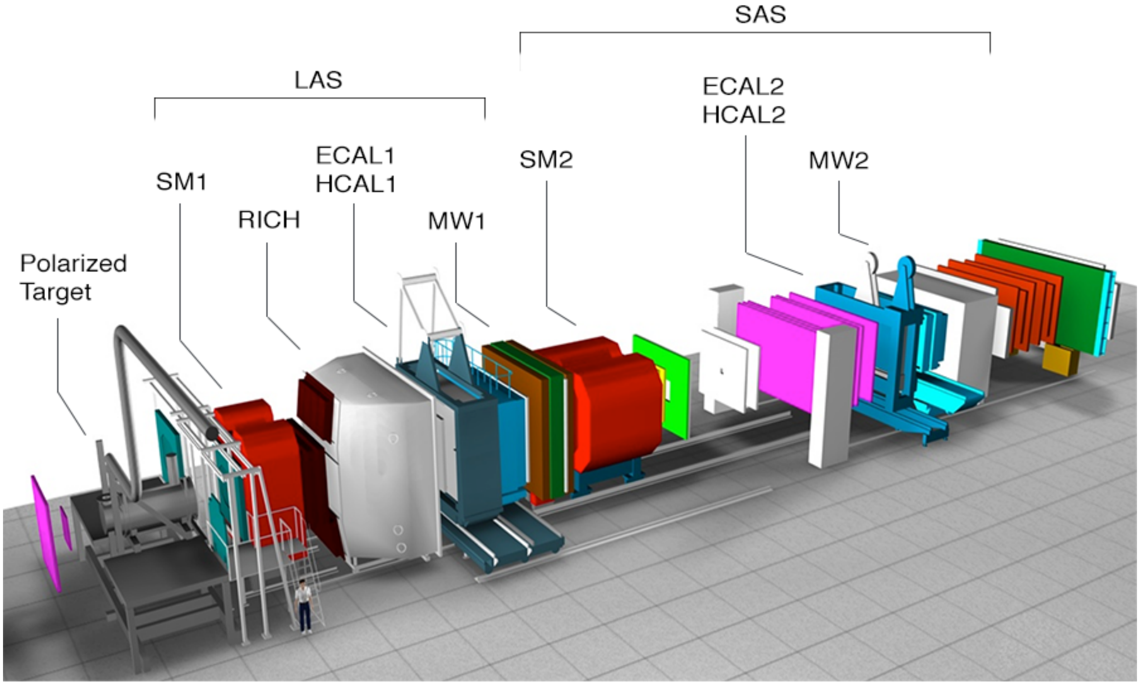

Figure 3.2: Artistic view of the COMPASS spectrometer.

3.1 The M2 Beam Line

The 1.13 km long tunnel, connecting the SPS and COMPASS, is called M2 beam line. When operating in muon mode, it transforms the initial proton beam (400 GeV/c) into a secondary collimated and momentum selected muon beam (up to 200 GeV/c). Therefore, within each 16.8 s lasting SPS cycle, spills of $1.2 \cdot 10^{13}$ protons are decoupled during an extraction time of 4.8 s and impinged on a beryllium target with 500 mm thickness (T6). As displayed in Fig. 3.3, produced kaons and pions are transported through a 600 m long channel with alternately focusing and defocusing quadrupoles (FODOs) while they decay partially into muons. The hadronic fraction of the beam is then stopped in a hadron absorber of beryllium at the end of the tunnel, while the muons are brought up to surface level by another 250 m long FODO channel and directed through the BMS. This complex is formed by six hodoscopes, a dipole magnet and a set of quadrupoles, and answers the purposes to measure the muons momenta on an event by event base, to focus them, and bent them back to the horizontal alignment.

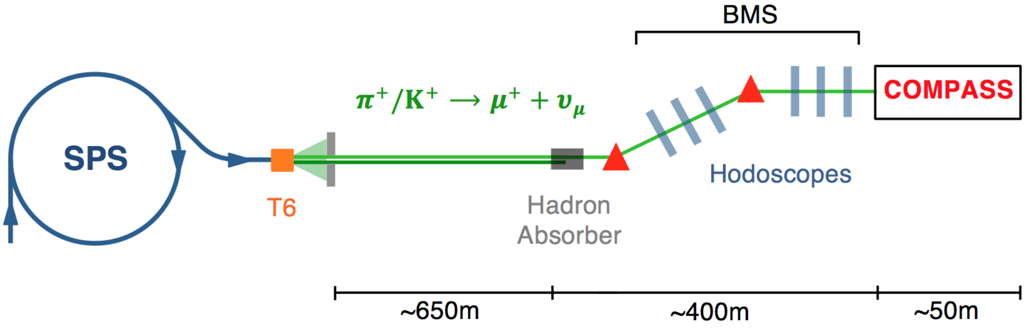

Figure 3.3: Schematic layout of the M2 beam line between SPS and COMPASS.

The muons are naturally polarized because of the parity violating weak decay they result of. However, their degree of polarization depends on their momentum. As a compromise between muon flux and polarization degree, a nominal momentum of 160 GeV/c is chosen for standard data taking, what corresponds to a muon flux of $2 \cdot 10^8$ muons per spill and a polarization percentage of around 80 %. Unlike this setting in 2007, in the year 2011 the momentum was chosen to be 200 GeV/c in order to cover a lower x-range in measurements of the structure function $g_1^P(x, Q^2)$ and to permit a more accurate extraction of the corresponding polarized PDFs. As a consequence the muon flux is reduced to $1 \cdot 10^8$ muons per spill.

3.2 The Polarized Target

The COMPASS physics program puts challenging requirements on the target construction. So has the small cross section of muon-nucleon interactions to be compensated in order to achieve a suitable luminosity and hence to allow for high accuracy measurements. Furthermore, target spin dependent measurements require a high polarizability of the target material and the possibility of optionally polarizing it longitudinal or transverse with respect to the beam axis. To make up for these requirements, a solid state NH_3-target with a high density of polarizable nucleons was used in 2007 and 2011. The ammonia crystals are contained in three independently polarizable cylindrical cells with a diameter of 4 cm and lengths of 30 cm, 60 cm, and 30 cm. By polarizing the two outer cells opposite to the central cell and exposing them to the same muon flux, one can measure both polarizations simultaneously and reduce the systematic uncertainties due to acceptance or beam flux effects on measurements of spin-dependent asymmetries.

The polarization is generated using Dynamic Nuclear Polarization (DNP). Therefore a 2.5 T homogeneous solenoid field is used, pointing along the beam axis, and a microwave irradiation of a suitable frequency to manipulate the spin states being longitudinally directed. The spin relaxation is suppressed by freezing the spin states at a temperature of around 50 mK, generated by a ^{3}He/^{4}He dilution refrigerator system. For measurements in transverse mode, the spins are rotated adiabatically into transverse direction, using a 0.5 T dipole field. The target polarization is permanently measured, using Nuclear Magnetic Resonance (NMR) coils along the target cells. A technical drawing of the whole apparatus, enclosing the target cells, is displayed in Fig. 3.4.

Even though only the protons of the hydrogen can be polarized, leading to a comparable small dilution factor of about 15 %, high polarization values of almost 90 % make ammonia the material of choice for muon programs on proton targets.

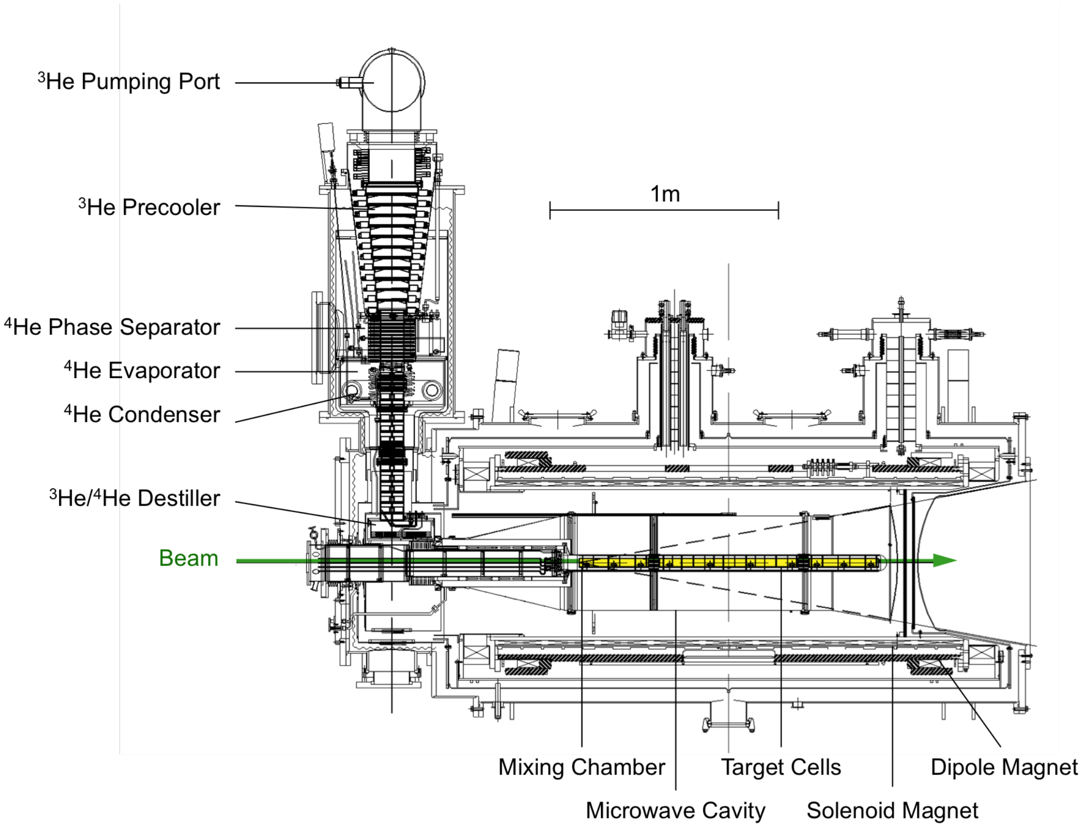

Figure 3.4: The COMPASS target cryostat, target (yellow) and polarization magnet [72](modified).

In order to minimize time dependent systematic uncertainties, entering from acceptance effects, the solenoid current is reversed at least once per day. After some weeks the microwave setting is reversed to avoid further acceptance effects from the solenoid field orientation. The polarization of the two outer cells is in each configuration opposite to the one of the center cell, as shown in Fig. 3.5. For the purpose of analysis, the central cell is regarded as two identical cells, whereas the cells are numbered from 1 to 4.

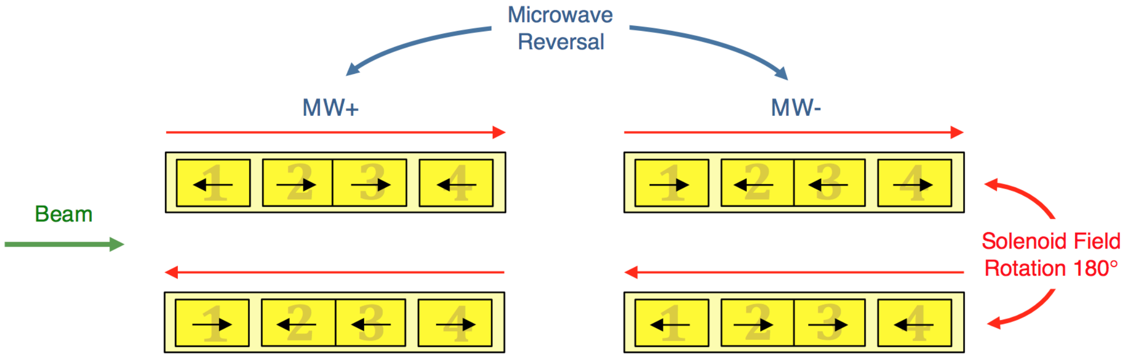

Figure 3.5: Target polarization settings in longitudinal mode. The black arrows indicate the polarizations of the cells 1 to 4. The beam direction points right with opposite polarization.

3.3 The Spectrometer

The two-stage spectrometer directly follows the target apparatus. It has a total length of about 60 m and answers the purpose to detect and characterize the final state particles. It is equipped with tracking detectors, allowing to determine the momentum to charge ratio of charged particles out of the bending of their trajectories when passing one of the dipole magnets, and to reconstruct the vertex position and the scattering angles by backpropagating the scattered particles. The setup is completed by calorimeters, a RICH detector for particle identification and hadron absorbers to identify muons. The spectrometer components are briefly described in the following sections.

3.3.1 Tracking Detectors

The particle trajectories are detected by a large variety of tracking detectors, distributed over the entire spectrometer length. As the particle flux and the kinematical phase space depend significantly on the distance from the beam axis, the used tracking technologies are chosen to match the respective requirements, regarding their particle rate capability, as well as their resolution of space and time. The used tracking detectors can be classified into three categories, depending on their angular acceptance. The main characteristics of the several detectors are listed in Tab. 3.1.

Very Small Area Trackers (VSAT)

Up to a radial distance of 5 cm, SciFi (Scintillating Fibre) stations, Silicon Microstrips and Pixel-GEMs (Gaseos Electron Multipliers) are used. Their data rate capability match the high particle flux (up to $5 \cdot 10^7$ Hz/cm^2) and their excellent spatial or time resolution make them ideally suited for beam particle tracking and vertex reconstruction.

Small Area Trackers (SAT)

In a radial distance of 5 cm till 40 cm from the beam axis, the particle flux decreases by two orders of magnitude (maximal $3 \cdot 10^5$ Hz/cm^2), hence a weaker time resolution is required. This area is covered by GEMs and Micromegas (Micromesh Gaseous Structure) with central dead-zones of 5 cm diameter.

Large Area Trackers (LAT)

The large area tracking is done using MWPC (Multi-Wire Proportional Chamber) stations, Straw Drift Tubes and DC (Drift Chamber) stations. Their active areas cover several square meters, leaving central dead-zones of 40 cm, and ensure 180 mrad of total acceptance and a good spatial resolution.

Table 3.1: Overview of the tracking detector types, grouped according to their acceptance. The characteristic parameters, including the dimensions of the active areas, as well as the spatial and time resolution (σ_s and σ_t) are listed [72].

Detector Type		Active Area [cm^2]	σ_s [μm]	σ_t [ns]
VSAT	SciFi	3.9×3.9 - 12.3×12.3	130 - 210	0.35 - 0.45
	Silicon Strips	5×7	8 - 11	2.5
	Pixel-GEM	10×10	95	9.9
SAT	GEM	31×31	70	12
	Micromegas	40×40	90	9
LAT	MWPC	178×90 - 178×120	1600	-
	DC	180×127	190 - 500	-
	Straws	280×323	190	-

3.3.2 Particle Identification

The COMPASS spectrometer includes several devices for particle identification (PID). Of great importance, even for inclusive DIS measurements, is the clear discriminability between scattered muons and other particles. This task is performed by Muon Filter systems, so called Muon Walls (MW1 & MW2 & MW3), placed in both spectrometer stages. For further identification of other final state particles, electromagnetic (ECAL1 & ECAL2) and hadronic (HCAL1 & HCAL2) calorimeters, as well as a RICH counter can be used. Although this study doesn't include hadron type specific measurements, all PID detectors are briefly described for completeness.

Muon Walls

Each Muon Wall consists of a hadron absorber, called Muon Filter (MF), enclosed by several tracking devices. A particle is then identified as a muon, if it is detected on both sides of the MF. The MW1, placed on the end of the LAS, is made up of an iron absorber of 60 cm thickness and two stations of gaseous wire detectors, called Mini Drift Tubes (MDTs). The MW2, contained in the SAS, is composed of a 2.4 m thick concrete absorber and Drift Tube detectors. MW3 is made up of an 40 cm thick iron absorber.

Calorimeters

Two electromagnetic calorimeters, one in each stage of the spectrometer, can be used to measure the energy of photons and electrons. They consist of lead glass modules of several types, and shashlik type modules in the innermost region of ECAL2, causing the incoming charged particle to produce electromagnetic showers by means of bremsstrahlung and pair production. By measuring the intensity of the emitted Cherenkov light, using Photo Multiplier Tubes (PMTs), the particles energy can be determined.

The energy of strong interacting particles is measured in hadronic calorimeters, placed in front of the Muon Walls. They are sampling calorimeters, consisting of alternating iron and scintillator plates. The incoming particle initiates a cascade of secondary particles through inelastic reactions in the iron layers. Their energy is measured through the radiation of photons in the scintillator layers of the calorimeter, detected and transformed into electric signals by PMTs. The quick response of the scintillators make the hadronic calorimeters suited for triggering inelastic muon scattering events.

The RICH-1 Detector

A Ring Imaging CHerenkov (RICH) detector in the LAS, called RICH-1, serves for excellent distinction of kaons, pions, protons and electrons. Its technology takes advantage of the Cherenkov effect, describing the emission of characteristic lightcones by particles, when passing through a dielectric medium (here C_4F_{10}) with a larger velocity than the velocity of light in that medium. The particles type can then be determined by calculating its invariant mass from the opening angle of the lightcone and the particles momentum.

3.4 The Trigger System

Due to limitations regarding the buffer-time and the available disk space, a fast selective storage process on hardware level is necessary in order to accomplish data storage in a high rate environment. The COMPASS trigger system is designed to serve this purpose. In a very short time less then 1 μs, it provides read-out signals to the front-end electronics and launches the data acquisition in case of a physical interesting event. The system consists of various scintillating hodoscopes, placed along the spectrometer, and the two hadron calorimeters HCAL1 and HCAL2, as shown in Fig. 3.7. Their signals are combined to subtriggers, requiring coincidences in two hodoscopes, called inner trigger IT (H4I & H5I), middle trigger MT (H4M & H5M), ladder trigger LT (H4L & H5L), outer trigger OT (H3O & H4O), and large angle spectrometer trigger LAST (H1 & H2).

The subtriggers can be grouped in three classes:

Inclusive Triggers (Inclusive MT, OT, LT)

> The trigger decision of the inclusive triggers bases on the information of scattered muons only. They require coincidences of space and time of the corresponding hodoscope signals, and that the muon trajectory points to the target. In case of small scattering angles, the trigger decision bases on the energy loss of the scattered muon, determined from its deflection in the two spectrometer magnets.

Semi-inclusive Triggers (IT, MT, LAST)

> In addition to coincidences in the hodoscopes, the semi-inclusive triggers require a certain energy deposit in one of the hadron calorimeters.

Calorimetric Triggers (CT)

> The calorimetric trigger makes use only of the calorimeters. By requiring the measured energy deposit to exceed the expected energy loss of a single muon, it complements the hodoscope-based triggers.

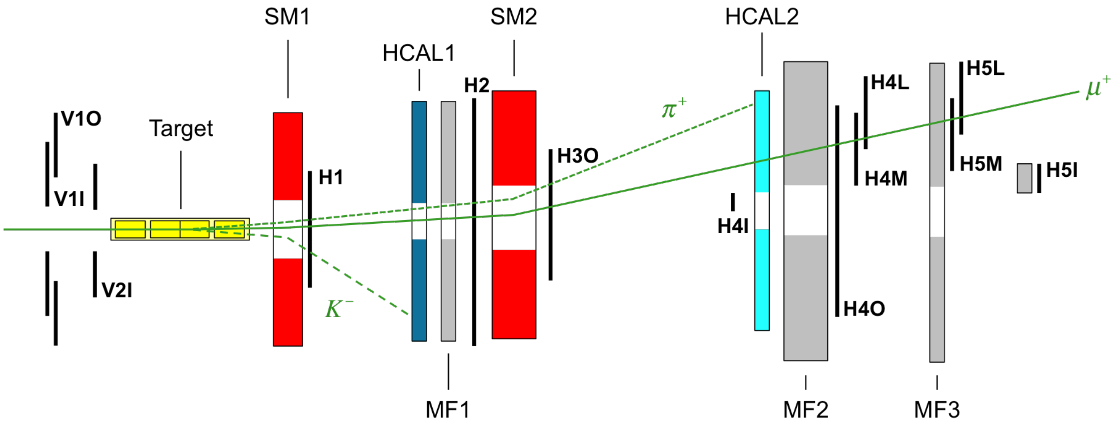

Figure 3.6: Positioning of the relevant trigger system components, including trigger hodoscopes, the hadron calorimeters and the muon filters. Shown is the setup of 2011.

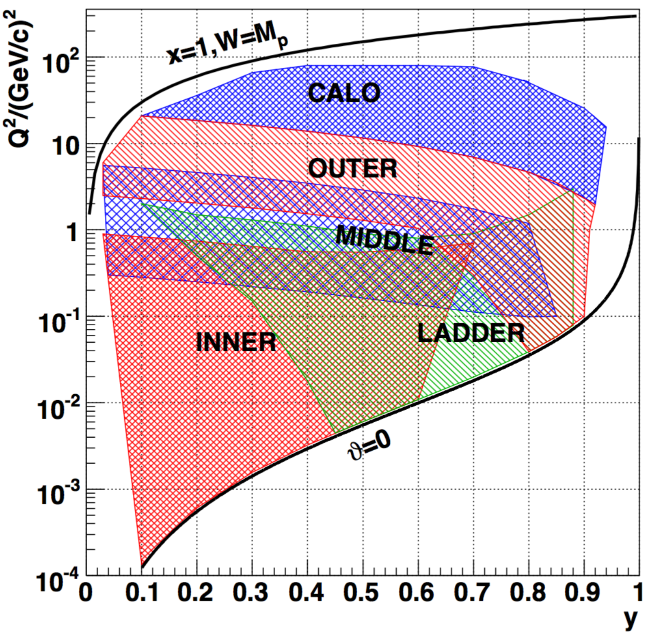

Figure 3.7: Kinematic range in Q^2 and y, covered by the several trigger subsystems for a 160 GeV muon beam. The thick lines indicate the kinematic limits for elastic scattering ($x_{Bj} = 1, W = M_p$) and forward scattering ($\theta = 0$) [74].

As shown in Fig. 3.7, the subtriggers completely cover the major kinematic range in Q^2 and y of COMPASS. In 2010, the LAST trigger was additionally installed to extend the covered range to lower Q^2, not included in the graphic.

The trigger system is completed by a veto trigger system, consisting of two scintillating hodoscopes placed in front of the target, leaving the central region around the beam uncovered. It is used to avoid false trigger decisions caused by halo muons, not crossing the target volume, but being detected in the trigger hodoscopes in the spectrometer.

3.5 Data Acquisition and Event Reconstruction

The COMPASS readout system has to cope with instantaneous trigger rates of about 100 kHz and typical event sizes of 45 kB, summing up to around 580 TB of recorded data per year. To meet these challenging requirements, an entirely new Data Acquisition (DAQ) system was developed, schematically shown in Fig. 3.8. The analog signals, coming from over 300 000 detector channels, are converted to digital units by either TDC[1]- or ADC[2]-cards, placed on front-end boards in closed proximity to the detectors. When receiving a trigger signal from the TCS (Trigger Control System), data is transferred to readout driver modules called CATCH (COMPASS Accumulate, Transfer and Control Hardware) and GeSiCA (GEM and Silicon Control and Acquisition), and completed by integrating also time synchronization information from the TCS. From the readout modules the final data is transported via optical

---

[1] **T**ime to **D**igital **C**onverter

[2] **A**nalog to **D**igital **C**onverter

links (S-LINK) to the Readout Buffer PCs, where it is buffered in form of sub-events. The data is processed in parallel by twelve Event Builders and combined to global events, including the complete information of all detectors. The raw data is merged to so called chunks of 1 GB and automatically stored on CASTOR[1].

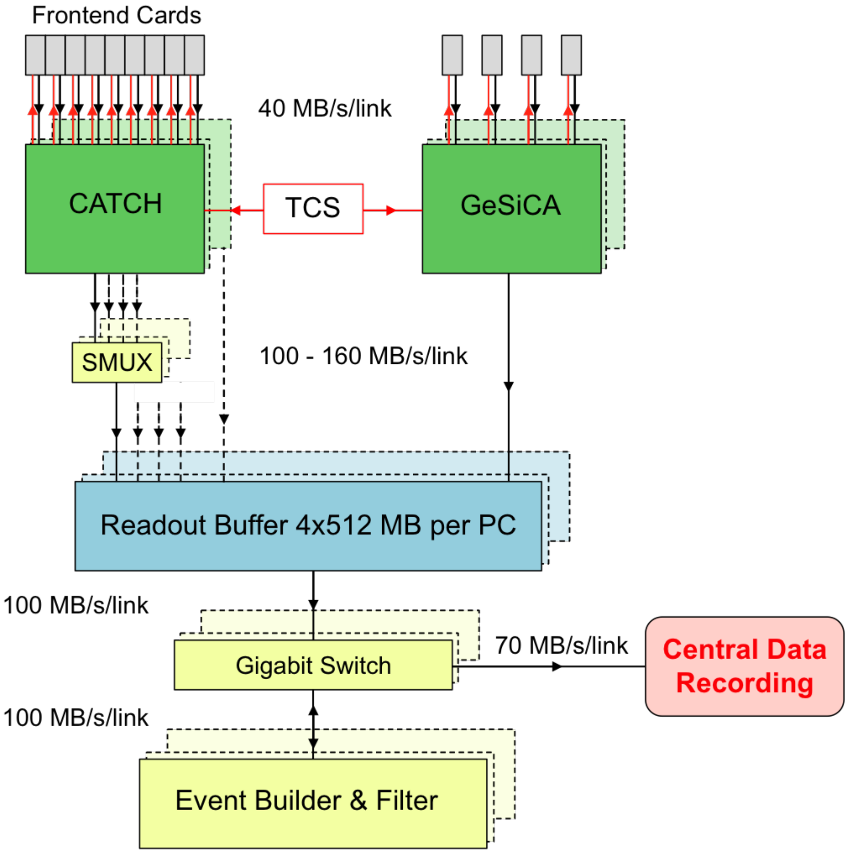

Figure 3.8: Architecture of the COMPASS data acquisition system [72, 73](modified).

The event reconstruction, meaning the transformation of the raw data into physical quantities, is realized by the internally developed software CORAL[2]. It is a fully object orientated software package, based on C++, processing the event reconstruction as schematically illustrated in Fig. 3.9. Except decoding, the reconstruction process is basically identical for both real and Monte Carlo (MC) generated data. In a first step, the initial data words are decoded to retrieve information about the detector channels. Hits coming from the same particle are then grouped to so called clusters and linked to their geometrical position in the main reference system of the experiment. The next phase contains the actual reconstruction of physical quantities used for analysis. In a last step, the information on tracks, calorimeter clusters,

---

[1] CERN **A**dvanced **STOR**age

[2] **CO**MPASS **R**econstruction and **A**na**L**ysis

vertices and particle IDs are stored into so called mDST[1]-files, using the format of ROOT[2] trees.

The main tool to analyze physical processes at COMPASS is the software package PHAST[3]. It provides C++ routines, allowing to easily access information on analytically interesting physical quantities from the mDST-files.

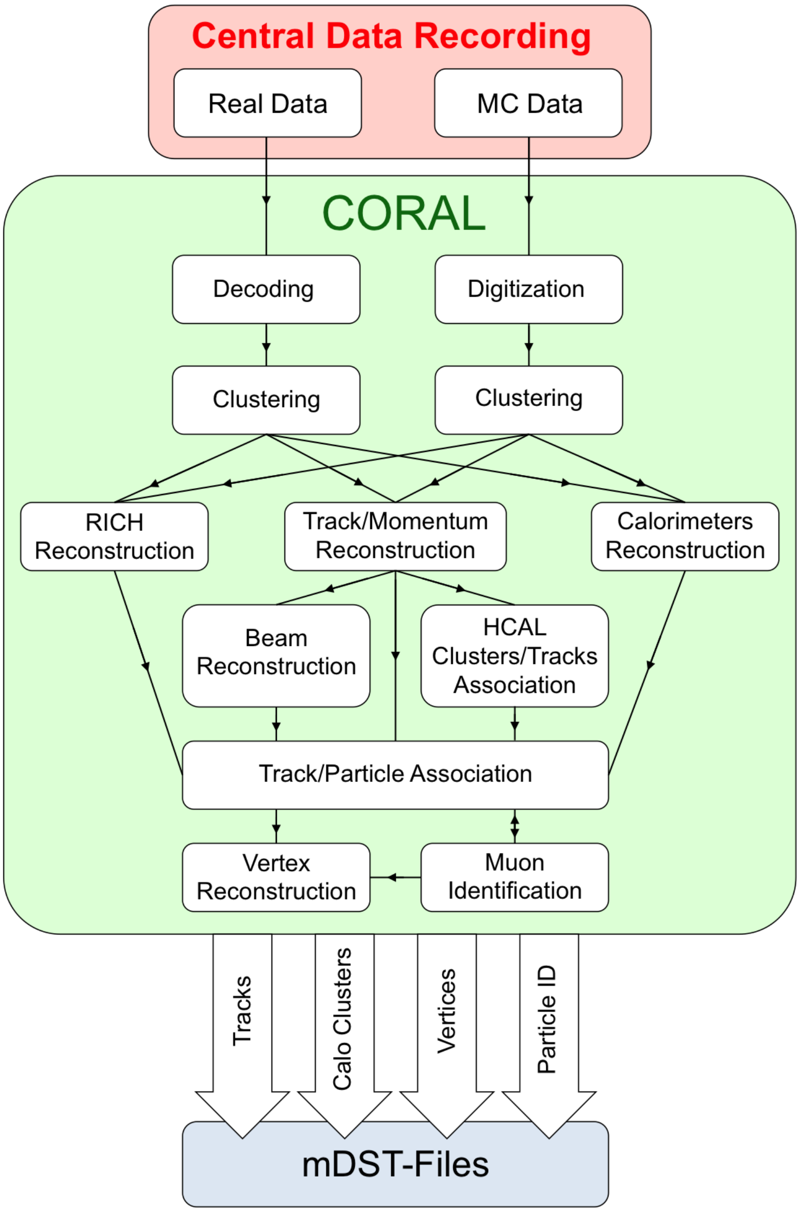

Figure 3.9: Reconstruction of real data and MC data at COMPASS [72](modified).

---

[1] **m**ini **D**ata **S**ummary **T**ape

[2] ROOT is an analysis software package, provided by CERN.

[3] **PH**ysics **A**nalysis **S**oftware **T**ools.

4. Data

The present study comprises the analysis of data taken in the years 2007 and 2011. In both years a three celled longitudinally polarized ammonia target was used, although the beam energy averaged 160 GeV in 2007 and 200 GeV in 2011. To allow for a distinctive analysis, the study is carried out for both years separately. Nevertheless, final asymmetry results are combined in case of satisfying compatibility, assuming their dependence on the beam energy to be negligible.

The following sections describe in detail the data selection, from the initial to the finally analyzed data samples, for both years and both analyses. Following this, the remaining data is finally checked for compatibility, comparing the distributions of important variables between subsamples from single weeks of data taking, as well as between the two target polarization configurations within each week. The final data samples are discussed in Sec. 4.4.

For reasons of clarity the main focus will be set on the hadron pair analysis. Thus statistics and distribution plots of the one hadron analysis can be found in the appendix A.5.

4.1 Initial Data Samples

The initial data samples contain data from 9 weeks for 2007 and 11 weeks for 2011. The data, reconstructed with CORAL and stored in mDST-files, are initially reduced in view of DIS analyses and written to so called μDST-files. The following basic DIS precuts reduce the initial amount of data to about 15 %:

- At least one reconstructed primary vertex
- At least one reconstructed scattered muon
- Photon virtuality $Q^2 > 1\,(\mathrm{GeV/c})^2$
- Fractional energy of the virtual photon $y < 0.95$.

4.2 Data Quality and Grouping

The study of asymmetries requires a best possible stability of used data to minimize adulterating effects. So can, for instance, detector problems cause changes of acceptance and thus lead to non-vanishing false asymmetries. Though the performance of all detectors is permanently monitored online during the data taking, additional quality checks are needed to ensure the data stability. This is done offline, using the reconstructed data with $Q^2 > 1\,(\mathrm{GeV/c})^2$ [75–77].

In a first step, a spill by spill analysis is performed to eliminate spills with short time detector instabilities. For this purpose several characteristic variables are checked for stability, such as the number of primary vertices per event, the number of beam tracks per event and the number of tracks per primary vertex. This is done on a spill by spill basis, comparing the mean values of each spill with those of its neighboring spills within a gliding window of 1200 spills. A neighboring spill is then counted as a good neighbor, if all of its mean values lie within chosen limits around those of the regarded spill. A threshold can be set to define the required minimal number of good neighbors to mark a spill as good.

The bad spill criteria are tuned week wise, varying the RMS window width in multiples of its standard deviation σ to pursue the best separation of good and bad spills. As an example, Fig. 4.1 shows the impact of the above described bad spill study for the number of tracks per primary vertex for W30 in 2011. Here, the red points mark spills with less than 300 good neighbors within boundaries of 5σ. They were thus excluded from the analyses.

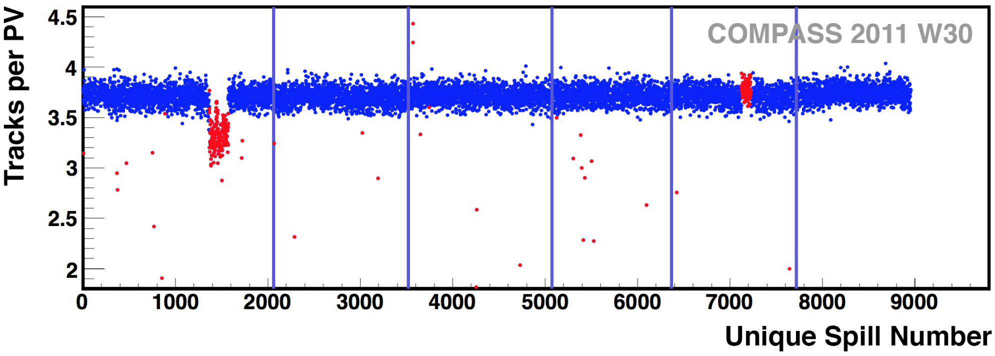

Figure 4.1: Example distribution of number of tracks per primary vertex vs the unique spill number for 2011 W30. Bad spills are marked red, good ones in blue. The vertical lines indicate solenoid field reversals.

The bad spill numbers, resulting from the above described procedure, are written into so called badspill lists and excluded from the analyses [78]. A whole run is discarded if more than 80 % of its spills are bad. Tab. 4.1 gives an overview of the bad spill statistics and the production settings of the initial data samples.

To eliminate instabilities on larger time scale, such as alignment or magnetic field issues, additional quality checks are performed on a run by run basis. This analysis makes use of physical quantities like the Bjorken scaling variable x, measured in μ-e

elastic scattering events, or the mass of K_0 from the exclusive ρ reproduction. The good runs are then sorted into stable groups of balanced statistics between the two polarization settings, where one week can contain several groups [79]. However, in the present analyses the asymmetries are extracted week wise to guarantee enough statistics for the used binned fit methods. Nevertheless only runs are included in the analyses, that are listed in the provided grouping lists.

Table 4.1: Overview of the production settings for each year, microwave setting and week. The numbers of initial and bad spills as well as their percental fraction are also listed.

Year		2007				
MW	**Week**	**Slot**	**CORAL**	**Spills**	**Bad Spills**	**%**
MW+	W32	2	2008-8-13	24840	2701	10.87
	W33	2	2008-8-13	19742	1447	7.33
	W34	2	2008-8-13	8291	765	9.23
	W44	2	2008-6-23	26345	1847	7.01
	W45	3	2008-3-12	7867	348	4.42
MW−	W35	2	2008-8-13	23006	2244	9.75
	W36	2	2008-8-13	26618	2379	8.94
	W37	2	2008-7-11	22616	1860	8.22
	W38	2	2008-7-07	5352	1091	20.38

Year		2011				
MW	**Week**	**Slot**	**CORAL**	**Spills**	**Bad Spills**	**%**
MW+	W36	1	2011-12-14	13393	679	5.07
	W38	1	2011-12-14	7027	223	3.17
	W39	1	2011-12-14	17538	487	2.78
	W41	1	2011-12-14	15138	368	2.43
	W43	1	2011-12-14	10674	473	4.43
MW−	W25	1	2011-12-14	8748	2509	28.68
	W27	1	2011-12-14	22168	1931	8.71
	W30	1	2011-12-14	8956	555	6.20
	W31	1	2011-12-14	6942	657	9.46
	W32	1	2011-12-14	6469	1740	26.90
	W33	1	2011-12-14	1807	484	26.78

4.3 Data Selection

To restrict the data to the topology and kinematic range of the considered processes several cuts were applied. These requirements are basically the same for both years, only differing regarding the energy of the incident muon and the quality of its track, as there is no accessible information for 2007 data from the beam momentum station. The applied cuts are listed in Tab. 4.2 and will be in detail motivated in the following.

4.3.1 Topology

The analyses of this work, both the single hadron and the dihadron study, are basically characterized by a similar topology. One incident muon scatters on a target nucleon, whereas the interacting parton fragments in one or more hadrons. For practical reasons it is initially only required to find at least two outgoing tracks, one to be later associated to the scattered muon and one to a hadron. In case of more than one hadron being detected in the final state, hadron pairs can be built.

4.3.2 Best Primary Vertex

The position of interaction between the incident muon and the target nucleon is called primary vertex. Since it is likely to reconstruct more than one primary vertex, the one with the highest number of associated outgoing tracks and the smallest χ^2 of its reconstruction fit is chosen. This selection is concluded in the PHAST routine PaEvent::iBestPrimaryVertex.

To furthermore ensure the interaction of the incident muon with one of the target nucleons, the best primary vertex has to be found inside of one of the target cells. Therefore the vertex coordinates are limited to the target geometry of the respective year, using the PHAST routine PaAlgo::InTarget. The Z_{prim}-distributions of the hadron pair samples with and without the applied cuts on Z_{prim} are shown in the upper row of Fig. 4.2. Here, the three cell structure of the target is clearly visible for both years.

The uncertainty of the z position is displayed in the bottom row of Fig. 4.2. As the distance of the target cells is 5 cm, the small uncertainties ensure a correct assignment of the primary vertex to a certain cell. This is of high importance for the extraction of asymmetries, because it implies the correct assignment of the right target polarization value to a certain event.

Fig. 4.3 shows the horizontal and vertical positions of the primary vertices. While the radial cut is set to $r < 1.9\,\text{cm}$ for both years, the different target shifts are taken into account. The two dashed red circles indicate the front and the back shape of the cylindrical cut accounting for a slight skew of the target along the z axis.

Table 4.2: Overview of the applied cuts.

<table>
<tr><th>Year</th><th>2007</th><th>2011</th></tr>
<tr><td>Cut Type</td><td colspan="2">Criteria</td></tr>
<tr><td>Topology</td><td colspan="2">Best primary vertex (PaEvent::iBestPrimaryVertex)
1 incident muon μ
Number of outgoing tracks $N_{\text{out}} \geq 2$</td></tr>
<tr><td rowspan="2">Incident μ</td><td colspan="2">$\chi^2_{\text{red}}(\mu) < 10$
μ is beam (PaParticle::IsBeam)
Beam crosses all target cells (PaAlgo::CrossCells)</td></tr>
<tr><td>$140 < p(\mu)/(\text{GeV/c}) < 180$</td><td>$185 < p(\mu)/(\text{GeV/c}) < 215$
$0.01 < LH_{\text{back}} < 1.0$
$N_{\text{BMS}} > 2$</td></tr>
<tr><td>Scattered μ'</td><td colspan="2">Is scattered μ' (PaVertex::iMuPrim(false, true, true, false,30))
$\chi^2_{\text{red}}(\mu') < 10$
$Z_{\text{first}}(\mu') < 350\,\text{cm}$
$350\,\text{cm} < Z_{\text{last}}(\mu') < 3300\,\text{cm}$</td></tr>
<tr><td>Vertex</td><td colspan="2">Vertex inside target (PaAlgo::InTarget)</td></tr>
<tr><td>Kinematics</td><td colspan="2">$Q^2 > 1\,(\text{GeV/c})^2$
$W > 5\,\text{GeV/c}^2$
$0.0025 < x < 0.7$
$0.1 < y < 0.9$</td></tr>
<tr><td>Hadrons</td><td colspan="2">$X/X_0(h) < 10$
$\chi^2_{\text{red}}(h) < 10$
$Z_{\text{first}}(h) < 350\,\text{cm}$
$350\,\text{cm} < Z_{\text{last}}(h) < 3300\,\text{cm}$</td></tr>
<tr><td>Single Hadron Analysis</td><td colspan="2">$0.2 < z(h) < 1.0$
$P_{hT} > 0.1\,\text{GeV/c}$</td></tr>
<tr><td>Hadron Pair Analysis</td><td colspan="2">$q(h_1) = +1$, $q(h_2) = -1$
$0.1 < z(h_{1/2}) < 1.0$
$0.1 < x_F(h_{1/2}) < 1.0$
$E_{\text{miss}} > 3\,\text{GeV}$
$R_T > 0.07$</td></tr>
</table>

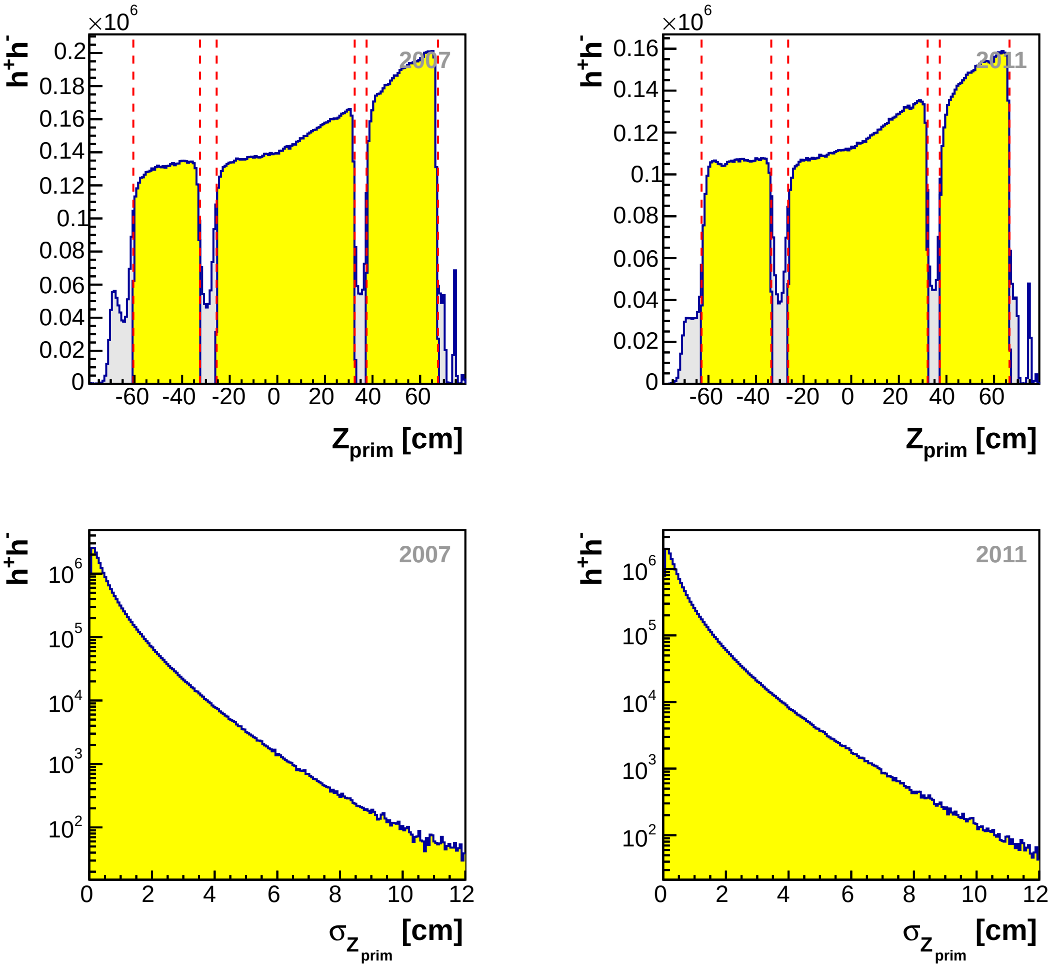

Figure 4.2: Distribution of the Z coordinate (top) and its uncertainty (bottom) of the best primary vertex before (grey) and after (color) application of the associated cuts. The cuts are marked with dashed red lines.

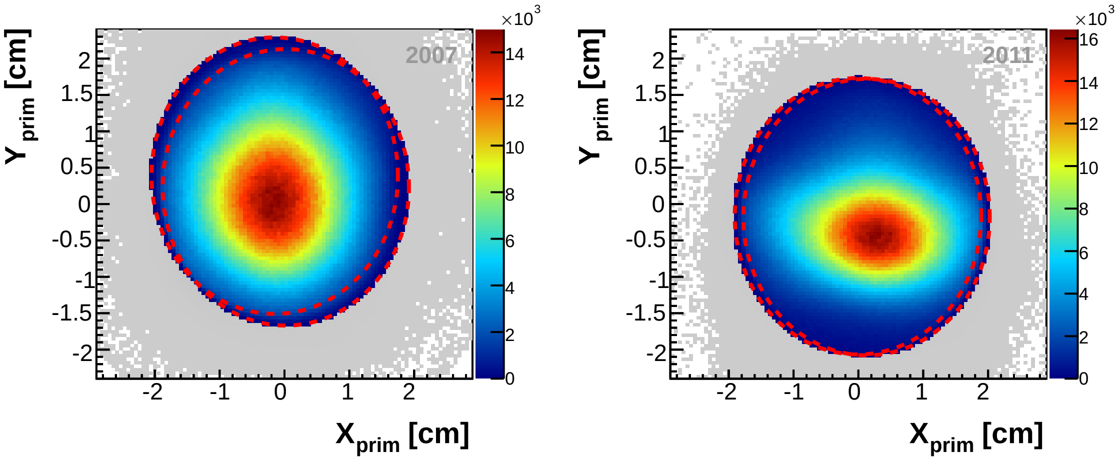

Figure 4.3: X coordinate versus Y coordinate of the best primary vertex before (greyscale) and after (colorscale) application of the associated cuts. The two dashed red circles indicate the front and the back shape of the cylindrical cut accounting for a slight skew of the target along the z axis.

4.3.3 Incident and Scattered Muon

The incident muon is defined as the beam particle associated to the best primary vertex, which is determined using the PHAST routine PaParticle::IsBeam. In order to ensure a proper quality of its track, the corresponding χ^2_{red} is chosen to be smaller than 10. Additionally the extrapolated track of the beam particle is required to cross all three target cells to ensure a balanced muon flux through the whole target by applying the PHAST routine PaAlgo::CrossCells.

The beam momentum, measured in the BMS, is limited to the range $140\,\mathrm{GeV/c} < p(\mu) < 180\,\mathrm{GeV/c}$ for 2007 and to $185\,\mathrm{GeV/c} < p(\mu) < 215\,\mathrm{GeV/c}$ for 2011 data. Fig. 4.4 shows the measured momenta, distributed around the respective nominal beam energy. The spiked shape on the right tale of the 2011 distribution could be credited to granulazation effects from the BMS planes, which arose with the use of a new BMS reconstruction software [80].

As there exists accessible information about BMS hits only for 2011 data, this year's beam momentum reconstruction quality can be further tuned. This is done by requiring more than two hits in the BMS planes and $0.01 < LH_{\mathrm{back}} < 1.0$, using the likelihood of the back propagation algorithm LH_{back} as a measure of goodness of the beam momentum reconstruction.

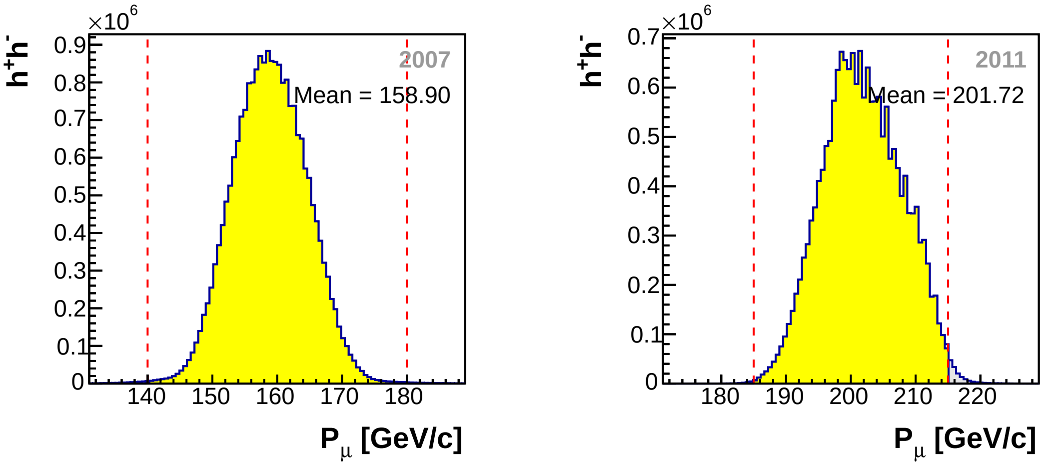

Figure 4.4: Momentum distribution of the incident muon before (grey) and after (color) application of the associated cuts. The cuts are marked with dashed red lines.

As scattered muon the outgoing particle is chosen that is tagged as such by the reconstruction software CORAL, using the PHAST routine PaVertex::iMuPrim. To first identify the outgoing particle as a muon, this function requires the outgoing particle to pass more than 30 radiation lengths, its last detection to take place after the Muon Filter 1 and its sign of charge to be equal to the one of the incident muon. Should more than one outgoing particle match these requirements the event is discarded.

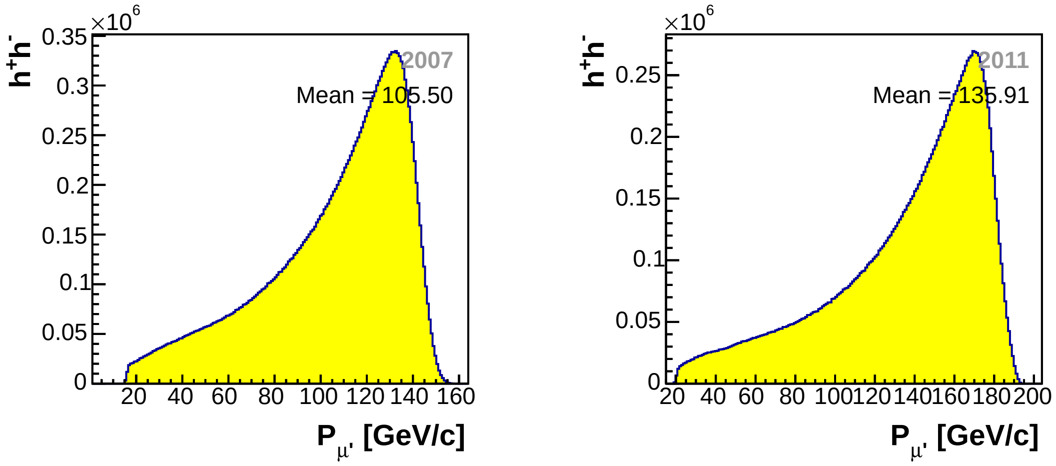

Figure 4.5: Momentum distribution of the scattered muon after application of the associated cuts.

4.3.4 Kinematics

In order to ensure the event to match the kinematic characteristics of a deep inelastic scattering process the following cuts are applied. The negative square of the virtual photon's four momentum is limited to $Q^2 > 1\,(\mathrm{GeV/c})^2$ to guarantee the resolution of partons inside the proton. Hadronic resonances are suppressed by restricting the data on events with invariant masses of the hadronic final states $W > 5\,\mathrm{GeV/c^2}$. Furthermore the fractional energy of the virtual photon is limited to $0.1 < y < 0.9$. Here, the lower y cut guarantees the inelasticity of the process and rejects events, where halo or background muons are misidentified as scattered muons. The upper y cut rejects events, where radiative corrections become not negligible. To restrict the data to COMPASS kinematics the Bjorken scaling variable is additionally limited to $0.0025 < x < 0.7$.

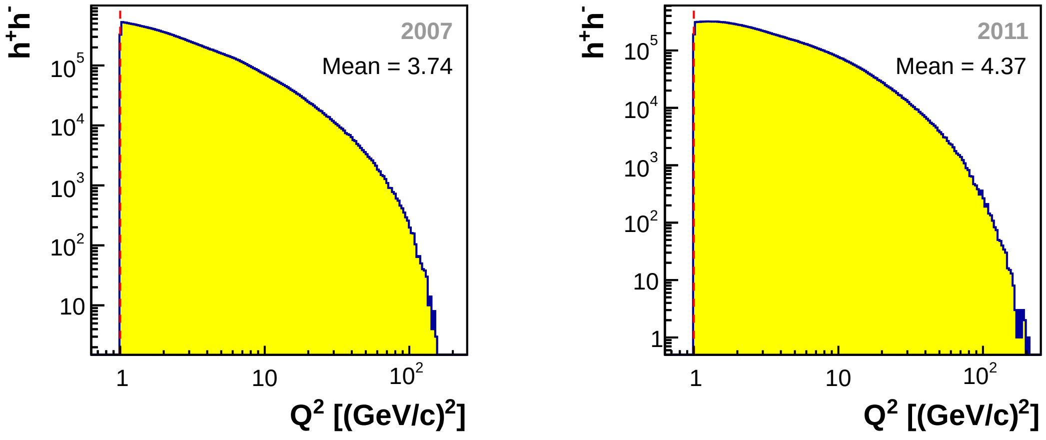

Figure 4.6: Distribution of Q^2 before (grey) and after (color) application of the associated cut. The cut is marked with a dashed red line.

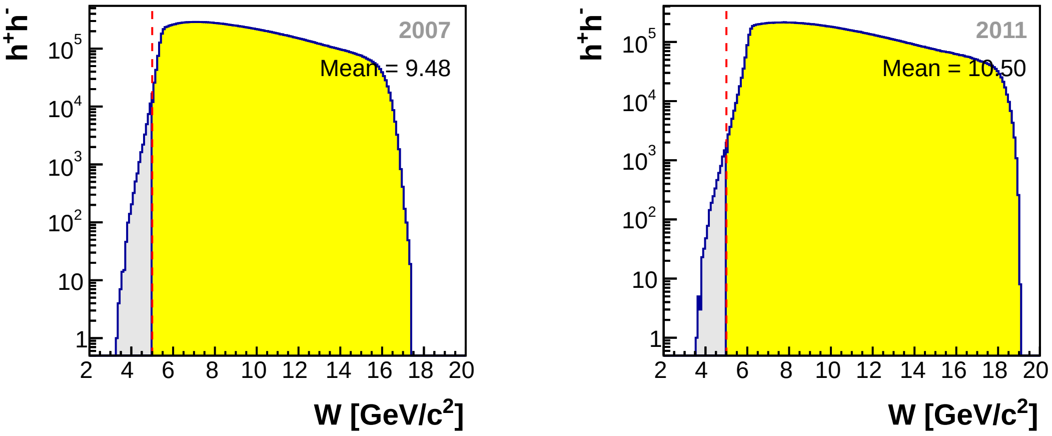

Figure 4.7: Distribution of W before (grey) and after (color) application of the associated cut. The cut is marked with a dashed red line.

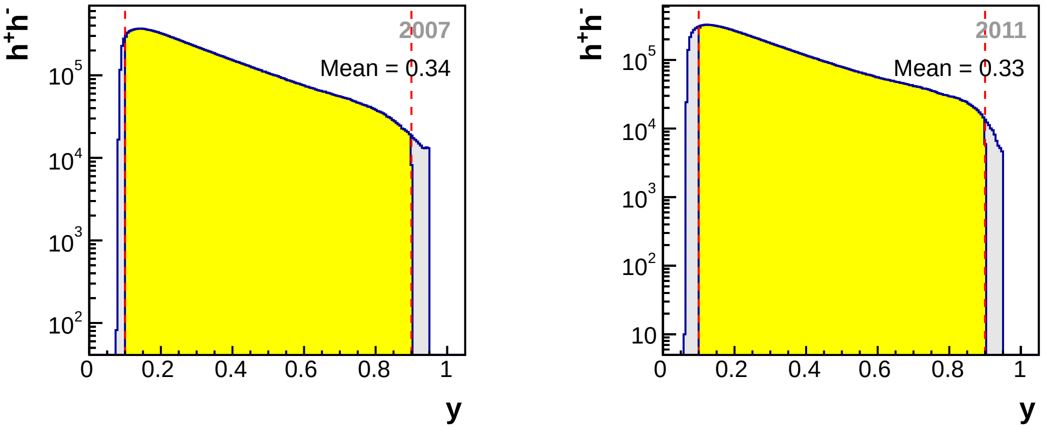

Figure 4.8: Distribution of y before (grey) and after (color) application of the associated cuts. The cuts are marked with dashed red lines.

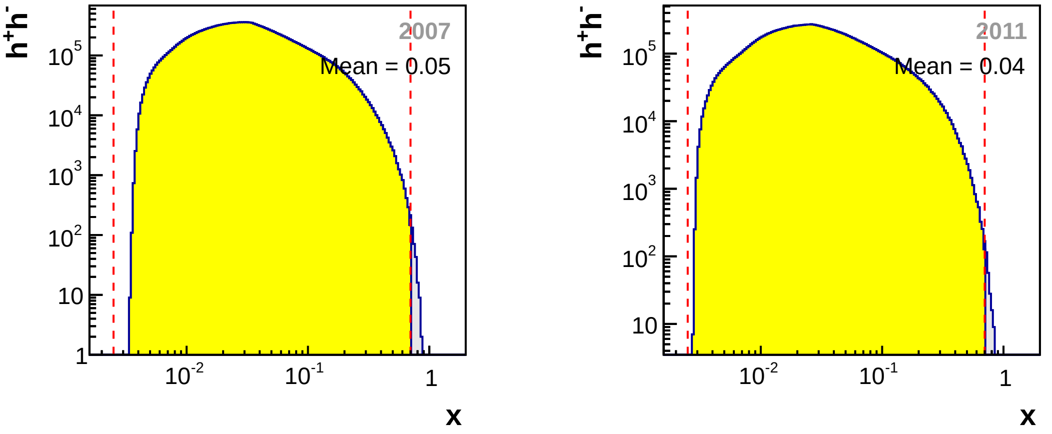

Figure 4.9: Distribution of x before (grey) and after (color) application of the associated cuts. The cuts are marked with dashed red lines.

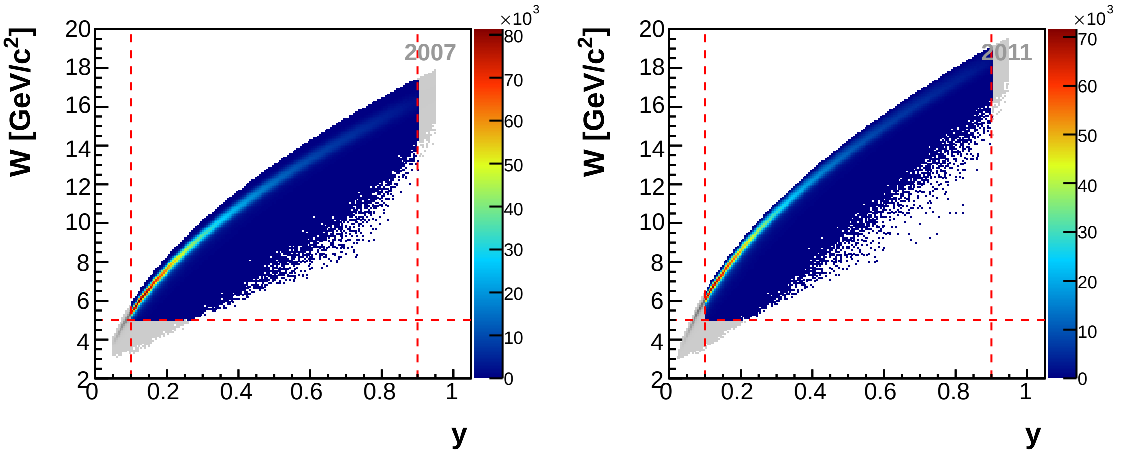

Figure 4.10: W vs y before (greyscale) and after (colorscale) application of the associated cuts. The cuts are marked with dashed red lines.

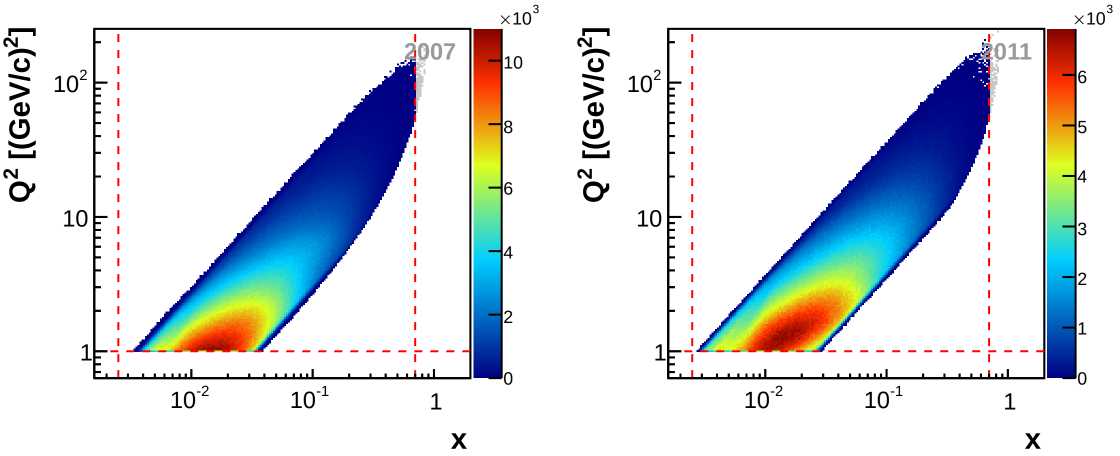

Figure 4.11: Kinematical phase space of Q^2 vs x before (greyscale) and after (colorscale) application of the associated cuts. The cuts are marked with dashed red lines.

4.3.5 Hadrons

Each outgoing particle that is associated to the best primary vertex, except the scattered muon, is checked to be a hadron. This is done requiring its track to fulfill $\chi^2_{\mathrm{red}}(h) < 10$ and to pass less than 10 radiation lengths. Its first detection point should be found in front ($Z_{\mathrm{first}}(h) < 350\,\mathrm{cm}$), its last measured point behind ($Z_{\mathrm{last}}(h) > 350\,\mathrm{cm}$) of the deflecting magnet SM1 in order to ensure a good momentum measurement. To reject misidentified muons it is further required to find the last detection point in front of muon filter 2 via $Z_{\mathrm{last}}(h) < 3300\,\mathrm{cm}$.

The following additional hadronic cuts are applied only for the single hadron analysis. First each hadron needs to carry a fractional energy $z(h) > 0.2$ to ensure current fragmentation. To furthermore guarantee a well-defined hadronic plane, and then a good resolution of the measured azimuthal angle ϕ_h, a transverse momentum with respect to the virtual photon direction $P_{hT} > 0.1\,\mathrm{GeV/c}$ is required.

4.3.6 Hadron Pairs

For each event all possible combinations of two hadrons with opposite charge are built, while the first hadron is required to be positively charged for the reason of discriminability. Here, the fractional energy of each hadron is limited to $0.1 < z(h_{1/2}) < 1.0$ (Fig. 4.12). Additionally, the Feynman scaling variable, defined as the ratio of the longitudinal momentum of the hadron in the center of mass frame divided by the total energy $x_{\mathrm{F}}(h_i) = P_z(h_i)/\sqrt{s}$, is limited to $0.1 < x_{\mathrm{F}}(h_{1/2}) < 1.0$ in order to reject hadrons originating from the target fragmentation. Fig. 4.16 shows the correlation between x_{F} and z for hadrons in the hadron pair sample. Furthermore a minimal missing energy of 3 GeV is required in order to remove exclusive events from the sample. The missing energy is defined as

$$E_{\mathrm{miss}} = \frac{(P + q - P_h)^2 - q^2}{2M} = \frac{M_X^2 - M^2}{2M}, \tag{4.1}$$

where P, q and P_h are the four-momenta of the proton, the virtual photon and the produced hadron pair, respectively. M_X describes the mass of the undetected recoiling system. The impact of this cut is visible in Fig. 4.13 as cut-off of the exclusive peak around $E_{\mathrm{miss}} = 0\,\mathrm{GeV}$.

To ensure a good definition of the measured angles, here ϕ_h and ϕ_R, the absolute relative momentum between the two hadrons is limited to $R_T > 0.07\,\mathrm{GeV/c}$, as it was introduced in previous studies of the same task on transversely polarized protons [81, 82]. This cut sort of replaces the usually used P_{hT}-cut on single hadrons, since the hadronic planes in case of hadron pairs are spread by the virtual photon and either the sum or the difference of their four momenta.

The final invariant mass distribution is shown in Fig. 4.15. One can clearly locate the K_0-peak at around $0.49\,\mathrm{GeV/c^2}$ as well as the ρ_0-peak at around $0.77\,\mathrm{GeV/c^2}$. Fig. 4.17 shows an additional impact of the $R_T > 0.07\,\mathrm{GeV/c}$, as it ensures linear correlation between the invariant mass and R_T.

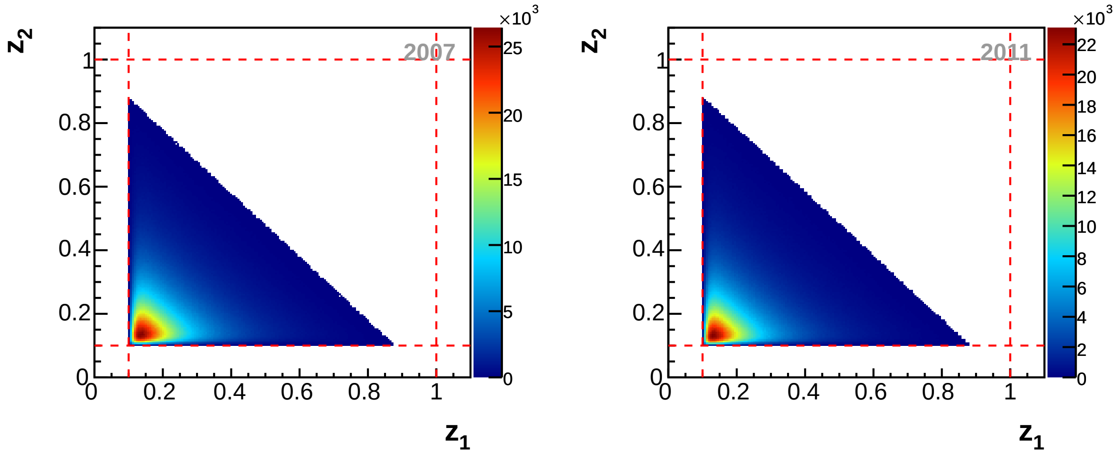

Figure 4.12: Energy fractions z_2 vs z_1 before (grey) and after (color) application of the associated cuts. The cuts are marked with dashed red lines.

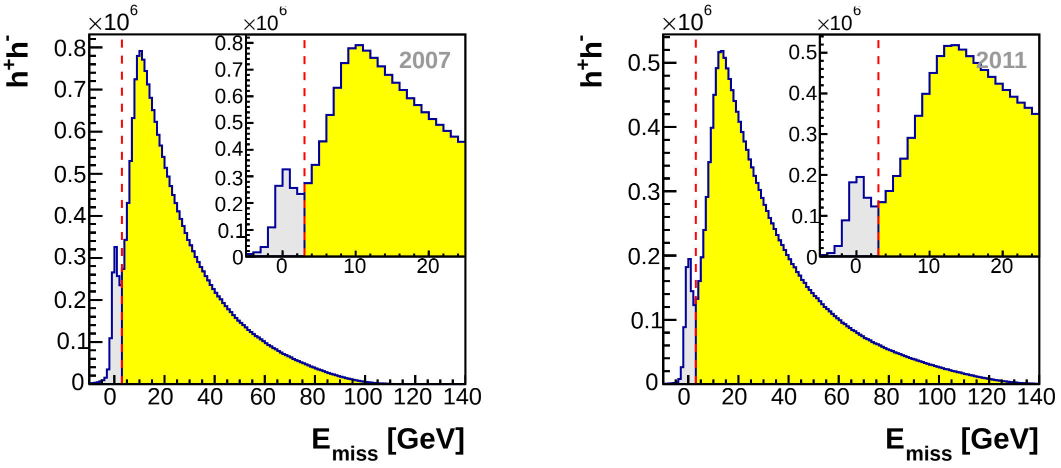

Figure 4.13: Distribution of the missing energy before (grey) and after (color) application of the associated cut. The cut is marked with a dashed red line.

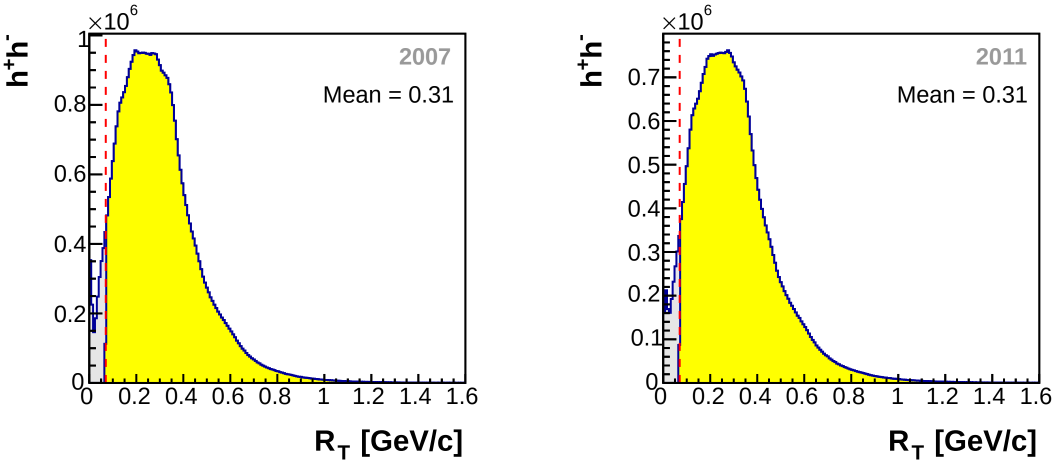

Figure 4.14: Distribution of R_T before (grey) and after (color) application of the associated cut. The cut is marked with a dashed red line.

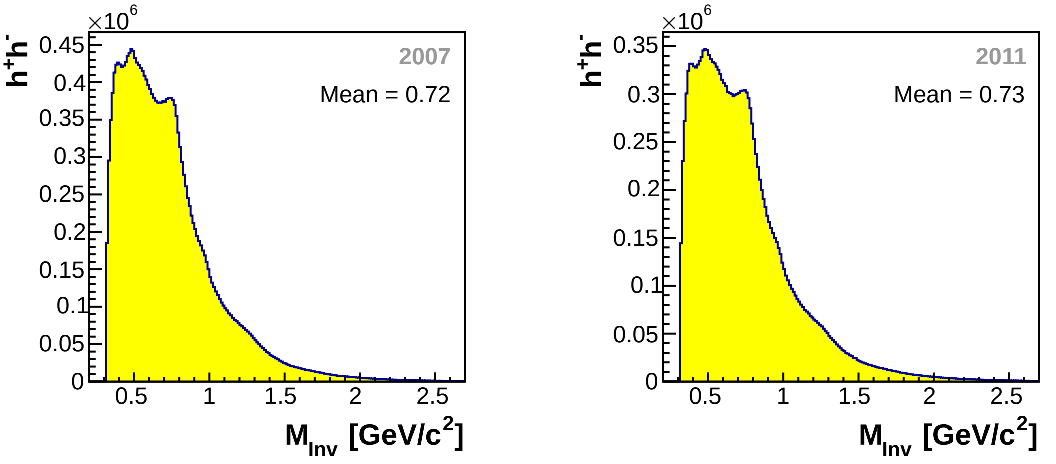

Figure 4.15: Distribution of the invariant mass after application of the associated cuts.

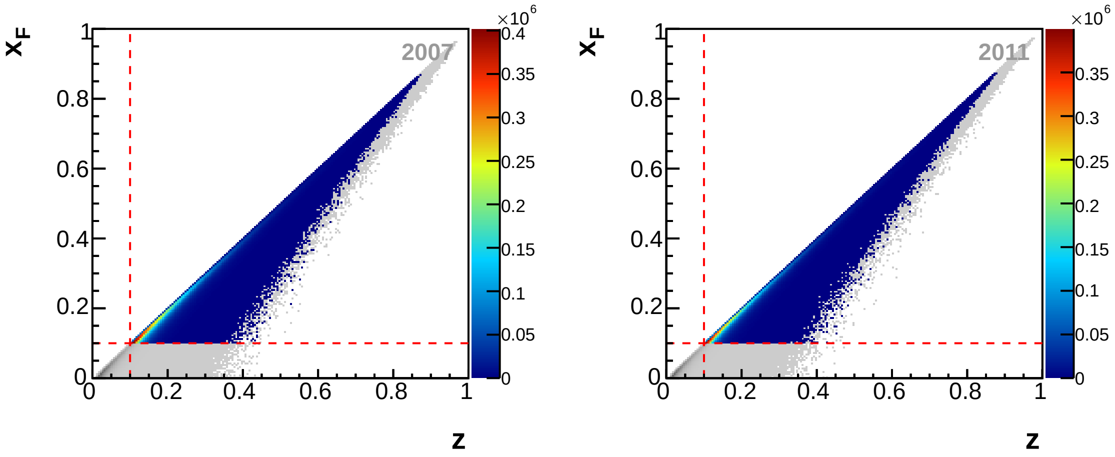

Figure 4.16: $x_{\mathrm{F},i}$ vs z_i before (greyscale) and after (colorscale) application of the associated cuts. The cuts are marked with dashed red lines.

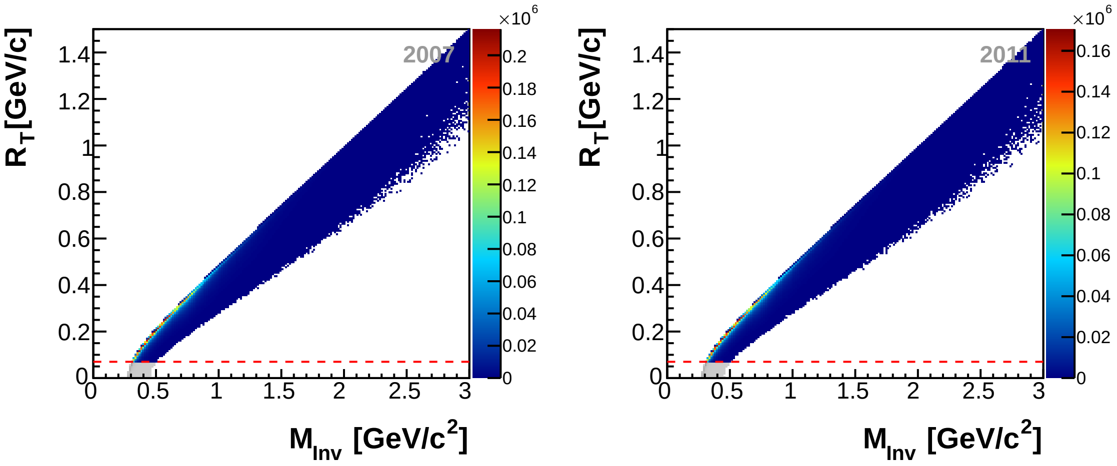

Figure 4.17: R_T vs M_{inv} before (greyscale) and after (colorscale) application of the associated cut. The cut is marked with a dashed red line.

4.4 Final Data Samples

In the following, the final data samples after application of the respective cuts are discussed, separately for the hadron pair and the single hadron analysis. For each analysis, respective statistics are given and important variables are discussed.

4.4.1 Final Two Hadron Data Samples

Tab. 4.3 shows the event and pair numbers per microwave setting, target polarization configuration and week. Although the overall numbers of hadron pairs per week differ significantly, the final data samples meet the statistical requirements of asymmetry extractions: a sufficiently balanced statistics regarding both the two polarization settings and the two microwave settings. They contain about $21.6 \cdot 10^6$ hadron pairs for 2007 and $17.9 \cdot 10^6$ for 2011 and show a constant pair multiplicity of 1.3 hadron pairs per SIDIS event.

Table 4.3: Final statistics of SIDIS events and h^+h^--pairs for each year, microwave setting, week, and polarization configuration.

Year		2007					
Setting		$+--+$		$-++-$		Both	
MW	**Week**	**Events**	$\boldsymbol{h^+h^-}$	**Events**	$\boldsymbol{h^+h^-}$	**Events**	$\boldsymbol{h^+h^-}$
MW+	W32	1388719	1843427	1113740	1477943	2502459	3321370
	W33	1099097	1462185	967784	1286026	2066881	2748211
	W34	603852	801100	269271	357613	873123	1158713
	W44	1151890	1537174	1411745	1883484	2563635	3420658
	W45	263238	350421	141751	188568	404989	538989
	Total	4506796	5994307	3904291	5193634	8411087	11187941
MW−	W35	1246868	1653884	1081330	1436066	2328198	3089950
	W36	1432501	1897447	1305372	1730766	2737873	3628213
	W37	1125555	1496325	1184722	1574971	2310277	3071296
	W38	271005	362835	209119	279396	480124	642231
	Total	4075929	5410491	3780543	5021199	7856472	10431690

Year		2011					
Setting		$+--+$		$-++-$		Both	
MW	**Week**	**Events**	$\boldsymbol{h^+h^-}$	**Events**	$\boldsymbol{h^+h^-}$	**Events**	$\boldsymbol{h^+h^-}$
MW+	W36	764345	1023069	934496	1249238	1698841	2272307
	W38	358067	477894	383735	512614	741802	990508
	W39	750349	1002278	999407	1334873	1749756	2337151
	W41	988938	1322982	850742	1137992	1839680	2460974
	W43	563010	750333	629699	838880	1192709	1589213
	Total	3424709	4576556	3798079	5073597	7222788	9650153
MW−	W25	495854	664185	336047	449060	831901	1113245
	W27	1421611	1905546	1214157	1625211	2635768	3530757
	W30	610755	818293	527929	705348	1138684	1523641
	W31	291513	390263	437650	584684	729163	974947
	W32	316608	423749	322571	431622	639179	855371
	W33	100754	134863	73785	98999	174539	233862
	Total	3237095	4336899	2912139	3894924	6149234	8231823

4.4.1.1 Angular Distributions

The azimuthal angles ϕ_h and ϕ_R, involved in the two hadron analysis, are displayed in Fig. 4.18, exemplarily for 2011. Corresponding plots for 2007 are appended in Sec. A.4 and don't show notable differences.

The angular distribution of θ, describing the angle between the positive hadron and the total four-momentum of the hadron pair in its center of mass frame, is depicted on the upper left of Fig. 4.19, exemplarily for 2011. It is symmetrically distributed around a mean value of approximately $\pi/2$. As a consequence, the θ-dependent modulations, involved in the two hadron cross section, shown in the further pads of Fig. 4.19, are characterized by mean values close to either 0 or 1. The mean values of the θ-dependent terms, appearing later as prefactors of the particular structure functions, are evaluated per kinematic bin, also used for the extraction of asymmetries. The results for both years are shown in Fig. 4.20, showing compatible values. They are found to be independent of x and M_{inv}, whereas for z a weak dependence is observed. In general, a clear dominance of $\sin(\theta)$- and $\sin^2(\theta)$-weighted structure functions can be concluded.

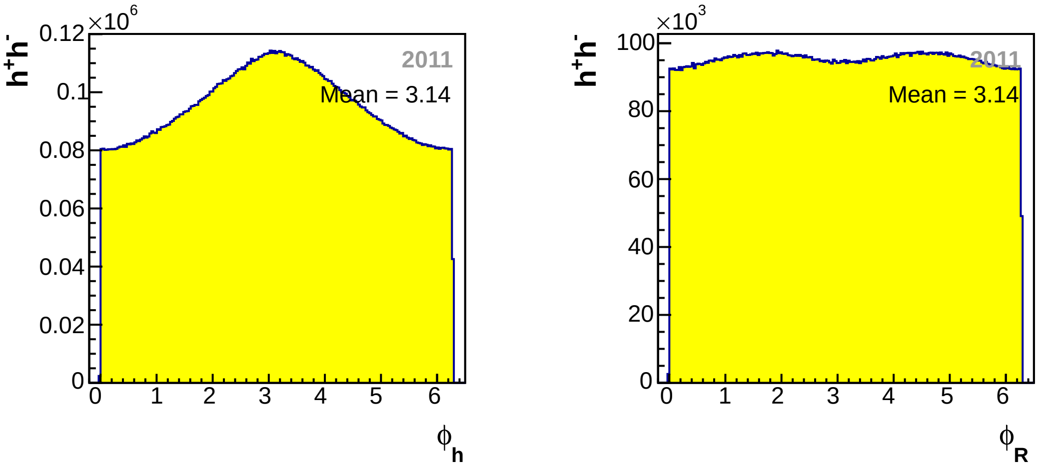

Figure 4.18: Distributions of the azimuthal angles ϕ_h (left) and ϕ_R (right) for 2011.

4.4.1.2 Kinematic Distributions

The mean values of important kinematic variables per kinematic bin, used for the extraction of hadron pair asymmetries, are depicted in Fig. 4.21 for both years. The different beam energies, 160 GeV in 2007 and 200 GeV in 2011, explain the main deviations in Q^2, y, and W. The other variables, considered for the extraction of asymmetries, show comparable values. The numerical values are collected in A.4.

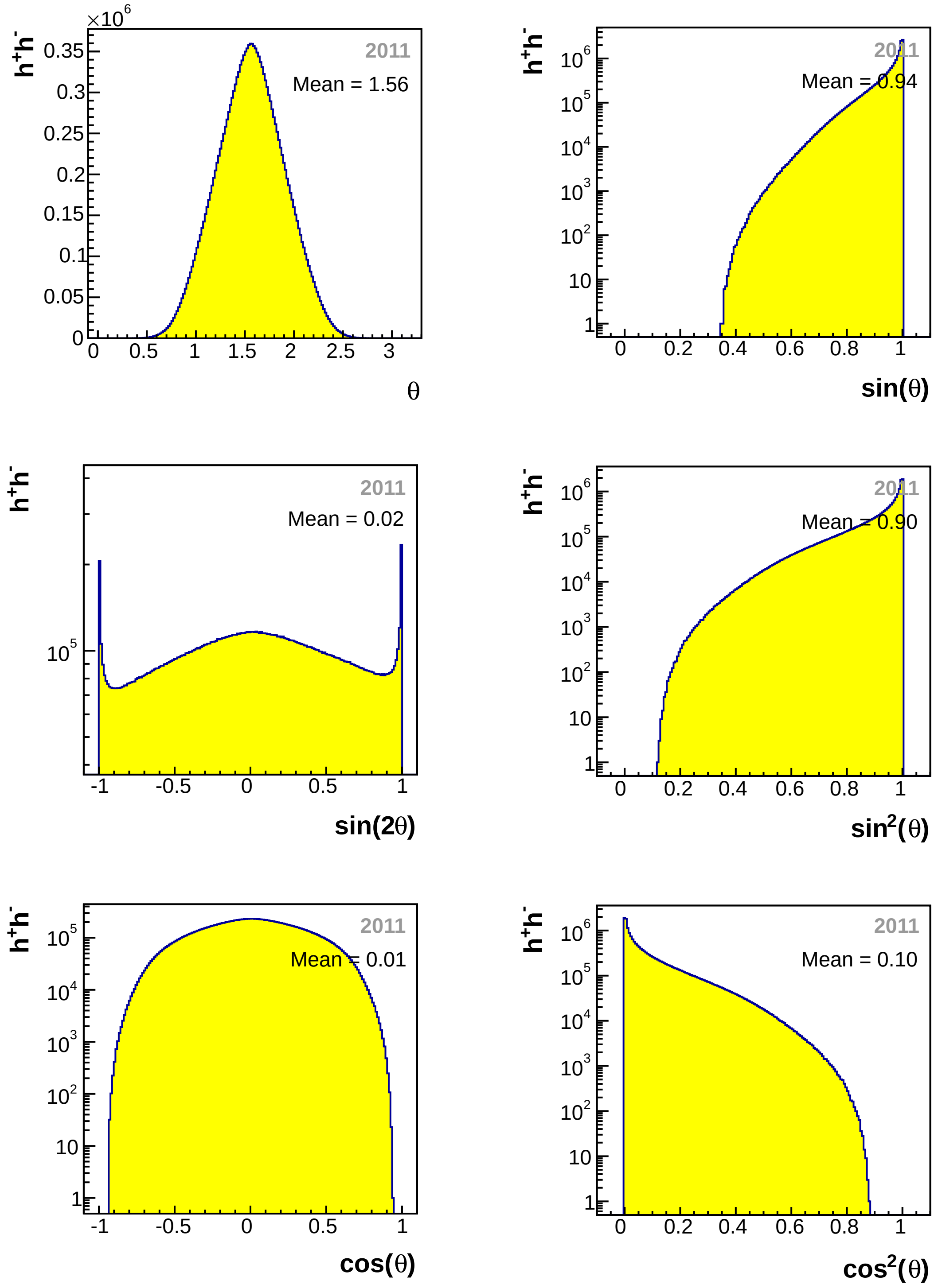

Figure 4.19: Distributions of the angle θ and the θ-dependent modulations of the hadron pair cross section for 2011.

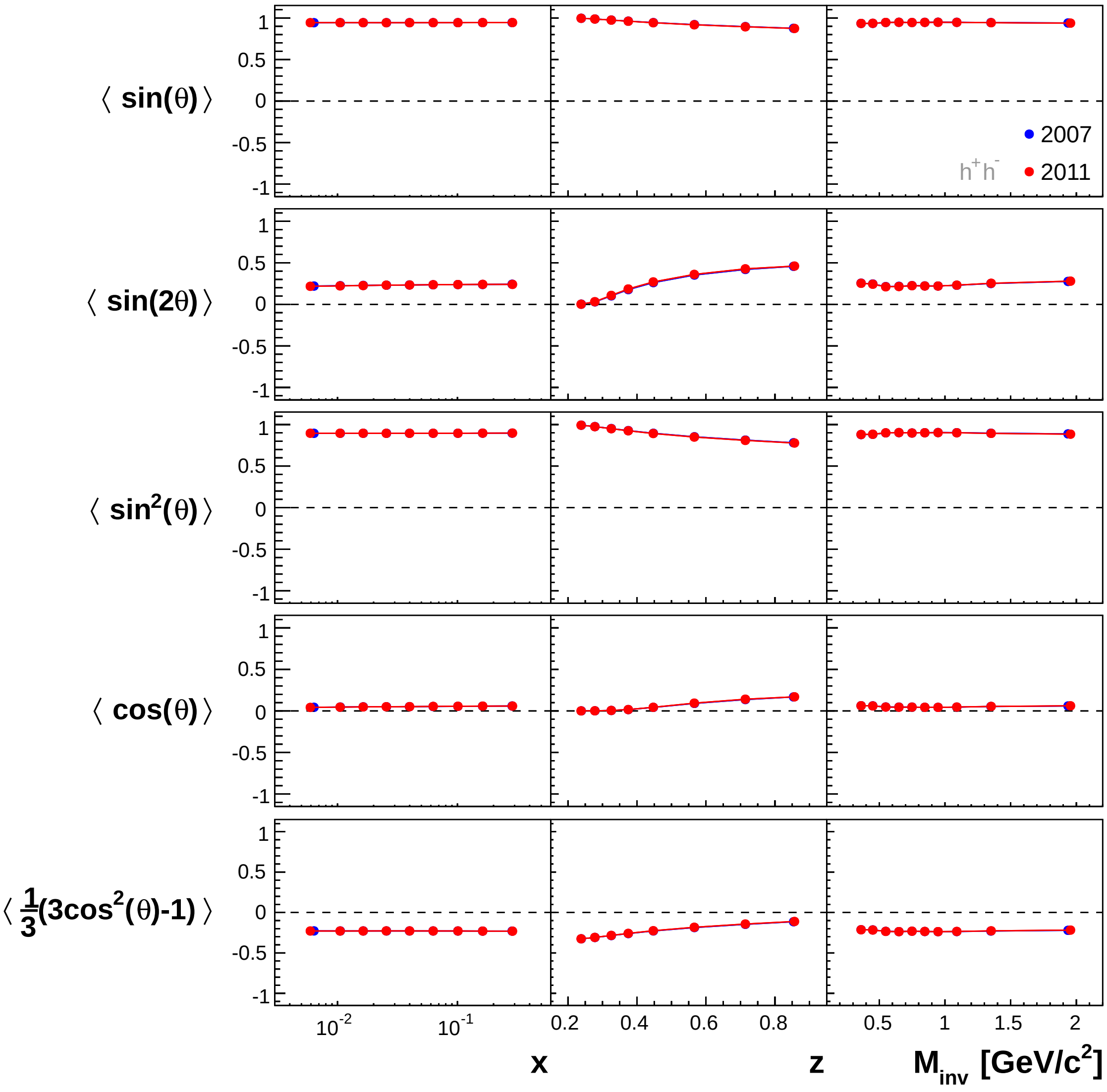

Figure 4.20: Mean values of θ-dependent prefactors per kinematic bin, used also for the extraction of azimuthal asymmetries.

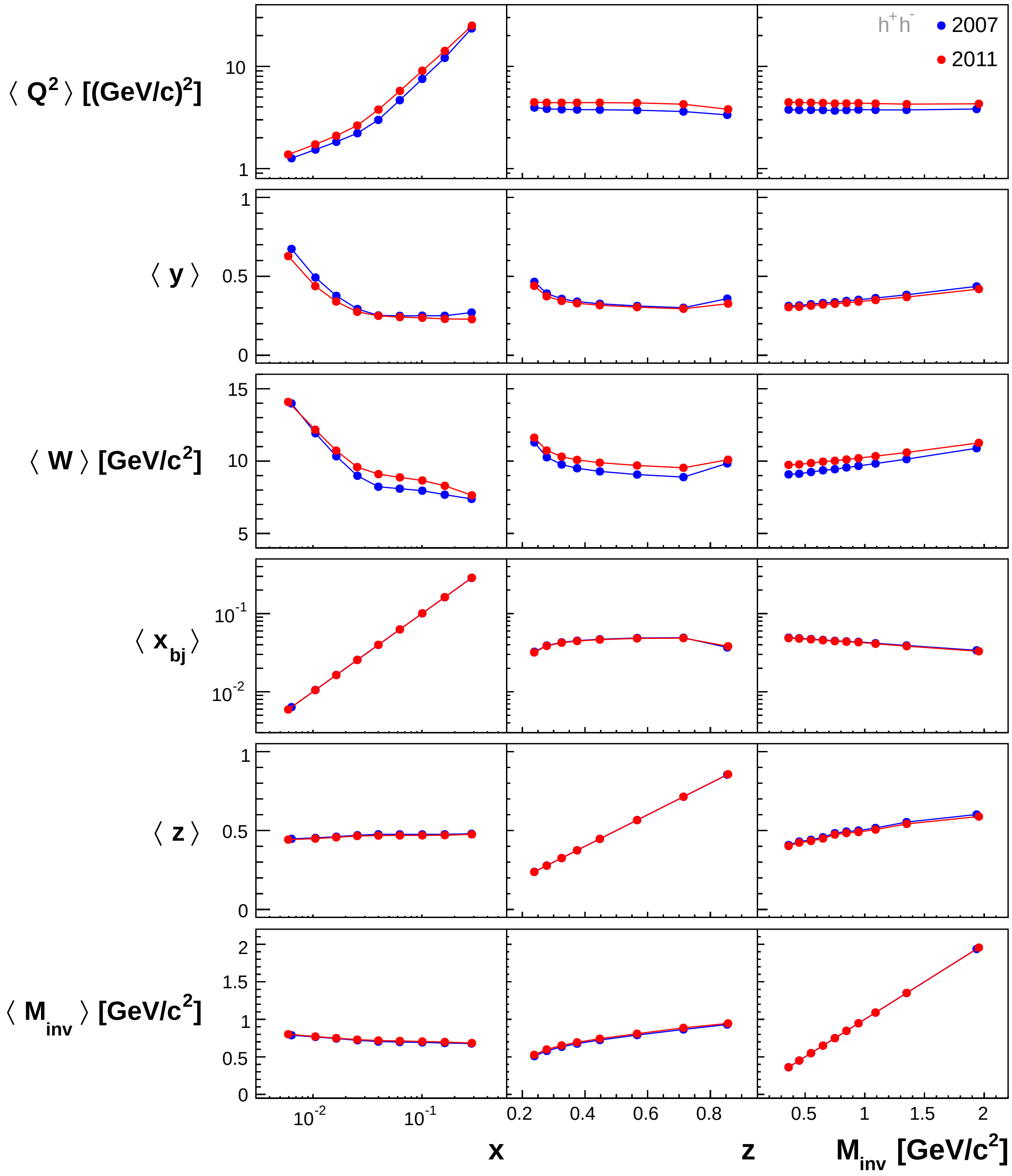

Figure 4.21: Mean values of important kinematic variables per kinematic bin, used also for the extraction of azimuthal asymmetries.

4.4.1.3 Stability of the Final Data Sample

The stability of the data is a crucial requirement for the extraction of asymmetries. To complete the previous data quality studies, outlined in Sec. 4.2, distributions of important variables are visually checked for consistency. As the asymmetries are extracted on basis of weekly subsamples, the distributions from different weeks, as well as distributions from different target polarization settings within one week, are compared on basis of their ratios.

As an example, Fig. 4.22 shows the ratios of angular distributions of each week with the most populated week, which is week 36 for 2007 and week 27 for 2011. The results indicate a general compatibility of the angular distributions for all weeks of the 2011 data. A comparable stability can be concluded for 2007 with the exception of week 44, where notable deviations are present. However, results of later compatibility studies on the resulting azimuthal asymmetries seem not to be affected by this observation. Corresponding ratio plots for kinematic variables indicate a general stability for the weeks of both years. They are collected in Sec. A.4.

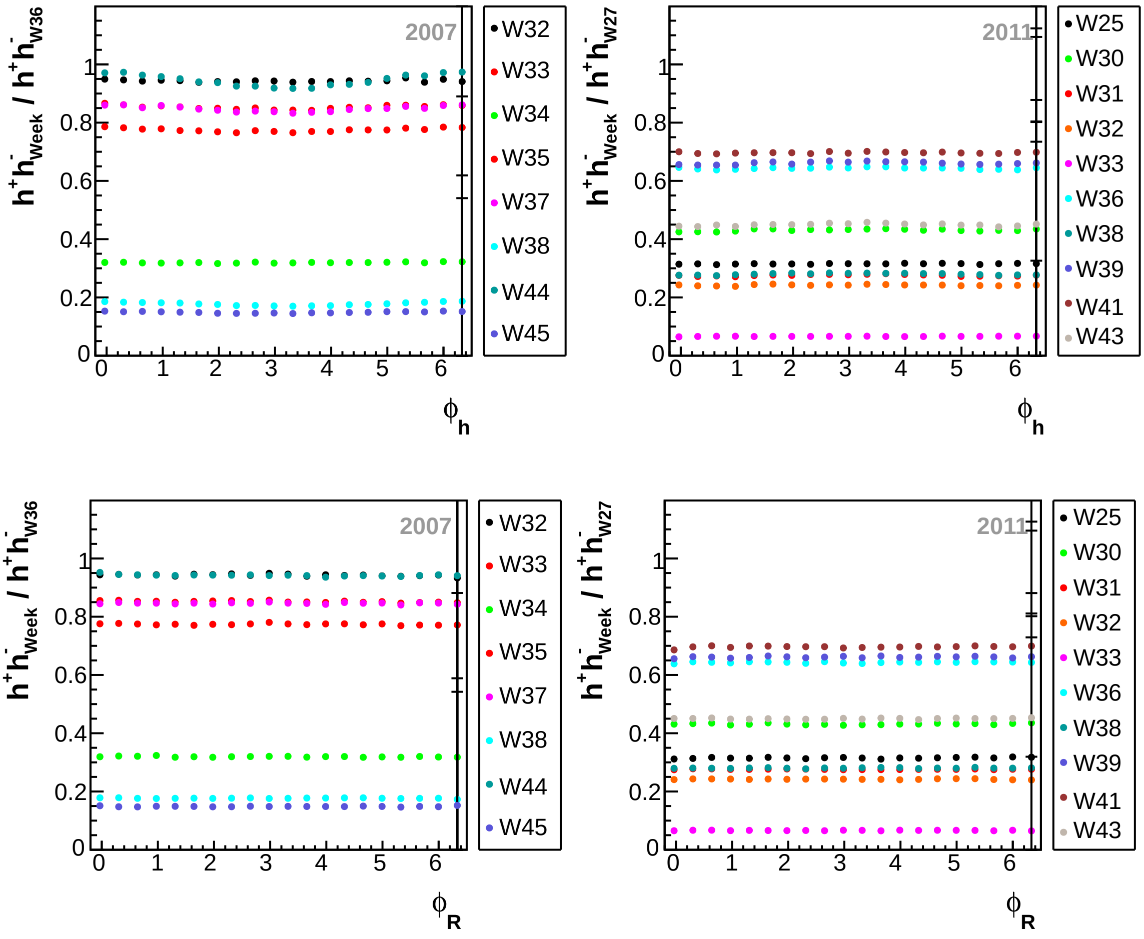

Figure 4.22: Ratios of the angular distributions from a particular week with the corresponding distribution from the most populated week.

Furthermore, ratios of angular distributions from subsamples with different polarization configuration are considered for each week, depicted in Fig. 4.23. The distributions do not seem to be affected substantially by the solenoid current changes. This can also be concluded from the ratio plots of kinematic variables, appended in Sec. A.4.

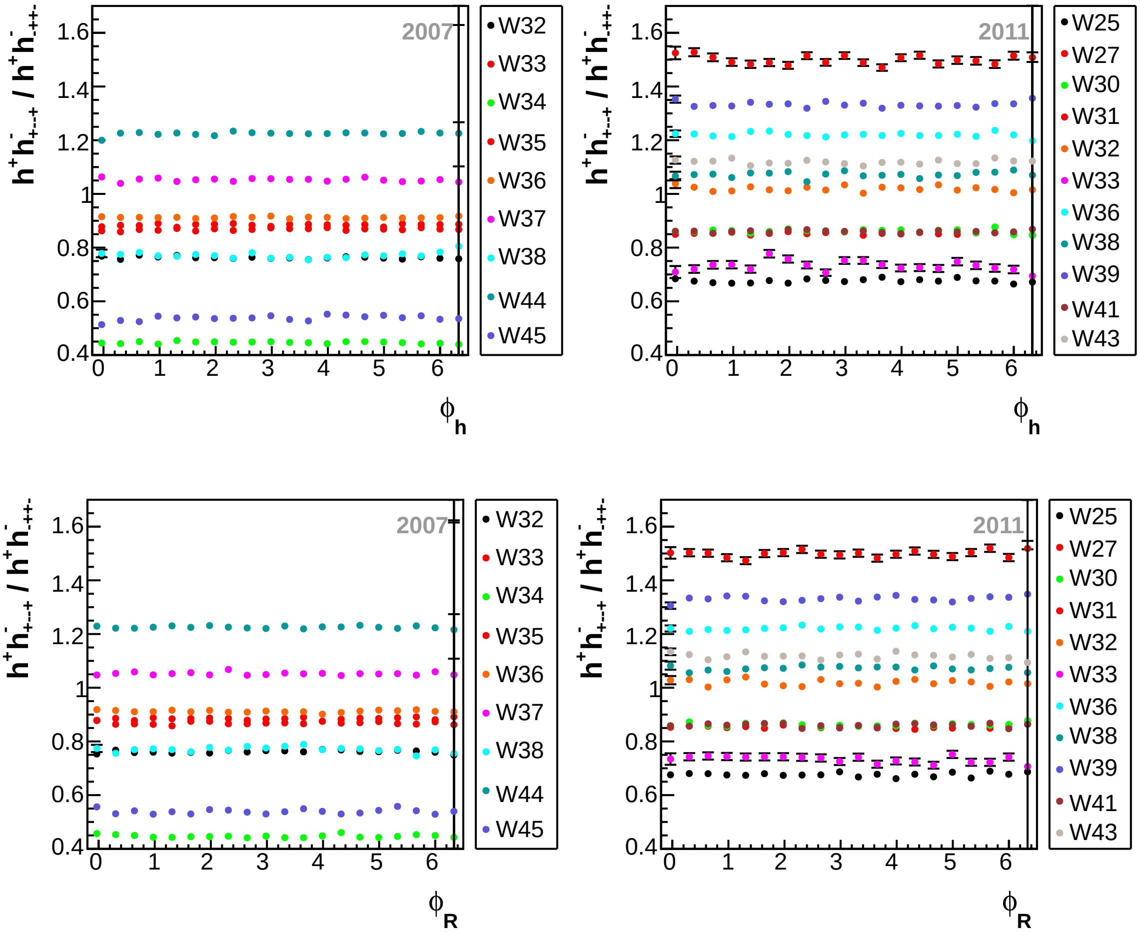

Figure 4.23: Ratios of the angular distributions from the two target polarization settings per week.

4.4.2 Final One Hadron Data Samples

The final statistics of the one hadron data samples from both years are given in Tab. 4.4 for positive and in Tab. 4.5 for negative hadrons. In total, the 2007 data contains about $27.5 \cdot 10^6$ positive and $21.6 \cdot 10^6$ negative hadrons, whereas for 2011 approximately $21.0 \cdot 10^6$ positive and $17.0 \cdot 10^6$ negative hadrons where detected. The numbers indicate a stable multiplicity of 1.06 h^+ and 1.04 h^- per event for all weeks of both years. When comparing the statistics from different microwave settings, as well as from different target polarization settings, a sufficient balance can be concluded.

Table 4.4: Final statistics of SIDIS events and positively charged hadrons for each year, microwave setting, week, and polarization configuration.

Year		2007					
Setting		$+--+$		$-++-$		Both	
MW	**Week**	**Events**	$\boldsymbol{h^+}$	**Events**	$\boldsymbol{h^+}$	**Events**	$\boldsymbol{h^+}$
MW+	W32	2223270	2347887	1784364	1884788	4007634	4232675
	W33	1756594	1857028	1547645	1635129	3304239	3492157
	W34	962693	1016969	430913	455125	1393606	1472094
	W44	1839044	1946131	2255150	2385972	4094194	4332103
	W45	420595	444878	225853	238800	646448	683678
	Total	7202196	7612893	6243925	6599814	13446121	14212707
MW−	W35	1991836	2103135	1728285	1826100	3720121	3929235
	W36	2292367	2419624	2092039	2209273	4384406	4628897
	W37	1791652	1893658	1886351	1994054	3678003	3887712
	W38	431853	457664	334350	353999	766203	811663
	Total	6507708	6874081	6041025	6383426	12548733	13257507

Year		2011					
Setting		$+--+$		$-++-$		Both	
MW	**Week**	**Events**	$\boldsymbol{h^+}$	**Events**	$\boldsymbol{h^+}$	**Events**	$\boldsymbol{h^+}$
MW+	W36	1137377	1200619	1392059	1469610	2529436	2670229
	W38	533830	563414	572313	603803	1106143	1167217
	W39	1119440	1181343	1489358	1572610	2608798	2753953
	W41	1469850	1551776	1263094	1333891	2732944	2885667
	W43	845105	891500	944907	996587	1790012	1888087
	Total	5105602	5388652	5661731	5976501	10767333	11365153
MW−	W25	737072	778240	499334	526782	1236406	1305022
	W27	2118726	2237879	1805649	1906670	3924375	4144549
	W30	909399	960504	786631	830035	1696030	1790539
	W31	433683	457899	649577	685423	1083260	1143322
	W32	472004	498228	479579	506462	951583	1004690
	W33	150834	159299	109460	115646	260294	274945
	Total	4821718	5092049	4330230	4571018	9151948	9663067

Table 4.5: Final statistics of SIDIS events and negatively charged hadrons for each year, microwave setting, week, and polarization configuration.

Year		2007					
Setting		$+--+$		$-++-$		Both	
MW	**Week**	**Events**	$\boldsymbol{h^-}$	**Events**	$\boldsymbol{h^-}$	**Events**	$\boldsymbol{h^-}$
MW+	W32	1766609	1844347	1422241	1484485	3188850	3328832
	W33	1396300	1458502	1231363	1286033	2627663	2744535
	W34	768423	802424	342797	358048	1111220	1160472
	W44	1466443	1532792	1799806	1880816	3266249	3413608
	W45	332859	347480	180675	188603	513534	536083
	Total	5730634	5985545	4976882	5197985	10707516	11183530
MW−	W35	1588895	1658317	1375098	1435132	2963993	3093449
	W36	1820895	1899952	1660679	1732986	3481574	3632938
	W37	1428834	1491765	1503789	1570743	2932623	3062508
	W38	343104	358716	265131	277238	608235	635954
	Total	5181728	5408750	4804697	5016099	9986425	10424849

Year		2011					
Setting		$+--+$		$-++-$		Both	
MW	**Week**	**Events**	$\boldsymbol{h^-}$	**Events**	$\boldsymbol{h^-}$	**Events**	$\boldsymbol{h^-}$
MW+	W36	932936	973653	1134035	1183136	2066971	2156789
	W38	437119	455734	466986	486855	904105	942589
	W39	914411	953676	1211075	1262975	2125486	2216651
	W41	1200746	1252820	1031700	1076392	2232446	2329212
	W43	689007	718556	769318	802051	1458325	1520607
	Total	4174219	4354439	4613114	4811409	8787333	9165848
MW−	W25	602420	628346	410676	428418	1013096	1056764
	W27	1722867	1797735	1479342	1543575	3202209	3341310
	W30	741024	773187	644281	672359	1385305	1445546
	W31	353011	368220	531898	554825	884909	923045
	W32	384262	400858	393062	410379	777324	811237
	W33	122547	127872	90328	94198	212875	222070
	Total	3926131	4096218	3549587	3703754	7475718	7799972

4.4.2.1 Angular Distributions

Both years distributions of the azimuthal angle ϕ_h are depicted in Fig. 4.24, together for positively and negatively charged hadrons. Their stability is checked in analogy to the two hadron case by building ratios of the distributions from single weeks (Fig. 4.25), as well as of distributions from different target polarization settings per week (Fig. 4.26). The results reveal a general coincidence with the results for ϕ_h in the two hadron case, indicating a stable measurement with exception of week 44 of year 2007, where small deviations can be noted in the global comparison.

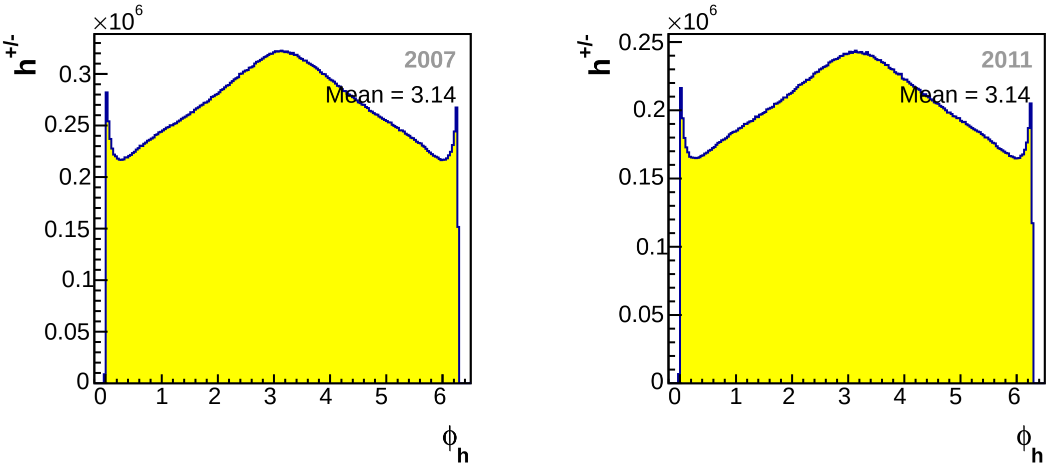

Figure 4.24: Distribution of the azimuthal angle ϕ_h.

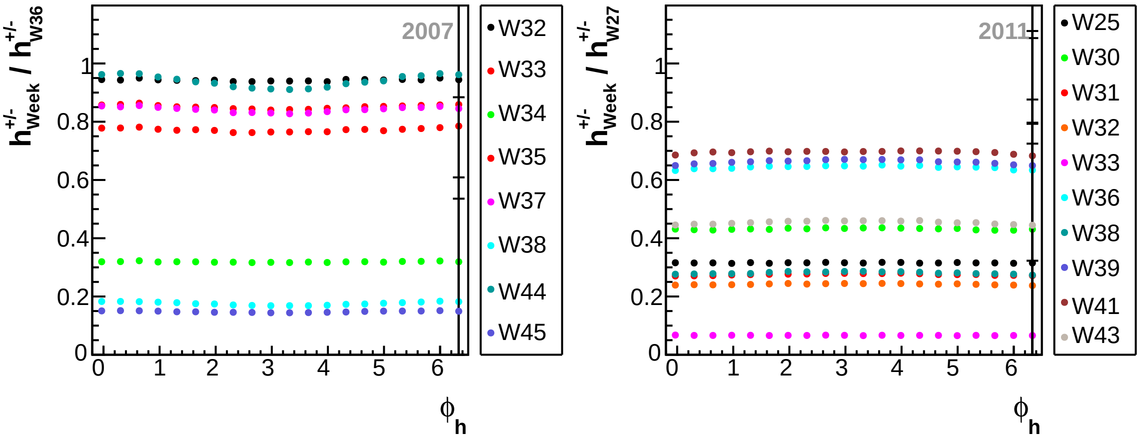

Figure 4.25: Ratios of the ϕ_h-distribution from a particular week with the corresponding distribution from the most populated week.

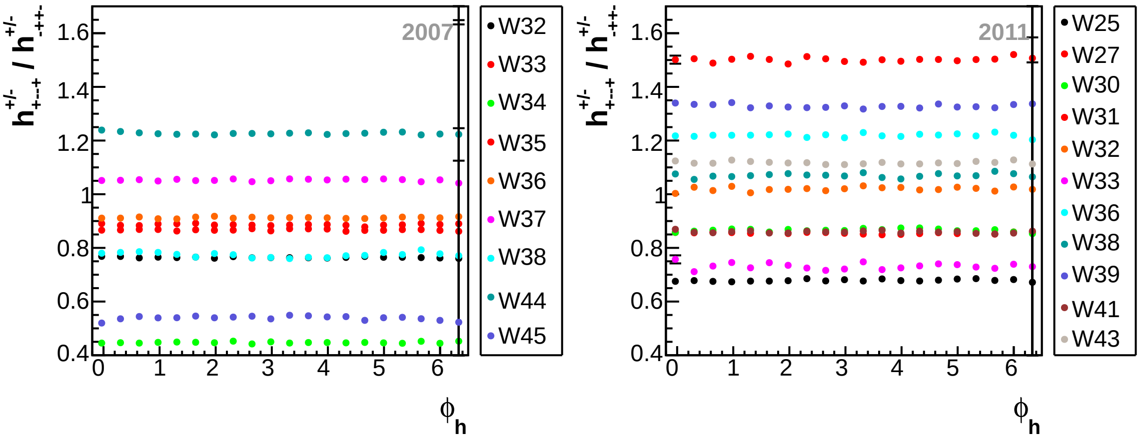

Figure 4.26: Ratios of the ϕ_h-distributions from the two target polarization settings per week.

4.4.2.2 Kinematic Distributions

The kinematic distributions for single hadrons are compatible with the two hadron case. They are appended in Sec. A.5. Fig. 4.27 shows the mean values of important variables in bins of x, z and P_{hT}, used for the extraction of asymmetries in the one hadron analysis, exemplarily for positively charged hadrons. The numerical values are also given in the appendix, separately for h^+ and h^-.

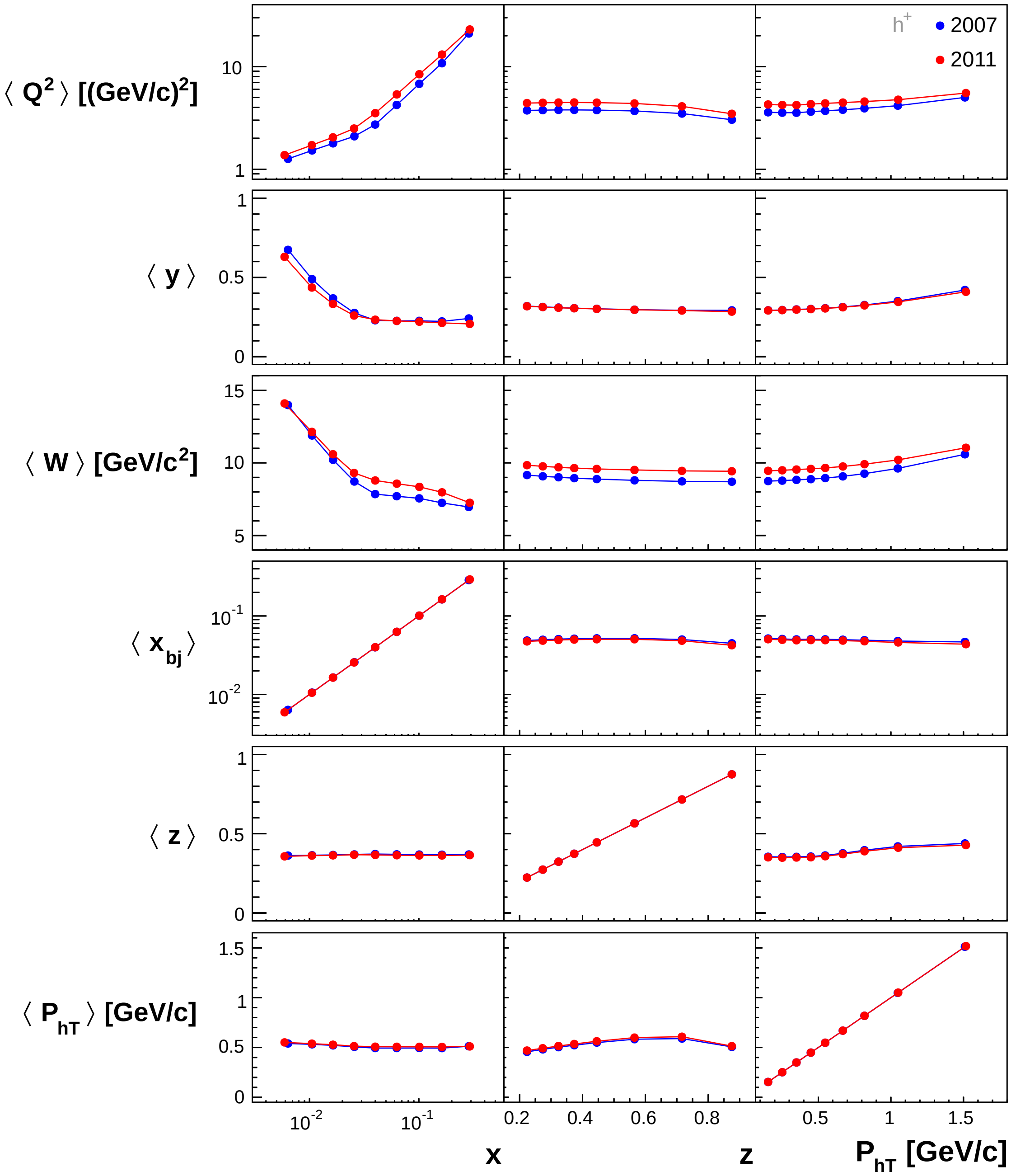

Figure 4.27: Mean values of important kinematic variables for h^+ per kinematic bin, used also for the extraction of azimuthal asymmetries.

5. Asymmetry Extraction

Measuring spin dependent azimuthal asymmetries is a challenging task and puts high requirements on the experimental setup, as well as on the data analysis techniques. As they are expected to be of the order of a few percent, they are highly sensitive to instabilities of the experimental setup, such as acceptance variations during the data taking. To take the best advantage from the available data set and to minimize experimentally inevitable systematic effects on analysis level, several extraction methods were used in this work. The most simple method is the so called Product Ratio (PR) method, where the asymmetries are accessed from a binned fit of constructed counting ratios, whereas the fit is performed one dimensionally for each of the angular basis arguments of the underlying cross section (1D PR). More sophisticated methods base on maximization of likelihood estimators, which is here used in two types, binned in two dimensions (2D LH) and unbinned (UB LH). The considered methods are discussed in detail in the following subchapters.

The procedure of analysis for each of the mentioned extraction methods, chosen in this work to extract asymmetries from the final data sample, is as follows. In a first step, raw asymmetries are extracted in bins of certain kinematical variables, the underlying PDFs and FFs are expected to depend on. These are x, z and M_{inv} in the two hadron, and x, z and P_{hT} in the one hadron analysis. The bin ranges for common variables are the same for both analysis, the one hadron and the two hadron, and are in detail listed in A.3. In order to minimize possible systematic effects, the raw asymmetries are extracted period-by-period, where each period corresponds to one week of data taking including sub-periods of different target polarization configurations. In a second step, the physical asymmetries are evaluated by correcting the raw asymmetries, accounting for the dilution of the target material, the polarization values of the beam and the target, as well as for the asymmetry dependent depolarization factors. The raw asymmetry correction is in detail outlined in Sec. 5.3. The final asymmetries are then evaluated by building the weighted means of the weekly asymmetries per kinematical bin.

5.1 Product Ratio Method

The Product Ratio (PR) method bases on the ratio

$$r_{1234}(\phi_h, \phi_R) = \prod_{i=1}^{4} \frac{N_i^+(\phi_h, \phi_R)}{N_i^-(\phi_h, \phi_R)}, \tag{5.1}$$

where the numbers $N_i^\pm(\phi_h, \phi_R)$ are numbers of single hadrons, respectively hadron pairs, originating from cell i with polarization state $+$ or $-$, as already introduced in Eq. (2.98). In first order of the modulation terms $A_{XU}(\phi_h, \phi_R)$ and $A_{XL}(\phi_h, \phi_R)$, defined in Sec. 2.4 for both types of analysis, this ratio is only sensitive on the modulation function $A_{XL}(\phi_h, \phi_R)$, containing the longitudinal raw asymmetries. Its approximation reads

$$r_{1234}(\phi_h, \phi_R) = C(\phi_h, \phi_R)\left(1 + 8A_{XL}(\phi_h, \phi_R)\right). \tag{5.2}$$

The prefactor

$$C(\phi_h, \phi_R) = \prod_{i=1}^{4} \frac{c_i^+(\phi_h, \phi_R)}{c_i^-(\phi_h, \phi_R)} \tag{5.3}$$

with $c_i^\pm(\phi_h, \phi_R) = \Phi_i^\pm a_i^\pm(\phi_h, \phi_R) n_i \sigma_{UU}$ can be reasonably assumed to be constant and closed to 1, as

- the flux is the same for all cells during each polarization configuration, because only events are selected where the beam crosses all cells

$$\Phi_1^\pm = \Phi_2^\mp = \Phi_3^\mp = \Phi_4^\pm \;\Rightarrow\; \prod_{i=1}^{4} \frac{\Phi_i^+}{\Phi_i^-} = 1, \tag{5.4}$$

- the ratio of acceptances before and after the polarization reversal is approximately equal for all cells

$$\frac{a_1^+(\phi_h, \phi_R)}{a_1^-(\phi_h, \phi_R)} = \frac{a_2^-(\phi_h, \phi_R)}{a_2^+(\phi_h, \phi_R)} = \frac{a_3^-(\phi_h, \phi_R)}{a_3^+(\phi_h, \phi_R)} = \frac{a_4^+(\phi_h, \phi_R)}{a_4^-(\phi_h, \phi_R)} \;\Rightarrow\; \prod_{i=1}^{4} \frac{a_i^+(\phi_h, \phi_R)}{a_i^-(\phi_h, \phi_R)} = 1, \tag{5.5}$$

- the target material is not changed during the data taking ($n_i^+ = n_i^-$).

Within this work, a one dimensional PR fitting technique is chosen, where the ratio $r_{1234}(\phi_h, \phi_R)$ is built separately for contributing independent angular arguments Θ_j, and fitted with adapted one dimensional fit functions $f_j(\Theta_j)$. Considering the two hadron analysis, $A_{XL}(\phi_h, \phi_R)$ is based on the six azimuthal angles

$$\Theta_1 = \phi_h - \phi_R \tag{5.6}$$
$$\Theta_2 = \phi_h \tag{5.7}$$
$$\Theta_3 = \phi_h + \phi_R \tag{5.8}$$
$$\Theta_4 = \phi_R \tag{5.9}$$
$$\Theta_5 = 3\phi_h - \phi_R \tag{5.10}$$
$$\Theta_6 = 4\phi_h - 2\phi_R. \tag{5.11}$$

By fitting $r_{1234}(\Theta_j)$ with the appropriate one dimensional fit function out of

$$\begin{aligned} f_1(\Theta_1) = 1 + 8\Big(&a^1_{LL,\mathrm{Raw},1} + a^{\sin(\phi_h-\phi_R)}_{UL,\mathrm{Raw}}\sin(\Theta_1) + a^{\sin(2\phi_h-2\phi_R)}_{UL,\mathrm{Raw}}\sin(2\Theta_1) \\ &+ a^{\cos(\phi_h-\phi_R)}_{LL,\mathrm{Raw}}\cos(\Theta_1) + a^{\cos(2\phi_h-2\phi_R)}_{LL,\mathrm{Raw}}\cos(2\Theta_1)\Big) \end{aligned} \tag{5.12}$$

$$f_2(\Theta_2) = 1 + 8\Big(a^1_{LL,\mathrm{Raw},2} + a^{\sin(2\phi_h)}_{UL,\mathrm{Raw}}\sin(2\Theta_2)\Big) \tag{5.13}$$

$$f_3(\Theta_3) = 1 + 8\Big(a^1_{LL,\mathrm{Raw},3} + a^{\sin(\phi_h+\phi_R)}_{UL,\mathrm{Raw}}\sin(\Theta_3)\Big) \tag{5.14}$$

$$f_4(\Theta_4) = 1 + 8\Big(a^1_{LL,\mathrm{Raw},4} + a^{\sin(2\phi_R)}_{UL,\mathrm{Raw}}\sin(2\Theta_4)\Big) \tag{5.15}$$

$$f_5(\Theta_5) = 1 + 8\Big(a^1_{LL,\mathrm{Raw},5} + a^{\sin(3\phi_h-\phi_R)}_{UL,\mathrm{Raw}}\sin(\Theta_5)\Big) \tag{5.16}$$

$$f_6(\Theta_6) = 1 + 8\Big(a^1_{LL,\mathrm{Raw},6} + a^{\sin(4\phi_h-2\phi_R)}_{UL,\mathrm{Raw}}\sin(\Theta_6)\Big), \tag{5.17}$$

the raw asymmetries can be identified with the fitted parameters

$$A^{m(\phi_h,\phi_R)}_{XL,\mathrm{Raw}} = a^{m(\phi_h,\phi_R)}_{XL,\mathrm{Raw}}. \tag{5.18}$$

Note that, beside the full set of azimuthal asymmetries, this method further allows to extract the integrated asymmetry A^1_{LL}. As it is kept as free parameter in each of the fit functions, six separately extracted values result in each bin.

Considering the one hadron case, all raw asymmetries can be extracted from a single one dimensional fit, as $A_{XL}(\phi_h, \phi_R)$ only depends on the azimuthal angle $\Theta = \phi_h$. Here, the fit function reads

$$f(\Theta) = 1 + 8\Big(a^1_{LL,\mathrm{Raw}} + a^{\sin(\phi_h)}_{UL,\mathrm{Raw}}\sin(\Theta) + a^{\sin(2\phi_h)}_{UL,\mathrm{Raw}}\sin(2\Theta) + a^{\cos(\phi_h)}_{LL,\mathrm{Raw}}\cos(\Theta)\Big). \tag{5.19}$$

In any case, the ratio $r_{1234}(\Theta_j)$ is fitted on 16 bins in $\Theta_j \in [0, 2\pi]$, using the χ^2-minimization technique, provided by the MINUIT package of ROOT. The error on $r_{1234}(\Theta_j)$ per bin is propagated as

$$\Delta r_{1234,\mathrm{bin}}(\Theta_j) = \sqrt{\sum_{i=1}^{4}\left(\frac{1}{N^+_{i,\mathrm{bin}}(\Theta_j)} + \frac{1}{N^-_{i,\mathrm{bin}}(\Theta_j)}\right)}. \tag{5.20}$$

A remark should be given on the used notation “r_{1234}”, chosen to clarify the type of asymmetry and the considered cells, used for its calculation. The letter indicates, if the asymmetry is a real physical spin asymmetry (r), or a constructed false asymmetry for systematic studies (f). As asymmetries of all types can also be constructed out of subsamples, including only two cells, the cell numbers are given to indicate the considered cells. The following notifications are used within this work to specify types of asymmetries:

A_{r1234}	Real Asymmetry
A_{r12}/A_{r34}	Upstream/Downstream Real Asymmetry
A_{f14}/A_{f23}	Outer/Inner False Asymmetry

5.2 Likelihood Methods

The following discussion on likelihood methods will be limited to the unbinned case, as a two dimensional approach is only reasonable in case of the two hadron analysis, and was also there mainly used to generate starting values for the unbinned method. For a detailed description of the two dimensional binned approach, the reader may be referred to the Refs. [82, 83].

The unbinned maximum likelihood method bases on a probabilistic approach, where the probability for detecting a hadron pair, respectively a single hadron, with azimuthal angles ϕ_h and ϕ_R is parametrized as a probability density function of the form

$$p_i^{\pm}(\phi_h, \phi_R) = a_i^{\pm}(\phi_h, \phi_R) \cdot (1 + A_{XU}(\phi_h, \phi_R) \pm A_{XL}(\phi_h, \phi_R)) \,, \tag{5.21}$$

where $a_i^{\pm}(\phi_h, \phi_R)$ is the acceptance for a specific cell i, while $A_{XU}(\phi_h, \phi_R)$ and $A_{XL}(\phi_h, \phi_R)$ denote the target spin independent and dependent angular modulation terms.

An extended maximum likelihood fit is performed, where the probability density function $p_i^{\pm}(\phi_h, \phi_R)$ is replaced by the function $P_i^{\pm}(\phi_h, \phi_R) = \mu_i^{\pm} \cdot p_i^{\pm}(\phi_h, \phi_R)$, which is normalized to the theoretically predicted number of events $\mu_i^{\pm}$:

$$\int_0^{2\pi} \int_0^{2\pi} P_i^{\pm}(\phi_h, \phi_R)\, d\phi_h d\phi_R = \mu_i^{\pm}. \tag{5.22}$$

The likelihood function to be maximized reads

$$\mathcal{L} = \prod_{i=1}^{4} \left[\left(e^{\mu_i^+} \prod_{m=1}^{N_i^+} P_i^+(\phi_{h_m}, \phi_{R_m}) \right)^{\frac{\bar{N}}{N_i^+}} \cdot \left(e^{\mu_i^-} \prod_{n=1}^{N_i^-} P_i^-(\phi_{h_n}, \phi_{R_n}) \right)^{\frac{\bar{N}}{N_i^-}} \right]. \tag{5.23}$$

Considering the necessary weighting with the powers $\bar{N}/N_i^{\pm}$ [84], where the average number of events per cell is $\bar{N} = \frac{1}{8}\sum_{i=1}^{4}\left(N_i^+ + N_i^-\right)$, to account for possibly unbalanced statistics between the cells and further assuming the acceptance change per cell $i \in \{1, 2, 3, 4\}$ to be describable by a single constant

$$c_i = \frac{a_i^-(\phi_h, \phi_R)}{a_i^+(\phi_h, \phi_R)}, \tag{5.24}$$

the maximum likelihood estimator becomes

$$\begin{aligned}\mathcal{L} = \prod_{i=1}^{4} \Bigg[&\left(e^{\mu_i^+} \prod_{m=1}^{N_i^+} a_i^+(\phi_{h_m}, \phi_{R_m}) \cdot (1 + A_{XU}(\phi_{h_m}, \phi_{R_m}) + A_{XL}(\phi_{h_m}, \phi_{R_m})) \right)^{\frac{\bar{N}}{N_i^+}} \\ &\cdot \left(e^{\mu_i^-} \prod_{n=1}^{N_i^-} c_i a_i^+(\phi_{h_n}, \phi_{R_n}) \cdot (1 + A_{XU}(\phi_{h_n}, \phi_{R_n}) - A_{XL}(\phi_{h_n}, \phi_{R_n})) \right)^{\frac{\bar{N}}{N_i^-}} \Bigg].\end{aligned} \tag{5.25}$$

For practical reasons the acceptance terms $a_i^+(\phi_h, \phi_R)$ are assumed to be describable by single constants a_i^+, which was found to be valid in Monte Carlo studies [83][85]. Consequently $\mu_i^{\pm}$ can be estimated as $\mu_i^{\pm} = 4\pi^2 a_i^{\pm}$ and the free fit parameters of this estimator are the acceptances a_1^+, ..., a_4^+, the acceptance changes c_1, ..., c_4, and the amplitudes of the angular modulations. These amplitudes can be identified with the wanted raw asymmetries.

Instead of the direct maximization of the likelihood function, it is technically more convenient to minimize its negative logarithm and to neglect constant terms, as they are expected not to contribute to the minimization. The minimization of $-\ln(\mathcal{L})$ is implemented using the Broyden-Fletcher-Goldfarb-Shanno (BFGS) algorithm from the GNU scientific library [86, 87].

The key advantage of the unbinned likelihood method, in comparison to the binned methods 1D PR and 2D LH, is its stable convergence also with low statistics. Another benefit, important for the present study, is the possibility to include also terms in the fit, that correspond to an unpolarized target. For these reasons, the final results of this work are obtained using the UB LH method.

It has to be mentioned for completeness, that the likelihood methods can be also used to extract asymmetries from subsamples, including only data from two cells for instance. Hence, also upstream/downstream real and outer/inner false asymmetries can be studied with these methods.

5.3 Raw Asymmetry Correction

The modulation amplitudes $A_{XL,\mathrm{Raw}}^{m(\phi_h,\phi_R)}$, extracted with any of the discussed methods, have to be corrected for the dilution of the target f, the respective polarization of the beam and target, P_B and P_T, and the corresponding depolarization factors $D_{XL}^{m(\phi_h,\phi_R)}$ in order to achieve physical asymmetries $A_{XL}^{m(\phi_h,\phi_R)}$. We review the corresponding formulas from Eq. (2.104):

$$A_{UL}^{m(\phi_h,\phi_R)} = \frac{A_{UL,\mathrm{Raw}}^{m(\phi_h,\phi_R)}}{\langle f|P_T|D_{UL}^{m(\phi_h,\phi_R)}\rangle} \qquad\qquad A_{LL}^{m(\phi_h,\phi_R)} = \frac{A_{LL,\mathrm{Raw}}^{m(\phi_h,\phi_R)}}{\langle fP_B|P_T|D_{LL}^{m(\phi_h,\phi_R)}\rangle}.$$

The certain correction factors derivate slightly for the considered data samples of 2007 and 2011, mainly due to the different beam energies. Considering the two hadron case exemplarily, their mean values per kinematical bin, averaged over the certain year of data taking, are displayed in Fig. 5.2 and are numerically listed in A.4. The following list summarizes their certain characteristics.

Dilution Factor f

The dilution factor f represents the fraction of polarizable target material. Considering pure ammonia NH_3, one could naively assume a dilution factor of $3/17 = 0.18$, since only the three hydrogen nucleons are polarizable. For a more realistic calculation, the dilution factor is commonly defined as the ratio of nucleon numbers, weighted with their corresponding unpolarized total cross sections:

$$f = \frac{n_p\overline{\sigma}_p^{\mathrm{tot}}}{n_p\overline{\sigma}_p^{\mathrm{tot}} + \sum_A n_A\overline{\sigma}_A^{\mathrm{tot}}} = \frac{n_p}{n_p + \sum_A n_A\frac{\overline{\sigma}_A^{\mathrm{tot}}}{\overline{\sigma}_p^{\mathrm{tot}}}}. \tag{5.26}$$

Here, p indicates a hydrogen nucleon and A any other isotope contained in the target [88]. The total spin-independent cross section $\overline{\sigma}^{\mathrm{tot}}$ is related to the Born approximated cross section $\overline{\sigma}^{1\gamma}$ by

$$\overline{\sigma}^{\mathrm{tot}} = \overline{\sigma}^{1\gamma} + \overline{\sigma}^{\mathrm{el}} + \overline{\sigma}^{\mathrm{qel}} + \overline{\sigma}^{\mathrm{incl}}, \tag{5.27}$$

involving elastic, quasi-elastic and inclusive contributions. Considering semi-inclusive reactions, the elastic and quasi-elastic cross sections σ^{el} and $\overline{\sigma}^{\mathrm{qel}}$ vanish, since the detection of at least one final state hadron ensures the inelasticity of the process [89]. At low x-values, the dilution factor for hadron-tagged reactions is consequently larger than for inclusive ones. For the calculation of the dilution factor, the fraction $\overline{\sigma}_A^{\mathrm{tot}}/\overline{\sigma}_p^{\mathrm{tot}}$ is approximated by the ratio of unpolarized structure functions F_2^A/F_2^p, using parametrizations from NMC [90] and EMC [91]. Higher order corrections, including vertex and vacuum polarization radiation, are taken into account by applying the additional correction factor

$$\rho(x,y) = \nu\frac{\overline{\sigma}^{1\gamma}}{\overline{\sigma}^{\mathrm{tot}}}, \tag{5.28}$$

where the values are obtained from tables, pregenerated with TERAD [92]. In practice, the dilution factor is evaluated event wise using the PHAST routine

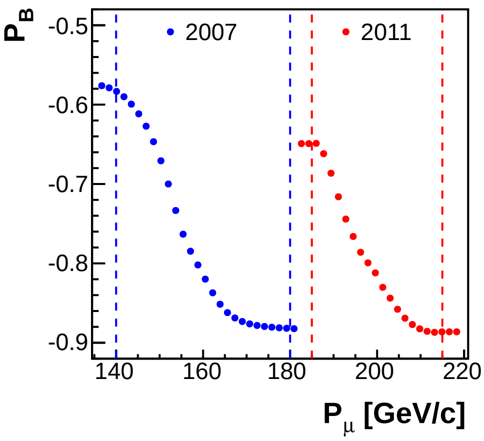

Figure 5.1: Beam polarization as a function of the beam momentum for 2007 (blue) and 2011 (red).

PaAlgo::GetDilutionFactor, which returns the dilution factor for a given cell and specific values for x and y, with a relative error of about 1% for 2007 and 2% for 2011 [23, 93]. It averages around 0.15 for both years of data taking.

Beam Polarization P_B

Due to the different beam energies during the two years of data taking, the beam polarization P_B differs for the considered data samples. It averages -0.79 in 2007 and -0.83 in 2011, and is measured with 5% uncertainty [23, 93]. Fig. 5.1 shows the beam polarization as a function of the muon momentum for both years. Only beam spin dependent asymmetries have to be corrected for this quantity.

Target Polarization P_T

The absolute target polarization $|P_T|$ is of the order of 0.87 for both years and is measured per run with 2% accuracy in 2007 and 3.5% in 2011 [23, 93]. It needs to be taken into account for all target spin dependent asymmetries.

Depolarization Factors $D_{XL}^{m(\phi_h,\phi_R)}$

The depolarization factors appear as kinematic prefactors of the angular modulations $m(\phi_h, \phi_R)$ in the considered cross sections. They describe the spin fraction, being transferred from the lepton to the virtual photon and are therefore dependent on the virtual photon polarization parameter ε, introduced in Eq. (2.53). The following depolarization factors can be defined:

$$D_{UL}^{(1)} := 1 \qquad D_{UL}^{(2)} := \varepsilon \qquad D_{UL}^{(3)} := \sqrt{2\varepsilon(1+\varepsilon^2)} \tag{5.29}$$

$$D_{LL}^{(1)} := \sqrt{1-\varepsilon} \qquad D_{LL}^{(2)} := \sqrt{2\varepsilon(1-\varepsilon)}. \tag{5.30}$$

The weekly raw asymmetries are corrected with the arithmetic mean of the product of correction factors, following the above Eq. (2.104), whereas the product is evaluated per hadron pair, respectively single hadron. The resulting total correction factors per kinematic bin, averaged over a whole year, are shown in Fig. 5.3 exemplarily for the two hadron analysis. In both analyses, the overall correction factors average around 0.1 to 0.2 for single spin and −0.05 for double spin asymmetries. Consequently, the raw asymmetries are effectively scaled by a factor of about 10 to 5, respectively −20, in order to obtain the physical asymmetries.

The systematic uncertainties of the correction factors have to be taken into account for the evaluation of the systematic error of the final asymmetries. The total multiplicative systematic errors are estimated as quadratic sum of the individual errors:

$$\frac{\Delta A_{UL}^{m(\phi_h,\phi_R)}}{A_{UL}^{m(\phi_h,\phi_R)}} = \sqrt{\left(\frac{\Delta f}{f}\right)^2 + \left(\frac{\Delta P_T}{P_T}\right)^2} \tag{5.31}$$

$$\frac{\Delta A_{LL}^{m(\phi_h,\phi_R)}}{A_{LL}^{m(\phi_h,\phi_R)}} = \sqrt{\left(\frac{\Delta f}{f}\right)^2 + \left(\frac{\Delta P_B}{P_B}\right)^2 + \left(\frac{\Delta P_T}{P_T}\right)^2}. \tag{5.32}$$

The systematic uncertainties, contributing to the corrected asymmetries, are listed in Tab. 5.1 for both years, including the resulting total multiplicative uncertainty for single- and double-spin asymmetries.

Table 5.1: Multiplicative systematic errors, contributing to the systematic uncertainty of the corrected asymmetries, for 2007 and 2011 [23, 93].

Year		2007	2011
Dilution Factor	$\Delta f/f$	0.01	0.02
Beam Polarization	$\Delta P_B/P_B$	0.05	0.05
Target Polarization	$\Delta P_T/P_T$	0.02	0.035
Total	$\Delta A_{UL}^{m(\phi_h,\phi_R)}/A_{UL}^{m(\phi_h,\phi_R)}$	0.022	0.040
	$\Delta A_{LL}^{m(\phi_h,\phi_R)}/A_{LL}^{m(\phi_h,\phi_R)}$	0.055	0.064

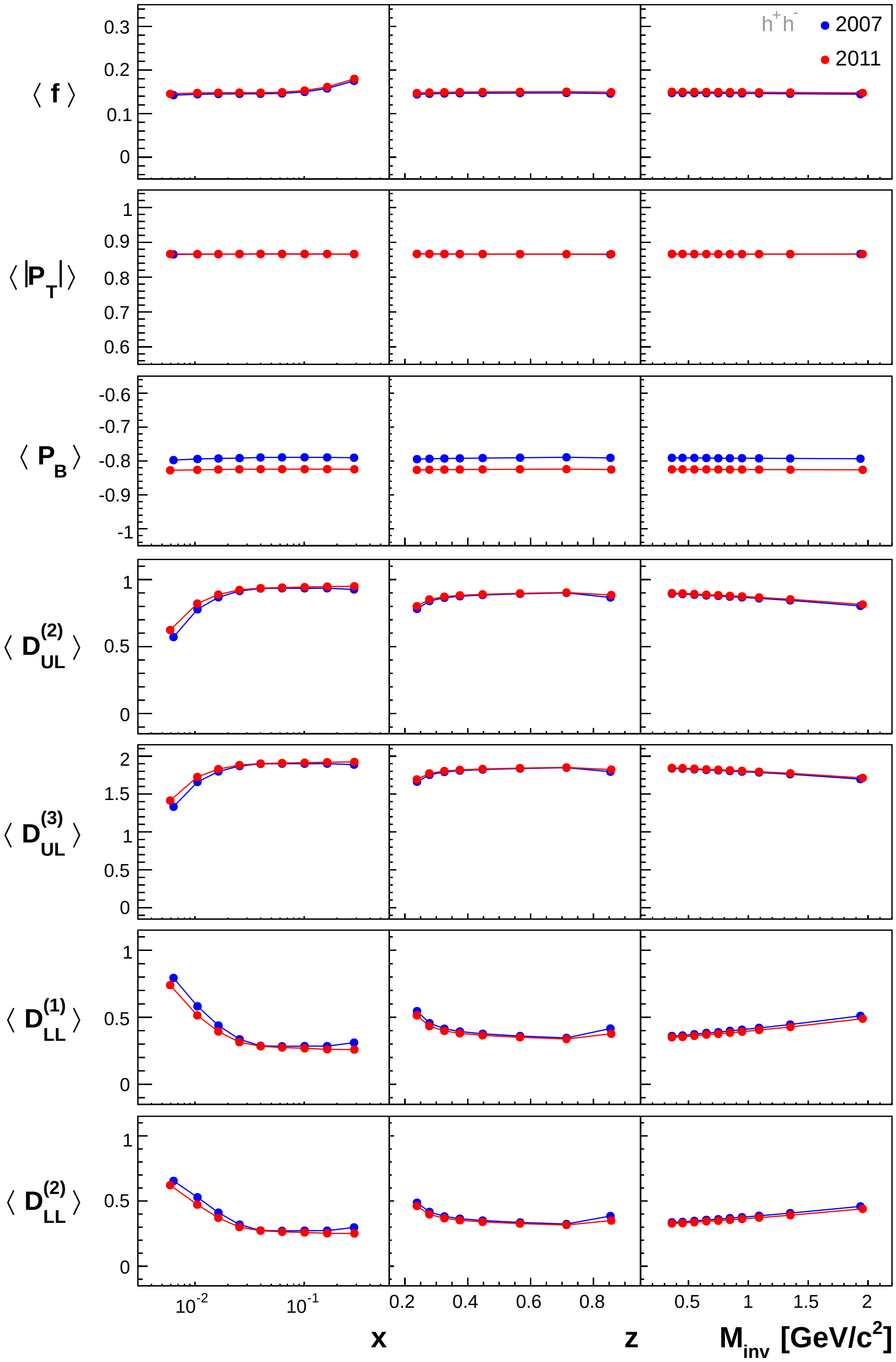

Figure 5.2: Mean values of the dilution factor f, the absolute target polarization $|P_T|$, the beam polarization P_B and the depolarization factors $D_{XL}^{(i)}$ in bins of x, z and M_{inv} in the h^+h^- analysis for both years. $D_{UL}^{(1)}$ is not displayed as it is constantly one.

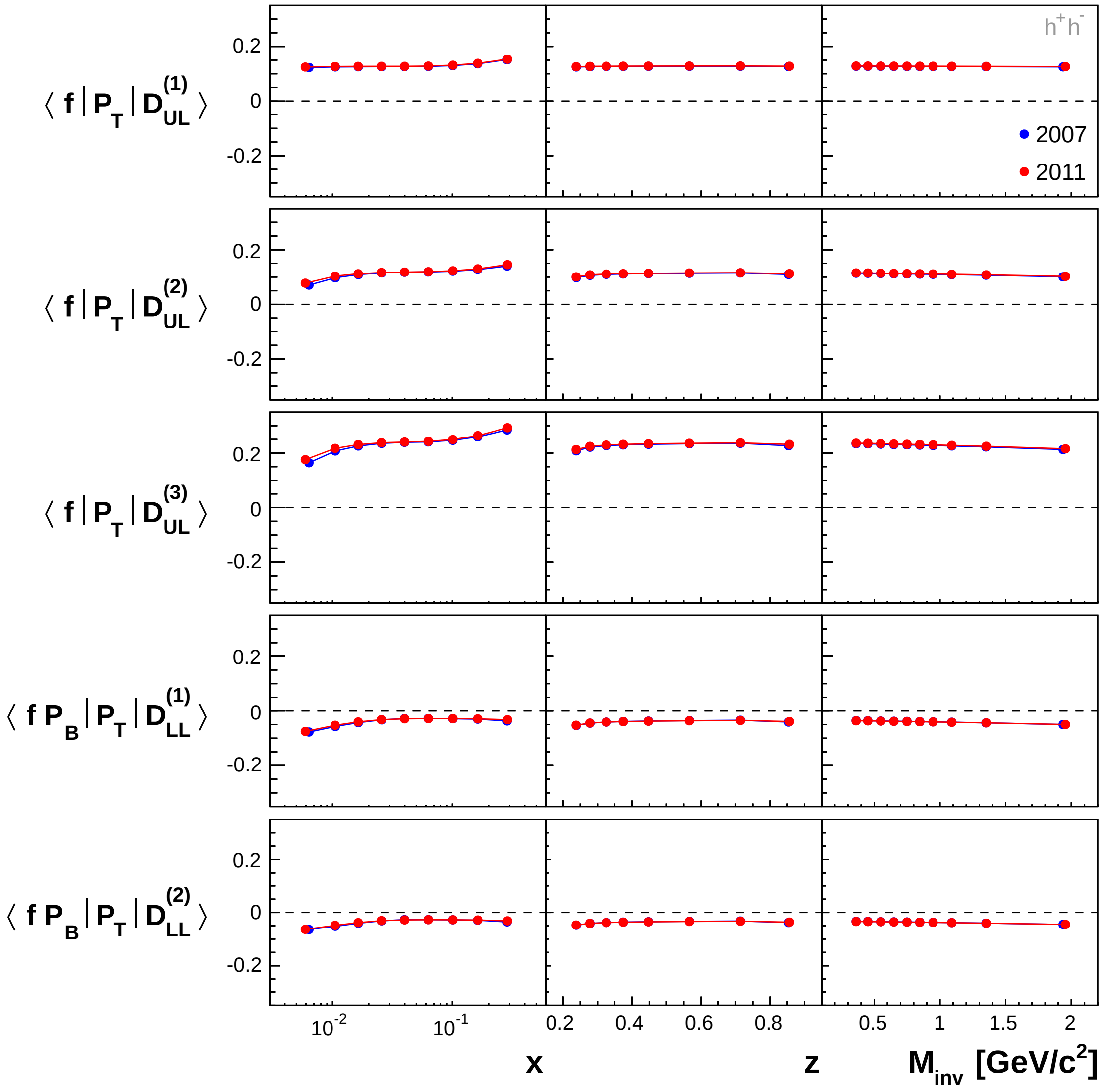

Figure 5.3: Mean values of the correction factors in bins of x, z and M_{inv} in the h^+h^- analysis for both years.

6. Two Hadron Analysis

This chapter is dedicated to the analysis of longitudinal target spin dependent asymmetries in two hadron SIDIS at leading twist, covering the study of seven single spin and two double spin azimuthal asymmetries. The results, extracted from the data samples of 2007 and 2011, are initially presented and discussed on basis of statistical errors only, followed by a detailed study of systematic error sources for each year separately. This includes the comparison of the different extraction methods 1D PR and UB LH, time dependent compatibility studies both on the level of weekly asymmetries and on the level of microwave settings, as well as the estimation of acceptance effects. The latter is performed by studying partial real and false asymmetries, extracted from combinations of data from two cells only. The final results, obtained from the UB LH method, are presented and discussed in more detail in Sec. 6.4, including their systematic uncertainty.

6.1 Azimuthal Asymmetries

In Fig. 6.1, the UB LH results for both years are plotted against the kinematic variables x, z and M_{inv}, where the error bars are purely statistical so far and the values for 2011 are manually rightshifted for a better visibility. No evident dependence on any of the kinematic variables is distinguished. All asymmetries are relatively closely distributed around zero. The mean azimuthal asymmetries are consequently compatible with zero within at least two standard deviations and are in acceptable agreement for 2007 and 2011. They are also compatible in the three kinematic variables per year. The overall mean values, evaluated as the arithmetic mean of the mean asymmetries in bins of x, z and M_{inv}, are separately depicted in Fig. 6.2 for clarity. Here, the largest error of the considered mean asymmetries is taken as statistical uncertainty.

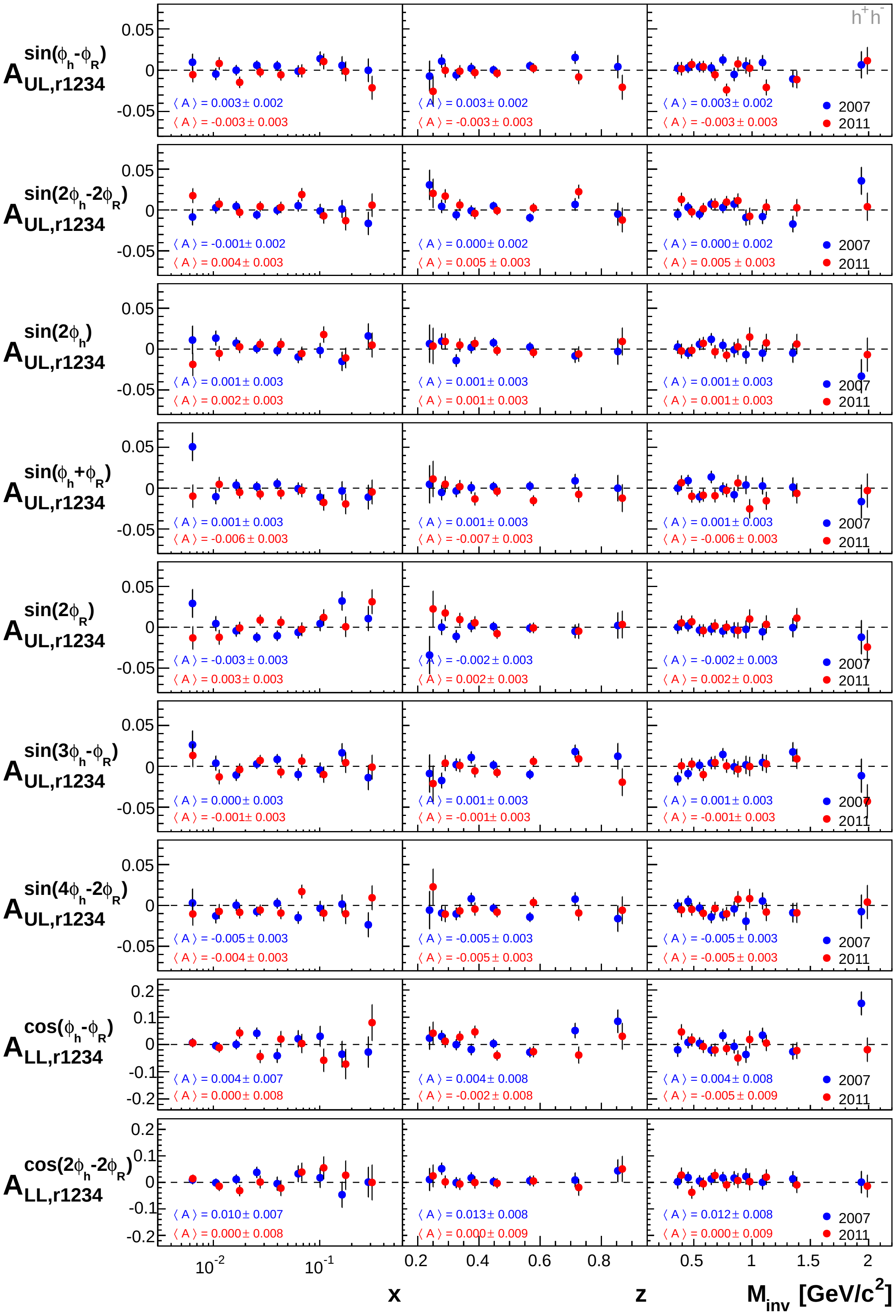

Figure 6.1: Azimuthal asymmetries from the UB LH method for 2007 and 2011 data. Corresponding mean values are also displayed. Please note the different scaling of the y axis for double-spin-asymmetries here and in the following.

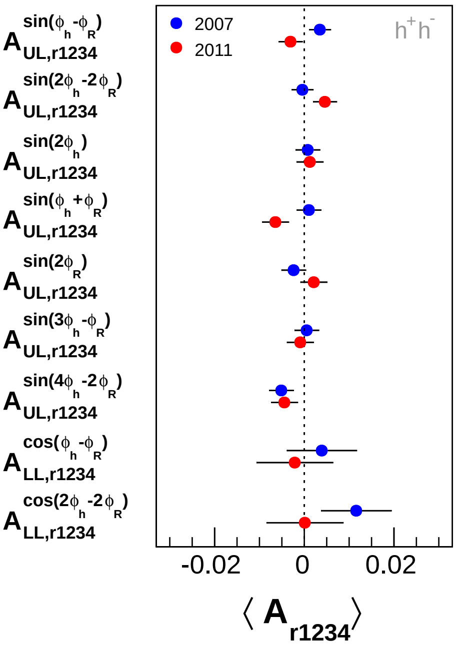

Figure 6.2: Mean azimuthal asymmetries from the UB LH method for 2007 and 2011 data.

6.2 Systematic Studies

The analysis of azimuthal asymmetries requires a high precision, ideally free from systematic error sources. This concerns the choice of the estimator as well as the stability of the experimental setup. Several tests were performed, to study the quality of the results and to estimate their systematic uncertainties:

- Compatibility of results from different extraction methods
- Compatibility of results from different weeks and microwave settings
- Study of false asymmetries on different target subsamples
- Compatibility of results with physical asymmetries from target subsamples

All systematic studies have been carried out for each year and each azimuthal asymmetry individually on the level of already corrected asymmetries. The same studies on raw asymmetries didn't reveal notable differences, confirming the correction not to affect the systematics of the results. Nevertheless, the systematic uncertainties of the correction factors have to be taken into account in the evaluation of the overall systematic uncertainties.

The following study covers an independent analysis of both years. For the reason of readability, the main concentration is put on data from 2011, while corresponding plots for the year 2007 are collected in A.4.

6.2.1 Compatibility of Methods

As described in Chapter 5, two independent methods were used to extract asymmetries: the 1D PR method, based on a quite simple approach to disentangle the asymmetries with a binned fit, and the more sophisticated UB LH method. Although the latter method is known to minimize systematic biases, it can not be considered free from systematics. Unfortunately no Monte Carlo data is available to test the reliability of the results, obtained from the UB LH method. Consequently, there is no alternative other than to estimate possible methodical systematics from comparison of the two methods.

The results from both methods are shown in Fig. 6.3, exemplarily for year 2011. Apparently, the asymmetries are in good agreement, both per kinematic bin and concerning the mean values per kinematic variable. To quantify deviations on the whole, including the asymmetries from all weeks, the following pulls are considered:

$$\text{Pull} = \frac{A_{\text{UB LH}} - A_{\text{1D PR}}}{\sigma_{\text{stat}}}. \tag{6.1}$$

The pull distributions for year 2011 are depicted in Fig. 6.4, including a gaussian fit. The number of entries corresponds to the total number of asymmetries, evaluated in 27 kinematical bins for 11 weeks in 2011. Although the pull distributions indicate a basic agreement of the two methods, differences among the asymmetries are visible, especially in the modulations $m(2\phi_h - 2\phi_R)$. It's reasonable to assign the RMS and half of the shifted mean as systematic uncertainties on the final results. The resulting relative uncertainties are listed in Tab. 6.1 for both years, showing consistent values. The corresponding plots for 2007 can be found in A.4.

Table 6.1: Systematic uncertainties for 2007 and 2011, resulting of the compatibility study of different methods.

Year	2007	2011
$A_{XL}^{m(\phi_h,\phi_R)}$	$\sigma_{\text{sys}}^{\text{meth}}/\sigma_{\text{stat}}$	
$A_{UL}^{\sin(\phi_h-\phi_R)}$	0.18	0.17
$A_{UL}^{\sin(2\phi_h-2\phi_R)}$	0.28	0.25
$A_{UL}^{\sin(2\phi_h)}$	0.17	0.17
$A_{UL}^{\sin(\phi_h+\phi_R)}$	0.17	0.18
$A_{UL}^{\sin(2\phi_R)}$	0.15	0.18
$A_{UL}^{\sin(3\phi_h-\phi_R)}$	0.19	0.16
$A_{UL}^{\sin(4\phi_h-2\phi_R)}$	0.14	0.19
$A_{LL}^{\cos(\phi_h-\phi_R)}$	0.19	0.17
$A_{LL}^{\cos(2\phi_h-2\phi_R)}$	0.28	0.27

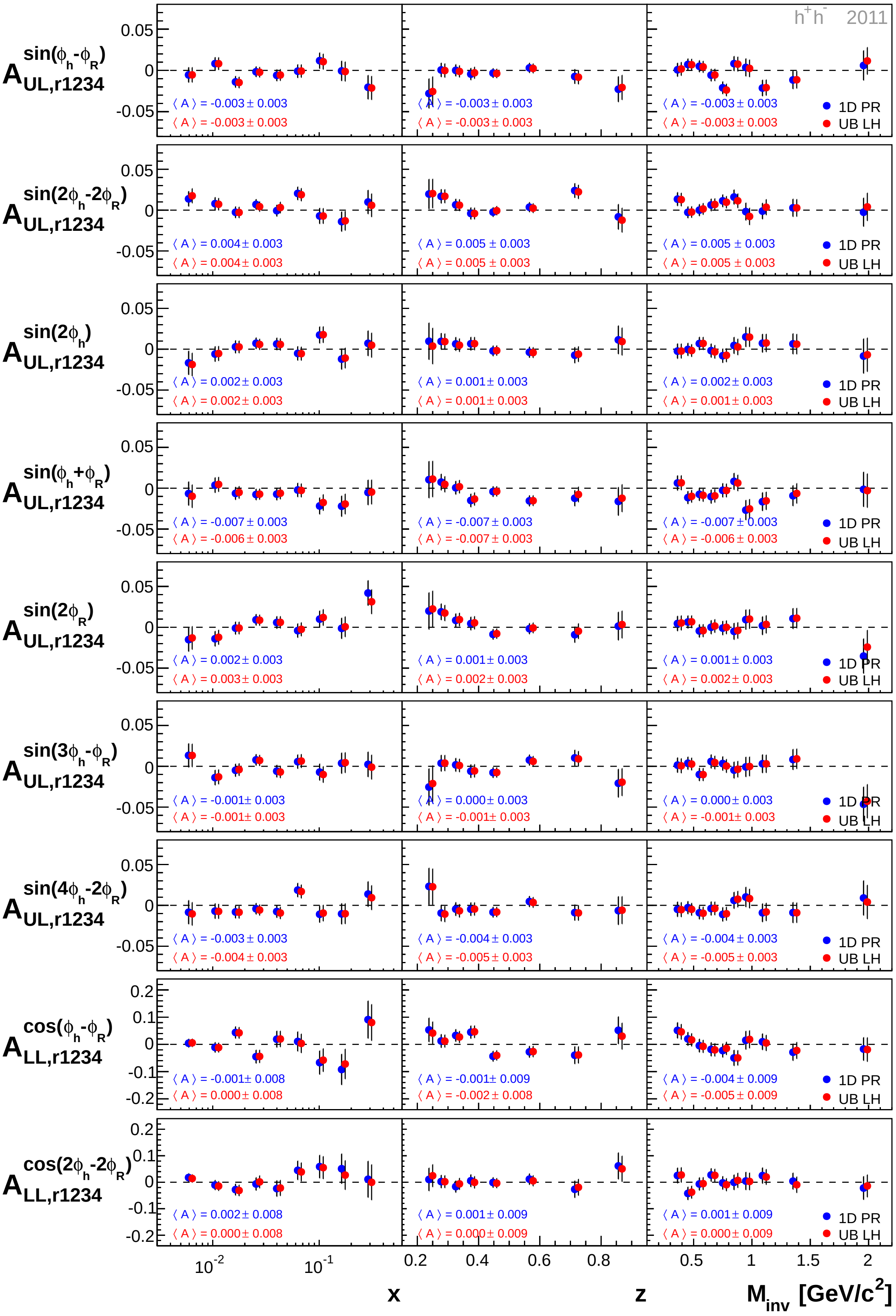

Figure 6.3: Comparison of the azimuthal asymmetries, extracted with the methods 1D PR and UB LH, for 2011.

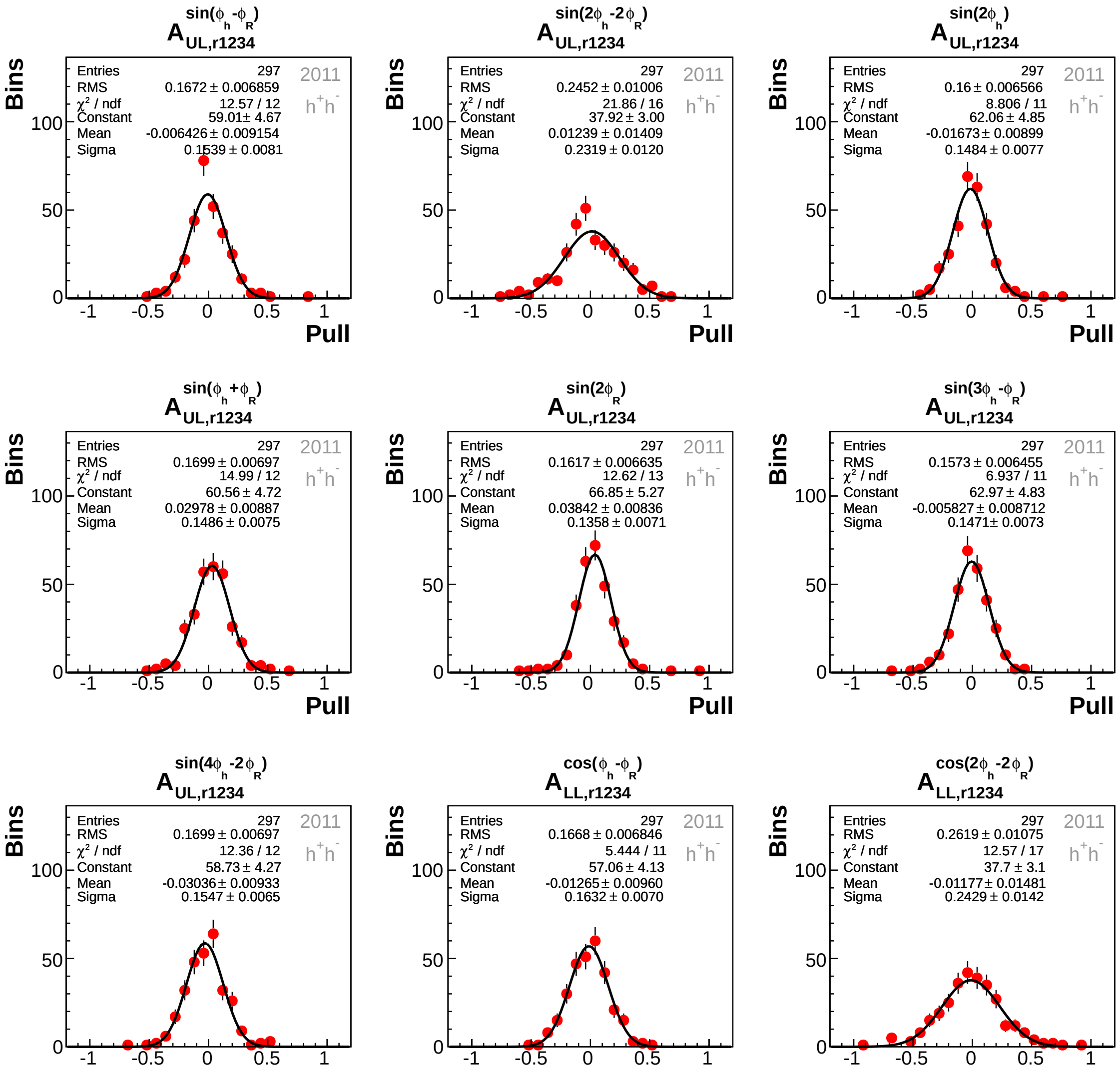

Figure 6.4: Pull distributions between asymmetries extracted with the UB LH and the 1D PR method for 2011. The gaussian fit, corresponding statistical values and fit parameters are also displayed.

6.2.2 Compatibility of Weeks

The azimuthal asymmetries, presented in the previous section, are evaluated as weighted means of weekly asymmetries per kinematic bin. As the measured asymmetries are potentially sensitive to changes in the experimental conditions over the data taking period, their self-consistency is considered as a main source of systematic uncertainties. A measure for the consistency of all values $A_{i,j}$, where i indicates the kinematic bin and j the number of the week, entering in the calculation of the final mean value of a certain asymmetry, is given by pulls of the form

$$\mathrm{Pull} = \frac{A_{i,j} - \langle A_i \rangle}{\sqrt{\sigma^2_{A_{i,j}} - \sigma^2_{\langle A_i \rangle}}}. \tag{6.2}$$

Considering a stable set of weekly asymmetries per bin, the pull distributions should be centered around 0 with a gaussian width σ_{Pull} of 1. In case of instabilities of the spectrometer, such as acceptance changes, an efficiency drop or misalignment, the distributions would appear more broad.

The pull distributions for year 2011 are exemplarily depicted for the UB LH method in Fig. 6.5, including a gaussian fit. The stability requirements are well fulfilled by all pull distributions except the double spin asymmetry $A_{LL}^{\cos(\phi_h+\phi_R)}$, where its pull indicates a relatively large instability. Regarding the summary plots in Fig. 6.6 and 6.7, where the essential quantities for both extraction methods are displayed, slightly larger instabilities of the results from 2007 can be concluded for some asymmetries, whereas the $A_{LL}^{\cos(\phi_h+\phi_R)}$ appears more stable. The larger errors of the mean values result of the fact, that the 2007 data comprises less weeks than 2011.

In order to investigate possible origins of observed instabilities, also the stability of weekly mean asymmetries is considered. Fig. 6.8 and Fig. 6.9 show the mean asymmetries for each week of 2011 and 2007, respectively. The three columns correspond to the kinematic variables x, z and M_{inv} from left to right, showing overall consistent results. In agreement with the previous study on basis of weekly asymmetries, also the mean single spin asymmetries appear to be stable with time, where single discordant values are expected within statistical fluctuations. Regarding the two double spin asymmetries, an instability with time is notable again for the $\cos(\phi_h + \phi_R)$ moment in 2011, characterized by a sign change after W33. This corresponds to the date, when the microwave setting was changed in 2011. Regarding year 2007 in Fig. 6.9, where the microwave setting was changed after W34 and again after W38, no such instabilities can be concluded by eye. In order to investigate the dependence of the results on the respective microwave setting, this is studied in more detail in the next section.

The instability of the results over time is considered as a major influence on the systematic uncertainties of the final asymmetries. It's reasonable to assign systematic uncertainties on basis of the discussed pull distributions. The corresponding RMS is taken to estimate the certain systematic uncertainties:

$$\frac{\sigma_{\mathrm{sys}}^{\mathrm{stab}}}{\sigma_{\mathrm{stat}}} = \sqrt{|\mathrm{RMS}^2 - 1|}. \tag{6.3}$$

Table 6.2: Systematic uncertainties for 2007 and 2011, resulting of the compatibility study of the weekly results.

Year	2007	2011
$A_{XL}^{m(\phi_h,\phi_R)}$	$\sigma_{\mathrm{sys}}^{\mathrm{stab}}/\sigma_{\mathrm{stat}}$	
$A_{UL}^{\sin(\phi_h-\phi_R)}$	0.29	0.28
$A_{UL}^{\sin(2\phi_h-2\phi_R)}$	0.37	0.30
$A_{UL}^{\sin(2\phi_h)}$	0.33	0.40
$A_{UL}^{\sin(\phi_h+\phi_R)}$	0.21	0.13
$A_{UL}^{\sin(2\phi_R)}$	0.46	0.32
$A_{UL}^{\sin(3\phi_h-\phi_R)}$	0.53	0.25
$A_{UL}^{\sin(4\phi_h-2\phi_R)}$	0.28	0.13
$A_{LL}^{\cos(\phi_h-\phi_R)}$	0.65	0.69
$A_{LL}^{\cos(2\phi_h-2\phi_R)}$	0.42	0.28

The resulting systematic uncertainties are listed in Tab. 6.2 for both years. It can be concluded, that both years results are comparably stable with time.

6.2.3 Compatibility of Microwave Settings

The previous compatibility study of results from single weeks suggests the assumption, that an incompatibility of the results from the two microwave settings could affect the systematics of the final results for certain azimuthal asymmetries. Fig. 6.10 and Fig. 6.11 show the results from different microwave settings for the two years, whereas the mean asymmetries are depicted in the summary plots in Fig. 6.12. Although the bin wise comparison of the single spin asymmetries show occasional strong deviations for both years, the mean values are found to be in agreement. Only the double spin asymmetry $A_{r1234}^{\cos(\phi_h+\phi_R)}$ reveals an incompatibility of the microwave settings in 2011. This is in agreement with the observations made in the previous section and is already taken into account in the systematic uncertainty $\sigma_{\mathrm{sys}}^{\mathrm{stab}}$.

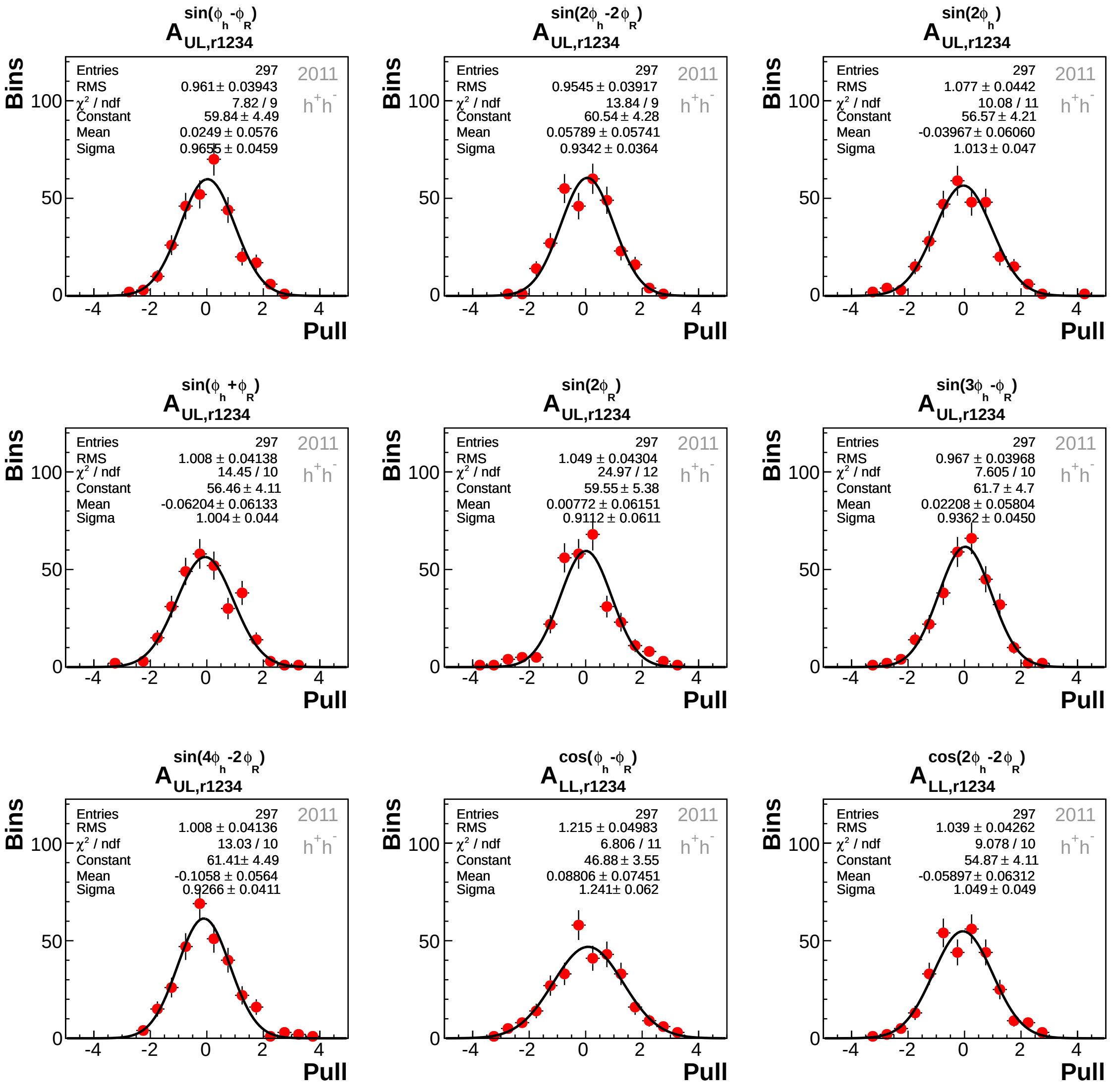

Figure 6.5: Stability pull distributions of asymmetries, extracted with the UB LH method, for 2011. The gaussian fit, corresponding statistical values and fit parameters are also displayed.

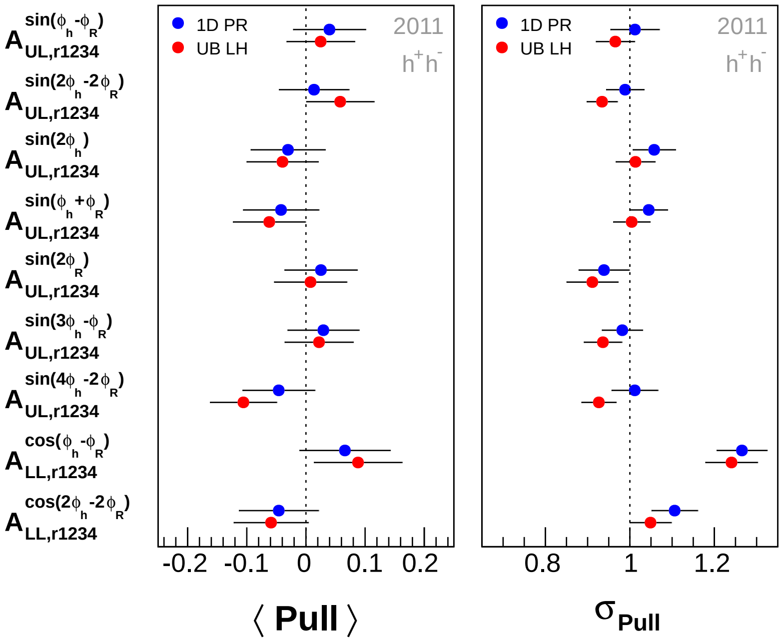

Figure 6.6: Mean values and σ_{Pull} of the stability pull distributions, evaluated with the 1D PR and the UB LH method, for 2011.

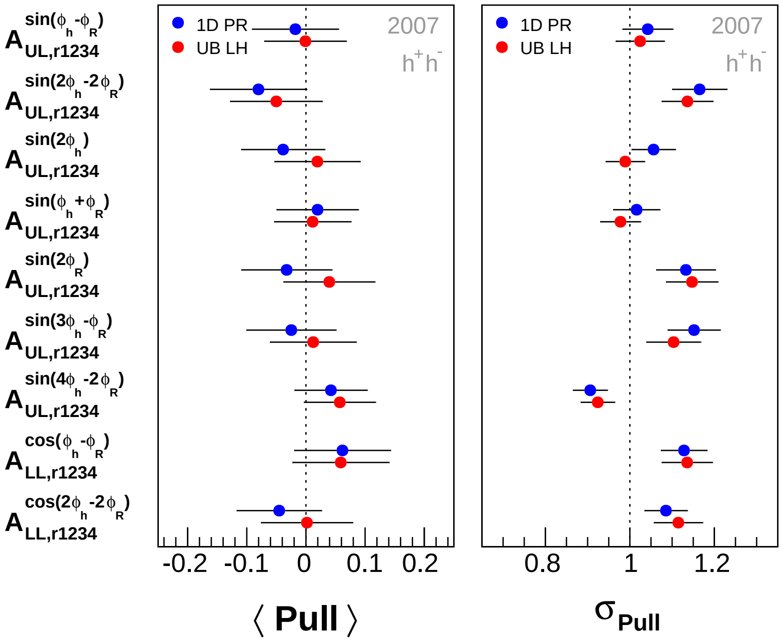

Figure 6.7: Mean values and σ_{Pull} of the stability pull distributions, evaluated with the 1D PR and the UB LH method, for 2007.

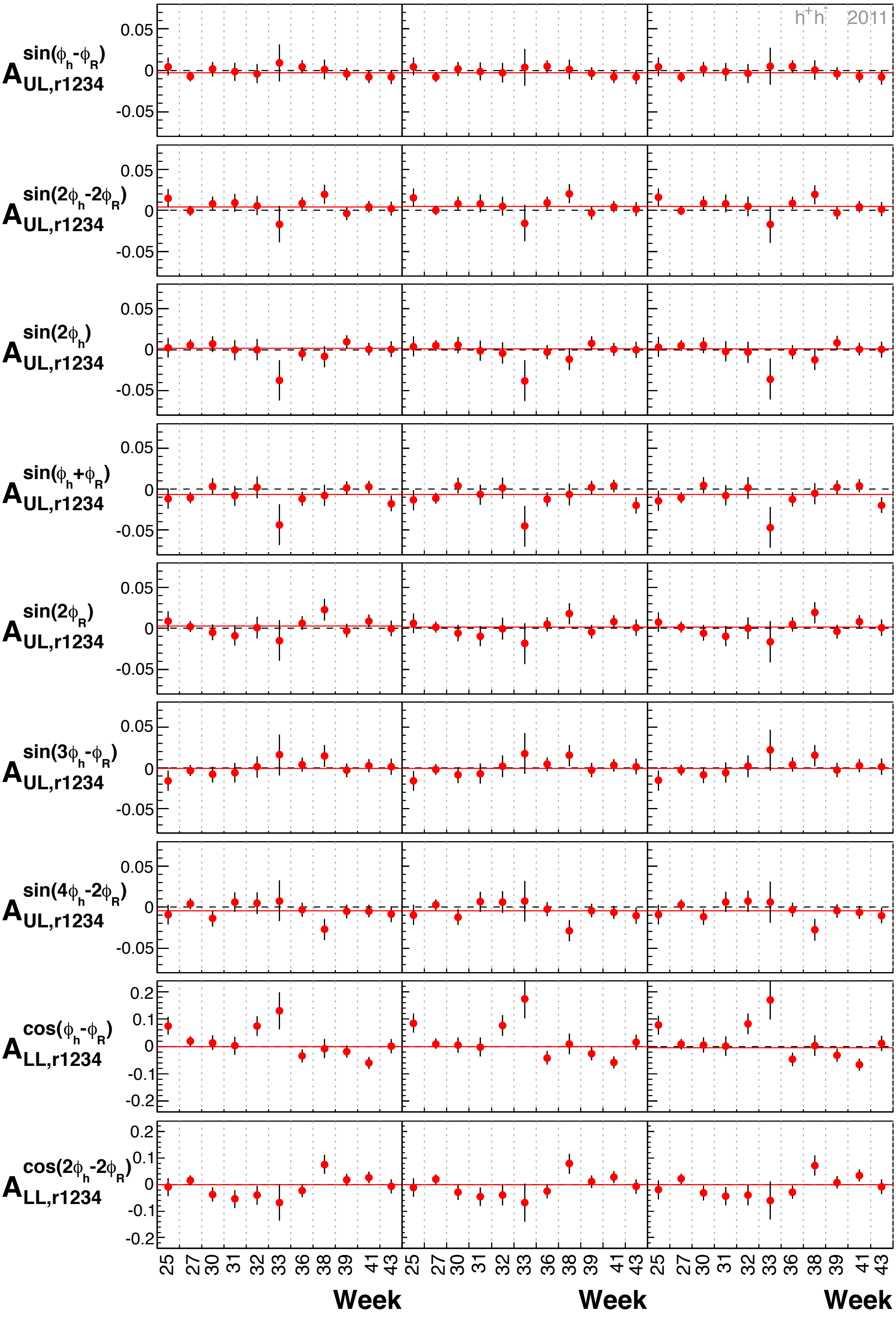

Figure 6.8: Mean asymmetries for each week of 2011. The three columns correspond to the kinematic variables x, z and M_{inv} from left to right. The red horizontal lines indicate the respective mean values.

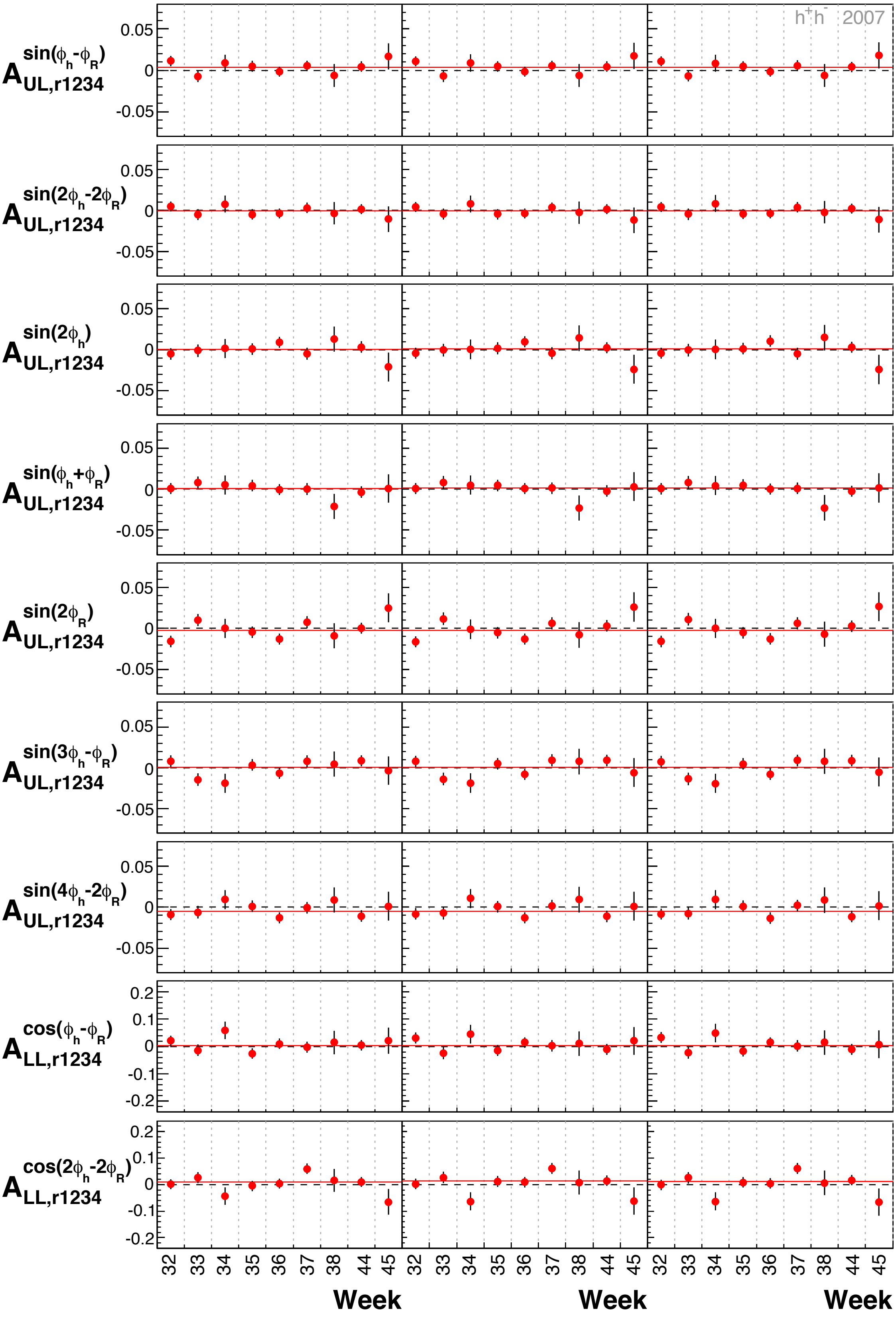

Figure 6.9: Mean asymmetries for each week of 2007. The three columns correspond to the kinematic variables x, z and M_{inv} from left to right. The red horizontal lines indicate the respective mean values.

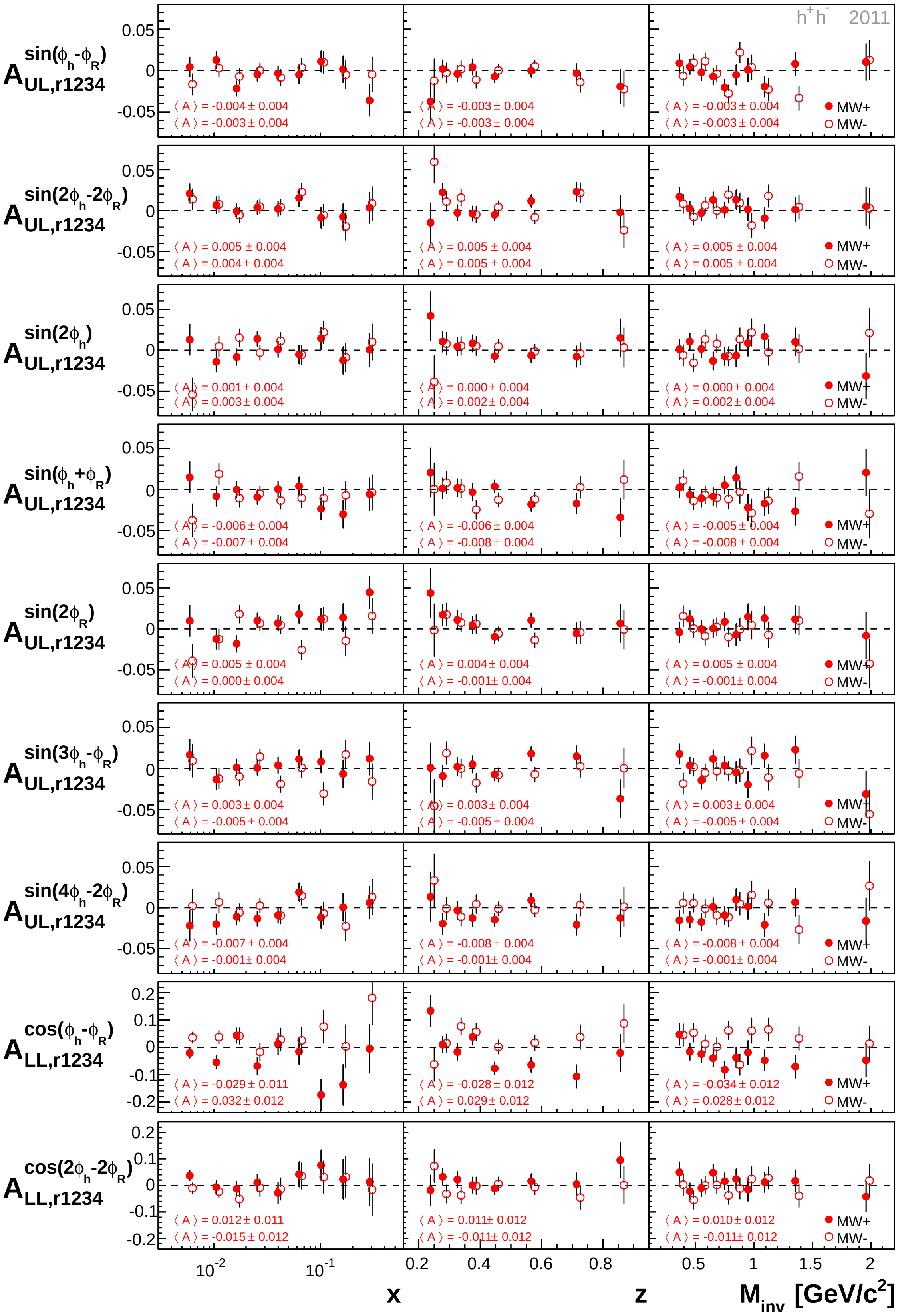

Figure 6.10: Comparison of asymmetries from the two microwave settings for 2011. Corresponding mean values are also displayed.

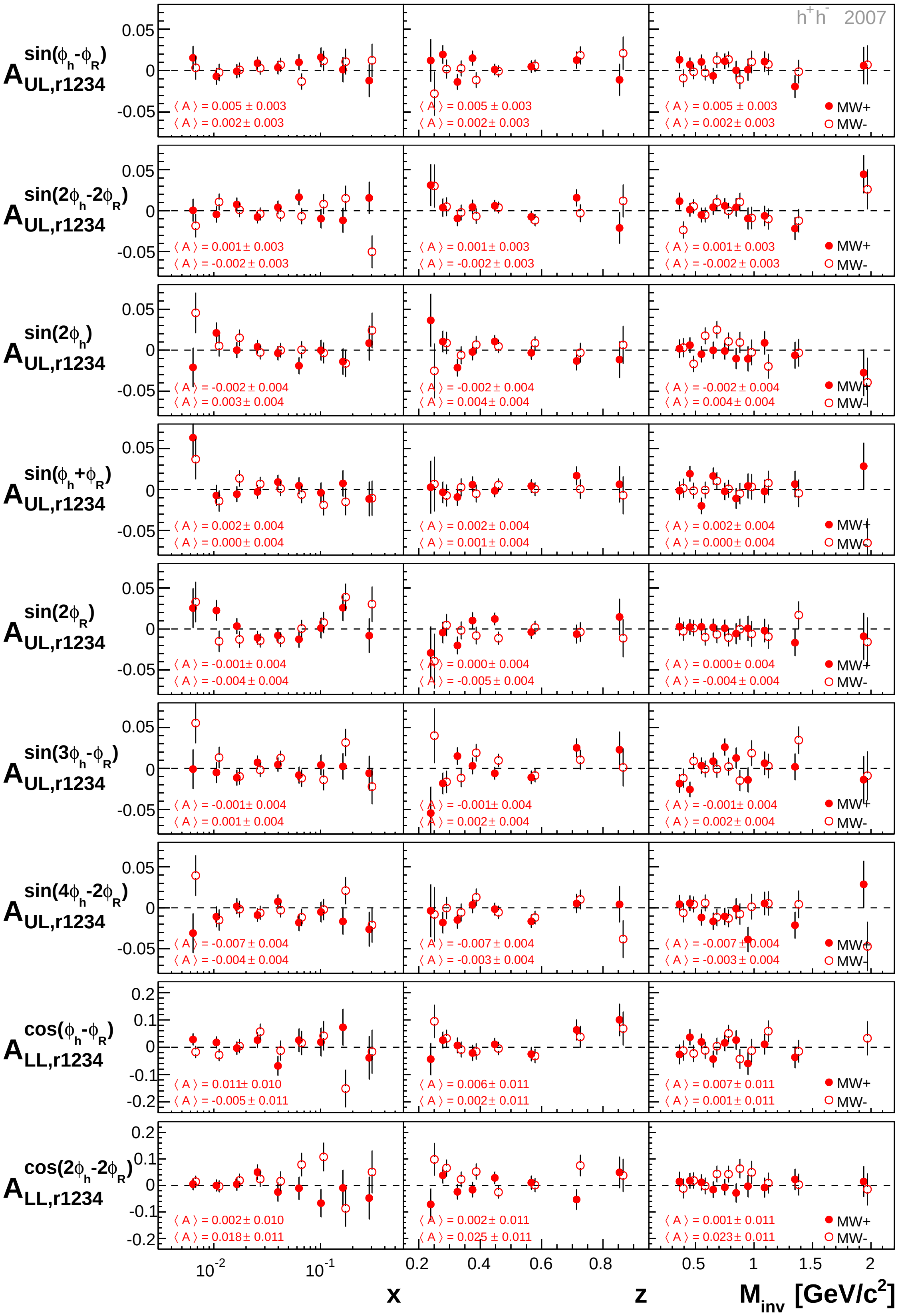

Figure 6.11: Comparison of asymmetries from the two microwave settings for 2007. Corresponding mean values are also displayed.

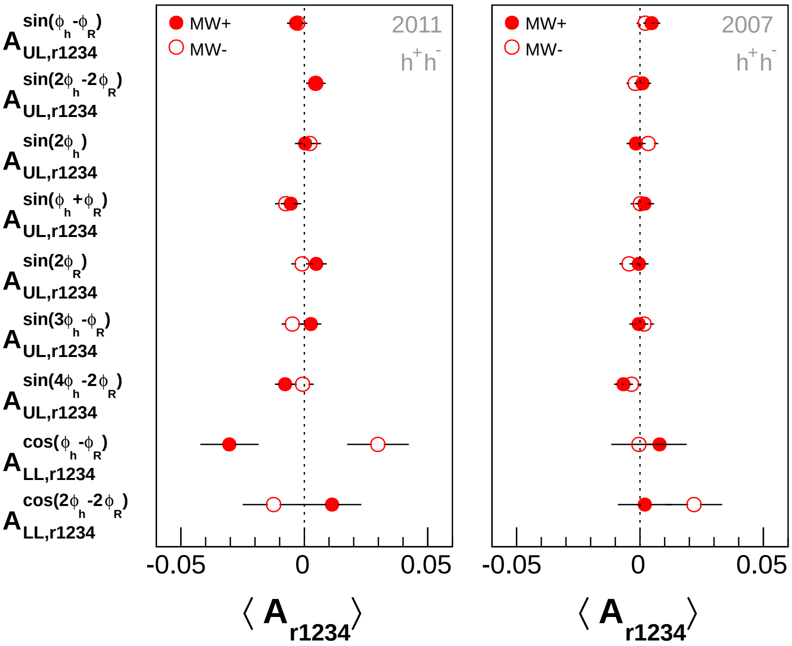

Figure 6.12: Comparison of mean asymmetries from the two microwave settings for 2011 and 2007.

6.2.4 Asymmetries from Target Subsamples

Asymmetries can be also extracted from target subsamples, for instance from data of only the two upstream or the two downstream cells. By fitting the corresponding ratios

$$r12 = \frac{N_1^+ N_2^+}{N_1^- N_2^-} \qquad\qquad r34 = \frac{N_3^+ N_4^+}{N_3^- N_4^-} \tag{6.4}$$

with appropriate fit functions, the upstream and downstream real asymmetries can be extracted separately, denoted as $A_{r12}^{m(\phi_h,\phi_R)}$ and $A_{r34}^{m(\phi_h,\phi_R)}$. At first approximation, half of their sum should give same results as extracted from the total data set at once:

$$A_{r1234}^{m(\phi_h,\phi_R)} = \frac{1}{2}\left(A_{r12}^{m(\phi_h,\phi_R)} + A_{r34}^{m(\phi_h,\phi_R)}\right). \tag{6.5}$$

This is the case within a small systematic uncertainty of at most 3% of the statistical error for all asymmetries, as the pull distributions in Fig. 6.13 and 6.14 show for both years. Here, the pulls are calculated for each week and kinematic bin as

$$\text{Pull} = \frac{A_{(r12+r34)/2} - A_{r1234}}{\sigma_{\text{stat}}}. \tag{6.6}$$

Due to its small size, compared to systematic uncertainties from other sources, this systematic error will be neglected in the estimation of the final systematic uncertainties.

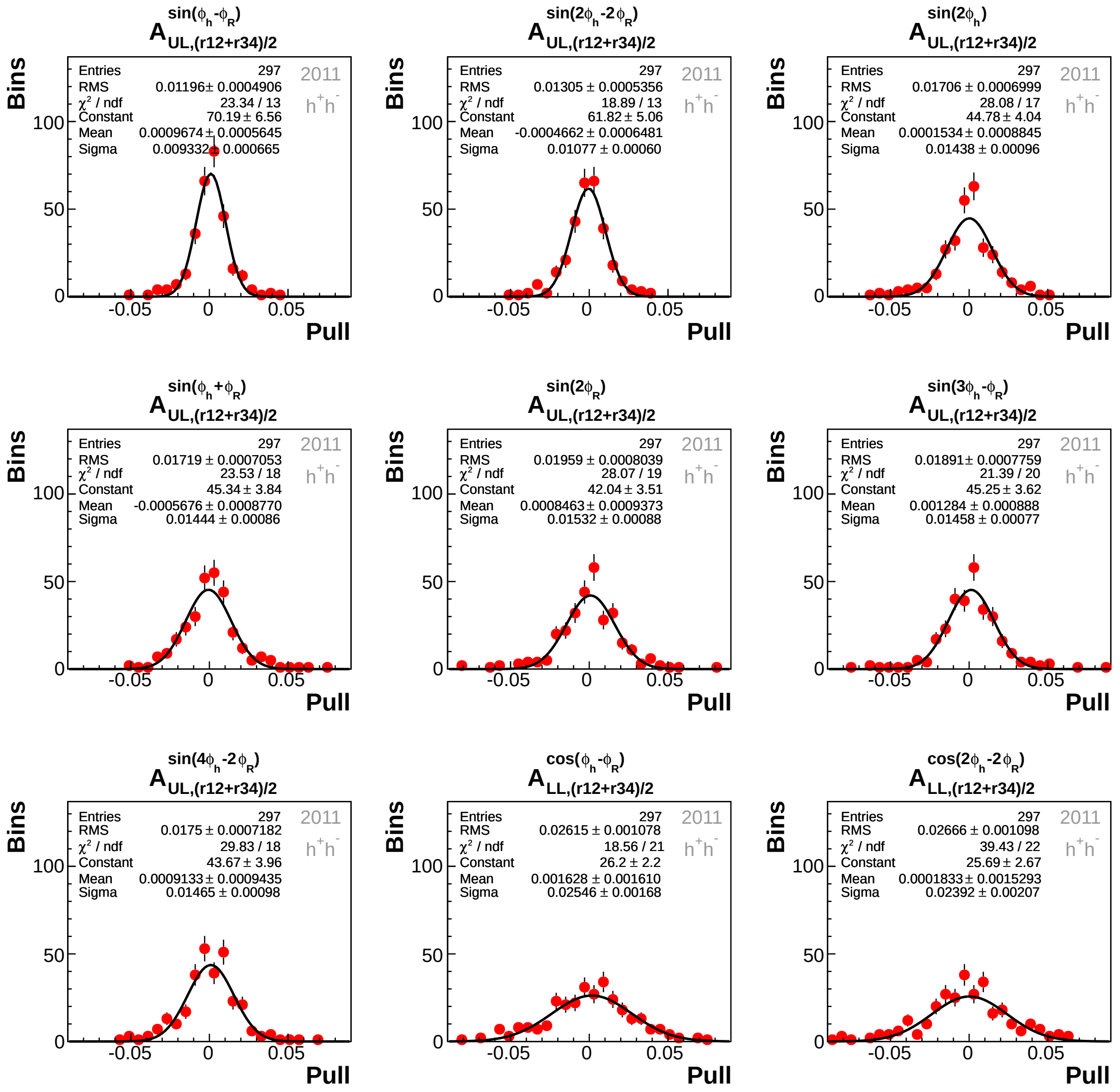

Figure 6.13: Pull distributions between asymmetries $A_{(r12+r34)/2}^{m(\phi_h,\phi_R)}$ and $A_{r1234}^{m(\phi_h,\phi_R)}$, for 2011. The gaussian fit, corresponding statistical values and fit parameters are also displayed.

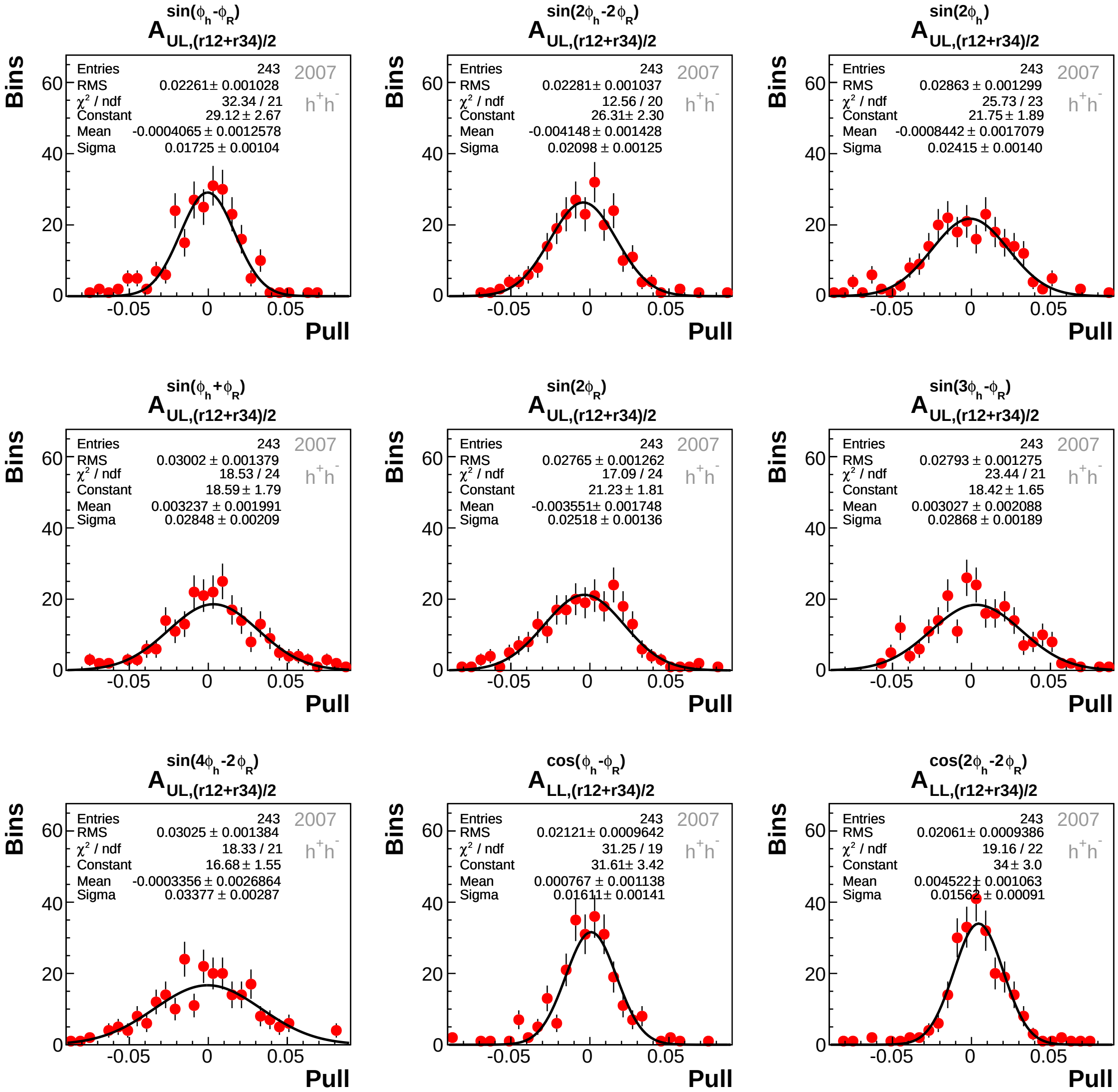

Figure 6.14: Pull distributions between asymmetries $A^{m(\phi_h,\phi_R)}_{(r12+r34)/2}$ and $A^{m(\phi_h,\phi_R)}_{r1234}$, for 2007. The gaussian fit, corresponding statistical values and fit parameters are also displayed.

6.2.5 False Asymmetries

The presented methods to extract asymmetries are all based on the assumption, that acceptance changes between the cells, caused by polarization setting changes for instance, cancel within each week. To verify this, it is common to study so called false asymmetries by combining data from only two cells in a way, such that the extracted asymmetries are expected to be purely sensitive to acceptance changes of the single cells. The considered ratios are

$$f_{14} = \frac{N_1^+ N_4^-}{N_1^- N_4^+} \qquad\qquad f_{23} = \frac{N_2^+ N_3^-}{N_2^- N_3^+}, \tag{6.7}$$

combining either data from the two outer cells or the two inner cells. Considering the acceptance to depend on the azimuthal angles ϕ_h and ϕ_R, it is reasonable to expect the main contribution to the measured physical asymmetry $A_{\text{meas}}^{m(\phi_h,\phi_R)}$ to originate from its appropriate acceptance fourier term. For each of the nine involved modulations $m(\phi_h, \phi_R)$, one can then write the number of hadron pairs, originating from a cell i with polarization $\pm$ as

$$N_i^{\pm} = c_i^{\pm}\left(1 + \alpha_i^{\pm} m(\phi_h, \phi_R)\right)\left(1 \pm A_{\text{true}}^{m(\phi_h,\phi_R)} m(\phi_h, \phi_R)\right). \tag{6.8}$$

Here, the prefactor $c_i^{\pm}$ comprises the muon flux, the number of target nucleons, and the non-azimuthal part of the unpolarized cross section. The $\alpha_i^{\pm}$ denote the acceptance amplitudes of a certain modulation and $A_{\text{true}}^{m(\phi_h,\phi_R)}$ is the corresponding true asymmetry. By inserting Eq. (6.8) in Eq. (6.7) and assigning opposite polarizations to $N_3^{\pm}$ and $N_4^{\pm}$, one obtains the following $O(m(\phi_h, \phi_R))$ approximations for the outer false asymmetries $A_{f14}^{m(\phi_h,\phi_R)}$ and inner false asymmetries $A_{f23}^{m(\phi_h,\phi_R)}$:

$$A_{f14}^{m(\phi_h,\phi_R)} = A_{f14,\text{true}}^{m(\phi_h,\phi_R)} + \frac{1}{4}\left(\alpha_1^+ - \alpha_1^- - \alpha_4^+ + \alpha_4^-\right) \tag{6.9}$$

$$A_{f23}^{m(\phi_h,\phi_R)} = A_{f23,\text{true}}^{m(\phi_h,\phi_R)} + \frac{1}{4}\left(\alpha_2^+ - \alpha_2^- - \alpha_3^+ + \alpha_3^-\right). \tag{6.10}$$

In both cases, the data is combined in a way that physical asymmetries should cancel, hence one can assume both true asymmetries to be zero. Considering real asymmetries, inserting 6.8 in the real ratio r_{1234} from Eq. (5.1), yields the following relation of real and false asymmetries:

$$A_{r1234}^{m(\phi_h,\phi_R)} = A_{r1234,\text{true}}^{m(\phi_h,\phi_R)} + \frac{1}{2}\left(A_{f14}^{m(\phi_h,\phi_R)} - A_{f23}^{m(\phi_h,\phi_R)}\right). \tag{6.11}$$

Hence, half the difference of the false asymmetries serves as an estimate of the bias of the measured asymmetries due to acceptance instabilities along the target. The shortcut $A_{(f14-f23)/2}^{m(\phi_h,\phi_R)}$ is used in the following for this quantity. Another estimate of acceptance instabilities is half the sum of false asymmetries, accordingly written

$A^{m(\phi_h,\phi_R)}_{(f14+f23)/2}$. Fig. 6.15 and Fig. 6.16 show the final false asymmetries for both years. They are small of size and mainly compatible with zero within statistical fluctuations. The systematic uncertainty is estimated by the weighted mean of deviations in terms of the statistical error, reduced in quadrature by the expected value of 0.68, calculated from all bins via

$$\frac{\sigma_{\text{sys}}^{(f14\pm f23)/2}}{\sigma_{\text{stat}}} = \sqrt{\left(\frac{\sum_{i=1}^{N_{\text{bins}}} \frac{\left|A^i_{(f14\pm f23)/2}\right|}{\sigma_i}\frac{1}{\sigma_i^2}}{\sum_{i=1}^{N_{\text{bins}}}\frac{1}{\sigma_i^2}}\right)^2 - 0.68^2}. \tag{6.12}$$

Should the determinant be negative, an uncertainty of zero is assigned. The resulting values are listed in Tab. 6.3 for both years separately, indicating no strong deviations. The systematic uncertainty is around half of the statistical error for all asymmetries. For the final systematic uncertainty $\sigma_{\text{sys}}^{\text{false}}$, the larger of the two values is assigned.

False asymmetries can be also constructed from the upstream and downstream physical asymmetries $A^{m(\phi_h,\phi_R)}_{r12}$ and $A^{m(\phi_h,\phi_R)}_{r34}$. It is approximately

$$A^{m(\phi_h,\phi_R)}_{(f14-f23)/2} = A^{m(\phi_h,\phi_R)}_{(r12-r34)/2}. \tag{6.13}$$

Their compatibility is confirmed by the narrow pull distributions in Fig. 6.17 and Fig. 6.18, where the pulls are calculated per kinematic bin and week as

$$\text{Pull} = \frac{A_{(r12-r34)/2} - A_{(f14-f23)/2}}{\sigma_{\text{stat}}}. \tag{6.14}$$

As a consequence also the systematic uncertainties, estimated from $A^{m(\phi_h,\phi_R)}_{(r12-r34)/2}$ following Eq. (6.12), coincide with the ones from $A^{m(\phi_h,\phi_R)}_{(f14-f23)/2}$.

Table 6.3: Systematic uncertainties for 2007 and 2011, resulting of the study of false asymmetries.

Year	2007		2011	
$A^{m(\phi_h,\phi_R)}_{XL}$	$(f14-f23)/2$	$(f14+f23)/2$	$(f14-f23)/2$	$(f14+f23)/2$
$A^{\sin(\phi_h-\phi_R)}_{UL}$	0.39	0.48	0.41	0.47
$A^{\sin(2\phi_h-2\phi_R)}_{UL}$	0.50	0.50	0.47	0.50
$A^{\sin(2\phi_h)}_{UL}$	0.37	0.53	0.52	0.46
$A^{\sin(\phi_h+\phi_R)}_{UL}$	0.67	0.50	0.51	0.54
$A^{\sin(2\phi_R)}_{UL}$	0.43	0.35	0.65	0.59
$A^{\sin(3\phi_h-\phi_R)}_{UL}$	0.44	0.36	0.43	0.52
$A^{\sin(4\phi_h-2\phi_R)}_{UL}$	0.54	0.44	0.36	0.47
$A^{\cos(\phi_h-\phi_R)}_{LL}$	0.48	0.60	0.70	0.51
$A^{\cos(2\phi_h-2\phi_R)}_{LL}$	0.43	0.40	0.45	0.51

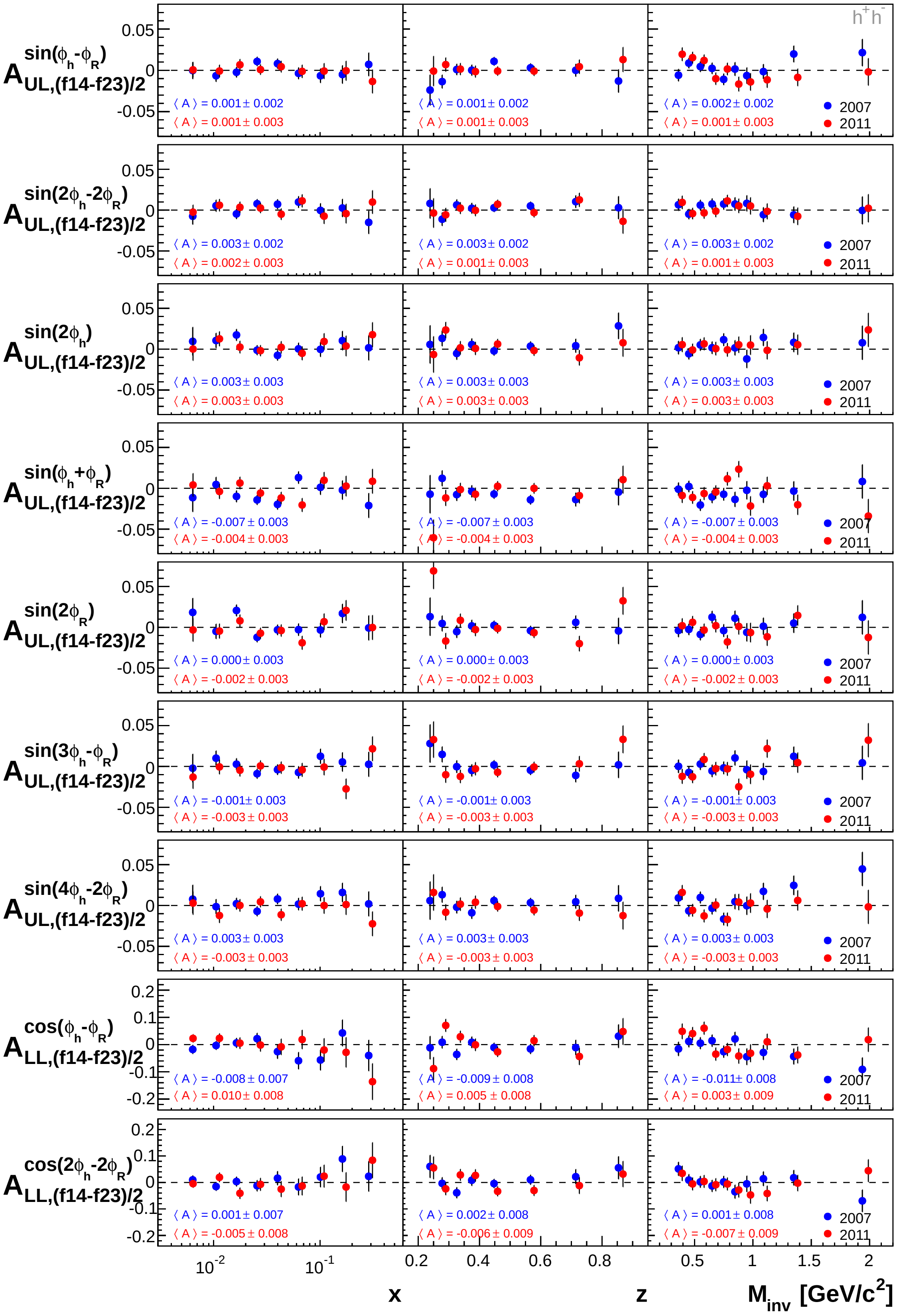

Figure 6.15: Azimuthal false asymmetries $A^{m(\phi_h,\phi_R)}_{(f14-f23)/2}$ from 2007 and 2011 data. Corresponding mean values are also displayed.

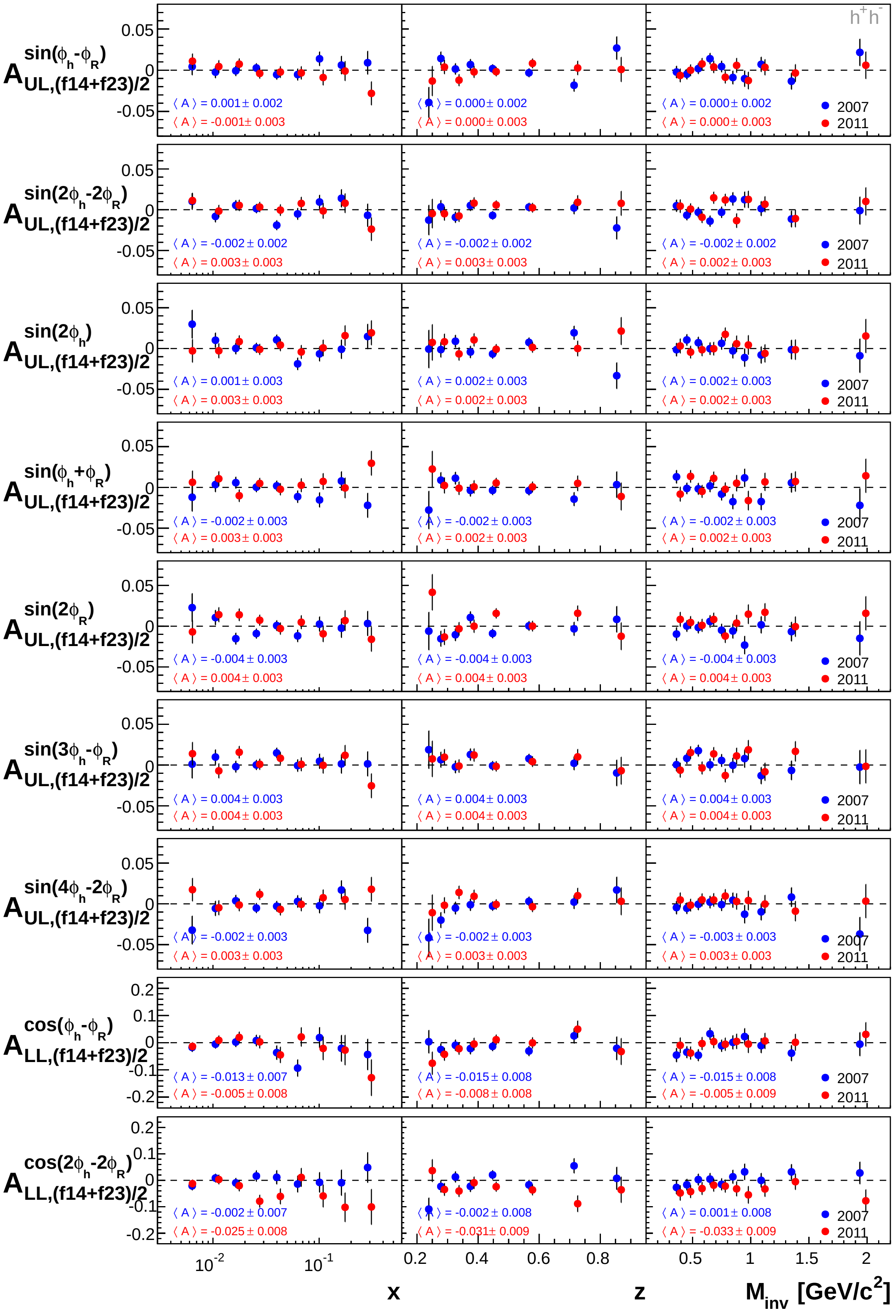

Figure 6.16: Azimuthal false asymmetries $A^{m(\phi_h,\phi_R)}_{(f14+f23)/2}$ from 2007 and 2011 data. Corresponding mean values are also displayed.

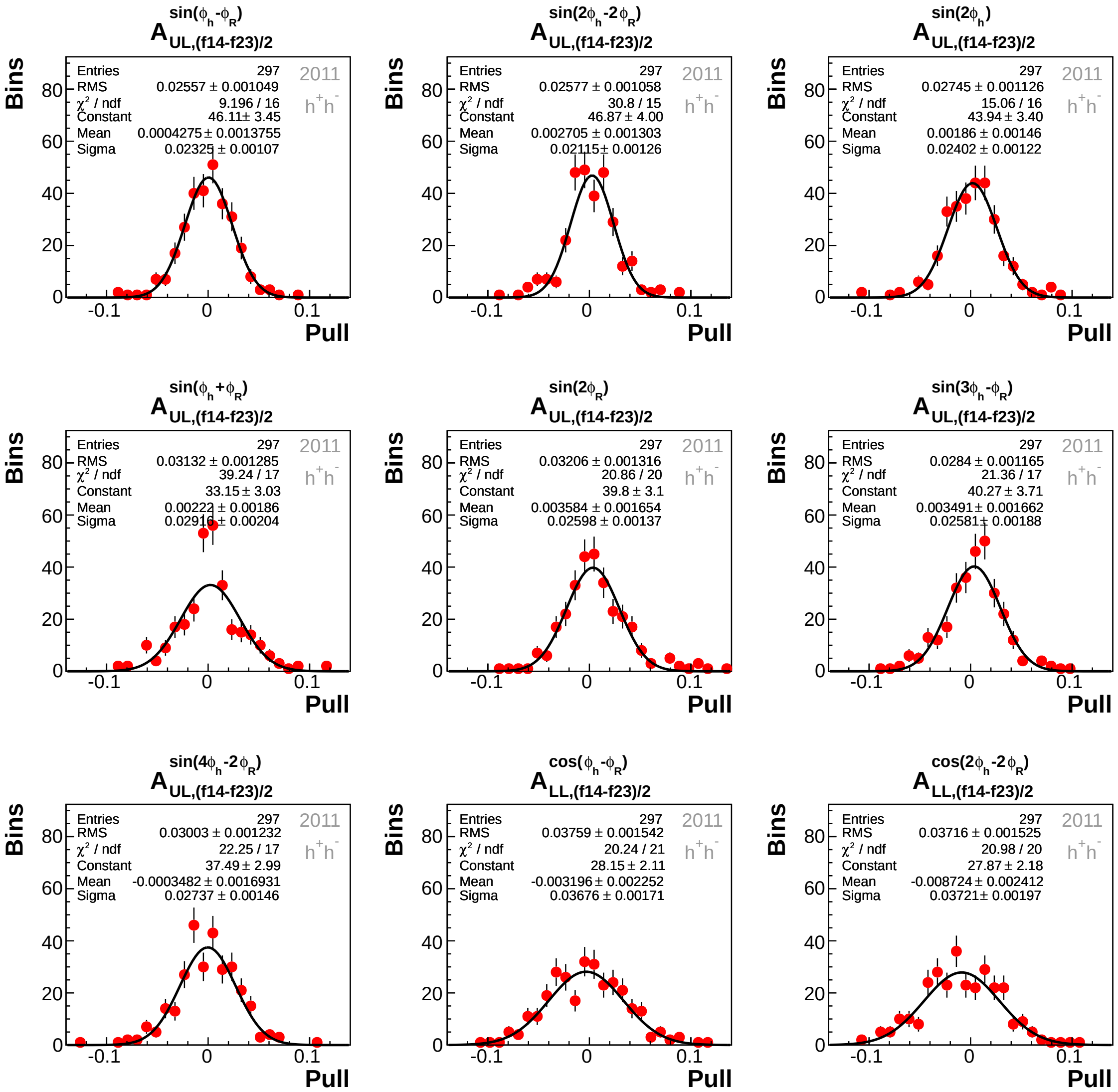

Figure 6.17: Pull distributions between $A^{m(\phi_h,\phi_R)}_{(f14-f23)/2}$ and $A^{m(\phi_h,\phi_R)}_{(r12-r34)/2}$ for 2011. The gaussian fit, corresponding statistical values and fit parameters are also displayed.

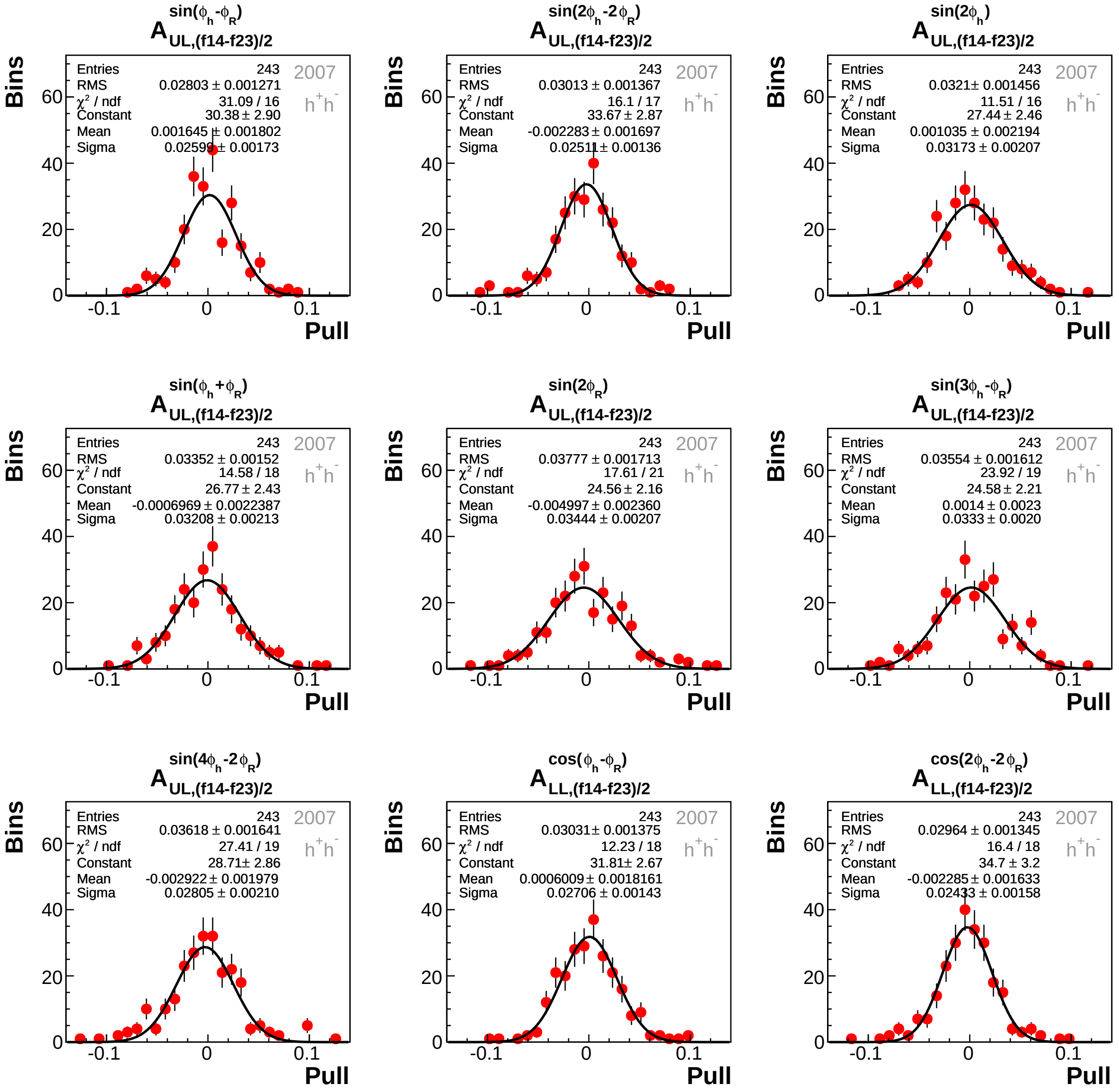

Figure 6.18: Pull distributions between $A^{m(\phi_h,\phi_R)}_{(f14-f23)/2}$ and $A^{m(\phi_h,\phi_R)}_{(r12-r34)/2}$ for 2007. The gaussian fit, corresponding statistical values and fit parameters are also displayed.

Table 6.4: Final additive systematic uncertainties for 2007 and 2011.

Year	2007	2011
$A_{XL}^{m(\phi_h,\phi_R)}$	$\sigma_{\text{sys}}^{\text{add}}/\sigma_{\text{stat}}$	
$A_{UL}^{\sin(\phi_h-\phi_R)}$	0.59	0.57
$A_{UL}^{\sin(2\phi_h-2\phi_R)}$	0.68	0.63
$A_{UL}^{\sin(2\phi_h)}$	0.65	0.68
$A_{UL}^{\sin(\phi_h+\phi_R)}$	0.72	0.58
$A_{UL}^{\sin(2\phi_R)}$	0.65	0.75
$A_{UL}^{\sin(3\phi_h-\phi_R)}$	0.71	0.60
$A_{UL}^{\sin(4\phi_h-2\phi_R)}$	0.62	0.52
$A_{LL}^{\cos(\phi_h-\phi_R)}$	0.9	1.00
$A_{LL}^{\cos(2\phi_h-2\phi_R)}$	0.66	0.64

6.3 Final Systematic Uncertainty

All uncorrelated systematic uncertainties, that were estimated in the above systematic studies, are taken into account for the evaluation of the final systematic uncertainty of a certain azimuthal asymmetry. This includes the additive systematic errors $\sigma_{\text{sys}}^{\text{meth}}$ (Tab. 6.1), $\sigma_{\text{sys}}^{\text{stab}}$ (Tab. 6.2) and $\sigma_{\text{sys}}^{\text{false}}$ (Tab. 6.3), all summed up in quadrature to

$$\sigma_{\text{sys}}^{\text{add}} = \sqrt{\left(\sigma_{\text{sys}}^{\text{meth}}\right)^2 + \left(\sigma_{\text{sys}}^{\text{stab}}\right)^2 + \left(\sigma_{\text{sys}}^{\text{false}}\right)^2}. \tag{6.15}$$

The results for this quantity are listed in Tab. 6.4 for each azimuthal asymmetry, separately for the studied years. Further systematics, resulting from the correction of the raw asymmetries, are taken into account by the multiplicative error $\Delta A_{XL}^{m(\phi_h,\phi_R)}$. As already concluded in Sec. 5.3, it amounts 2.2% for single spin asymmetries and 5.5% for double spin asymmetries in 2007, respectively 4.0% and 6.4% in 2011. The final systematic uncertainty in a kinematic bin i is calculated for each asymmetry as

$$\sigma_{\text{sys},i} = \sqrt{\left(\sigma_{\text{sys}}^{\text{add}} \cdot \sigma_{\text{stat,i}}\right)^2 + \left(\Delta A_{XL}^{m(\phi_h,\phi_R)} \cdot A_{XL,i}^{m(\phi_h,\phi_R)}\right)^2}. \tag{6.16}$$

6.4 Results

A visual comparison of the final azimuthal asymmetries, extracted with the UB LH method from the 2007 and 2011 data, is shown in Fig. 6.19 in bins of x, z and M_{inv}. The numerical values are appended in Sec. A.4. As already concluded on basis of statistical errors at the beginning of this section, no eminent kinematic dependence is observed on any of the considered variables. All asymmetries are quite narrowly distributed around zero with respect to statistics, involving the corresponding mean values to be consequently compatible with zero within at least three standard deviations for occasional cases. Taking the systematic uncertainties into consideration, these conclusions are further asserted. The corresponding mean values are depicted in the left summary plot in Fig. 6.19, where the systematic uncertainties are indicated as bars on the left.

Comparing the results from the two years, a rough agreement can be concluded, however suffering from large uncertainties. Incompatibilities concerning the results from particular microwave settings, showing up in the study of the A^1_{LL} asymmetry, can not be concluded. The corresponding plots can be found in Fig. A.15 and Fig. A.16. Assuming the Q^2-evolution of the considered asymmetries to be negligible within experimental accuracy, it's reasonable to estimate the weighted means of results from both years, although different beam energies were used. This is done for each bin, considering only statistical weights. To avoid double counting of systematic uncertainties, the corresponding systematic uncertainty is assigned following Eq. 6.16. Here, the additive uncertainty $\sigma^{\rm add}_{\rm sys}$ with the larger corresponding absolute error $\sigma^{\rm add}_{\rm sys} \cdot \sigma_{\rm sys,i}$ is chosen for each kinematic bin. The bin wise results are shown in Fig. 6.21, whereas corresponding mean values are depicted in the right summary plot in Fig. 6.19. All asymmetries are found to be compatible with zero within experimental precision, except the $\sin 4\phi_h - 2\phi_R$ moment, where the asymmetry is found to be slightly negative. Regarding the bin wise results in Fig. 6.21, a weak x-dependence could be interpreted in the high x-region for some of the asymmetries, especially for $A_{UL}^{\sin(\phi_h-\phi_R)}$ and $A_{UL}^{\sin(2\phi_R)}$.

The numerical mean values are listed in Tab. 6.6, including statistical and systematic uncertainties.

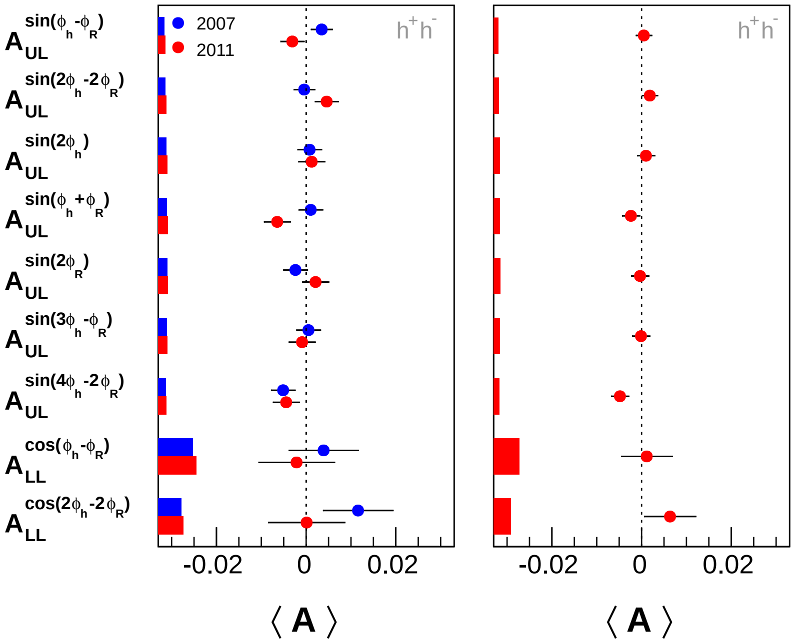

Figure 6.19: Left: Comparison of mean azimuthal asymmetries from 2007 and 2011 data. Right: Overall mean azimuthal asymmetries from both years. The bars indicate the corresponding systematic uncertainty.

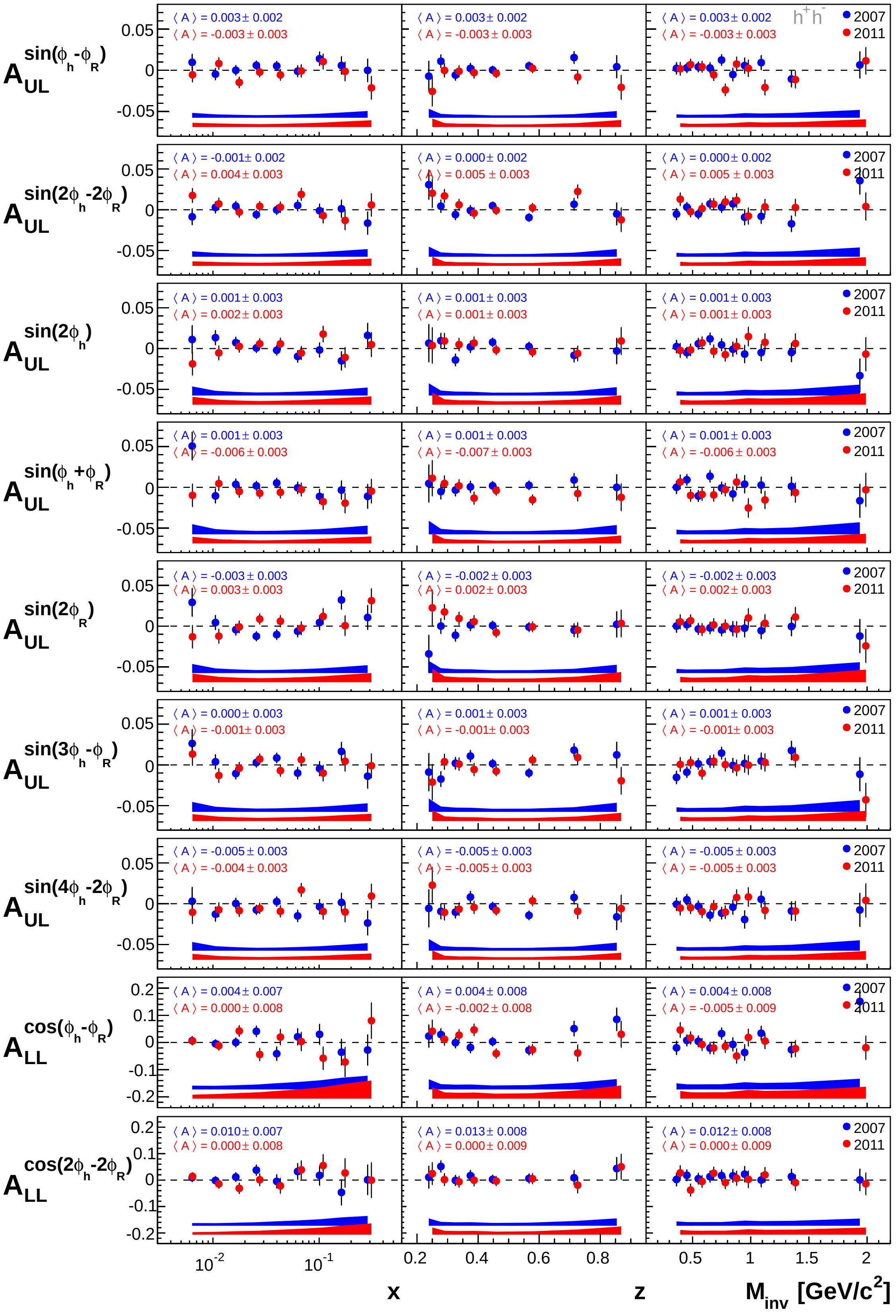

Figure 6.20: Azimuthal asymmetries from 2007 and 2011 data. The error bands indicate the systematic uncertainties. Corresponding mean values are also displayed.

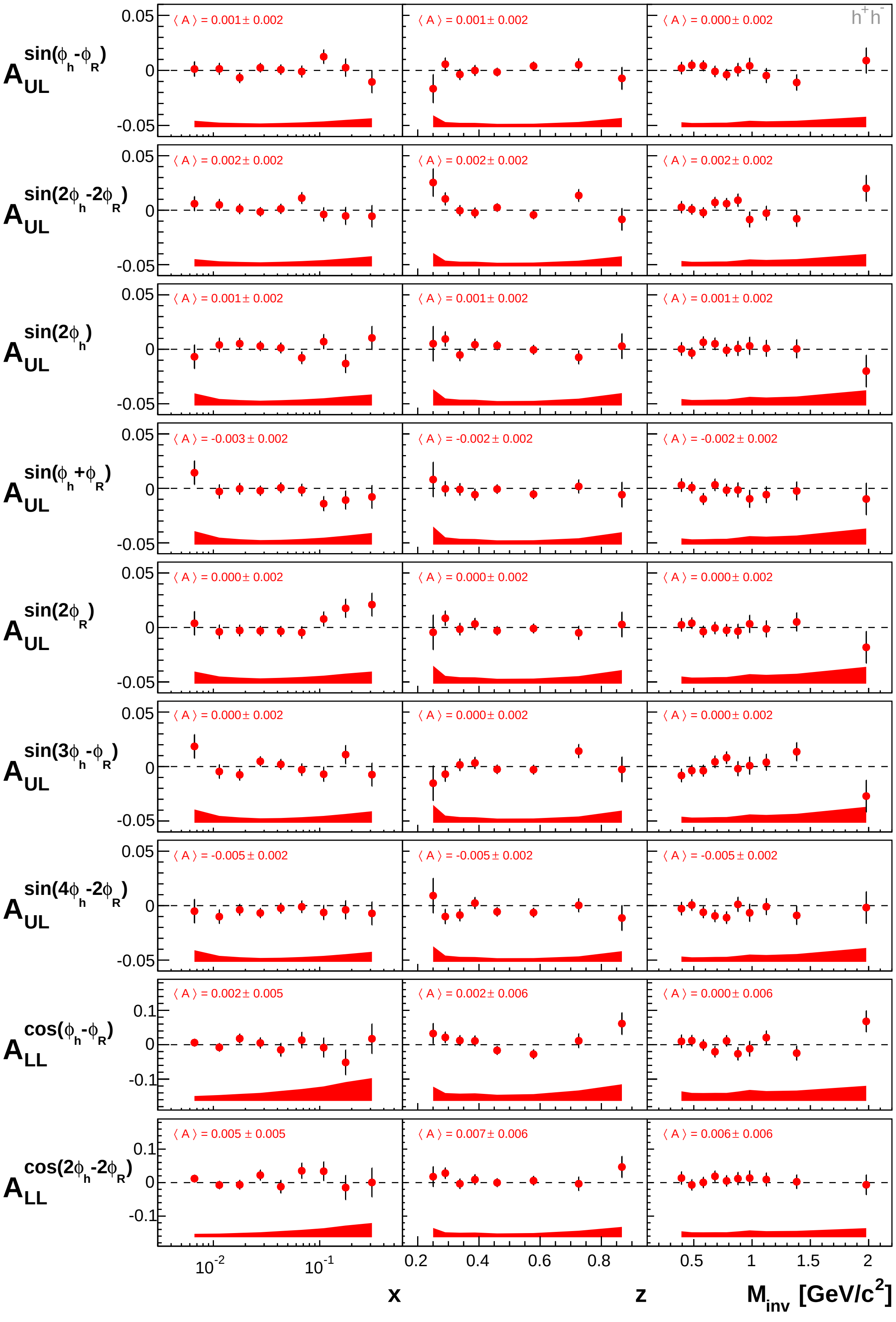

Figure 6.21: Azimuthal asymmetries for the whole data set. The error band indicates the systematic uncertainties. Corresponding mean values are also displayed.

Table 6.5: Mean azimuthal asymmetries for 2007 and 2011, including the statistical and systematic uncertainties.

Year	2007	2011
$A_{UL}^{\sin(\phi_h-\phi_R)}$	0.003 ± 0.002 ± 0.001	-0.003 ± 0.003 ± 0.002
$A_{UL}^{\sin(2\phi_h-2\phi_R)}$	0.000 ± 0.002 ± 0.002	0.005 ± 0.003 ± 0.002
$A_{UL}^{\sin(2\phi_h)}$	0.001 ± 0.003 ± 0.002	0.001 ± 0.003 ± 0.002
$A_{UL}^{\sin(\phi_h+\phi_R)}$	0.001 ± 0.003 ± 0.002	-0.006 ± 0.003 ± 0.002
$A_{UL}^{\sin(2\phi_R)}$	-0.002 ± 0.003 ± 0.002	0.002 ± 0.003 ± 0.002
$A_{UL}^{\sin(3\phi_h-\phi_R)}$	0.001 ± 0.003 ± 0.002	-0.001 ± 0.003 ± 0.002
$A_{UL}^{\sin(4\phi_h-2\phi_R)}$	-0.005 ± 0.003 ± 0.002	-0.004 ± 0.003 ± 0.002
$A_{LL}^{\cos(\phi_h-\phi_R)}$	0.004 ± 0.008 ± 0.008	-0.002 ± 0.009 ± 0.009
$A_{LL}^{\cos(2\phi_h-2\phi_R)}$	0.012 ± 0.008 ± 0.005	0.000 ± 0.009 ± 0.006

Table 6.6: Mean azimuthal asymmetries for the whole data set, including the statistical and systematic uncertainties.

	2007 & 2011
$A_{UL}^{\sin(\phi_h-\phi_R)}$	0.000 ± 0.002 ± 0.001
$A_{UL}^{\sin(2\phi_h-2\phi_R)}$	0.002 ± 0.002 ± 0.001
$A_{UL}^{\sin(2\phi_h)}$	0.001 ± 0.002 ± 0.001
$A_{UL}^{\sin(\phi_h+\phi_R)}$	-0.002 ± 0.002 ± 0.001
$A_{UL}^{\sin(2\phi_R)}$	0.000 ± 0.002 ± 0.001
$A_{UL}^{\sin(3\phi_h-\phi_R)}$	0.000 ± 0.002 ± 0.001
$A_{UL}^{\sin(4\phi_h-2\phi_R)}$	-0.005 ± 0.002 ± 0.001
$A_{LL}^{\cos(\phi_h-\phi_R)}$	0.001 ± 0.006 ± 0.006
$A_{LL}^{\cos(2\phi_h-2\phi_R)}$	0.006 ± 0.006 ± 0.004

7. One Hadron Analysis

In this chapter, the analysis of azimuthal asymmetries in one hadron SIDIS is outlined. Three asymmetries are considered, namely the two single spin asymmetries $A_{LU}^{\sin(\phi_h)}$ and $A_{LU}^{\sin(2\phi_h)}$, and the double spin asymmetry $A_{LL}^{\cos(\phi_h)}$, whereas they are analyzed for positive and negative hadrons separately. The study is performed in analogy to the two hadron case and will, in order to avoid repetitions, be presented in abbreviated form, concentrating on specific conclusions in the one hadron case. For a detailed description of the analysis framework, the reader may be referred to the previous chapter.

As already outlined in Sec. 2.5, the considered one hadron asymmetries were already measured by HERMES [50, 51] and CLAS [56], however in different kinematic regions and with less statistics. A comparison of the results from this work with former measurements and available model predictions is presented in Sec. 7.3, supporting essentially new conclusions.

7.1 Azimuthal Asymmetries

All asymmetries are extracted in bins of the variables x, z and the absolute transverse momentum of the detected hadron P_{hT}. Fig. 7.1 shows the UB LH results for both years, whereas the errors are only statistical so far. A general compatibility can be naively concluded from the visual comparison of the two years results, as well as from comparing the mean values from the three kinematic variables per year. Regarding the results for the $\sin(\phi_h)$ moment, a strong rise with x is obvious in case of positive hadrons, whereas in the central x-region results for 2007 are slightly larger than those from 2011. A slight x-dependence seems also to be present for the $\sin(2\phi_h)$ moment, falling for positive and rising for negative hadrons. Concerning the double spin asymmetry $A_{LL}^{\cos(\phi_h)}$, no such tendencies are observed. The results for this asymmetry are compatible with zero within statistical uncertainties for both years. In order to manifest these vague conclusions, the systematic uncertainties will be estimated in the following section, allowing for a final discussion of the overall results from both years in Sec. 7.3.

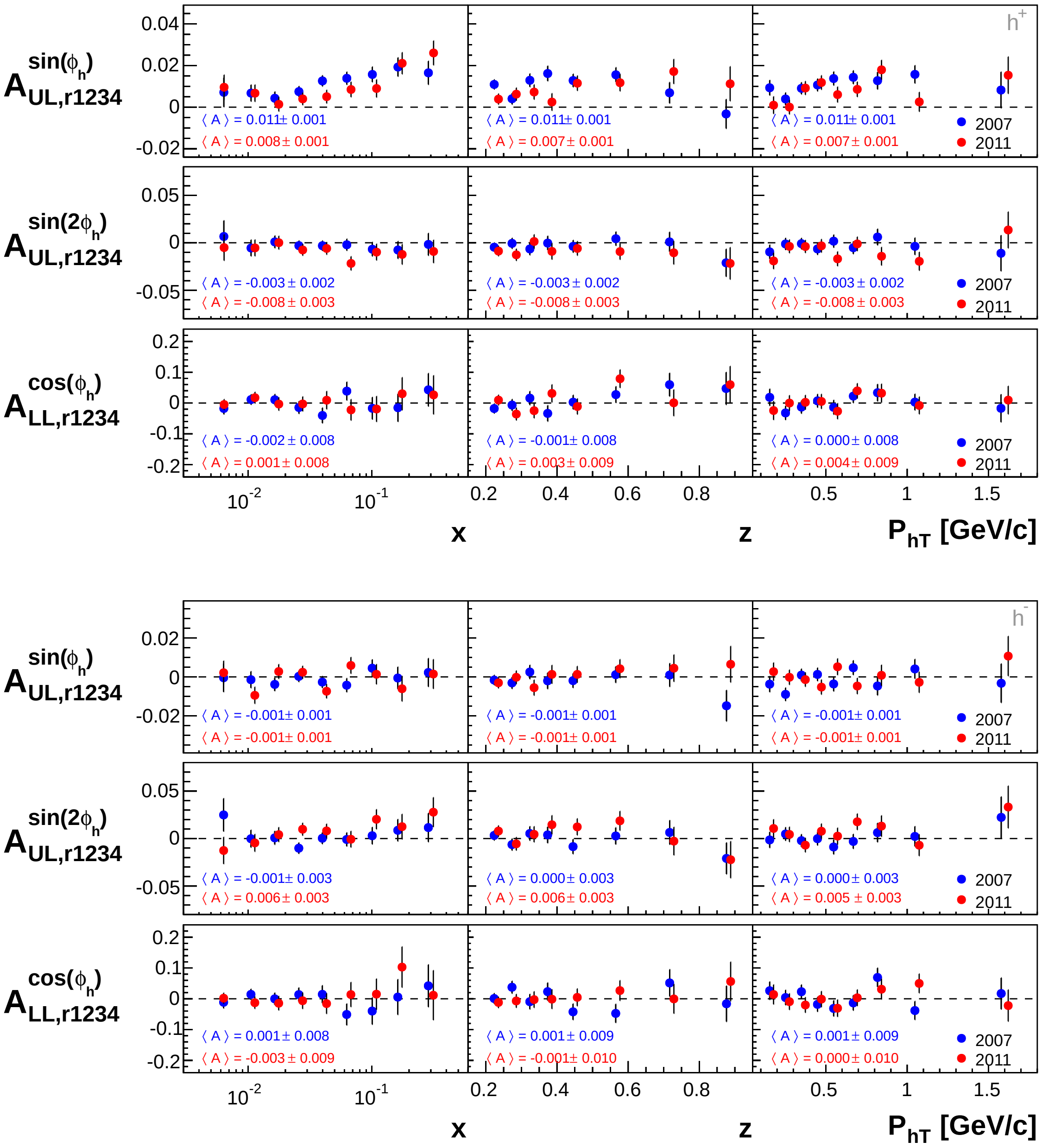

Figure 7.1: Azimuthal asymmetries from the UB LH method for 2007 and 2011 data for h^+ (top) and h^- (bottom). Corresponding mean values are also displayed.

7.2 Systematic Studies

The investigation of systematic influences for one hadron SIDIS follows analogue steps as performed in case of the two hadron analysis, outlined in the previous chapter. The following discussion will hence be reduced to the essential conclusions. For more detailed descriptions and formulas, the reader may be referred to the corresponding subsections in Sec. 6.2.

7.2.1 Compatibility of Methods

The used methods to extract asymmetries, namely the one dimensional product ratio method 1D PR and the unbinned maximum likelihood method UB LH, are checked for compatibility regarding the corresponding pull distributions of their differences, depicted in Fig. 7.2 for 2007 and in Fig. 7.3 for 2011. Their widths indicate a comparable agreement of the two methods to the two hadron case. However, the $\sin(2\phi_h)$ moment shows larger deviations, compared to the other asymmetries. Especially for 2007, a strong left shift indicates overall larger values from the 1D PR method. This is taken into account in the systematic uncertainty, summing up half of the shifted mean and the RMS. The resulting systematic uncertainties $\sigma_{\text{sys}}^{\text{meth}}$ are listed in Tab. 7.1 for each year, asymmetry, and hadron type. The comparison plots of both years results are appended in Fig. A.25 and Fig. A.26.

7.2.2 Compatibility of Weeks

In order to check the consistency of the results from all weeks, differences of week wise results with the corresponding weighted mean per kinematic bin are investigated, following Eq. (6.2). The resulting pull distributions in Fig. A.28 and Fig. A.27 show a satisfying compatibility for all asymmetries and both data sets, characterized by their means being compatible with zero and their widths being compatible to one within at least two standard deviations. The individual systematics are taken into account by estimating the systematic uncertainty $\sigma_{\text{sys}}^{\text{stab}}$ with the use of the specific RMS values, following Eq. 6.3. The relative uncertainties are given in Tab. 7.1.

The time dependent systematic studies are also extended to the comparison of weekly mean results, as well as on the comparison of results from different microwave settings for each year. As these studies reveal nothing conspicuous, the corresponding plots are appended in Fig. A.29 till Fig. A.34.

7.2.3 Asymmetries from Target Subsamples

The combination $A_{(r12+r34)/2}^{m(\phi_h)}$ of asymmetries from the two upstream and the two downstream cells coincides with the presented results, extracted from the data of all cells at once. This can be concluded from the pull distributions between the two asymmetry types for both years, shown in Fig. A.35 and A.36 in the appendix. It is noticeable, that the single spin asymmetries are characterized by a broader pull distribution then the double spin asymmetries in case of 2011, while for 2007 it is opposite. Nevertheless, the overall comparably small widths allow to neglect these systematic error sources in the final calculation of the systematic uncertainty.

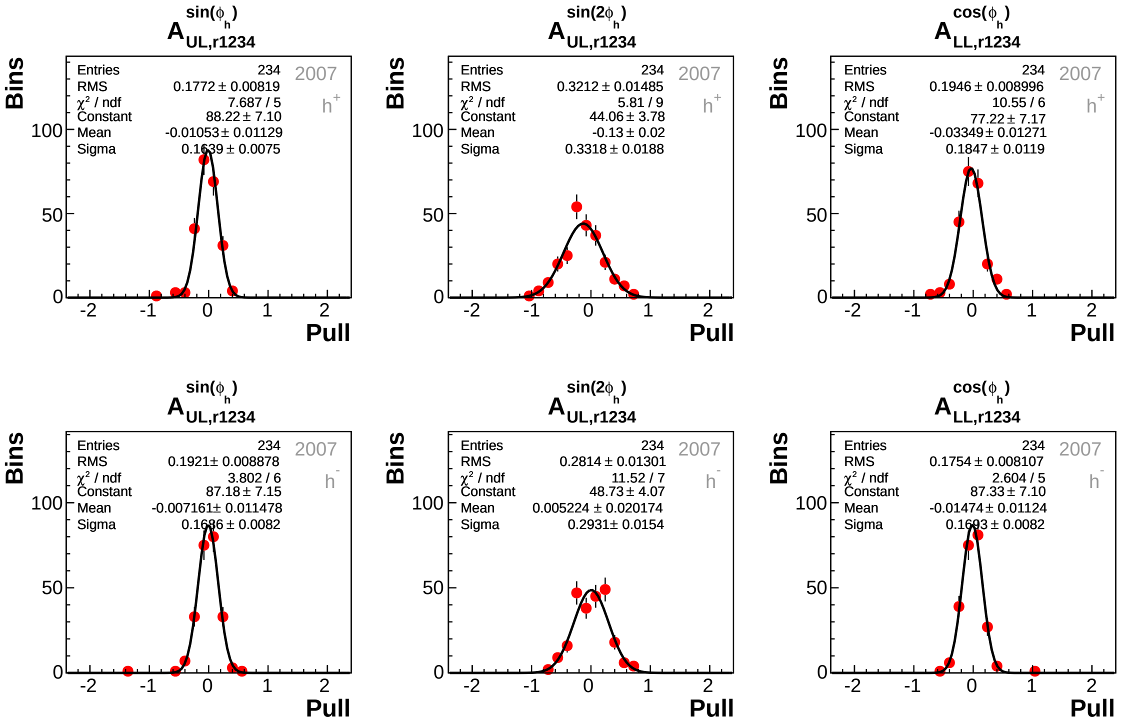

Figure 7.2: Pull distributions for h^+ (top) and h^- (bottom) between asymmetries extracted with the UB LH and the 1D PR method for 2007. The gaussian fit, corresponding statistical values and fit parameters are also displayed.

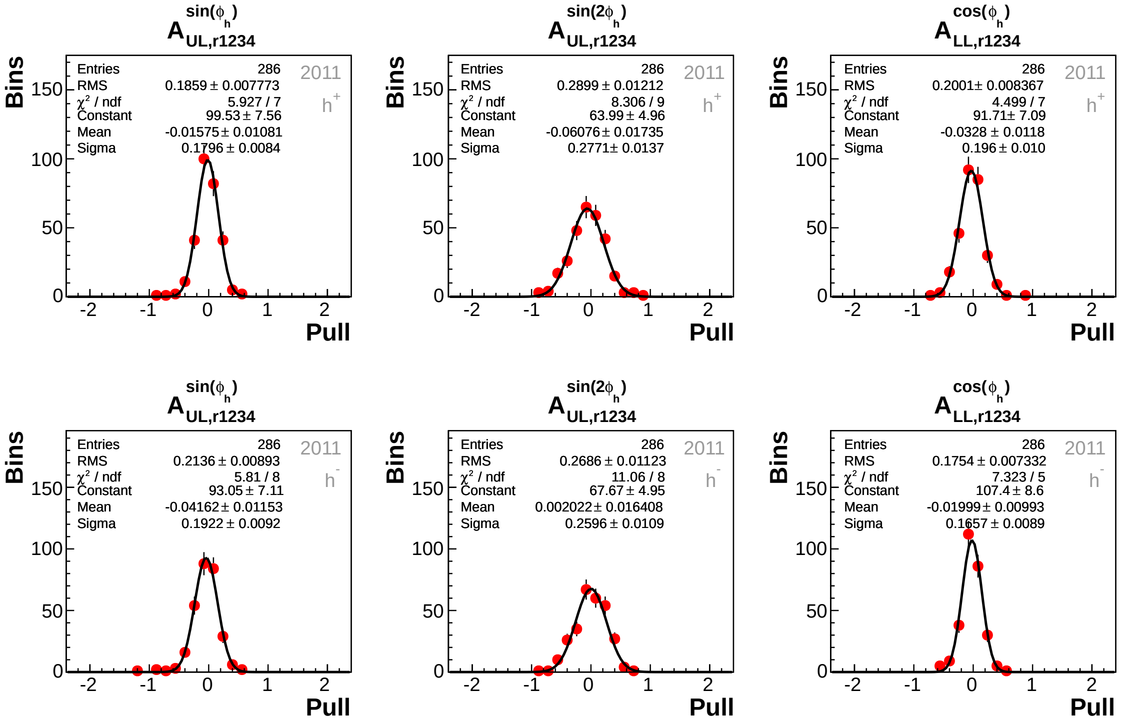

Figure 7.3: Pull distributions for h^+ (top) and h^- (bottom) between asymmetries extracted with the UB LH and the 1D PR method for 2011. The gaussian fit, corresponding statistical values and fit parameters are also displayed.

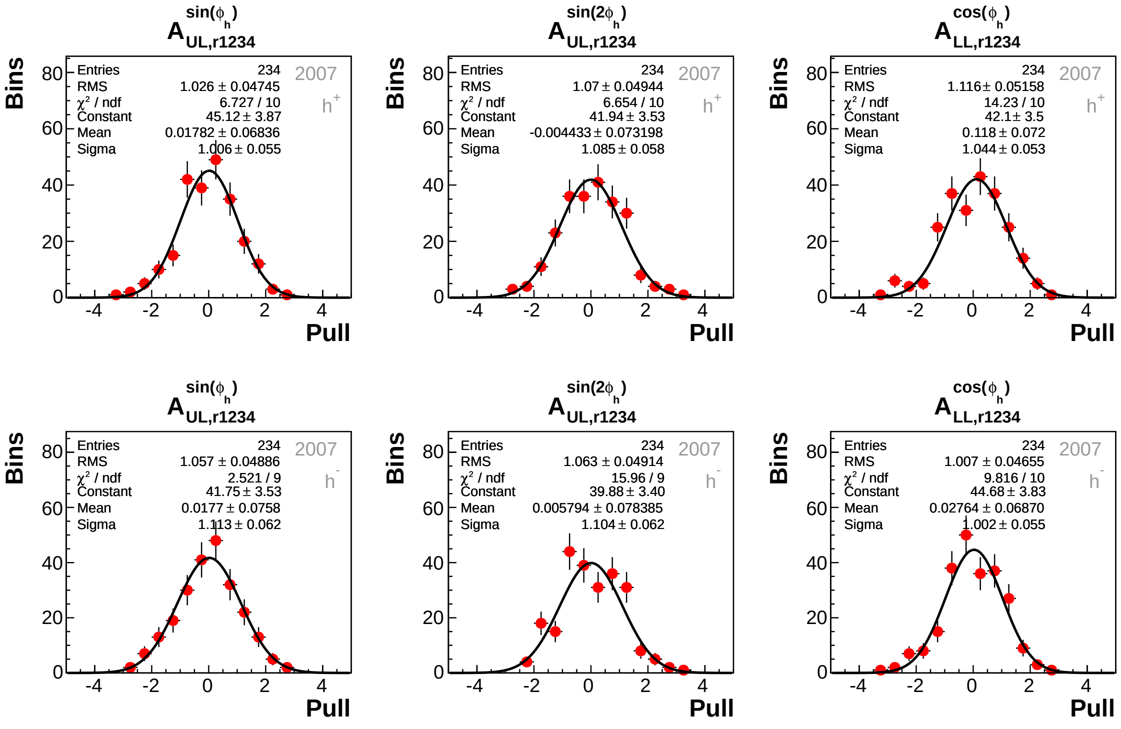

Figure 7.4: Stability pull distributions of asymmetries for h^+ (top) and h^- (bottom), extracted with the UB LH method, for 2007. The gaussian fit, corresponding statistical values and fit parameters are also displayed.

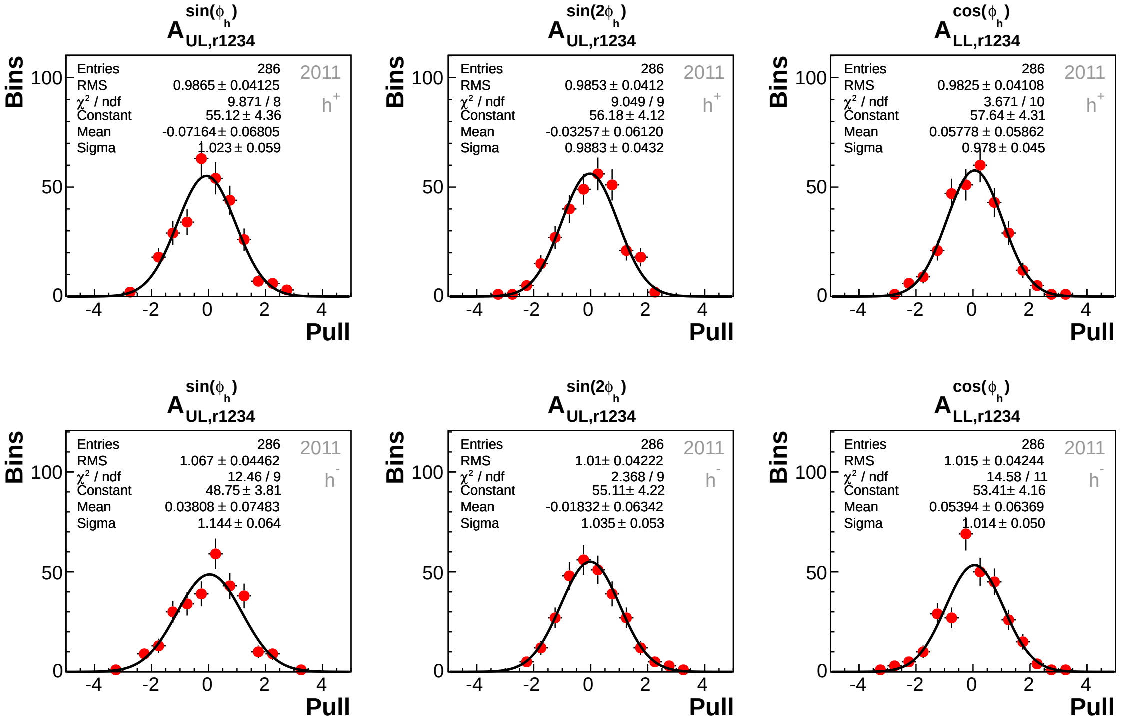

Figure 7.5: Stability pull distributions of asymmetries for h^+ (top) and h^- (bottom), extracted with the UB LH method, for 2011. The gaussian fit, corresponding statistical values and fit parameters are also displayed.

7.2.4 False Asymmetries

From the study of the false asymmetries $A^{m(\phi_h)}_{(f14-f23)/2}$ and $A^{m(\phi_h)}_{(f14+f23)/2}$ it can be concluded, that acceptance effects between the cells have to be accounted for with around half of the statistical error for all asymmetries, both hadron charges, and both years. This is comparable to the two hadron case. The concrete numerical systematic uncertainties $\sigma^{\text{false}}_{\text{sys}}$, estimated following Eq. (6.12), are listed in Tab. 7.1. For the sake of completeness, the results for both false asymmetry types are displayed in Fig. A.37 and Fig. A.38.

7.2.5 Final Systematic Uncertainty

The systematic uncertainties, resulting of the previous studies, are collected in Tab. 7.1 for both years and hadron charges. As it is done in the two hadron study, the certain error sources are assumed to be uncorrelated, allowing to estimate an overall additive systematic uncertainty $\sigma^{\text{false}}_{\text{sys}}$ by the square root of their quadratic sum. The numerical results are also given in Tab. 7.1. Again, the systematic uncertainty due to the correction of the raw asymmetries is taken into account as a multiplicative uncertainty $\Delta A^{m(\phi_h,\phi_R)}_{XL}$. The calculation of the final systematic uncertainty per bin follows Eq. (6.16), also used in the two hadron study. The systematic uncertainties are in size comparable to the two hadron studies and show no peculiarities, regarding the two years and the two hadron charges.

Table 7.1: Systematic uncertainties, relative to the statistical error, for 2007 and 2011.

Year	2007				2011			
$A^{m(\phi_h)}_{XL}$	$\sigma^{\text{meth}}_{\text{sys}}$	$\sigma^{\text{stab}}_{\text{sys}}$	$\sigma^{\text{false}}_{\text{sys}}$	$\sigma^{\text{add}}_{\text{sys}}$	$\sigma^{\text{meth}}_{\text{sys}}$	$\sigma^{\text{stab}}_{\text{sys}}$	$\sigma^{\text{false}}_{\text{sys}}$	$\sigma^{\text{add}}_{\text{sys}}$
h^+								
$A^{\sin(\phi_h)}_{UL}$	0.18	0.23	0.55	0.62	0.19	0.16	0.31	0.40
$A^{\sin(2\phi_h)}_{UL}$	0.39	0.38	0.57	0.79	0.32	0.26	0.57	0.70
$A^{\cos(\phi_h)}_{LL}$	0.21	0.50	0.39	0.67	0.22	0.19	0.41	0.50
h^-								
$A^{\sin(\phi_h)}_{UL}$	0.20	0.34	0.51	0.64	0.23	0.37	0.43	0.61
$A^{\sin(2\phi_h)}_{UL}$	0.28	0.36	0.58	0.74	0.27	0.14	0.50	0.58
$A^{\cos(\phi_h)}_{LL}$	0.18	0.12	0.47	0.52	0.19	0.17	0.49	0.55

7.3 Results

Three azimuthal asymmetries were measured in one hadron SIDIS, the two single spin asymmetries $A_{UL}^{\sin(\phi_h)}$ and $A_{UL}^{\sin(2\phi_h)}$, as well as the double spin asymmetry $A_{LL}^{\cos(\phi_h)}$. The study was performed for both data sets separately, distinguishing positive and negative hadrons. The results, extracted in bins of x, z and P_{hT} with the UB LH method, are displayed in Fig. 7.7 for both years separately, whereas Fig. 7.8 shows their averaged results. The mean values are depicted in Fig. 7.6.

Several remarkable conclusions can be drawn from the results, involving interesting physical interpretations. At this point, the main observations are summarized, postponing their physical discussion to the context of a comparison with results from other experiments and model predictions, outlined in the next section.

The $\sin(\phi_h)$ moment shows an evident increase with rising x for positive hadrons, not present for negative hadrons. This is observed for both years, however the results from 2007 are found to be larger in the central x region. Nevertheless, the results are in agreement within their statistical and systematic uncertainties. For positively charged hadrons, a weak increase seems also to be present in the P_{hT} region up to around 1 GeV/c. The average mean asymmetry for positive hadrons amounts

$$A_{UL,h^+}^{\sin(\phi_h)} = 0.009 \pm 0.001(\text{stat}) \pm 0.001(\text{sys}). \qquad (7.1)$$

A further observation concerns the $A_{UL}^{\sin(2\phi_h)}$. Being compatible with zero for low x, it seems to be slightly decreasing for positive and slightly increasing for negative hadrons in the valence x region. For positively charged hadrons, a negative overall mean value

$$A_{UL,h^+}^{\sin(2\phi_h)} = -0.005 \pm 0.002(\text{stat}) \pm 0.001(\text{sys}) \qquad (7.2)$$

is found, while the mean result for negative hadrons is compatible with zero.

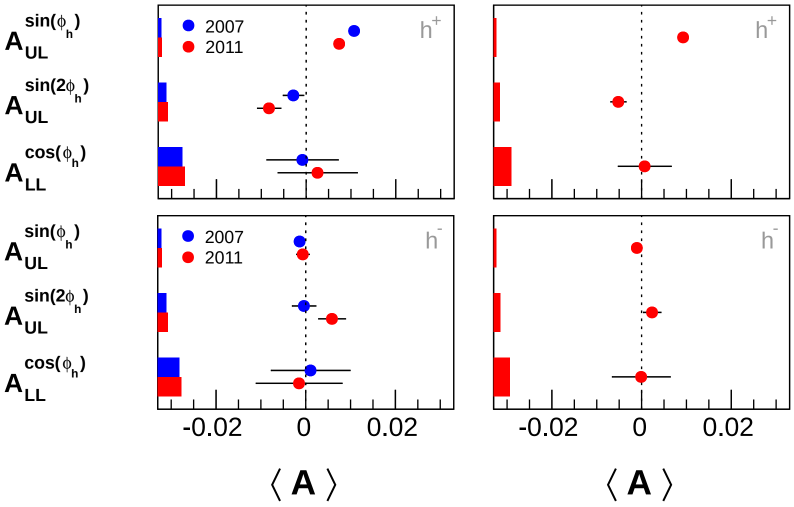

Figure 7.6: Left: Comparison of mean azimuthal asymmetries from 2007 and 2011 data. Right: Overall mean azimuthal asymmetries from both years. The bars indicate the corresponding systematic uncertainties.

The mean double spin asymmetry $A_{LL}^{\cos(\phi_h)}$ is found to be compatible with zero for both positive and negative hadrons. Regarding the bin wise results, no clear indication of a kinematic dependence can be observed.

The numerical results are summarized in the following tables, separately per year in Tab. 7.2, and averaged over the whole data set in Tab. 7.3. The bin wise results can be found in the appendix A.5.

Table 7.2: Mean azimuthal asymmetries for 2007 and 2011, including the statistical and systematic uncertainties.

Year	2007	2011
h^+		
$A_{UL}^{\sin(\phi_h)}$	0.011 ± 0.001 ± 0.001	0.007 ± 0.001 ± 0.001
$A_{UL}^{\sin(2\phi_h)}$	-0.003 ± 0.002 ± 0.002	-0.008 ± 0.003 ± 0.002
$A_{LL}^{\cos(\phi_h)}$	-0.001 ± 0.008 ± 0.005	0.003 ± 0.009 ± 0.006
h^-		
$A_{UL}^{\sin(\phi_h)}$	-0.001 ± 0.001 ± 0.001	-0.001 ± 0.001 ± 0.001
$A_{UL}^{\sin(2\phi_h)}$	0.000 ± 0.003 ± 0.002	0.006 ± 0.003 ± 0.002
$A_{LL}^{\cos(\phi_h)}$	0.001 ± 0.009 ± 0.005	-0.001 ± 0.010 ± 0.005

Table 7.3: Mean azimuthal asymmetries for the whole data set, including the statistical and systematic uncertainties.

	h^+	h^-
$A_{UL}^{\sin(\phi_h)}$	0.009 ± 0.001 ± 0.001	-0.001 ± 0.001 ± 0.001
$A_{UL}^{\sin(2\phi_h)}$	-0.005 ± 0.002 ± 0.001	0.002 ± 0.002 ± 0.001
$A_{LL}^{\cos(\phi_h)}$	0.001 ± 0.006 ± 0.004	0.000 ± 0.007 ± 0.004

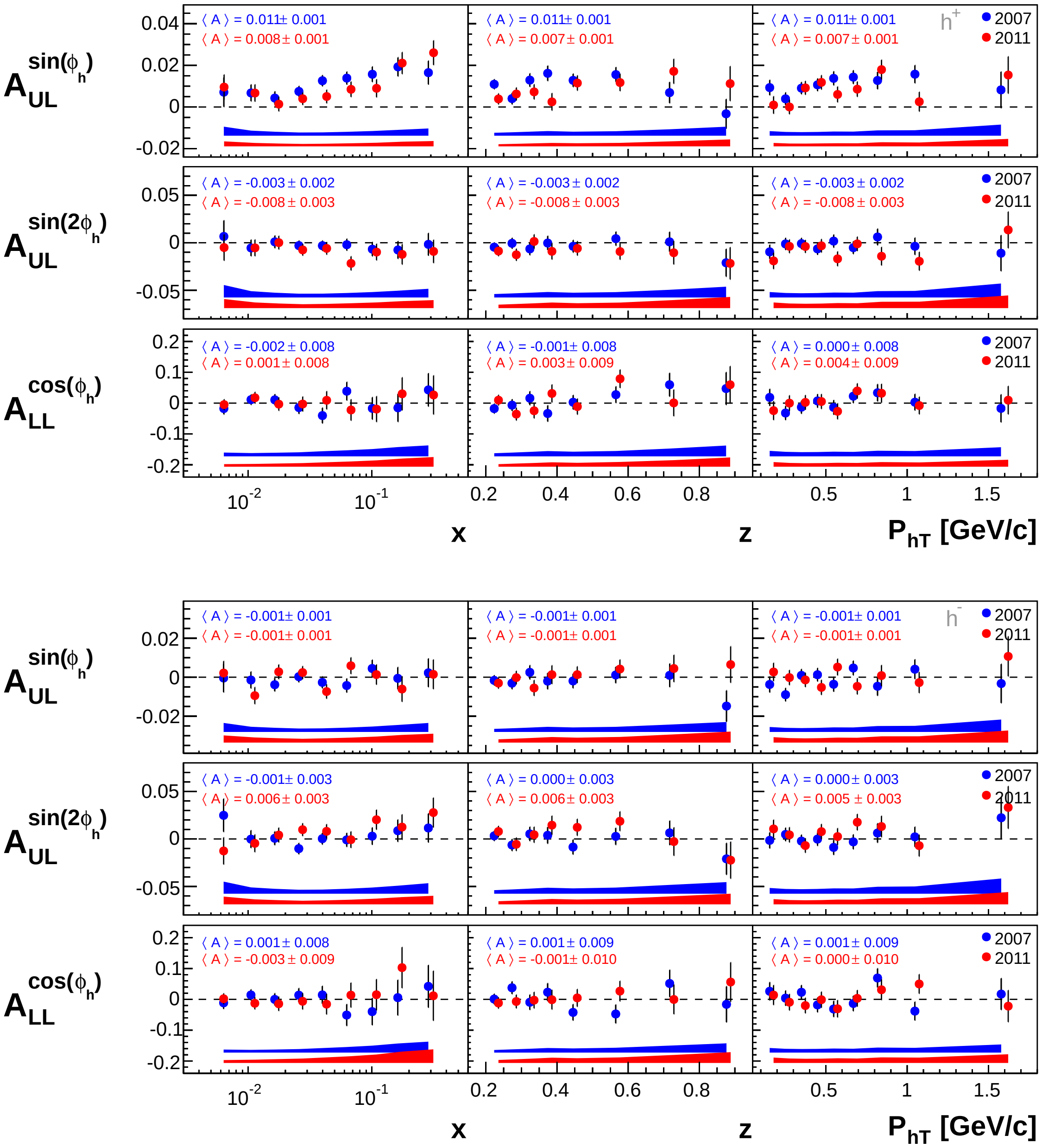

Figure 7.7: Azimuthal asymmetries from 2007 and 2011 data for h^+ (top) and h^- (bottom). The error bands indicate the systematic uncertainties. Corresponding mean values are also displayed.

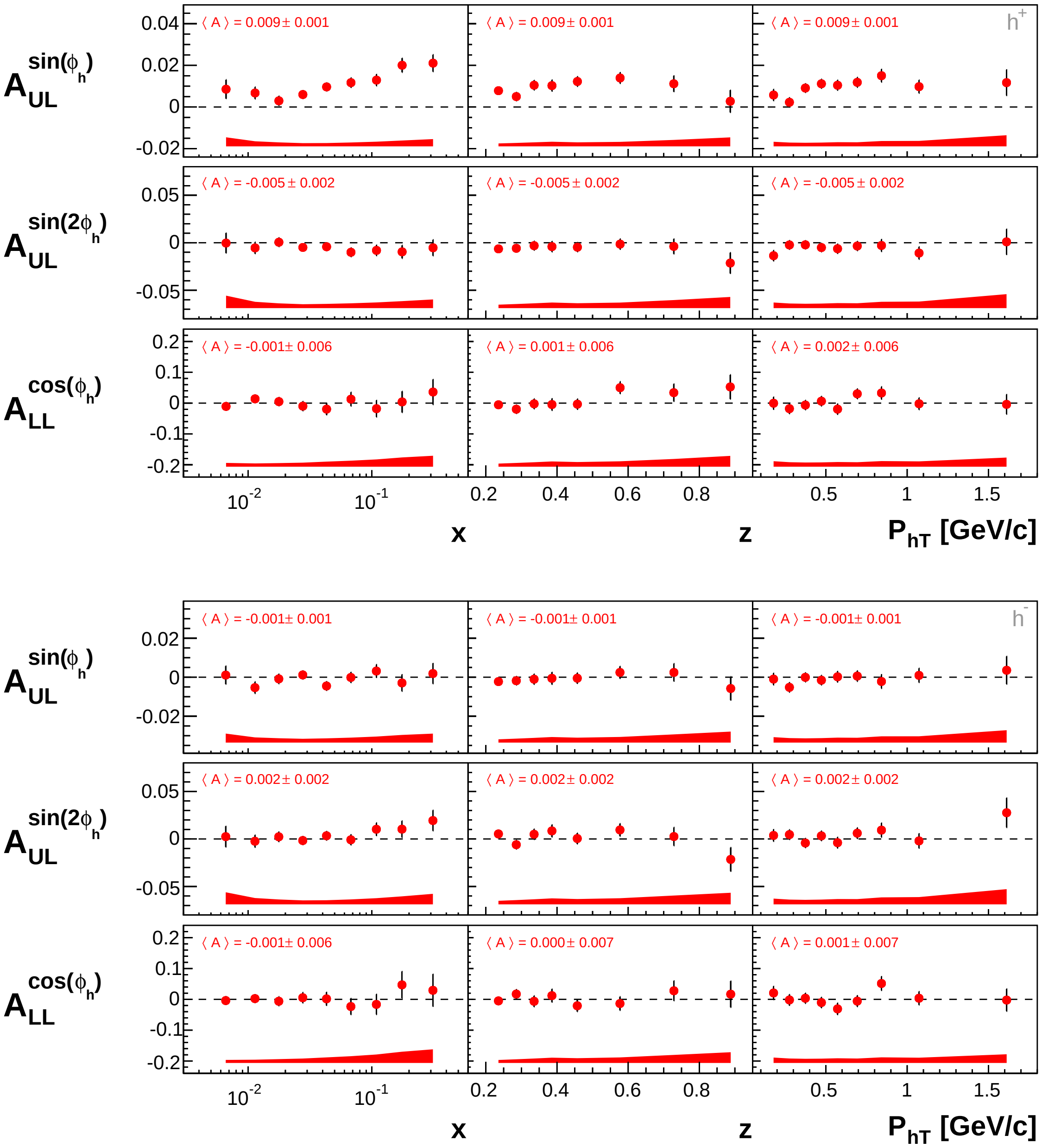

Figure 7.8: Azimuthal asymmetries from 2007 and 2011 data for h^+ (top) and h^- (bottom). The error bands indicate the systematic uncertainties. Corresponding mean values are also displayed.

7.3.1 Comparison with Results from Other Experiments and Model Predictions

As outlined in Sec. 2.5, target spin asymmetries in SIDIS off longitudinally polarized protons were already measured by HERMES [50, 51] and CLAS [56]. Their results on the single spin asymmetries $A_{UL}^{\sin(\phi_h)}$ and $A_{UL}^{\sin(2\phi_h)}$ gave evidence of measurable spin effects, related to intrinsic transverse parton momenta, and triggered a lot of interest in spin dependent TMD PDFs and FFs. However, the data was suffering from low statistics and a limited kinematic range so far. With the present combined analysis, using COMPASS data from 2007 and 2011, the statistical uncertainty is reduced significantly, revealing results of great value for the study of spin phenomena inside nucleons.

Fig. 7.9 shows the results on the leading twist single spin asymmetry $A_{UL}^{\sin(2\phi_h)}$ for positively (left) and negatively (right) charged hadrons, compared to the results from HERMES [50] and CLAS [56] on identified pions, as well as to available model predictions from Refs. [61, 94] (AEGMST). For convenience, here and in the following models are denoted in an abbreviated way by the first letters of their authors names. Note, that the HERMES and CLAS data was rescaled, accounting for the depolarization factor, that was not included in their original released results. While results from HERMES were found to be consistent with zero, the present analysis reveals a sizable asymmetry in the high-x region of opposite sign for h^+ and h^-. In fact, a sizable asymmetry was already measured by CLAS, however of negative sign for both π^+ and π^-. Hence, the presented results are the first, that are in agreement with AEGMST-model predictions, based on results on the Collins Function $H_1^\perp$, extracted from measurements in SIDIS [57, 95–97] and e^+e^- annihilation [58]

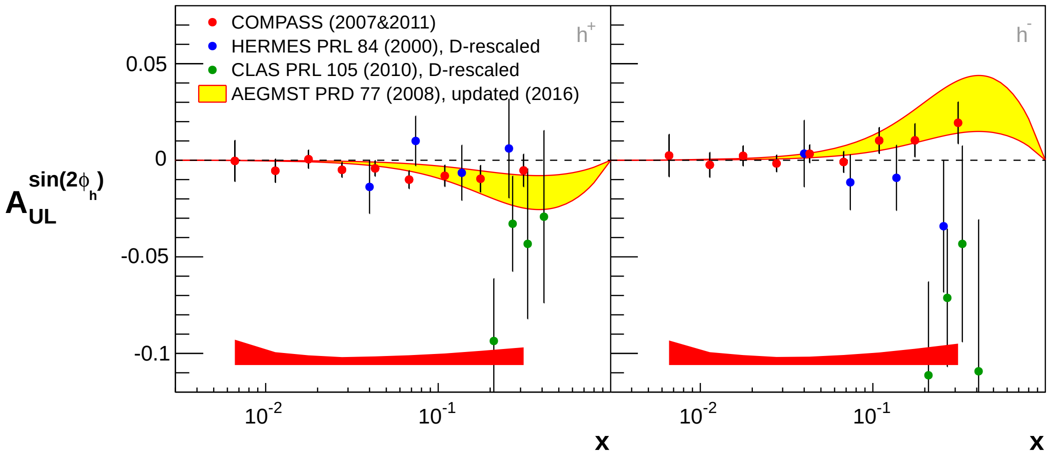

Figure 7.9: Comparison of results for $A_{UL}^{\sin(2\phi_h)}$ for h^+ (left) and h^- (right) with rescaled results from HERMES [50] and CLAS [56] and available model predictions [61, 94]. The red error band on the bottom indicates the systematic uncertainties of the COMPASS results, while the yellow error band is due to the present uncertainty of the Collins Function.

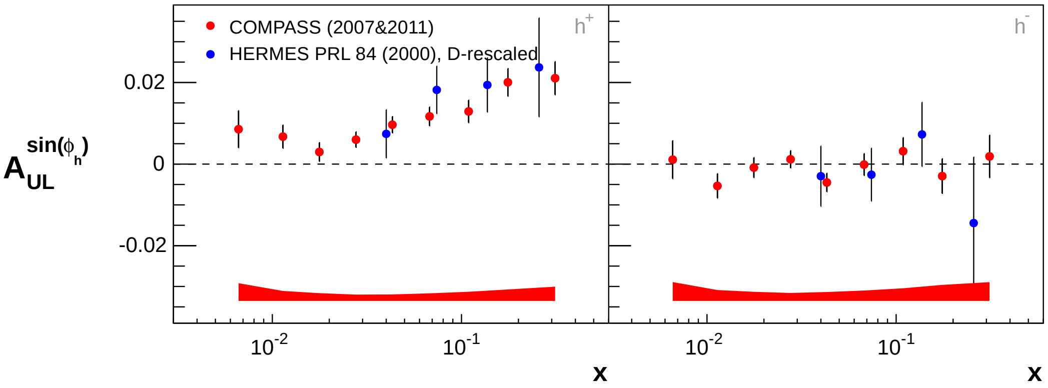

Figure 7.10: Comparison of results for $A_{UL}^{\sin(\phi_h)}$ for h^+ (left) and h^- (right) with results from HERMES [50]. The error band indicates the systematic uncertainties of the COMPASS results.

processes, and assuming the Wandzura-Wilczek (WW) approximation[1] to be valid also for $h_{1L}^{q\perp}$:

$$h_{1L}^{q\perp} \approx -x^2 \int_x^1 \frac{\mathrm{d}y}{y^2}\, h_1^q. \tag{7.3}$$

In order to model the transversity distribution h_1^q, predictions from the chiral quark soliton model (χQSM) were used [99]. The compatibility of the predicted asymmetry with the experimental results from this work suggests the WW-like assumption in Eq. (7.3) for $h_{1L}^{q\perp}$ to be reasonable and motivates its application in the description of subleading asymmetries as well, such as $A_{UL}^{\sin(\phi_h)}$.

In Fig. 7.10 the results on the subleading single spin azimuthal asymmetry $A_{UL}^{\sin(\phi_h)}$ for positively (left) and negatively (right) charged hadrons are compared to the results from HERMES on identified pions [50]. A significant non-zero asymmetry can be confirmed for h^+, while for h^- the results are found to be compatible with zero. This observation confirms the former interpretation, that there is a large difference between favored and disfavored FFs [50]. The $\sin(\phi_h)$-moment of the one hadron SIDIS cross section involves contributions from several higher-twist PDFs and FFs, making it difficult to prorate their particular influence on the measured observable. The results from $A_{UL}^{\sin(\phi_h)}$ could shed light on this issue, as they suggest the contribution from genuine collinear twist-3 PDFs to be negligible.

Concerning the double spin asymmetry $A_{LL}^{\cos(\phi_h)}$, there are predictions available for this asymmetry from two models, based on essentially different theoretical approaches. Calculations from Ref. [59] (AEKP) consider a leading order ansatz, assuming a simple factorized gaussian model for the p_T- and k_T-dependence of involved TMD PDFs and FFs. When not taking into account negligible contributions

---

[1] QCD-equations of motion allow to relate TMD PDFs and pure twist-3 interaction dependent PDFs. In the WW-approximation, contributions from pure twist-3 PDFs are neglected [98]. This concept could be experimentally confirmed only in case of g_T so far.

from transverse spin components, the contributing TMD PDFs are $f_1^q(x, p_T^2)$ and $g_{1L}^q(x, p_T^2)$. They are modeled as

$$f_1^q(x, p_T^2) = f_1^q(x)\,\frac{1}{\pi\mu_0^2}\exp\left(-\frac{p_T^2}{\mu_0^2}\right) \tag{7.4}$$

$$g_{1L}^q(x, p_T^2) = g_1^q(x)\,\frac{1}{\pi\mu_2^2}\exp\left(-\frac{p_T^2}{\mu_2^2}\right), \tag{7.5}$$

including the p_T-integrated unpolarized distribution function $f_1^q(x)$, taken from Ref. [100], and the helicity distribution function $g_1^q(x)$, for which the "standard scenario" parametrization from Ref. [101] was used. The contributing leading twist TMD FF $D_1^q(z, k_T^2)$ is factorized analogously as

$$D_1^q(z, k_T^2) = D_1^q(z)\,\frac{1}{\pi\mu_D^2}\exp\left(-\frac{k_T^2}{\mu_D^2}\right), \tag{7.6}$$

with $D_1^q(z)$ describing the k_T-integrated unpolarized FF, adopted from Ref. [102]. The respective average partonic transverse momenta are given by the parameters μ_0^2, μ_2^2 and μ_D^2, being kept equal for all quark flavors for simplicity. Following the fitted result from Ref. [103], μ_0^2 and μ_D^2 were set to 0.25 (GeV/c)^2, respectively 0.20 (GeV/c)^2. The free parameter μ_2^2 was chosen to take four different values 0.10, 0.15, 0.20 and 0.25 (GeV/c)^2.

The second model, presented in Ref. [104] (MWDLM), bases on an alternative approach. It considers twist-3 effects arising from the genuine twist-3 TMD PDFs $g_L^{q\perp}$ and e_L^q, calculated in the framework of the spectator model. Two different propagators of the vector diquark were chosen for their calculation, resulting in two different sets of TMD PDFs. "Set1" is motivated by the light-cone formalism [105], whereas "Set2" originates from a different form used in Ref. [106]. Concerning the involved leading twist TMD FFs, a parametrization for $H_1^{q\perp}(z, k_T^2)$ was adopted from Ref. [32], while $D_1^q(z, k_T^2)$ is factorized as it was done in the latter model. Here, the integrated FF $D_1^q(z)$ is adopted from the leading order set of Ref. [107], obtained from a global QCD analysis, which is compatible to the one used in the latter model.

In order to compare with the experimental results from this work, predictions from both models were recalculated to match the kinematics of the used COMPASS data [108][109]. It has to be mentioned, that simple factorization with unintegrated distributions can be assumed to hold up to values of $P_{hT} < 1$ GeV/c. In the high-P_{hT} region pQCD corrections of higher order have to be taken into account [110]. As can be seen in Fig. 4.27, the used COMPASS data is dominated by low-P_{hT} contributions in all bins of x and z. MWDLM-calculations were consequently restricted to $P_{hT} <$ 1 GeV/c. The AEKP-calculations were carried out for $z < 0.85$ to exclude exclusive contamination.

The experimental and theoretical results are shown in Fig. 7.11 for h^+ (left) and h^- (right). The models predictions are found to be roughly compatible when considering "Set1" from MWDLM, both predicting a negative asymmetry of weak kinematic dependence, which is supposed to increase slightly for higher values of the

μ_2^2-parameter. For "Set2", a surprisingly small asymmetry is predicted, indicated as the dashed blue line. The experimental results in x are found to be in satisfying agreement with the predictions, whereas for the other kinematic variables larger deviations are present. Unfortunately, relatively large experimental uncertainties do not allow to qualitatively assess the different models.

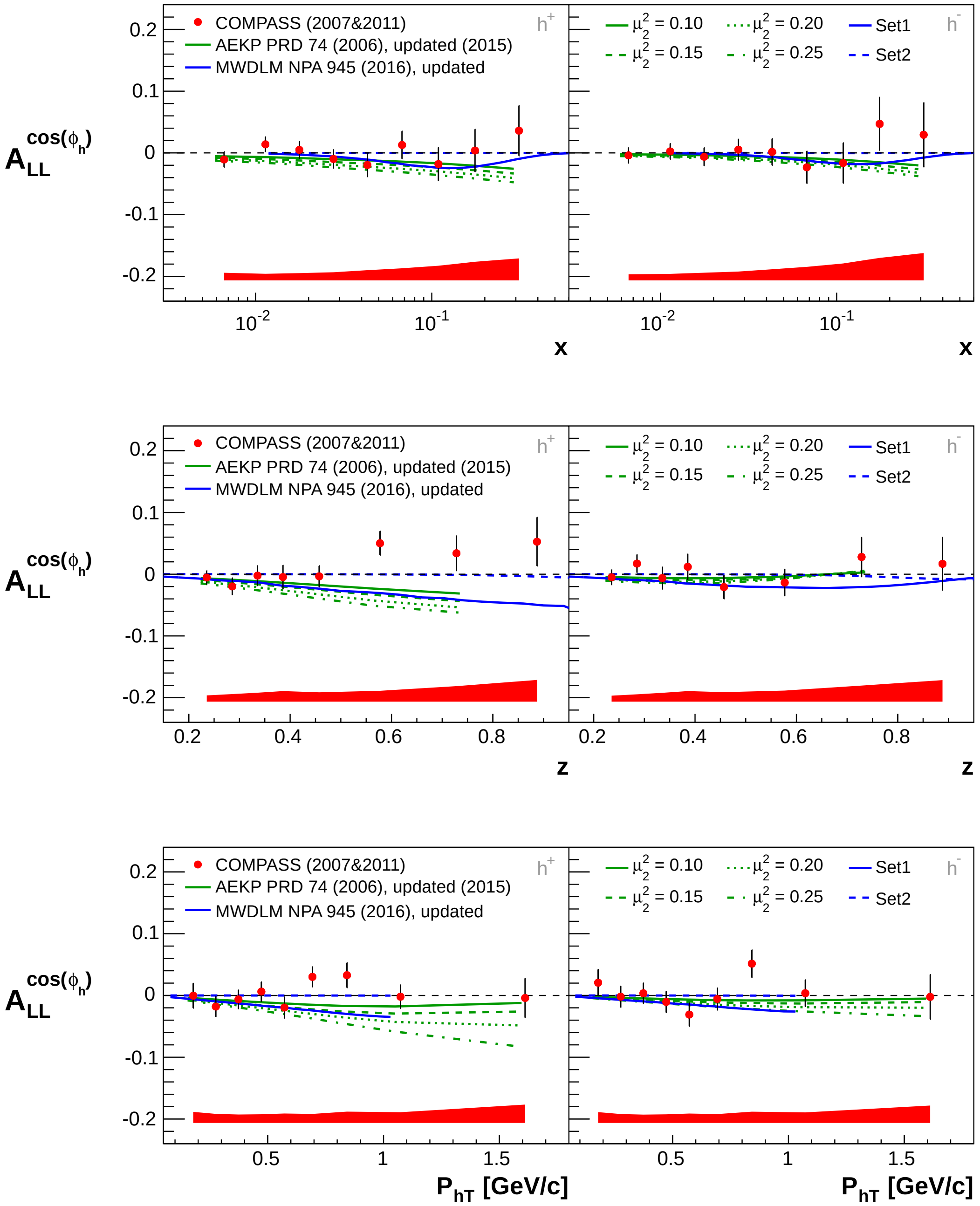

Figure 7.11: Comparison of results for $A_{LL}^{\cos(\phi_h)}$ for h^+ (left) and h^- (right) with available model predictions [59, 104]. The error band indicates the systematic uncertainties of the COMPASS results.

8. Analysis of the A_1^p Asymmetries

The one dimensional PR method, used as an alternative to the UB LH method to extract azimuthal asymmetries, gives also access to the cross section asymmetry A_1^p. Being already measured with high accuracy in DIS and one hadron SIDIS at various experiments, a comparison study with existing results can be used to confirm a general consistency of the procedure of analysis, used to disentangle azimuthal asymmetries in the one and two hadron analysis. This chapter comprises a brief summary of corresponding systematic studies, concluding with a more detailed discussion on the compatibility of results from the different analyses, as well as with results from existing literature.

For the reason of comparability, the analysis of the A_1^p asymmetry is discussed simultaneously for single hadrons and hadron pairs. As there were used six one dimensional fit functions to extract the azimuthal asymmetries in the two hadron analysis, one for each independent azimuthal argument Θ_i, a set of six associated values for $A_{1,i}^p$ results. They are found to be in sufficient agreement within all kinematic bins and all weeks to allow for a simplified comprehensive study on basis of their arithmetic mean values, maintaining the statistical errors[2]. In case of the one hadron study, all azimuthal asymmetries are accessed by a single one dimensional fit, contributing results for positively and negatively charged hadrons to the present analysis of A_1^p.

8.1 Systematic Studies

The estimation of the systematic uncertainty of A_1^p is basically performed in analogy to the azimuthal asymmetry studies. The following discussion is therefore reduced to the essentials, referring the reader to the corresponding subsection in Sec. 6.2 for detailed explanations.

---

[2] An analogue study was carried out for the six individual results $A_{1,i}^p$, resulting in compatible conclusions. See Fig. A.39 for a comparison of the final results.

As the A_1^p asymmetry is accessed with the 1D PR method only, a general systematic uncertainty of $\sigma_{\text{sys}}^{\text{meth}}/\sigma_{\text{stat}} = 0.25$ is assigned, which is roughly the outcome of the method compatibility studies in case of azimuthal asymmetries.

The stability pull distributions, including results from all kinematic bins and all weeks, are shown in Fig. 8.1. All distributions, corresponding to the different analyses (columns) for the two years (rows), are characterized by a relatively large RMS. This is taken into account in the calculation of the systematic uncertainty $\sigma_{\text{sys}}^{\text{stab}}$, following Eq. (6.3). The resulting values are listed in Tab. 8.1. The observed instability can be traced back to markable deviations of the results from different microwave settings, depicted in the comparison plots of Fig. 8.3 for 2007 and Fig. 8.4 for 2011. Obvious differences are visible in the central x region for all analyses, most pronounced for positive hadrons in 2011. When comparing the results from same microwave settings of the two years, these deviations seem to originate from MW-. Regarding the weekly mean asymmetries, depicted in Fig. 8.7 and Fig. 8.8, strong variations can be noted. Sudden jumps seem to be caused by microwave reversals, following week 33 and week 38 in 2007, and week 33 in 2011. However, results from different analyses show a varying severity.

The compatibility of the results $A_{1,r1234}^p$ with those, extracted from data subsamples from the upstream and the downstream half of the target $A_{1,(r12+r34)/2}^p$, is reasonably satisfying. Although the comparison pull distributions in Fig. 8.2 appear slightly broader then in case of azimuthal asymmetries, systematics are concluded to be of negligible size.

The study of false asymmetries, namely $A_{1,(f14-f23)/2}^p$ and $A_{1,(f14+f23)/2}^p$, reveal comparable results as in case of azimuthal asymmetries. They are well compatible with zero, shown in Fig. 8.9 and Fig. 8.10, with occasional deviations in certain kinematic bins. The corresponding systematic uncertainties, estimated as the larger weighted mean of deviations from all bins via Eq. 6.12, is assigned individually per analysis and year. The resulting values $\sigma_{\text{sys}}^{\text{false}}$ are listed in Tab. 8.1.

The final systematic uncertainties are estimated in analogy to the case of azimuthal asymmetries, including the combined additive systematic uncertainty $\sigma_{\text{sys}}^{\text{add}}$, as well as the multiplicative uncertainty $\Delta A_{LL}^{m(\phi_h,\phi_R)}$ due to the raw asymmetry correction.

Table 8.1: Systematic uncertainties of A_1^p for the different analyses, relative to the statistical error, for 2007 and 2011.

Year	2007				2011			
Analysis	$\sigma_{\text{sys}}^{\text{meth}}$	$\sigma_{\text{sys}}^{\text{stab}}$	$\sigma_{\text{sys}}^{\text{false}}$	$\sigma_{\text{sys}}^{\text{add}}$	$\sigma_{\text{sys}}^{\text{meth}}$	$\sigma_{\text{sys}}^{\text{stab}}$	$\sigma_{\text{sys}}^{\text{false}}$	$\sigma_{\text{sys}}^{\text{add}}$
h^+	0.25	0.66	0.49	0.86	0.25	0.59	0.64	0.91
h^-	0.25	0.55	0.43	0.74	0.25	0.48	0.40	0.67
h^+h^-	0.25	0.76	0.67	1.04	0.25	0.62	0.67	0.95

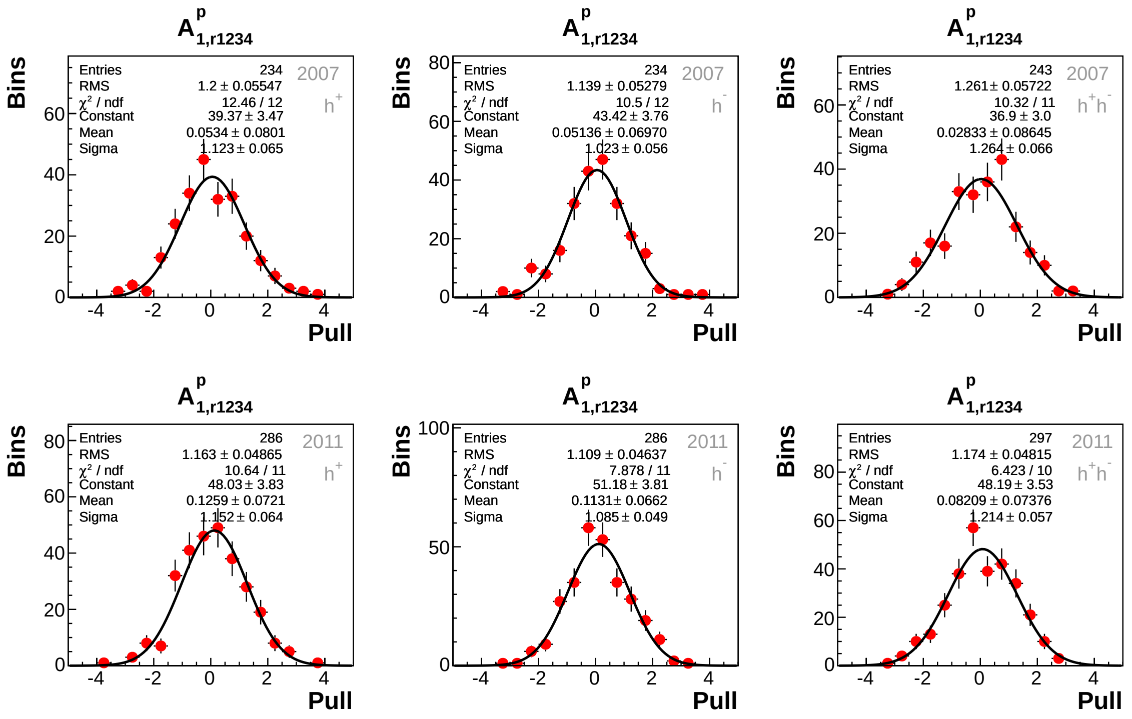

Figure 8.1: Stability pull distributions of A_1^p from the different analyses for 2007 (top) and 2011 (bottom). The gaussian fit, corresponding statistical values and fit parameters are also displayed.

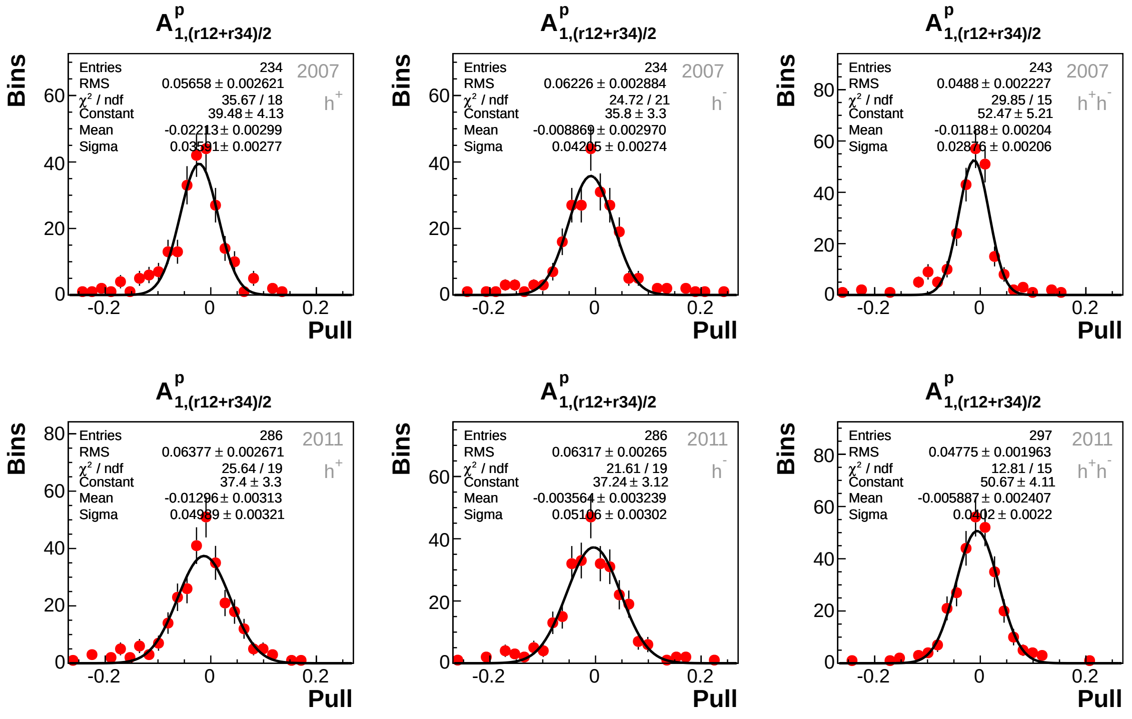

Figure 8.2: Pull distributions between $A^p_{1,(r12+r34)/2}$ and $A^p_{1,r1234}$ from the different analyses for 2007 (top) and 2011 (bottom). The gaussian fit, corresponding statistical values and fit parameters are also displayed.

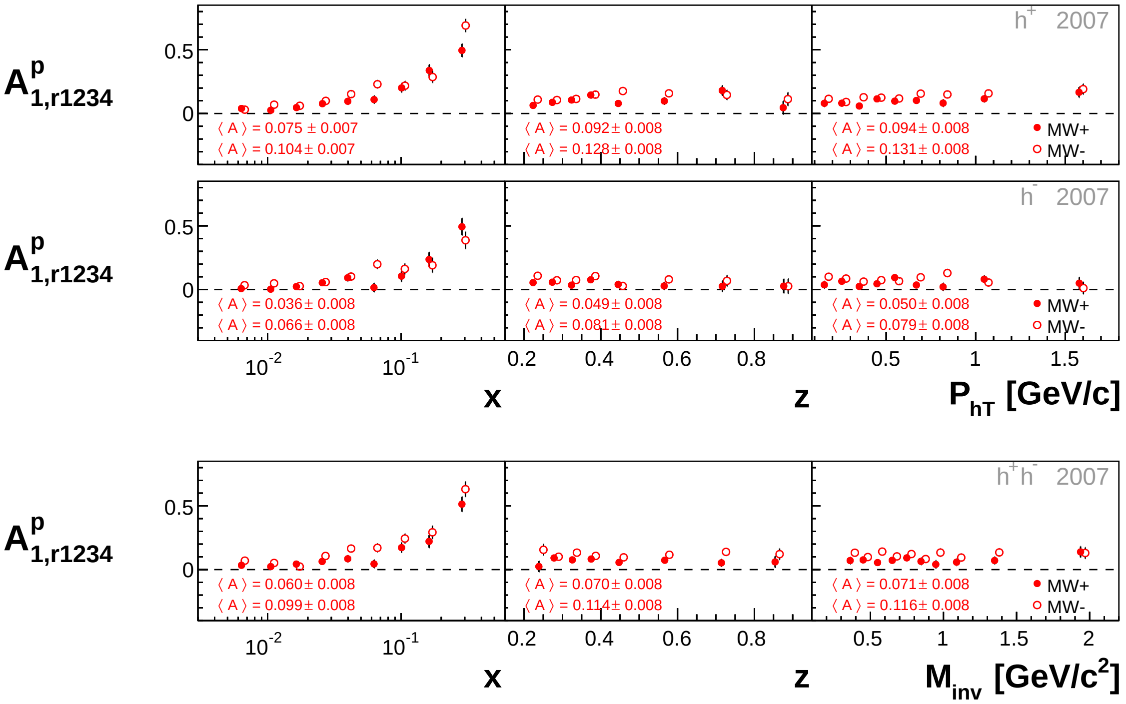

Figure 8.3: Comparison of A_1^p from different microwave settings for h^+ and h^-(top) and h^+h^-(bottom) for 2007. Corresponding mean values are also displayed.

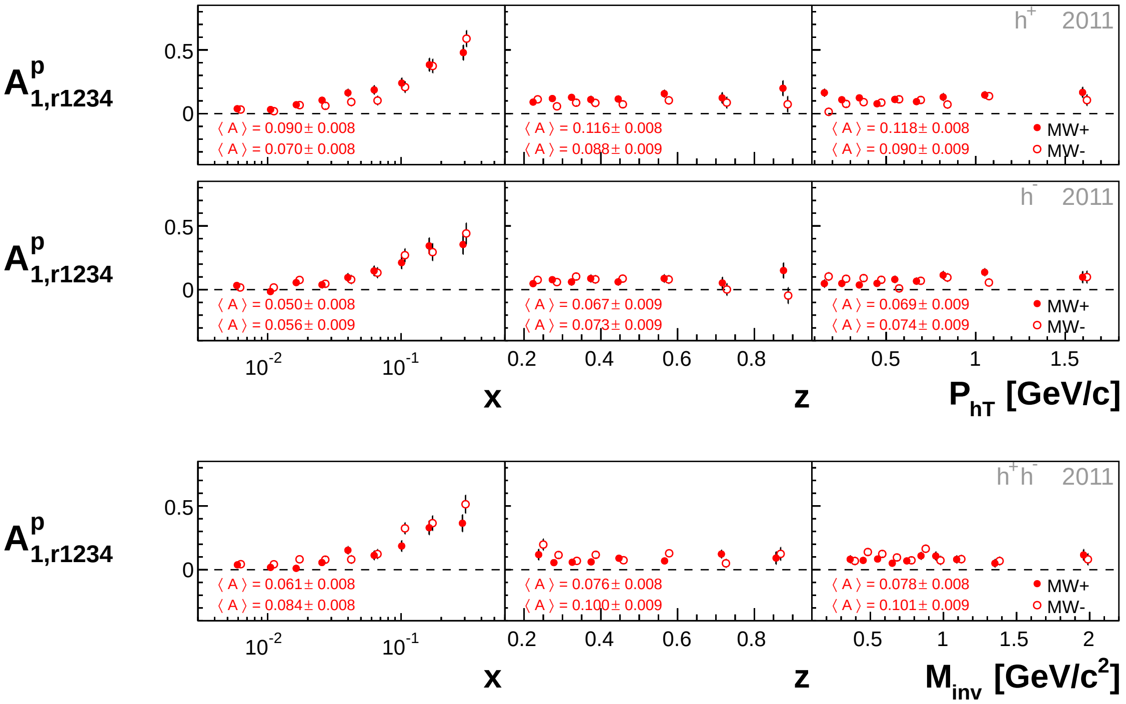

Figure 8.4: Comparison of A_1^p from different microwave settings for h^+ and h^-(top) and h^+h^-(bottom) for 2011. Corresponding mean values are also displayed.

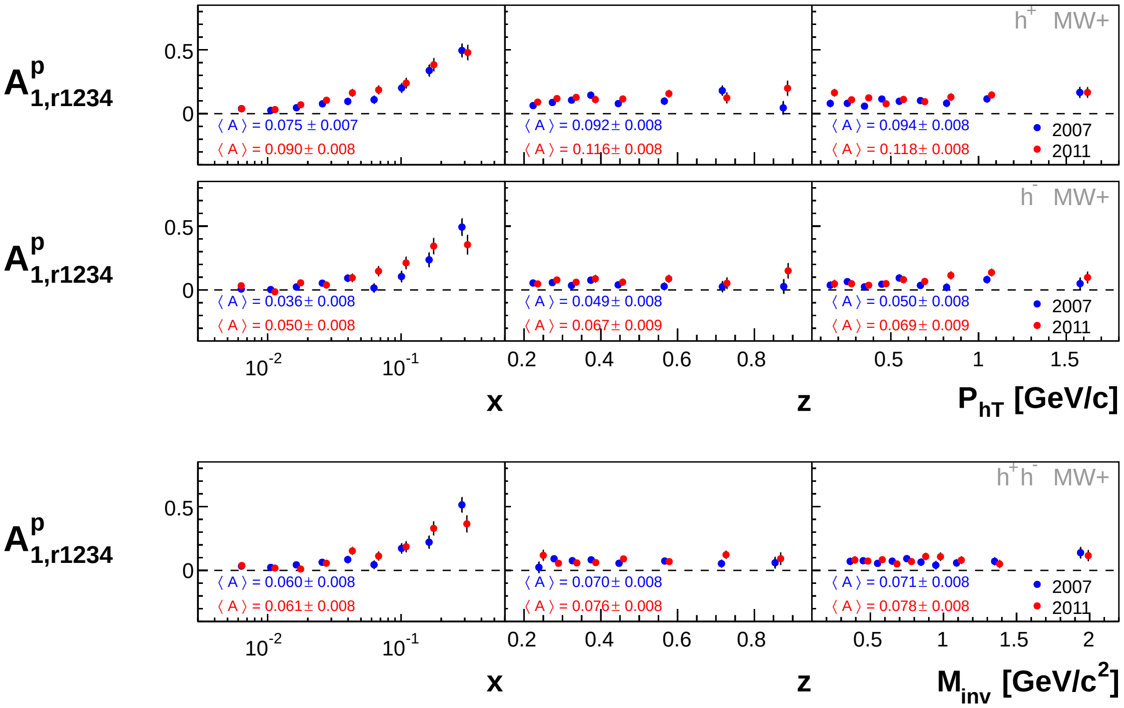

Figure 8.5: Comparison of A_1^p from MW+ for h^+ and h^-(top) and h^+h^-(bottom) for 2007 and 2011. Corresponding mean values are also displayed.

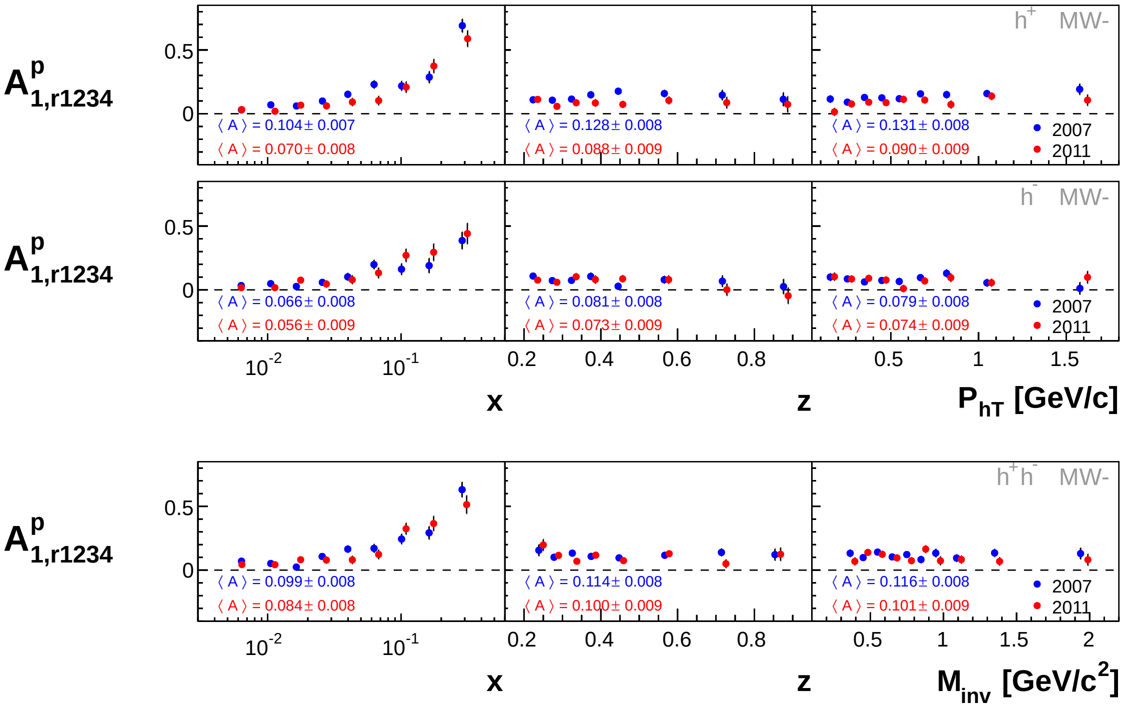

Figure 8.6: Comparison of A_1^p from MW- for h^+ and h^-(top) and h^+h^-(bottom) for 2007 and 2011. Corresponding mean values are also displayed.

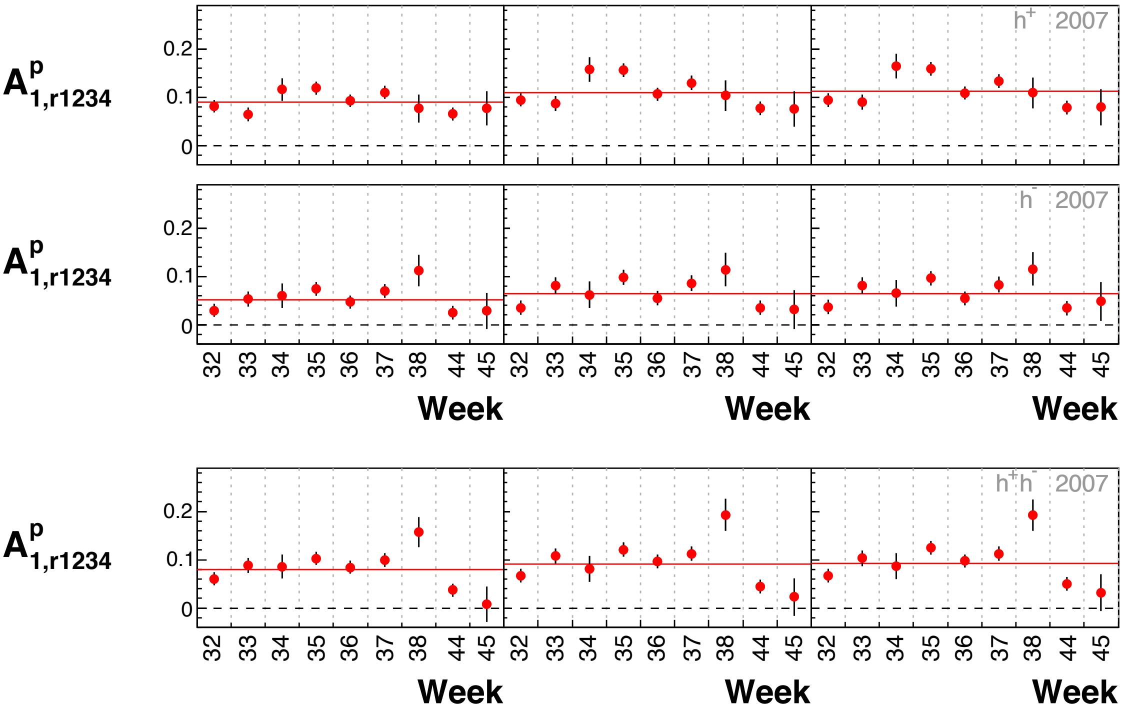

Figure 8.7: Mean A_1^p asymmetries for each week of 2007. The three columns correspond to the kinematic variables x, z and P_{hT} from left to right for h^+ and h^-(top), and to x, z and M_{inv} for h^+h^-(bottom).

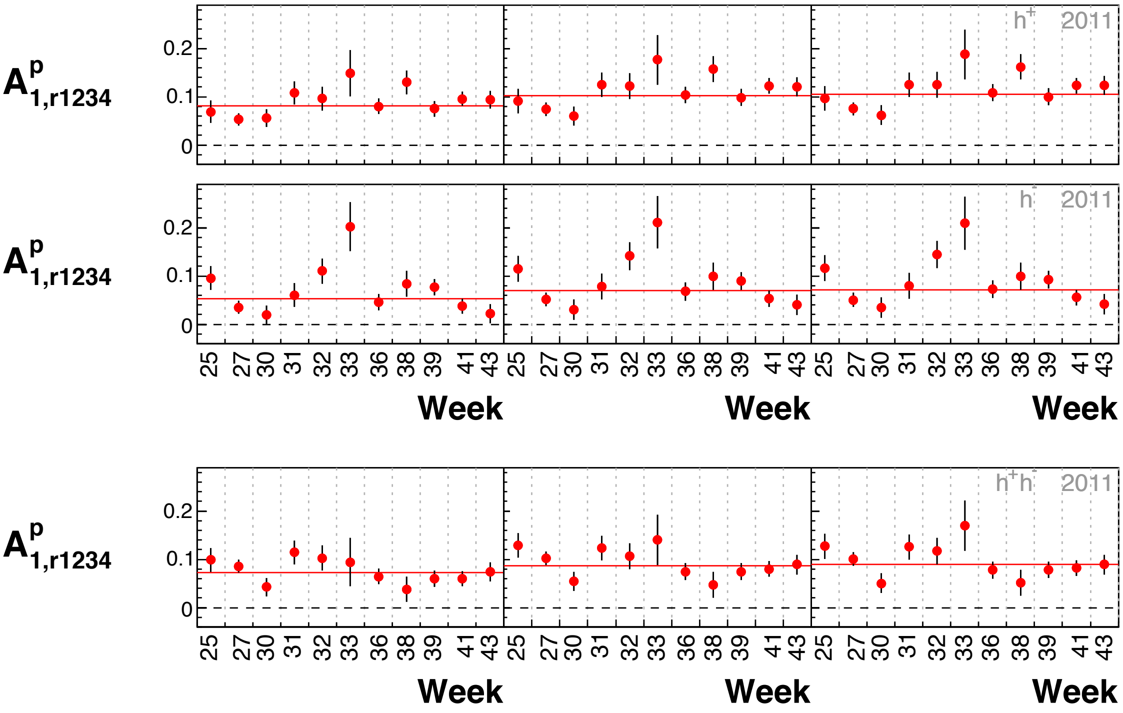

Figure 8.8: Mean A_1^p asymmetries for each week of 2011. The three columns correspond to the kinematic variables x, z and P_{hT} from left to right for h^+ and h^-(top), and to x, z and M_{inv} for h^+h^-(bottom).

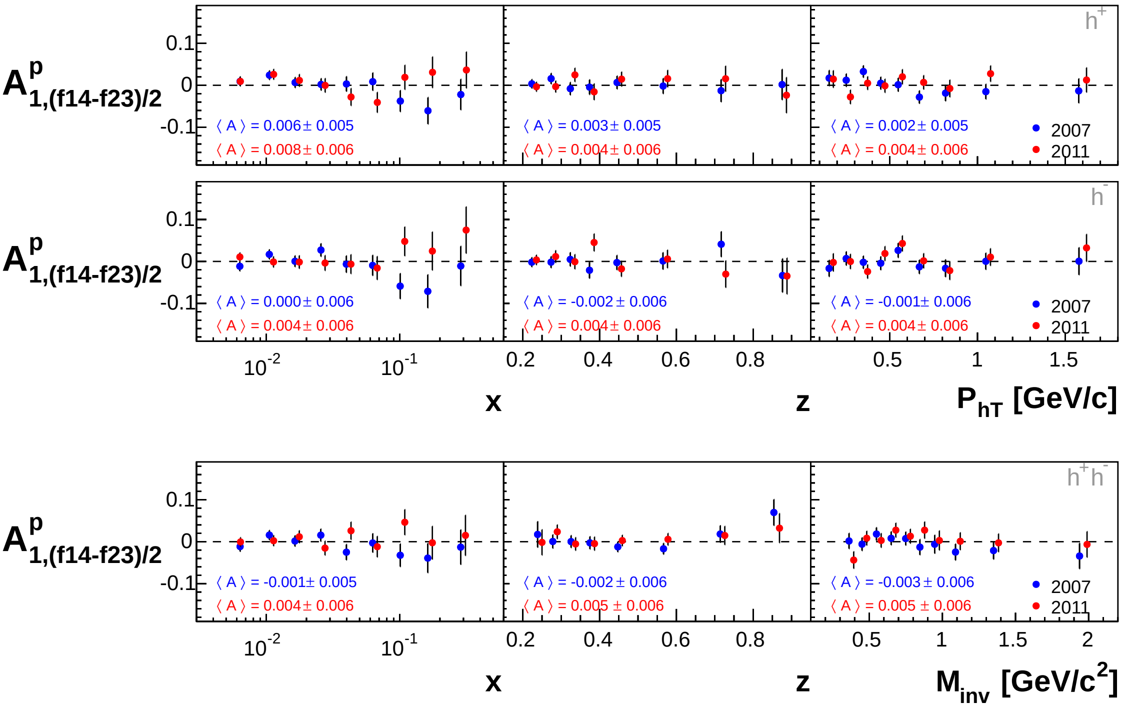

Figure 8.9: False asymmetries $A^p_{1,(f14-f23)/2}$ for h^+ and h^-(top) and h^+h^-(bottom) from 2007 and 2011 data. Corresponding mean values are also displayed.

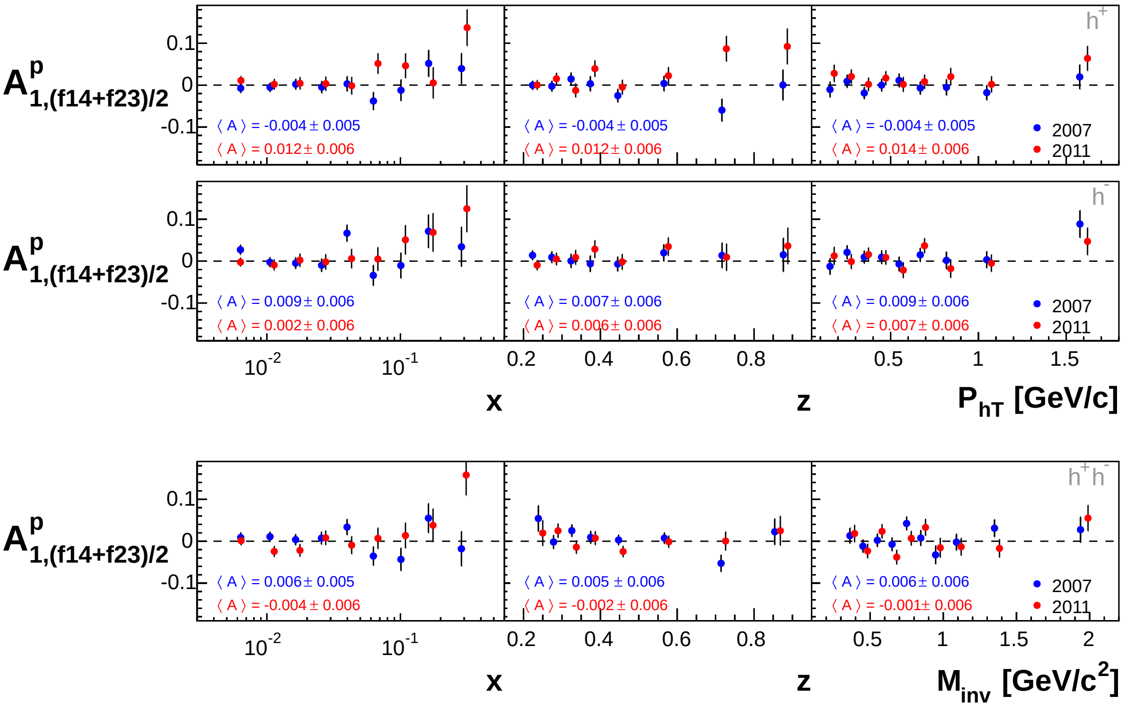

Figure 8.10: False asymmetries $A^p_{1,(f14+f23)/2}$ for h^+ and h^-(top) and h^+h^-(bottom) from 2007 and 2011 data. Corresponding mean values are also displayed.

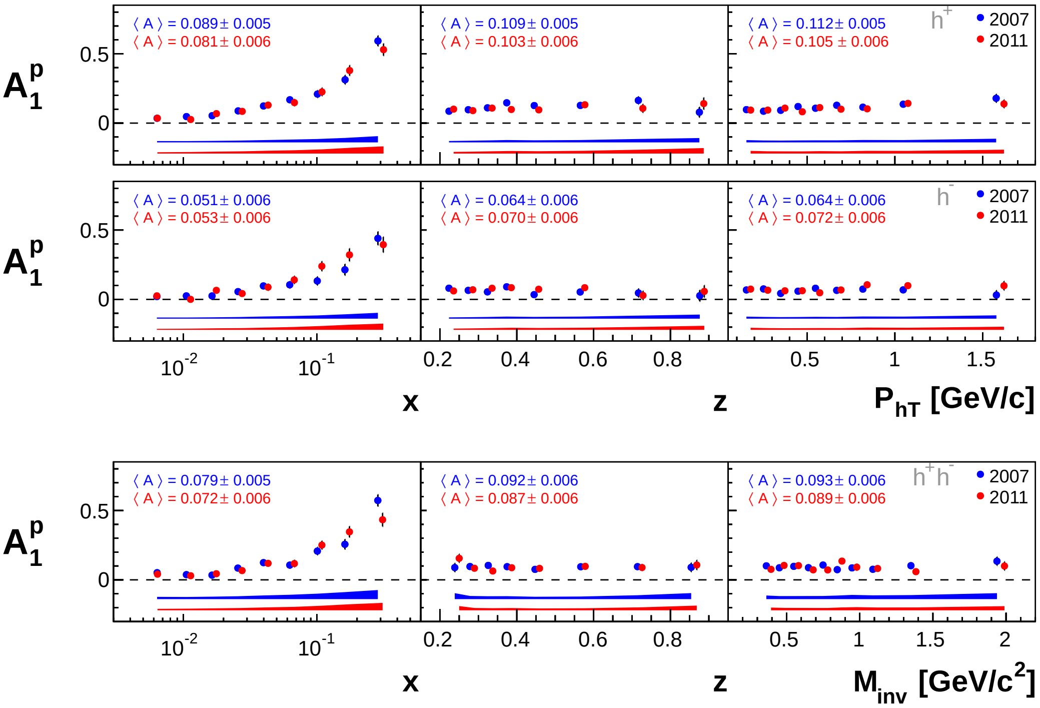

Figure 8.11: A_1^p for h^+ and h^-(top) and h^+h^-(bottom) from 2007 and 2011 data. Corresponding mean values are also displayed.

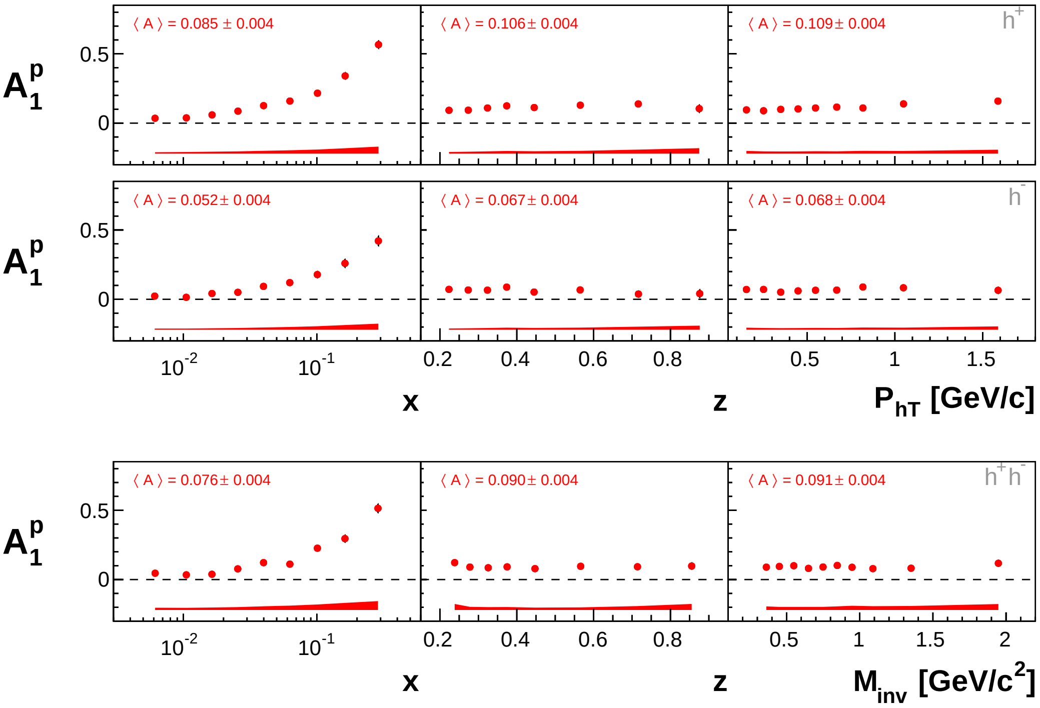

Figure 8.12: A_1^p for h^+ and h^-(top) and h^+h^-(bottom) from the whole data set. Corresponding mean values are also displayed.

8.2 Results and Conclusions

Both years results of the double spin asymmetry A_1^p, obtained from the 1D PR method for each of the analyses, are displayed in Fig. 8.11. The systematic uncertainties are indicated as bands on the bottom of each plot. In all cases, the expected characteristic rise with x is observed, confirming a general consistency of the procedure of analysis. Regarding the other kinematic variables, no evident dependence is observed. However, differences in certain bins are present between the two years, especially in the higher x region. Nevertheless, the mean values are compatible within their statistical uncertainty for each kinematic variable. This doesn't hold true when comparing the mean values of the three kinematic variables themselves. Here, the mean values in x are found to be smaller than the others in all analyses and years. This effect can be traced back to the correction of asymmetries, as it doesn't appear for raw asymmetries, see Fig. A.41. This effect is known and could be minimized by an event-by-event weighting, accounting for the correction factors [111]. Fig. 8.12 shows the weighted mean of the results from both years. The numerical results are collected in the appendix in Sec. A.6.

8.3 Comparison with Results from Other Experiments

As outlined in Sec. 2.5, the double spin asymmetry A_1^p was already measured in one hadron SIDIS by various experiments. A comparison of the results from the present work with existing world data is shown in Fig. 8.13, indicating a general agreement. Considering only COMPASS results, deviations seem to be present in the upper x-region in case of negatively charged hadrons, where the results from this work appear throughout larger.

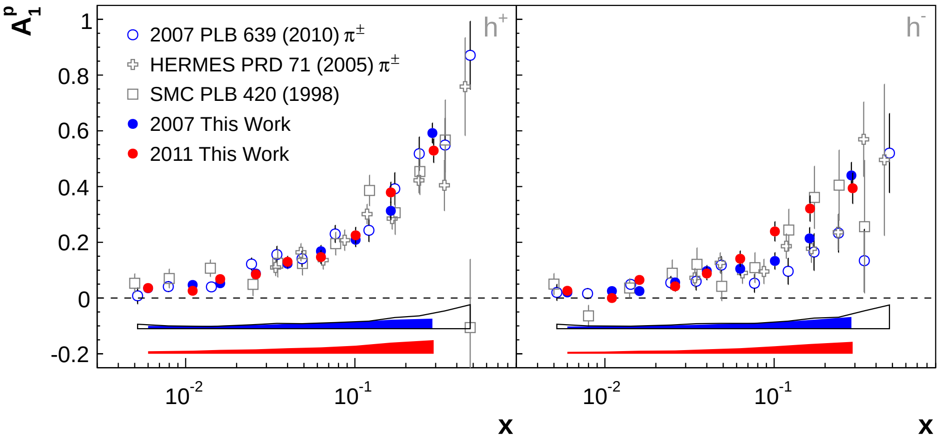

Figure 8.13: Comparison of the results for A_1^p for h^+ (left) and h^+ (right) with published results from COMPASS for identified charged pions [69] and other world data (HERMES [68], SMC [67]). The filled error bands indicate the corresponding systematic uncertainties, whereas the not filled error bands correspond to the published COMPASS results.

Fig. 8.14 shows the comparison of the averaged results from both years with AEKP-model predictions [59]. As already outlined in the context of the one hadron double spin asymmetry $A_{LL}^{\cos(\phi_h)}$, this model considers leading order and bases on gaussian-factorization. Considering A_1^p as a function of x, the predictions are in very good agreement with the experimental results. A rough agreement can also be concluded in z and P_{hT}, indicating a favored p_T-width of $\mu_2^2 = 0.25$.

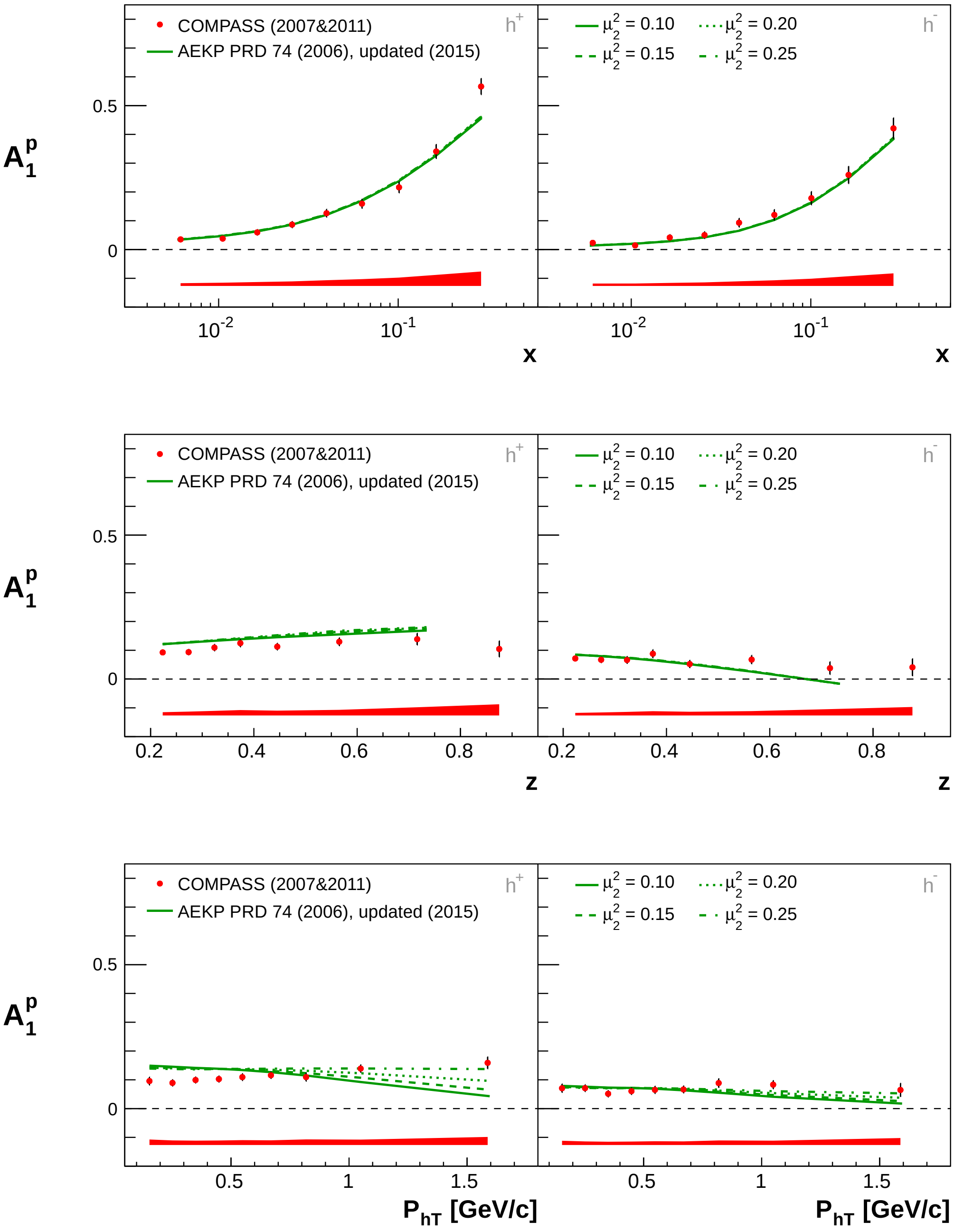

Figure 8.14: Comparison of results for A_1^p for h^+ (left) and h^- (right) with available model predictions [59]. The error band indicates the systematic uncertainties of the COMPASS results.

9. Two Hadron Asymmetries at Twist-3

The collinear two hadron SIDIS cross section at twist-3 has the same structure as the one hadron SIDIS TMD cross section from Eq. (2.62) - Eq. (2.65), with ϕ_h replaced by ϕ_R. Considering a longitudinally polarized target, two twist-3 asymmetries can be investigated, namely the single-spin asymmetry $A_{UL}^{\sin(\phi_R)}$ and the double-spin asymmetry $A_{LL}^{\cos(\phi_R)}$.

Using the partial wave decomposition of collinear leading twist DiFFs from Eq. (2.76) and Eq. (2.77), and analogously for the involved genuine twist-3 IFFs $\tilde{D}$ and $\tilde{G}$ [48], the considered asymmetries can be approximated in COMPASS kinematics as [112]

$$A_{UL}^{\sin(\phi_R)} = -\frac{M}{Q}\frac{|\boldsymbol{R}|}{M_h}\,\frac{\sum_q e_q^2\left[x h_L^q(x) H_1^{\angle q,sp}(z,M_h^2) + \frac{M_h}{Mz} g_1^q(x)\tilde{G}^{\angle q,sp}(z,M_h^2)\right]}{\sum_q e_q^2 f_1^q(x) D_1^{q,ss+pp}(z,M_h^2)} \tag{9.1}$$

$$A_{LL}^{\cos(\phi_R)} = \frac{M}{Q}\frac{|\boldsymbol{R}|}{M_h}\,\frac{\sum_q e_q^2\left[x e_L^q(x) H_1^{\angle q,sp}(z,M_h^2) - \frac{M_h}{Mz} g_1^q(x)\tilde{D}^{\angle q,sp}(z,M_h^2)\right]}{\sum_q e_q^2 f_1^q(x) D_1^{q,ss+pp}(z,M_h^2)}. \tag{9.2}$$

The purpose of measuring asymmetries of subleading twist is manifold. In general, such observables provide sensitivity to so far largely unexplored quark-gluon correlations, which are of importance for a complete understanding of the dynamics inside nucleons. In particular, measuring $A_{UL}^{\sin(\phi_R)}$ can provide information about the unknown collinear twist-3 PDF h_L. The importance of pure twist-3 contributions, hence the validity of the Wandzura-Wilczek approximation, can be directly addressed by measuring the double spin asymmetry $A_{LL}^{\cos(\phi_R)}$.

Both asymmetries are measured by extending the corresponding fitting procedures (1D PR and UB LH) of the leading twist two hadron analysis, described in Sec. 5, in order to account for the additional modulations $\sin(\phi_R)$ and $\cos(\phi_R)$. Also here the results from the UB LH method are chosen to estimate the final asymmetries. The analytical procedure to obtain the final physical asymmetries is analogue to the previous studies, i. e. raw asymmetries are measured from subsamples of one week each and corrected to obtain weekly physical asymmetries before building their weighted mean in order to obtain the final results per year. The correction of the extracted raw asymmetries is straightforward:

$$A_{UL}^{\sin(\phi_R)} = \frac{A_{UL,\mathrm{Raw}}^{\sin(\phi_R)}}{\langle f|P_T|D_{UL}^{(3)}\rangle} \qquad A_{LL}^{\cos(\phi_R)} = \frac{A_{LL,\mathrm{Raw}}^{\cos(\phi_R)}}{\langle fP_B|P_T|D_{LL}^{(2)}\rangle}. \tag{9.3}$$

The bin wise mean values of the certain correction factors for each year, namely the dilution factor f, the beam and the target polarizations P_B and $|P_T|$, as well as of the depolarization factors $D_{XL}^{(i)}$ are displayed within Fig. 5.2. The mean values of the respective products, shown in Fig. 5.3, indicate effective scaling factors of the raw asymmetries and the corresponding statistical uncertainties of about 5 in case of the single spin asymmetry $A_{UL}^{\sin(\phi_R)}$, respectively of about -20 for the double spin asymmetry $A_{LL}^{\cos(\phi_R)}$.

9.1 Systematic Studies

Systematics are studied in the same way as it was done in case of the other analyses, presented in the previous chapters. Therefore the following discussion concentrates on the main conclusions, referring the reader to Sec. 6.2, where the particular steps are explained in detail. Corresponding plots are collected in the appendix in Sec. A.7.

The results from the two different extraction methods, namely the 1D PR and the UB LH method, displayed in Fig. A.42, are found to be in satisfying agreement. Nevertheless, a methodical uncertainty is taken into account by assigning a relative systematic uncertainty $\sigma_{\mathrm{sys}}^{\mathrm{meth}}/\sigma^{\mathrm{stat}}$, calculated as the sum of the RMS and half of the shifted mean from the respective pull distributions, estimated using Eq. (6.1) and depicted in Fig. A.43. The resulting relative systematic errors average around 20% of the statistical error for both asymmetries for both years data sets. The numerical values are given in Tab. 9.1.

Time dependent instabilities of the results are considered as a major source of systematic uncertainty. Fig. A.44 shows the stability pull distributions, estimated following Eq. (6.2). The respective RMS values, all found compatible with 1 within at least around two standard deviations, reflect statistically expected fluctuations. As it was done in the previous analyses, the square root of the difference of the squared RMS and the expectation value 1 (Eq. (6.3)) is chosen as corresponding relative systematic uncertainty $\sigma_{\mathrm{sys}}^{\mathrm{stab}}/\sigma^{\mathrm{stat}}$. The resulting uncertainties are all found to average around 40% of the statistical error and are listed in Tab. 9.1.

To further investigate the time dependent stability of the results, also the weekly mean asymmetries are considered. They are shown in Fig. A.45 as a function of the week number, separately for both years, whereas the columns correspond to the variables x, z and M_{inv}. Fluctuations are found to be statistically expected for both asymmetries, whereas $A_{UL}^{\sin(\phi_R)}$ appears slightly broader distributed then $A_{LL}^{\cos(\phi_R)}$. A markable deviation is present for the result of $A_{UL}^{\sin(\phi_R)}$ from W34 of 2007, which corresponds to the microwave setting MW+. Comparing the results from the different microwave settings, depicted in Fig. A.46, one finds a similar situation as in case of the other two hadron azimuthal asymmetries, characterized by large occasional deviations in certain kinematic bins, here most pronounced for $A_{UL}^{\sin(\phi_R)}$ from 2011. Although not satisfying, one can still conclude a rough overall agreement of the results within statistical uncertainties.

The considered results $A_{r1234}^{m(\phi_h,\phi_R)}$ and those, obtained by separately fitting the data from the upstream and the downstream half of the target, $A_{(r12+r34)/2}^{m(\phi_h,\phi_R)}$, are found to be in good agreement. This is reflected by the small widths of the corresponding pull distributions, shown in Fig. A.47. Therefore, systematics arising from the combinatoric use of data from target subsamples are assumed to be negligible.

From the study of the false asymmetries $A_{(f14\pm f23)/2}^{m(\phi_h,\phi_R)}$ and $A_{(r12-r34)/2}^{m(\phi_h,\phi_R)}$, one can conclude moderate influences from acceptance variations between the cells. The corresponding systematic uncertainties, estimated as described in Sec. 6.2.5, are found to measure around 60% of the statistical error for both asymmetries from both years and hence dominate the studied systematic effects. The detailed values are given in Tab. 9.1. Corresponding pull distributions are attached in Fig. A.48 and Fig. A.49.

All systematic uncertainties, namely $\sigma_{\text{sys}}^{\text{meth}}$, $\sigma_{\text{sys}}^{\text{stab}}$ and $\sigma_{\text{sys}}^{\text{false}}$, are combined in quadrature to estimate the overall additive systematic uncertainty $\sigma_{\text{sys}}^{\text{add}}$, separately per asymmetry and year. They are also listed in Tab. 9.1 and don't exceed 84% of the statistical error. For the evaluation of the systematic uncertainties of the averaged results, calculated as statistically weighted results from both years, the additive systematic uncertainty with the larger value of $\sigma_{\text{sys}}^{\text{add}} \cdot \sigma_{\text{stat}}$ is chosen. The final systematic error per kinematic bin is calculated via Eq. (6.16), accounting also for the multiplicative systematic uncertainty $\Delta A^{m(\phi_h,\phi_R)}$, which is caused by the raw asymmetry correction due to systematic uncertainties of the dilution factor, as well as of the beam and target polarizations.

Table 9.1: Systematic uncertainties, relative to the statistical error, for 2007 and 2011.

Year	2007				2011			
$A_{XL}^{m(\phi_R)}$	$\sigma_{\text{sys}}^{\text{meth}}$	$\sigma_{\text{sys}}^{\text{stab}}$	$\sigma_{\text{sys}}^{\text{false}}$	$\sigma_{\text{sys}}^{\text{add}}$	$\sigma_{\text{sys}}^{\text{meth}}$	$\sigma_{\text{sys}}^{\text{stab}}$	$\sigma_{\text{sys}}^{\text{false}}$	$\sigma_{\text{sys}}^{\text{add}}$
$A_{UL}^{\sin(\phi_R)}$	0.21	0.35	0.64	0.76	0.20	0.46	0.59	0.77
$A_{LL}^{\cos(\phi_R)}$	0.19	0.39	0.72	0.84	0.17	0.38	0.54	0.68

9.2 Results

The results of the twist-3 asymmetries $A_{UL}^{\sin(\phi_R)}$ and $A_{LL}^{\cos(\phi_R)}$, extracted in bins of x, z and M_{inv} with the UB LH method, are shown in Fig. 9.1, separately per year on the top, and averaged on the bottom. The error bands indicate the respective systematic uncertainties. For both years, the single spin asymmetry $A_{UL}^{\sin(\phi_R)}$ is found to be clearly positive over the entire kinematical ranges. Concerning the double spin asymmetry $A_{LL}^{\cos(\phi_R)}$, the bin wise results tempt to be compatible with zero within overall uncertainties, although the mean results from both years indicate a tendency to be negative. The corresponding mean values are given in Tab. 9.2. The mean values of the averaged results measure

$$A_{UL}^{\sin(\phi_R)} = \quad 0.005 \pm 0.001(\mathrm{stat}) \pm 0.001(\mathrm{sys}) \tag{9.4}$$

$$A_{LL}^{\cos(\phi_R)} = -0.013 \pm 0.006(\mathrm{stat}) \pm 0.005(\mathrm{sys}). \tag{9.5}$$

The results for $A_{UL}^{\sin(\phi_R)}$ are of great value in order to access the collinear twist-3 PDF $h_L(x)$, which is among the missing puzzle pieces to complete the collinear picture of the nucleon spin-structure at subleading twist. Compared to the case of single hadron SIDIS, where higher-twist PDFs appear convoluted with FFs in a p_T-dependent integral, the extraction from the two hadron asymmetry involves clear benefits. When assuming Wandzura-Wilzcek approximation, $\tilde{G}^{\angle}$ vanishes, and the observable $A_{UL}^{\sin(\phi_R)}$ is exclusively sensitive to $h_L(x)$, which appears in a simple product with the recently measured IFF $H_1^{\angle}$ [113].

Assuming the gauge-link to be the only source of T-odd behavior, the PDF $e_L(x)$ should not contribute to the double spin asymmetry $A_{LL}^{\cos(\phi_R)}$. The fact, that this asymmetry is found to be small within the experimental precision could consequently corroborate the Wandzura-Wilzcek assumption of negligible quark-gluon correlations on the fragmentation side, here encoded in the pure twist-3 IFF $\tilde{D}^{\angle}$.

Table 9.2: Mean azimuthal asymmetries for 2007 and 2011, including the statistical and systematic uncertainties.

Year	2007	2011
$A_{UL}^{\sin(\phi_R)}$	0.004 ± 0.001 ± 0.001	0.006 ± 0.001 ± 0.001
$A_{LL}^{\cos(\phi_R)}$	-0.013 ± 0.008 ± 0.007	-0.013 ± 0.009 ± 0.008

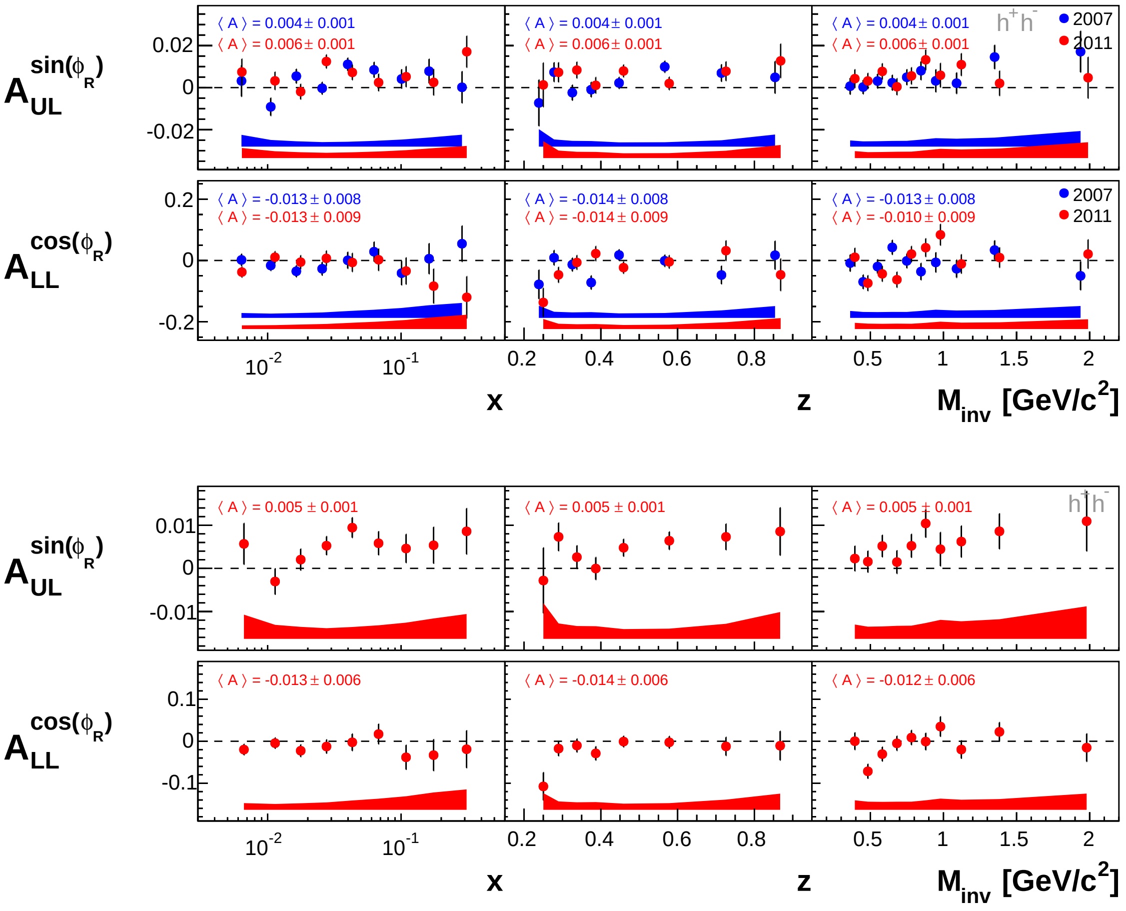

Figure 9.1: Azimuthal asymmetries from 2007 and 2011 (top) and for the whole data set (bottom). The error bands indicate the systematic uncertainties. Corresponding mean values are also displayed.

10. Summary

This thesis comprises a comprehensive study of longitudinal target spin asymmetries, measured in semi-inclusive muoproduction of unidentified hadrons and hadron pairs off longitudinally polarized protons at COMPASS. The analysis is based on data, recorded in the years 2007 and 2011 by scattering a high-energetic muon beam of 160 GeV/c, respectively 200 GeV/c, off a longitudinally polarized NH_3 target. Results of high accuracy could be obtained, covering a wide kinematic range.

Although the experimental setup was basically identical in both years, and one can reasonably assume influences from the different beam energies to be negligible within the given experimental uncertainties, both years were treated individually in order to allow for a differentiated analysis. To reduce systematics due to time dependent instabilities, results were extracted from weekly samples. Systematic uncertainties are evaluated using the results from these samples, considering both experimental and methodic uncertainty sources. For this purpose, two independent estimators were used to extract asymmetries, namely the so called one dimensional binned product ratio method and an unbinned likelihood method. The respective results were found to be well compatible. The systematic uncertainties turned out to be dominated by acceptance variations between data subsamples of opposite target polarization configuration within the weekly samples, caused by instabilities of the experimental setup. Nevertheless, overall systematics are found to be considerably smaller then the statistical uncertainties. Final results were obtained from the unbinned likelihood method.

The observables of this study, namely azimuthal asymmetries of the detected final state hadrons, can be interpreted within the QCD parton model in terms of parton distribution functions and fragmentation functions. They encode the non-perturbative information on the spin-substructure of the proton, respectively of the spin related fragmentation mechanisms of the current quark. The studied azimuthal asymmetries are in particular sensitive to suppressed effects, such as spin-orbit or quark-gluon correlations. Their measurement is of great interest in order to obtain an understanding about the three-dimensional spin structure of the nucleon, the role of quark-gluon interactions and dynamics inside hadrons in general.

Two Hadron Analysis

Particular emphasis was put on the investigation of azimuthal asymmetries of hadron pairs, composed by oppositely charged hadrons in the final state. Although hadron pair azimuthal asymmetries have been already intensively studied in SIDIS off transversely polarized targets, only marginal information on respective longitudinal target spin asymmetries has been obtained so far. When taking into account intrinsic transverse momenta of struck quarks, the respective longitudinal cross section involves a set of nine azimuthal asymmetries. Within this thesis all nine asymmetries were extracted in kinematic bins of x, z and the invariant mass of the hadron pair M_{inv}. All nine azimuthal asymmetries were found to be mostly compatible with zero over the entire kinematical range.

Two further hadron pair azimuthal asymmetries were extracted, namely the single spin asymmetry $A_{UL}^{\sin(\phi_R)}$ and the double spin asymmetry $A_{LL}^{\cos(\phi_R)}$. Both arise at subleading twist, which means they are suppressed by $1/Q$ with respect to leading twist asymmetries, and survive the integration over intrinsic transverse momenta of struck quarks. Hence, they can be interpreted in a simple collinear framework, offering a technically cleaner way to access involved PDFs than in TMD interpretations. In general, higher twist asymmetries can provide insights to largely unexplored quark-gluon correlations, which are of high interest for the understanding of dynamics inside hadrons. In particular, the results on the single spin asymmetry $A_{UL}^{\sin(\phi_R)}$, in an average measured to

$$A_{UL}^{\sin(\phi_R)} = \quad 0.005 \pm 0.001(\text{stat}) \pm 0.001(\text{sys}),$$

can be used for a first determination of the collinear twist-three PDF h_L, describing the distribution of transversely polarized quarks in a nucleon with longitudinal spin orientation, which is among the missing puzzle pieces to complete the one-dimensional picture of the proton at subleading twist. The double spin asymmetry $A_{LL}^{\cos(\phi_R)}$ was found to average

$$A_{LL}^{\cos(\phi_R)} = -0.013 \pm 0.006(\text{stat}) \pm 0.005(\text{sys}).$$

Since this asymmetry is solely related to the genuine twist-three IFF $\tilde{D}^{\sphericalangle}$, the obtained results provide information about the importance of pure twist-three fragmentation mechanisms.

One Hadron Analysis

An additional analysis was carried out, considering azimuthal asymmetries of single hadrons. Similar studies have yet been performed by the HERMES [50–52] and CLAS [55, 56] collaborations, however with much larger experimental uncertainties and covering more limited kinematic domains. At COMPASS, longitudinal single hadron azimuthal asymmetries were so far only measured on a deuteron target and found to be compatible with zero [62]. The respective single hadron TMD SIDIS cross section involves three azimuthal asymmetries. These are the leading twist asymmetry $A_{UL}^{\sin(2\phi_h)}$ and the subleading twist amplitudes $A_{UL}^{\sin(\phi_h)}$ and $A_{LL}^{\cos(\phi_h)}$. They were extracted in bins of x, z and the transverse momentum of the outgoing hadron P_{hT}, whereas hadrons with opposite charge were distinguished. The results on the leading twist asymmetry $A_{UL}^{\sin(2\phi_h)}$ are the first, which can qualitatively confirm present model predictions, characterized by small values of opposite sign for positive and negative hadrons in the valence x-region. The corresponding mean asymmetries are

$$\begin{aligned} A_{UL,h^+}^{\sin(2\phi_h)} &= -0.005 \pm 0.002(\text{stat}) \pm 0.001(\text{sys}) \\ A_{UL,h^-}^{\sin(2\phi_h)} &= 0.002 \pm 0.002(\text{stat}) \pm 0.001(\text{sys}). \end{aligned}$$

where the hadron charge is indicated by the subscript h^+, respectively h^-. The results can be further useful for a global fit of the Worm-Gear TMD PDF $h_{1L}^{\perp}$, since it appears coupled to the Collins FF $H_1^{\perp}$, which is currently being addressed in global fits by different groups of phenomenologists. The results on the subleading single spin asymmetry $A_{UL}^{\sin(\phi_h)}$ were found to be in agreement with previous measurements from HERMES, characterized by an evident increase with x in case of positive hadrons and an entire compatibility with zero for negative hadrons. The average asymmetries measure

$$\begin{aligned} A_{UL,h^+}^{\sin(\phi_h)} &= 0.009 \pm 0.001(\text{stat}) \pm 0.001(\text{sys}) \\ A_{UL,h^-}^{\sin(\phi_h)} &= -0.001 \pm 0.001(\text{stat}) \pm 0.001(\text{sys}). \end{aligned}$$

Assuming Wandzura-Wilczek approximation, this asymmetry can be related to the leading twist TMD PDF $h_{1L}^{\perp}$. It can be used to validate the negligibility of subleading contributions within phenomenological frameworks. Alternatively it may indicate the potential importance of twist-three contributions. The double spin asymmetry $A_{LL}^{\cos(\phi_h)}$ emerged to be compatible with available predictions based on Wandzura-Wilczek approximation and twist-three approaches. Unfortunately, the achieved experimental precision does not allow to give any preference.

Analysis of the A_1^p Asymmetries

As a byproduct of the presented analyses on azimuthal asymmetries, also corresponding cross section asymmetries for single hadrons, respectively hadron pairs, were obtained. At a first look, the single hadron asymmetries A_{1,h^+}^p and A_{1,h^-}^p turned out to be in sufficient agreement with previous measurements for pions from COMPASS, other world data and model predictions, allowing to conclude a general consistency of the procedure of analysis. Since these asymmetries were so far only investigated in bins of x, the presented results could be used for further tuning of existing theoretical models. In particular, as suggested in Ref. [59], it may allow to determine the gaussian p_T-width of the involved TMD PDF g_{1L}.

Summarizing the presented analyses, the obtained results provide an abundance of new information on spin related mechanisms inside hadrons and fragmentation processes. They can serve as valuable input for global analyses of parton distribution functions and fragmentation functions as well as for the validation of theoretical model approaches.

A. Appendix

A.1 Definitions, Notations and Conventions

A.1.1 Light-Cone-Coordinates

Considering a particle to have large momentum along a respective axis, commonly the z-axis, it is theoretically convenient to change to light-cone coordinates in a collinear frame. For any arbitrary Minkowski four-vector $a^\mu = (a^0, a^1, a^2, a^3)$, its light-cone-components a^+ and a^- are defined as

$$a^+ = \frac{a^0 + a^3}{\sqrt{2}} \qquad\qquad a^- = \frac{a^0 - a^3}{\sqrt{2}}, \tag{A.1}$$

and the transverse components are collected in a bidimensional vector $\boldsymbol{a}_T = (a^1, a^2)$. The four-vector a^μ then reads in light-cone-coordinates

$$a^\mu = \left[a^+, a^-, a^1, a^2\right] = \left[a^+, a^-, \boldsymbol{a}_T\right]. \tag{A.2}$$

The scalar product of two vectors in light-cone-coordinates a and b is defined as

$$\begin{aligned} a \cdot b &= a^+ b^- + a^- b^+ - \boldsymbol{a}_T \cdot \boldsymbol{b}_T \\ &= a^+ b^- + a^- b^+ - a^1 b^1 - a^2 b^2. \end{aligned} \tag{A.3}$$

The transformation to light-cone-coordinates can be written as an expansion in the basis of the Sudakov-vectors $n_+ = (1, 0, 0, 0)$ and $n_- = (0, 1, 0, 0)$, such that

$$a^\mu = a^+ n_+ + a^- n_- + a_T. \tag{A.4}$$

Considering a particle to move fast in z-direction with $P^\mu = (P^0, P^1, P^2, P^3)$ and $P_T = (0, 0)$, its four-vector reads in light-cone coordinates

$$P^\mu = \left[P^+, \frac{M^2}{2P^+}, 0, 0\right], \tag{A.5}$$

since $P^\mu P_\mu = M^2 = (P^0)^2 - (P^3)^2 = (P^0 + P^3)(P^0 - P^3) = 2P^+P^-$. In case of DIS, the dominance of the +-component allows to neglect the other components, involving obvious advantages in theoretical approaches.

A.1.2 Dirac Matrices

The four Dirac matrices are defined as

$$\gamma^0 \;:=\; \begin{pmatrix} 1 & 0 & 0 & 0 \\ 0 & 1 & 0 & 0 \\ 0 & 0 & -1 & 0 \\ 0 & 0 & 0 & -1 \end{pmatrix} \qquad \gamma^1 := \begin{pmatrix} 0 & 0 & 0 & 1 \\ 0 & 0 & 1 & 0 \\ 0 & -1 & 0 & 0 \\ -1 & 0 & 0 & 0 \end{pmatrix} \tag{A.6}$$

$$\gamma^2 \;:=\; \begin{pmatrix} 0 & 0 & 0 & -i \\ 0 & 0 & i & 0 \\ 0 & i & 0 & 0 \\ -i & 0 & 0 & 0 \end{pmatrix} \qquad \gamma^3 := \begin{pmatrix} 0 & 0 & 1 & 0 \\ 0 & 0 & 0 & -1 \\ -1 & 0 & 0 & 0 \\ 0 & 1 & 0 & 0 \end{pmatrix}. \tag{A.7}$$

They fulfill the Dirac Algebra, being anticommutative and fulfilling the conditions $\gamma^0\gamma^0 = \mathbf{1}$ and $\gamma^1\gamma^1 = \gamma^2\gamma^2 = \gamma^3\gamma^3 = -\mathbf{1}$. It is additionally useful to define a fifth matrix as the product of the above Dirac matrices as

$$\gamma^5 := i\gamma^0\gamma^1\gamma^2\gamma^3 = \begin{pmatrix} 0 & 0 & 0 & 1 \\ 0 & 0 & 1 & 0 \\ 0 & 1 & 0 & 0 \\ 1 & 0 & 0 & 0 \end{pmatrix}, \tag{A.8}$$

with $\gamma^5\gamma^5 = \mathbf{1}$ and $\gamma^5\gamma^\mu = -\gamma^\mu\gamma^5$.

The light-cone components of the Dirac matrices are

$$\gamma^\pm = \frac{1}{\sqrt{2}}\left(\gamma^0 \pm \gamma^3\right). \tag{A.9}$$

A.1.3 Feynman-Slash Notation

The Feynman-slash transforms a given four-vector A^μ into a 4×4 matrix, following the convention

$$\not{A} := \sum_{\mu=0}^{3} \gamma^\mu A_\mu, \tag{A.10}$$

where the γ^μ are Dirac matrices.

A.2 Structure Functions in terms of PDFs and FFs

Each structure function occuring in Eqs.(2.62)-(2.65) and Eqs.(2.80)-(2.83) can be written as sums of weighted convolutions of the form

$$\mathcal{I}\,[...] = \sum_q e_q^2 \int d^2\boldsymbol{p}_T d^2\boldsymbol{k}_T \delta\left(\boldsymbol{p}_T - \boldsymbol{k}_T - \frac{\boldsymbol{P}_{h\perp}}{z}\right)[...]. \tag{A.11}$$

Note, that the variables P_{hT} and z refer to the transverse momentum, respectively the energy fraction, of single hadrons in case of one hadron SIDIS. In two hadron SIDIS, they describe analogue properties of the common hadron pair, hence $P_{hT} = P_{hT,1} + P_{hT,2}$ and $z = z_1 + z_2$.

A.2.1 One Hadron Structure Functions

$$F_{UU,T} = \mathcal{I}\Big[f_1 D_1\Big] \tag{A.12}$$

$$F_{UU,L} = 0 \tag{A.13}$$

$$\begin{aligned} F_{UU}^{\cos(\phi_h)} = \frac{2M}{Q}\mathcal{I}\Big[&- \frac{\boldsymbol{k}_T \hat{\boldsymbol{P}}_{h\perp}}{M_h}\left(xhH_1^\perp + \frac{M_h}{Mz} f_1 \tilde{D}^\perp\right) \\ &- \frac{\boldsymbol{p}_T \hat{\boldsymbol{P}}_{h\perp}}{M}\left(xf^\perp D_1 + \frac{M_h}{Mz} h_1^\perp \tilde{H}\right)\Big] \end{aligned} \tag{A.14}$$

$$F_{UU}^{\cos(2\phi_h)} = \mathcal{I}\Big[- \frac{2(\boldsymbol{p}_T \hat{\boldsymbol{P}}_{h\perp})(\boldsymbol{k}_T \hat{\boldsymbol{P}}_{h\perp}) - \boldsymbol{p}_T \boldsymbol{k}_T}{MM_h} h_1^\perp H_1^\perp\Big] \tag{A.15}$$

$$\begin{aligned} F_{LU}^{\sin(\phi_h)} = \frac{2M}{Q}\mathcal{I}\Big[&- \frac{\boldsymbol{k}_T \hat{\boldsymbol{P}}_{h\perp}}{M_h}\left(xeH_1^\perp + \frac{M_h}{Mz} f_1 \tilde{G}^\perp\right) \\ &+ \frac{\boldsymbol{p}_T \hat{\boldsymbol{P}}_{h\perp}}{M}\left(xg^\perp D_1 + \frac{M_h}{Mz} h_1^\perp \tilde{E}\right)\Big] \end{aligned} \tag{A.16}$$

$$\begin{aligned} F_{UL}^{\sin(\phi_h)} = \frac{2M}{Q}\mathcal{I}\Big[&- \frac{\boldsymbol{k}_T \hat{\boldsymbol{P}}_{h\perp}}{M_h}\left(xh_L H_1^\perp + \frac{M_h}{Mz} g_{1L} \tilde{G}^\perp\right) \\ &+ \frac{\boldsymbol{p}_T \hat{\boldsymbol{P}}_{h\perp}}{M}\left(xf_L^\perp D_1 - \frac{M_h}{Mz} h_{1L}^\perp \tilde{H}\right)\Big] \end{aligned} \tag{A.17}$$

$$F_{UL}^{\sin(2\phi_h)} = \mathcal{I}\Big[- \frac{2(\boldsymbol{p}_T \hat{\boldsymbol{P}}_{h\perp})(\boldsymbol{k}_T \hat{\boldsymbol{P}}_{h\perp}) - \boldsymbol{p}_T \boldsymbol{k}_T}{MM_h} h_{1L}^\perp H_1^\perp\Big] \tag{A.18}$$

$$F_{LL} = \mathcal{I}\Big[g_{1L} D_1\Big] \tag{A.19}$$

$$\begin{aligned} F_{LL}^{\cos(\phi_h)} = \frac{2M}{Q}\mathcal{I}\Big[&\frac{\boldsymbol{k}_T \hat{\boldsymbol{P}}_{h\perp}}{M_h}\left(xe_L H_1^\perp + \frac{M_h}{Mz} g_{1L} \tilde{D}^\perp\right) \\ &- \frac{\boldsymbol{p}_T \hat{\boldsymbol{P}}_{h\perp}}{M}\left(xg_L^\perp D_1 + \frac{M_h}{Mz} h_{1L}^\perp \tilde{E}\right)\Big] \end{aligned} \tag{A.20}$$

A.2.2 Two Hadron Structure Functions

$$F_{UU,T} = \mathcal{I}\left[f_1\left(\frac{1}{4}D^s_{1,UU} + \frac{3}{4}D^p_{1,UU}\right)\right] \tag{A.21}$$

$$F_{UU,L} = 0 \tag{A.22}$$

$$F_{UU}^{\cos\theta} = \mathcal{I}\left[f_1 D_{1,UL}\right] \tag{A.23}$$

$$F_{UU}^{\frac{1}{3}\left(3\cos^2\theta - 1\right)} = \mathcal{I}\left[f_1\left(\frac{3}{4}D_{1,LL}\right)\right] \tag{A.24}$$

$$F_{UU}^{\cos(\phi_h-\phi_R)\sin\theta} = -\mathcal{I}\left[\frac{\boldsymbol{k}_T\hat{\boldsymbol{P}}_{h\perp}}{M_h}f_1\left(-\frac{M_h}{|\boldsymbol{k}_T|}D_{1,UT}\right)\right] \tag{A.25}$$

$$F_{UU}^{\cos(\phi_h-\phi_R)\sin 2\theta} = -\mathcal{I}\left[\frac{\boldsymbol{k}_T\hat{\boldsymbol{P}}_{h\perp}}{M_h}f_1\left(-\frac{M_h}{2|\boldsymbol{k}_T|}D_{1,LT}\right)\right] \tag{A.26}$$

$$F_{UU}^{\cos(2\phi_h-2\phi_R)\sin^2\theta} = -\mathcal{I}\left[\frac{2\left(\boldsymbol{k}_T\hat{\boldsymbol{P}}_{h\perp}\right)^2 - \boldsymbol{k}_T^2}{M_h^2}f_1\left(-\frac{M_h^2}{|\boldsymbol{k}_T|^2}D_{1,TT}\right)\right] \tag{A.27}$$

$$\begin{aligned} F_{UU}^{\cos(2\phi_h)} = -\mathcal{I}\Bigg[&\frac{2\left(\boldsymbol{p}_T\hat{\boldsymbol{P}}_{h\perp}\right)\left(\boldsymbol{k}_T\hat{\boldsymbol{P}}_{h\perp}\right) - \boldsymbol{p}_T\boldsymbol{k}_T}{MM_h} \\ &h_1^\perp\left(\frac{1}{4}H^{\perp s}_{1,UU} + \frac{3}{4}H^{\perp p}_{1,UU}\right)\Bigg] \end{aligned} \tag{A.28}$$

$$F_{UU}^{\cos(2\phi_h)\cos\theta} = -\mathcal{I}\left[\frac{2\left(\boldsymbol{p}_T\hat{\boldsymbol{P}}_{h\perp}\right)\left(\boldsymbol{k}_T\hat{\boldsymbol{P}}_{h\perp}\right) - \boldsymbol{p}_T\boldsymbol{k}_T}{MM_h}h_1^\perp H^\perp_{1,UL}\right] \tag{A.29}$$

$$F_{UU}^{\cos(2\phi_h)\frac{1}{3}\left(3\cos^2\theta-1\right)} = -\mathcal{I}\left[\frac{2\left(\boldsymbol{p}_T\hat{\boldsymbol{P}}_{h\perp}\right)\left(\boldsymbol{k}_T\hat{\boldsymbol{P}}_{h\perp}\right) - \boldsymbol{p}_T\boldsymbol{k}_T}{MM_h}h_1^\perp\left(\frac{3}{4}H^\perp_{1,LL}\right)\right] \tag{A.30}$$

$$F_{UU}^{\cos(\phi_h+\phi_R)\sin\theta} = \mathcal{I}\left[\frac{\boldsymbol{p}_T\hat{\boldsymbol{P}}_{h\perp}}{M}h_1^\perp\left(-\frac{|\boldsymbol{R}|}{M_h}H^\angle_{1,UT}\right)\right] \tag{A.31}$$

$$F_{UU}^{\cos(\phi_h+\phi_R)\sin 2\theta} = \mathcal{I}\left[\frac{\boldsymbol{p}_T\hat{\boldsymbol{P}}_{h\perp}}{M}h_1^\perp\left(-\frac{|\boldsymbol{R}|}{2M_h}H^\angle_{1,LT}\right)\right] \tag{A.32}$$

$$F_{UU}^{\cos(2\phi_R)\sin^2\theta} = \mathcal{I}\left[\frac{\boldsymbol{p}_T\hat{\boldsymbol{P}}_{h\perp}}{MM_h}h_1^\perp\left(-\frac{|\boldsymbol{R}|}{|\boldsymbol{k}_T|}H^\angle_{1,TT}\right)\right] \tag{A.33}$$

$$\begin{aligned} F_{UU}^{\cos(3\phi_h-\phi_R)\sin\theta} = \mathcal{I}\Bigg[&\frac{4\left(\boldsymbol{p}_T\hat{\boldsymbol{P}}_{h\perp}\right)\left(\boldsymbol{k}_T\hat{\boldsymbol{P}}_{h\perp}\right)^2 - 2\left(\boldsymbol{p}_T\boldsymbol{k}_T\right)\left(\boldsymbol{k}_T\hat{\boldsymbol{P}}_{h\perp}\right) - \boldsymbol{k}_T^2\left(\boldsymbol{p}_T\hat{\boldsymbol{P}}_{h\perp}\right)}{2MM_h^2} \\ &h_1^\perp\left(-\frac{2M_h}{|\boldsymbol{k}_T|}H^\perp_{1,UT}\right)\Bigg] \end{aligned} \tag{A.34}$$

$$\begin{aligned} F_{UU}^{\cos(3\phi_h-\phi_R)\sin 2\theta} = \mathcal{I}\Bigg[& \frac{4\left(\boldsymbol{p}_T\hat{\boldsymbol{P}}_{h\perp}\right)\left(\boldsymbol{k}_T\hat{\boldsymbol{P}}_{h\perp}\right)^2 - 2\left(\boldsymbol{p}_T\boldsymbol{k}_T\right)\left(\boldsymbol{k}_T\hat{\boldsymbol{P}}_{h\perp}\right) - \boldsymbol{k}_T^2\left(\boldsymbol{p}_T\hat{\boldsymbol{P}}_{h\perp}\right)}{2MM_h^2} \\ & h_1^\perp\left(-\frac{M_h}{|\boldsymbol{k}_T|}H_{1,LT}^\perp\right)\Bigg] \end{aligned} \tag{A.35}$$

$$\begin{aligned} F_{UU}^{\cos(4\phi_h-2\phi_R)\sin^2\theta} = \mathcal{I}\Bigg[& \frac{\left(\boldsymbol{k}_T^2 - 4(\boldsymbol{k}_T\hat{\boldsymbol{P}}_{h\perp})^2\right)\left(\boldsymbol{p}_T\boldsymbol{k}_T - 4\left(\boldsymbol{p}_T\hat{\boldsymbol{P}}_{h\perp}\right)\left(\boldsymbol{k}_T\hat{\boldsymbol{P}}_{h\perp}\right)\right)}{2MM_h^3} \\ & - \frac{8\left(\boldsymbol{p}_T\hat{\boldsymbol{P}}_{h\perp}\right)\left(\boldsymbol{k}_T\hat{\boldsymbol{P}}_{h\perp}\right)^3}{2MM_h^3} h_1^\perp\left(-\frac{2M_h^2}{|\boldsymbol{k}_T|^2}H_{1,TT}^\perp\right)\Bigg] \end{aligned} \tag{A.36}$$

$$F_{LU}^{\sin(\phi_h-\phi_R)\sin\theta} = -\mathcal{I}\left[\frac{\boldsymbol{k}_T\hat{\boldsymbol{P}}_{h\perp}}{M_h} f_1\left(\frac{|\boldsymbol{R}|}{M_h}G_{1,UT}^\perp\right)\right] \tag{A.37}$$

$$F_{LU}^{\sin(\phi_h-\phi_R)\sin 2\theta} = -\mathcal{I}\left[\frac{\boldsymbol{k}_T\hat{\boldsymbol{P}}_{h\perp}}{M_h} f_1\left(\frac{|\boldsymbol{R}|}{2M_h}G_{1,LT}^\perp\right)\right] \tag{A.38}$$

$$F_{LU}^{\sin(2\phi_h-2\phi_R)\sin^2\theta} = -\mathcal{I}\left[\frac{2\left(\boldsymbol{k}_T\hat{\boldsymbol{P}}_{h\perp}\right)^2 - \boldsymbol{k}_T^2}{M_h^2} f_1\left(\frac{|\boldsymbol{R}|}{2|\boldsymbol{k}_T|}G_{1,TT}^\perp\right)\right] \tag{A.39}$$

$$F_{UL}^{\sin(\phi_h-\phi_R)\sin\theta} = \mathcal{I}\left[\frac{\boldsymbol{k}_T\hat{\boldsymbol{P}}_{h\perp}}{M_h} g_{1L}\left(\frac{|\boldsymbol{R}|}{M_h}G_{1,UT}^\perp\right)\right] \tag{A.40}$$

$$F_{UL}^{\sin(\phi_h-\phi_R)\sin 2\theta} = \mathcal{I}\left[\frac{\boldsymbol{k}_T\hat{\boldsymbol{P}}_{h\perp}}{M_h} g_{1L}\left(\frac{|\boldsymbol{R}|}{2M_h}G_{1,LT}^\perp\right)\right] \tag{A.41}$$

$$F_{UL}^{\sin(2\phi_h-2\phi_R)\sin^2\theta} = \mathcal{I}\left[\frac{2\left(\boldsymbol{k}_T\hat{\boldsymbol{P}}_{h\perp}\right)^2 - \boldsymbol{k}_T^2}{M_h^2} g_{1L}\left(\frac{|\boldsymbol{R}|}{2|\boldsymbol{k}_T|}G_{1,TT}^\perp\right)\right] \tag{A.42}$$

$$\begin{aligned} F_{UL}^{\sin(2\phi_h)} = \mathcal{I}\Bigg[& \frac{2\left(\boldsymbol{p}_T\hat{\boldsymbol{P}}_{h\perp}\right)\left(\boldsymbol{k}_T\hat{\boldsymbol{P}}_{h\perp}\right) - \boldsymbol{p}_T\boldsymbol{k}_T}{MM_h} \\ & h_{1L}^\perp\left(\frac{1}{4}H_{1,UU}^{\perp s} + \frac{3}{4}H_{1,UU}^{\perp p}\right)\Bigg] \end{aligned} \tag{A.43}$$

$$F_{UL}^{\sin(2\phi_h)\cos\theta} = \mathcal{I}\left[\frac{2\left(\boldsymbol{p}_T\hat{\boldsymbol{P}}_{h\perp}\right)\left(\boldsymbol{k}_T\hat{\boldsymbol{P}}_{h\perp}\right) - \boldsymbol{p}_T\boldsymbol{k}_T}{MM_h} h_{1L}^\perp H_{1,UL}^\perp\right] \tag{A.44}$$

$$F_{UL}^{\sin(2\phi_h)\frac{1}{3}\left(3\cos^2\theta-1\right)} = \mathcal{I}\left[\frac{2\left(\boldsymbol{p}_T\hat{\boldsymbol{P}}_{h\perp}\right)\left(\boldsymbol{k}_T\hat{\boldsymbol{P}}_{h\perp}\right) - \boldsymbol{p}_T\boldsymbol{k}_T}{MM_h} h_{1L}^\perp\left(\frac{3}{4}H_{1,LL}^\perp\right)\right] \tag{A.45}$$

$$F_{UL}^{\sin(\phi_h+\phi_R)\sin\theta} = -\mathcal{I}\left[\frac{\boldsymbol{p}_T\hat{\boldsymbol{P}}_{h\perp}}{M} h_{1L}^\perp\left(-\frac{|\boldsymbol{R}|}{M_h}H_{1,UT}^\measuredangle\right)\right] \tag{A.46}$$

$$F_{UL}^{\sin(\phi_h+\phi_R)\sin 2\theta} = -\mathcal{I}\left[\frac{\boldsymbol{p}_T\hat{\boldsymbol{P}}_{h\perp}}{M} h_{1L}^\perp\left(-\frac{|\boldsymbol{R}|}{2M_h}H_{1,LT}^\measuredangle\right)\right] \tag{A.47}$$

$$F_{UL}^{\sin(2\phi_R)\sin^2\theta} = -\mathcal{I}\left[\frac{\boldsymbol{p}_T\boldsymbol{k}_T}{MM_h} h_{1L}^{\perp}\left(-\frac{|\boldsymbol{R}|}{|\boldsymbol{k}_T|}H_{1,TT}^{\angle}\right)\right] \tag{A.48}$$

$$\begin{aligned} F_{UL}^{\sin(3\phi_h-\phi_R)\sin\theta} = & -\mathcal{I}\Bigg[\frac{4\left(\boldsymbol{p}_T\hat{\boldsymbol{P}}_{h\perp}\right)\left(\boldsymbol{k}_T\hat{\boldsymbol{P}}_{h\perp}\right)^2 - 2\left(\boldsymbol{p}_T\boldsymbol{k}_T\right)\left(\boldsymbol{k}_T\hat{\boldsymbol{P}}_{h\perp}\right) - \boldsymbol{k}_T^2\left(\boldsymbol{p}_T\hat{\boldsymbol{P}}_{h\perp}\right)}{2MM_h^2} \\ & h_{1L}^{\perp}\left(-\frac{2M_h}{|\boldsymbol{k}_T|}H_{1,UT}^{\perp}\right)\Bigg] \end{aligned} \tag{A.49}$$

$$\begin{aligned} F_{UL}^{\sin(3\phi_h-\phi_R)\sin2\theta} = & -\mathcal{I}\Bigg[\frac{4\left(\boldsymbol{p}_T\hat{\boldsymbol{P}}_{h\perp}\right)\left(\boldsymbol{k}_T\hat{\boldsymbol{P}}_{h\perp}\right)^2 - 2\left(\boldsymbol{p}_T\boldsymbol{k}_T\right)\left(\boldsymbol{k}_T\hat{\boldsymbol{P}}_{h\perp}\right) - \boldsymbol{k}_T^2\left(\boldsymbol{p}_T\hat{\boldsymbol{P}}_{h\perp}\right)}{2MM_h^2} \\ & h_{1L}^{\perp}\left(-\frac{M_h}{|\boldsymbol{k}_T|}H_{1,LT}^{\perp}\right)\Bigg] \end{aligned} \tag{A.50}$$

$$\begin{aligned} F_{UL}^{\sin(4\phi_h-2\phi_R)\sin^2\theta} = & -\mathcal{I}\Bigg[\frac{\left(\boldsymbol{k}_T^2 - 4(\boldsymbol{k}_T\hat{\boldsymbol{P}}_{h\perp})^2\right)\left(\boldsymbol{p}_T\boldsymbol{k}_T - 4\left(\boldsymbol{p}_T\hat{\boldsymbol{P}}_{h\perp}\right)\left(\boldsymbol{k}_T\hat{\boldsymbol{P}}_{h\perp}\right)\right)}{2MM_h^3} \\ & - \frac{8\left(\boldsymbol{p}_T\hat{\boldsymbol{P}}_{h\perp}\right)\left(\boldsymbol{k}_T\hat{\boldsymbol{P}}_{h\perp}\right)^3}{2MM_h^3} h_{1L}^{\perp}\left(-\frac{2M_h^2}{|\boldsymbol{k}_T|^2}H_{1,TT}^{\perp}\right)\Bigg] \end{aligned} \tag{A.51}$$

$$F_{LL} = \mathcal{I}\left[g_{1L}\left(\frac{1}{4}D_{1,UU}^{s} + \frac{3}{4}D_{1,UU}^{p}\right)\right] \tag{A.52}$$

$$F_{LL}^{\cos\theta} = \mathcal{I}\Big[g_{1L}D_{1,UL}\Big] \tag{A.53}$$

$$F_{LL}^{\frac{1}{3}\left(3\cos^2\theta-1\right)} = \mathcal{I}\left[g_{1L}\left(\frac{3}{4}D_{1,LL}\right)\right] \tag{A.54}$$

$$F_{LL}^{\cos(\phi_h-\phi_R)\sin\theta} = -\mathcal{I}\left[\frac{\boldsymbol{k}_T\hat{\boldsymbol{P}}_{h\perp}}{M_h} g_{1L}\left(-\frac{M_h}{|\boldsymbol{k}_T|}D_{1,UT}\right)\right] \tag{A.55}$$

$$F_{LL}^{\cos(\phi_h-\phi_R)\sin2\theta} = -\mathcal{I}\left[\frac{\boldsymbol{k}_T\hat{\boldsymbol{P}}_{h\perp}}{M_h} g_{1L}\left(-\frac{M_h}{2|\boldsymbol{k}_T|}D_{1,LT}\right)\right] \tag{A.56}$$

$$F_{LL}^{\cos(2\phi_h-2\phi_R)\sin^2\theta} = -\mathcal{I}\left[\frac{2\left(\boldsymbol{k}_T\hat{\boldsymbol{P}}_{h\perp}\right)^2 - \boldsymbol{k}_T^2}{M_h^2} g_{1L}\left(-\frac{M_h^2}{|\boldsymbol{k}_T|^2}D_{1,TT}\right)\right] \tag{A.57}$$

A.3 Binning

Table A.1: Binning, used for the extraction of asymmetries. The asymmetries are extracted in bins of x, z and P_{hT} in the one hadron analysis, while in case of hadron pairs the considered variables are x, z and M_{inv}.

Bin	x	z	P_{hT} [GeV/c]	M_{inv} [GeV/c^2]
0	$[0.0025, 0.0080)$	$[0.20, 0.25)$	$[0.10, 0.20)$	$[0.0, 0.4)$
1	$[0.0080, 0.0130)$	$[0.25, 0.30)$	$[0.20, 0.30)$	$[0.4, 0.5)$
2	$[0.0130, 0.0200)$	$[0.30, 0.35)$	$[0.30, 0.40)$	$[0.5, 0.6)$
3	$[0.0200, 0.0320)$	$[0.35, 0.40)$	$[0.40, 0.50)$	$[0.6, 0.7)$
4	$[0.0320, 0.0500)$	$[0.40, 0.50)$	$[0.50, 0.60)$	$[0.7, 0.8)$
5	$[0.0500, 0.0800)$	$[0.50, 0.65)$	$[0.60, 0.75)$	$[0.8, 0.9)$
6	$[0.0800, 0.1300)$	$[0.65, 0.80)$	$[0.75, 0.90)$	$[0.9, 1.0)$
7	$[0.1300, 0.2100)$	$[0.80, 1.00)$	$[0.90, 1.30)$	$[1.0, 1.2)$
8	$[0.2100, 0.7000)$		$[0.13, 10.00)$	$[1.2, 1.6)$
9				$[1.6, 100.0)$

A.4 Two Hadron Analysis Material

Table A.2: Mean Values of relevant variables for the h^+h^- analysis in bins of x, z, and M_{inv} for 2007.

h^+h^-										2007
					x					
Bin	Range	$\langle x\rangle$	$\langle z\rangle$	$\langle M_{\text{inv}}\rangle$ [GeV/c^2]	$\langle Q^2\rangle$ [(GeV/c)^2]	$\langle y\rangle$	$\langle W\rangle$ [GeV/c^2]	$\langle f\rangle$	$\langle \lvert P_T\rvert\rangle$	$\langle P_B\rangle$
0	$[0.0025, 0.0080)$	0.006	0.448	0.788	1.260	0.674	13.985	0.142	0.865	-0.798
1	$[0.0080, 0.0130)$	0.011	0.453	0.765	1.532	0.492	11.926	0.144	0.866	-0.794
2	$[0.0130, 0.0200)$	0.016	0.461	0.744	1.826	0.377	10.331	0.145	0.866	-0.793
3	$[0.0200, 0.0320)$	0.026	0.470	0.721	2.215	0.293	8.985	0.145	0.867	-0.792
4	$[0.0320, 0.0500)$	0.040	0.476	0.704	2.992	0.252	8.228	0.146	0.867	-0.790
5	$[0.0500, 0.0800)$	0.063	0.476	0.698	4.664	0.250	8.093	0.146	0.867	-0.789
6	$[0.0800, 0.1300)$	0.101	0.476	0.693	7.526	0.251	7.955	0.150	0.867	-0.789
7	$[0.1300, 0.2100)$	0.162	0.476	0.684	12.089	0.250	7.678	0.158	0.867	-0.790
8	$[0.2100, 0.7000)$	0.286	0.480	0.678	23.477	0.271	7.385	0.175	0.866	-0.791
					z					
Bin	Range	$\langle x\rangle$	$\langle z\rangle$	$\langle M_{\text{inv}}\rangle$ [GeV/c^2]	$\langle Q^2\rangle$ [(GeV/c)^2]	$\langle y\rangle$	$\langle W\rangle$ [GeV/c^2]	$\langle f\rangle$	$\langle \lvert P_T\rvert\rangle$	$\langle P_B\rangle$
0	$[0.20, 0.25)$	0.032	0.238	0.510	3.951	0.465	11.291	0.144	0.867	-0.795
1	$[0.25, 0.30)$	0.039	0.278	0.580	3.839	0.392	10.263	0.145	0.867	-0.794
2	$[0.30, 0.35)$	0.043	0.326	0.634	3.794	0.357	9.760	0.146	0.867	-0.793
3	$[0.35, 0.40)$	0.045	0.375	0.676	3.773	0.340	9.503	0.147	0.867	-0.792
4	$[0.40, 0.50)$	0.047	0.447	0.724	3.761	0.326	9.286	0.147	0.866	-0.792
5	$[0.50, 0.65)$	0.049	0.567	0.791	3.722	0.312	9.069	0.147	0.866	-0.791
6	$[0.65, 0.80)$	0.049	0.714	0.865	3.612	0.301	8.893	0.147	0.866	-0.789
7	$[0.80, 1.00)$	0.037	0.854	0.931	3.349	0.359	9.840	0.146	0.865	-0.791
					M_{inv}					
Bin	Range	$\langle x\rangle$	$\langle z\rangle$	$\langle M_{\text{inv}}\rangle$ [GeV/c^2]	$\langle Q^2\rangle$ [(GeV/c)^2]	$\langle y\rangle$	$\langle W\rangle$ [GeV/c^2]	$\langle f\rangle$	$\langle \lvert P_T\rvert\rangle$	$\langle P_B\rangle$
0	$[0.0, 0.4)$	0.049	0.408	0.362	3.772	0.313	9.080	0.147	0.867	-0.791
1	$[0.4, 0.5)$	0.048	0.430	0.451	3.739	0.316	9.125	0.147	0.867	-0.791
2	$[0.5, 0.6)$	0.047	0.441	0.549	3.747	0.323	9.243	0.147	0.866	-0.791
3	$[0.6, 0.7)$	0.046	0.457	0.650	3.735	0.331	9.362	0.147	0.866	-0.791
4	$[0.7, 0.8)$	0.045	0.483	0.749	3.688	0.336	9.438	0.147	0.866	-0.792
5	$[0.8, 0.9)$	0.044	0.493	0.846	3.733	0.344	9.559	0.146	0.866	-0.792
6	$[0.9, 1.0)$	0.044	0.500	0.947	3.772	0.352	9.665	0.146	0.866	-0.792
7	$[1.0, 1.2)$	0.042	0.516	1.090	3.751	0.362	9.828	0.146	0.866	-0.792
8	$[1.2, 1.6)$	0.039	0.554	1.350	3.745	0.383	10.134	0.146	0.866	-0.793
9	$[1.6, 100.0)$	0.034	0.602	1.937	3.821	0.437	10.888	0.145	0.867	-0.793

Table A.3: Mean Values of relevant variables for the h^+h^- analysis in bins of x, z, and M_{inv} for 2011.

h^+h^-										2011
					x					
Bin	Range	$\langle x\rangle$	$\langle z\rangle$	$\langle M_{\text{inv}}\rangle$ [GeV/c^2]	$\langle Q^2\rangle$ [(GeV/c)^2]	$\langle y\rangle$	$\langle W\rangle$ [GeV/c^2]	$\langle f\rangle$	$\langle \lvert P_T\rvert\rangle$	$\langle P_B\rangle$
0	$[0.0025, 0.0080)$	0.006	0.443	0.801	1.371	0.628	14.087	0.145	0.867	-0.828
1	$[0.0080, 0.0130)$	0.011	0.449	0.771	1.723	0.438	12.168	0.147	0.866	-0.826
2	$[0.0130, 0.0200)$	0.016	0.457	0.750	2.091	0.340	10.725	0.148	0.866	-0.825
3	$[0.0200, 0.0320)$	0.026	0.466	0.730	2.638	0.275	9.587	0.148	0.866	-0.825
4	$[0.0320, 0.0500)$	0.040	0.468	0.718	3.770	0.250	9.098	0.148	0.866	-0.824
5	$[0.0500, 0.0800)$	0.063	0.469	0.712	5.745	0.242	8.875	0.149	0.866	-0.824
6	$[0.0800, 0.1300)$	0.101	0.469	0.705	9.058	0.237	8.659	0.153	0.866	-0.824
7	$[0.1300, 0.2100)$	0.162	0.471	0.698	14.158	0.231	8.293	0.161	0.866	-0.824
8	$[0.2100, 0.7000)$	0.288	0.476	0.684	25.010	0.228	7.637	0.180	0.866	-0.825
					z					
Bin	Range	$\langle x\rangle$	$\langle z\rangle$	$\langle M_{\text{inv}}\rangle$ [GeV/c^2]	$\langle Q^2\rangle$ [(GeV/c)^2]	$\langle y\rangle$	$\langle W\rangle$ [GeV/c^2]	$\langle f\rangle$	$\langle \lvert P_T\rvert\rangle$	$\langle P_B\rangle$
0	$[0.20, 0.25)$	0.032	0.238	0.527	4.450	0.440	11.618	0.147	0.866	-0.827
1	$[0.25, 0.30)$	0.039	0.278	0.599	4.413	0.373	10.732	0.148	0.866	-0.826
2	$[0.30, 0.35)$	0.042	0.325	0.652	4.411	0.344	10.305	0.149	0.866	-0.826
3	$[0.35, 0.40)$	0.045	0.375	0.694	4.412	0.329	10.081	0.149	0.866	-0.825
4	$[0.40, 0.50)$	0.046	0.447	0.742	4.414	0.317	9.891	0.150	0.866	-0.825
5	$[0.50, 0.65)$	0.048	0.566	0.808	4.385	0.305	9.698	0.150	0.866	-0.825
6	$[0.65, 0.80)$	0.049	0.714	0.886	4.260	0.295	9.536	0.150	0.866	-0.824
7	$[0.80, 1.00)$	0.038	0.857	0.945	3.801	0.327	10.094	0.149	0.866	-0.825
					M_{inv}					
Bin	Range	$\langle x\rangle$	$\langle z\rangle$	$\langle M_{\text{inv}}\rangle$ [GeV/c^2]	$\langle Q^2\rangle$ [(GeV/c)^2]	$\langle y\rangle$	$\langle W\rangle$ [GeV/c^2]	$\langle f\rangle$	$\langle \lvert P_T\rvert\rangle$	$\langle P_B\rangle$
0	$[0.0, 0.4)$	0.049	0.402	0.362	4.453	0.305	9.736	0.150	0.866	-0.825
1	$[0.4, 0.5)$	0.048	0.423	0.451	4.422	0.307	9.771	0.150	0.866	-0.825
2	$[0.5, 0.6)$	0.047	0.434	0.549	4.415	0.314	9.862	0.150	0.866	-0.825
3	$[0.6, 0.7)$	0.046	0.449	0.650	4.384	0.321	9.959	0.150	0.866	-0.825
4	$[0.7, 0.8)$	0.044	0.474	0.749	4.322	0.326	10.019	0.150	0.866	-0.825
5	$[0.8, 0.9)$	0.044	0.484	0.846	4.337	0.333	10.109	0.149	0.866	-0.825
6	$[0.9, 1.0)$	0.043	0.491	0.947	4.367	0.339	10.198	0.149	0.866	-0.825
7	$[1.0, 1.2)$	0.041	0.506	1.090	4.321	0.350	10.343	0.149	0.866	-0.825
8	$[1.2, 1.6)$	0.038	0.542	1.352	4.268	0.369	10.595	0.148	0.866	-0.826
9	$[1.6, 100.0)$	0.033	0.589	1.955	4.298	0.419	11.257	0.147	0.866	-0.826

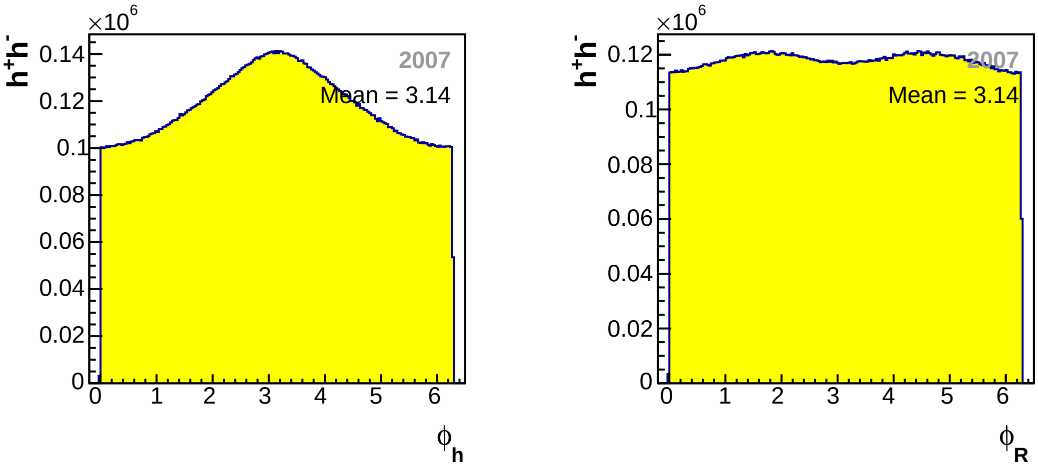

Figure A.1: Distributions of the azimuthal angles ϕ_h (left) and ϕ_R (right) for 2007.

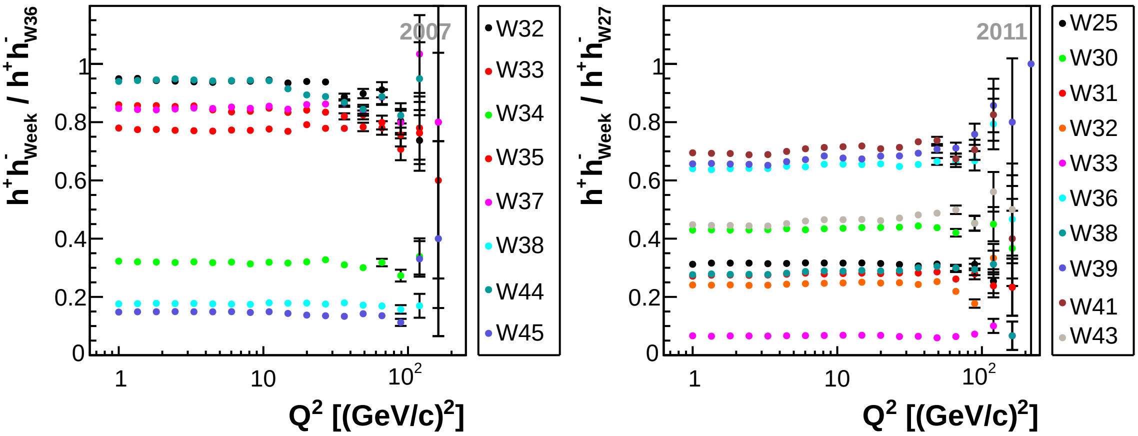

Figure A.2: Ratios of the Q^2-distributions from a particular week with the corresponding distribution from the most populated week.

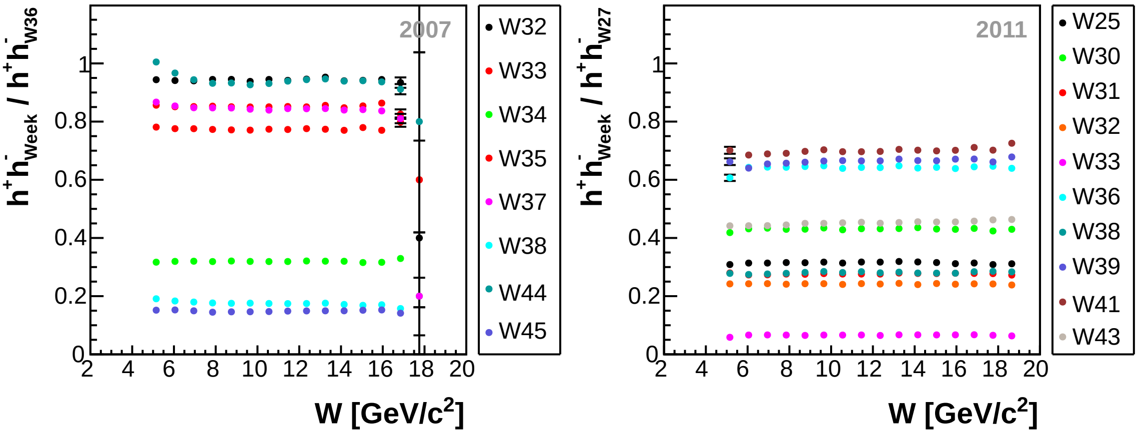

Figure A.3: Ratios of the W-distributions from a particular week with the corresponding distribution from the most populated week.

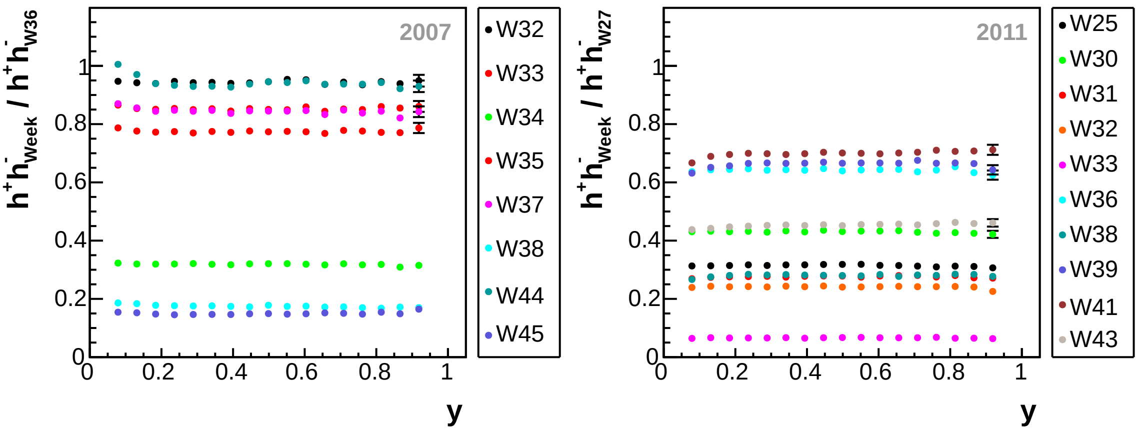

Figure A.4: Ratios of the y-distributions from a particular week with the corresponding distribution from the most populated week.

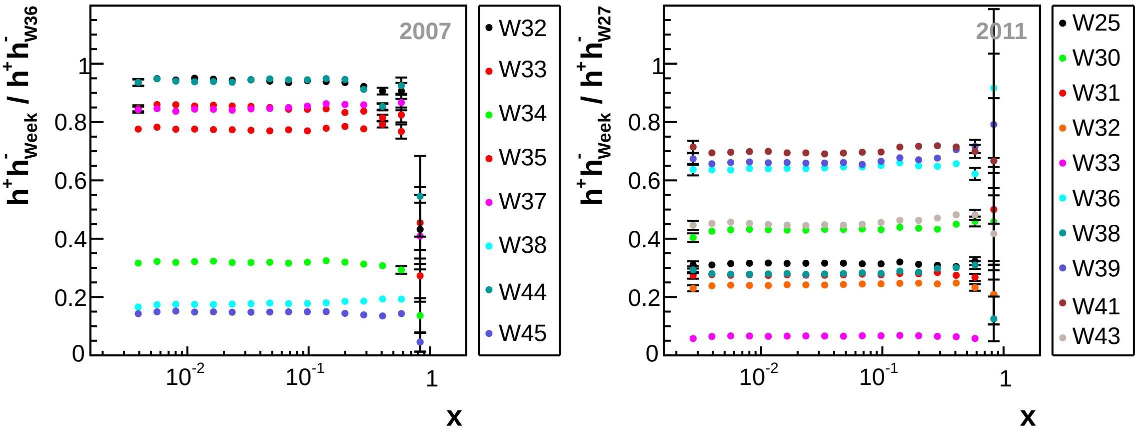

Figure A.5: Ratios of the x-distributions from a particular week with the corresponding distribution from the most populated week.

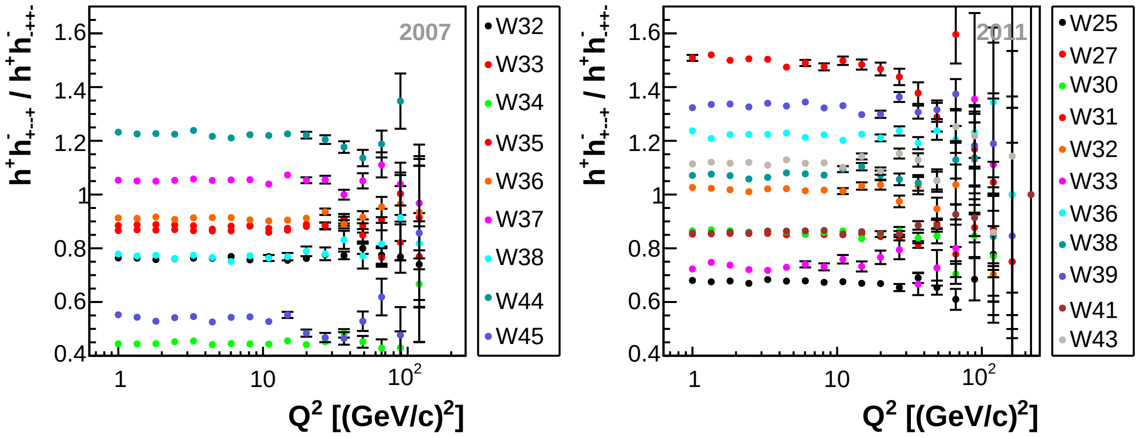

Figure A.6: Ratios of the Q^2-distributions from the two target polarization settings per week.

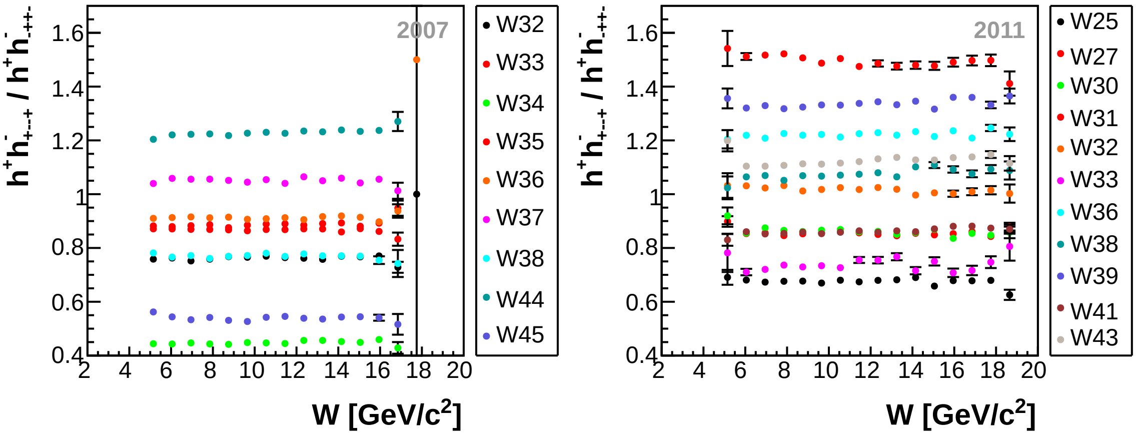

Figure A.7: Ratios of the W-distributions from the two target polarization settings per week.

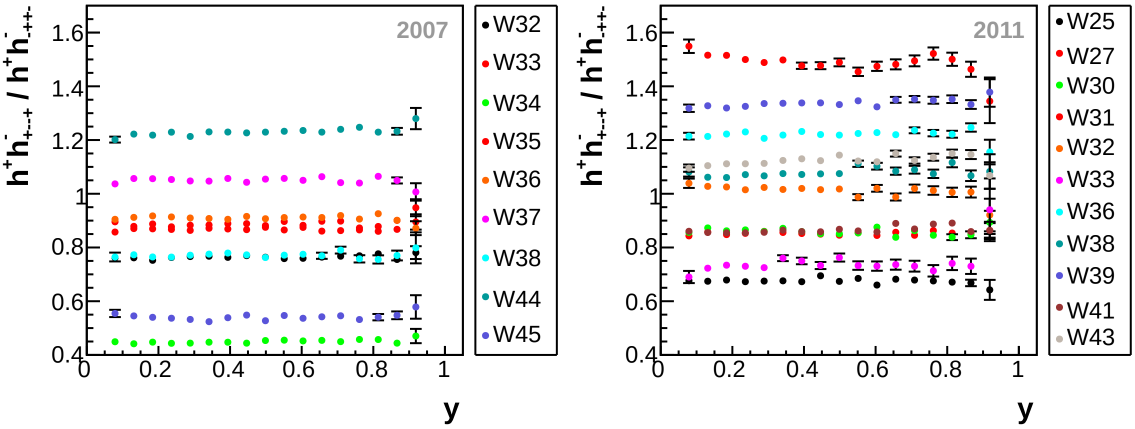

Figure A.8: Ratios of the y-distributions from the two target polarization settings per week.

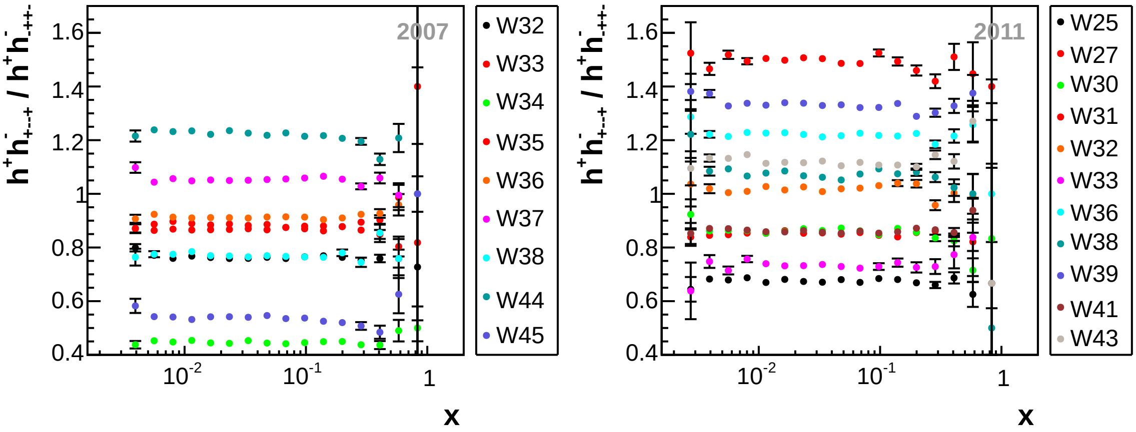

Figure A.9: Ratios of the x-distributions from the two target polarization settings per week.

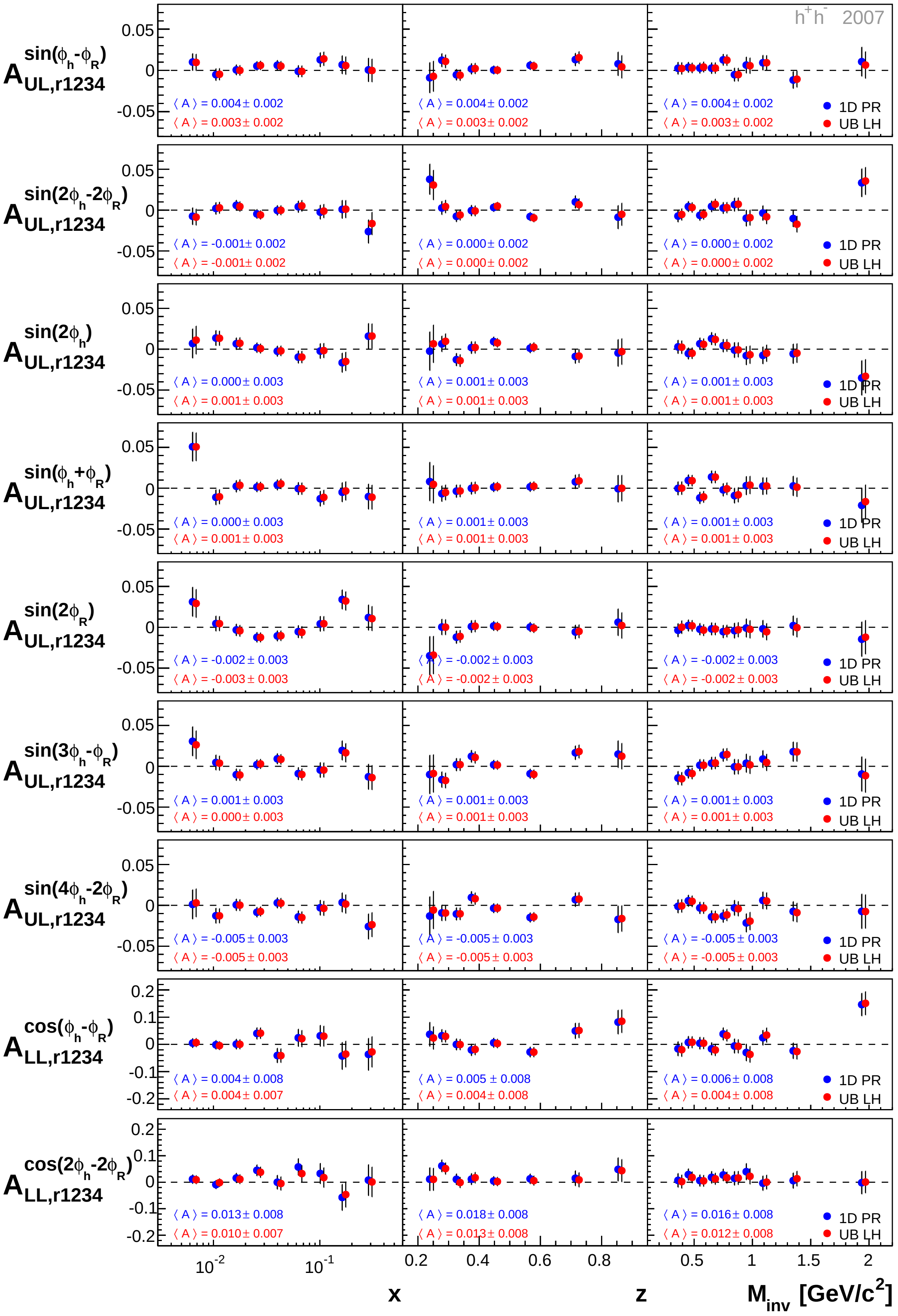

Figure A.10: Comparison of the azimuthal asymmetries, extracted with the methods 1D PR and UB LH, for 2007.

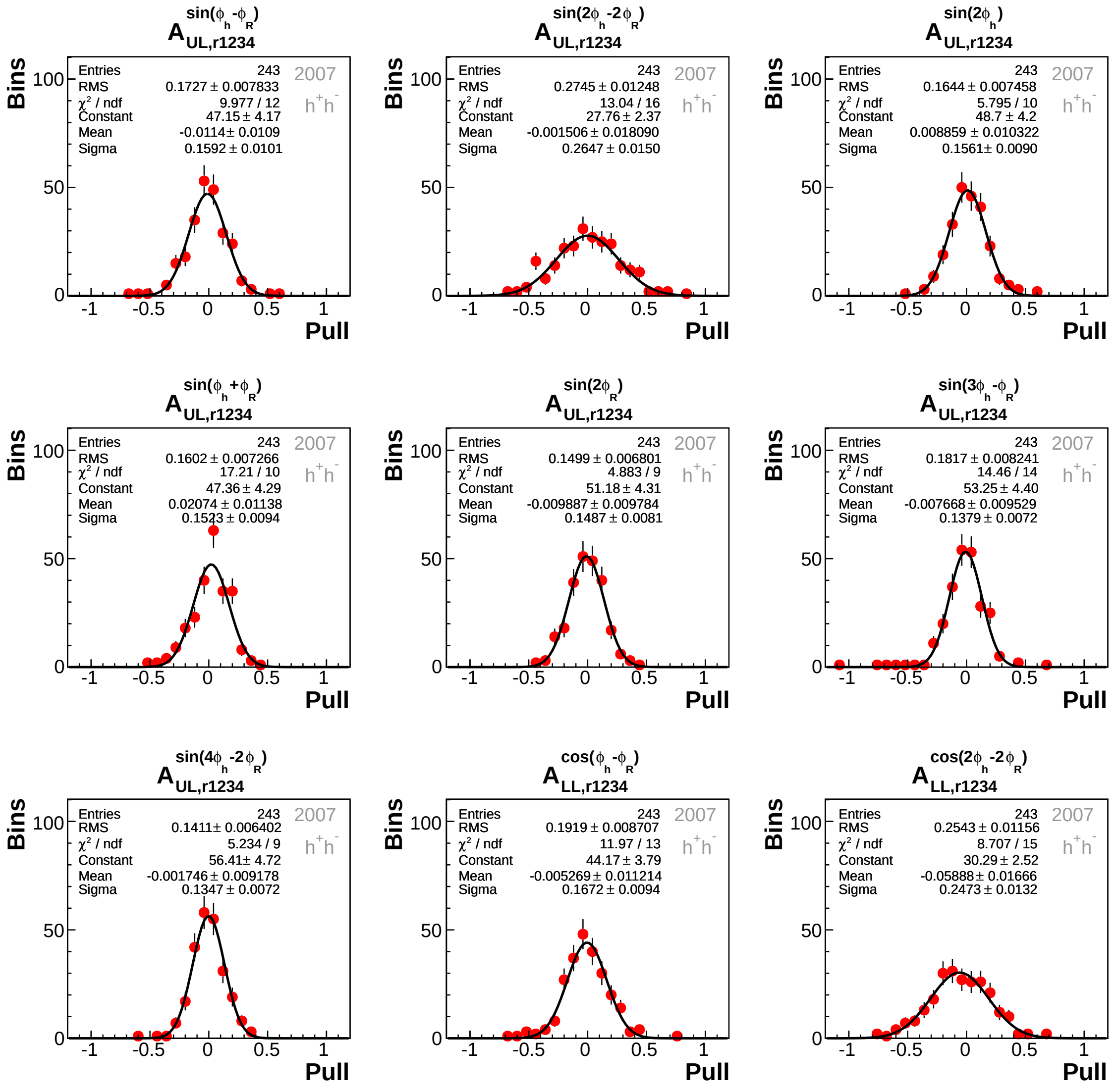

Figure A.11: Pull distributions between asymmetries extracted with the UB LH and the 1D PR method for 2007. The gaussian fit, corresponding statistical values and fit parameters are also displayed.

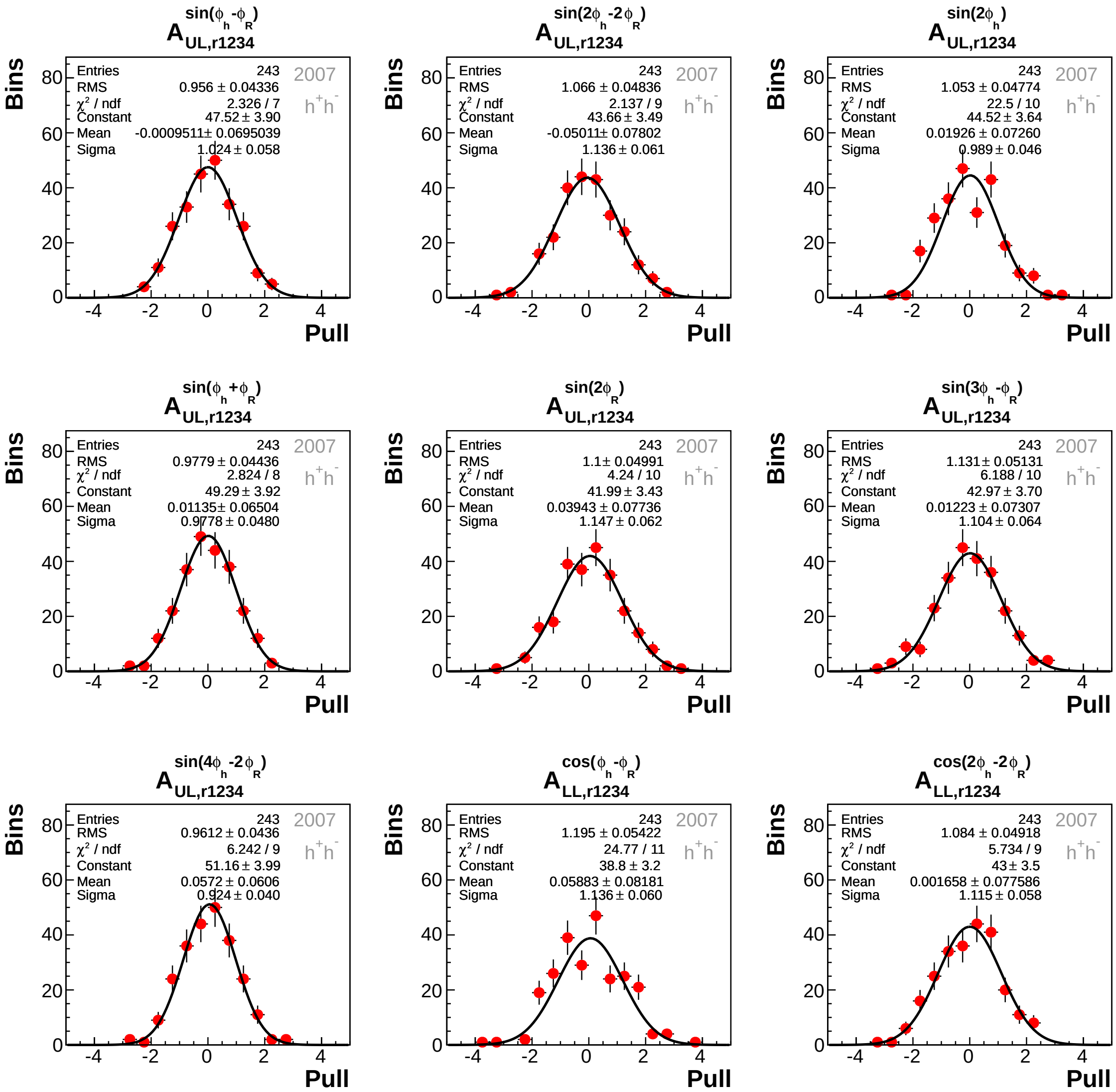

Figure A.12: Stability pull distributions of asymmetries, extracted with the UB LH method, for 2007. The gaussian fit, corresponding statistical values and fit parameters are also displayed.

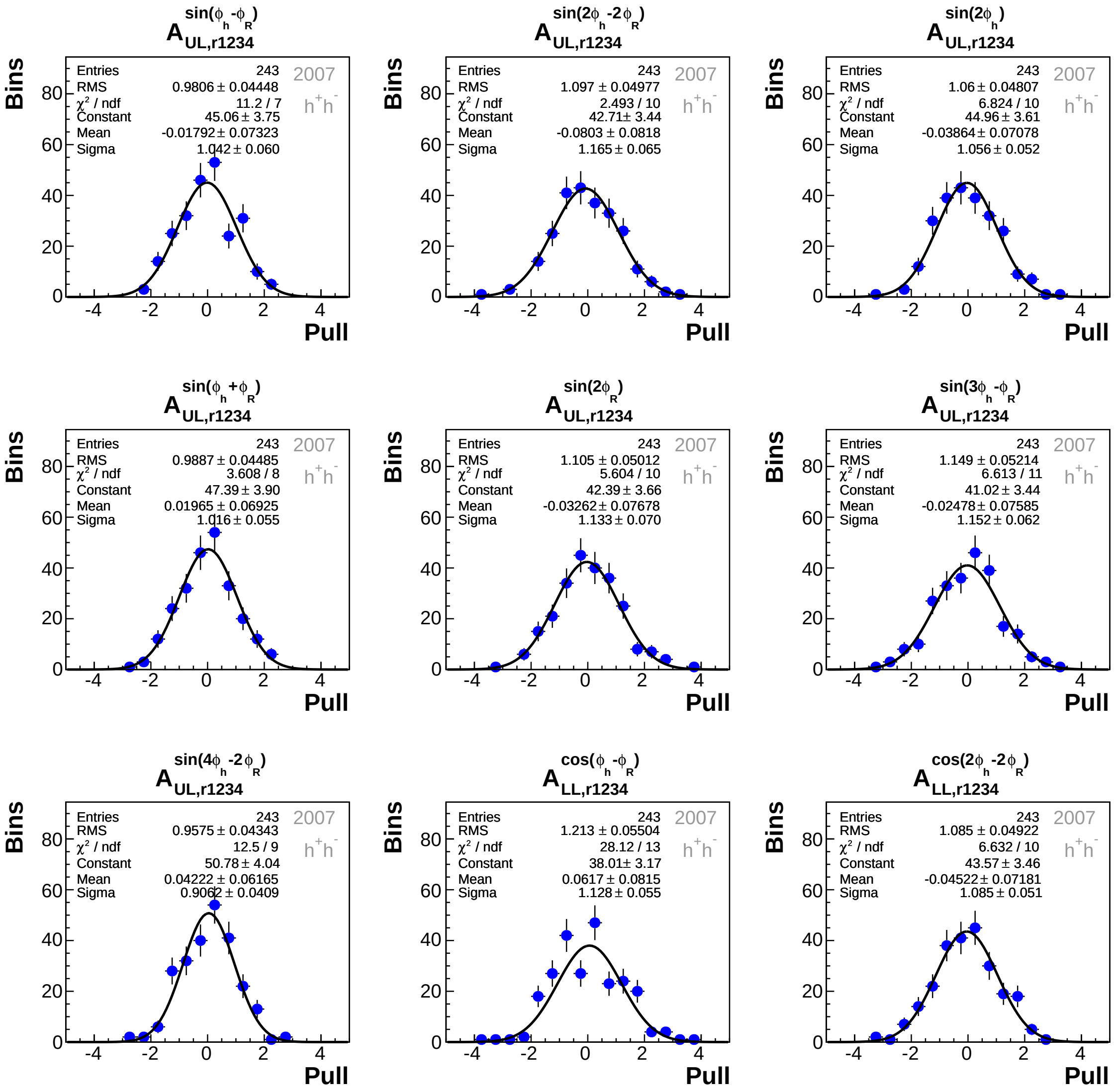

Figure A.13: Stability pull distributions of asymmetries, extracted with the 1D PR method, for 2007. The gaussian fit, corresponding statistical values and fit parameters are also displayed.

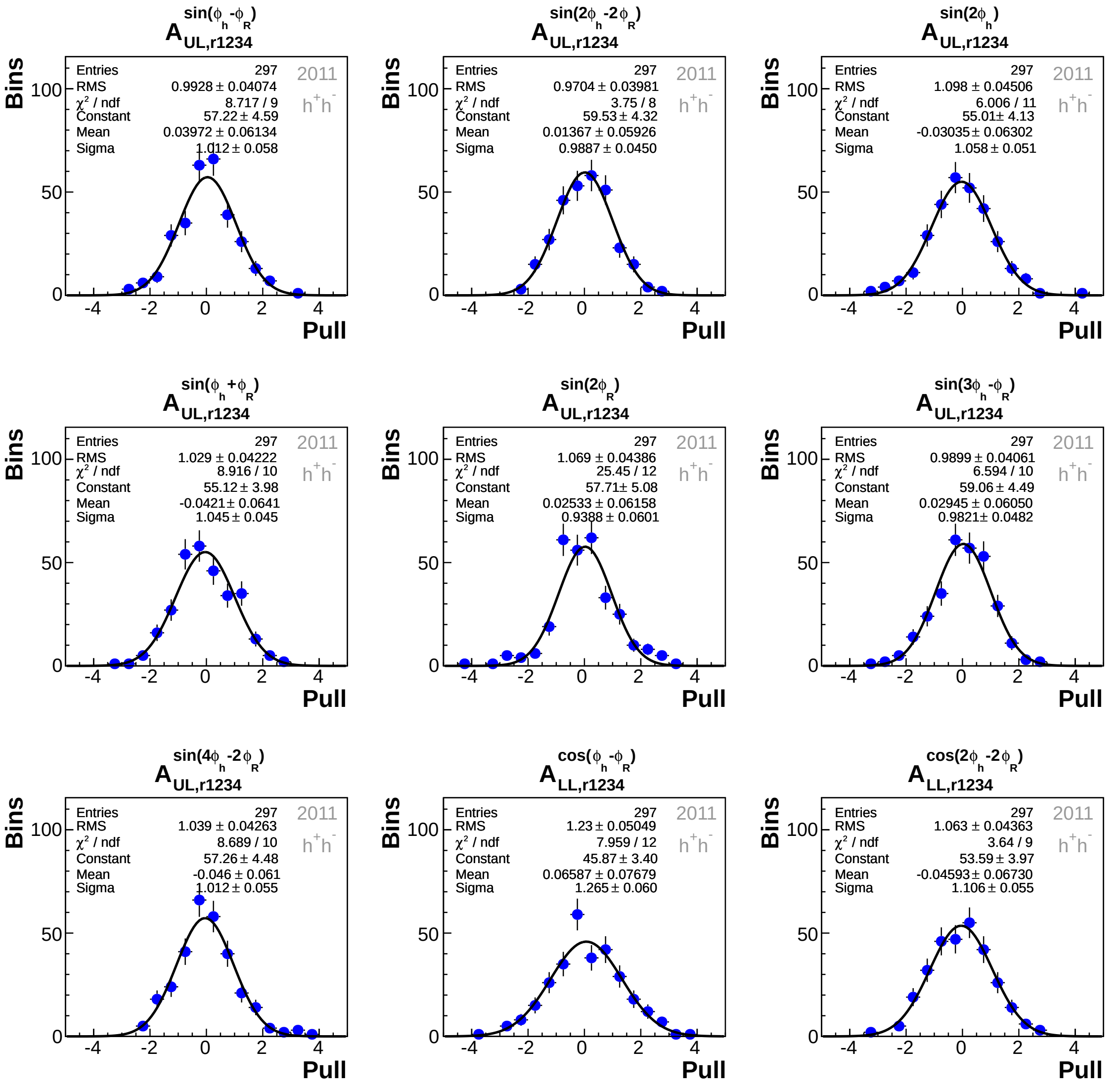

Figure A.14: Stability pull distributions of asymmetries, extracted with the 1D PR method, for 2011. The gaussian fit, corresponding statistical values and fit parameters are also displayed.

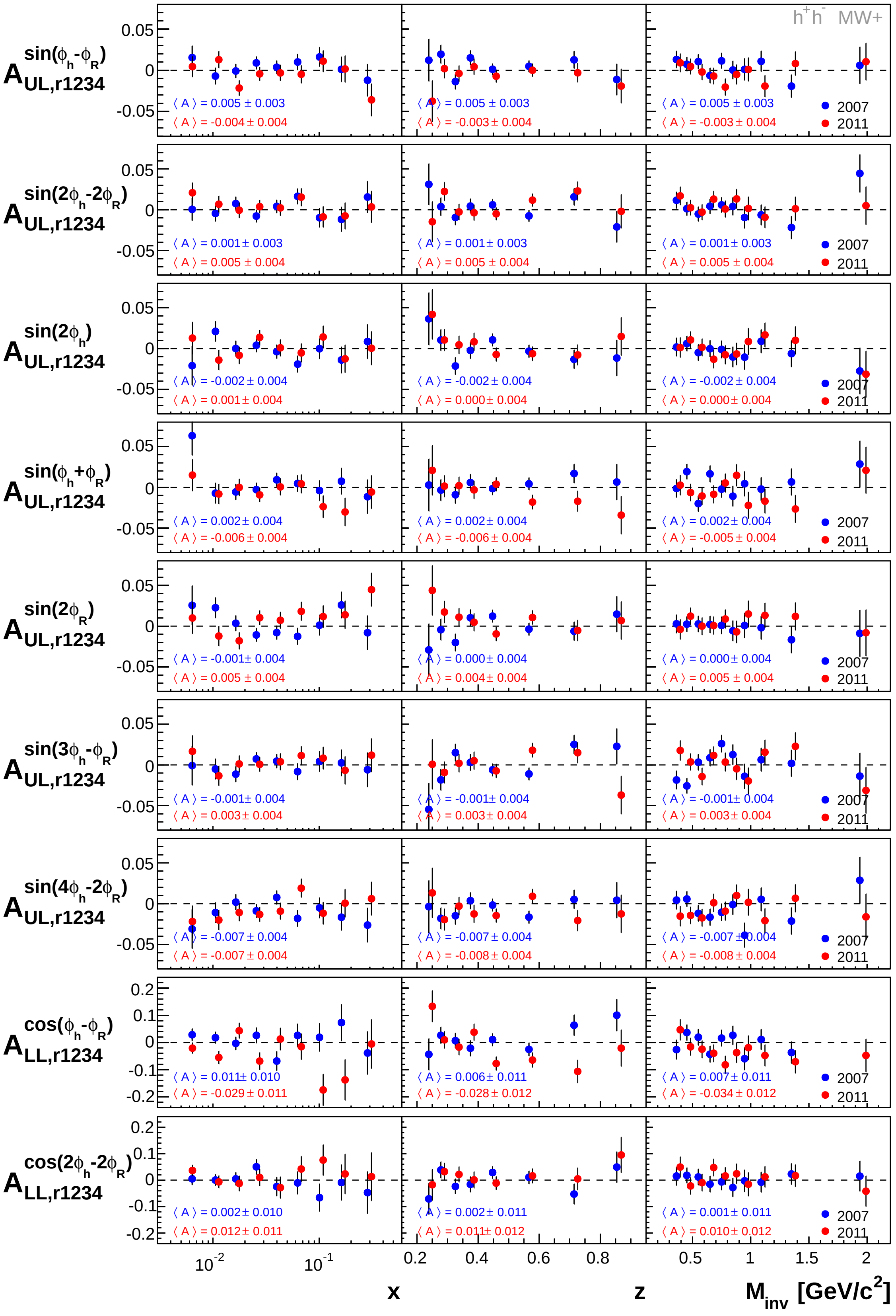

Figure A.15: Comparison of asymmetries from MW+ for 2007 and 2011. Corresponding mean values are also displayed.

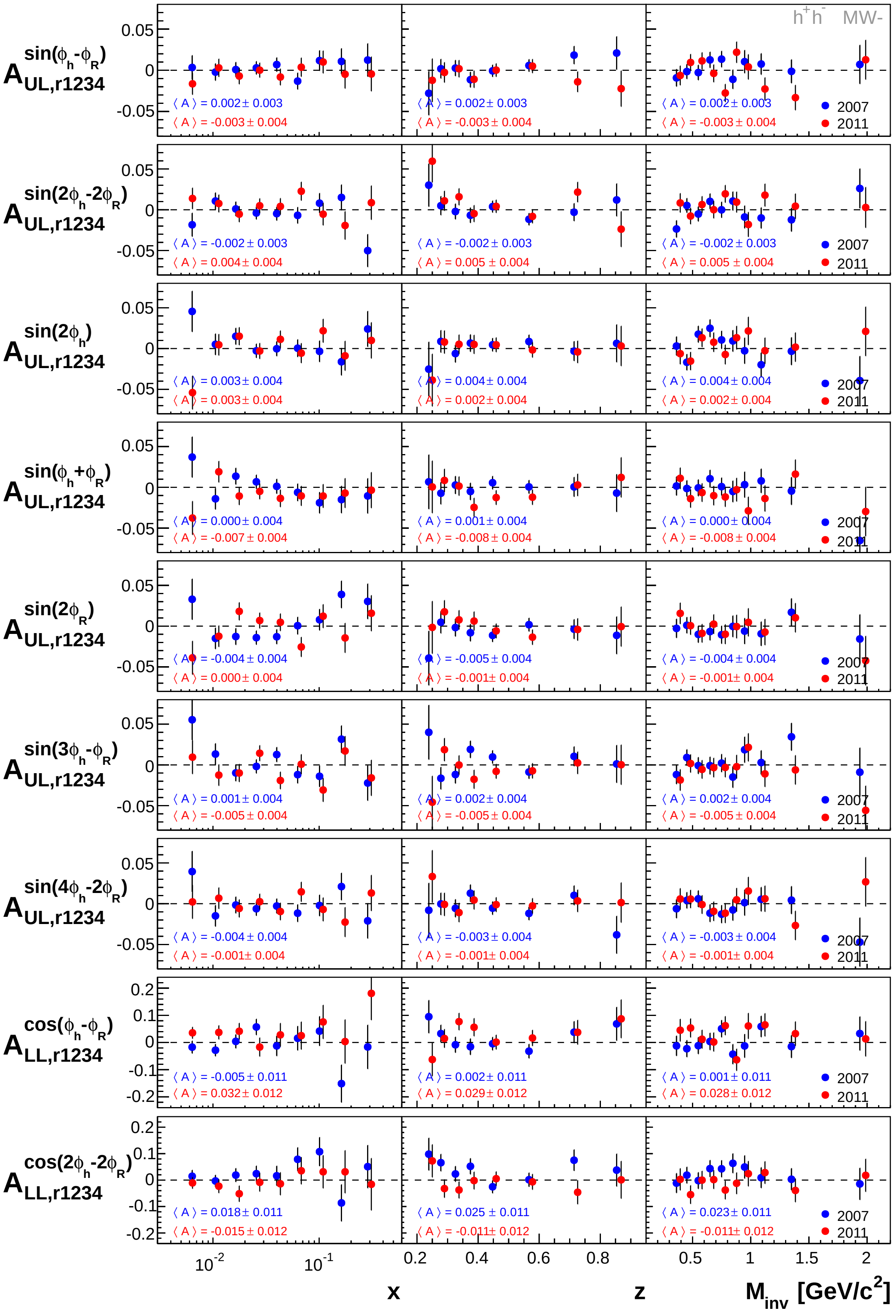

Figure A.16: Comparison of asymmetries from MW- for 2007 and 2011. Corresponding mean values are also displayed.

Table A.4: Results of $A_{UL}^{\sin(\phi_h-\phi_R)}$ for h^+h^- in bins of x, z, and $M_{\mathrm{inv}}$for 2007.

h^+h^-			2007
x			
Bin	Range	$\langle x \rangle$	$A_{UL}^{\sin(\phi_h-\phi_R)}$
0	$[0.0025, 0.0080)$	0.006	0.010 ± 0.010 ± 0.006
1	$[0.0080, 0.0130)$	0.011	-0.005 ± 0.007 ± 0.004
2	$[0.0130, 0.0200)$	0.016	0.000 ± 0.006 ± 0.004
3	$[0.0200, 0.0320)$	0.026	0.006 ± 0.005 ± 0.003
4	$[0.0320, 0.0500)$	0.040	0.005 ± 0.006 ± 0.003
5	$[0.0500, 0.0800)$	0.063	-0.001 ± 0.007 ± 0.004
6	$[0.0800, 0.1300)$	0.101	0.014 ± 0.008 ± 0.005
7	$[0.1300, 0.2100)$	0.162	0.006 ± 0.011 ± 0.006
8	$[0.2100, 0.7000)$	0.286	0.000 ± 0.014 ± 0.008
z			
Bin	Range	$\langle z \rangle$	$A_{UL}^{\sin(\phi_h-\phi_R)}$
0	$[0.20, 0.25)$	0.238	-0.007 ± 0.018 ± 0.011
1	$[0.25, 0.30)$	0.278	0.011 ± 0.008 ± 0.005
2	$[0.30, 0.35)$	0.326	-0.006 ± 0.007 ± 0.004
3	$[0.35, 0.40)$	0.375	0.002 ± 0.006 ± 0.004
4	$[0.40, 0.50)$	0.447	0.000 ± 0.005 ± 0.003
5	$[0.50, 0.65)$	0.567	0.005 ± 0.005 ± 0.003
6	$[0.65, 0.80)$	0.714	0.015 ± 0.007 ± 0.004
7	$[0.80, 1.00)$	0.854	0.004 ± 0.014 ± 0.008
M_{inv}			
Bin	Range	$\langle M_{\mathrm{inv}} \rangle$ [GeV/c^2]	$A_{UL}^{\sin(\phi_h-\phi_R)}$
0	$[0.0, 0.4)$	0.362	0.002 ± 0.007 ± 0.004
1	$[0.4, 0.5)$	0.451	0.003 ± 0.006 ± 0.004
2	$[0.5, 0.6)$	0.549	0.004 ± 0.006 ± 0.004
3	$[0.6, 0.7)$	0.650	0.003 ± 0.007 ± 0.004
4	$[0.7, 0.8)$	0.749	0.012 ± 0.007 ± 0.004
5	$[0.8, 0.9)$	0.846	-0.005 ± 0.008 ± 0.005
6	$[0.9, 1.0)$	0.947	0.006 ± 0.009 ± 0.006
7	$[1.0, 1.2)$	1.090	0.009 ± 0.009 ± 0.005
8	$[1.2, 1.6)$	1.350	-0.011 ± 0.010 ± 0.006
9	$[1.6, 100.0)$	1.938	0.007 ± 0.016 ± 0.010

Table A.5: Results of $A_{UL}^{\sin(\phi_h-\phi_R)}$ for h^+h^- in bins of x, z, and $M_{\mathrm{inv}}$for 2011.

h^+h^-			2011
x			
Bin	Range	$\langle x \rangle$	$A_{UL}^{\sin(\phi_h-\phi_R)}$
0	$[0.0025, 0.0080)$	0.006	-0.005 ± 0.009 ± 0.005
1	$[0.0080, 0.0130)$	0.011	0.008 ± 0.007 ± 0.004
2	$[0.0130, 0.0200)$	0.016	-0.015 ± 0.007 ± 0.004
3	$[0.0200, 0.0320)$	0.026	-0.002 ± 0.006 ± 0.003
4	$[0.0320, 0.0500)$	0.040	-0.006 ± 0.007 ± 0.004
5	$[0.0500, 0.0800)$	0.063	-0.001 ± 0.008 ± 0.004
6	$[0.0800, 0.1300)$	0.101	0.011 ± 0.009 ± 0.005
7	$[0.1300, 0.2100)$	0.162	-0.001 ± 0.012 ± 0.007
8	$[0.2100, 0.7000)$	0.288	-0.021 ± 0.014 ± 0.008
z			
Bin	Range	$\langle z \rangle$	$A_{UL}^{\sin(\phi_h-\phi_R)}$
0	$[0.20, 0.25)$	0.238	-0.026 ± 0.018 ± 0.010
1	$[0.25, 0.30)$	0.278	0.000 ± 0.008 ± 0.005
2	$[0.30, 0.35)$	0.325	-0.001 ± 0.007 ± 0.004
3	$[0.35, 0.40)$	0.375	-0.003 ± 0.007 ± 0.004
4	$[0.40, 0.50)$	0.447	-0.004 ± 0.005 ± 0.003
5	$[0.50, 0.65)$	0.566	0.002 ± 0.006 ± 0.003
6	$[0.65, 0.80)$	0.714	-0.008 ± 0.008 ± 0.005
7	$[0.80, 1.00)$	0.857	-0.021 ± 0.015 ± 0.008
M_{inv}			
Bin	Range	$\langle M_{\mathrm{inv}} \rangle$ [GeV/c^2]	$A_{UL}^{\sin(\phi_h-\phi_R)}$
0	$[0.0, 0.4)$	0.362	0.002 ± 0.008 ± 0.005
1	$[0.4, 0.5)$	0.451	0.007 ± 0.007 ± 0.004
2	$[0.5, 0.6)$	0.549	0.004 ± 0.007 ± 0.004
3	$[0.6, 0.7)$	0.650	-0.006 ± 0.007 ± 0.004
4	$[0.7, 0.8)$	0.749	-0.024 ± 0.007 ± 0.004
5	$[0.8, 0.9)$	0.846	0.008 ± 0.009 ± 0.005
6	$[0.9, 1.0)$	0.947	0.002 ± 0.010 ± 0.006
7	$[1.0, 1.2)$	1.090	-0.021 ± 0.009 ± 0.005
8	$[1.2, 1.6)$	1.352	-0.011 ± 0.010 ± 0.006
9	$[1.6, 100.0)$	1.957	0.012 ± 0.016 ± 0.009

Table A.6: Results of $A_{UL}^{\sin(\phi_h-\phi_R)}$ for h^+h^- in bins of x, z, and M_{inv}.

h^+h^-			2007 & 2011
		x	
Bin	Range	$\langle x\rangle$	$A_{UL}^{\sin(\phi_h-\phi_R)}$
0	$[0.0025, 0.0080)$	0.006	0.001 ± 0.007 ± 0.006
1	$[0.0080, 0.0130)$	0.011	0.001 ± 0.005 ± 0.004
2	$[0.0130, 0.0200)$	0.016	-0.007 ± 0.004 ± 0.004
3	$[0.0200, 0.0320)$	0.026	0.002 ± 0.004 ± 0.003
4	$[0.0320, 0.0500)$	0.040	0.001 ± 0.004 ± 0.004
5	$[0.0500, 0.0800)$	0.063	-0.001 ± 0.005 ± 0.004
6	$[0.0800, 0.1300)$	0.101	0.012 ± 0.006 ± 0.005
7	$[0.1300, 0.2100)$	0.162	0.003 ± 0.008 ± 0.007
8	$[0.2100, 0.7000)$	0.287	-0.010 ± 0.010 ± 0.008
		z	
Bin	Range	$\langle z\rangle$	$A_{UL}^{\sin(\phi_h-\phi_R)}$
0	$[0.20, 0.25)$	0.238	-0.017 ± 0.013 ± 0.011
1	$[0.25, 0.30)$	0.278	0.006 ± 0.006 ± 0.005
2	$[0.30, 0.35)$	0.326	-0.004 ± 0.005 ± 0.004
3	$[0.35, 0.40)$	0.375	0.000 ± 0.005 ± 0.004
4	$[0.40, 0.50)$	0.447	-0.002 ± 0.004 ± 0.003
5	$[0.50, 0.65)$	0.566	0.004 ± 0.004 ± 0.003
6	$[0.65, 0.80)$	0.714	0.005 ± 0.006 ± 0.005
7	$[0.80, 1.00)$	0.855	-0.007 ± 0.010 ± 0.008
		M_{inv}	
Bin	Range	$\langle M_{\mathrm{inv}}\rangle$ [GeV/c^2]	$A_{UL}^{\sin(\phi_h-\phi_R)}$
0	$[0.0, 0.4)$	0.362	0.002 ± 0.005 ± 0.005
1	$[0.4, 0.5)$	0.451	0.005 ± 0.005 ± 0.004
2	$[0.5, 0.6)$	0.549	0.004 ± 0.005 ± 0.004
3	$[0.6, 0.7)$	0.650	-0.001 ± 0.005 ± 0.004
4	$[0.7, 0.8)$	0.749	-0.004 ± 0.005 ± 0.004
5	$[0.8, 0.9)$	0.846	0.001 ± 0.006 ± 0.005
6	$[0.9, 1.0)$	0.947	0.004 ± 0.007 ± 0.006
7	$[1.0, 1.2)$	1.090	-0.005 ± 0.006 ± 0.005
8	$[1.2, 1.6)$	1.351	-0.011 ± 0.007 ± 0.006
9	$[1.6, 100.0)$	1.947	0.009 ± 0.011 ± 0.010

Table A.7: Results of $A_{UL}^{\sin(2\phi_h-2\phi_R)}$ for h^+h^- in bins of x, z, and $M_{\mathrm{inv}}$for 2007.

h^+h^-			2007
		x	
Bin	Range	$\langle x\rangle$	$A_{UL}^{\sin(2\phi_h-2\phi_R)}$
0	$[0.0025, 0.0080)$	0.006	-0.009 ± 0.010 ± 0.007
1	$[0.0080, 0.0130)$	0.011	0.003 ± 0.007 ± 0.005
2	$[0.0130, 0.0200)$	0.016	0.004 ± 0.006 ± 0.004
3	$[0.0200, 0.0320)$	0.026	-0.006 ± 0.005 ± 0.004
4	$[0.0320, 0.0500)$	0.040	0.000 ± 0.006 ± 0.004
5	$[0.0500, 0.0800)$	0.063	0.005 ± 0.007 ± 0.005
6	$[0.0800, 0.1300)$	0.101	-0.001 ± 0.008 ± 0.006
7	$[0.1300, 0.2100)$	0.162	0.001 ± 0.011 ± 0.007
8	$[0.2100, 0.7000)$	0.286	-0.016 ± 0.014 ± 0.009
		z	
Bin	Range	$\langle z\rangle$	$A_{UL}^{\sin(2\phi_h-2\phi_R)}$
0	$[0.20, 0.25)$	0.238	0.031 ± 0.018 ± 0.012
1	$[0.25, 0.30)$	0.278	0.004 ± 0.008 ± 0.005
2	$[0.30, 0.35)$	0.326	-0.006 ± 0.006 ± 0.004
3	$[0.35, 0.40)$	0.375	-0.001 ± 0.006 ± 0.004
4	$[0.40, 0.50)$	0.447	0.005 ± 0.005 ± 0.003
5	$[0.50, 0.65)$	0.567	-0.010 ± 0.005 ± 0.003
6	$[0.65, 0.80)$	0.714	0.007 ± 0.007 ± 0.005
7	$[0.80, 1.00)$	0.854	-0.005 ± 0.014 ± 0.009
		M_{inv}	
Bin	Range	$\langle M_{\mathrm{inv}}\rangle$ [GeV/c^2]	$A_{UL}^{\sin(2\phi_h-2\phi_R)}$
0	$[0.0, 0.4)$	0.362	-0.005 ± 0.007 ± 0.005
1	$[0.4, 0.5)$	0.451	0.003 ± 0.006 ± 0.004
2	$[0.5, 0.6)$	0.549	-0.005 ± 0.006 ± 0.004
3	$[0.6, 0.7)$	0.650	0.007 ± 0.006 ± 0.004
4	$[0.7, 0.8)$	0.749	0.003 ± 0.007 ± 0.004
5	$[0.8, 0.9)$	0.846	0.007 ± 0.008 ± 0.005
6	$[0.9, 1.0)$	0.947	-0.009 ± 0.009 ± 0.006
7	$[1.0, 1.2)$	1.090	-0.008 ± 0.009 ± 0.006
8	$[1.2, 1.6)$	1.350	-0.017 ± 0.010 ± 0.007
9	$[1.6, 100.0)$	1.938	0.036 ± 0.017 ± 0.011

Table A.8: Results of $A_{UL}^{\sin(2\phi_h-2\phi_R)}$ for h^+h^- in bins of x, z, and $M_{\mathrm{inv}}$for 2011.

h^+h^-			2011
		x	
Bin	Range	$\langle x\rangle$	$A_{UL}^{\sin(2\phi_h-2\phi_R)}$
0	$[0.0025, 0.0080)$	0.006	0.018 ± 0.009 ± 0.006
1	$[0.0080, 0.0130)$	0.011	0.007 ± 0.007 ± 0.005
2	$[0.0130, 0.0200)$	0.016	-0.003 ± 0.007 ± 0.004
3	$[0.0200, 0.0320)$	0.026	0.004 ± 0.006 ± 0.004
4	$[0.0320, 0.0500)$	0.040	0.003 ± 0.007 ± 0.004
5	$[0.0500, 0.0800)$	0.063	0.019 ± 0.008 ± 0.005
6	$[0.0800, 0.1300)$	0.101	-0.007 ± 0.009 ± 0.006
7	$[0.1300, 0.2100)$	0.162	-0.013 ± 0.012 ± 0.007
8	$[0.2100, 0.7000)$	0.288	0.006 ± 0.014 ± 0.009
		z	
Bin	Range	$\langle z\rangle$	$A_{UL}^{\sin(2\phi_h-2\phi_R)}$
0	$[0.20, 0.25)$	0.238	0.020 ± 0.018 ± 0.011
1	$[0.25, 0.30)$	0.278	0.017 ± 0.008 ± 0.005
2	$[0.30, 0.35)$	0.325	0.006 ± 0.007 ± 0.004
3	$[0.35, 0.40)$	0.375	-0.004 ± 0.007 ± 0.004
4	$[0.40, 0.50)$	0.447	-0.001 ± 0.005 ± 0.003
5	$[0.50, 0.65)$	0.566	0.002 ± 0.006 ± 0.004
6	$[0.65, 0.80)$	0.714	0.022 ± 0.008 ± 0.005
7	$[0.80, 1.00)$	0.857	-0.012 ± 0.015 ± 0.009
		M_{inv}	
Bin	Range	$\langle M_{\mathrm{inv}}\rangle$ [GeV/c^2]	$A_{UL}^{\sin(2\phi_h-2\phi_R)}$
0	$[0.0, 0.4)$	0.362	0.013 ± 0.008 ± 0.005
1	$[0.4, 0.5)$	0.451	-0.002 ± 0.007 ± 0.004
2	$[0.5, 0.6)$	0.549	0.001 ± 0.007 ± 0.004
3	$[0.6, 0.7)$	0.650	0.007 ± 0.007 ± 0.005
4	$[0.7, 0.8)$	0.749	0.010 ± 0.007 ± 0.005
5	$[0.8, 0.9)$	0.846	0.011 ± 0.009 ± 0.005
6	$[0.9, 1.0)$	0.947	-0.008 ± 0.010 ± 0.006
7	$[1.0, 1.2)$	1.090	0.004 ± 0.009 ± 0.006
8	$[1.2, 1.6)$	1.352	0.003 ± 0.010 ± 0.007
9	$[1.6, 100.0)$	1.957	0.004 ± 0.017 ± 0.011

Table A.9: Results of $A_{UL}^{\sin(2\phi_h-2\phi_R)}$ for h^+h^- in bins of x, z, and M_{inv}.

h^+h^-			2007 & 2011
		x	
Bin	Range	$\langle x\rangle$	$A_{UL}^{\sin(2\phi_h-2\phi_R)}$
0	$[0.0025, 0.0080)$	0.006	0.006 ± 0.007 ± 0.007
1	$[0.0080, 0.0130)$	0.011	0.005 ± 0.005 ± 0.005
2	$[0.0130, 0.0200)$	0.016	0.001 ± 0.004 ± 0.004
3	$[0.0200, 0.0320)$	0.026	-0.001 ± 0.004 ± 0.004
4	$[0.0320, 0.0500)$	0.040	0.001 ± 0.004 ± 0.004
5	$[0.0500, 0.0800)$	0.063	0.011 ± 0.005 ± 0.005
6	$[0.0800, 0.1300)$	0.101	-0.004 ± 0.006 ± 0.006
7	$[0.1300, 0.2100)$	0.162	-0.005 ± 0.008 ± 0.007
8	$[0.2100, 0.7000)$	0.287	-0.006 ± 0.010 ± 0.009
		z	
Bin	Range	$\langle z\rangle$	$A_{UL}^{\sin(2\phi_h-2\phi_R)}$
0	$[0.20, 0.25)$	0.238	0.025 ± 0.013 ± 0.012
1	$[0.25, 0.30)$	0.278	0.010 ± 0.006 ± 0.005
2	$[0.30, 0.35)$	0.326	0.000 ± 0.005 ± 0.004
3	$[0.35, 0.40)$	0.375	-0.002 ± 0.005 ± 0.004
4	$[0.40, 0.50)$	0.447	0.002 ± 0.004 ± 0.003
5	$[0.50, 0.65)$	0.566	-0.004 ± 0.004 ± 0.004
6	$[0.65, 0.80)$	0.714	0.014 ± 0.006 ± 0.005
7	$[0.80, 1.00)$	0.855	-0.008 ± 0.010 ± 0.009
		M_{inv}	
Bin	Range	$\langle M_{\mathrm{inv}}\rangle$ [GeV/c^2]	$A_{UL}^{\sin(2\phi_h-2\phi_R)}$
0	$[0.0, 0.4)$	0.362	0.003 ± 0.005 ± 0.005
1	$[0.4, 0.5)$	0.451	0.001 ± 0.004 ± 0.004
2	$[0.5, 0.6)$	0.549	-0.002 ± 0.005 ± 0.004
3	$[0.6, 0.7)$	0.650	0.007 ± 0.005 ± 0.005
4	$[0.7, 0.8)$	0.749	0.006 ± 0.005 ± 0.005
5	$[0.8, 0.9)$	0.846	0.009 ± 0.006 ± 0.005
6	$[0.9, 1.0)$	0.947	-0.009 ± 0.007 ± 0.006
7	$[1.0, 1.2)$	1.090	-0.003 ± 0.006 ± 0.006
8	$[1.2, 1.6)$	1.351	-0.008 ± 0.007 ± 0.007
9	$[1.6, 100.0)$	1.947	0.020 ± 0.012 ± 0.011

Table A.10: Results of $A_{UL}^{\sin(2\phi_h)}$ for h^+h^- in bins of x, z, and $M_{\mathrm{inv}}$for 2007.

h^+h^-			2007
x			
Bin	Range	$\langle x\rangle$	$A_{UL}^{\sin(2\phi_h)}$
0	$[0.0025, 0.0080)$	0.006	0.011 ± 0.017 ± 0.011
1	$[0.0080, 0.0130)$	0.011	0.013 ± 0.009 ± 0.006
2	$[0.0130, 0.0200)$	0.016	0.007 ± 0.007 ± 0.004
3	$[0.0200, 0.0320)$	0.026	0.001 ± 0.006 ± 0.004
4	$[0.0320, 0.0500)$	0.040	-0.002 ± 0.006 ± 0.004
5	$[0.0500, 0.0800)$	0.063	-0.010 ± 0.007 ± 0.005
6	$[0.0800, 0.1300)$	0.101	-0.002 ± 0.009 ± 0.006
7	$[0.1300, 0.2100)$	0.162	-0.015 ± 0.011 ± 0.007
8	$[0.2100, 0.7000)$	0.286	0.016 ± 0.015 ± 0.010
z			
Bin	Range	$\langle z\rangle$	$A_{UL}^{\sin(2\phi_h)}$
0	$[0.20, 0.25)$	0.238	0.007 ± 0.023 ± 0.015
1	$[0.25, 0.30)$	0.278	0.010 ± 0.009 ± 0.006
2	$[0.30, 0.35)$	0.326	-0.014 ± 0.007 ± 0.005
3	$[0.35, 0.40)$	0.375	0.002 ± 0.007 ± 0.005
4	$[0.40, 0.50)$	0.447	0.008 ± 0.005 ± 0.004
5	$[0.50, 0.65)$	0.567	0.002 ± 0.006 ± 0.004
6	$[0.65, 0.80)$	0.714	-0.008 ± 0.008 ± 0.005
7	$[0.80, 1.00)$	0.854	-0.003 ± 0.016 ± 0.010
M_{inv}			
Bin	Range	$\langle M_{\mathrm{inv}}\rangle$ [GeV/c^2]	$A_{UL}^{\sin(2\phi_h)}$
0	$[0.0, 0.4)$	0.362	0.002 ± 0.008 ± 0.005
1	$[0.4, 0.5)$	0.451	-0.005 ± 0.007 ± 0.004
2	$[0.5, 0.6)$	0.549	0.006 ± 0.007 ± 0.004
3	$[0.6, 0.7)$	0.650	0.012 ± 0.007 ± 0.005
4	$[0.7, 0.8)$	0.749	0.005 ± 0.007 ± 0.005
5	$[0.8, 0.9)$	0.846	-0.001 ± 0.009 ± 0.006
6	$[0.9, 1.0)$	0.947	-0.007 ± 0.011 ± 0.007
7	$[1.0, 1.2)$	1.090	-0.005 ± 0.010 ± 0.007
8	$[1.2, 1.6)$	1.350	-0.005 ± 0.012 ± 0.008
9	$[1.6, 100.0)$	1.938	-0.033 ± 0.021 ± 0.013

Table A.11: Results of $A_{UL}^{\sin(2\phi_h)}$ for h^+h^- in bins of x, z, and $M_{\mathrm{inv}}$for 2011.

h^+h^-			2011
x			
Bin	Range	$\langle x\rangle$	$A_{UL}^{\sin(2\phi_h)}$
0	$[0.0025, 0.0080)$	0.006	-0.019 ± 0.014 ± 0.010
1	$[0.0080, 0.0130)$	0.011	-0.005 ± 0.009 ± 0.006
2	$[0.0130, 0.0200)$	0.016	0.003 ± 0.007 ± 0.005
3	$[0.0200, 0.0320)$	0.026	0.006 ± 0.007 ± 0.004
4	$[0.0320, 0.0500)$	0.040	0.006 ± 0.007 ± 0.005
5	$[0.0500, 0.0800)$	0.063	-0.005 ± 0.008 ± 0.006
6	$[0.0800, 0.1300)$	0.101	0.018 ± 0.010 ± 0.007
7	$[0.1300, 0.2100)$	0.162	-0.011 ± 0.012 ± 0.008
8	$[0.2100, 0.7000)$	0.288	0.005 ± 0.015 ± 0.010
z			
Bin	Range	$\langle z\rangle$	$A_{UL}^{\sin(2\phi_h)}$
0	$[0.20, 0.25)$	0.238	0.004 ± 0.022 ± 0.015
1	$[0.25, 0.30)$	0.278	0.009 ± 0.010 ± 0.007
2	$[0.30, 0.35)$	0.325	0.005 ± 0.008 ± 0.005
3	$[0.35, 0.40)$	0.375	0.007 ± 0.008 ± 0.005
4	$[0.40, 0.50)$	0.447	-0.002 ± 0.006 ± 0.004
5	$[0.50, 0.65)$	0.566	-0.004 ± 0.006 ± 0.004
6	$[0.65, 0.80)$	0.714	-0.006 ± 0.009 ± 0.006
7	$[0.80, 1.00)$	0.857	0.009 ± 0.017 ± 0.011
M_{inv}			
Bin	Range	$\langle M_{\mathrm{inv}}\rangle$ [GeV/c^2]	$A_{UL}^{\sin(2\phi_h)}$
0	$[0.0, 0.4)$	0.362	-0.002 ± 0.009 ± 0.006
1	$[0.4, 0.5)$	0.451	-0.002 ± 0.007 ± 0.005
2	$[0.5, 0.6)$	0.549	0.007 ± 0.008 ± 0.005
3	$[0.6, 0.7)$	0.650	-0.003 ± 0.008 ± 0.005
4	$[0.7, 0.8)$	0.749	-0.007 ± 0.008 ± 0.006
5	$[0.8, 0.9)$	0.846	0.003 ± 0.010 ± 0.007
6	$[0.9, 1.0)$	0.947	0.015 ± 0.012 ± 0.008
7	$[1.0, 1.2)$	1.090	0.008 ± 0.011 ± 0.007
8	$[1.2, 1.6)$	1.352	0.006 ± 0.012 ± 0.008
9	$[1.6, 100.0)$	1.957	-0.007 ± 0.021 ± 0.014

Table A.12: Results of $A_{UL}^{\sin(2\phi_h)}$ for h^+h^- in bins of x, z, and M_{inv}.

h^+h^-			2007 & 2011
		x	
Bin	Range	$\langle x \rangle$	$A_{UL}^{\sin(2\phi_h)}$
0	$[0.0025, 0.0080)$	0.006	-0.007 ± 0.011 ± 0.011
1	$[0.0080, 0.0130)$	0.011	0.004 ± 0.006 ± 0.006
2	$[0.0130, 0.0200)$	0.016	0.005 ± 0.005 ± 0.005
3	$[0.0200, 0.0320)$	0.026	0.003 ± 0.004 ± 0.004
4	$[0.0320, 0.0500)$	0.040	0.001 ± 0.005 ± 0.005
5	$[0.0500, 0.0800)$	0.063	-0.008 ± 0.005 ± 0.006
6	$[0.0800, 0.1300)$	0.101	0.007 ± 0.007 ± 0.007
7	$[0.1300, 0.2100)$	0.162	-0.013 ± 0.008 ± 0.008
8	$[0.2100, 0.7000)$	0.287	0.010 ± 0.011 ± 0.010
		z	
Bin	Range	$\langle z \rangle$	$A_{UL}^{\sin(2\phi_h)}$
0	$[0.20, 0.25)$	0.238	0.005 ± 0.016 ± 0.015
1	$[0.25, 0.30)$	0.278	0.009 ± 0.007 ± 0.007
2	$[0.30, 0.35)$	0.326	-0.005 ± 0.005 ± 0.005
3	$[0.35, 0.40)$	0.375	0.004 ± 0.005 ± 0.005
4	$[0.40, 0.50)$	0.447	0.003 ± 0.004 ± 0.004
5	$[0.50, 0.65)$	0.566	0.000 ± 0.004 ± 0.004
6	$[0.65, 0.80)$	0.714	-0.007 ± 0.006 ± 0.006
7	$[0.80, 1.00)$	0.855	0.003 ± 0.012 ± 0.011
		M_{inv}	
Bin	Range	$\langle M_{\text{inv}} \rangle$ [GeV/c^2]	$A_{UL}^{\sin(2\phi_h)}$
0	$[0.0, 0.4)$	0.362	0.000 ± 0.006 ± 0.006
1	$[0.4, 0.5)$	0.451	-0.004 ± 0.005 ± 0.005
2	$[0.5, 0.6)$	0.549	0.006 ± 0.005 ± 0.005
3	$[0.6, 0.7)$	0.650	0.005 ± 0.005 ± 0.005
4	$[0.7, 0.8)$	0.749	-0.001 ± 0.005 ± 0.006
5	$[0.8, 0.9)$	0.846	0.001 ± 0.007 ± 0.007
6	$[0.9, 1.0)$	0.947	0.003 ± 0.008 ± 0.008
7	$[1.0, 1.2)$	1.090	0.001 ± 0.007 ± 0.007
8	$[1.2, 1.6)$	1.351	0.000 ± 0.008 ± 0.008
9	$[1.6, 100.0)$	1.947	-0.020 ± 0.015 ± 0.014

Table A.13: Results of $A_{UL}^{\sin(\phi_h+\phi_R)}$ for h^+h^- in bins of x, z, and $M_{\text{inv}}$for 2007.

h^+h^-			2007
		x	
Bin	Range	$\langle x \rangle$	$A_{UL}^{\sin(\phi_h+\phi_R)}$
0	$[0.0025, 0.0080)$	0.006	0.051 ± 0.017 ± 0.012
1	$[0.0080, 0.0130)$	0.011	-0.010 ± 0.009 ± 0.006
2	$[0.0130, 0.0200)$	0.016	0.004 ± 0.007 ± 0.005
3	$[0.0200, 0.0320)$	0.026	0.002 ± 0.006 ± 0.004
4	$[0.0320, 0.0500)$	0.040	0.005 ± 0.006 ± 0.004
5	$[0.0500, 0.0800)$	0.063	-0.001 ± 0.007 ± 0.005
6	$[0.0800, 0.1300)$	0.101	-0.011 ± 0.009 ± 0.006
7	$[0.1300, 0.2100)$	0.162	-0.003 ± 0.011 ± 0.008
8	$[0.2100, 0.7000)$	0.286	-0.011 ± 0.015 ± 0.011
		z	
Bin	Range	$\langle z \rangle$	$A_{UL}^{\sin(\phi_h+\phi_R)}$
0	$[0.20, 0.25)$	0.238	0.005 ± 0.023 ± 0.017
1	$[0.25, 0.30)$	0.278	-0.005 ± 0.009 ± 0.007
2	$[0.30, 0.35)$	0.326	-0.003 ± 0.007 ± 0.005
3	$[0.35, 0.40)$	0.375	0.001 ± 0.007 ± 0.005
4	$[0.40, 0.50)$	0.447	0.002 ± 0.005 ± 0.004
5	$[0.50, 0.65)$	0.567	0.002 ± 0.006 ± 0.004
6	$[0.65, 0.80)$	0.714	0.009 ± 0.008 ± 0.006
7	$[0.80, 1.00)$	0.854	0.000 ± 0.016 ± 0.011
		M_{inv}	
Bin	Range	$\langle M_{\text{inv}} \rangle$ [GeV/c^2]	$A_{UL}^{\sin(\phi_h+\phi_R)}$
0	$[0.0, 0.4)$	0.362	0.000 ± 0.008 ± 0.006
1	$[0.4, 0.5)$	0.451	0.009 ± 0.007 ± 0.005
2	$[0.5, 0.6)$	0.549	-0.011 ± 0.007 ± 0.005
3	$[0.6, 0.7)$	0.650	0.014 ± 0.007 ± 0.005
4	$[0.7, 0.8)$	0.749	-0.001 ± 0.007 ± 0.005
5	$[0.8, 0.9)$	0.846	-0.008 ± 0.009 ± 0.006
6	$[0.9, 1.0)$	0.947	0.004 ± 0.011 ± 0.008
7	$[1.0, 1.2)$	1.090	0.003 ± 0.010 ± 0.007
8	$[1.2, 1.6)$	1.350	0.001 ± 0.012 ± 0.008
9	$[1.6, 100.0)$	1.938	-0.016 ± 0.021 ± 0.015

Table A.14: Results of $A_{UL}^{\sin(\phi_h+\phi_R)}$ for h^+h^- in bins of x, z, and $M_{\text{inv}}$for 2011.

h^+h^-			2011
		x	
Bin	Range	$\langle x\rangle$	$A_{UL}^{\sin(\phi_h+\phi_R)}$
0	$[0.0025, 0.0080)$	0.006	-0.010 ± 0.014 ± 0.008
1	$[0.0080, 0.0130)$	0.011	0.005 ± 0.009 ± 0.005
2	$[0.0130, 0.0200)$	0.016	-0.005 ± 0.007 ± 0.004
3	$[0.0200, 0.0320)$	0.026	-0.007 ± 0.006 ± 0.004
4	$[0.0320, 0.0500)$	0.040	-0.006 ± 0.007 ± 0.004
5	$[0.0500, 0.0800)$	0.063	-0.003 ± 0.008 ± 0.005
6	$[0.0800, 0.1300)$	0.101	-0.018 ± 0.010 ± 0.006
7	$[0.1300, 0.2100)$	0.162	-0.019 ± 0.012 ± 0.007
8	$[0.2100, 0.7000)$	0.288	-0.005 ± 0.015 ± 0.009
		z	
Bin	Range	$\langle z\rangle$	$A_{UL}^{\sin(\phi_h+\phi_R)}$
0	$[0.20, 0.25)$	0.238	0.011 ± 0.022 ± 0.013
1	$[0.25, 0.30)$	0.278	0.005 ± 0.010 ± 0.006
2	$[0.30, 0.35)$	0.325	0.002 ± 0.008 ± 0.005
3	$[0.35, 0.40)$	0.375	-0.013 ± 0.008 ± 0.005
4	$[0.40, 0.50)$	0.447	-0.004 ± 0.006 ± 0.003
5	$[0.50, 0.65)$	0.566	-0.015 ± 0.006 ± 0.004
6	$[0.65, 0.80)$	0.714	-0.008 ± 0.009 ± 0.005
7	$[0.80, 1.00)$	0.857	-0.012 ± 0.017 ± 0.010
		M_{inv}	
Bin	Range	$\langle M_{\text{inv}}\rangle$ [GeV/c^2]	$A_{UL}^{\sin(\phi_h+\phi_R)}$
0	$[0.0, 0.4)$	0.362	0.007 ± 0.009 ± 0.005
1	$[0.4, 0.5)$	0.451	-0.010 ± 0.007 ± 0.004
2	$[0.5, 0.6)$	0.549	-0.009 ± 0.008 ± 0.004
3	$[0.6, 0.7)$	0.650	-0.009 ± 0.008 ± 0.005
4	$[0.7, 0.8)$	0.749	-0.003 ± 0.008 ± 0.005
5	$[0.8, 0.9)$	0.846	0.006 ± 0.010 ± 0.006
6	$[0.9, 1.0)$	0.947	-0.025 ± 0.012 ± 0.007
7	$[1.0, 1.2)$	1.090	-0.015 ± 0.011 ± 0.006
8	$[1.2, 1.6)$	1.352	-0.006 ± 0.012 ± 0.007
9	$[1.6, 100.0)$	1.957	-0.003 ± 0.021 ± 0.012

Table A.15: Results of $A_{UL}^{\sin(\phi_h+\phi_R)}$ for h^+h^- in bins of x, z, and M_{inv}.

h^+h^-			2007 & 2011
		x	
Bin	Range	$\langle x\rangle$	$A_{UL}^{\sin(\phi_h+\phi_R)}$
0	$[0.0025, 0.0080)$	0.006	0.014 ± 0.011 ± 0.012
1	$[0.0080, 0.0130)$	0.011	-0.003 ± 0.006 ± 0.006
2	$[0.0130, 0.0200)$	0.016	0.000 ± 0.005 ± 0.005
3	$[0.0200, 0.0320)$	0.026	-0.002 ± 0.004 ± 0.004
4	$[0.0320, 0.0500)$	0.040	0.001 ± 0.005 ± 0.004
5	$[0.0500, 0.0800)$	0.063	-0.002 ± 0.005 ± 0.005
6	$[0.0800, 0.1300)$	0.101	-0.014 ± 0.007 ± 0.006
7	$[0.1300, 0.2100)$	0.162	-0.011 ± 0.008 ± 0.008
8	$[0.2100, 0.7000)$	0.287	-0.008 ± 0.010 ± 0.011
		z	
Bin	Range	$\langle z\rangle$	$A_{UL}^{\sin(\phi_h+\phi_R)}$
0	$[0.20, 0.25)$	0.238	0.008 ± 0.016 ± 0.017
1	$[0.25, 0.30)$	0.278	0.000 ± 0.007 ± 0.007
2	$[0.30, 0.35)$	0.326	-0.001 ± 0.005 ± 0.005
3	$[0.35, 0.40)$	0.375	-0.006 ± 0.005 ± 0.005
4	$[0.40, 0.50)$	0.447	-0.001 ± 0.004 ± 0.004
5	$[0.50, 0.65)$	0.566	-0.005 ± 0.004 ± 0.004
6	$[0.65, 0.80)$	0.714	0.002 ± 0.006 ± 0.006
7	$[0.80, 1.00)$	0.855	-0.006 ± 0.011 ± 0.011
		M_{inv}	
Bin	Range	$\langle M_{\text{inv}}\rangle$ [GeV/c^2]	$A_{UL}^{\sin(\phi_h+\phi_R)}$
0	$[0.0, 0.4)$	0.362	0.003 ± 0.006 ± 0.006
1	$[0.4, 0.5)$	0.451	0.001 ± 0.005 ± 0.005
2	$[0.5, 0.6)$	0.549	-0.010 ± 0.005 ± 0.005
3	$[0.6, 0.7)$	0.650	0.003 ± 0.005 ± 0.005
4	$[0.7, 0.8)$	0.749	-0.002 ± 0.005 ± 0.005
5	$[0.8, 0.9)$	0.846	-0.001 ± 0.007 ± 0.006
6	$[0.9, 1.0)$	0.947	-0.010 ± 0.008 ± 0.008
7	$[1.0, 1.2)$	1.090	-0.006 ± 0.007 ± 0.007
8	$[1.2, 1.6)$	1.351	-0.002 ± 0.008 ± 0.008
9	$[1.6, 100.0)$	1.947	-0.010 ± 0.015 ± 0.015

Table A.16: Results of $A_{UL}^{\sin(2\phi_R)}$ for h^+h^- in bins of x, z, and $M_{\text{inv}}$for 2007.

h^+h^-			2007
		x	
Bin	Range	$\langle x \rangle$	$A_{UL}^{\sin(2\phi_R)}$
0	$[0.0025, 0.0080)$	0.006	0.029 ± 0.017 ± 0.011
1	$[0.0080, 0.0130)$	0.011	0.004 ± 0.009 ± 0.006
2	$[0.0130, 0.0200)$	0.016	-0.004 ± 0.007 ± 0.004
3	$[0.0200, 0.0320)$	0.026	-0.012 ± 0.006 ± 0.004
4	$[0.0320, 0.0500)$	0.040	-0.010 ± 0.006 ± 0.004
5	$[0.0500, 0.0800)$	0.063	-0.006 ± 0.007 ± 0.005
6	$[0.0800, 0.1300)$	0.101	0.004 ± 0.009 ± 0.006
7	$[0.1300, 0.2100)$	0.162	0.032 ± 0.011 ± 0.007
8	$[0.2100, 0.7000)$	0.286	0.011 ± 0.015 ± 0.010
		z	
Bin	Range	$\langle z \rangle$	$A_{UL}^{\sin(2\phi_R)}$
0	$[0.20, 0.25)$	0.238	-0.034 ± 0.023 ± 0.015
1	$[0.25, 0.30)$	0.278	0.000 ± 0.009 ± 0.006
2	$[0.30, 0.35)$	0.326	-0.011 ± 0.007 ± 0.005
3	$[0.35, 0.40)$	0.375	0.001 ± 0.007 ± 0.005
4	$[0.40, 0.50)$	0.447	0.001 ± 0.005 ± 0.004
5	$[0.50, 0.65)$	0.567	-0.001 ± 0.006 ± 0.004
6	$[0.65, 0.80)$	0.714	-0.005 ± 0.008 ± 0.005
7	$[0.80, 1.00)$	0.854	0.002 ± 0.016 ± 0.010
		M_{inv}	
Bin	Range	$\langle M_{\text{inv}} \rangle$ [GeV/c^2]	$A_{UL}^{\sin(2\phi_R)}$
0	$[0.0, 0.4)$	0.362	0.000 ± 0.008 ± 0.005
1	$[0.4, 0.5)$	0.451	0.002 ± 0.007 ± 0.004
2	$[0.5, 0.6)$	0.549	-0.004 ± 0.007 ± 0.004
3	$[0.6, 0.7)$	0.650	-0.002 ± 0.007 ± 0.005
4	$[0.7, 0.8)$	0.749	-0.005 ± 0.007 ± 0.005
5	$[0.8, 0.9)$	0.846	-0.003 ± 0.009 ± 0.006
6	$[0.9, 1.0)$	0.947	-0.003 ± 0.011 ± 0.007
7	$[1.0, 1.2)$	1.090	-0.006 ± 0.010 ± 0.007
8	$[1.2, 1.6)$	1.350	0.000 ± 0.012 ± 0.008
9	$[1.6, 100.0)$	1.938	-0.012 ± 0.021 ± 0.013

Table A.17: Results of $A_{UL}^{\sin(2\phi_R)}$ for h^+h^- in bins of x, z, and $M_{\text{inv}}$for 2011.

h^+h^-			2011
		x	
Bin	Range	$\langle x \rangle$	$A_{UL}^{\sin(2\phi_R)}$
0	$[0.0025, 0.0080)$	0.006	-0.013 ± 0.014 ± 0.011
1	$[0.0080, 0.0130)$	0.011	-0.012 ± 0.009 ± 0.007
2	$[0.0130, 0.0200)$	0.016	-0.001 ± 0.007 ± 0.006
3	$[0.0200, 0.0320)$	0.026	0.009 ± 0.006 ± 0.005
4	$[0.0320, 0.0500)$	0.040	0.006 ± 0.007 ± 0.005
5	$[0.0500, 0.0800)$	0.063	-0.003 ± 0.008 ± 0.006
6	$[0.0800, 0.1300)$	0.101	0.012 ± 0.010 ± 0.007
7	$[0.1300, 0.2100)$	0.162	0.001 ± 0.012 ± 0.009
8	$[0.2100, 0.7000)$	0.288	0.031 ± 0.015 ± 0.011
		z	
Bin	Range	$\langle z \rangle$	$A_{UL}^{\sin(2\phi_R)}$
0	$[0.20, 0.25)$	0.238	0.022 ± 0.022 ± 0.016
1	$[0.25, 0.30)$	0.278	0.017 ± 0.010 ± 0.007
2	$[0.30, 0.35)$	0.325	0.009 ± 0.008 ± 0.006
3	$[0.35, 0.40)$	0.375	0.005 ± 0.008 ± 0.006
4	$[0.40, 0.50)$	0.447	-0.008 ± 0.006 ± 0.005
5	$[0.50, 0.65)$	0.566	-0.001 ± 0.006 ± 0.005
6	$[0.65, 0.80)$	0.714	-0.005 ± 0.009 ± 0.007
7	$[0.80, 1.00)$	0.857	0.003 ± 0.017 ± 0.012
		M_{inv}	
Bin	Range	$\langle M_{\text{inv}} \rangle$ [GeV/c^2]	$A_{UL}^{\sin(2\phi_R)}$
0	$[0.0, 0.4)$	0.362	0.005 ± 0.009 ± 0.007
1	$[0.4, 0.5)$	0.451	0.007 ± 0.007 ± 0.006
2	$[0.5, 0.6)$	0.549	-0.004 ± 0.008 ± 0.006
3	$[0.6, 0.7)$	0.650	0.002 ± 0.008 ± 0.006
4	$[0.7, 0.8)$	0.749	0.000 ± 0.008 ± 0.006
5	$[0.8, 0.9)$	0.846	-0.004 ± 0.010 ± 0.007
6	$[0.9, 1.0)$	0.947	0.010 ± 0.012 ± 0.009
7	$[1.0, 1.2)$	1.090	0.004 ± 0.011 ± 0.008
8	$[1.2, 1.6)$	1.352	0.011 ± 0.012 ± 0.009
9	$[1.6, 100.0)$	1.957	-0.024 ± 0.021 ± 0.015

Table A.18: Results of $A_{UL}^{\sin(2\phi_R)}$ for h^+h^- in bins of x, z, and $M_{\rm inv}$.

h^+h^-			2007 & 2011
		x	
Bin	Range	$\langle x\rangle$	$A_{UL}^{\sin(2\phi_R)}$
0	$[0.0025, 0.0080)$	0.006	0.004 ± 0.011 ± 0.011
1	$[0.0080, 0.0130)$	0.011	-0.004 ± 0.006 ± 0.007
2	$[0.0130, 0.0200)$	0.016	-0.003 ± 0.005 ± 0.006
3	$[0.0200, 0.0320)$	0.026	-0.003 ± 0.004 ± 0.005
4	$[0.0320, 0.0500)$	0.040	-0.004 ± 0.005 ± 0.005
5	$[0.0500, 0.0800)$	0.063	-0.005 ± 0.005 ± 0.006
6	$[0.0800, 0.1300)$	0.101	0.008 ± 0.007 ± 0.007
7	$[0.1300, 0.2100)$	0.162	0.018 ± 0.008 ± 0.009
8	$[0.2100, 0.7000)$	0.287	0.021 ± 0.011 ± 0.011
		z	
Bin	Range	$\langle z\rangle$	$A_{UL}^{\sin(2\phi_R)}$
0	$[0.20, 0.25)$	0.238	-0.004 ± 0.016 ± 0.016
1	$[0.25, 0.30)$	0.278	0.008 ± 0.007 ± 0.007
2	$[0.30, 0.35)$	0.326	-0.002 ± 0.005 ± 0.006
3	$[0.35, 0.40)$	0.375	0.003 ± 0.005 ± 0.006
4	$[0.40, 0.50)$	0.447	-0.003 ± 0.004 ± 0.004
5	$[0.50, 0.65)$	0.566	-0.001 ± 0.004 ± 0.005
6	$[0.65, 0.80)$	0.714	-0.005 ± 0.006 ± 0.007
7	$[0.80, 1.00)$	0.855	0.003 ± 0.011 ± 0.012
		$M_{\rm inv}$	
Bin	Range	$\langle M_{\rm inv}\rangle$ [GeV/c^2]	$A_{UL}^{\sin(2\phi_R)}$
0	$[0.0, 0.4)$	0.362	0.002 ± 0.006 ± 0.007
1	$[0.4, 0.5)$	0.451	0.004 ± 0.005 ± 0.006
2	$[0.5, 0.6)$	0.549	-0.004 ± 0.005 ± 0.006
3	$[0.6, 0.7)$	0.650	-0.001 ± 0.005 ± 0.006
4	$[0.7, 0.8)$	0.749	-0.003 ± 0.005 ± 0.006
5	$[0.8, 0.9)$	0.846	-0.004 ± 0.007 ± 0.007
6	$[0.9, 1.0)$	0.947	0.003 ± 0.008 ± 0.009
7	$[1.0, 1.2)$	1.090	-0.001 ± 0.007 ± 0.008
8	$[1.2, 1.6)$	1.351	0.005 ± 0.008 ± 0.009
9	$[1.6, 100.0)$	1.947	-0.018 ± 0.015 ± 0.015

Table A.19: Results of $A_{UL}^{\sin(3\phi_h-\phi_R)}$ for h^+h^- in bins of x, z, and $M_{\rm inv}$for 2007.

h^+h^-			2007
		x	
Bin	Range	$\langle x\rangle$	$A_{UL}^{\sin(3\phi_h-\phi_R)}$
0	$[0.0025, 0.0080)$	0.006	0.026 ± 0.017 ± 0.012
1	$[0.0080, 0.0130)$	0.011	0.004 ± 0.009 ± 0.006
2	$[0.0130, 0.0200)$	0.016	-0.011 ± 0.007 ± 0.005
3	$[0.0200, 0.0320)$	0.026	0.003 ± 0.006 ± 0.004
4	$[0.0320, 0.0500)$	0.040	0.009 ± 0.006 ± 0.004
5	$[0.0500, 0.0800)$	0.063	-0.010 ± 0.007 ± 0.005
6	$[0.0800, 0.1300)$	0.101	-0.005 ± 0.009 ± 0.006
7	$[0.1300, 0.2100)$	0.162	0.017 ± 0.011 ± 0.008
8	$[0.2100, 0.7000)$	0.286	-0.014 ± 0.015 ± 0.011
		z	
Bin	Range	$\langle z\rangle$	$A_{UL}^{\sin(3\phi_h-\phi_R)}$
0	$[0.20, 0.25)$	0.238	-0.009 ± 0.023 ± 0.016
1	$[0.25, 0.30)$	0.278	-0.017 ± 0.009 ± 0.007
2	$[0.30, 0.35)$	0.326	0.002 ± 0.007 ± 0.005
3	$[0.35, 0.40)$	0.375	0.011 ± 0.007 ± 0.005
4	$[0.40, 0.50)$	0.447	0.002 ± 0.005 ± 0.004
5	$[0.50, 0.65)$	0.567	-0.010 ± 0.006 ± 0.004
6	$[0.65, 0.80)$	0.714	0.018 ± 0.008 ± 0.006
7	$[0.80, 1.00)$	0.854	0.012 ± 0.016 ± 0.011
		$M_{\rm inv}$	
Bin	Range	$\langle M_{\rm inv}\rangle$ [GeV/c^2]	$A_{UL}^{\sin(3\phi_h-\phi_R)}$
0	$[0.0, 0.4)$	0.362	-0.015 ± 0.008 ± 0.006
1	$[0.4, 0.5)$	0.451	-0.009 ± 0.007 ± 0.005
2	$[0.5, 0.6)$	0.549	0.001 ± 0.007 ± 0.005
3	$[0.6, 0.7)$	0.650	0.004 ± 0.007 ± 0.005
4	$[0.7, 0.8)$	0.749	0.014 ± 0.007 ± 0.005
5	$[0.8, 0.9)$	0.846	-0.001 ± 0.009 ± 0.006
6	$[0.9, 1.0)$	0.947	0.002 ± 0.011 ± 0.008
7	$[1.0, 1.2)$	1.090	0.005 ± 0.010 ± 0.007
8	$[1.2, 1.6)$	1.350	0.018 ± 0.012 ± 0.008
9	$[1.6, 100.0)$	1.938	-0.011 ± 0.021 ± 0.015

Table A.20: Results of $A_{UL}^{\sin(3\phi_h-\phi_R)}$ for h^+h^- in bins of x, z, and $M_{\text{inv}}$for 2011.

h^+h^-			2011
		x	
Bin	Range	$\langle x\rangle$	$A_{UL}^{\sin(3\phi_h-\phi_R)}$
0	$[0.0025, 0.0080)$	0.006	0.013 ± 0.014 ± 0.008
1	$[0.0080, 0.0130)$	0.011	-0.013 ± 0.009 ± 0.005
2	$[0.0130, 0.0200)$	0.016	-0.004 ± 0.007 ± 0.004
3	$[0.0200, 0.0320)$	0.026	0.007 ± 0.006 ± 0.004
4	$[0.0320, 0.0500)$	0.040	-0.007 ± 0.007 ± 0.004
5	$[0.0500, 0.0800)$	0.063	0.006 ± 0.008 ± 0.005
6	$[0.0800, 0.1300)$	0.101	-0.010 ± 0.010 ± 0.006
7	$[0.1300, 0.2100)$	0.162	0.004 ± 0.012 ± 0.007
8	$[0.2100, 0.7000)$	0.288	-0.001 ± 0.015 ± 0.009
		z	
Bin	Range	$\langle z\rangle$	$A_{UL}^{\sin(3\phi_h-\phi_R)}$
0	$[0.20, 0.25)$	0.238	-0.021 ± 0.022 ± 0.013
1	$[0.25, 0.30)$	0.278	0.004 ± 0.010 ± 0.006
2	$[0.30, 0.35)$	0.325	0.001 ± 0.008 ± 0.005
3	$[0.35, 0.40)$	0.375	-0.006 ± 0.008 ± 0.005
4	$[0.40, 0.50)$	0.447	-0.008 ± 0.006 ± 0.004
5	$[0.50, 0.65)$	0.566	0.006 ± 0.006 ± 0.004
6	$[0.65, 0.80)$	0.714	0.009 ± 0.009 ± 0.006
7	$[0.80, 1.00)$	0.857	-0.019 ± 0.017 ± 0.010
		M_{inv}	
Bin	Range	$\langle M_{\text{inv}}\rangle$ [GeV/c^2]	$A_{UL}^{\sin(3\phi_h-\phi_R)}$
0	$[0.0, 0.4)$	0.362	0.001 ± 0.009 ± 0.005
1	$[0.4, 0.5)$	0.451	0.003 ± 0.007 ± 0.004
2	$[0.5, 0.6)$	0.549	-0.010 ± 0.008 ± 0.005
3	$[0.6, 0.7)$	0.650	0.005 ± 0.008 ± 0.005
4	$[0.7, 0.8)$	0.749	0.000 ± 0.008 ± 0.005
5	$[0.8, 0.9)$	0.846	-0.004 ± 0.010 ± 0.006
6	$[0.9, 1.0)$	0.947	0.000 ± 0.012 ± 0.007
7	$[1.0, 1.2)$	1.090	0.003 ± 0.011 ± 0.006
8	$[1.2, 1.6)$	1.352	0.009 ± 0.012 ± 0.007
9	$[1.6, 100.0)$	1.957	-0.043 ± 0.021 ± 0.012

Table A.21: Results of $A_{UL}^{\sin(3\phi_h-\phi_R)}$ for h^+h^- in bins of x, z, and M_{inv}.

h^+h^-			2007 & 2011
		x	
Bin	Range	$\langle x\rangle$	$A_{UL}^{\sin(3\phi_h-\phi_R)}$
0	$[0.0025, 0.0080)$	0.006	0.018 ± 0.011 ± 0.012
1	$[0.0080, 0.0130)$	0.011	-0.005 ± 0.006 ± 0.006
2	$[0.0130, 0.0200)$	0.016	-0.008 ± 0.005 ± 0.005
3	$[0.0200, 0.0320)$	0.026	0.005 ± 0.004 ± 0.004
4	$[0.0320, 0.0500)$	0.040	0.002 ± 0.005 ± 0.004
5	$[0.0500, 0.0800)$	0.063	-0.003 ± 0.005 ± 0.005
6	$[0.0800, 0.1300)$	0.101	-0.007 ± 0.007 ± 0.006
7	$[0.1300, 0.2100)$	0.162	0.011 ± 0.008 ± 0.008
8	$[0.2100, 0.7000)$	0.287	-0.007 ± 0.011 ± 0.011
		z	
Bin	Range	$\langle z\rangle$	$A_{UL}^{\sin(3\phi_h-\phi_R)}$
0	$[0.20, 0.25)$	0.238	-0.015 ± 0.016 ± 0.016
1	$[0.25, 0.30)$	0.278	-0.007 ± 0.007 ± 0.007
2	$[0.30, 0.35)$	0.326	0.002 ± 0.005 ± 0.005
3	$[0.35, 0.40)$	0.375	0.003 ± 0.005 ± 0.005
4	$[0.40, 0.50)$	0.447	-0.003 ± 0.004 ± 0.004
5	$[0.50, 0.65)$	0.566	-0.003 ± 0.004 ± 0.004
6	$[0.65, 0.80)$	0.714	0.014 ± 0.006 ± 0.006
7	$[0.80, 1.00)$	0.855	-0.003 ± 0.011 ± 0.011
		M_{inv}	
Bin	Range	$\langle M_{\text{inv}}\rangle$ [GeV/c^2]	$A_{UL}^{\sin(3\phi_h-\phi_R)}$
0	$[0.0, 0.4)$	0.362	-0.008 ± 0.006 ± 0.006
1	$[0.4, 0.5)$	0.451	-0.004 ± 0.005 ± 0.005
2	$[0.5, 0.6)$	0.549	-0.004 ± 0.005 ± 0.005
3	$[0.6, 0.7)$	0.650	0.004 ± 0.005 ± 0.005
4	$[0.7, 0.8)$	0.749	0.008 ± 0.005 ± 0.005
5	$[0.8, 0.9)$	0.846	-0.002 ± 0.007 ± 0.006
6	$[0.9, 1.0)$	0.947	0.001 ± 0.008 ± 0.008
7	$[1.0, 1.2)$	1.090	0.004 ± 0.007 ± 0.007
8	$[1.2, 1.6)$	1.351	0.014 ± 0.008 ± 0.008
9	$[1.6, 100.0)$	1.947	-0.027 ± 0.015 ± 0.015

Table A.22: Results of $A_{UL}^{\sin(4\phi_h-2\phi_R)}$ for h^+h^- in bins of x, z, and $M_{\mathrm{inv}}$for 2007.

h^+h^-			2007
		x	
Bin	Range	$\langle x\rangle$	$A_{UL}^{\sin(4\phi_h-2\phi_R)}$
0	$[0.0025, 0.0080)$	0.006	0.003 ± 0.017 ± 0.011
1	$[0.0080, 0.0130)$	0.011	-0.013 ± 0.009 ± 0.006
2	$[0.0130, 0.0200)$	0.016	0.000 ± 0.007 ± 0.004
3	$[0.0200, 0.0320)$	0.026	-0.008 ± 0.006 ± 0.004
4	$[0.0320, 0.0500)$	0.040	0.003 ± 0.006 ± 0.004
5	$[0.0500, 0.0800)$	0.063	-0.015 ± 0.007 ± 0.004
6	$[0.0800, 0.1300)$	0.101	-0.004 ± 0.009 ± 0.005
7	$[0.1300, 0.2100)$	0.162	0.002 ± 0.011 ± 0.007
8	$[0.2100, 0.7000)$	0.286	-0.024 ± 0.015 ± 0.009
		z	
Bin	Range	$\langle z\rangle$	$A_{UL}^{\sin(4\phi_h-2\phi_R)}$
0	$[0.20, 0.25)$	0.238	-0.006 ± 0.023 ± 0.014
1	$[0.25, 0.30)$	0.278	-0.009 ± 0.009 ± 0.006
2	$[0.30, 0.35)$	0.326	-0.010 ± 0.007 ± 0.005
3	$[0.35, 0.40)$	0.375	0.008 ± 0.007 ± 0.004
4	$[0.40, 0.50)$	0.447	-0.003 ± 0.005 ± 0.003
5	$[0.50, 0.65)$	0.567	-0.014 ± 0.006 ± 0.003
6	$[0.65, 0.80)$	0.714	0.008 ± 0.008 ± 0.005
7	$[0.80, 1.00)$	0.854	-0.016 ± 0.016 ± 0.010
		M_{inv}	
Bin	Range	$\langle M_{\mathrm{inv}}\rangle$ [GeV/c^2]	$A_{UL}^{\sin(4\phi_h-2\phi_R)}$
0	$[0.0, 0.4)$	0.362	-0.001 ± 0.008 ± 0.005
1	$[0.4, 0.5)$	0.451	0.005 ± 0.007 ± 0.004
2	$[0.5, 0.6)$	0.549	-0.003 ± 0.007 ± 0.004
3	$[0.6, 0.7)$	0.650	-0.014 ± 0.007 ± 0.005
4	$[0.7, 0.8)$	0.749	-0.012 ± 0.007 ± 0.005
5	$[0.8, 0.9)$	0.846	-0.004 ± 0.009 ± 0.006
6	$[0.9, 1.0)$	0.947	-0.019 ± 0.011 ± 0.007
7	$[1.0, 1.2)$	1.090	0.005 ± 0.010 ± 0.006
8	$[1.2, 1.6)$	1.350	-0.009 ± 0.012 ± 0.007
9	$[1.6, 100.0)$	1.938	-0.008 ± 0.021 ± 0.013

Table A.23: Results of $A_{UL}^{\sin(4\phi_h-2\phi_R)}$ for h^+h^- in bins of x, z, and $M_{\mathrm{inv}}$for 2011.

h^+h^-			2011
		x	
Bin	Range	$\langle x\rangle$	$A_{UL}^{\sin(4\phi_h-2\phi_R)}$
0	$[0.0025, 0.0080)$	0.006	-0.010 ± 0.014 ± 0.007
1	$[0.0080, 0.0130)$	0.011	-0.007 ± 0.009 ± 0.005
2	$[0.0130, 0.0200)$	0.016	-0.008 ± 0.007 ± 0.004
3	$[0.0200, 0.0320)$	0.026	-0.006 ± 0.006 ± 0.003
4	$[0.0320, 0.0500)$	0.040	-0.009 ± 0.007 ± 0.004
5	$[0.0500, 0.0800)$	0.063	0.017 ± 0.008 ± 0.004
6	$[0.0800, 0.1300)$	0.101	-0.009 ± 0.010 ± 0.005
7	$[0.1300, 0.2100)$	0.162	-0.010 ± 0.012 ± 0.006
8	$[0.2100, 0.7000)$	0.288	0.009 ± 0.015 ± 0.008
		z	
Bin	Range	$\langle z\rangle$	$A_{UL}^{\sin(4\phi_h-2\phi_R)}$
0	$[0.20, 0.25)$	0.238	0.023 ± 0.022 ± 0.011
1	$[0.25, 0.30)$	0.278	-0.011 ± 0.010 ± 0.005
2	$[0.30, 0.35)$	0.325	-0.007 ± 0.008 ± 0.004
3	$[0.35, 0.40)$	0.375	-0.005 ± 0.008 ± 0.004
4	$[0.40, 0.50)$	0.447	-0.008 ± 0.006 ± 0.003
5	$[0.50, 0.65)$	0.566	0.004 ± 0.006 ± 0.003
6	$[0.65, 0.80)$	0.714	-0.009 ± 0.009 ± 0.005
7	$[0.80, 1.00)$	0.857	-0.006 ± 0.017 ± 0.009
		M_{inv}	
Bin	Range	$\langle M_{\mathrm{inv}}\rangle$ [GeV/c^2]	$A_{UL}^{\sin(4\phi_h-2\phi_R)}$
0	$[0.0, 0.4)$	0.362	-0.005 ± 0.009 ± 0.005
1	$[0.4, 0.5)$	0.451	-0.005 ± 0.007 ± 0.004
2	$[0.5, 0.6)$	0.549	-0.010 ± 0.008 ± 0.004
3	$[0.6, 0.7)$	0.650	-0.004 ± 0.008 ± 0.004
4	$[0.7, 0.8)$	0.749	-0.010 ± 0.008 ± 0.004
5	$[0.8, 0.9)$	0.846	0.008 ± 0.010 ± 0.005
6	$[0.9, 1.0)$	0.947	0.008 ± 0.012 ± 0.006
7	$[1.0, 1.2)$	1.090	-0.008 ± 0.011 ± 0.006
8	$[1.2, 1.6)$	1.352	-0.009 ± 0.012 ± 0.006
9	$[1.6, 100.0)$	1.957	0.004 ± 0.021 ± 0.011

Table A.24: Results of $A_{UL}^{\sin(4\phi_h-2\phi_R)}$ for h^+h^- in bins of x, z, and M_{inv}.

h^+h^-			2007 & 2011
x			
Bin	Range	$\langle x\rangle$	$A_{UL}^{\sin(4\phi_h-2\phi_R)}$
0	$[0.0025, 0.0080)$	0.006	-0.005 ± 0.011 ± 0.011
1	$[0.0080, 0.0130)$	0.011	-0.010 ± 0.006 ± 0.005
2	$[0.0130, 0.0200)$	0.016	-0.004 ± 0.005 ± 0.004
3	$[0.0200, 0.0320)$	0.026	-0.007 ± 0.004 ± 0.004
4	$[0.0320, 0.0500)$	0.040	-0.002 ± 0.005 ± 0.004
5	$[0.0500, 0.0800)$	0.063	-0.001 ± 0.005 ± 0.004
6	$[0.0800, 0.1300)$	0.101	-0.006 ± 0.007 ± 0.005
7	$[0.1300, 0.2100)$	0.162	-0.004 ± 0.008 ± 0.007
8	$[0.2100, 0.7000)$	0.287	-0.007 ± 0.011 ± 0.009
z			
Bin	Range	$\langle z\rangle$	$A_{UL}^{\sin(4\phi_h-2\phi_R)}$
0	$[0.20, 0.25)$	0.238	0.009 ± 0.016 ± 0.014
1	$[0.25, 0.30)$	0.278	-0.010 ± 0.007 ± 0.006
2	$[0.30, 0.35)$	0.326	-0.009 ± 0.005 ± 0.005
3	$[0.35, 0.40)$	0.375	0.002 ± 0.005 ± 0.004
4	$[0.40, 0.50)$	0.447	-0.006 ± 0.004 ± 0.003
5	$[0.50, 0.65)$	0.566	-0.006 ± 0.004 ± 0.003
6	$[0.65, 0.80)$	0.714	0.000 ± 0.006 ± 0.005
7	$[0.80, 1.00)$	0.855	-0.011 ± 0.011 ± 0.010
M_{inv}			
Bin	Range	$\langle M_{\mathrm{inv}}\rangle$ [GeV/c^2]	$A_{UL}^{\sin(4\phi_h-2\phi_R)}$
0	$[0.0, 0.4)$	0.362	-0.003 ± 0.006 ± 0.005
1	$[0.4, 0.5)$	0.451	0.001 ± 0.005 ± 0.004
2	$[0.5, 0.6)$	0.549	-0.006 ± 0.005 ± 0.004
3	$[0.6, 0.7)$	0.650	-0.009 ± 0.005 ± 0.005
4	$[0.7, 0.8)$	0.749	-0.011 ± 0.005 ± 0.005
5	$[0.8, 0.9)$	0.846	0.001 ± 0.007 ± 0.006
6	$[0.9, 1.0)$	0.947	-0.007 ± 0.008 ± 0.007
7	$[1.0, 1.2)$	1.090	-0.001 ± 0.007 ± 0.006
8	$[1.2, 1.6)$	1.351	-0.009 ± 0.008 ± 0.007
9	$[1.6, 100.0)$	1.947	-0.002 ± 0.015 ± 0.013

Table A.25: Results of $A_{LL}^{\cos(\phi_h-\phi_R)}$ for h^+h^- in bins of x, z, and $M_{\mathrm{inv}}$for 2007.

h^+h^-			2007
x			
Bin	Range	$\langle x\rangle$	$A_{LL}^{\cos(\phi_h-\phi_R)}$
0	$[0.0025, 0.0080)$	0.006	0.006 ± 0.015 ± 0.014
1	$[0.0080, 0.0130)$	0.011	-0.005 ± 0.015 ± 0.013
2	$[0.0130, 0.0200)$	0.016	0.000 ± 0.017 ± 0.016
3	$[0.0200, 0.0320)$	0.026	0.041 ± 0.020 ± 0.018
4	$[0.0320, 0.0500)$	0.040	-0.041 ± 0.025 ± 0.023
5	$[0.0500, 0.0800)$	0.063	0.021 ± 0.030 ± 0.027
6	$[0.0800, 0.1300)$	0.101	0.030 ± 0.037 ± 0.033
7	$[0.1300, 0.2100)$	0.162	-0.036 ± 0.048 ± 0.043
8	$[0.2100, 0.7000)$	0.286	-0.028 ± 0.056 ± 0.051
z			
Bin	Range	$\langle z\rangle$	$A_{LL}^{\cos(\phi_h-\phi_R)}$
0	$[0.20, 0.25)$	0.238	0.023 ± 0.042 ± 0.038
1	$[0.25, 0.30)$	0.278	0.029 ± 0.022 ± 0.020
2	$[0.30, 0.35)$	0.326	-0.001 ± 0.020 ± 0.018
3	$[0.35, 0.40)$	0.375	-0.018 ± 0.020 ± 0.018
4	$[0.40, 0.50)$	0.447	0.003 ± 0.016 ± 0.015
5	$[0.50, 0.65)$	0.567	-0.029 ± 0.018 ± 0.016
6	$[0.65, 0.80)$	0.714	0.051 ± 0.027 ± 0.025
7	$[0.80, 1.00)$	0.854	0.085 ± 0.042 ± 0.038
M_{inv}			
Bin	Range	$\langle M_{\mathrm{inv}}\rangle$ [GeV/c^2]	$A_{LL}^{\cos(\phi_h-\phi_R)}$
0	$[0.0, 0.4)$	0.362	-0.020 ± 0.025 ± 0.023
1	$[0.4, 0.5)$	0.451	0.008 ± 0.021 ± 0.019
2	$[0.5, 0.6)$	0.549	0.004 ± 0.021 ± 0.019
3	$[0.6, 0.7)$	0.650	-0.021 ± 0.021 ± 0.019
4	$[0.7, 0.8)$	0.749	0.033 ± 0.021 ± 0.019
5	$[0.8, 0.9)$	0.846	-0.007 ± 0.025 ± 0.022
6	$[0.9, 1.0)$	0.947	-0.037 ± 0.029 ± 0.027
7	$[1.0, 1.2)$	1.090	0.034 ± 0.027 ± 0.024
8	$[1.2, 1.6)$	1.350	-0.026 ± 0.028 ± 0.026
9	$[1.6, 100.0)$	1.938	0.151 ± 0.043 ± 0.039

Table A.26: Results of $A_{LL}^{\cos(\phi_h-\phi_R)}$ for h^+h^- in bins of x, z, and $M_{\text{inv}}$for 2011.

h^+h^-			2011
		x	
Bin	Range	$\langle x \rangle$	$A_{LL}^{\cos(\phi_h-\phi_R)}$
0	$[0.0025, 0.0080)$	0.006	0.006 ± 0.014 ± 0.014
1	$[0.0080, 0.0130)$	0.011	-0.012 ± 0.017 ± 0.017
2	$[0.0130, 0.0200)$	0.016	0.042 ± 0.020 ± 0.020
3	$[0.0200, 0.0320)$	0.026	-0.044 ± 0.023 ± 0.023
4	$[0.0320, 0.0500)$	0.040	0.020 ± 0.029 ± 0.029
5	$[0.0500, 0.0800)$	0.063	0.004 ± 0.035 ± 0.035
6	$[0.0800, 0.1300)$	0.101	-0.058 ± 0.042 ± 0.042
7	$[0.1300, 0.2100)$	0.162	-0.072 ± 0.055 ± 0.055
8	$[0.2100, 0.7000)$	0.288	0.080 ± 0.066 ± 0.066
		z	
Bin	Range	$\langle z \rangle$	$A_{LL}^{\cos(\phi_h-\phi_R)}$
0	$[0.20, 0.25)$	0.238	0.041 ± 0.042 ± 0.042
1	$[0.25, 0.30)$	0.278	0.012 ± 0.023 ± 0.023
2	$[0.30, 0.35)$	0.325	0.027 ± 0.021 ± 0.021
3	$[0.35, 0.40)$	0.375	0.046 ± 0.022 ± 0.022
4	$[0.40, 0.50)$	0.447	-0.041 ± 0.018 ± 0.018
5	$[0.50, 0.65)$	0.566	-0.026 ± 0.020 ± 0.020
6	$[0.65, 0.80)$	0.714	-0.039 ± 0.031 ± 0.031
7	$[0.80, 1.00)$	0.857	0.030 ± 0.048 ± 0.048
		M_{inv}	
Bin	Range	$\langle M_{\text{inv}} \rangle$ [GeV/c^2]	$A_{LL}^{\cos(\phi_h-\phi_R)}$
0	$[0.0, 0.4)$	0.362	0.046 ± 0.028 ± 0.028
1	$[0.4, 0.5)$	0.451	0.017 ± 0.023 ± 0.023
2	$[0.5, 0.6)$	0.549	-0.007 ± 0.023 ± 0.023
3	$[0.6, 0.7)$	0.650	-0.020 ± 0.023 ± 0.023
4	$[0.7, 0.8)$	0.749	-0.015 ± 0.023 ± 0.023
5	$[0.8, 0.9)$	0.846	-0.050 ± 0.027 ± 0.027
6	$[0.9, 1.0)$	0.947	0.018 ± 0.032 ± 0.032
7	$[1.0, 1.2)$	1.090	0.005 ± 0.029 ± 0.029
8	$[1.2, 1.6)$	1.352	-0.022 ± 0.030 ± 0.030
9	$[1.6, 100.0)$	1.957	-0.019 ± 0.044 ± 0.044

Table A.27: Results of $A_{LL}^{\cos(\phi_h-\phi_R)}$ for h^+h^- in bins of x, z, and M_{inv}.

h^+h^-			2007 & 2011
		x	
Bin	Range	$\langle x \rangle$	$A_{LL}^{\cos(\phi_h-\phi_R)}$
0	$[0.0025, 0.0080)$	0.006	0.006 ± 0.011 ± 0.014
1	$[0.0080, 0.0130)$	0.011	-0.008 ± 0.011 ± 0.017
2	$[0.0130, 0.0200)$	0.016	0.018 ± 0.013 ± 0.020
3	$[0.0200, 0.0320)$	0.026	0.005 ± 0.015 ± 0.023
4	$[0.0320, 0.0500)$	0.040	-0.015 ± 0.019 ± 0.029
5	$[0.0500, 0.0800)$	0.063	0.013 ± 0.023 ± 0.035
6	$[0.0800, 0.1300)$	0.101	-0.008 ± 0.028 ± 0.042
7	$[0.1300, 0.2100)$	0.162	-0.051 ± 0.036 ± 0.055
8	$[0.2100, 0.7000)$	0.287	0.017 ± 0.043 ± 0.066
		z	
Bin	Range	$\langle z \rangle$	$A_{LL}^{\cos(\phi_h-\phi_R)}$
0	$[0.20, 0.25)$	0.238	0.032 ± 0.029 ± 0.042
1	$[0.25, 0.30)$	0.278	0.021 ± 0.016 ± 0.023
2	$[0.30, 0.35)$	0.326	0.012 ± 0.014 ± 0.021
3	$[0.35, 0.40)$	0.375	0.011 ± 0.015 ± 0.022
4	$[0.40, 0.50)$	0.447	-0.017 ± 0.012 ± 0.018
5	$[0.50, 0.65)$	0.566	-0.028 ± 0.013 ± 0.020
6	$[0.65, 0.80)$	0.714	0.011 ± 0.020 ± 0.031
7	$[0.80, 1.00)$	0.855	0.061 ± 0.032 ± 0.048
		M_{inv}	
Bin	Range	$\langle M_{\text{inv}} \rangle$ [GeV/c^2]	$A_{LL}^{\cos(\phi_h-\phi_R)}$
0	$[0.0, 0.4)$	0.362	0.010 ± 0.019 ± 0.028
1	$[0.4, 0.5)$	0.451	0.012 ± 0.016 ± 0.023
2	$[0.5, 0.6)$	0.549	-0.001 ± 0.015 ± 0.023
3	$[0.6, 0.7)$	0.650	-0.020 ± 0.016 ± 0.023
4	$[0.7, 0.8)$	0.749	0.011 ± 0.016 ± 0.023
5	$[0.8, 0.9)$	0.846	-0.027 ± 0.018 ± 0.027
6	$[0.9, 1.0)$	0.947	-0.012 ± 0.022 ± 0.032
7	$[1.0, 1.2)$	1.090	0.021 ± 0.019 ± 0.029
8	$[1.2, 1.6)$	1.351	-0.025 ± 0.021 ± 0.030
9	$[1.6, 100.0)$	1.947	0.068 ± 0.031 ± 0.044

Table A.28: Results of $A_{LL}^{\cos(2\phi_h-2\phi_R)}$ for h^+h^- in bins of x, z, and $M_{\text{inv}}$for 2007.

h^+h^-			2007
		x	
Bin	Range	$\langle x\rangle$	$A_{LL}^{\cos(2\phi_h-2\phi_R)}$
0	$[0.0025, 0.0080)$	0.006	0.009 ± 0.016 ± 0.010
1	$[0.0080, 0.0130)$	0.011	-0.002 ± 0.015 ± 0.010
2	$[0.0130, 0.0200)$	0.016	0.011 ± 0.017 ± 0.012
3	$[0.0200, 0.0320)$	0.026	0.038 ± 0.020 ± 0.013
4	$[0.0320, 0.0500)$	0.040	-0.005 ± 0.026 ± 0.017
5	$[0.0500, 0.0800)$	0.063	0.033 ± 0.031 ± 0.020
6	$[0.0800, 0.1300)$	0.101	0.018 ± 0.037 ± 0.025
7	$[0.1300, 0.2100)$	0.162	-0.047 ± 0.048 ± 0.032
8	$[0.2100, 0.7000)$	0.286	0.001 ± 0.056 ± 0.037
		z	
Bin	Range	$\langle z\rangle$	$A_{LL}^{\cos(2\phi_h-2\phi_R)}$
0	$[0.20, 0.25)$	0.238	0.011 ± 0.042 ± 0.028
1	$[0.25, 0.30)$	0.278	0.052 ± 0.022 ± 0.015
2	$[0.30, 0.35)$	0.326	-0.001 ± 0.020 ± 0.013
3	$[0.35, 0.40)$	0.375	0.017 ± 0.020 ± 0.014
4	$[0.40, 0.50)$	0.447	0.003 ± 0.016 ± 0.011
5	$[0.50, 0.65)$	0.567	0.006 ± 0.018 ± 0.012
6	$[0.65, 0.80)$	0.714	0.009 ± 0.027 ± 0.018
7	$[0.80, 1.00)$	0.854	0.044 ± 0.042 ± 0.028
		M_{inv}	
Bin	Range	$\langle M_{\text{inv}}\rangle$ [GeV/c^2]	$A_{LL}^{\cos(2\phi_h-2\phi_R)}$
0	$[0.0, 0.4)$	0.362	0.002 ± 0.025 ± 0.017
1	$[0.4, 0.5)$	0.451	0.018 ± 0.021 ± 0.014
2	$[0.5, 0.6)$	0.549	0.005 ± 0.021 ± 0.014
3	$[0.6, 0.7)$	0.650	0.013 ± 0.022 ± 0.014
4	$[0.7, 0.8)$	0.749	0.017 ± 0.022 ± 0.014
5	$[0.8, 0.9)$	0.846	0.016 ± 0.025 ± 0.017
6	$[0.9, 1.0)$	0.947	0.022 ± 0.030 ± 0.020
7	$[1.0, 1.2)$	1.090	0.000 ± 0.027 ± 0.018
8	$[1.2, 1.6)$	1.350	0.013 ± 0.028 ± 0.019
9	$[1.6, 100.0)$	1.938	0.001 ± 0.041 ± 0.027

Table A.29: Results of $A_{LL}^{\cos(2\phi_h-2\phi_R)}$ for h^+h^- in bins of x, z, and $M_{\text{inv}}$for 2011.

h^+h^-			2011
		x	
Bin	Range	$\langle x\rangle$	$A_{LL}^{\cos(2\phi_h-2\phi_R)}$
0	$[0.0025, 0.0080)$	0.006	0.014 ± 0.015 ± 0.009
1	$[0.0080, 0.0130)$	0.011	-0.015 ± 0.017 ± 0.011
2	$[0.0130, 0.0200)$	0.016	-0.031 ± 0.021 ± 0.013
3	$[0.0200, 0.0320)$	0.026	0.001 ± 0.023 ± 0.015
4	$[0.0320, 0.0500)$	0.040	-0.022 ± 0.029 ± 0.019
5	$[0.0500, 0.0800)$	0.063	0.039 ± 0.035 ± 0.022
6	$[0.0800, 0.1300)$	0.101	0.055 ± 0.042 ± 0.027
7	$[0.1300, 0.2100)$	0.162	0.027 ± 0.055 ± 0.035
8	$[0.2100, 0.7000)$	0.288	0.000 ± 0.067 ± 0.043
		z	
Bin	Range	$\langle z\rangle$	$A_{LL}^{\cos(2\phi_h-2\phi_R)}$
0	$[0.20, 0.25)$	0.238	0.025 ± 0.042 ± 0.027
1	$[0.25, 0.30)$	0.278	0.002 ± 0.023 ± 0.015
2	$[0.30, 0.35)$	0.325	-0.006 ± 0.021 ± 0.014
3	$[0.35, 0.40)$	0.375	-0.001 ± 0.022 ± 0.014
4	$[0.40, 0.50)$	0.447	-0.004 ± 0.018 ± 0.012
5	$[0.50, 0.65)$	0.566	0.005 ± 0.020 ± 0.013
6	$[0.65, 0.80)$	0.714	-0.019 ± 0.031 ± 0.020
7	$[0.80, 1.00)$	0.857	0.051 ± 0.048 ± 0.031
		M_{inv}	
Bin	Range	$\langle M_{\text{inv}}\rangle$ [GeV/c^2]	$A_{LL}^{\cos(2\phi_h-2\phi_R)}$
0	$[0.0, 0.4)$	0.362	0.027 ± 0.028 ± 0.018
1	$[0.4, 0.5)$	0.451	-0.038 ± 0.023 ± 0.015
2	$[0.5, 0.6)$	0.549	-0.005 ± 0.023 ± 0.015
3	$[0.6, 0.7)$	0.650	0.026 ± 0.024 ± 0.015
4	$[0.7, 0.8)$	0.749	-0.009 ± 0.024 ± 0.015
5	$[0.8, 0.9)$	0.846	0.007 ± 0.028 ± 0.018
6	$[0.9, 1.0)$	0.947	0.003 ± 0.032 ± 0.021
7	$[1.0, 1.2)$	1.090	0.020 ± 0.029 ± 0.018
8	$[1.2, 1.6)$	1.352	-0.010 ± 0.030 ± 0.019
9	$[1.6, 100.0)$	1.957	-0.014 ± 0.042 ± 0.027

Table A.30: Results of $A_{LL}^{\cos(2\phi_h-2\phi_R)}$ for h^+h^- in bins of x, z, and M_{inv}.

h^+h^-			2007 & 2011
		x	
Bin	Range	$\langle x\rangle$	$A_{LL}^{\cos(2\phi_h-2\phi_R)}$
0	$[0.0025, 0.0080)$	0.006	0.012 ± 0.011 ± 0.010
1	$[0.0080, 0.0130)$	0.011	-0.007 ± 0.011 ± 0.011
2	$[0.0130, 0.0200)$	0.016	-0.006 ± 0.013 ± 0.013
3	$[0.0200, 0.0320)$	0.026	0.022 ± 0.015 ± 0.015
4	$[0.0320, 0.0500)$	0.040	-0.012 ± 0.019 ± 0.019
5	$[0.0500, 0.0800)$	0.063	0.035 ± 0.023 ± 0.022
6	$[0.0800, 0.1300)$	0.101	0.034 ± 0.028 ± 0.027
7	$[0.1300, 0.2100)$	0.162	-0.015 ± 0.036 ± 0.035
8	$[0.2100, 0.7000)$	0.287	0.000 ± 0.043 ± 0.043
		z	
Bin	Range	$\langle z\rangle$	$A_{LL}^{\cos(2\phi_h-2\phi_R)}$
0	$[0.20, 0.25)$	0.238	0.018 ± 0.030 ± 0.028
1	$[0.25, 0.30)$	0.278	0.028 ± 0.016 ± 0.015
2	$[0.30, 0.35)$	0.326	-0.004 ± 0.015 ± 0.014
3	$[0.35, 0.40)$	0.375	0.009 ± 0.015 ± 0.014
4	$[0.40, 0.50)$	0.447	0.000 ± 0.012 ± 0.012
5	$[0.50, 0.65)$	0.566	0.006 ± 0.013 ± 0.013
6	$[0.65, 0.80)$	0.714	-0.004 ± 0.020 ± 0.020
7	$[0.80, 1.00)$	0.855	0.047 ± 0.032 ± 0.031
		M_{inv}	
Bin	Range	$\langle M_{\text{inv}}\rangle$ [GeV/c^2]	$A_{LL}^{\cos(2\phi_h-2\phi_R)}$
0	$[0.0, 0.4)$	0.362	0.014 ± 0.019 ± 0.018
1	$[0.4, 0.5)$	0.451	-0.007 ± 0.016 ± 0.015
2	$[0.5, 0.6)$	0.549	0.000 ± 0.016 ± 0.015
3	$[0.6, 0.7)$	0.650	0.019 ± 0.016 ± 0.015
4	$[0.7, 0.8)$	0.749	0.005 ± 0.016 ± 0.015
5	$[0.8, 0.9)$	0.846	0.012 ± 0.019 ± 0.018
6	$[0.9, 1.0)$	0.947	0.013 ± 0.022 ± 0.021
7	$[1.0, 1.2)$	1.090	0.009 ± 0.020 ± 0.018
8	$[1.2, 1.6)$	1.351	0.003 ± 0.021 ± 0.019
9	$[1.6, 100.0)$	1.947	-0.007 ± 0.029 ± 0.027

A.5 One Hadron Analysis Material

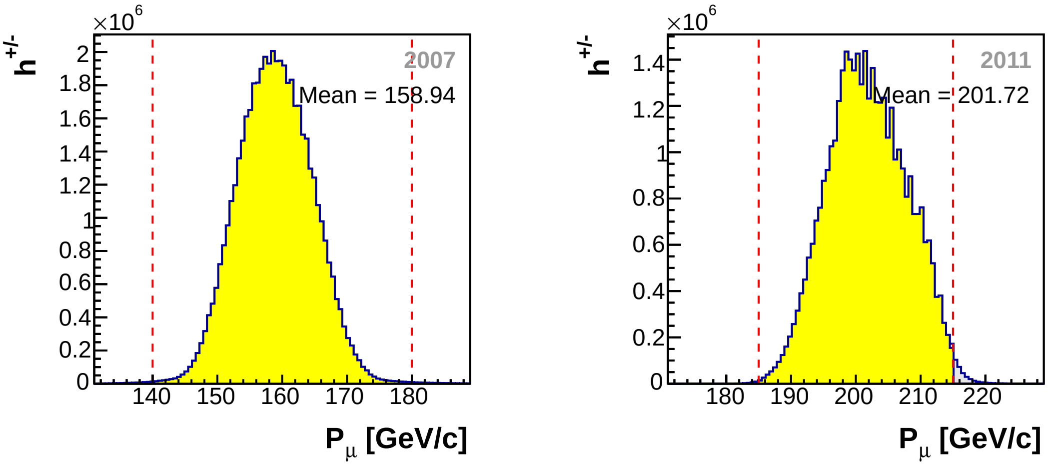

Figure A.17: Momentum distribution of the incident muon before (grey) and after (color) application of the associated cuts. The cuts are marked with dashed red lines.

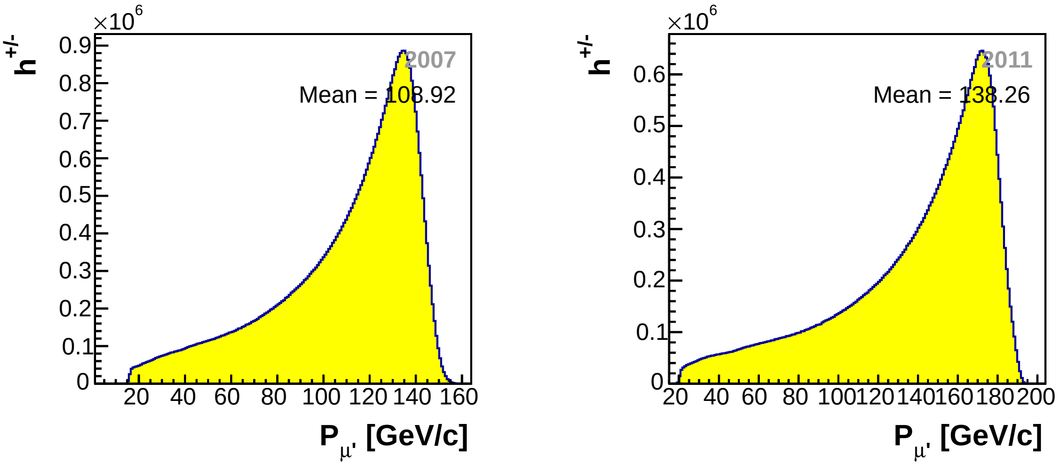

Figure A.18: Momentum distribution of the scattered muon after application of the associated cuts.

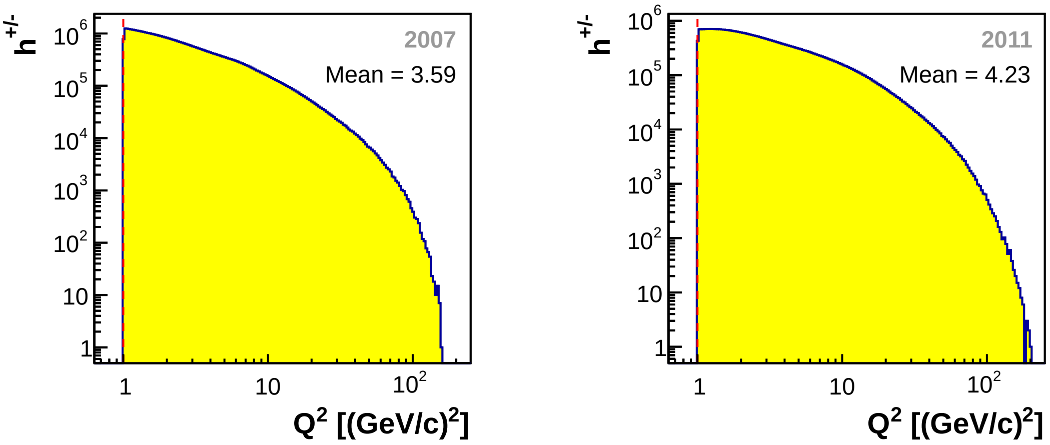

Figure A.19: Distribution of Q^2 before (grey) and after (color) application of the associated cuts. The cut is marked with a dashed red line.

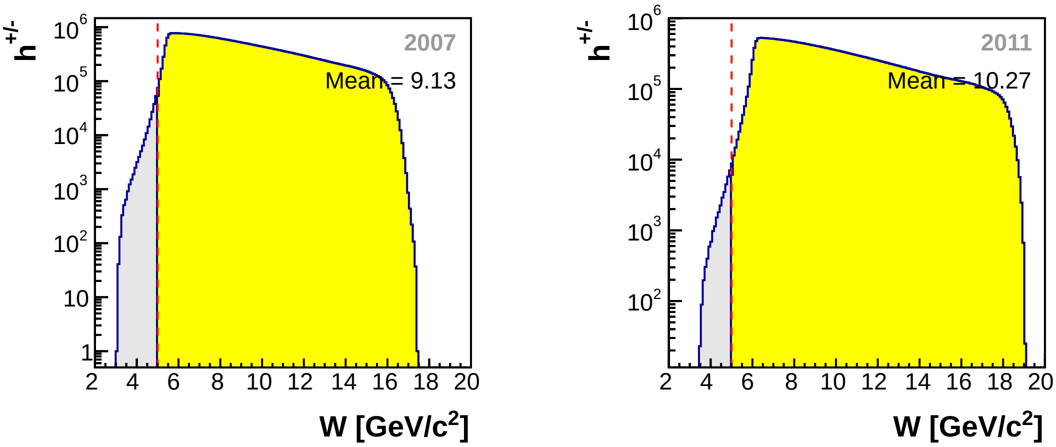

Figure A.20: Distribution of W before (grey) and after (color) application of the associated cuts. The cut is marked with a dashed red line.

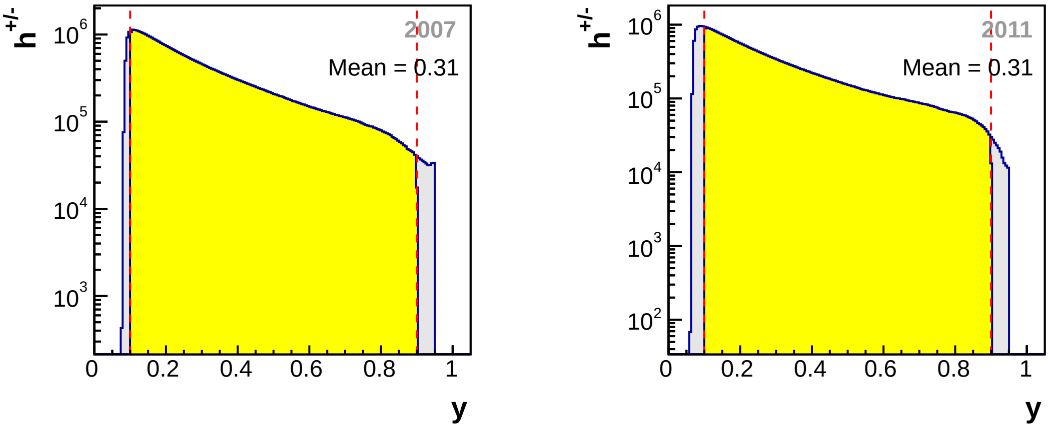

Figure A.21: Distribution of y before (grey) and after (color) application of the associated cuts. The cuts are marked with dashed red lines.

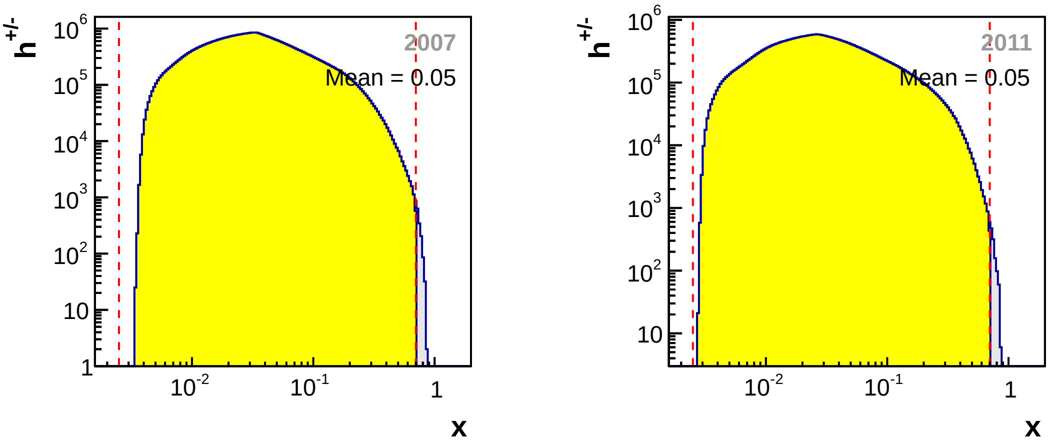

Figure A.22: Distribution of x before (grey) and after (color) application of the associated cuts. The cuts are marked with dashed red lines.

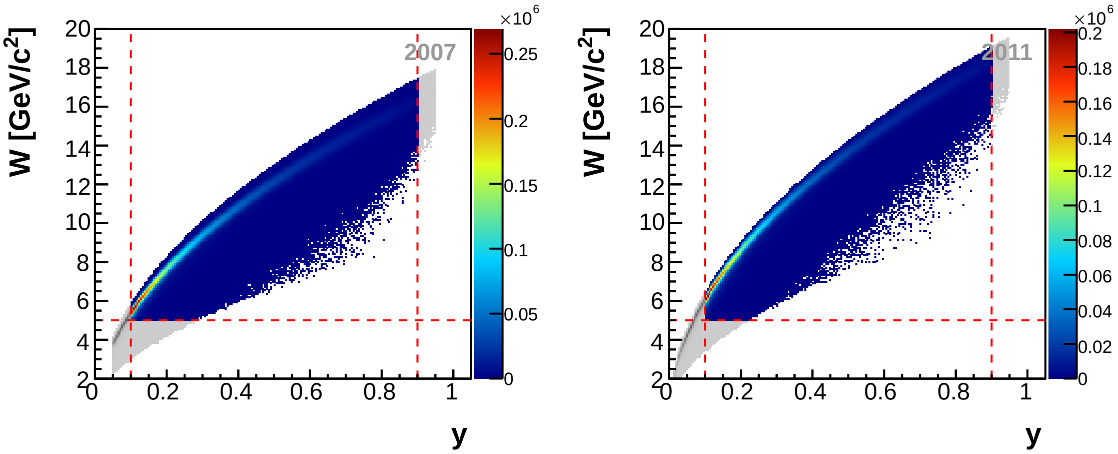

Figure A.23: W vs y before (greyscale) and after (colorscale) application of the associated cuts. The cuts are marked with dashed red lines.

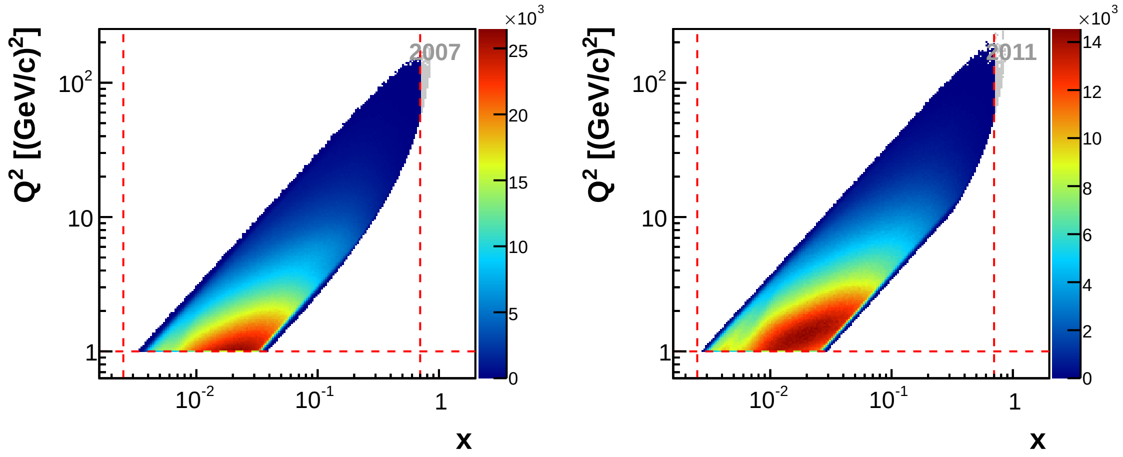

Figure A.24: Kinematical phase space of Q vs x before (greyscale) and after (colorscale) application of the associated cuts. The cuts are marked with dashed red lines.

Table A.31: Mean Values of relevant variables for the h^+ analysis in bins of x, z, and P_{hT} for 2007.

h^+										2007
					x					
Bin	Range	$\langle x \rangle$	$\langle z \rangle$	$\langle P_{\mathrm{hT}} \rangle$ [GeV/c]	$\langle Q^2 \rangle$ [(GeV/c)^2]	$\langle y \rangle$	$\langle W \rangle$ [GeV/c^2]	$\langle f \rangle$	$\langle \lvert P_T \rvert \rangle$	$\langle P_B \rangle$
0	$[0.0025, 0.0080)$	0.006	0.362	0.540	1.260	0.674	13.981	0.142	0.867	-0.798
1	$[0.0080, 0.0130)$	0.011	0.364	0.532	1.523	0.489	11.882	0.144	0.868	-0.795
2	$[0.0130, 0.0200)$	0.016	0.366	0.522	1.786	0.368	10.209	0.145	0.868	-0.793
3	$[0.0200, 0.0320)$	0.026	0.369	0.506	2.091	0.276	8.716	0.146	0.868	-0.793
4	$[0.0320, 0.0500)$	0.040	0.372	0.494	2.722	0.229	7.848	0.146	0.868	-0.790
5	$[0.0500, 0.0800)$	0.063	0.370	0.494	4.225	0.226	7.703	0.147	0.868	-0.790
6	$[0.0800, 0.1300)$	0.101	0.369	0.495	6.793	0.226	7.555	0.150	0.868	-0.790
7	$[0.1300, 0.2100)$	0.163	0.368	0.494	10.779	0.223	7.245	0.158	0.868	-0.790
8	$[0.2100, 0.7000)$	0.287	0.369	0.513	21.010	0.241	6.961	0.176	0.868	-0.791
					z					
Bin	Range	$\langle x \rangle$	$\langle z \rangle$	$\langle P_{\mathrm{hT}} \rangle$ [GeV/c]	$\langle Q^2 \rangle$ [(GeV/c)^2]	$\langle y \rangle$	$\langle W \rangle$ [GeV/c^2]	$\langle f \rangle$	$\langle \lvert P_T \rvert \rangle$	$\langle P_B \rangle$
0	$[0.20, 0.25)$	0.049	0.224	0.457	3.739	0.319	9.160	0.147	0.868	-0.793
1	$[0.25, 0.30)$	0.050	0.274	0.481	3.761	0.314	9.074	0.147	0.868	-0.792
2	$[0.30, 0.35)$	0.051	0.324	0.503	3.783	0.310	9.008	0.147	0.868	-0.792
3	$[0.35, 0.40)$	0.051	0.374	0.523	3.782	0.306	8.947	0.147	0.868	-0.792
4	$[0.40, 0.50)$	0.052	0.445	0.549	3.765	0.302	8.883	0.147	0.868	-0.791
5	$[0.50, 0.65)$	0.052	0.565	0.583	3.696	0.296	8.797	0.148	0.868	-0.791
6	$[0.65, 0.80)$	0.050	0.716	0.590	3.486	0.293	8.725	0.147	0.868	-0.790
7	$[0.80, 1.00)$	0.045	0.875	0.506	3.033	0.292	8.701	0.147	0.868	-0.788
					P_{hT}					
Bin	Range	$\langle x \rangle$	$\langle z \rangle$	$\langle P_{\mathrm{hT}} \rangle$ [GeV/c]	$\langle Q^2 \rangle$ [(GeV/c)^2]	$\langle y \rangle$	$\langle W \rangle$ [GeV/c^2]	$\langle f \rangle$	$\langle \lvert P_T \rvert \rangle$	$\langle P_B \rangle$
0	$[0.10, 0.20)$	0.052	0.355	0.155	3.583	0.293	8.745	0.148	0.868	-0.791
1	$[0.20, 0.30)$	0.051	0.353	0.252	3.554	0.294	8.776	0.147	0.868	-0.791
2	$[0.30, 0.40)$	0.050	0.354	0.350	3.550	0.298	8.830	0.147	0.868	-0.791
3	$[0.40, 0.50)$	0.051	0.356	0.449	3.634	0.301	8.877	0.147	0.868	-0.792
4	$[0.50, 0.60)$	0.050	0.363	0.548	3.703	0.306	8.951	0.147	0.868	-0.792
5	$[0.60, 0.75)$	0.050	0.377	0.669	3.792	0.313	9.069	0.147	0.868	-0.792
6	$[0.75, 0.90)$	0.049	0.396	0.818	3.917	0.326	9.257	0.147	0.868	-0.793
7	$[0.90, 1.30)$	0.048	0.420	1.048	4.159	0.350	9.617	0.147	0.868	-0.793
8	$[0.13, 10.00)$	0.047	0.439	1.510	5.005	0.420	10.589	0.146	0.868	-0.794

Table A.32: Mean Values of relevant variables for the h^- analysis in bins of x, z, and P_{hT} for 2007.

h^-										2007
					x					
Bin	Range	$\langle x\rangle$	$\langle z\rangle$	$\langle P_{\mathrm{hT}}\rangle$ [GeV/c]	$\langle Q^2\rangle$ [(GeV/c)^2]	$\langle y\rangle$	$\langle W\rangle$ [GeV/c^2]	$\langle f\rangle$	$\langle \lvert P_T\rvert\rangle$	$\langle P_B\rangle$
0	$[0.0025, 0.0080)$	0.006	0.368	0.527	1.260	0.676	14.012	0.142	0.867	-0.798
1	$[0.0080, 0.0130)$	0.011	0.363	0.523	1.530	0.492	11.923	0.144	0.868	-0.795
2	$[0.0130, 0.0200)$	0.016	0.361	0.514	1.798	0.371	10.251	0.145	0.868	-0.793
3	$[0.0200, 0.0320)$	0.026	0.362	0.499	2.110	0.279	8.762	0.146	0.868	-0.792
4	$[0.0320, 0.0500)$	0.040	0.362	0.486	2.746	0.232	7.888	0.146	0.868	-0.790
5	$[0.0500, 0.0800)$	0.063	0.357	0.488	4.253	0.228	7.737	0.147	0.868	-0.789
6	$[0.0800, 0.1300)$	0.101	0.350	0.489	6.810	0.227	7.578	0.150	0.868	-0.789
7	$[0.1300, 0.2100)$	0.162	0.345	0.489	10.791	0.224	7.263	0.158	0.868	-0.789
8	$[0.2100, 0.7000)$	0.286	0.342	0.508	21.066	0.242	6.980	0.176	0.868	-0.791
					z					
Bin	Range	$\langle x\rangle$	$\langle z\rangle$	$\langle P_{\mathrm{hT}}\rangle$ [GeV/c]	$\langle Q^2\rangle$ [(GeV/c)^2]	$\langle y\rangle$	$\langle W\rangle$ [GeV/c^2]	$\langle f\rangle$	$\langle \lvert P_T\rvert\rangle$	$\langle P_B\rangle$
0	$[0.20, 0.25)$	0.046	0.223	0.457	3.593	0.328	9.294	0.147	0.868	-0.793
1	$[0.25, 0.30)$	0.046	0.273	0.483	3.556	0.324	9.231	0.147	0.868	-0.792
2	$[0.30, 0.35)$	0.046	0.324	0.506	3.516	0.321	9.185	0.147	0.868	-0.792
3	$[0.35, 0.40)$	0.046	0.374	0.525	3.454	0.319	9.156	0.147	0.868	-0.792
4	$[0.40, 0.50)$	0.045	0.445	0.547	3.365	0.318	9.132	0.147	0.868	-0.791
5	$[0.50, 0.65)$	0.044	0.565	0.569	3.183	0.316	9.109	0.147	0.868	-0.791
6	$[0.65, 0.80)$	0.041	0.717	0.553	2.894	0.313	9.061	0.147	0.868	-0.790
7	$[0.80, 1.00)$	0.037	0.876	0.448	2.532	0.305	8.975	0.147	0.868	-0.788
					P_{hT}					
Bin	Range	$\langle x\rangle$	$\langle z\rangle$	$\langle P_{\mathrm{hT}}\rangle$ [GeV/c]	$\langle Q^2\rangle$ [(GeV/c)^2]	$\langle y\rangle$	$\langle W\rangle$ [GeV/c^2]	$\langle f\rangle$	$\langle \lvert P_T\rvert\rangle$	$\langle P_B\rangle$
0	$[0.10, 0.20)$	0.046	0.356	0.155	3.293	0.306	8.949	0.147	0.868	-0.791
1	$[0.20, 0.30)$	0.046	0.351	0.252	3.265	0.306	8.971	0.147	0.868	-0.791
2	$[0.30, 0.40)$	0.045	0.351	0.350	3.273	0.310	9.031	0.147	0.868	-0.791
3	$[0.40, 0.50)$	0.046	0.349	0.449	3.372	0.314	9.090	0.147	0.868	-0.792
4	$[0.50, 0.60)$	0.046	0.352	0.548	3.461	0.320	9.169	0.147	0.868	-0.792
5	$[0.60, 0.75)$	0.045	0.362	0.669	3.552	0.328	9.300	0.147	0.868	-0.792
6	$[0.75, 0.90)$	0.045	0.377	0.818	3.656	0.341	9.487	0.146	0.868	-0.793
7	$[0.90, 1.30)$	0.043	0.399	1.048	3.826	0.364	9.836	0.146	0.868	-0.793
8	$[0.13, 10.00)$	0.040	0.422	1.511	4.317	0.425	10.698	0.145	0.868	-0.794

Table A.33: Mean Values of relevant variables for the h^+ analysis in bins of x, z, and P_{hT} for 2011.

h^+ 2011

x

Bin	Range	$\langle x \rangle$	$\langle z \rangle$	$\langle P_{\mathrm{hT}} \rangle$ [GeV/c]	$\langle Q^2 \rangle$ [(GeV/c)^2]	$\langle y \rangle$	$\langle W \rangle$ [GeV/c^2]	$\langle f \rangle$	$\langle \lvert P_T \rvert \rangle$	$\langle P_B \rangle$
0	$[0.0025, 0.0080)$	0.006	0.357	0.551	1.370	0.630	14.089	0.145	0.867	-0.828
1	$[0.0080, 0.0130)$	0.011	0.362	0.539	1.716	0.436	12.132	0.147	0.867	-0.826
2	$[0.0130, 0.0200)$	0.016	0.364	0.528	2.044	0.333	10.594	0.148	0.867	-0.825
3	$[0.0200, 0.0320)$	0.026	0.368	0.514	2.491	0.260	9.305	0.148	0.866	-0.825
4	$[0.0320, 0.0500)$	0.040	0.366	0.508	3.517	0.233	8.788	0.148	0.867	-0.824
5	$[0.0500, 0.0800)$	0.063	0.364	0.507	5.356	0.225	8.568	0.149	0.867	-0.824
6	$[0.0800, 0.1300)$	0.101	0.363	0.507	8.425	0.220	8.348	0.153	0.866	-0.824
7	$[0.1300, 0.2100)$	0.163	0.363	0.506	13.102	0.213	7.971	0.161	0.867	-0.824
8	$[0.2100, 0.7000)$	0.292	0.365	0.511	22.993	0.207	7.251	0.181	0.867	-0.824

z

Bin	Range	$\langle x \rangle$	$\langle z \rangle$	$\langle P_{\mathrm{hT}} \rangle$ [GeV/c]	$\langle Q^2 \rangle$ [(GeV/c)^2]	$\langle y \rangle$	$\langle W \rangle$ [GeV/c^2]	$\langle f \rangle$	$\langle \lvert P_T \rvert \rangle$	$\langle P_B \rangle$
0	$[0.20, 0.25)$	0.047	0.223	0.470	4.409	0.318	9.841	0.150	0.867	-0.825
1	$[0.25, 0.30)$	0.048	0.274	0.493	4.438	0.313	9.760	0.150	0.867	-0.825
2	$[0.30, 0.35)$	0.049	0.324	0.515	4.462	0.309	9.692	0.150	0.867	-0.825
3	$[0.35, 0.40)$	0.050	0.374	0.535	4.470	0.305	9.639	0.150	0.867	-0.825
4	$[0.40, 0.50)$	0.050	0.445	0.563	4.453	0.301	9.581	0.150	0.866	-0.825
5	$[0.50, 0.65)$	0.050	0.565	0.599	4.373	0.296	9.511	0.150	0.867	-0.825
6	$[0.65, 0.80)$	0.048	0.716	0.608	4.100	0.291	9.446	0.150	0.867	-0.824
7	$[0.80, 1.00)$	0.042	0.875	0.514	3.467	0.284	9.422	0.150	0.866	-0.823

P_{hT}

Bin	Range	$\langle x \rangle$	$\langle z \rangle$	$\langle P_{\mathrm{hT}} \rangle$ [GeV/c]	$\langle Q^2 \rangle$ [(GeV/c)^2]	$\langle y \rangle$	$\langle W \rangle$ [GeV/c^2]	$\langle f \rangle$	$\langle \lvert P_T \rvert \rangle$	$\langle P_B \rangle$
0	$[0.10, 0.20)$	0.051	0.351	0.155	4.274	0.292	9.452	0.150	0.867	-0.825
1	$[0.20, 0.30)$	0.050	0.349	0.252	4.225	0.293	9.487	0.150	0.867	-0.825
2	$[0.30, 0.40)$	0.049	0.350	0.350	4.212	0.297	9.540	0.150	0.867	-0.825
3	$[0.40, 0.50)$	0.049	0.351	0.449	4.308	0.300	9.585	0.150	0.867	-0.825
4	$[0.50, 0.60)$	0.049	0.358	0.548	4.380	0.304	9.650	0.150	0.867	-0.825
5	$[0.60, 0.75)$	0.049	0.371	0.669	4.459	0.311	9.751	0.150	0.867	-0.825
6	$[0.75, 0.90)$	0.048	0.389	0.818	4.563	0.323	9.908	0.150	0.866	-0.825
7	$[0.90, 1.30)$	0.046	0.412	1.051	4.756	0.345	10.206	0.149	0.867	-0.826
8	$[0.13, 10.00)$	0.044	0.428	1.517	5.518	0.409	11.039	0.148	0.867	-0.826

Table A.34: Mean Values of relevant variables for the h^- analysis in bins of x, z, and P_{hT} for 2011.

h^-										2011
					x					
Bin	Range	$\langle x\rangle$	$\langle z\rangle$	$\langle P_{\mathrm{hT}}\rangle$ [GeV/c]	$\langle Q^2\rangle$ [(GeV/c)^2]	$\langle y\rangle$	$\langle W\rangle$ [GeV/c^2]	$\langle f\rangle$	$\langle \lvert P_T\rvert\rangle$	$\langle P_B\rangle$
0	$[0.0025, 0.0080)$	0.006	0.367	0.538	1.374	0.637	14.118	0.145	0.867	-0.828
1	$[0.0080, 0.0130)$	0.010	0.362	0.531	1.732	0.441	12.173	0.147	0.867	-0.826
2	$[0.0130, 0.0200)$	0.016	0.360	0.521	2.068	0.337	10.644	0.148	0.867	-0.825
3	$[0.0200, 0.0320)$	0.026	0.361	0.506	2.522	0.263	9.358	0.148	0.867	-0.825
4	$[0.0320, 0.0500)$	0.040	0.356	0.501	3.552	0.236	8.830	0.148	0.867	-0.824
5	$[0.0500, 0.0800)$	0.063	0.350	0.502	5.389	0.227	8.600	0.149	0.866	-0.824
6	$[0.0800, 0.1300)$	0.101	0.344	0.501	8.437	0.221	8.367	0.153	0.866	-0.824
7	$[0.1300, 0.2100)$	0.163	0.339	0.501	13.105	0.214	7.984	0.161	0.867	-0.824
8	$[0.2100, 0.7000)$	0.291	0.338	0.506	22.993	0.208	7.272	0.181	0.866	-0.824
					z					
Bin	Range	$\langle x\rangle$	$\langle z\rangle$	$\langle P_{\mathrm{hT}}\rangle$ [GeV/c]	$\langle Q^2\rangle$ [(GeV/c)^2]	$\langle y\rangle$	$\langle W\rangle$ [GeV/c^2]	$\langle f\rangle$	$\langle \lvert P_T\rvert\rangle$	$\langle P_B\rangle$
0	$[0.20, 0.25)$	0.044	0.223	0.470	4.212	0.327	9.957	0.150	0.867	-0.825
1	$[0.25, 0.30)$	0.045	0.273	0.496	4.165	0.323	9.899	0.150	0.867	-0.825
2	$[0.30, 0.35)$	0.044	0.324	0.518	4.114	0.322	9.863	0.150	0.867	-0.825
3	$[0.35, 0.40)$	0.044	0.374	0.538	4.047	0.321	9.835	0.150	0.867	-0.825
4	$[0.40, 0.50)$	0.043	0.445	0.561	3.918	0.321	9.821	0.150	0.867	-0.825
5	$[0.50, 0.65)$	0.041	0.565	0.584	3.692	0.322	9.811	0.149	0.867	-0.825
6	$[0.65, 0.80)$	0.037	0.717	0.569	3.331	0.321	9.787	0.149	0.867	-0.825
7	$[0.80, 1.00)$	0.033	0.876	0.453	2.825	0.311	9.743	0.149	0.867	-0.824
					P_{hT}					
Bin	Range	$\langle x\rangle$	$\langle z\rangle$	$\langle P_{\mathrm{hT}}\rangle$ [GeV/c]	$\langle Q^2\rangle$ [(GeV/c)^2]	$\langle y\rangle$	$\langle W\rangle$ [GeV/c^2]	$\langle f\rangle$	$\langle \lvert P_T\rvert\rangle$	$\langle P_B\rangle$
0	$[0.10, 0.20)$	0.044	0.354	0.155	3.879	0.308	9.634	0.150	0.867	-0.825
1	$[0.20, 0.30)$	0.044	0.349	0.252	3.848	0.308	9.666	0.150	0.867	-0.825
2	$[0.30, 0.40)$	0.043	0.348	0.350	3.848	0.311	9.720	0.150	0.867	-0.825
3	$[0.40, 0.50)$	0.044	0.346	0.449	3.953	0.315	9.778	0.150	0.867	-0.825
4	$[0.50, 0.60)$	0.044	0.349	0.548	4.043	0.321	9.850	0.150	0.867	-0.825
5	$[0.60, 0.75)$	0.043	0.358	0.669	4.122	0.328	9.962	0.149	0.867	-0.825
6	$[0.75, 0.90)$	0.042	0.372	0.818	4.210	0.340	10.127	0.149	0.866	-0.826
7	$[0.90, 1.30)$	0.041	0.393	1.050	4.353	0.362	10.437	0.149	0.867	-0.826
8	$[0.13, 10.00)$	0.038	0.415	1.518	4.839	0.419	11.200	0.148	0.867	-0.827

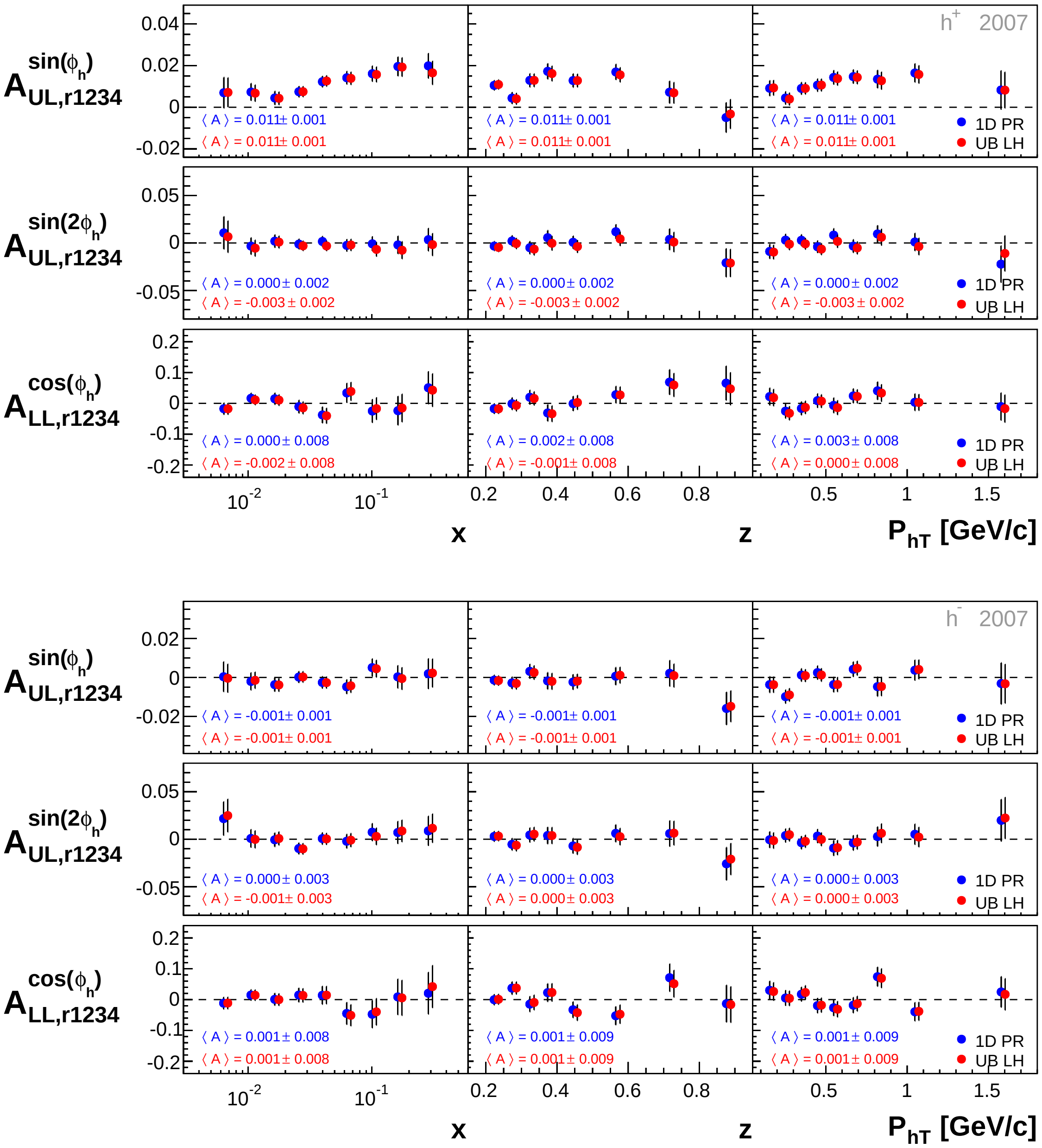

Figure A.25: Comparison of the azimuthal asymmetries, extracted with the methods 1D PR and UB LH, for h^+ (top) and h^- (bottom) for 2007.

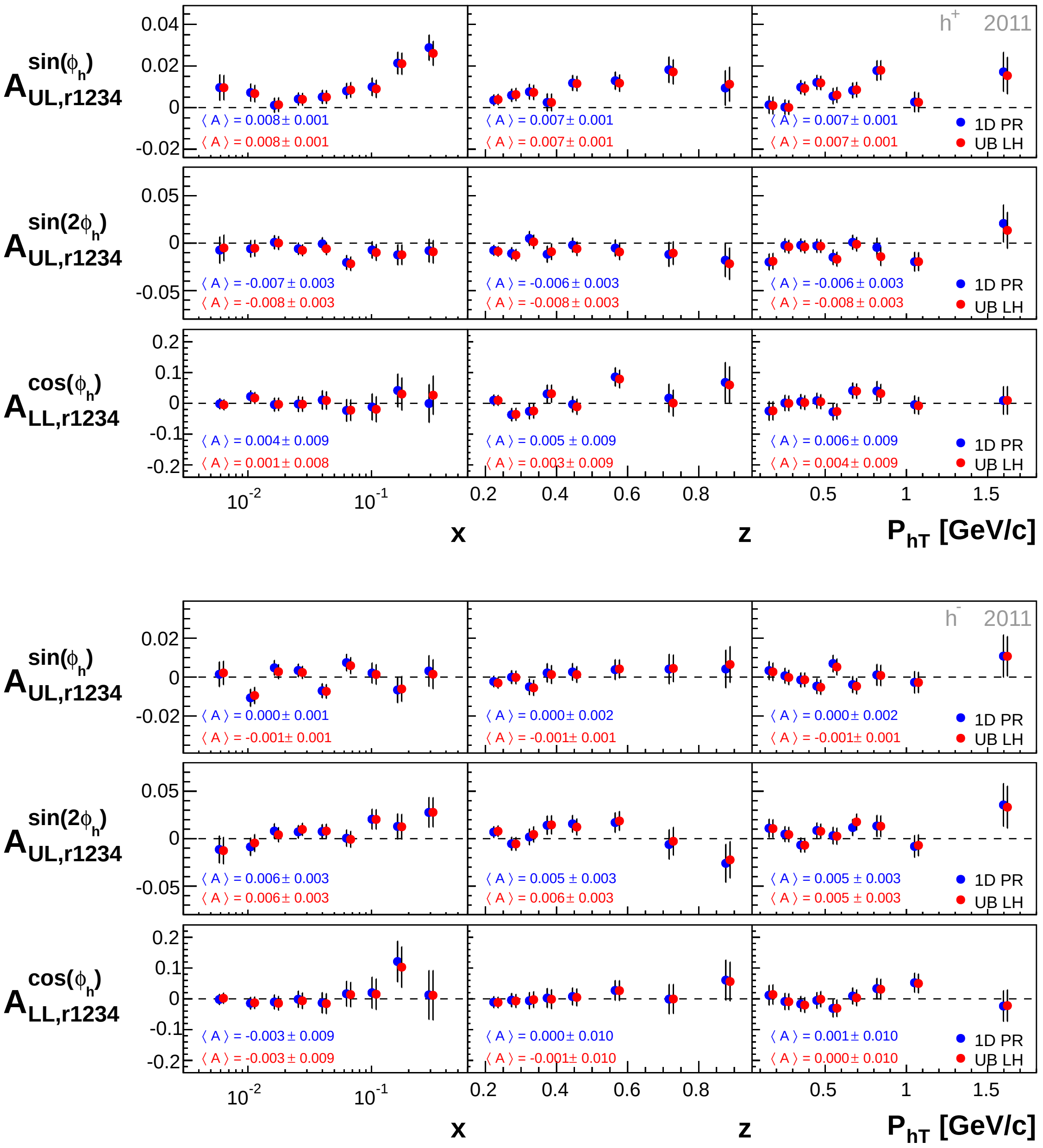

Figure A.26: Comparison of the azimuthal asymmetries, extracted with the methods 1D PR and UB LH, for h^+ (top) and h^- (bottom) for 2011.

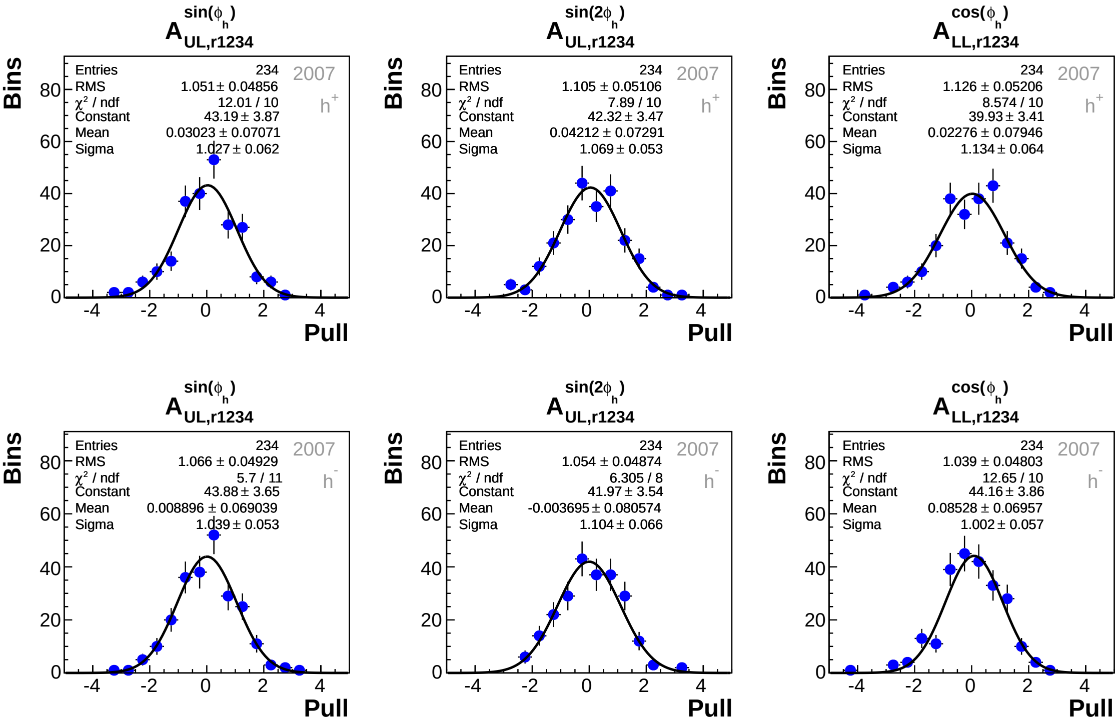

Figure A.27: Stability pull distributions of asymmetries for h^+ (top) and h^- (bottom), extracted with the 1D PR method, for 2007. The gaussian fit, corresponding statistical values and fit parameters are also displayed.

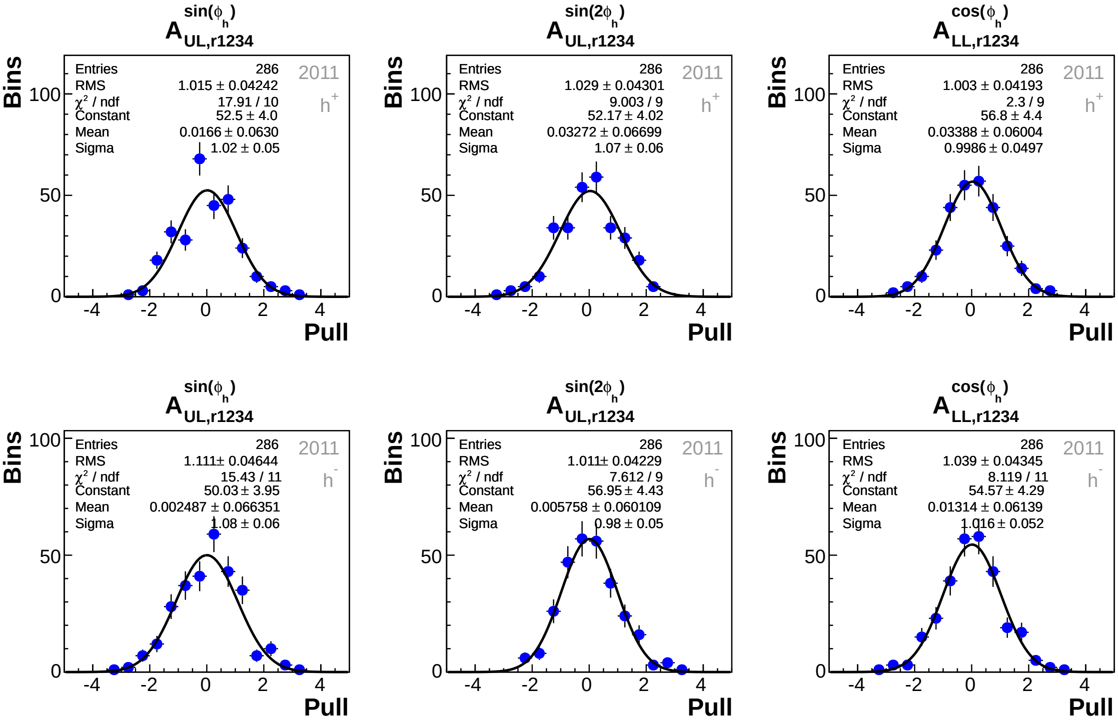

Figure A.28: Stability pull distributions of asymmetries for h^+ (top) and h^- (bottom), extracted with the 1D PR method, for 2011. The gaussian fit, corresponding statistical values and fit parameters are also displayed.

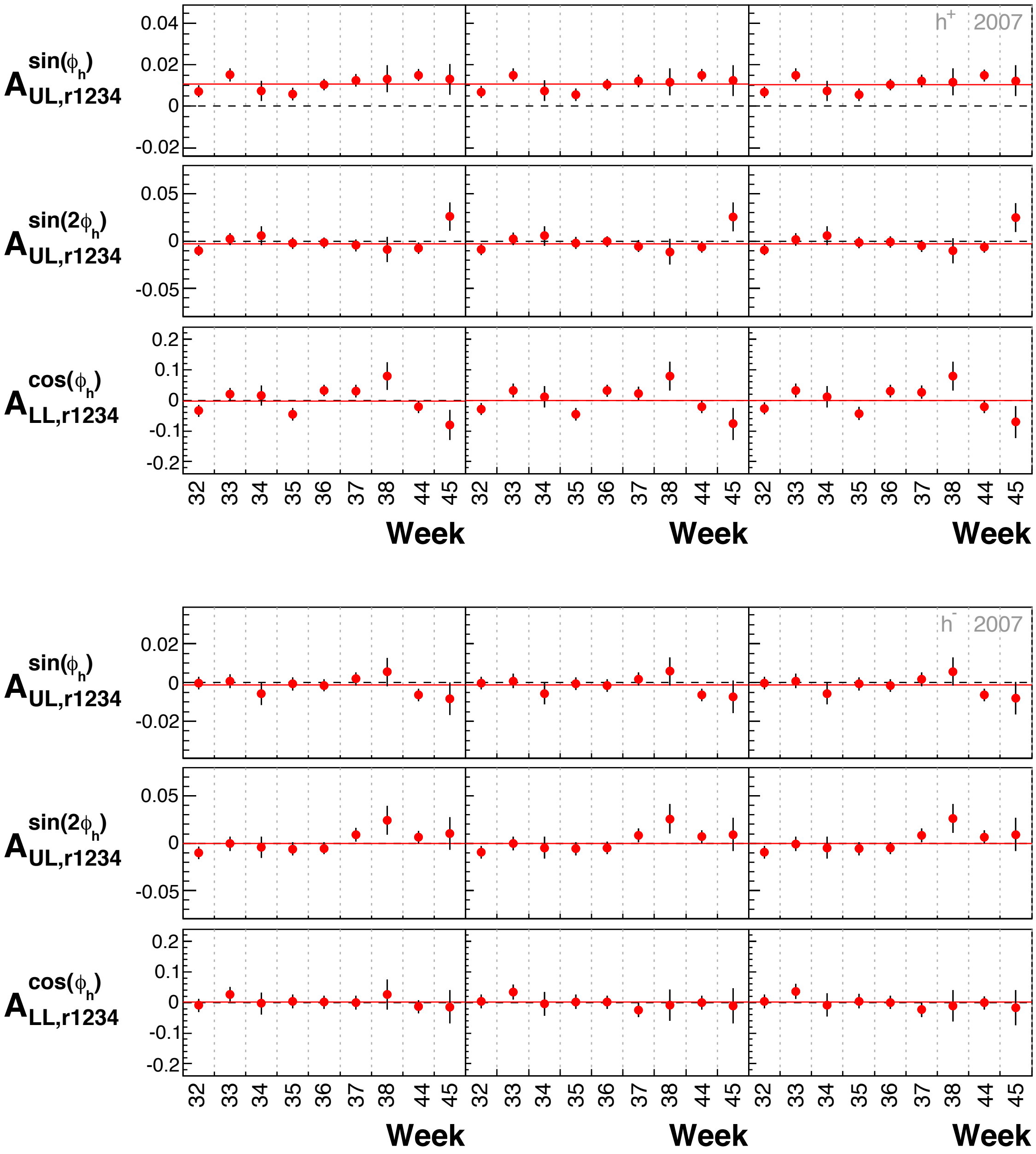

Figure A.29: Mean asymmetries for each week of 2007 for h^+ (top) and h^- (bottom). The three columns correspond to the kinematic variables x, z and P_{hT}. The red horizontal lines indicate the respective mean values.

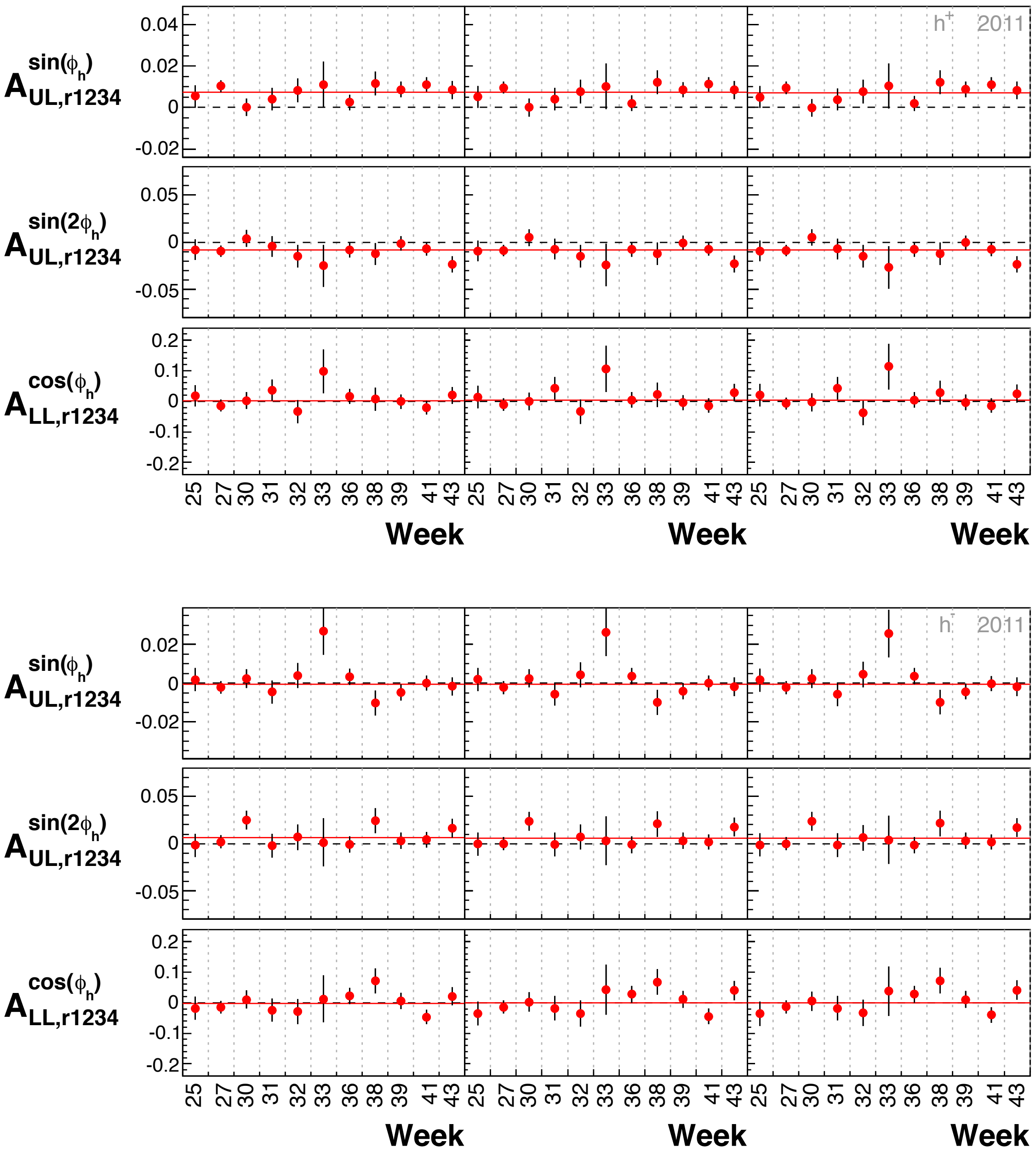

Figure A.30: Mean asymmetries for each week of 2007 for h^+ (top) and h^- (bottom). The three columns correspond to the kinematic variables x, z and P_{hT}. The red horizontal lines indicate the respective mean values.

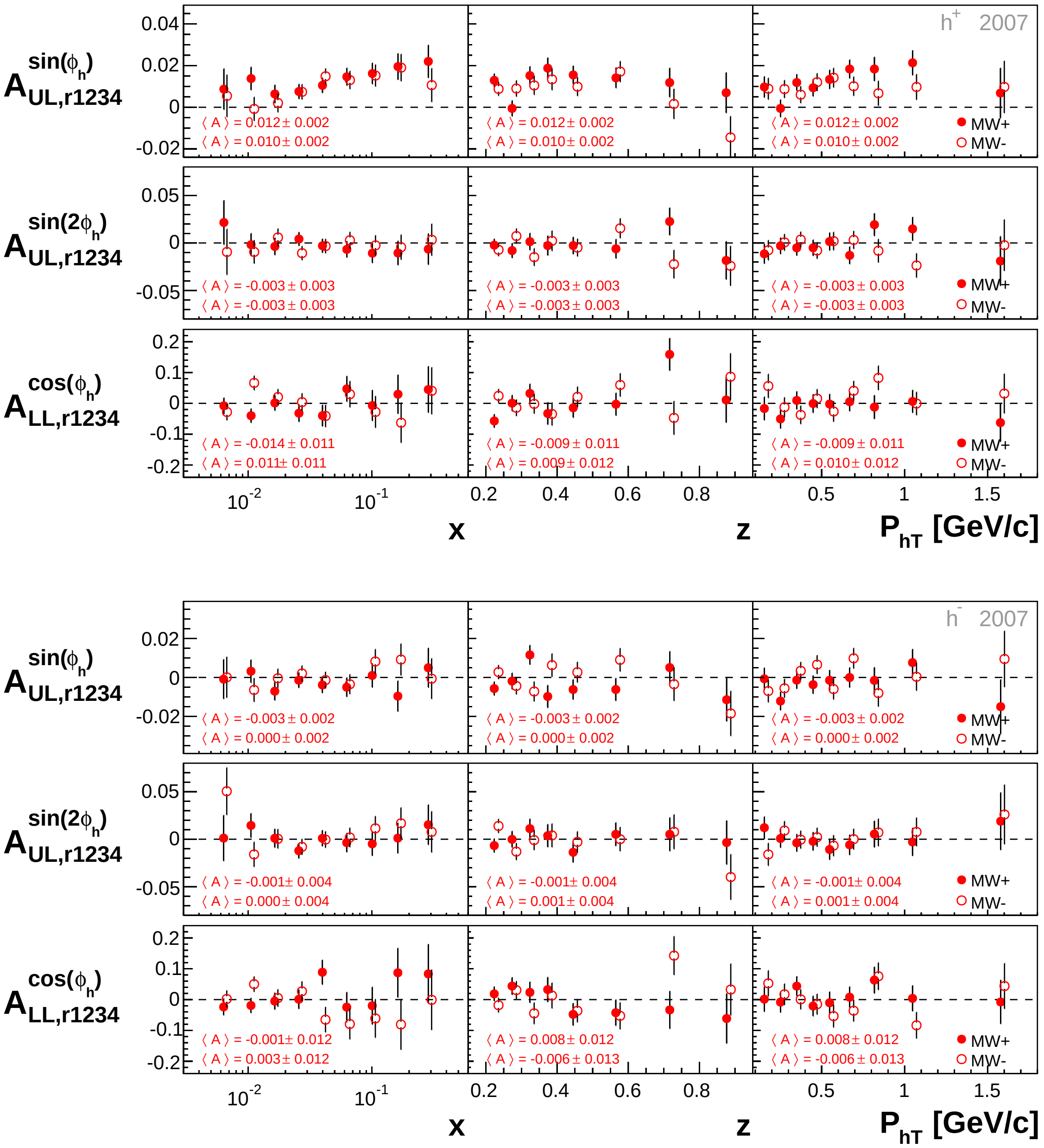

Figure A.31: Comparison of asymmetries from the two microwave settings for h^+ (top) and h^- (bottom) for 2007.

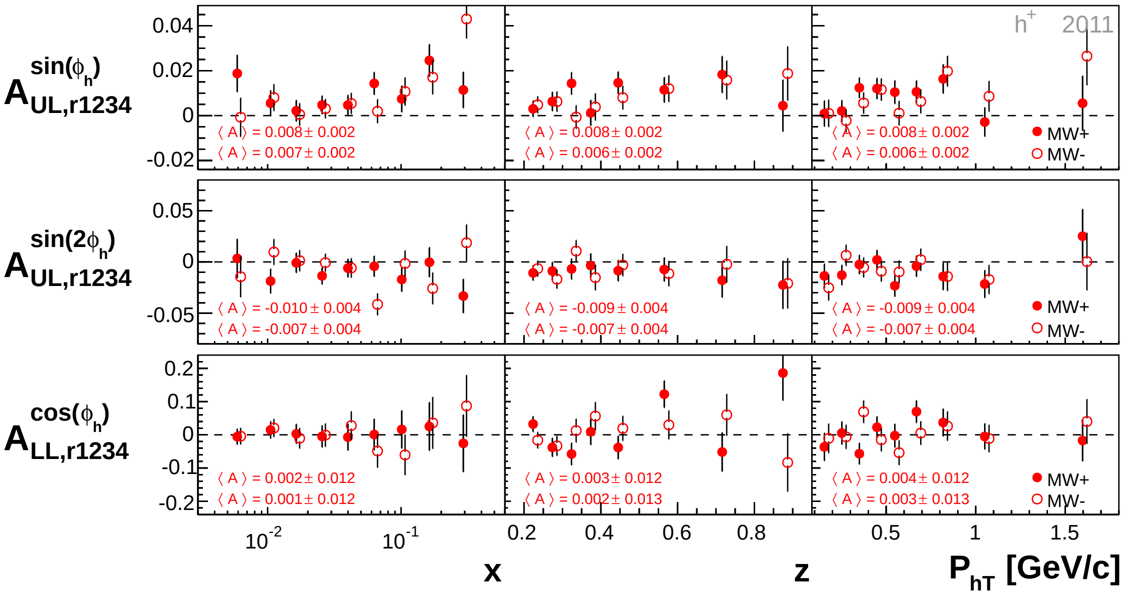

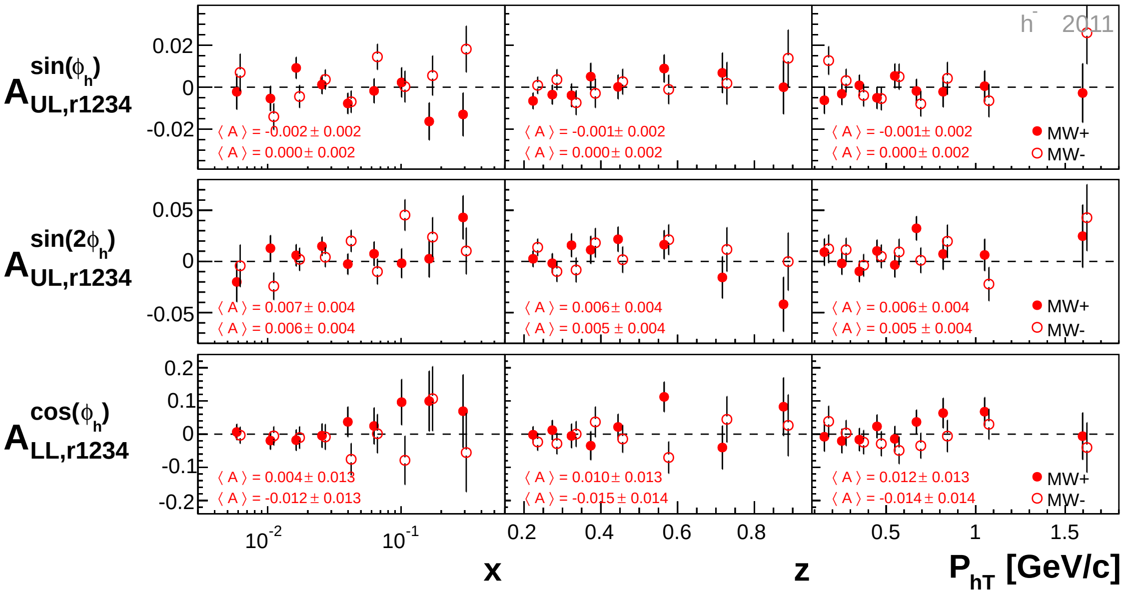

Figure A.32: Comparison of asymmetries from the two microwave settings for h^+ (top) and h^- (bottom) for 2011.

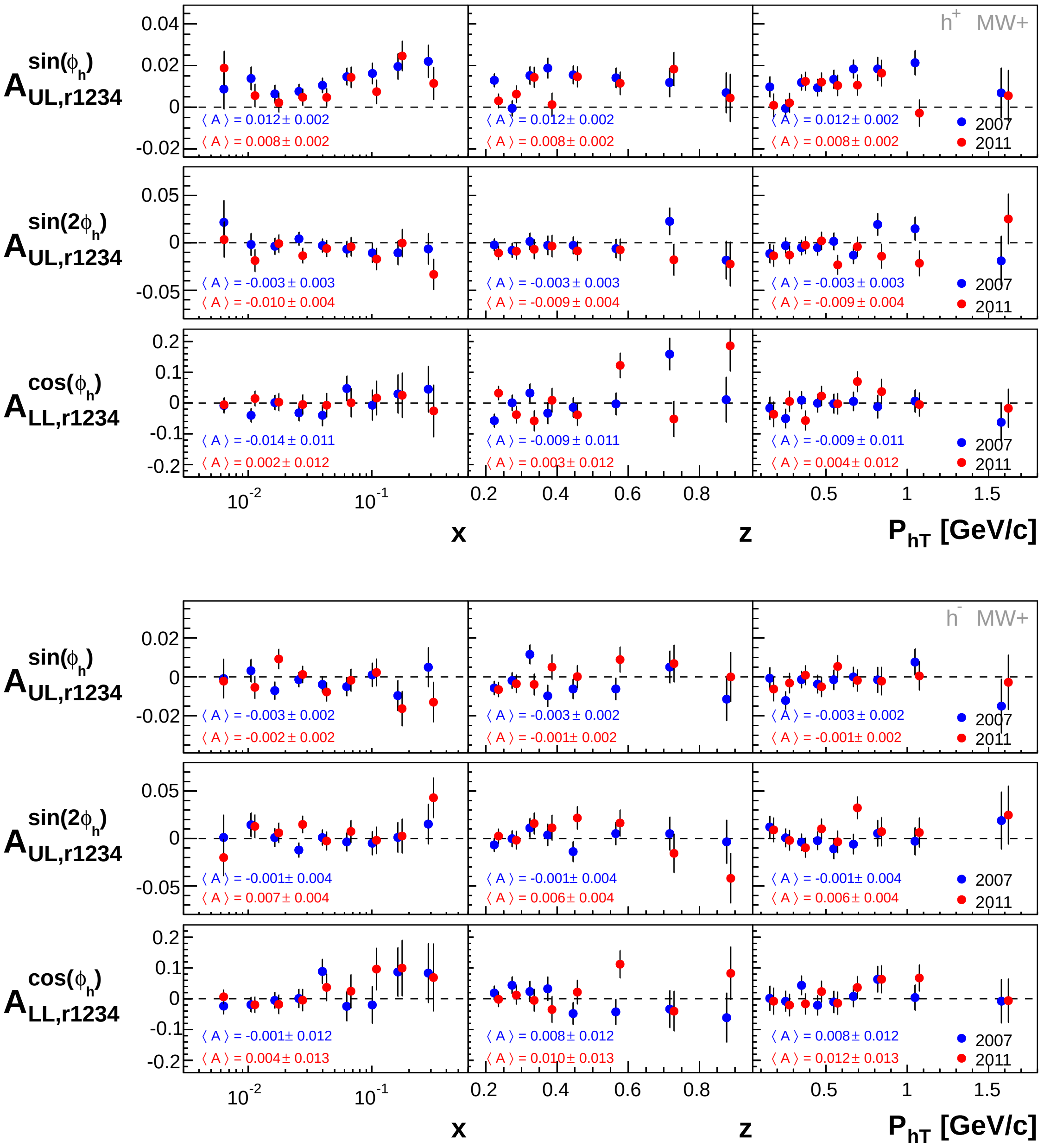

Figure A.33: Comparison of asymmetries from MW+ for h^+ (top) and h^- (bottom) for 2007 and 2011.

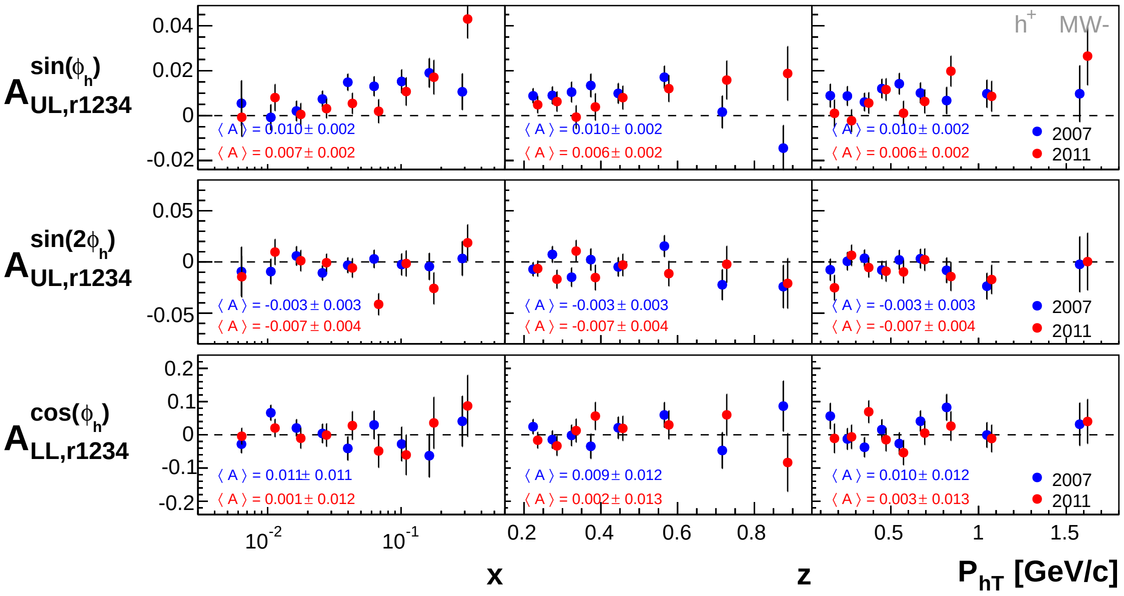

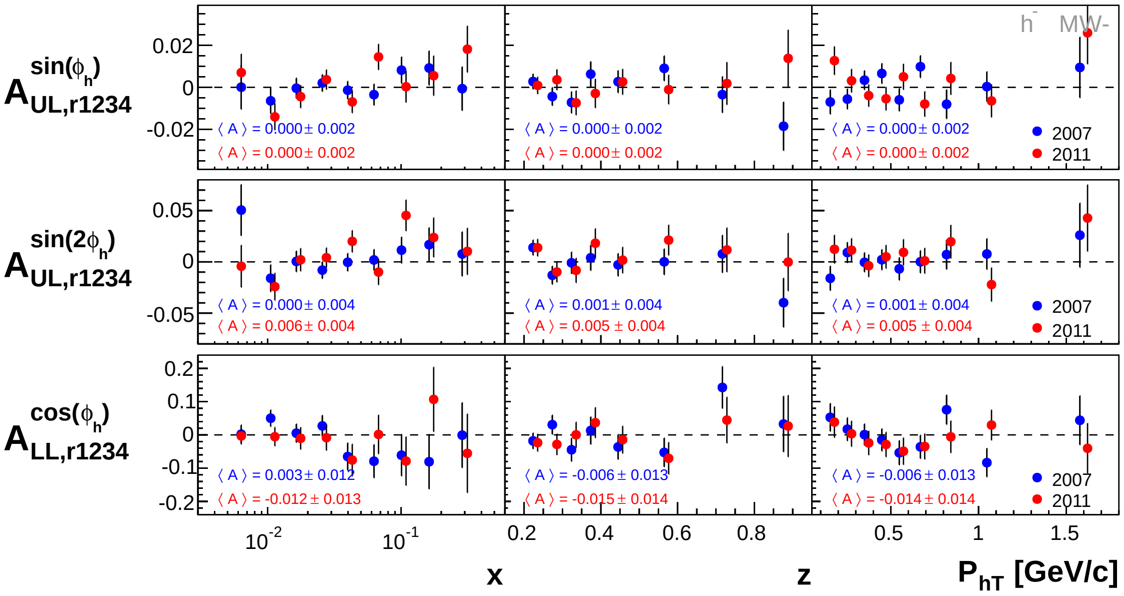

Figure A.34: Comparison of asymmetries from MW- for h^+ (top) and h^- (bottom) for 2007 and 2011.

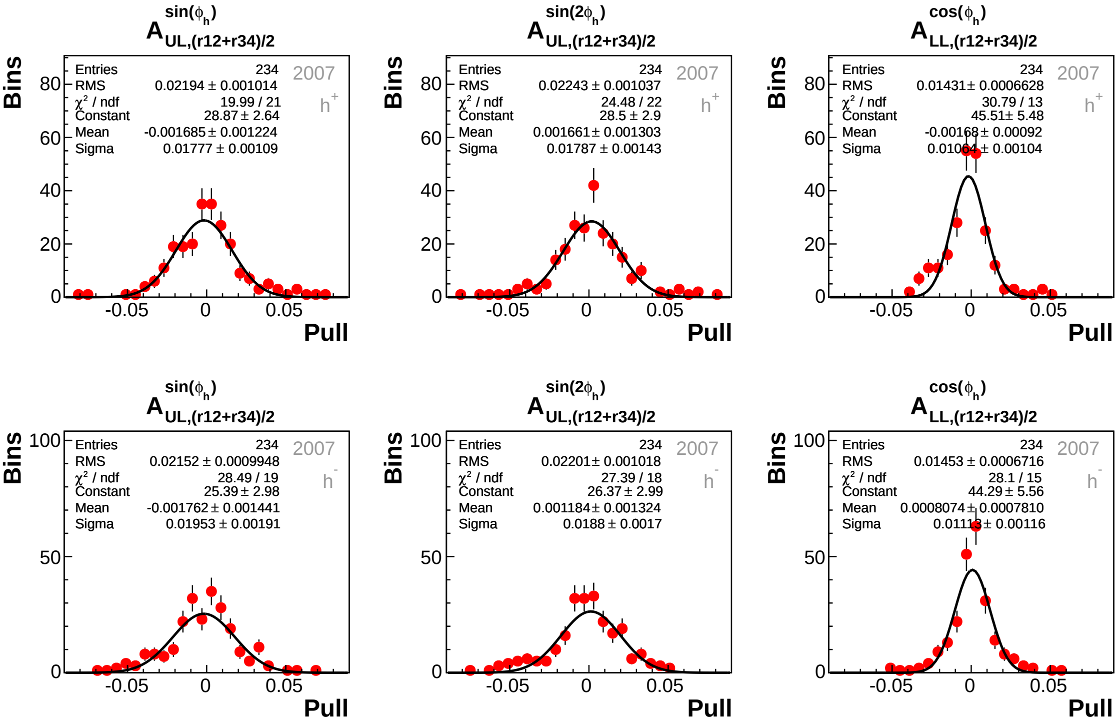

Figure A.35: Pull distributions for h^+ (top) and h^- (bottom) between asymmetries $A^{m(\phi_h)}_{(r12+r34)/2}$ and $A^{m(\phi_h)}_{r1234}$, for 2007. The gaussian fit, corresponding statistical values and fit parameters are also displayed.

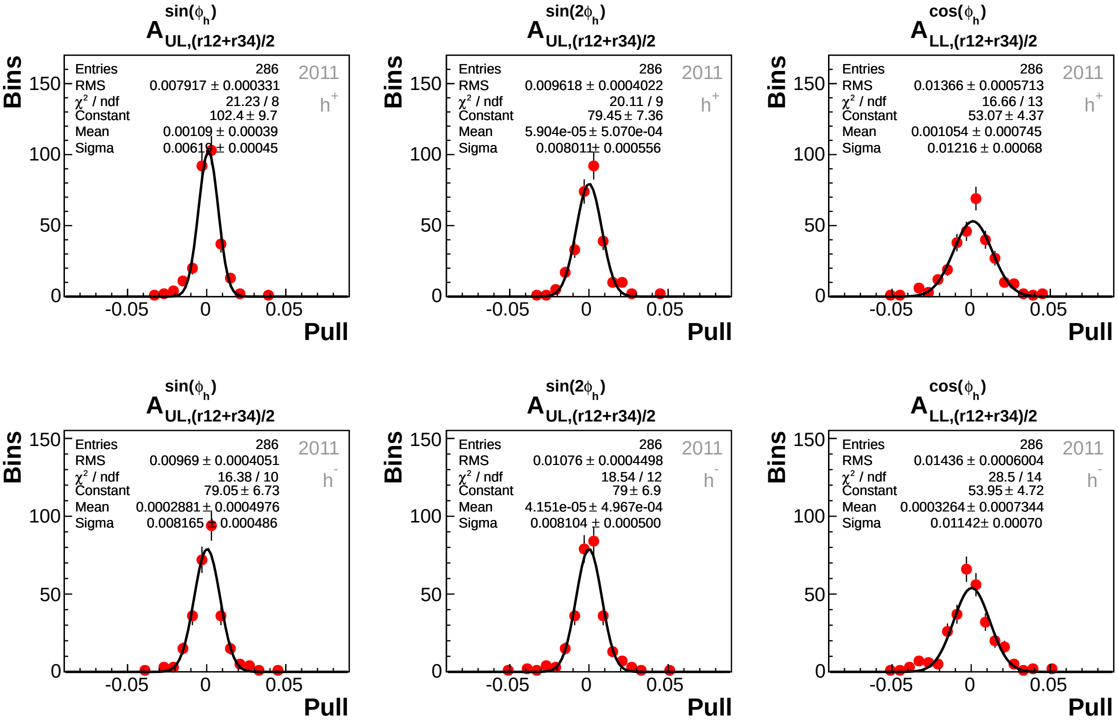

Figure A.36: Pull distributions for h^+ (top) and h^- (bottom) between asymmetries $A^{m(\phi_h)}_{(r12+r34)/2}$ and $A^{m(\phi_h)}_{r1234}$, for 2011. The gaussian fit, corresponding statistical values and fit parameters are also displayed.

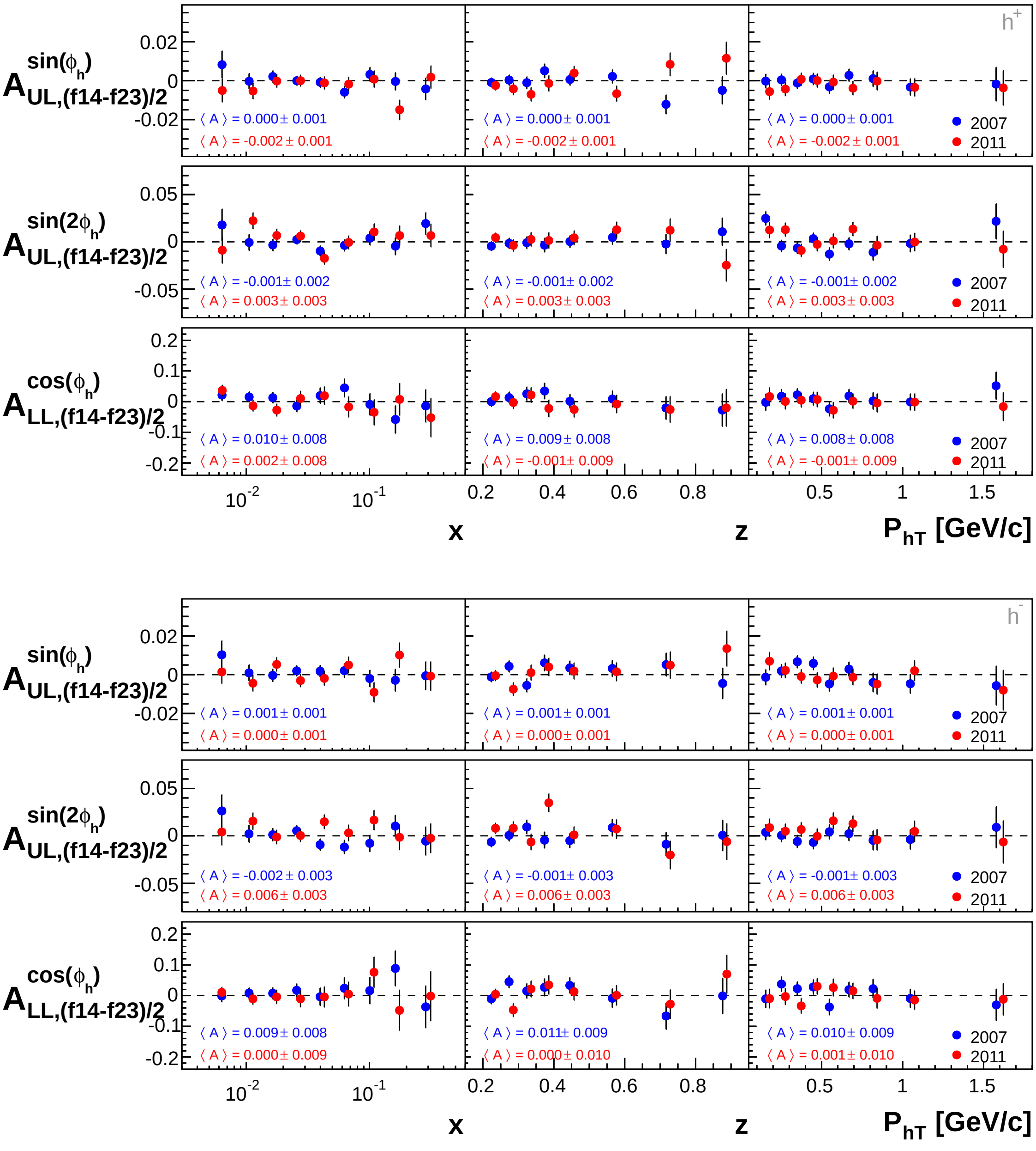

Figure A.37: Azimuthal false asymmetries $A_{(f14-f23)/2}^{m(\phi_h)}$ for h^+ (top) and h^- (bottom) from 2007 and 2011 data. Corresponding mean values are also displayed.

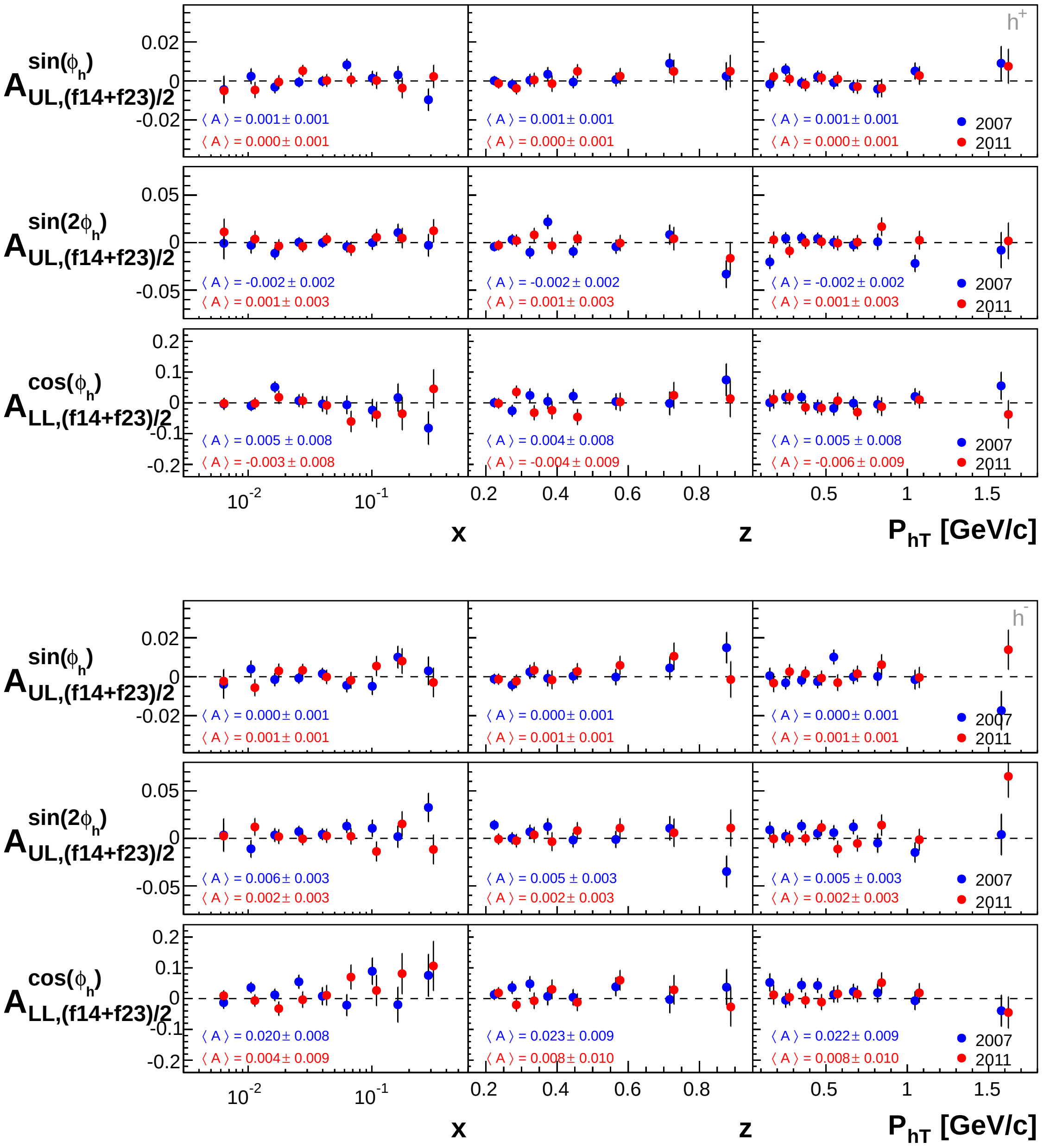

Figure A.38: Azimuthal false asymmetries $A^{m(\phi_h)}_{(f14+f23)/2}$ for h^+ (top) and h^- (bottom) from 2007 and 2011 data. Corresponding mean values are also displayed.

Table A.35: Results of $A_{UL}^{\sin(\phi_h)}$ for h^+ in bins of x, z, and P_{hT} for 2007.

h^+			2007
		x	
Bin	Range	$\langle x\rangle$	$A_{UL}^{\sin(\phi_h)}$
0	$[0.0025, 0.0080)$	0.006	0.007 ± 0.007 ± 0.004
1	$[0.0080, 0.0130)$	0.011	0.007 ± 0.004 ± 0.002
2	$[0.0130, 0.0200)$	0.016	0.004 ± 0.003 ± 0.002
3	$[0.0200, 0.0320)$	0.026	0.007 ± 0.002 ± 0.002
4	$[0.0320, 0.0500)$	0.040	0.013 ± 0.003 ± 0.002
5	$[0.0500, 0.0800)$	0.063	0.014 ± 0.003 ± 0.002
6	$[0.0800, 0.1300)$	0.101	0.016 ± 0.004 ± 0.002
7	$[0.1300, 0.2100)$	0.163	0.019 ± 0.004 ± 0.003
8	$[0.2100, 0.7000)$	0.287	0.016 ± 0.006 ± 0.003
		z	
Bin	Range	$\langle z\rangle$	$A_{UL}^{\sin(\phi_h)}$
0	$[0.20, 0.25)$	0.224	0.011 ± 0.002 ± 0.001
1	$[0.25, 0.30)$	0.274	0.004 ± 0.003 ± 0.002
2	$[0.30, 0.35)$	0.324	0.013 ± 0.003 ± 0.002
3	$[0.35, 0.40)$	0.374	0.016 ± 0.004 ± 0.002
4	$[0.40, 0.50)$	0.445	0.013 ± 0.003 ± 0.002
5	$[0.50, 0.65)$	0.565	0.016 ± 0.003 ± 0.002
6	$[0.65, 0.80)$	0.716	0.007 ± 0.005 ± 0.003
7	$[0.80, 1.00)$	0.875	-0.003 ± 0.007 ± 0.004
		P_{hT}	
Bin	Range	$\langle P_{hT}\rangle$ [GeV/c]	$A_{UL}^{\sin(\phi_h)}$
0	$[0.10, 0.20)$	0.155	0.009 ± 0.004 ± 0.002
1	$[0.20, 0.30)$	0.252	0.004 ± 0.003 ± 0.002
2	$[0.30, 0.40)$	0.350	0.009 ± 0.003 ± 0.002
3	$[0.40, 0.50)$	0.449	0.011 ± 0.003 ± 0.002
4	$[0.50, 0.60)$	0.548	0.014 ± 0.003 ± 0.002
5	$[0.60, 0.75)$	0.669	0.014 ± 0.003 ± 0.002
6	$[0.75, 0.90)$	0.818	0.013 ± 0.004 ± 0.003
7	$[0.90, 1.30)$	1.048	0.016 ± 0.004 ± 0.003
8	$[0.13, 10.00)$	1.577	0.008 ± 0.009 ± 0.005

Table A.36: Results of $A_{UL}^{\sin(\phi_h)}$ for h^+ in bins of x, z, and P_{hT} for 2011.

h^+			2011
		x	
Bin	Range	$\langle x\rangle$	$A_{UL}^{\sin(\phi_h)}$
0	$[0.0025, 0.0080)$	0.006	0.010 ± 0.006 ± 0.002
1	$[0.0080, 0.0130)$	0.011	0.007 ± 0.004 ± 0.002
2	$[0.0130, 0.0200)$	0.016	0.001 ± 0.003 ± 0.001
3	$[0.0200, 0.0320)$	0.026	0.004 ± 0.003 ± 0.001
4	$[0.0320, 0.0500)$	0.040	0.005 ± 0.003 ± 0.001
5	$[0.0500, 0.0800)$	0.063	0.008 ± 0.004 ± 0.001
6	$[0.0800, 0.1300)$	0.101	0.009 ± 0.004 ± 0.002
7	$[0.1300, 0.2100)$	0.163	0.021 ± 0.005 ± 0.002
8	$[0.2100, 0.7000)$	0.292	0.026 ± 0.006 ± 0.002
		z	
Bin	Range	$\langle z\rangle$	$A_{UL}^{\sin(\phi_h)}$
0	$[0.20, 0.25)$	0.223	0.004 ± 0.003 ± 0.001
1	$[0.25, 0.30)$	0.274	0.006 ± 0.003 ± 0.001
2	$[0.30, 0.35)$	0.324	0.007 ± 0.004 ± 0.001
3	$[0.35, 0.40)$	0.374	0.002 ± 0.004 ± 0.002
4	$[0.40, 0.50)$	0.445	0.012 ± 0.004 ± 0.001
5	$[0.50, 0.65)$	0.565	0.012 ± 0.004 ± 0.002
6	$[0.65, 0.80)$	0.716	0.017 ± 0.006 ± 0.002
7	$[0.80, 1.00)$	0.875	0.011 ± 0.008 ± 0.003
		P_{hT}	
Bin	Range	$\langle P_{hT}\rangle$ [GeV/c]	$A_{UL}^{\sin(\phi_h)}$
0	$[0.10, 0.20)$	0.155	0.001 ± 0.004 ± 0.002
1	$[0.20, 0.30)$	0.252	0.000 ± 0.003 ± 0.001
2	$[0.30, 0.40)$	0.350	0.009 ± 0.003 ± 0.001
3	$[0.40, 0.50)$	0.449	0.012 ± 0.003 ± 0.001
4	$[0.50, 0.60)$	0.548	0.006 ± 0.004 ± 0.001
5	$[0.60, 0.75)$	0.669	0.009 ± 0.004 ± 0.001
6	$[0.75, 0.90)$	0.818	0.018 ± 0.005 ± 0.002
7	$[0.90, 1.30)$	1.051	0.003 ± 0.005 ± 0.002
8	$[0.13, 10.00)$	1.597	0.015 ± 0.009 ± 0.004

Table A.37: Results of $A_{UL}^{\sin(\phi_h)}$ for h^+ in bins of x, z, and P_{hT}.

h^+			2007 & 2011
		x	
Bin	Range	$\langle x \rangle$	$A_{UL}^{\sin(\phi_h)}$
0	$[0.0025, 0.0080)$	0.006	0.009 ± 0.005 ± 0.004
1	$[0.0080, 0.0130)$	0.011	0.007 ± 0.003 ± 0.002
2	$[0.0130, 0.0200)$	0.016	0.003 ± 0.002 ± 0.002
3	$[0.0200, 0.0320)$	0.026	0.006 ± 0.002 ± 0.002
4	$[0.0320, 0.0500)$	0.040	0.010 ± 0.002 ± 0.002
5	$[0.0500, 0.0800)$	0.063	0.012 ± 0.002 ± 0.002
6	$[0.0800, 0.1300)$	0.101	0.013 ± 0.003 ± 0.002
7	$[0.1300, 0.2100)$	0.163	0.020 ± 0.003 ± 0.003
8	$[0.2100, 0.7000)$	0.289	0.021 ± 0.004 ± 0.003
		z	
Bin	Range	$\langle z \rangle$	$A_{UL}^{\sin(\phi_h)}$
0	$[0.20, 0.25)$	0.223	0.008 ± 0.002 ± 0.001
1	$[0.25, 0.30)$	0.274	0.005 ± 0.002 ± 0.002
2	$[0.30, 0.35)$	0.324	0.010 ± 0.002 ± 0.002
3	$[0.35, 0.40)$	0.374	0.010 ± 0.003 ± 0.002
4	$[0.40, 0.50)$	0.445	0.012 ± 0.002 ± 0.002
5	$[0.50, 0.65)$	0.565	0.014 ± 0.003 ± 0.002
6	$[0.65, 0.80)$	0.716	0.011 ± 0.004 ± 0.003
7	$[0.80, 1.00)$	0.875	0.003 ± 0.005 ± 0.004
		P_{hT}	
Bin	Range	$\langle P_{hT} \rangle$ [GeV/c]	$A_{UL}^{\sin(\phi_h)}$
0	$[0.10, 0.20)$	0.155	0.006 ± 0.003 ± 0.002
1	$[0.20, 0.30)$	0.252	0.002 ± 0.002 ± 0.002
2	$[0.30, 0.40)$	0.350	0.009 ± 0.002 ± 0.002
3	$[0.40, 0.50)$	0.449	0.011 ± 0.002 ± 0.002
4	$[0.50, 0.60)$	0.548	0.010 ± 0.002 ± 0.002
5	$[0.60, 0.75)$	0.669	0.012 ± 0.002 ± 0.002
6	$[0.75, 0.90)$	0.818	0.015 ± 0.003 ± 0.003
7	$[0.90, 1.30)$	1.049	0.010 ± 0.003 ± 0.003
8	$[0.13, 10.00)$	1.587	0.012 ± 0.006 ± 0.005

Table A.38: Results of $A_{UL}^{\sin(\phi_h)}$ for h^- in bins of x, z, and P_{hT} for 2007.

h^-			2007
		x	
Bin	Range	$\langle x \rangle$	$A_{UL}^{\sin(\phi_h)}$
0	$[0.0025, 0.0080)$	0.006	0.000 ± 0.007 ± 0.005
1	$[0.0080, 0.0130)$	0.011	-0.001 ± 0.004 ± 0.003
2	$[0.0130, 0.0200)$	0.016	-0.004 ± 0.003 ± 0.002
3	$[0.0200, 0.0320)$	0.026	0.000 ± 0.003 ± 0.002
4	$[0.0320, 0.0500)$	0.040	-0.003 ± 0.003 ± 0.002
5	$[0.0500, 0.0800)$	0.063	-0.004 ± 0.003 ± 0.002
6	$[0.0800, 0.1300)$	0.101	0.004 ± 0.004 ± 0.003
7	$[0.1300, 0.2100)$	0.162	-0.001 ± 0.006 ± 0.004
8	$[0.2100, 0.7000)$	0.286	0.002 ± 0.007 ± 0.005
		z	
Bin	Range	$\langle z \rangle$	$A_{UL}^{\sin(\phi_h)}$
0	$[0.20, 0.25)$	0.223	-0.002 ± 0.002 ± 0.002
1	$[0.25, 0.30)$	0.273	-0.003 ± 0.003 ± 0.002
2	$[0.30, 0.35)$	0.324	0.002 ± 0.003 ± 0.002
3	$[0.35, 0.40)$	0.374	-0.002 ± 0.004 ± 0.003
4	$[0.40, 0.50)$	0.445	-0.002 ± 0.004 ± 0.002
5	$[0.50, 0.65)$	0.565	0.001 ± 0.004 ± 0.003
6	$[0.65, 0.80)$	0.717	0.001 ± 0.006 ± 0.004
7	$[0.80, 1.00)$	0.876	-0.015 ± 0.008 ± 0.005
		P_{hT}	
Bin	Range	$\langle P_{hT} \rangle$ [GeV/c]	$A_{UL}^{\sin(\phi_h)}$
0	$[0.10, 0.20)$	0.155	-0.004 ± 0.004 ± 0.003
1	$[0.20, 0.30)$	0.252	-0.009 ± 0.003 ± 0.002
2	$[0.30, 0.40)$	0.350	0.001 ± 0.003 ± 0.002
3	$[0.40, 0.50)$	0.449	0.001 ± 0.003 ± 0.002
4	$[0.50, 0.60)$	0.548	-0.004 ± 0.004 ± 0.002
5	$[0.60, 0.75)$	0.669	0.005 ± 0.004 ± 0.002
6	$[0.75, 0.90)$	0.818	-0.005 ± 0.005 ± 0.003
7	$[0.90, 1.30)$	1.048	0.004 ± 0.005 ± 0.003
8	$[0.13, 10.00)$	1.578	-0.003 ± 0.010 ± 0.006

Table A.39: Results of $A_{UL}^{\sin(\phi_h)}$ for h^- in bins of x, z, and P_{hT} for 2011.

h^-			2011
		x	
Bin	Range	$\langle x \rangle$	$A_{UL}^{\sin(\phi_h)}$
0	$[0.0025, 0.0080)$	0.006	0.002 ± 0.006 ± 0.004
1	$[0.0080, 0.0130)$	0.010	-0.009 ± 0.004 ± 0.003
2	$[0.0130, 0.0200)$	0.016	0.003 ± 0.004 ± 0.002
3	$[0.0200, 0.0320)$	0.026	0.002 ± 0.003 ± 0.002
4	$[0.0320, 0.0500)$	0.040	-0.007 ± 0.004 ± 0.002
5	$[0.0500, 0.0800)$	0.063	0.006 ± 0.004 ± 0.003
6	$[0.0800, 0.1300)$	0.101	0.001 ± 0.005 ± 0.003
7	$[0.1300, 0.2100)$	0.163	-0.006 ± 0.006 ± 0.004
8	$[0.2100, 0.7000)$	0.291	0.001 ± 0.007 ± 0.005
		z	
Bin	Range	$\langle z \rangle$	$A_{UL}^{\sin(\phi_h)}$
0	$[0.20, 0.25)$	0.223	-0.003 ± 0.003 ± 0.002
1	$[0.25, 0.30)$	0.273	0.000 ± 0.003 ± 0.002
2	$[0.30, 0.35)$	0.324	-0.006 ± 0.004 ± 0.002
3	$[0.35, 0.40)$	0.374	0.001 ± 0.005 ± 0.003
4	$[0.40, 0.50)$	0.445	0.001 ± 0.004 ± 0.003
5	$[0.50, 0.65)$	0.565	0.004 ± 0.005 ± 0.003
6	$[0.65, 0.80)$	0.717	0.004 ± 0.007 ± 0.004
7	$[0.80, 1.00)$	0.876	0.006 ± 0.009 ± 0.006
		P_{hT}	
Bin	Range	$\langle P_{hT} \rangle$ [GeV/c]	$A_{UL}^{\sin(\phi_h)}$
0	$[0.10, 0.20)$	0.155	0.003 ± 0.005 ± 0.003
1	$[0.20, 0.30)$	0.252	0.000 ± 0.004 ± 0.002
2	$[0.30, 0.40)$	0.350	-0.001 ± 0.004 ± 0.002
3	$[0.40, 0.50)$	0.449	-0.005 ± 0.004 ± 0.002
4	$[0.50, 0.60)$	0.548	0.005 ± 0.004 ± 0.003
5	$[0.60, 0.75)$	0.669	-0.005 ± 0.004 ± 0.002
6	$[0.75, 0.90)$	0.818	0.001 ± 0.005 ± 0.003
7	$[0.90, 1.30)$	1.050	-0.003 ± 0.005 ± 0.003
8	$[0.13, 10.00)$	1.597	0.011 ± 0.010 ± 0.006

Table A.40: Results of $A_{UL}^{\sin(\phi_h)}$ for h^- in bins of x, z, and P_{hT}.

h^-			2007 & 2011
		x	
Bin	Range	$\langle x \rangle$	$A_{UL}^{\sin(\phi_h)}$
0	$[0.0025, 0.0080)$	0.006	0.001 ± 0.005 ± 0.005
1	$[0.0080, 0.0130)$	0.011	-0.005 ± 0.003 ± 0.003
2	$[0.0130, 0.0200)$	0.016	-0.001 ± 0.002 ± 0.002
3	$[0.0200, 0.0320)$	0.026	0.001 ± 0.002 ± 0.002
4	$[0.0320, 0.0500)$	0.040	-0.005 ± 0.002 ± 0.002
5	$[0.0500, 0.0800)$	0.063	0.000 ± 0.003 ± 0.003
6	$[0.0800, 0.1300)$	0.101	0.003 ± 0.003 ± 0.003
7	$[0.1300, 0.2100)$	0.162	-0.003 ± 0.004 ± 0.004
8	$[0.2100, 0.7000)$	0.289	0.002 ± 0.005 ± 0.005
		z	
Bin	Range	$\langle z \rangle$	$A_{UL}^{\sin(\phi_h)}$
0	$[0.20, 0.25)$	0.223	-0.002 ± 0.002 ± 0.002
1	$[0.25, 0.30)$	0.273	-0.002 ± 0.002 ± 0.002
2	$[0.30, 0.35)$	0.324	-0.001 ± 0.003 ± 0.002
3	$[0.35, 0.40)$	0.374	-0.001 ± 0.003 ± 0.003
4	$[0.40, 0.50)$	0.445	-0.001 ± 0.003 ± 0.003
5	$[0.50, 0.65)$	0.565	0.002 ± 0.003 ± 0.003
6	$[0.65, 0.80)$	0.717	0.002 ± 0.004 ± 0.004
7	$[0.80, 1.00)$	0.876	-0.006 ± 0.006 ± 0.006
		P_{hT}	
Bin	Range	$\langle P_{hT} \rangle$ [GeV/c]	$A_{UL}^{\sin(\phi_h)}$
0	$[0.10, 0.20)$	0.155	-0.001 ± 0.003 ± 0.003
1	$[0.20, 0.30)$	0.252	-0.005 ± 0.002 ± 0.002
2	$[0.30, 0.40)$	0.350	0.000 ± 0.002 ± 0.002
3	$[0.40, 0.50)$	0.449	-0.002 ± 0.002 ± 0.002
4	$[0.50, 0.60)$	0.548	0.000 ± 0.003 ± 0.003
5	$[0.60, 0.75)$	0.669	0.001 ± 0.003 ± 0.002
6	$[0.75, 0.90)$	0.818	-0.002 ± 0.004 ± 0.003
7	$[0.90, 1.30)$	1.049	0.001 ± 0.004 ± 0.003
8	$[0.13, 10.00)$	1.588	0.004 ± 0.007 ± 0.006

Table A.41: Results of $A_{UL}^{\sin(2\phi_h)}$ for h^+ in bins of x, z, and P_{hT} for 2007.

h^+			2007
		x	
Bin	Range	$\langle x \rangle$	$A_{UL}^{\sin(2\phi_h)}$
0	$[0.0025, 0.0080)$	0.006	0.007 ± 0.017 ± 0.013
1	$[0.0080, 0.0130)$	0.011	-0.005 ± 0.008 ± 0.007
2	$[0.0130, 0.0200)$	0.016	0.001 ± 0.006 ± 0.005
3	$[0.0200, 0.0320)$	0.026	-0.003 ± 0.005 ± 0.004
4	$[0.0320, 0.0500)$	0.040	-0.003 ± 0.005 ± 0.004
5	$[0.0500, 0.0800)$	0.063	-0.002 ± 0.006 ± 0.005
6	$[0.0800, 0.1300)$	0.101	-0.007 ± 0.007 ± 0.006
7	$[0.1300, 0.2100)$	0.163	-0.008 ± 0.009 ± 0.007
8	$[0.2100, 0.7000)$	0.287	-0.002 ± 0.012 ± 0.009
		z	
Bin	Range	$\langle z \rangle$	$A_{UL}^{\sin(2\phi_h)}$
0	$[0.20, 0.25)$	0.224	-0.005 ± 0.005 ± 0.004
1	$[0.25, 0.30)$	0.274	-0.001 ± 0.005 ± 0.004
2	$[0.30, 0.35)$	0.324	-0.006 ± 0.006 ± 0.005
3	$[0.35, 0.40)$	0.374	0.000 ± 0.007 ± 0.006
4	$[0.40, 0.50)$	0.445	-0.004 ± 0.006 ± 0.005
5	$[0.50, 0.65)$	0.565	0.004 ± 0.007 ± 0.006
6	$[0.65, 0.80)$	0.716	0.001 ± 0.010 ± 0.008
7	$[0.80, 1.00)$	0.875	-0.021 ± 0.014 ± 0.011
		P_{hT}	
Bin	Range	$\langle P_{hT} \rangle$ [GeV/c]	$A_{UL}^{\sin(2\phi_h)}$
0	$[0.10, 0.20)$	0.155	-0.010 ± 0.007 ± 0.006
1	$[0.20, 0.30)$	0.252	-0.001 ± 0.006 ± 0.005
2	$[0.30, 0.40)$	0.350	-0.001 ± 0.006 ± 0.004
3	$[0.40, 0.50)$	0.449	-0.006 ± 0.006 ± 0.005
4	$[0.50, 0.60)$	0.548	0.002 ± 0.007 ± 0.005
5	$[0.60, 0.75)$	0.669	-0.005 ± 0.006 ± 0.005
6	$[0.75, 0.90)$	0.818	0.006 ± 0.008 ± 0.007
7	$[0.90, 1.30)$	1.048	-0.004 ± 0.009 ± 0.007
8	$[0.13, 10.00)$	1.577	-0.011 ± 0.019 ± 0.015

Table A.42: Results of $A_{UL}^{\sin(2\phi_h)}$ for h^+ in bins of x, z, and P_{hT} for 2011.

h^+			2011
		x	
Bin	Range	$\langle x \rangle$	$A_{UL}^{\sin(2\phi_h)}$
0	$[0.0025, 0.0080)$	0.006	-0.005 ± 0.014 ± 0.010
1	$[0.0080, 0.0130)$	0.011	-0.005 ± 0.009 ± 0.006
2	$[0.0130, 0.0200)$	0.016	0.000 ± 0.007 ± 0.005
3	$[0.0200, 0.0320)$	0.026	-0.008 ± 0.006 ± 0.004
4	$[0.0320, 0.0500)$	0.040	-0.006 ± 0.006 ± 0.004
5	$[0.0500, 0.0800)$	0.063	-0.022 ± 0.007 ± 0.005
6	$[0.0800, 0.1300)$	0.101	-0.010 ± 0.009 ± 0.006
7	$[0.1300, 0.2100)$	0.163	-0.012 ± 0.010 ± 0.007
8	$[0.2100, 0.7000)$	0.292	-0.009 ± 0.012 ± 0.008
		z	
Bin	Range	$\langle z \rangle$	$A_{UL}^{\sin(2\phi_h)}$
0	$[0.20, 0.25)$	0.223	-0.009 ± 0.005 ± 0.004
1	$[0.25, 0.30)$	0.274	-0.013 ± 0.006 ± 0.004
2	$[0.30, 0.35)$	0.324	0.001 ± 0.007 ± 0.005
3	$[0.35, 0.40)$	0.374	-0.009 ± 0.008 ± 0.006
4	$[0.40, 0.50)$	0.445	-0.006 ± 0.007 ± 0.005
5	$[0.50, 0.65)$	0.565	-0.009 ± 0.008 ± 0.006
6	$[0.65, 0.80)$	0.716	-0.011 ± 0.012 ± 0.008
7	$[0.80, 1.00)$	0.875	-0.022 ± 0.017 ± 0.012
		P_{hT}	
Bin	Range	$\langle P_{hT} \rangle$ [GeV/c]	$A_{UL}^{\sin(2\phi_h)}$
0	$[0.10, 0.20)$	0.155	-0.019 ± 0.008 ± 0.006
1	$[0.20, 0.30)$	0.252	-0.004 ± 0.007 ± 0.005
2	$[0.30, 0.40)$	0.350	-0.004 ± 0.007 ± 0.005
3	$[0.40, 0.50)$	0.449	-0.003 ± 0.007 ± 0.005
4	$[0.50, 0.60)$	0.548	-0.017 ± 0.008 ± 0.005
5	$[0.60, 0.75)$	0.669	-0.001 ± 0.007 ± 0.005
6	$[0.75, 0.90)$	0.818	-0.014 ± 0.010 ± 0.007
7	$[0.90, 1.30)$	1.051	-0.019 ± 0.010 ± 0.007
8	$[0.13, 10.00)$	1.597	0.013 ± 0.019 ± 0.013

Table A.43: Results of $A_{UL}^{\sin(2\phi_h)}$ for h^+ in bins of x, z, and P_{hT}.

h^+			2007 & 2011
		x	
Bin	Range	$\langle x \rangle$	$A_{UL}^{\sin(2\phi_h)}$
0	$[0.0025, 0.0080)$	0.006	0.000 ± 0.011 ± 0.013
1	$[0.0080, 0.0130)$	0.011	-0.005 ± 0.006 ± 0.007
2	$[0.0130, 0.0200)$	0.016	0.001 ± 0.005 ± 0.005
3	$[0.0200, 0.0320)$	0.026	-0.005 ± 0.004 ± 0.004
4	$[0.0320, 0.0500)$	0.040	-0.004 ± 0.004 ± 0.004
5	$[0.0500, 0.0800)$	0.063	-0.010 ± 0.005 ± 0.005
6	$[0.0800, 0.1300)$	0.101	-0.008 ± 0.006 ± 0.006
7	$[0.1300, 0.2100)$	0.163	-0.010 ± 0.007 ± 0.007
8	$[0.2100, 0.7000)$	0.289	-0.005 ± 0.008 ± 0.009
		z	
Bin	Range	$\langle z \rangle$	$A_{UL}^{\sin(2\phi_h)}$
0	$[0.20, 0.25)$	0.223	-0.006 ± 0.003 ± 0.004
1	$[0.25, 0.30)$	0.274	-0.006 ± 0.004 ± 0.004
2	$[0.30, 0.35)$	0.324	-0.003 ± 0.005 ± 0.005
3	$[0.35, 0.40)$	0.374	-0.004 ± 0.006 ± 0.006
4	$[0.40, 0.50)$	0.445	-0.005 ± 0.005 ± 0.005
5	$[0.50, 0.65)$	0.565	-0.001 ± 0.005 ± 0.006
6	$[0.65, 0.80)$	0.716	-0.004 ± 0.008 ± 0.008
7	$[0.80, 1.00)$	0.875	-0.021 ± 0.011 ± 0.012
		P_{hT}	
Bin	Range	$\langle P_{hT} \rangle$ [GeV/c]	$A_{UL}^{\sin(2\phi_h)}$
0	$[0.10, 0.20)$	0.155	-0.014 ± 0.005 ± 0.006
1	$[0.20, 0.30)$	0.252	-0.002 ± 0.005 ± 0.005
2	$[0.30, 0.40)$	0.350	-0.002 ± 0.004 ± 0.005
3	$[0.40, 0.50)$	0.449	-0.005 ± 0.004 ± 0.005
4	$[0.50, 0.60)$	0.548	-0.006 ± 0.005 ± 0.005
5	$[0.60, 0.75)$	0.669	-0.003 ± 0.005 ± 0.005
6	$[0.75, 0.90)$	0.818	-0.003 ± 0.006 ± 0.007
7	$[0.90, 1.30)$	1.049	-0.011 ± 0.006 ± 0.007
8	$[0.13, 10.00)$	1.587	0.001 ± 0.013 ± 0.015

Table A.44: Results of $A_{UL}^{\sin(2\phi_h)}$ for h^- in bins of x, z, and P_{hT} for 2007.

h^-			2007
		x	
Bin	Range	$\langle x \rangle$	$A_{UL}^{\sin(2\phi_h)}$
0	$[0.0025, 0.0080)$	0.006	0.025 ± 0.017 ± 0.013
1	$[0.0080, 0.0130)$	0.011	0.000 ± 0.009 ± 0.007
2	$[0.0130, 0.0200)$	0.016	0.001 ± 0.007 ± 0.005
3	$[0.0200, 0.0320)$	0.026	-0.010 ± 0.006 ± 0.004
4	$[0.0320, 0.0500)$	0.040	0.000 ± 0.006 ± 0.004
5	$[0.0500, 0.0800)$	0.063	-0.001 ± 0.007 ± 0.005
6	$[0.0800, 0.1300)$	0.101	0.003 ± 0.009 ± 0.006
7	$[0.1300, 0.2100)$	0.162	0.009 ± 0.011 ± 0.008
8	$[0.2100, 0.7000)$	0.286	0.012 ± 0.015 ± 0.011
		z	
Bin	Range	$\langle z \rangle$	$A_{UL}^{\sin(2\phi_h)}$
0	$[0.20, 0.25)$	0.223	0.003 ± 0.005 ± 0.004
1	$[0.25, 0.30)$	0.273	-0.006 ± 0.006 ± 0.004
2	$[0.30, 0.35)$	0.324	0.005 ± 0.007 ± 0.005
3	$[0.35, 0.40)$	0.374	0.004 ± 0.009 ± 0.006
4	$[0.40, 0.50)$	0.445	-0.009 ± 0.008 ± 0.006
5	$[0.50, 0.65)$	0.565	0.003 ± 0.009 ± 0.006
6	$[0.65, 0.80)$	0.717	0.006 ± 0.013 ± 0.009
7	$[0.80, 1.00)$	0.876	-0.021 ± 0.016 ± 0.012
		P_{hT}	
Bin	Range	$\langle P_{hT} \rangle$ [GeV/c]	$A_{UL}^{\sin(2\phi_h)}$
0	$[0.10, 0.20)$	0.155	-0.001 ± 0.008 ± 0.006
1	$[0.20, 0.30)$	0.252	0.005 ± 0.007 ± 0.005
2	$[0.30, 0.40)$	0.350	-0.002 ± 0.006 ± 0.005
3	$[0.40, 0.50)$	0.449	0.000 ± 0.007 ± 0.005
4	$[0.50, 0.60)$	0.548	-0.009 ± 0.008 ± 0.006
5	$[0.60, 0.75)$	0.669	-0.003 ± 0.007 ± 0.006
6	$[0.75, 0.90)$	0.818	0.006 ± 0.010 ± 0.007
7	$[0.90, 1.30)$	1.048	0.002 ± 0.010 ± 0.008
8	$[0.13, 10.00)$	1.578	0.022 ± 0.022 ± 0.016

Table A.45: Results of $A_{UL}^{\sin(2\phi_h)}$ for h^- in bins of x, z, and P_{hT} for 2011.

h^-			2011
		x	
Bin	Range	$\langle x \rangle$	$A_{UL}^{\sin(2\phi_h)}$
0	$[0.0025, 0.0080)$	0.006	-0.013 ± 0.014 ± 0.008
1	$[0.0080, 0.0130)$	0.010	-0.005 ± 0.009 ± 0.005
2	$[0.0130, 0.0200)$	0.016	0.004 ± 0.008 ± 0.004
3	$[0.0200, 0.0320)$	0.026	0.010 ± 0.007 ± 0.004
4	$[0.0320, 0.0500)$	0.040	0.008 ± 0.007 ± 0.004
5	$[0.0500, 0.0800)$	0.063	-0.001 ± 0.008 ± 0.005
6	$[0.0800, 0.1300)$	0.101	0.020 ± 0.010 ± 0.006
7	$[0.1300, 0.2100)$	0.163	0.013 ± 0.013 ± 0.008
8	$[0.2100, 0.7000)$	0.291	0.028 ± 0.015 ± 0.009
		z	
Bin	Range	$\langle z \rangle$	$A_{UL}^{\sin(2\phi_h)}$
0	$[0.20, 0.25)$	0.223	0.008 ± 0.006 ± 0.003
1	$[0.25, 0.30)$	0.273	-0.006 ± 0.007 ± 0.004
2	$[0.30, 0.35)$	0.324	0.004 ± 0.008 ± 0.005
3	$[0.35, 0.40)$	0.374	0.015 ± 0.010 ± 0.006
4	$[0.40, 0.50)$	0.445	0.012 ± 0.009 ± 0.005
5	$[0.50, 0.65)$	0.565	0.019 ± 0.010 ± 0.006
6	$[0.65, 0.80)$	0.717	-0.003 ± 0.015 ± 0.009
7	$[0.80, 1.00)$	0.876	-0.022 ± 0.019 ± 0.011
		P_{hT}	
Bin	Range	$\langle P_{hT} \rangle$ [GeV/c]	$A_{UL}^{\sin(2\phi_h)}$
0	$[0.10, 0.20)$	0.155	0.011 ± 0.009 ± 0.005
1	$[0.20, 0.30)$	0.252	0.004 ± 0.008 ± 0.005
2	$[0.30, 0.40)$	0.350	-0.007 ± 0.007 ± 0.004
3	$[0.40, 0.50)$	0.449	0.008 ± 0.008 ± 0.005
4	$[0.50, 0.60)$	0.548	0.003 ± 0.009 ± 0.005
5	$[0.60, 0.75)$	0.669	0.018 ± 0.008 ± 0.005
6	$[0.75, 0.90)$	0.818	0.013 ± 0.011 ± 0.006
7	$[0.90, 1.30)$	1.050	-0.007 ± 0.011 ± 0.007
8	$[0.13, 10.00)$	1.597	0.033 ± 0.022 ± 0.013

Table A.46: Results of $A_{UL}^{\sin(2\phi_h)}$ for h^- in bins of x, z, and P_{hT}.

h^-			2007 & 2011
		x	
Bin	Range	$\langle x \rangle$	$A_{UL}^{\sin(2\phi_h)}$
0	$[0.0025, 0.0080)$	0.006	0.002 ± 0.011 ± 0.013
1	$[0.0080, 0.0130)$	0.011	-0.002 ± 0.006 ± 0.007
2	$[0.0130, 0.0200)$	0.016	0.002 ± 0.005 ± 0.005
3	$[0.0200, 0.0320)$	0.026	-0.002 ± 0.004 ± 0.004
4	$[0.0320, 0.0500)$	0.040	0.003 ± 0.005 ± 0.004
5	$[0.0500, 0.0800)$	0.063	-0.001 ± 0.005 ± 0.005
6	$[0.0800, 0.1300)$	0.101	0.010 ± 0.007 ± 0.006
7	$[0.1300, 0.2100)$	0.162	0.010 ± 0.009 ± 0.008
8	$[0.2100, 0.7000)$	0.289	0.019 ± 0.011 ± 0.011
		z	
Bin	Range	$\langle z \rangle$	$A_{UL}^{\sin(2\phi_h)}$
0	$[0.20, 0.25)$	0.223	0.005 ± 0.004 ± 0.004
1	$[0.25, 0.30)$	0.273	-0.006 ± 0.005 ± 0.004
2	$[0.30, 0.35)$	0.324	0.005 ± 0.005 ± 0.005
3	$[0.35, 0.40)$	0.374	0.008 ± 0.006 ± 0.006
4	$[0.40, 0.50)$	0.445	0.000 ± 0.006 ± 0.006
5	$[0.50, 0.65)$	0.565	0.009 ± 0.007 ± 0.006
6	$[0.65, 0.80)$	0.717	0.003 ± 0.010 ± 0.009
7	$[0.80, 1.00)$	0.876	-0.022 ± 0.013 ± 0.012
		P_{hT}	
Bin	Range	$\langle P_{hT} \rangle$ [GeV/c]	$A_{UL}^{\sin(2\phi_h)}$
0	$[0.10, 0.20)$	0.155	0.004 ± 0.006 ± 0.006
1	$[0.20, 0.30)$	0.252	0.005 ± 0.005 ± 0.005
2	$[0.30, 0.40)$	0.350	-0.004 ± 0.005 ± 0.005
3	$[0.40, 0.50)$	0.449	0.003 ± 0.005 ± 0.005
4	$[0.50, 0.60)$	0.548	-0.004 ± 0.006 ± 0.006
5	$[0.60, 0.75)$	0.669	0.006 ± 0.006 ± 0.006
6	$[0.75, 0.90)$	0.818	0.009 ± 0.007 ± 0.007
7	$[0.90, 1.30)$	1.049	-0.002 ± 0.008 ± 0.008
8	$[0.13, 10.00)$	1.588	0.028 ± 0.015 ± 0.016

Table A.47: Results of $A_{LL}^{\cos(\phi_h)}$ for h^+ in bins of x, z, and P_{hT} for 2007.

h^+			2007
		x	
Bin	Range	$\langle x\rangle$	$A_{LL}^{\cos(\phi_h)}$
0	$[0.0025, 0.0080)$	0.006	-0.018 ± 0.018 ± 0.012
1	$[0.0080, 0.0130)$	0.011	0.011 ± 0.016 ± 0.011
2	$[0.0130, 0.0200)$	0.016	0.011 ± 0.018 ± 0.012
3	$[0.0200, 0.0320)$	0.026	-0.015 ± 0.020 ± 0.013
4	$[0.0320, 0.0500)$	0.040	-0.040 ± 0.025 ± 0.017
5	$[0.0500, 0.0800)$	0.063	0.039 ± 0.029 ± 0.020
6	$[0.0800, 0.1300)$	0.101	-0.017 ± 0.035 ± 0.024
7	$[0.1300, 0.2100)$	0.163	-0.015 ± 0.045 ± 0.030
8	$[0.2100, 0.7000)$	0.287	0.043 ± 0.053 ± 0.036
		z	
Bin	Range	$\langle z\rangle$	$A_{LL}^{\cos(\phi_h)}$
0	$[0.20, 0.25)$	0.224	-0.018 ± 0.015 ± 0.010
1	$[0.25, 0.30)$	0.274	-0.007 ± 0.018 ± 0.012
2	$[0.30, 0.35)$	0.324	0.016 ± 0.022 ± 0.015
3	$[0.35, 0.40)$	0.374	-0.034 ± 0.026 ± 0.017
4	$[0.40, 0.50)$	0.445	0.003 ± 0.023 ± 0.015
5	$[0.50, 0.65)$	0.565	0.027 ± 0.026 ± 0.017
6	$[0.65, 0.80)$	0.716	0.060 ± 0.037 ± 0.025
7	$[0.80, 1.00)$	0.875	0.047 ± 0.052 ± 0.035
		P_{hT}	
Bin	Range	$\langle P_{hT}\rangle$ [GeV/c]	$A_{LL}^{\cos(\phi_h)}$
0	$[0.10, 0.20)$	0.155	0.018 ± 0.027 ± 0.018
1	$[0.20, 0.30)$	0.252	-0.032 ± 0.022 ± 0.015
2	$[0.30, 0.40)$	0.350	-0.013 ± 0.020 ± 0.014
3	$[0.40, 0.50)$	0.449	0.007 ± 0.021 ± 0.014
4	$[0.50, 0.60)$	0.548	-0.014 ± 0.023 ± 0.015
5	$[0.60, 0.75)$	0.669	0.023 ± 0.022 ± 0.015
6	$[0.75, 0.90)$	0.818	0.034 ± 0.027 ± 0.018
7	$[0.90, 1.30)$	1.048	0.003 ± 0.026 ± 0.017
8	$[0.13, 10.00)$	1.577	-0.017 ± 0.044 ± 0.030

Table A.48: Results of $A_{LL}^{\cos(\phi_h)}$ for h^+ in bins of x, z, and P_{hT} for 2011.

h^+			2011
		x	
Bin	Range	$\langle x\rangle$	$A_{LL}^{\cos(\phi_h)}$
0	$[0.0025, 0.0080)$	0.006	-0.005 ± 0.017 ± 0.008
1	$[0.0080, 0.0130)$	0.011	0.017 ± 0.018 ± 0.009
2	$[0.0130, 0.0200)$	0.016	-0.003 ± 0.021 ± 0.010
3	$[0.0200, 0.0320)$	0.026	-0.003 ± 0.023 ± 0.012
4	$[0.0320, 0.0500)$	0.040	0.009 ± 0.029 ± 0.014
5	$[0.0500, 0.0800)$	0.063	-0.022 ± 0.034 ± 0.017
6	$[0.0800, 0.1300)$	0.101	-0.019 ± 0.041 ± 0.021
7	$[0.1300, 0.2100)$	0.163	0.030 ± 0.053 ± 0.026
8	$[0.2100, 0.7000)$	0.292	0.026 ± 0.063 ± 0.031
		z	
Bin	Range	$\langle z\rangle$	$A_{LL}^{\cos(\phi_h)}$
0	$[0.20, 0.25)$	0.223	0.010 ± 0.017 ± 0.008
1	$[0.25, 0.30)$	0.274	-0.036 ± 0.020 ± 0.010
2	$[0.30, 0.35)$	0.324	-0.025 ± 0.024 ± 0.012
3	$[0.35, 0.40)$	0.374	0.031 ± 0.028 ± 0.014
4	$[0.40, 0.50)$	0.445	-0.011 ± 0.025 ± 0.013
5	$[0.50, 0.65)$	0.565	0.079 ± 0.029 ± 0.015
6	$[0.65, 0.80)$	0.716	0.001 ± 0.043 ± 0.021
7	$[0.80, 1.00)$	0.875	0.060 ± 0.060 ± 0.030
		P_{hT}	
Bin	Range	$\langle P_{hT}\rangle$ [GeV/c]	$A_{LL}^{\cos(\phi_h)}$
0	$[0.10, 0.20)$	0.155	-0.024 ± 0.030 ± 0.015
1	$[0.20, 0.30)$	0.252	0.000 ± 0.025 ± 0.012
2	$[0.30, 0.40)$	0.350	0.002 ± 0.023 ± 0.011
3	$[0.40, 0.50)$	0.449	0.005 ± 0.023 ± 0.012
4	$[0.50, 0.60)$	0.548	-0.027 ± 0.025 ± 0.013
5	$[0.60, 0.75)$	0.669	0.039 ± 0.024 ± 0.012
6	$[0.75, 0.90)$	0.818	0.032 ± 0.030 ± 0.015
7	$[0.90, 1.30)$	1.051	-0.008 ± 0.028 ± 0.014
8	$[0.13, 10.00)$	1.597	0.010 ± 0.045 ± 0.023

Table A.49: Results of $A_{LL}^{\cos(\phi_h)}$ for h^+ in bins of x, z, and P_{hT}.

h^+			2007 & 2011
		x	
Bin	Range	$\langle x\rangle$	$A_{LL}^{\cos(\phi_h)}$
0	$[0.0025, 0.0080)$	0.006	-0.011 ± 0.012 ± 0.012
1	$[0.0080, 0.0130)$	0.011	0.014 ± 0.012 ± 0.011
2	$[0.0130, 0.0200)$	0.016	0.005 ± 0.013 ± 0.012
3	$[0.0200, 0.0320)$	0.026	-0.010 ± 0.015 ± 0.013
4	$[0.0320, 0.0500)$	0.040	-0.020 ± 0.019 ± 0.017
5	$[0.0500, 0.0800)$	0.063	0.013 ± 0.022 ± 0.020
6	$[0.0800, 0.1300)$	0.101	-0.018 ± 0.027 ± 0.024
7	$[0.1300, 0.2100)$	0.163	0.004 ± 0.034 ± 0.030
8	$[0.2100, 0.7000)$	0.289	0.036 ± 0.041 ± 0.036
		z	
Bin	Range	$\langle z\rangle$	$A_{LL}^{\cos(\phi_h)}$
0	$[0.20, 0.25)$	0.223	-0.005 ± 0.011 ± 0.010
1	$[0.25, 0.30)$	0.274	-0.020 ± 0.014 ± 0.012
2	$[0.30, 0.35)$	0.324	-0.002 ± 0.016 ± 0.015
3	$[0.35, 0.40)$	0.374	-0.005 ± 0.019 ± 0.017
4	$[0.40, 0.50)$	0.445	-0.003 ± 0.017 ± 0.015
5	$[0.50, 0.65)$	0.565	0.050 ± 0.019 ± 0.018
6	$[0.65, 0.80)$	0.716	0.034 ± 0.028 ± 0.025
7	$[0.80, 1.00)$	0.875	0.053 ± 0.039 ± 0.035
		P_{hT}	
Bin	Range	$\langle P_{hT}\rangle$ [GeV/c]	$A_{LL}^{\cos(\phi_h)}$
0	$[0.10, 0.20)$	0.155	0.000 ± 0.020 ± 0.018
1	$[0.20, 0.30)$	0.252	-0.018 ± 0.016 ± 0.015
2	$[0.30, 0.40)$	0.350	-0.006 ± 0.015 ± 0.014
3	$[0.40, 0.50)$	0.449	0.006 ± 0.016 ± 0.014
4	$[0.50, 0.60)$	0.548	-0.020 ± 0.017 ± 0.015
5	$[0.60, 0.75)$	0.669	0.030 ± 0.016 ± 0.015
6	$[0.75, 0.90)$	0.818	0.033 ± 0.020 ± 0.018
7	$[0.90, 1.30)$	1.049	-0.002 ± 0.019 ± 0.017
8	$[0.13, 10.00)$	1.587	-0.004 ± 0.032 ± 0.030

Table A.50: Results of $A_{LL}^{\cos(\phi_h)}$ for h^- in bins of x, z, and P_{hT} for 2007.

h^-			2007
		x	
Bin	Range	$\langle x\rangle$	$A_{LL}^{\cos(\phi_h)}$
0	$[0.0025, 0.0080)$	0.006	-0.011 ± 0.019 ± 0.010
1	$[0.0080, 0.0130)$	0.011	0.014 ± 0.017 ± 0.009
2	$[0.0130, 0.0200)$	0.016	0.000 ± 0.019 ± 0.010
3	$[0.0200, 0.0320)$	0.026	0.014 ± 0.022 ± 0.011
4	$[0.0320, 0.0500)$	0.040	0.014 ± 0.028 ± 0.015
5	$[0.0500, 0.0800)$	0.063	-0.051 ± 0.034 ± 0.018
6	$[0.0800, 0.1300)$	0.101	-0.040 ± 0.043 ± 0.023
7	$[0.1300, 0.2100)$	0.162	0.006 ± 0.057 ± 0.030
8	$[0.2100, 0.7000)$	0.286	0.042 ± 0.068 ± 0.036
		z	
Bin	Range	$\langle z\rangle$	$A_{LL}^{\cos(\phi_h)}$
0	$[0.20, 0.25)$	0.223	0.001 ± 0.016 ± 0.008
1	$[0.25, 0.30)$	0.273	0.038 ± 0.020 ± 0.011
2	$[0.30, 0.35)$	0.324	-0.009 ± 0.024 ± 0.012
3	$[0.35, 0.40)$	0.374	0.023 ± 0.029 ± 0.015
4	$[0.40, 0.50)$	0.445	-0.042 ± 0.026 ± 0.014
5	$[0.50, 0.65)$	0.565	-0.047 ± 0.030 ± 0.016
6	$[0.65, 0.80)$	0.717	0.051 ± 0.043 ± 0.023
7	$[0.80, 1.00)$	0.876	-0.016 ± 0.058 ± 0.030
		P_{hT}	
Bin	Range	$\langle P_{hT}\rangle$ [GeV/c]	$A_{LL}^{\cos(\phi_h)}$
0	$[0.10, 0.20)$	0.155	0.026 ± 0.029 ± 0.015
1	$[0.20, 0.30)$	0.252	0.004 ± 0.024 ± 0.012
2	$[0.30, 0.40)$	0.350	0.023 ± 0.022 ± 0.012
3	$[0.40, 0.50)$	0.449	-0.018 ± 0.023 ± 0.012
4	$[0.50, 0.60)$	0.548	-0.031 ± 0.025 ± 0.013
5	$[0.60, 0.75)$	0.669	-0.013 ± 0.024 ± 0.013
6	$[0.75, 0.90)$	0.818	0.069 ± 0.031 ± 0.016
7	$[0.90, 1.30)$	1.048	-0.038 ± 0.029 ± 0.015
8	$[0.13, 10.00)$	1.578	0.017 ± 0.051 ± 0.026

Table A.51: Results of $A_{LL}^{\cos(\phi_h)}$ for h^- in bins of x, z, and P_{hT} for 2011.

h^-			2011
		x	
Bin	Range	$\langle x\rangle$	$A_{LL}^{\cos(\phi_h)}$
0	$[0.0025, 0.0080)$	0.006	0.002 ± 0.017 ± 0.009
1	$[0.0080, 0.0130)$	0.010	-0.013 ± 0.019 ± 0.011
2	$[0.0130, 0.0200)$	0.016	-0.014 ± 0.023 ± 0.012
3	$[0.0200, 0.0320)$	0.026	-0.006 ± 0.026 ± 0.014
4	$[0.0320, 0.0500)$	0.040	-0.016 ± 0.033 ± 0.018
5	$[0.0500, 0.0800)$	0.063	0.014 ± 0.040 ± 0.022
6	$[0.0800, 0.1300)$	0.101	0.015 ± 0.050 ± 0.027
7	$[0.1300, 0.2100)$	0.163	0.103 ± 0.066 ± 0.037
8	$[0.2100, 0.7000)$	0.291	0.012 ± 0.080 ± 0.044
		z	
Bin	Range	$\langle z\rangle$	$A_{LL}^{\cos(\phi_h)}$
0	$[0.20, 0.25)$	0.223	-0.012 ± 0.018 ± 0.010
1	$[0.25, 0.30)$	0.273	-0.007 ± 0.022 ± 0.012
2	$[0.30, 0.35)$	0.324	-0.003 ± 0.026 ± 0.014
3	$[0.35, 0.40)$	0.374	-0.001 ± 0.031 ± 0.017
4	$[0.40, 0.50)$	0.445	0.005 ± 0.028 ± 0.015
5	$[0.50, 0.65)$	0.565	0.027 ± 0.033 ± 0.018
6	$[0.65, 0.80)$	0.717	0.000 ± 0.047 ± 0.026
7	$[0.80, 1.00)$	0.876	0.056 ± 0.063 ± 0.035
		P_{hT}	
Bin	Range	$\langle P_{hT}\rangle$ [GeV/c]	$A_{LL}^{\cos(\phi_h)}$
0	$[0.10, 0.20)$	0.155	0.014 ± 0.032 ± 0.017
1	$[0.20, 0.30)$	0.252	-0.009 ± 0.026 ± 0.014
2	$[0.30, 0.40)$	0.350	-0.020 ± 0.025 ± 0.014
3	$[0.40, 0.50)$	0.449	-0.001 ± 0.025 ± 0.014
4	$[0.50, 0.60)$	0.548	-0.031 ± 0.027 ± 0.015
5	$[0.60, 0.75)$	0.669	0.003 ± 0.026 ± 0.014
6	$[0.75, 0.90)$	0.818	0.031 ± 0.033 ± 0.018
7	$[0.90, 1.30)$	1.050	0.050 ± 0.031 ± 0.017
8	$[0.13, 10.00)$	1.597	-0.022 ± 0.051 ± 0.028

Table A.52: Results of $A_{LL}^{\cos(\phi_h)}$ for h^- in bins of x, z, and P_{hT}.

h^-			2007 & 2011
		x	
Bin	Range	$\langle x\rangle$	$A_{LL}^{\cos(\phi_h)}$
0	$[0.0025, 0.0080)$	0.006	-0.004 ± 0.013 ± 0.010
1	$[0.0080, 0.0130)$	0.011	0.002 ± 0.013 ± 0.011
2	$[0.0130, 0.0200)$	0.016	-0.006 ± 0.015 ± 0.012
3	$[0.0200, 0.0320)$	0.026	0.005 ± 0.017 ± 0.014
4	$[0.0320, 0.0500)$	0.040	0.002 ± 0.021 ± 0.018
5	$[0.0500, 0.0800)$	0.063	-0.023 ± 0.026 ± 0.022
6	$[0.0800, 0.1300)$	0.101	-0.016 ± 0.033 ± 0.027
7	$[0.1300, 0.2100)$	0.162	0.047 ± 0.043 ± 0.036
8	$[0.2100, 0.7000)$	0.289	0.029 ± 0.052 ± 0.044
		z	
Bin	Range	$\langle z\rangle$	$A_{LL}^{\cos(\phi_h)}$
0	$[0.20, 0.25)$	0.223	-0.005 ± 0.012 ± 0.010
1	$[0.25, 0.30)$	0.273	0.017 ± 0.015 ± 0.012
2	$[0.30, 0.35)$	0.324	-0.006 ± 0.018 ± 0.014
3	$[0.35, 0.40)$	0.374	0.012 ± 0.021 ± 0.017
4	$[0.40, 0.50)$	0.445	-0.021 ± 0.019 ± 0.015
5	$[0.50, 0.65)$	0.565	-0.014 ± 0.022 ± 0.018
6	$[0.65, 0.80)$	0.717	0.028 ± 0.032 ± 0.026
7	$[0.80, 1.00)$	0.876	0.017 ± 0.043 ± 0.035
		P_{hT}	
Bin	Range	$\langle P_{hT}\rangle$ [GeV/c]	$A_{LL}^{\cos(\phi_h)}$
0	$[0.10, 0.20)$	0.155	0.021 ± 0.021 ± 0.017
1	$[0.20, 0.30)$	0.252	-0.002 ± 0.018 ± 0.014
2	$[0.30, 0.40)$	0.350	0.004 ± 0.016 ± 0.013
3	$[0.40, 0.50)$	0.449	-0.010 ± 0.017 ± 0.014
4	$[0.50, 0.60)$	0.548	-0.031 ± 0.019 ± 0.015
5	$[0.60, 0.75)$	0.669	-0.006 ± 0.018 ± 0.014
6	$[0.75, 0.90)$	0.818	0.051 ± 0.022 ± 0.018
7	$[0.90, 1.30)$	1.049	0.004 ± 0.021 ± 0.017
8	$[0.13, 10.00)$	1.588	-0.002 ± 0.036 ± 0.028

A.6 A_1^p Analysis Material

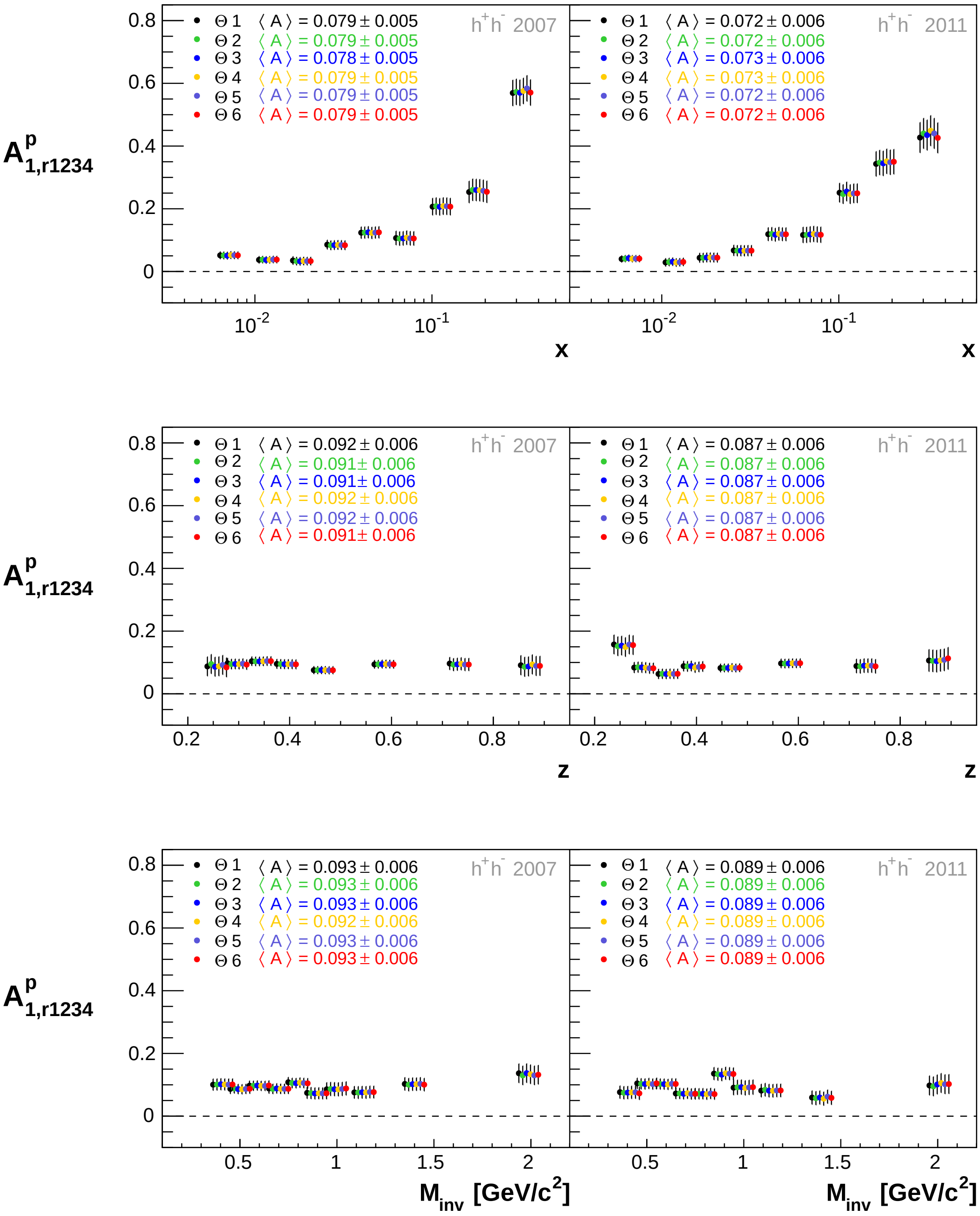

Figure A.39: A_1^p from the different 1D PR fits of the h^+h^- analysis for 2007 (left) and 2011 (right). The azimuthal angles Θ_i are defined in Eq. (5.6) to Eq. (5.11). Corresponding mean values are also displayed.

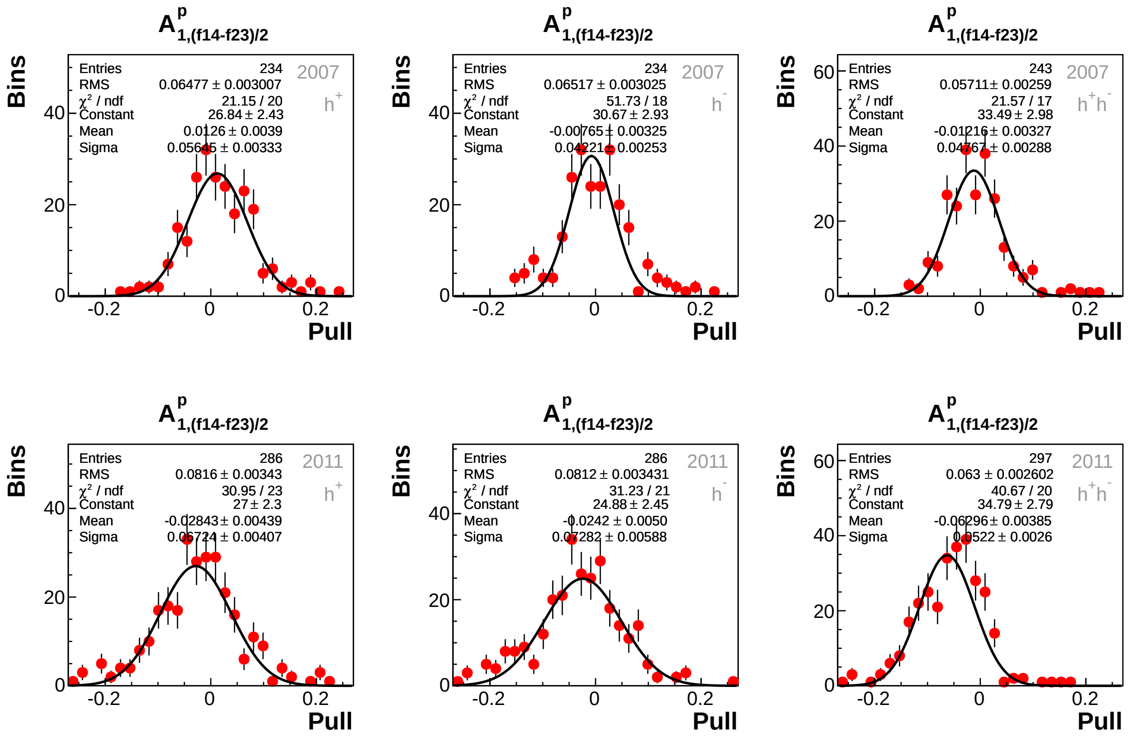

Figure A.40: Pull distributions between $A^p_{1,(f14-f23)/2}$ and $A^p_{1,(r12-r34)/2}$ from the different analyses for 2007 (top) and 2011 (bottom). The gaussian fit, corresponding statistical values and fit parameters are also displayed.

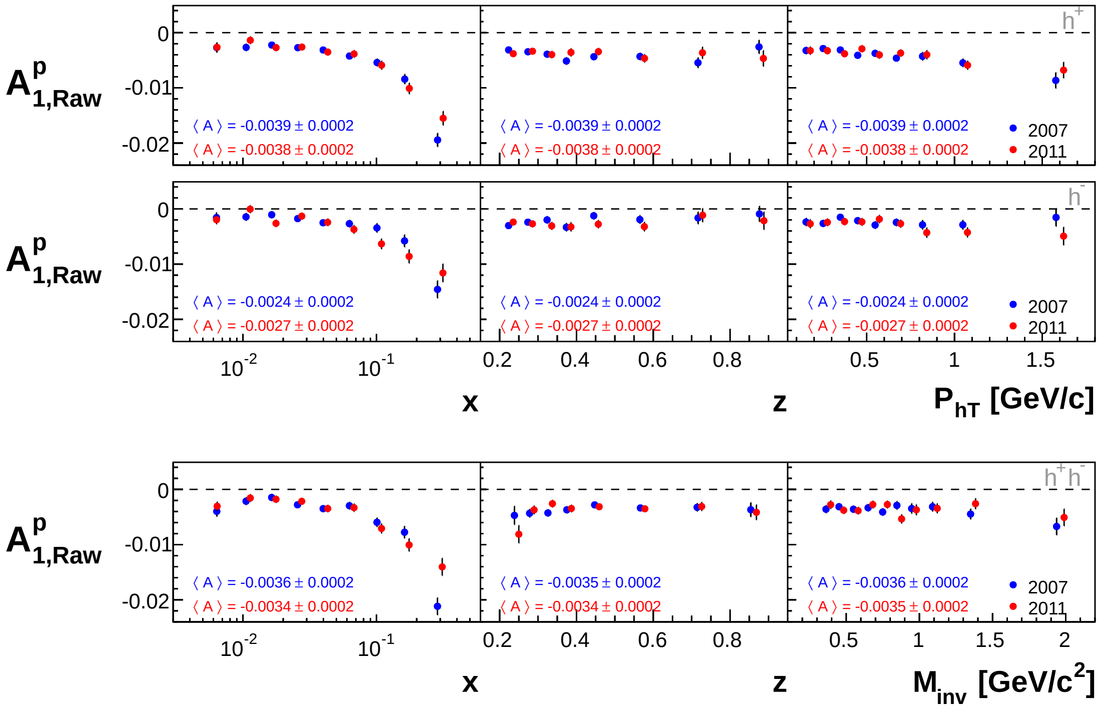

Figure A.41: $A^p_{1,\mathrm{Raw}}$ for h^+ and h^-(top) and h^+h^-(bottom) from 2007 and 2011 data. Corresponding mean values are also displayed.

Table A.53: Results of A_1^p for h^+ in bins of x, z, and P_{hT} for 2007.

h^+			2007
		x	
Bin	Range	$\langle x \rangle$	A_1^p
0	$[0.0025, 0.0080)$	0.006	0.035 ± 0.011 ± 0.010
1	$[0.0080, 0.0130)$	0.011	0.047 ± 0.011 ± 0.009
2	$[0.0130, 0.0200)$	0.016	0.053 ± 0.012 ± 0.011
3	$[0.0200, 0.0320)$	0.026	0.088 ± 0.014 ± 0.013
4	$[0.0320, 0.0500)$	0.040	0.123 ± 0.018 ± 0.017
5	$[0.0500, 0.0800)$	0.063	0.168 ± 0.021 ± 0.020
6	$[0.0800, 0.1300)$	0.101	0.209 ± 0.025 ± 0.024
7	$[0.1300, 0.2100)$	0.163	0.313 ± 0.032 ± 0.032
8	$[0.2100, 0.7000)$	0.287	0.592 ± 0.036 ± 0.045
		z	
Bin	Range	$\langle z \rangle$	A_1^p
0	$[0.20, 0.25)$	0.224	0.086 ± 0.010 ± 0.010
1	$[0.25, 0.30)$	0.274	0.097 ± 0.012 ± 0.012
2	$[0.30, 0.35)$	0.324	0.110 ± 0.015 ± 0.014
3	$[0.35, 0.40)$	0.374	0.147 ± 0.017 ± 0.017
4	$[0.40, 0.50)$	0.445	0.127 ± 0.015 ± 0.015
5	$[0.50, 0.65)$	0.565	0.127 ± 0.018 ± 0.017
6	$[0.65, 0.80)$	0.716	0.164 ± 0.027 ± 0.025
7	$[0.80, 1.00)$	0.875	0.078 ± 0.036 ± 0.031
		P_{hT}	
Bin	Range	$\langle P_{hT} \rangle$ [GeV/c]	A_1^p
0	$[0.10, 0.20)$	0.155	0.097 ± 0.018 ± 0.016
1	$[0.20, 0.30)$	0.252	0.086 ± 0.015 ± 0.014
2	$[0.30, 0.40)$	0.350	0.092 ± 0.014 ± 0.013
3	$[0.40, 0.50)$	0.449	0.119 ± 0.014 ± 0.014
4	$[0.50, 0.60)$	0.548	0.107 ± 0.016 ± 0.015
5	$[0.60, 0.75)$	0.669	0.129 ± 0.015 ± 0.015
6	$[0.75, 0.90)$	0.818	0.115 ± 0.019 ± 0.017
7	$[0.90, 1.30)$	1.048	0.136 ± 0.018 ± 0.017
8	$[0.13, 10.00)$	1.577	0.179 ± 0.029 ± 0.027

Table A.54: Results of A_1^p for h^+ in bins of x, z, and P_{hT} for 2011.

h^+			2011
		x	
Bin	Range	$\langle x \rangle$	A_1^p
0	$[0.0025, 0.0080)$	0.006	0.036 ± 0.010 ± 0.009
1	$[0.0080, 0.0130)$	0.011	0.026 ± 0.012 ± 0.011
2	$[0.0130, 0.0200)$	0.016	0.068 ± 0.014 ± 0.014
3	$[0.0200, 0.0320)$	0.026	0.085 ± 0.017 ± 0.016
4	$[0.0320, 0.0500)$	0.040	0.130 ± 0.020 ± 0.020
5	$[0.0500, 0.0800)$	0.063	0.147 ± 0.024 ± 0.023
6	$[0.0800, 0.1300)$	0.101	0.225 ± 0.029 ± 0.029
7	$[0.1300, 0.2100)$	0.163	0.379 ± 0.037 ± 0.040
8	$[0.2100, 0.7000)$	0.292	0.529 ± 0.043 ± 0.049
		z	
Bin	Range	$\langle z \rangle$	A_1^p
0	$[0.20, 0.25)$	0.223	0.101 ± 0.011 ± 0.012
1	$[0.25, 0.30)$	0.274	0.090 ± 0.014 ± 0.013
2	$[0.30, 0.35)$	0.324	0.108 ± 0.016 ± 0.016
3	$[0.35, 0.40)$	0.374	0.098 ± 0.019 ± 0.018
4	$[0.40, 0.50)$	0.445	0.095 ± 0.017 ± 0.016
5	$[0.50, 0.65)$	0.565	0.132 ± 0.020 ± 0.020
6	$[0.65, 0.80)$	0.716	0.106 ± 0.030 ± 0.028
7	$[0.80, 1.00)$	0.875	0.141 ± 0.042 ± 0.039
		P_{hT}	
Bin	Range	$\langle P_{hT} \rangle$ [GeV/c]	A_1^p
0	$[0.10, 0.20)$	0.155	0.094 ± 0.020 ± 0.019
1	$[0.20, 0.30)$	0.252	0.094 ± 0.017 ± 0.016
2	$[0.30, 0.40)$	0.350	0.108 ± 0.016 ± 0.015
3	$[0.40, 0.50)$	0.449	0.082 ± 0.016 ± 0.015
4	$[0.50, 0.60)$	0.548	0.112 ± 0.017 ± 0.017
5	$[0.60, 0.75)$	0.669	0.100 ± 0.016 ± 0.016
6	$[0.75, 0.90)$	0.818	0.103 ± 0.020 ± 0.019
7	$[0.90, 1.30)$	1.051	0.142 ± 0.019 ± 0.019
8	$[0.13, 10.00)$	1.597	0.138 ± 0.029 ± 0.028

Table A.55: Results of A_1^p for h^+ in bins of x, z, and P_{hT}.

h^+			2007 & 2011
x			
Bin	Range	$\langle x\rangle$	A_1^p
0	$[0.0025, 0.0080)$	0.006	0.035 ± 0.007 ± 0.010
1	$[0.0080, 0.0130)$	0.011	0.038 ± 0.008 ± 0.011
2	$[0.0130, 0.0200)$	0.016	0.060 ± 0.009 ± 0.014
3	$[0.0200, 0.0320)$	0.026	0.087 ± 0.011 ± 0.016
4	$[0.0320, 0.0500)$	0.040	0.126 ± 0.013 ± 0.020
5	$[0.0500, 0.0800)$	0.063	0.159 ± 0.016 ± 0.024
6	$[0.0800, 0.1300)$	0.101	0.216 ± 0.019 ± 0.029
7	$[0.1300, 0.2100)$	0.163	0.341 ± 0.024 ± 0.038
8	$[0.2100, 0.7000)$	0.289	0.566 ± 0.028 ± 0.050
z			
Bin	Range	$\langle z\rangle$	A_1^p
0	$[0.20, 0.25)$	0.223	0.093 ± 0.008 ± 0.011
1	$[0.25, 0.30)$	0.274	0.094 ± 0.009 ± 0.013
2	$[0.30, 0.35)$	0.324	0.109 ± 0.011 ± 0.016
3	$[0.35, 0.40)$	0.374	0.125 ± 0.013 ± 0.019
4	$[0.40, 0.50)$	0.445	0.113 ± 0.011 ± 0.017
5	$[0.50, 0.65)$	0.565	0.130 ± 0.013 ± 0.020
6	$[0.65, 0.80)$	0.716	0.139 ± 0.020 ± 0.029
7	$[0.80, 1.00)$	0.875	0.105 ± 0.027 ± 0.039
P_{hT}			
Bin	Range	$\langle P_{hT}\rangle$ [GeV/c]	A_1^p
0	$[0.10, 0.20)$	0.155	0.096 ± 0.013 ± 0.019
1	$[0.20, 0.30)$	0.252	0.089 ± 0.011 ± 0.016
2	$[0.30, 0.40)$	0.350	0.099 ± 0.010 ± 0.015
3	$[0.40, 0.50)$	0.449	0.103 ± 0.011 ± 0.016
4	$[0.50, 0.60)$	0.548	0.109 ± 0.012 ± 0.017
5	$[0.60, 0.75)$	0.669	0.116 ± 0.011 ± 0.016
6	$[0.75, 0.90)$	0.818	0.109 ± 0.014 ± 0.019
7	$[0.90, 1.30)$	1.049	0.139 ± 0.013 ± 0.019
8	$[0.13, 10.00)$	1.587	0.159 ± 0.020 ± 0.028

Table A.56: Results of A_1^p for h^- in bins of x, z, and P_{hT} for 2007.

h^-			2007
x			
Bin	Range	$\langle x\rangle$	A_1^p
0	$[0.0025, 0.0080)$	0.006	0.020 ± 0.011 ± 0.008
1	$[0.0080, 0.0130)$	0.011	0.025 ± 0.011 ± 0.008
2	$[0.0130, 0.0200)$	0.016	0.025 ± 0.013 ± 0.010
3	$[0.0200, 0.0320)$	0.026	0.056 ± 0.015 ± 0.012
4	$[0.0320, 0.0500)$	0.040	0.097 ± 0.020 ± 0.015
5	$[0.0500, 0.0800)$	0.063	0.105 ± 0.024 ± 0.019
6	$[0.0800, 0.1300)$	0.101	0.133 ± 0.030 ± 0.023
7	$[0.1300, 0.2100)$	0.162	0.214 ± 0.039 ± 0.031
8	$[0.2100, 0.7000)$	0.286	0.440 ± 0.047 ± 0.042
z			
Bin	Range	$\langle z\rangle$	A_1^p
0	$[0.20, 0.25)$	0.223	0.081 ± 0.011 ± 0.009
1	$[0.25, 0.30)$	0.273	0.065 ± 0.013 ± 0.010
2	$[0.30, 0.35)$	0.324	0.054 ± 0.016 ± 0.012
3	$[0.35, 0.40)$	0.374	0.091 ± 0.019 ± 0.015
4	$[0.40, 0.50)$	0.445	0.034 ± 0.017 ± 0.013
5	$[0.50, 0.65)$	0.565	0.053 ± 0.020 ± 0.015
6	$[0.65, 0.80)$	0.717	0.046 ± 0.030 ± 0.022
7	$[0.80, 1.00)$	0.876	0.026 ± 0.040 ± 0.029
P_{hT}			
Bin	Range	$\langle P_{hT}\rangle$ [GeV/c]	A_1^p
0	$[0.10, 0.20)$	0.155	0.068 ± 0.019 ± 0.015
1	$[0.20, 0.30)$	0.252	0.075 ± 0.016 ± 0.012
2	$[0.30, 0.40)$	0.350	0.043 ± 0.015 ± 0.011
3	$[0.40, 0.50)$	0.449	0.059 ± 0.016 ± 0.012
4	$[0.50, 0.60)$	0.548	0.080 ± 0.017 ± 0.013
5	$[0.60, 0.75)$	0.669	0.065 ± 0.016 ± 0.012
6	$[0.75, 0.90)$	0.818	0.074 ± 0.020 ± 0.016
7	$[0.90, 1.30)$	1.048	0.068 ± 0.019 ± 0.015
8	$[0.13, 10.00)$	1.578	0.031 ± 0.032 ± 0.024

Table A.57: Results of A_1^p for h^- in bins of x, z, and P_{hT} for 2011.

h^-			2011
		x	
Bin	Range	$\langle x \rangle$	A_1^p
0	$[0.0025, 0.0080)$	0.006	0.026 ± 0.010 ± 0.007
1	$[0.0080, 0.0130)$	0.010	0.000 ± 0.013 ± 0.008
2	$[0.0130, 0.0200)$	0.016	0.065 ± 0.015 ± 0.011
3	$[0.0200, 0.0320)$	0.026	0.042 ± 0.018 ± 0.012
4	$[0.0320, 0.0500)$	0.040	0.088 ± 0.023 ± 0.016
5	$[0.0500, 0.0800)$	0.063	0.141 ± 0.028 ± 0.020
6	$[0.0800, 0.1300)$	0.101	0.239 ± 0.035 ± 0.027
7	$[0.1300, 0.2100)$	0.163	0.321 ± 0.046 ± 0.035
8	$[0.2100, 0.7000)$	0.291	0.394 ± 0.055 ± 0.043
		z	
Bin	Range	$\langle z \rangle$	A_1^p
0	$[0.20, 0.25)$	0.223	0.061 ± 0.012 ± 0.009
1	$[0.25, 0.30)$	0.273	0.069 ± 0.014 ± 0.010
2	$[0.30, 0.35)$	0.324	0.080 ± 0.017 ± 0.012
3	$[0.35, 0.40)$	0.374	0.085 ± 0.021 ± 0.015
4	$[0.40, 0.50)$	0.445	0.073 ± 0.018 ± 0.013
5	$[0.50, 0.65)$	0.565	0.084 ± 0.021 ± 0.015
6	$[0.65, 0.80)$	0.717	0.028 ± 0.032 ± 0.021
7	$[0.80, 1.00)$	0.876	0.058 ± 0.043 ± 0.029
		P_{hT}	
Bin	Range	$\langle P_{hT} \rangle$ [GeV/c]	A_1^p
0	$[0.10, 0.20)$	0.155	0.074 ± 0.021 ± 0.015
1	$[0.20, 0.30)$	0.252	0.066 ± 0.017 ± 0.012
2	$[0.30, 0.40)$	0.350	0.062 ± 0.016 ± 0.011
3	$[0.40, 0.50)$	0.449	0.062 ± 0.017 ± 0.012
4	$[0.50, 0.60)$	0.548	0.048 ± 0.018 ± 0.013
5	$[0.60, 0.75)$	0.669	0.068 ± 0.017 ± 0.012
6	$[0.75, 0.90)$	0.818	0.105 ± 0.022 ± 0.016
7	$[0.90, 1.30)$	1.050	0.099 ± 0.020 ± 0.015
8	$[0.13, 10.00)$	1.597	0.098 ± 0.032 ± 0.022

Table A.58: Results of A_1^p for h^- in bins of x, z, and P_{hT}.

h^-			2007 & 2011
		x	
Bin	Range	$\langle x \rangle$	A_1^p
0	$[0.0025, 0.0080)$	0.006	0.023 ± 0.007 ± 0.008
1	$[0.0080, 0.0130)$	0.011	0.014 ± 0.008 ± 0.009
2	$[0.0130, 0.0200)$	0.016	0.042 ± 0.010 ± 0.011
3	$[0.0200, 0.0320)$	0.026	0.050 ± 0.012 ± 0.012
4	$[0.0320, 0.0500)$	0.040	0.093 ± 0.015 ± 0.016
5	$[0.0500, 0.0800)$	0.063	0.120 ± 0.018 ± 0.020
6	$[0.0800, 0.1300)$	0.101	0.178 ± 0.023 ± 0.025
7	$[0.1300, 0.2100)$	0.162	0.259 ± 0.030 ± 0.034
8	$[0.2100, 0.7000)$	0.289	0.421 ± 0.036 ± 0.044
		z	
Bin	Range	$\langle z \rangle$	A_1^p
0	$[0.20, 0.25)$	0.223	0.071 ± 0.008 ± 0.009
1	$[0.25, 0.30)$	0.273	0.067 ± 0.010 ± 0.011
2	$[0.30, 0.35)$	0.324	0.066 ± 0.012 ± 0.012
3	$[0.35, 0.40)$	0.374	0.088 ± 0.014 ± 0.015
4	$[0.40, 0.50)$	0.445	0.052 ± 0.012 ± 0.013
5	$[0.50, 0.65)$	0.565	0.068 ± 0.015 ± 0.015
6	$[0.65, 0.80)$	0.717	0.038 ± 0.022 ± 0.022
7	$[0.80, 1.00)$	0.876	0.041 ± 0.029 ± 0.030
		P_{hT}	
Bin	Range	$\langle P_{hT} \rangle$ [GeV/c]	A_1^p
0	$[0.10, 0.20)$	0.155	0.071 ± 0.014 ± 0.015
1	$[0.20, 0.30)$	0.252	0.071 ± 0.012 ± 0.012
2	$[0.30, 0.40)$	0.350	0.052 ± 0.011 ± 0.011
3	$[0.40, 0.50)$	0.449	0.061 ± 0.011 ± 0.012
4	$[0.50, 0.60)$	0.548	0.065 ± 0.012 ± 0.013
5	$[0.60, 0.75)$	0.669	0.066 ± 0.012 ± 0.013
6	$[0.75, 0.90)$	0.818	0.089 ± 0.015 ± 0.016
7	$[0.90, 1.30)$	1.049	0.083 ± 0.014 ± 0.015
8	$[0.13, 10.00)$	1.588	0.065 ± 0.023 ± 0.024

Table A.59: Results of A_1^p for h^+h^- in bins of x, z, and M_{inv} for 2007.

h^+h^-			2007
		x	
Bin	Range	$\langle x \rangle$	A_1^p
0	$[0.0025, 0.0080)$	0.006	0.052 ± 0.011 ± 0.016
1	$[0.0080, 0.0130)$	0.011	0.038 ± 0.011 ± 0.016
2	$[0.0130, 0.0200)$	0.016	0.033 ± 0.013 ± 0.018
3	$[0.0200, 0.0320)$	0.026	0.084 ± 0.015 ± 0.021
4	$[0.0320, 0.0500)$	0.040	0.124 ± 0.018 ± 0.027
5	$[0.0500, 0.0800)$	0.063	0.106 ± 0.022 ± 0.031
6	$[0.0800, 0.1300)$	0.101	0.207 ± 0.027 ± 0.039
7	$[0.1300, 0.2100)$	0.162	0.257 ± 0.035 ± 0.051
8	$[0.2100, 0.7000)$	0.286	0.574 ± 0.041 ± 0.066
		z	
Bin	Range	$\langle z \rangle$	A_1^p
0	$[0.20, 0.25)$	0.238	0.089 ± 0.031 ± 0.043
1	$[0.25, 0.30)$	0.278	0.095 ± 0.016 ± 0.023
2	$[0.30, 0.35)$	0.326	0.104 ± 0.014 ± 0.021
3	$[0.35, 0.40)$	0.375	0.095 ± 0.015 ± 0.021
4	$[0.40, 0.50)$	0.447	0.075 ± 0.012 ± 0.017
5	$[0.50, 0.65)$	0.567	0.095 ± 0.013 ± 0.019
6	$[0.65, 0.80)$	0.714	0.094 ± 0.020 ± 0.028
7	$[0.80, 1.00)$	0.854	0.089 ± 0.031 ± 0.043
		M_{inv}	
Bin	Range	$\langle M_{\text{inv}} \rangle$ [GeV/c^2]	A_1^p
0	$[0.0, 0.4)$	0.362	0.101 ± 0.018 ± 0.026
1	$[0.4, 0.5)$	0.451	0.087 ± 0.015 ± 0.022
2	$[0.5, 0.6)$	0.549	0.097 ± 0.015 ± 0.022
3	$[0.6, 0.7)$	0.650	0.087 ± 0.016 ± 0.022
4	$[0.7, 0.8)$	0.749	0.106 ± 0.016 ± 0.023
5	$[0.8, 0.9)$	0.846	0.073 ± 0.018 ± 0.026
6	$[0.9, 1.0)$	0.947	0.086 ± 0.021 ± 0.030
7	$[1.0, 1.2)$	1.090	0.076 ± 0.019 ± 0.027
8	$[1.2, 1.6)$	1.350	0.102 ± 0.020 ± 0.029
9	$[1.6, 100.0)$	1.938	0.133 ± 0.030 ± 0.043

Table A.60: Results of A_1^p for h^+h^- in bins of x, z, and M_{inv} for 2011.

h^+h^-			2011
		x	
Bin	Range	$\langle x \rangle$	A_1^p
0	$[0.0025, 0.0080)$	0.006	0.041 ± 0.010 ± 0.010
1	$[0.0080, 0.0130)$	0.011	0.030 ± 0.013 ± 0.012
2	$[0.0130, 0.0200)$	0.016	0.044 ± 0.015 ± 0.014
3	$[0.0200, 0.0320)$	0.026	0.067 ± 0.017 ± 0.016
4	$[0.0320, 0.0500)$	0.040	0.119 ± 0.021 ± 0.021
5	$[0.0500, 0.0800)$	0.063	0.118 ± 0.025 ± 0.024
6	$[0.0800, 0.1300)$	0.101	0.250 ± 0.030 ± 0.032
7	$[0.1300, 0.2100)$	0.162	0.347 ± 0.039 ± 0.042
8	$[0.2100, 0.7000)$	0.288	0.436 ± 0.048 ± 0.052
		z	
Bin	Range	$\langle z \rangle$	A_1^p
0	$[0.20, 0.25)$	0.238	0.154 ± 0.030 ± 0.030
1	$[0.25, 0.30)$	0.278	0.083 ± 0.017 ± 0.016
2	$[0.30, 0.35)$	0.325	0.064 ± 0.015 ± 0.015
3	$[0.35, 0.40)$	0.375	0.087 ± 0.016 ± 0.016
4	$[0.40, 0.50)$	0.447	0.083 ± 0.013 ± 0.013
5	$[0.50, 0.65)$	0.566	0.097 ± 0.014 ± 0.015
6	$[0.65, 0.80)$	0.714	0.089 ± 0.022 ± 0.021
7	$[0.80, 1.00)$	0.857	0.107 ± 0.035 ± 0.034
		M_{inv}	
Bin	Range	$\langle M_{\text{inv}} \rangle$ [GeV/c^2]	A_1^p
0	$[0.0, 0.4)$	0.362	0.075 ± 0.020 ± 0.020
1	$[0.4, 0.5)$	0.451	0.104 ± 0.017 ± 0.017
2	$[0.5, 0.6)$	0.549	0.103 ± 0.017 ± 0.017
3	$[0.6, 0.7)$	0.650	0.072 ± 0.017 ± 0.017
4	$[0.7, 0.8)$	0.749	0.071 ± 0.017 ± 0.017
5	$[0.8, 0.9)$	0.846	0.135 ± 0.020 ± 0.020
6	$[0.9, 1.0)$	0.947	0.092 ± 0.023 ± 0.023
7	$[1.0, 1.2)$	1.090	0.082 ± 0.021 ± 0.020
8	$[1.2, 1.6)$	1.352	0.059 ± 0.022 ± 0.021
9	$[1.6, 100.0)$	1.957	0.101 ± 0.031 ± 0.030

Table A.61: Results of A_1^p for h^+h^- in bins of x, z, and M_{inv}.

h^+h^-			2007 & 2011
		x	
Bin	Range	$\langle x\rangle$	A_1^p
0	$[0.0025, 0.0080)$	0.006	0.046 ± 0.008 ± 0.016
1	$[0.0080, 0.0130)$	0.011	0.034 ± 0.008 ± 0.015
2	$[0.0130, 0.0200)$	0.016	0.038 ± 0.010 ± 0.018
3	$[0.0200, 0.0320)$	0.026	0.077 ± 0.011 ± 0.021
4	$[0.0320, 0.0500)$	0.040	0.122 ± 0.014 ± 0.027
5	$[0.0500, 0.0800)$	0.063	0.111 ± 0.016 ± 0.031
6	$[0.0800, 0.1300)$	0.101	0.226 ± 0.020 ± 0.040
7	$[0.1300, 0.2100)$	0.162	0.297 ± 0.026 ± 0.051
8	$[0.2100, 0.7000)$	0.287	0.516 ± 0.031 ± 0.064
		z	
Bin	Range	$\langle z\rangle$	A_1^p
0	$[0.20, 0.25)$	0.238	0.122 ± 0.022 ± 0.043
1	$[0.25, 0.30)$	0.278	0.090 ± 0.011 ± 0.023
2	$[0.30, 0.35)$	0.326	0.085 ± 0.010 ± 0.021
3	$[0.35, 0.40)$	0.375	0.091 ± 0.011 ± 0.021
4	$[0.40, 0.50)$	0.447	0.079 ± 0.009 ± 0.017
5	$[0.50, 0.65)$	0.566	0.096 ± 0.010 ± 0.019
6	$[0.65, 0.80)$	0.714	0.092 ± 0.015 ± 0.028
7	$[0.80, 1.00)$	0.855	0.097 ± 0.023 ± 0.043
		M_{inv}	
Bin	Range	$\langle M_{\mathrm{inv}}\rangle$ [GeV/c^2]	A_1^p
0	$[0.0, 0.4)$	0.362	0.089 ± 0.013 ± 0.026
1	$[0.4, 0.5)$	0.451	0.095 ± 0.011 ± 0.022
2	$[0.5, 0.6)$	0.549	0.100 ± 0.011 ± 0.022
3	$[0.6, 0.7)$	0.650	0.080 ± 0.012 ± 0.022
4	$[0.7, 0.8)$	0.749	0.090 ± 0.012 ± 0.022
5	$[0.8, 0.9)$	0.846	0.101 ± 0.013 ± 0.026
6	$[0.9, 1.0)$	0.947	0.089 ± 0.016 ± 0.030
7	$[1.0, 1.2)$	1.090	0.079 ± 0.014 ± 0.027
8	$[1.2, 1.6)$	1.351	0.081 ± 0.015 ± 0.029
9	$[1.6, 100.0)$	1.947	0.117 ± 0.022 ± 0.043

A.7 Two Hadron Twist-3 Asymmetries Material

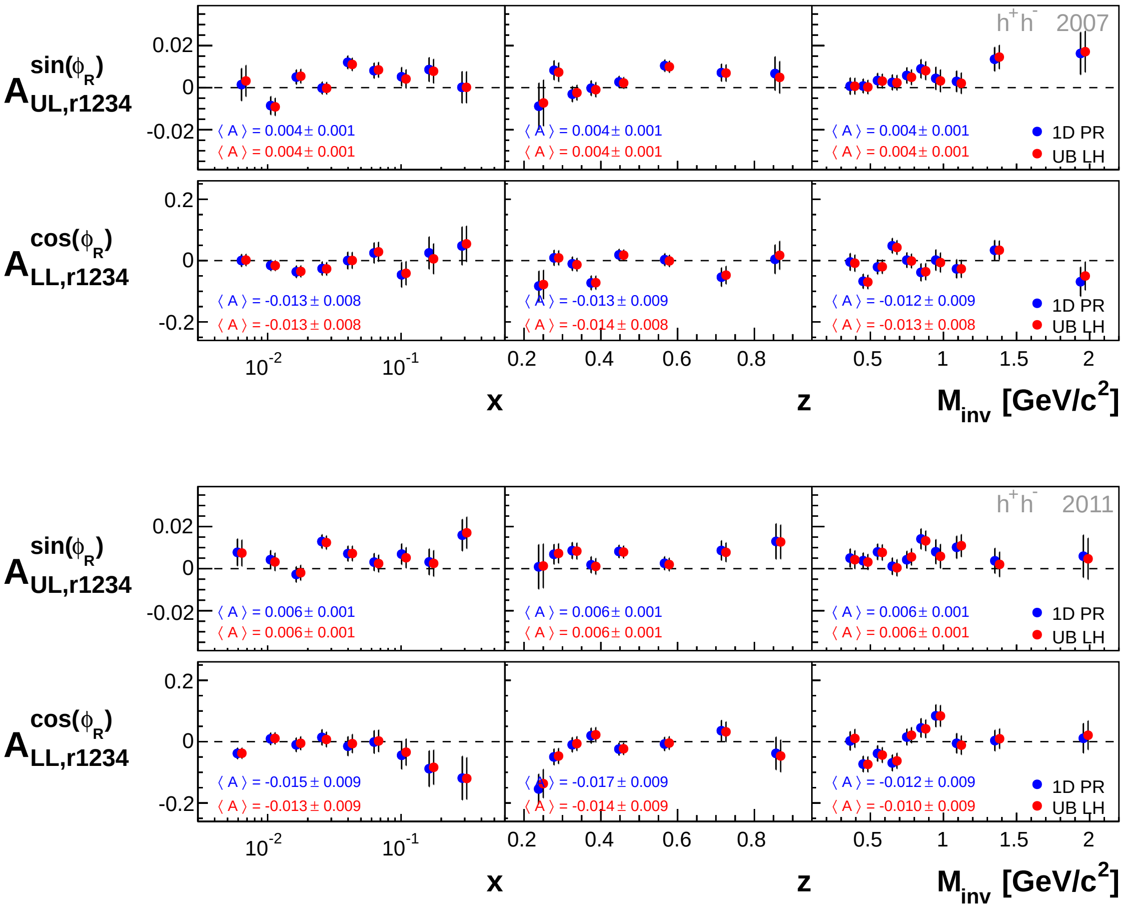

Figure A.42: Comparison of the azimuthal asymmetries, extracted with the methods 1D PR and UB LH, for 2007 (top) and 2011 (bottom). Corresponding mean values are also displayed.

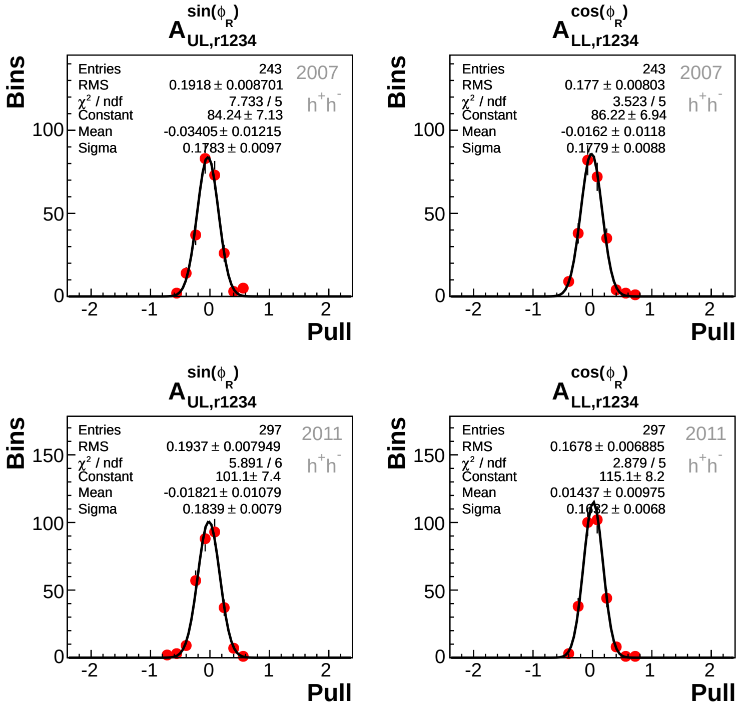

Figure A.43: Pull distributions between asymmetries extracted with the UB LH and the 1D PR method for 2007 (top) and 2011 (bottom). The gaussian fit, corresponding statistical values and fit parameters are also displayed.

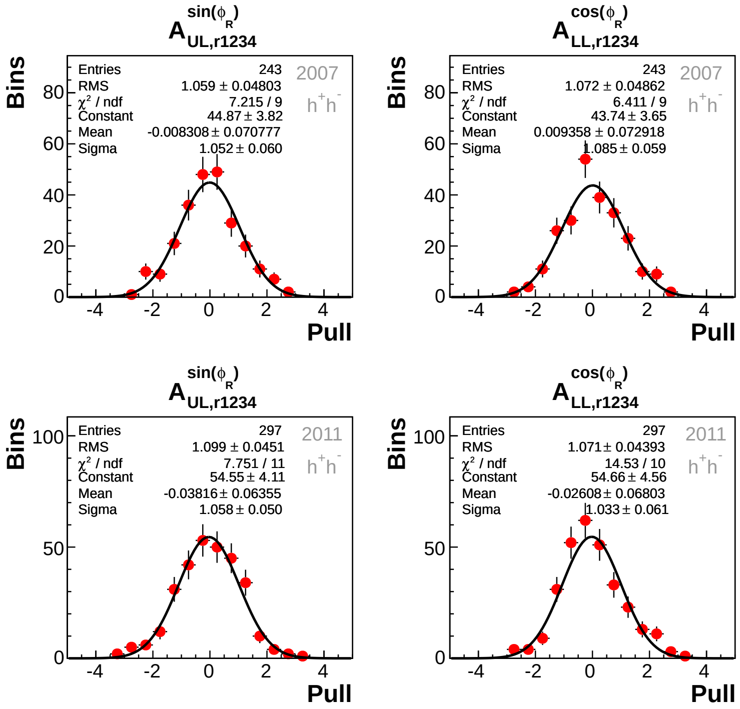

Figure A.44: Stability pull distributions of asymmetries, extracted with the UB LH method, for 2007 (top) and 2011 (bottom). The gaussian fit, corresponding statistical values and fit parameters are also displayed.

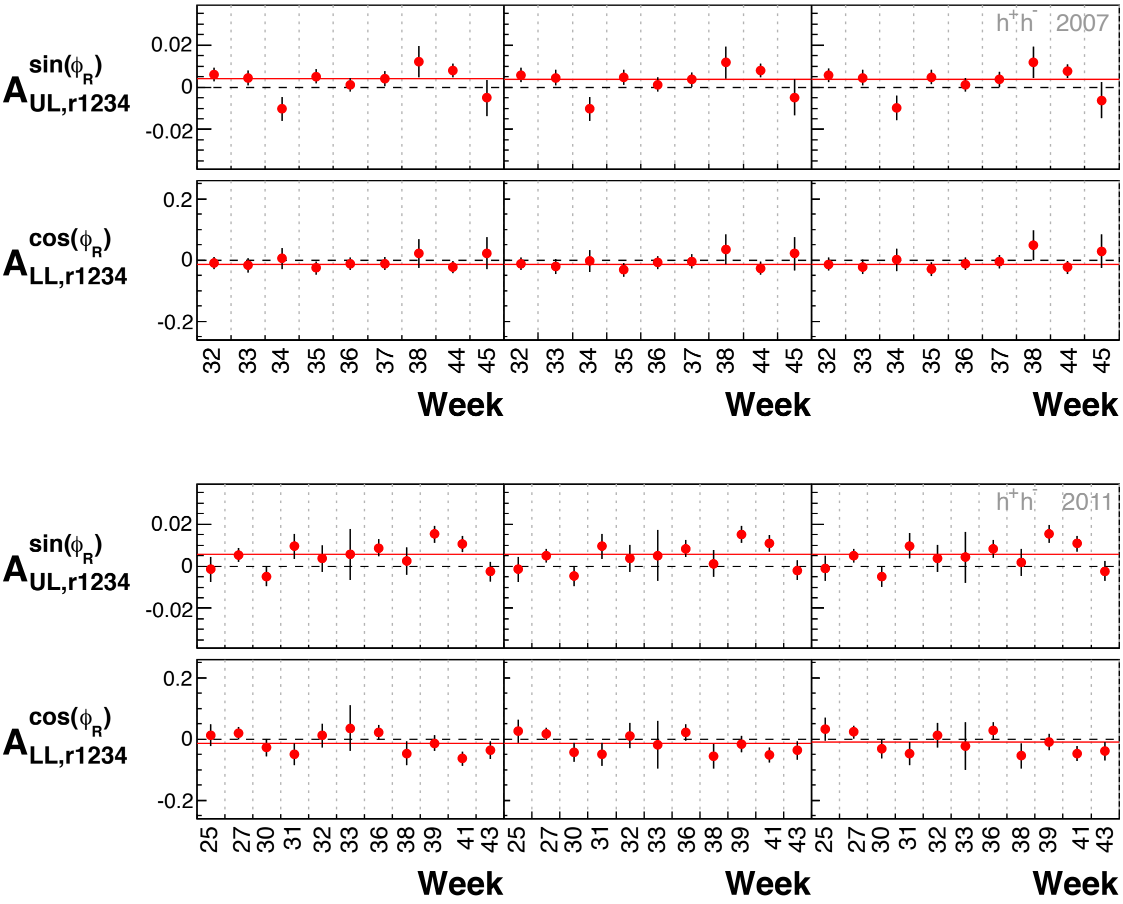

Figure A.45: Mean asymmetries for each week of 2007 (top) and 2011 (bottom). The three columns correspond to the kinematic variables x, z and M_{inv} from left to right. The red horizontal lines indicate the respective mean values.

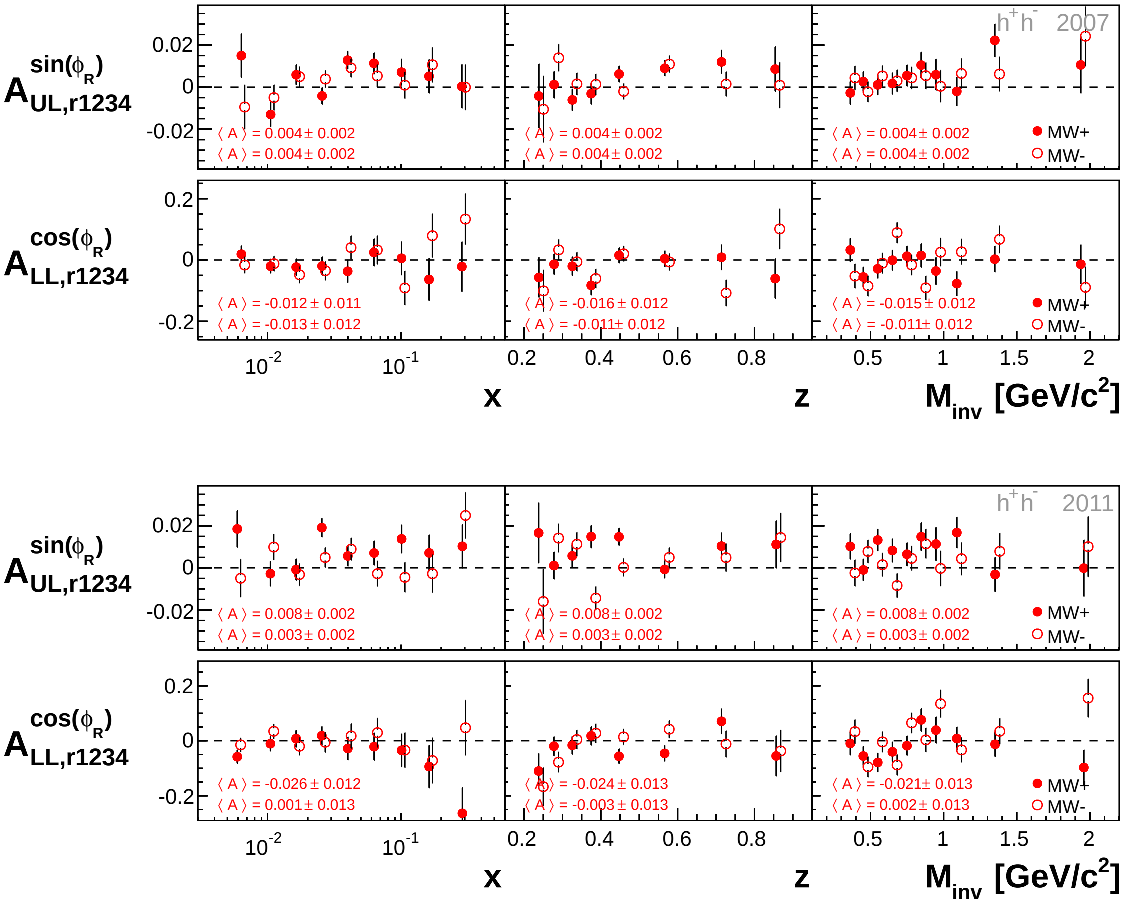

Figure A.46: Comparison of asymmetries from the two microwave settings for 2007 (top) and 2011 (bottom).

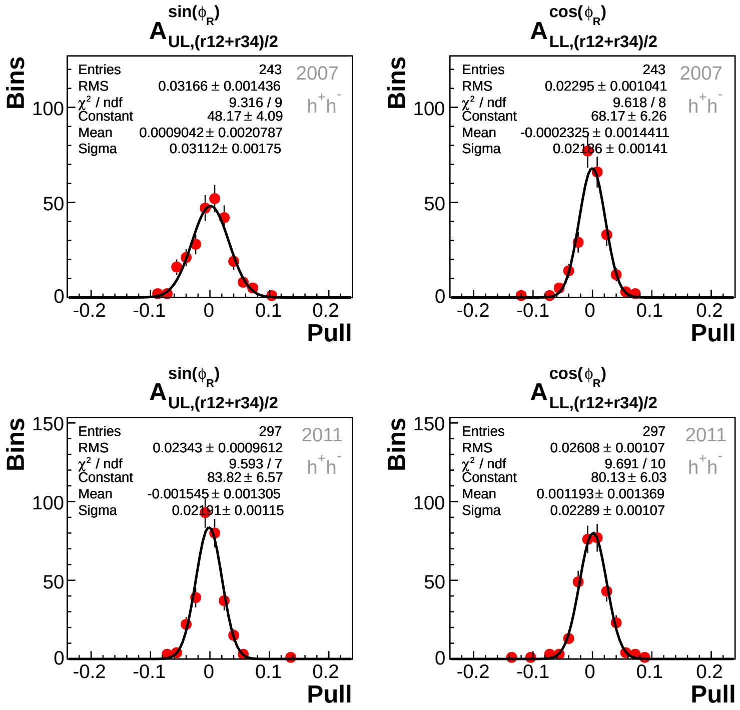

Figure A.47: Pull distributions between asymmetries $A^{m(\phi_R)}_{(r12+r34)/2}$ and $A^{m(\phi_R)}_{r1234}$ for 2007 (top) and 2011 (bottom). The gaussian fit, corresponding statistical values and fit parameters are also displayed.

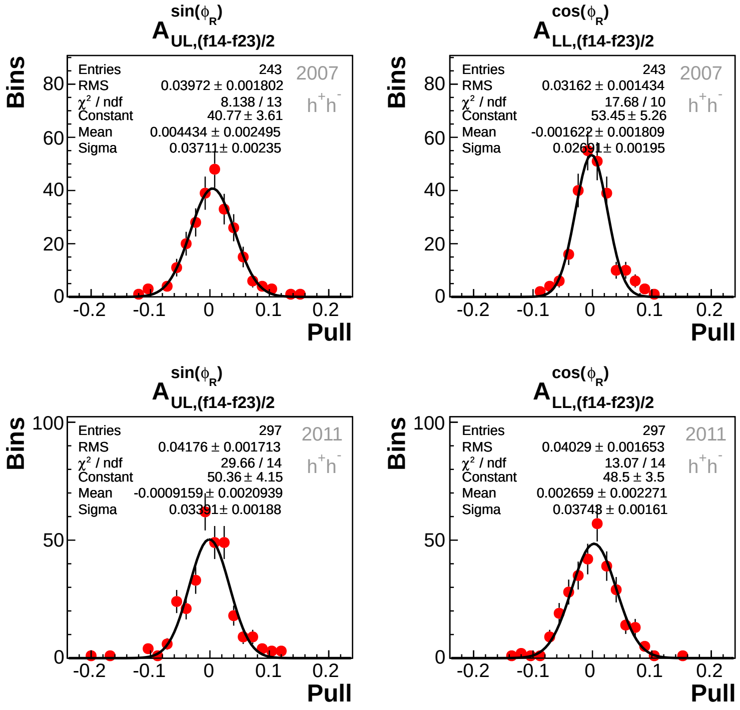

Figure A.48: Pull distributions between asymmetries $A^{m(\phi_R)}_{(f14-f23)/2}$ and $A^{m(\phi_R)}_{(r12-r34)/2}$ for 2007 (top) and 2011 (bottom). The gaussian fit, corresponding statistical values and fit parameters are also displayed.

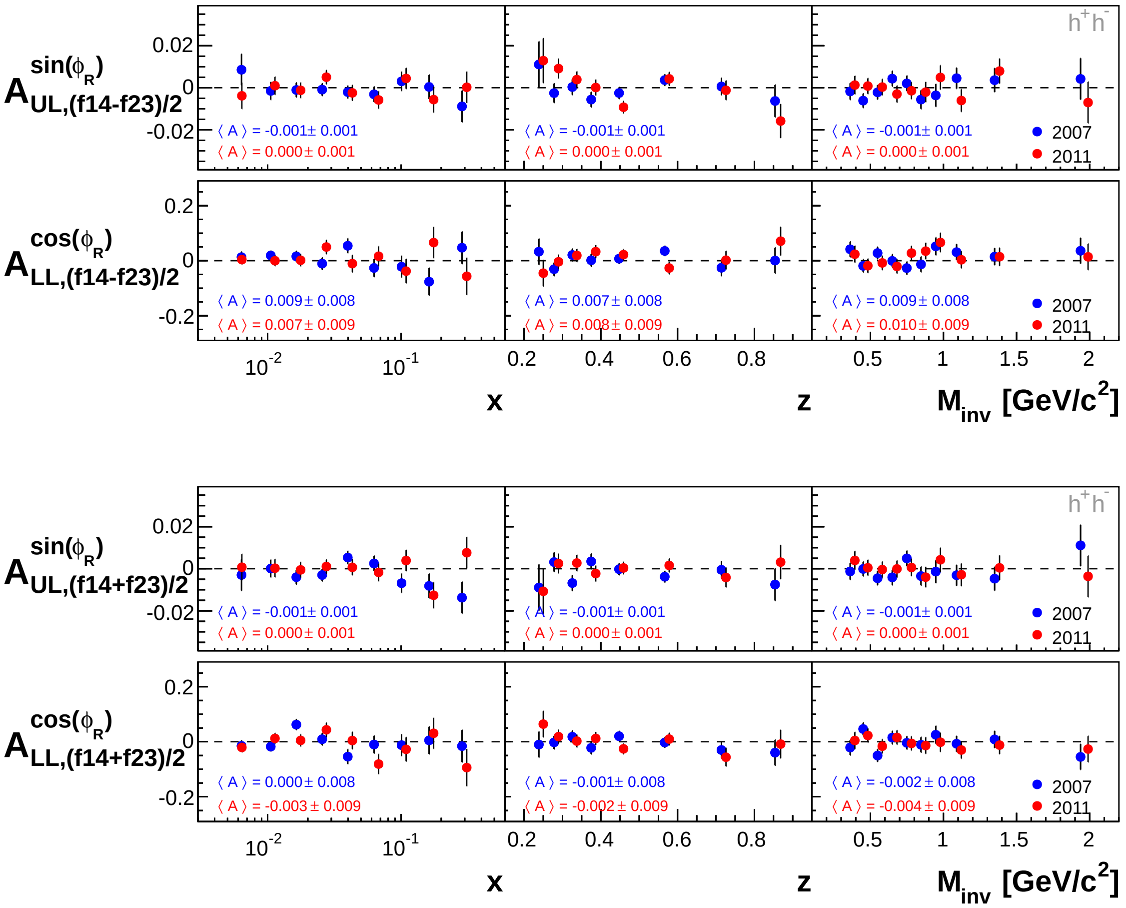

Figure A.49: Azimuthal false asymmetries $A^{m(\phi_R)}_{(f14-f23)/2}$ (top) and $A^{m(\phi_R)}_{(f14+f23)/2}$ (bottom) for 2007 and 2011 data.

Table A.62: Results of $A_{UL}^{\sin(\phi_R)}$ for h^+h^- in bins of x, z, and M_{inv} for 2007.

h^+h^-			2007
		x	
Bin	Range	$\langle x \rangle$	$A_{UL}^{\sin(\phi_R)}$
0	$[0.0025, 0.0080)$	0.006	0.001 ± 0.008 ± 0.006
1	$[0.0080, 0.0130)$	0.011	-0.009 ± 0.004 ± 0.003
2	$[0.0130, 0.0200)$	0.016	0.005 ± 0.003 ± 0.003
3	$[0.0200, 0.0320)$	0.026	0.000 ± 0.003 ± 0.002
4	$[0.0320, 0.0500)$	0.040	0.012 ± 0.003 ± 0.002
5	$[0.0500, 0.0800)$	0.063	0.008 ± 0.004 ± 0.003
6	$[0.0800, 0.1300)$	0.101	0.005 ± 0.004 ± 0.003
7	$[0.1300, 0.2100)$	0.162	0.009 ± 0.006 ± 0.004
8	$[0.2100, 0.7000)$	0.286	0.000 ± 0.007 ± 0.006
		z	
Bin	Range	$\langle z \rangle$	$A_{UL}^{\sin(\phi_R)}$
0	$[0.20, 0.25)$	0.238	-0.009 ± 0.011 ± 0.008
1	$[0.25, 0.30)$	0.278	0.008 ± 0.005 ± 0.003
2	$[0.30, 0.35)$	0.326	-0.003 ± 0.004 ± 0.003
3	$[0.35, 0.40)$	0.375	0.000 ± 0.004 ± 0.003
4	$[0.40, 0.50)$	0.447	0.003 ± 0.003 ± 0.002
5	$[0.50, 0.65)$	0.567	0.010 ± 0.003 ± 0.002
6	$[0.65, 0.80)$	0.714	0.007 ± 0.004 ± 0.003
7	$[0.80, 1.00)$	0.854	0.007 ± 0.008 ± 0.006
		M_{inv}	
Bin	Range	$\langle M_{\text{inv}} \rangle$ [GeV/c^2]	$A_{UL}^{\sin(\phi_R)}$
0	$[0.0, 0.4)$	0.362	0.001 ± 0.004 ± 0.003
1	$[0.4, 0.5)$	0.451	0.001 ± 0.003 ± 0.003
2	$[0.5, 0.6)$	0.549	0.003 ± 0.003 ± 0.003
3	$[0.6, 0.7)$	0.650	0.002 ± 0.004 ± 0.003
4	$[0.7, 0.8)$	0.749	0.006 ± 0.004 ± 0.003
5	$[0.8, 0.9)$	0.846	0.009 ± 0.004 ± 0.003
6	$[0.9, 1.0)$	0.947	0.004 ± 0.005 ± 0.004
7	$[1.0, 1.2)$	1.090	0.003 ± 0.005 ± 0.004
8	$[1.2, 1.6)$	1.350	0.014 ± 0.006 ± 0.004
9	$[1.6, 100.0)$	1.938	0.016 ± 0.010 ± 0.008

Table A.63: Results of $A_{UL}^{\sin(\phi_R)}$ for h^+h^- in bins of x, z, and M_{inv} for 2011.

h^+h^-			2011
		x	
Bin	Range	$\langle x \rangle$	$A_{UL}^{\sin(\phi_R)}$
0	$[0.0025, 0.0080)$	0.006	0.008 ± 0.006 ± 0.005
1	$[0.0080, 0.0130)$	0.011	0.004 ± 0.004 ± 0.003
2	$[0.0130, 0.0200)$	0.016	-0.003 ± 0.004 ± 0.003
3	$[0.0200, 0.0320)$	0.026	0.013 ± 0.003 ± 0.003
4	$[0.0320, 0.0500)$	0.040	0.007 ± 0.004 ± 0.003
5	$[0.0500, 0.0800)$	0.063	0.003 ± 0.004 ± 0.003
6	$[0.0800, 0.1300)$	0.101	0.007 ± 0.005 ± 0.004
7	$[0.1300, 0.2100)$	0.162	0.003 ± 0.006 ± 0.005
8	$[0.2100, 0.7000)$	0.288	0.016 ± 0.007 ± 0.006
		z	
Bin	Range	$\langle z \rangle$	$A_{UL}^{\sin(\phi_R)}$
0	$[0.20, 0.25)$	0.238	0.001 ± 0.010 ± 0.008
1	$[0.25, 0.30)$	0.278	0.007 ± 0.005 ± 0.004
2	$[0.30, 0.35)$	0.325	0.009 ± 0.004 ± 0.003
3	$[0.35, 0.40)$	0.375	0.002 ± 0.004 ± 0.003
4	$[0.40, 0.50)$	0.447	0.008 ± 0.003 ± 0.002
5	$[0.50, 0.65)$	0.566	0.003 ± 0.003 ± 0.002
6	$[0.65, 0.80)$	0.714	0.009 ± 0.005 ± 0.004
7	$[0.80, 1.00)$	0.857	0.013 ± 0.008 ± 0.006
		M_{inv}	
Bin	Range	$\langle M_{\text{inv}} \rangle$ [GeV/c^2]	$A_{UL}^{\sin(\phi_R)}$
0	$[0.0, 0.4)$	0.362	0.005 ± 0.004 ± 0.003
1	$[0.4, 0.5)$	0.451	0.004 ± 0.004 ± 0.003
2	$[0.5, 0.6)$	0.549	0.008 ± 0.004 ± 0.003
3	$[0.6, 0.7)$	0.650	0.001 ± 0.004 ± 0.003
4	$[0.7, 0.8)$	0.749	0.004 ± 0.004 ± 0.003
5	$[0.8, 0.9)$	0.846	0.014 ± 0.005 ± 0.004
6	$[0.9, 1.0)$	0.947	0.008 ± 0.006 ± 0.004
7	$[1.0, 1.2)$	1.090	0.010 ± 0.005 ± 0.004
8	$[1.2, 1.6)$	1.352	0.004 ± 0.006 ± 0.005
9	$[1.6, 100.0)$	1.957	0.006 ± 0.010 ± 0.008

Table A.64: Results of $A_{UL}^{\sin(\phi_R)}$ for h^+h^- in bins of x, z, and M_{inv}.

h^+h^-			2007 & 2011
		x	
Bin	Range	$\langle x\rangle$	$A_{UL}^{\sin(\phi_R)}$
0	$[0.0025, 0.0080)$	0.006	0.005 ± 0.005 ± 0.006
1	$[0.0080, 0.0130)$	0.011	-0.002 ± 0.003 ± 0.003
2	$[0.0130, 0.0200)$	0.016	0.001 ± 0.002 ± 0.003
3	$[0.0200, 0.0320)$	0.026	0.006 ± 0.002 ± 0.002
4	$[0.0320, 0.0500)$	0.040	0.010 ± 0.002 ± 0.003
5	$[0.0500, 0.0800)$	0.063	0.006 ± 0.003 ± 0.003
6	$[0.0800, 0.1300)$	0.101	0.006 ± 0.003 ± 0.004
7	$[0.1300, 0.2100)$	0.162	0.006 ± 0.004 ± 0.005
8	$[0.2100, 0.7000)$	0.287	0.008 ± 0.005 ± 0.006
		z	
Bin	Range	$\langle z\rangle$	$A_{UL}^{\sin(\phi_R)}$
0	$[0.20, 0.25)$	0.238	-0.004 ± 0.008 ± 0.008
1	$[0.25, 0.30)$	0.278	0.008 ± 0.003 ± 0.004
2	$[0.30, 0.35)$	0.326	0.002 ± 0.003 ± 0.003
3	$[0.35, 0.40)$	0.375	0.001 ± 0.003 ± 0.003
4	$[0.40, 0.50)$	0.447	0.005 ± 0.002 ± 0.002
5	$[0.50, 0.65)$	0.566	0.007 ± 0.002 ± 0.002
6	$[0.65, 0.80)$	0.714	0.008 ± 0.003 ± 0.004
7	$[0.80, 1.00)$	0.855	0.010 ± 0.006 ± 0.006
		M_{inv}	
Bin	Range	$\langle M_{\text{inv}}\rangle$ [GeV/c^2]	$A_{UL}^{\sin(\phi_R)}$
0	$[0.0, 0.4)$	0.362	0.003 ± 0.003 ± 0.003
1	$[0.4, 0.5)$	0.451	0.002 ± 0.002 ± 0.003
2	$[0.5, 0.6)$	0.549	0.005 ± 0.003 ± 0.003
3	$[0.6, 0.7)$	0.650	0.002 ± 0.003 ± 0.003
4	$[0.7, 0.8)$	0.749	0.005 ± 0.003 ± 0.003
5	$[0.8, 0.9)$	0.846	0.011 ± 0.003 ± 0.004
6	$[0.9, 1.0)$	0.947	0.006 ± 0.004 ± 0.004
7	$[1.0, 1.2)$	1.090	0.006 ± 0.004 ± 0.004
8	$[1.2, 1.6)$	1.351	0.009 ± 0.004 ± 0.005
9	$[1.6, 100.0)$	1.947	0.011 ± 0.007 ± 0.008

Table A.65: Results of $A_{LL}^{\cos(\phi_R)}$ for h^+h^- in bins of x, z, and M_{inv} for 2007.

h^+h^-			2007
		x	
Bin	Range	$\langle x\rangle$	$A_{LL}^{\cos(\phi_R)}$
0	$[0.0025, 0.0080)$	0.006	0.000 ± 0.020 ± 0.016
1	$[0.0080, 0.0130)$	0.011	-0.016 ± 0.017 ± 0.014
2	$[0.0130, 0.0200)$	0.016	-0.036 ± 0.019 ± 0.016
3	$[0.0200, 0.0320)$	0.026	-0.026 ± 0.022 ± 0.018
4	$[0.0320, 0.0500)$	0.040	0.000 ± 0.027 ± 0.023
5	$[0.0500, 0.0800)$	0.063	0.025 ± 0.033 ± 0.028
6	$[0.0800, 0.1300)$	0.101	-0.046 ± 0.040 ± 0.034
7	$[0.1300, 0.2100)$	0.162	0.025 ± 0.052 ± 0.044
8	$[0.2100, 0.7000)$	0.286	0.048 ± 0.062 ± 0.052
		z	
Bin	Range	$\langle z\rangle$	$A_{LL}^{\cos(\phi_R)}$
0	$[0.20, 0.25)$	0.238	-0.083 ± 0.049 ± 0.041
1	$[0.25, 0.30)$	0.278	0.009 ± 0.025 ± 0.021
2	$[0.30, 0.35)$	0.326	-0.010 ± 0.022 ± 0.019
3	$[0.35, 0.40)$	0.375	-0.073 ± 0.023 ± 0.019
4	$[0.40, 0.50)$	0.447	0.019 ± 0.018 ± 0.015
5	$[0.50, 0.65)$	0.567	0.003 ± 0.020 ± 0.016
6	$[0.65, 0.80)$	0.714	-0.054 ± 0.030 ± 0.025
7	$[0.80, 1.00)$	0.854	0.004 ± 0.047 ± 0.039
		M_{inv}	
Bin	Range	$\langle M_{\text{inv}}\rangle$ [GeV/c^2]	$A_{LL}^{\cos(\phi_R)}$
0	$[0.0, 0.4)$	0.362	-0.004 ± 0.028 ± 0.023
1	$[0.4, 0.5)$	0.451	-0.067 ± 0.023 ± 0.020
2	$[0.5, 0.6)$	0.549	-0.021 ± 0.023 ± 0.020
3	$[0.6, 0.7)$	0.650	0.048 ± 0.024 ± 0.020
4	$[0.7, 0.8)$	0.749	0.002 ± 0.024 ± 0.020
5	$[0.8, 0.9)$	0.846	-0.038 ± 0.028 ± 0.024
6	$[0.9, 1.0)$	0.947	0.002 ± 0.033 ± 0.028
7	$[1.0, 1.2)$	1.090	-0.027 ± 0.030 ± 0.025
8	$[1.2, 1.6)$	1.350	0.034 ± 0.032 ± 0.027
9	$[1.6, 100.0)$	1.938	-0.069 ± 0.047 ± 0.040

Table A.66: Results of $A_{LL}^{\cos(\phi_R)}$ for h^+h^- in bins of x, z, and M_{inv} for 2011.

h^+h^-			2011
		x	
Bin	Range	$\langle x\rangle$	$A_{LL}^{\cos(\phi_R)}$
0	$[0.0025, 0.0080)$	0.006	-0.038 ± 0.018 ± 0.012
1	$[0.0080, 0.0130)$	0.011	0.009 ± 0.019 ± 0.013
2	$[0.0130, 0.0200)$	0.016	-0.010 ± 0.022 ± 0.015
3	$[0.0200, 0.0320)$	0.026	0.014 ± 0.025 ± 0.017
4	$[0.0320, 0.0500)$	0.040	-0.015 ± 0.031 ± 0.021
5	$[0.0500, 0.0800)$	0.063	-0.001 ± 0.037 ± 0.025
6	$[0.0800, 0.1300)$	0.101	-0.044 ± 0.045 ± 0.031
7	$[0.1300, 0.2100)$	0.162	-0.088 ± 0.058 ± 0.040
8	$[0.2100, 0.7000)$	0.288	-0.119 ± 0.071 ± 0.049
		z	
Bin	Range	$\langle z\rangle$	$A_{LL}^{\cos(\phi_R)}$
0	$[0.20, 0.25)$	0.238	-0.154 ± 0.048 ± 0.034
1	$[0.25, 0.30)$	0.278	-0.050 ± 0.026 ± 0.018
2	$[0.30, 0.35)$	0.325	-0.010 ± 0.024 ± 0.016
3	$[0.35, 0.40)$	0.375	0.020 ± 0.025 ± 0.017
4	$[0.40, 0.50)$	0.447	-0.024 ± 0.020 ± 0.014
5	$[0.50, 0.65)$	0.566	-0.008 ± 0.022 ± 0.015
6	$[0.65, 0.80)$	0.714	0.036 ± 0.033 ± 0.023
7	$[0.80, 1.00)$	0.857	-0.038 ± 0.053 ± 0.036
		M_{inv}	
Bin	Range	$\langle M_{\text{inv}}\rangle$ [GeV/c^2]	$A_{LL}^{\cos(\phi_R)}$
0	$[0.0, 0.4)$	0.362	0.002 ± 0.030 ± 0.021
1	$[0.4, 0.5)$	0.451	-0.073 ± 0.026 ± 0.018
2	$[0.5, 0.6)$	0.549	-0.038 ± 0.025 ± 0.017
3	$[0.6, 0.7)$	0.650	-0.069 ± 0.026 ± 0.018
4	$[0.7, 0.8)$	0.749	0.015 ± 0.026 ± 0.018
5	$[0.8, 0.9)$	0.846	0.045 ± 0.030 ± 0.021
6	$[0.9, 1.0)$	0.947	0.084 ± 0.036 ± 0.025
7	$[1.0, 1.2)$	1.090	-0.005 ± 0.032 ± 0.022
8	$[1.2, 1.6)$	1.352	0.004 ± 0.033 ± 0.023
9	$[1.6, 100.0)$	1.957	0.011 ± 0.048 ± 0.033

Table A.67: Results of $A_{LL}^{\cos(\phi_R)}$ for h^+h^- in bins of x, z, and M_{inv}.

h^+h^-			2007 & 2011
		x	
Bin	Range	$\langle x\rangle$	$A_{LL}^{\cos(\phi_R)}$
0	$[0.0025, 0.0080)$	0.006	-0.021 ± 0.013 ± 0.016
1	$[0.0080, 0.0130)$	0.011	-0.005 ± 0.013 ± 0.014
2	$[0.0130, 0.0200)$	0.016	-0.025 ± 0.014 ± 0.016
3	$[0.0200, 0.0320)$	0.026	-0.009 ± 0.016 ± 0.018
4	$[0.0320, 0.0500)$	0.040	-0.006 ± 0.021 ± 0.023
5	$[0.0500, 0.0800)$	0.063	0.013 ± 0.024 ± 0.028
6	$[0.0800, 0.1300)$	0.101	-0.045 ± 0.030 ± 0.034
7	$[0.1300, 0.2100)$	0.162	-0.025 ± 0.039 ± 0.044
8	$[0.2100, 0.7000)$	0.287	-0.024 ± 0.047 ± 0.052
		z	
Bin	Range	$\langle z\rangle$	$A_{LL}^{\cos(\phi_R)}$
0	$[0.20, 0.25)$	0.238	-0.119 ± 0.034 ± 0.041
1	$[0.25, 0.30)$	0.278	-0.019 ± 0.018 ± 0.021
2	$[0.30, 0.35)$	0.326	-0.010 ± 0.016 ± 0.019
3	$[0.35, 0.40)$	0.375	-0.030 ± 0.017 ± 0.019
4	$[0.40, 0.50)$	0.447	-0.001 ± 0.013 ± 0.015
5	$[0.50, 0.65)$	0.566	-0.002 ± 0.015 ± 0.016
6	$[0.65, 0.80)$	0.714	-0.014 ± 0.022 ± 0.025
7	$[0.80, 1.00)$	0.855	-0.014 ± 0.035 ± 0.039
		M_{inv}	
Bin	Range	$\langle M_{\text{inv}}\rangle$ [GeV/c^2]	$A_{LL}^{\cos(\phi_R)}$
0	$[0.0, 0.4)$	0.362	-0.001 ± 0.020 ± 0.023
1	$[0.4, 0.5)$	0.451	-0.070 ± 0.017 ± 0.020
2	$[0.5, 0.6)$	0.549	-0.029 ± 0.017 ± 0.020
3	$[0.6, 0.7)$	0.650	-0.006 ± 0.018 ± 0.020
4	$[0.7, 0.8)$	0.749	0.008 ± 0.018 ± 0.020
5	$[0.8, 0.9)$	0.846	0.000 ± 0.021 ± 0.024
6	$[0.9, 1.0)$	0.947	0.040 ± 0.024 ± 0.028
7	$[1.0, 1.2)$	1.090	-0.017 ± 0.022 ± 0.025
8	$[1.2, 1.6)$	1.351	0.019 ± 0.023 ± 0.027
9	$[1.6, 100.0)$	1.947	-0.029 ± 0.034 ± 0.040

List of Figures

List of Tables

Bibliography

[1] D. M. Dennison, “A note on the Specific Heat of the Hydrogen Molecule”, *Proc. R. Soc. Lond. A* **115**(771) 483–486 (1927), doi:10.1098/rspa.1927.0105

[2] The EMC Collaboration, “A measurement of the spin asymmetry and determination of the structure function g_1 in deep inelastic muon-proton scattering”, *Phys. Lett. B* **206** 364–370 (1988), doi:10.1016/0370-2693(88)91523-7

[3] The COMPASS Collaboration, “Leading order determination of the gluon polarisation from DIS events with high-p_T hadron pairs”, *Phys. Rev. D* **718**(3) 922–930 (2013), doi:10.1016/j.physletb.2012.11.056, arXiv:1202.4064

[4] The COMPASS Collaboration, “Leading and next-to-leading order gluon polarisation in the nucleon and longitudinal double spin asymmetries from open charm muoproduction”, *Phys. Rev. D* **87** 052018 (2013), doi:10.1103/PhysRevD.87.052018, arXiv:1211.6849

[5] The COMPASS Collaboration, “Leading-order determination of the gluon polarisation using a novel method”, submitted to *Phys. Lett. B* (2015), arXiv:1512.05053

[6] E. D. Bloom et al., “High-Energy Inelastic $e - p$ Scattering at 6° and 10°”, *Phys. Rev. Lett.* **23** 930–934 (1969), doi:10.1103/PhysRevLett.23.930

[7] D. J. Gross and F. Wilczek, “Ultraviolet Behavior of Non-Abelian Gauge Theories”, *Phys. Rev. Lett.* **30**(26) 1343–1346 (1973), doi:10.1103/PhysRevLett.30.1343

[8] H. David Politzer, “Reliable Perturbative Results for Strong Interactions?”, *Phys. Rev. Lett.* **30**(26) 1346–1349 (1973), doi:10.1103/PhysRevLett.30.1346

[9] V. Barone and P. G. Ratcliffe, “Transverse Spin Physics”, World Scientific Ltd. (2003), ISBN 9812381015

[10] V. Barone, A. Drago, and P. G. Ratcliffe, “Transverse Polarisation of Quarks in Hadrons”, *Phys. Rept.* **359**(1–2) 1–168 (2002), doi:10.1016/S0370-1573(01)00051-5, arXiv:hep-ph/0104283

[11] A. V. Manohar, “An Introduction to Spin Dependent Deep Inelastic Scattering”, (1992), arXiv:hep-ph/9204208

[12] The Particle Data Group Collaboration, “Review of Particle Physics”, *Chin. Phys. C* **38**(9) 090001 (2014), doi:10.1088/1674-1137/38/9/090001

[13] J. D. Bjorken, "Asymptotic Sum Rules at Infinite Momentum", *Phys. Rev.* **179** 1547–1553 (1969), doi:10.1103/PhysRev.179.1547

[14] C. G. Callan and D. J. Gross, "High-Energy Electroproduction and the Constitution of the Electric Current", *Phys. Rev. Lett.* **22**(4) 156–159 (1969), doi:10.1103/PhysRevLett.22.156

[15] M. Breidenbach et al., "Observed Behavior of Highly Inelastic Electron-Proton Scattering", *Phys. Rev. Lett.* **23**(16) 935–939 (1969), doi:10.1103/PhysRevLett.23.935

[16] The ZEUS Collaboration, "Measurement of the neutral current cross section and F2 structure function for deep inelastic e+p scattering at HERA", *Eur. Phys. J. C* **21** 443–471 (2001), doi:10.1007/s100520100749, arXiv:hep-ex/0105090

[17] The H1 Collaboration, "Deep-inelastic inclusive *ep* scattering at low x and a determination of α_s", *Eur. Phys. J. C* **21** 33–61 (2001), doi:10.1007/s100520100720, arXiv:hep-ex/0105090

[18] The H1 Collaboration, "Measurement and QCD Analysis of Neutral Charged Current Cross Sections at HERA", *Eur. Phys. J. C* **30** 01–32 (2003), doi:10.1140/epjc/s2003-01257-6, arXiv:hep-ex/0304003

[19] L. W. Whitlow et al., "Precise measurements of the proton and deuteron structure functions from a global analysis of the SLAC deep inelastic electron scattering cross-sections", *Phys. Lett. B* **282** 475–482 (1992), doi:10.1016/0370-2693(92)90672-Q

[20] The BCDMS Collaboration, "A high statistics measurement of the proton structure functions $F_2(x, Q^2)$ and R from deep inelastic muon scattering at high Q^2", *Phys. Lett. B* **223** 485–489 (1989), doi:10.1016/0370-2693(89)91637-7

[21] The E665 Collaboration, "Proton and deuteron structure functions in muon scattering at 470 GeV", *Phys. Rev. D* **54** 3006–3056 (1996), doi:10.1103/PhysRevD.54.3006

[22] The New Muon Collaboration, "Measurement of the proton and deuteron structure functions, F_2^p and F_2^d, and of the ratio σ_L/σ_T", *Nucl. Phys. B* **483** 3–43 (1997), doi:10.1016/S0550-3213(96)00538-X, arXiv:hep-ph/9610231

[23] C. Adolph et al., "The Spin Structure Function g_1^{p} of the Proton and a Test of the Bjorken Sum Rule", *Phys. Lett. B* **753** 18–28 (2015), doi:10.1016/j.physletb.2015.11.064, arXiv:1503.08935

[24] A.D. Martin et al., "Martin-Stirling-Thorne-Watt Parton Distribution Functions", https://mstwpdf.hepforge.org

[25] W. Melnitchouk P. Jimenez-Delgado and J. F. Owens, "Parton momentum and helicity distributions in the nucleon", *J. Phys. G* **40**(9) 093102 (2013), doi:10.1088/0954-3899/40/9/093102, arXiv:1306.6515

[26] Z.-B. Kang et al., "Extraction of Quark Transversity Distribution and Collins Fragmentation Functions with QCD Evolution", *Phys. Rev. D* **93**(1) 014009 (2016), doi:10.1103/PhysRevD.93.014009, arXiv:1505.05589

[27] D. de Florian et al., "Extraction of spin-dependent parton densities and their uncertainties", *Phys. Rev. D* **80**(3) 034030 (2009), doi:10.1103/PhysRevD.80.034030, arXiv:0904.3821

[28] E. Leader et al., "Determination of polarized parton densities from a QCD analysis of inclusive and semi-inclusive deep inelastic scattering data", *Phys. Rev. D* **82**(11) 114018 (2010), doi:10.1103/PhysRevD.82.114018, arXiv:1010.0574

[29] J. Blümlein and H. Böttcher, "QCD Analysis of Polarized Deep Inelastic Scattering Data", *AIP Conf. Proc.* **602** 94–99 (2001), doi:10.1063/1.1435915, arXiv:hep-ph/0107317

[30] M. Hirai and S. Kumano, "Determination of gluon polarization from deep inelastic scattering and collider data", *Nucl. Phys. B* **813**(1–2) 106–122 (2009), doi:10.1016/j.nuclphysb.2008.12.026, arXiv:0808.0413

[31] P. Jimenez-Delgado, A. Accardi, and W. Melnitchouk, "Impact of hadronic and nuclear corrections on global analysis of spin-dependent parton distributions", *Phys. Rev. D* **89**(3) 034025 (2014), 10.1103/PhysRevD.89.034025, arXiv:1310.3734

[32] M. Anselmino et al., "Simultaneous extraction of transversity and Collins functions from new semi-inclusive deep inelastic scattering and e^+e^- data", *Phys. Rev. D* **87** 094019 (2013), doi:10.1103/PhysRevD.87.094019, arXiv:1303.3822

[33] R. N. Cahn, "Azimuthal dependence in leptoproduction: A simple parton model calculation", *Phys. Lett. B* **78**(2–3) 269–273 (1978), doi:http://dx.doi.org/10.1016/0370-2693(78)90020-5

[34] D. Sivers, "Single-spin production asymmetries from the hard scattering of pointlike constituents", *Phys. Rev. D* **41**(1) 83–90 (1990), doi:10.1103/PhysRevD.41.83

[35] H. Avakian et al., "Pretzelosity distribution function $h_{1T}^{\perp}$", *Contr. to Transversity 2008* (2008), arXiv:0808.3982

[36] D. Boer and P.J. Mulders, "Time-reversal odd distribution functions in leptoproduction", *Phys. Rev. D* **57**(9) 5780–5786 (1998), doi:10.1103/PhysRevD.57.5780, arXiv:hep-ph/9711485

[37] A. Bacchetta et al., "Semi-inclusive deep inelastic scattering at small transverse momentum", *JHEP* (2007), doi:10.1088/1126-6708/2007/02/093, arXiv:hep-ph/0611265

[38] D. Boer, "Overview of TMD evolution", *Int. J. Mod. Phys. Conf. Ser.* (2015), arXiv:1502.00899

[39] J. Collins, "Overview of TMD Factorization and Evolution", *Int. J. Mod. Phys. Conf. Ser.* **37** 1560021 (2015), doi:10.1142/S2010194515600216

[40] Shu-Yi Wei Kai-Bao Chen and Zuo-Tang Liang, "Three-dimensional imaging of the nucleon and semi-inclusive high-energy reactions", *Front. Phys.* **10**(6) 101204 (2015), doi:10.1007/s11467-015-0477-x, arXiv:1506.07302

[41] F. Hautmann et. al., "TMDlib and TMDplotter: library and plotting tools for transverse-momentum-dependent parton distributions", *Eur. Phys. J. C* **74** 3220 (2014), doi:10.1140/epjc/s10052-014-3220-9, arXiv:1408.3015

[42] S. J. Brodsky, D. S. Hwang, and I. Schmidt, "Final state interactions and single spin asymmetries in semiinclusive deep inelastic scattering", *Phys. Lett. B* **530** 99–107 (2002), doi:10.1016/S0370-2693(02)01320-5, arXiv:hep-ph/0201296

[43] S. J. Brodsky, D. S. Hwang, and I. Schmidt, "Initial state interactions and single spin asymmetries in Drell-Yan processes", *Nucl. Phys. B* **642** 344–356 (2002), doi:10.1016/S0550-3213(02)00617-X, arXiv:hep-ph/0206259

[44] J. C. Collins, "Leading twist single transverse-spin asymmetries: Drell-Yan and deep inelastic scattering", *Phys. Lett.* **B536** 43–48 (2002), doi:10.1016/S0370-2693(02)01819-1, arXiv:hep-ph/0204004

[45] K. Goeke, A. Metz, and M. Schlegel, "Parameterization of the quark-quark correlator of a spin-1/2 hadron", *Phys. Lett. B* **618** 90–96 (2005), doi:10.1016/j.physletb.2005.05.037, arXiv:hep-ph/0504130

[46] P. J. Mulders and R. D. Tangerman, "The Complete tree level result up to order 1/Q for polarized deep inelastic leptoproduction", *Nucl. Phys. B* **461** 197–237 (1996), doi:10.1016/0550-3213(95)00632-X, arXiv:hep-ph/9510301

[47] S. Gliske, A. Bacchetta, and M. Radici, "Production of two hadrons in semi-inclusive Deep Inelatic Scattering", *Phys. Rev. D* **90**(11) 114027 (2014), doi:10.1103/PhysRevD.90.114027, arXiv:1408.5721

[48] A. Bacchetta and M. Radici, "Partial wave analysis of two hadron fragmentation functions", *Phys. Rev. D* **67**(9) 094002 (2003), doi:10.1103/PhysRevD.67.094002, arXiv:hep-ph/0212300

[49] M. Diehl and S. Sapeta, "On the analysis of lepton scattering on longitudinally or transversely polarized protons", *Eur. Phys. J. C* **41** 515–533 (2005), arXiv:hep-ph/0503023

[50] The HERMES Collaboration, "Evidence for a Single-Spin Azimuthal Asymmetry in Semi-inclusive Pion Electroproduction", *Phys. Rev. Lett.* **84** 4047–4051 (2000), doi:10.1103/PhysRevLett.84.4047, arXiv:hep-ex/9910062

[51] The HERMES Collaboration, "Single-spin azimuthal asymmetries in electroproduction of neutral pions in semi-inclusive deep-inelastic scattering", *Phys. Rev. D* **64** 097101 (2001), doi:10.1103/PhysRevD.64.097101, arXiv:hep-ex/0104005

[52] The HERMES Collaboration, "Measurement of single-spin azimuthal asymmetries in semi-inclusive electroproduction of pions and kaons on a longitudinally polarised deuterium target", *Phys. Lett. B* **562**(3–4) 182–192 (2003), doi:10.1016/S0370-2693(03)00566-5, arXiv:hep-ex/0212039

[53] K.A. Oganessyan et al., "Sin(phi) azimuthal asymmetry in semi-inclusive electroproduction on longitudinally polarized nucleon", (1998), arXiv:hep-ph/9808368

[54] E. De Sanctis, W.-D. Nowak, and K. A. Oganessyan, "Single-spin azimuthal asymmetries in the "Reduced twist-3 approximation"", *Nucl. Phys. B* **483**(1–3) 69–73 (2000), doi:10.1016/S0370-2693(00)00596-7, arXiv:hep-ph/0002091

[55] H. Avakian, P. Bosted, V. Burkert, and L. Elouadrhiri, "New results on SIDIS SSA from Jefferson Lab", *AIP Conf. Proc.* **792** 945–948 (2005), doi:10.1063/1.2122193, arXiv:nucl-ex/0509032

[56] The CLAS Collaboration, "Measurement of Single and Double Spin Asymmetries in Deep Inelastic Pion Electroproduction with a Longitudinally Polarized Target", *Phys. Rev. Lett.* **105** 262002 (2010), doi:10.1103/PhysRevLett.105.262002, arXiv:1003.4549

[57] The HERMES Collaboration, "Single-spin asymmetries in semi-inclusive deep-inelastic scattering on a transversely polarized hydrogen target", *Phys. Rev. Lett.* **94** 012002 (2005), doi:10.1103/PhysRevLett.94.012002, arXiv:hep-ex/0408013

[58] The Belle Collaboration, "Measurement of Azimuthal Asymmetries in Inclusive Production of Hadron Pairs in e^+e^- Annihilation at Belle", *Phys. Rev. Lett.* **96** 232002 (2006), doi:10.1103/PhysRevLett.96.232002, arXiv:hep-ex/0507063

[59] M. Anselmino et al., "Transverse momentum dependence of the quark helicity distributions and the Cahn effect in double-spin asymmetry A_{LL} in semiinclusive DIS", *Phys. Rev. D* **74** 074015 (2006), doi:10.1103/PhysRevD.74.074015, arXiv:hep-ph/0608048

[60] H. Avakian et al., "Studies of Spin-Orbit Correlations with Longitudinally Polarized Target", *A 12 GeV Research Proposal to Jefferson Lab (PAC 32)* (2007), https://www.jlab.org/exp_prog/proposals/07/PR12-07-107.pdf

[61] H. Avakian et al., "Are there approximate relations among transverse momentum dependent distribution functions?", *Phys. Rev. D* **77** 014023 (2008), doi:10.1103/PhysRevD.77.014023, arXiv:0709.3253

[62] The COMPASS Collaboration, "Azimuthal asymmetries of charged hadrons produced by high-energy muons scattered off longitudinally polarised deuterons", *Eur. Phys. J. C* **70**(1) 39–49 (2010), doi:10.1140/epjc/s10052-010-1461-9, arXiv:1007.1562

[63] A. Martin, F. Bradamante, and V. Barone, “Extracting the transversity distributions from single-hadron and dihadron production”, *Phys. Rev. D* **91**(1) 014034 (2015), doi:10.1103/PhysRevD.91.014034, arXiv:1412.5946

[64] H. Avakian et al., “Studies of Dihadron Electroproduction in DIS with Unpolarized and Longitudinally Polarized Hydrogen and Deuterium Targets”, *A 12 GeV Research Proposal to Jefferson Lab (PAC 38)* (2011), https://wwwold.jlab.org/exp_prog/proposals/11/PR12-11-109.pdf

[65] S. A. Pereira, “Di-hadron production at Jefferson Lab.”, *Proceedings of Science* (2014), http://pos.sissa.it/archive/conferences/203/231/DIS2014_231.pdf

[66] The EMC Collaboration, “An investigation of the spin structure of the proton in deep inelastic scattering of polarised muons on polarised protons”, *Nucl. Phys. B* **328** 1–35 (1989), doi:10.1016/0550-3213(89)90089-8

[67] The SMC Collaboration, “Polarised quark distributions in the nucleon from semi-inclusive spin asymmetries”, *Phys. Lett. B* **420** 180–190 (1998), doi:10.1016/S0370-2693(97)01546-3, arXiv:hep-ex/9711008

[68] The HERMES Collaboration, “Quark helicity distributions in the nucleon for up, down, and strange quarks from semi-inclusive deep-inelastic scattering”, *Phys. Rev. D* **71** 012003 (2005), doi:10.1103/PhysRevD.71.012003, arXiv:hep-ex/0407032

[69] The COMPASS Collaboration, “Quark helicity distributions from longitudinal spin asymmetries in muon-proton and muon-deuteron scattering”, *Phys. Lett. B* **693**(3) 227–235 (2010), doi:10.1016/j.physletb.2010.08.034, arXiv:1007.4061

[70] D. de Florian et al., “Global Analysis of Helicity Parton Densities and Their Uncertainties”, *Phys. Rev. Lett.* **101** 072001 (2008), doi:10.1103/PhysRevLett.101.072001, arXiv:0804.0422

[71] O. A. Rondon-Aramayo, “Corrections to nucleon spin structure asymmetries measured on nuclear polarized targets”, *Phys. Rev. C* **60** 035201 (1999), doi:10.1103/PhysRevC.60.035201

[72] The COMPASS Collaboration, “The COMPASS Experiment at CERN”, *Nucl. Instrum. Meth. A* **577**(3) 455–518 (2007), doi:10.1016/j.nima.2007.03.026, arXiv:hep-ex/0703049

[73] The COMPASS Collaboration, “The COMPASS Setup for Physics with Hadron Beams”, *Nucl. Instrum. Meth. A* **779** 69–115 (2015), doi:10.1016/j.nima.2015.01.035, arXiv:1410.1797

[74] S. Koblitz, “Determination of the Gluon Polarisation from Open Charm Production at COMPASS”, Ph.D. thesis, University of Mainz (2008), https://inspirehep.net/record/897929/files/CERN-THESIS-2009-190.pdf

[75] E. Zemlyanichkina, “Quality check of 2011 data”, at COMPASS Analysis Meeting (2011), https://wwwcompass.cern.ch/compass/software/analysis/transparencies/2011/am_111115/zemlyanichkina_111115.pdf

[76] V. Andrieux, “Stability checks for 2011 data set”, at COMPASS Analysis Meeting (2012), https://wwwcompass.cern.ch/compass/software/analysis/transparencies/2012/am_120619/andrieux_120619.pdf

[77] V. Andrieux, “2011 Longitudinal - Analysis Status and First Results”, at COMPASS Analysis Meeting (2012), https://wwwcompass.cern.ch/compass/software/analysis/transparencies/2012/am_120809/andrieux_120809.pdf

[78] The COMPASS Collaboration, “Bad Spill Lists”, (2009, 2012), http://wwwcompass.cern.ch/compass/software/offline/input/stab/stability.html

[79] The COMPASS Collaboration, “Data Grouping”, (2009, 2012), http://wwwcompass.cern.ch/compass/software/offline/input/stab/grouping.html

[80] P. Sznajder, “The beam reconstruction”, at COMPASS GPD Meeting (2011), https://wwwcompass.cern.ch/compass/gpd/meetings/201305_15may_CERN/sznajder_150513_beam.pdf

[81] The COMPASS Collaboration, “Transverse spin effects in hadron-pair production from semi-inclusive deep inelastic scattering”, *Phys. Lett. B* **713** 10–16 (2012), doi:10.1016/j.physletb.2012.05.015, arXiv:1202.6150

[82] H. Wollny, “Measuring azimuthal asymmetries in semi-inclusive deep-inelastic scattering off transversely polarized protons”, Ph.D. thesis, University of Freiburg (2010), https://www.freidok.uni-freiburg.de/fedora/objects/freidok:7558/datastreams/FILE1/content

[83] A. Vossen, “Transverse Spin Asymmetries at the COMPASS Experiment”, Ph.D. thesis, University of Freiburg (2008), https://www.freidok.uni-freiburg.de/fedora/objects/freidok:5234/datastreams/FILE1/content

[84] A. Martin et al., “On the role of the acceptance in the Unbinned Maximum Likelihood Method”, COMPASS note 2009-13, https://wwwcompass.cern.ch/compass/notes/2009-13/2009-13.pdf

[85] B. Parsamyan, “SIDIS target longitudinal-spin dependent asymmetries: proton 2011 data”, at COMPASS Analysis Meeting (2015), https://wwwcompass.cern.ch/compass/software/analysis/transparencies/2015/am_150714/talks/Parsamyan_150714_AM_L.pdf

[86] R. Fletcher, “Practical Methods of Optimization”, John Wiley & Sons Ltd. (1987), ISBN 0471915475

[87] The GSL Team, “GNU Scientific Library”, Reference Manual (2015), https://www.gnu.org/software/gsl/manual/gsl-ref.pdf

[88] K. Gustafsson, “Computation of the Dilution Factor for the Year 2002 COMPASS Data”, COMPASS note 2003-3, http://wwwcompass.cern.ch/compass/notes/2003-3/2003-3.html

[89] The SMC Collaboration, "Spin asymmetries A_1 and structure functions g_1 of the proton and the deuteron from polarized high energy muon scattering", *Phys. Rev. D* **58**(11) 112001 (1998), doi:10.1103/PhysRevD.58.112001

[90] The EMC Collaboration, "The ratio F_2^n/F_2^p in deep inelastic muon scattering", *Nucl. Phys. B* **371**(1-2) 3–31 (1989), doi:10.1016/0550-3213(92)90227-3

[91] The EMC Collaboration, "A measurement of the ratio of the nucleon structure function in copper and deuterium", *Z. Phys. C* **57**(2) 211–218 (1993), doi:10.1007/BF01565050

[92] A. Akhundov, D. Y. Bardin, and N. M. Shumeiko, "Contribution of electromagnetic production of lepton pairs to inclusive cross-section of deep inelastic μp scattering", *Sov. J. Nucl. Phys.* **32** 234 (1980)

[93] The COMPASS Collaboration, "The spin-dependent structure function of the proton g_1^p and a test of the Bjorken sum rule", *Phys. Lett. B* **690** 466–472 (2010), doi:10.1016/j.physletb.2010.05.069, arXiv:1001.4654

[94] P. Schweitzer, Private Communications, (2016)

[95] The COMPASS Collaboration, "First measurement of the transverse spin asymmetries of the deuteron in semi-inclusive deep inelastic scattering", *Phys. Rev. Lett.* **94** 202002 (2005), doi:10.1103/PhysRevLett.94.202002, arXiv:hep-ex/0503002

[96] M. Diefenthaler, "Transversity measurements at HERMES", *AIP Conf. Proc.* **792** 933–936 (2005), doi:10.1063/1.2122190, arXiv:hep-ex/0507013

[97] The COMPASS Collaboration, "A new measurement of the Collins and Sivers asymmetries on a transversely polarised deuteron target", *Nucl. Phys. B* **765** 31–70 (2007), doi:10.1016/j.nuclphysb.2006.10.027, arXiv:hep-ex/0610068

[98] S. Wandzura and F. Wilczek, "Sum rules for spin-dependent electroproduction-test of relativistic constituent quarks", *Phys. Lett. B* **72**(2) 195–198 (1977), doi:10.1016/0370-2693(77)90700-6

[99] P. Schweitzer et al., "Transversity distributions in the nucleon in the large-N_c limit", *Phys. Rev. D* **64** 034013 (2001), doi:10.1103/PhysRevD.64.034013, arXiv:hep-ph/0101300

[100] M. Glück, E. Reya, and A. Vogt, "Dynamical parton distributions revisited", *Eur. Phys. J. C* **5**(3) 461–470 (1998), doi:10.1007/s100529800978, arXiv:hep-ph/9806404

[101] M. Glück et al., "Models for the polarized parton distributions of the nucleon", *Phys. Rev. D* **63** 094005 (2001), doi:10.1103/PhysRevD.63.094005, arXiv:hep-ph/0011215

[102] S. Kretzer, "Fragmentation functions from flavor-inclusive and flavor-tagged e^+e^- annihilations", *Phys. Rev. D* **62** 054001 (2000), doi:10.1103/PhysRevD.62.054001, arXiv:hep-ph/0003177

[103] M. Anselmino et al., "Role of Cahn and Sivers effects in deep inelastic scattering", *Phys. Rev. D* **71** 074006 (2005), doi:10.1103/PhysRevD.71.074006, arXiv:hep-ph/0501196

[104] W. Mao et al., "On the $\cos\phi_h$ asymmetry in electroproduction of pions in double longitudinally polarized process", *Nucl. Phys. A* **945** 153–167 (2016), doi:10.1016/j.nuclphysa.2015.10.004

[105] S. J. Brodsky et al., "Light-cone representation of the spin and orbital angular momentum of relativistic composite systems", *Nucl. Phys. B* **593**(1–2) 311 – 335 (2001), doi:10.1016/S0550-3213(00)00626-X

[106] A. Bacchetta, A. Schäfer, and J.-J. Yang, "Sivers function in a spectator model with axial-vector diquarks", *Phys. Lett. B* **578**(1–2) 109–118 (2004), doi:10.1016/j.physletb.2003.10.045, arXiv:hep-ph/0309246

[107] D. de Florian, R. Sassot, and M. Stratmann, "Global analysis of fragmentation functions for pions and kaons and their uncertainties", *Phys. Rev. D* **75** 114010 (2007), doi:10.1103/PhysRevD.75.114010, arXiv:hep-ph/0703242

[108] B. Parsamyan, Private Communications, (2016)

[109] Z. Lu, Private Communications, (2016)

[110] M. Anselmino et al., "Semi-Inclusive Deep Inelastic Scattering processes from small to large P_T", *Eur. Phys. J. A* **31**(3) 373–381 (2007), doi:10.1140/epja/i2007-10003-9, arXiv:hep-ph/0606286

[111] B. Parsamyan, "SIDIS-DY asymmetry extraction methods: Update on "six-asymmetries paper" – studies Global SIDIS-DY asymmetry extraction method", at COMPASS Analysis Meeting (2015), https://wwwcompass.cern.ch/compass/software/analysis/transparencies/2015/am_150514/talks/Parsamyan_150514_AM.pdf

[112] A. Bacchetta and M. Radici, "Two hadron semiinclusive production including subleading twist", *Phys.Rev.* **D69** 074026 (2004), doi:10.1103/PhysRevD.69.074026, arXiv:hep-ph/0311173

[113] A. Courtoy, A. Bacchetta, M. Radici, and A. Bianconi, "First extraction of interference fragmentation functions from e^+e^- data", *Phys. Rev. D* **85**(11) 114023 (2012), doi:10.1103/PhysRevD.85.114023, arXiv:1202.0323

Acknowledgements

This thesis would not have been possible without the encouragement and support from many people. I would like to express my deepest gratitude to

- my supervisor Prof. Dr. Horst Fischer for introducing me to the fascinating field of scientific research and his tireless and excellent support throughout the last years.
- Prof. Dr. Kay Königsmann for providing me the opportunity to join his working group and to participate in the research program of the COMPASS collaboration.
- all members of the COMPASS collaboration and the entire Königsmann working group for their continuous support and the warm and familiar atmosphere.
- Dr. Bakur Parsamyan for being both a cooperative colleague and lovely friend, accompanying me through all ups and downs.
- Dr. Aram Kotzinian and Dr. Peter Schweitzer for the fruitful discussions on the theory behind it all.
- Matthias Gorzellik, Philipp Jörg, Dr. Bakur Parsamyan, Christopher Regali, Dr. Peter Schweitzer and Tobias Szameitat for the careful proofreading of this thesis and their constructive criticism.
- my parents and sister for their unconditional love, trust and support.
- all my close friends beyond physics, for keeping my feet on the ground whenever my head was in the clouds, and for lifting me up whenever I was down.